Fibrillarin - a Central Regulator of Epithelial Integrity and Tumor Progression

विद्या वाचस्पति की
उपाधि की अपेक्षाओं की आंशिक पूर्ति में प्रस्तुत शोध प्रबंध

A thesis submitted in partial fulfillment of the requirements of the degree of Doctor of Philosophy

द्वारा / By

संतम साहा/Santam Saha

पंजीकरण सं. / Registration No.: **20203792**

शोध प्रबंध पर्यवेक्षक / Thesis Supervisor:

प्रोफ. कुंदन सेनगुप्ता/Prof. Kundan Sengupta

भारतीय विज्ञान शिक्षा एवं अनुसंधान संस्थान पुणे
INDIAN INSTITUTE OF SCIENCE EDUCATION AND RESEARCH PUNE

CERTIFICATE

Certified that the work incorporated in the thesis entitled "**Fibrillarin- a Central Regulator of Epithelial Integrity and Tumor Progression**" Submitted by **Santam Saha** was carried out by the candidate, under my supervision. The work presented here or any part of it has not been included in any other thesis submitted previously for the award of any degree or diploma from any other University or institution.

(Supervisor)

डॉ. कुंदन सेनगुप्ता/Dr. Kundan Sengupta
प्राध्यापक, जीवशास्त्र विभाग/Professor, Biology Department
भारतीय विज्ञान शिक्षा एवं अनुसंधान संस्थान
Indian Institute of Science Education & Research
पुणे / Pune- 411 008, भारत / India

Date: 14.01.2026

Declaration by Student

Name of Student: **Santam Saha**

Reg. No.: **20203792**

Thesis Supervisor(s): **Prof. Kundan Sengupta**

Department: **Department of Biology**

Date of joining program: **1st September 2020**

Date of Pre-Synopsis Seminar: **1st September 2025**

Title of Thesis: **Fibrillarin- a Central Regulator of Epithelial Integrity and Tumor Progression**

I declare that this written submission represents my idea in my own words and where others' ideas have been included; I have adequately cited and referenced the original sources. I declare that I have acknowledged collaborative work and discussions wherever such work has been included. I also declare that I have adhered to all principles of academic honesty and integrity and have not misrepresented or fabricated or falsified any idea/data/fact/source in my submission. I understand that violation of the above will be cause for disciplinary action by the Institute and can also evoke penal action from the sources which have thus not been properly cited or from whom proper permission has not been taken when needed.

The work reported in this thesis is the original work done by me under the guidance of

Prof. **Kundan Sengupta**
Date: **14.01.2026**

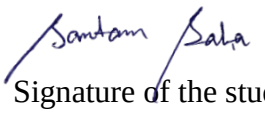

Signature of the student:

Acknowledgements

I would like to begin by expressing my sincere gratitude to my PhD supervisor, Dr. Kundan Sengupta, for providing me with the opportunity to pursue my doctoral research in the Chromosome Biology Laboratory. I am deeply thankful to him for his guidance and for his careful and critical reading of this thesis.

I am grateful to my Research Advisory Committee members, Dr. Krishanpal Karmodiya (IISER Pune), Dr. Deepa Subramanyam (NCCS Pune) and Dr. Jomon Joseph (NCCS Pune), for their critical evaluation of my research and for their valuable suggestions during RAC meetings. I also thank Dr. Richa Rikhy (IISER Pune) for her feedback on my work. I acknowledge the constructive suggestions and insights provided by Dr. Dimple Notani (NCBS Bangalore), in my RNA sequencing experiments.

I am extremely thankful to IISER Pune for providing comprehensive institutional support in the form of equipment, infrastructure, administrative assistance (Mrinalini Virkar, Kalpesh Thakare, Piyush Gadekar, Rupali Jadhav, Shabnam Patil, and Mahesh Rote), and intramural grants, all of which were essential for the successful completion of this work. I greatly appreciate the open-lab culture at IISER Pune, which fosters unrestricted sharing of equipment, reagents, and ideas across laboratories, and I thank the faculty and students who uphold this spirit. I also acknowledge the IISER Pune Microscopy Facility, particularly Vijay Vitthal, upon which my work relied extensively. I am thankful to Dr. Krishnaveni, National Facility for Gene Function in Health and Disease at IISER Pune. I am grateful to the funding agency- IISER Pune.

I would like to extend my special thanks to all current and former members of the Chromosome Biology Laboratory for their earlier contributions and procurements, which continued to support my work throughout my PhD. I am particularly grateful to Dr. Shalaka Patil for her guidance during the initial phase of my doctoral research. I also thank Dr. Ayantika Sengupta, whose early findings laid the foundation for my PhD project. I acknowledge the support of Balaji, Anish, Arnav, Priyam, Tanmay, Kshitij, and Chetna (Bugs and Drugs lab) who stood by me from the early stages of this journey and provided constant encouragement during some of the most challenging periods of my personal and professional life. I am thankful to Balaji for his assistance with ChIP experiments and to Priyojit for his help in generating experimental clones. Finally, I wish to acknowledge the setbacks and failures encountered along this journey, as well as the moments of fortune that accompanied them. Finally, I would like to express my

deepest gratitude to the failures that I have endured and my lucky stars. I am especially thankful to myself who survived this journey, did the needful and came out as a better version of myself.

Contents

Abstract

Epithelial integrity is maintained through coordinated regulation of cell–cell adhesion, apico–basal polarity, and transcriptional programs that preserve epithelial identity. Disruption of these processes underlies epithelial–to–mesenchymal transition (EMT), a key driver of cancer invasion and metastasis. Fibrillarin (FBL) is a conserved nucleolar protein best known for its essential role in ribosomal RNA biogenesis; however, emerging evidence suggests that its functions extend beyond ribosome assembly. Here, we identify a previously unrecognized role for FBL in safeguarding epithelial architecture by regulating chromatin-mediated control of cell polarity genes. Using colorectal (DLD-1) and breast epithelial (MCF10A[p53DN]) models, we show that FBL depletion leads to profound disruption of epithelial morphology, characterized by loss of cobblestone architecture, destabilization of adherens and tight junctions, and enhanced cell migration and invasion. Mechanistically, FBL loss induces clathrin- and dynamin-dependent internalization of E-cadherin without altering global endocytic flux, indicating selective perturbation of junctional trafficking. Transcriptomic analyses reveal significant deregulation of pathways associated with cell adhesion, apical membrane organization, and EMT, identifying the basolateral polarity regulator Scribble (SCRIB) as a key downstream effector of FBL function.We demonstrate that FBL depletion transcriptionally represses SCRIB through increased deposition of the repressive histone mark H3K27me3 at its promoter. This epigenetic silencing is driven by the relocalization of a subpopulation of EZH2, the catalytic component of Polycomb Repressive Complex 2 (PRC2), from the nucleolus to the nucleoplasm. Disruption of the FBL–EZH2 interaction, either by FBL depletion or deletion of its RNA-binding domain, enhances nucleoplasmic EZH2 occupancy at PRC2 target genes, including SCRIB, thereby promoting epithelial destabilization. Pharmacological inhibition of EZH2 restores Scribble expression, rescues E-cadherin localization, and suppresses aberrant cell migration, establishing the functional importance of nucleolar EZH2 sequestration.

Prolonged FBL depletion further induces EMT in breast epithelial cells, marked by activation of Akt signaling, upregulation of mesenchymal transcription factors (Snail, Twist, and Zeb1), and loss of epithelial markers. In vivo, FBL depletion enhances tumor growth and lung metastasis in xenograft models, correlating with reduced Scribble levels and altered EZH2 localization. Collectively, these findings uncover an FBL–EZH2–Scribble regulatory axis that links nucleolar function to chromatin regulation, epithelial identity, and metastatic progression, positioning fibrillarin as a critical suppressor of EMT and a potential therapeutic vulnerability in epithelial cancers.

Synopsis

Introduction

The nucleus is a highly organized organelle in which genomic and regulatory functions are compartmentalized into spatially distinct, membrane-less sub-domains (Pederson 2011). Nuclear proteins, while remaining in dynamic equilibrium with the nucleoplasm, self-organize into discrete nuclear bodies such as the nucleolus, nuclear speckles, transcription factories, and PML bodies (Handwerger and Gall 2006; Lallemand-Breitenbach and Thé 2010; Sleeman and Trinkle-Mulcahy 2014). This compartmentalization enables efficient coordination of essential nuclear processes by locally concentrating molecular components required for transcription, RNA processing, and chromatin regulation (Misteli 2010).

The nucleolus is the largest nuclear sub-compartment and is classically known as the site of RNA polymerase I–mediated ribosomal DNA (rDNA) transcription, rRNA processing, and ribosome assembly (Scheer and Hock 1999; Sirri et al. 2008). Ultrastructural studies have revealed that the nucleolus is further organized into three sub-domains: the fibrillar center (FC), dense fibrillar component (DFC), and granular component (GC), each corresponding to distinct stages of ribosome biogenesis (Pederson 2011). Although historically regarded as a ribosome factory, it is now evident that the nucleolus functions as a regulatory hub integrating transcriptional control, chromatin organization, stress responses, and cell fate decisions.

Despite lacking a bounding membrane, the nucleolus maintains a stable architecture while allowing rapid exchange of resident proteins with the nucleoplasm. Photobleaching experiments have demonstrated that nucleolar proteins such as fibrillarin, nucleolin, and nucleophosmin exhibit residence times of only seconds, raising fundamental questions regarding the mechanisms that preserve nucleolar integrity (Chen and Huang 2001; Shav-Tal et al. 2005). Disruption of nucleolar structure, either through inhibition of rDNA transcription or cellular stress, results in nucleolar disassembly and activation of the nucleolar stress response, leading to stabilization of p53 and induction of cell cycle arrest or apoptosis (James et al. 2014, 53; Kurki et al. 2004).

Recent studies have demonstrated that the nucleolus assembles through liquid–liquid phase separation (LLPS), driven by multivalent interactions between nucleolar proteins and RNA (Brangwynne et al. 2011; Feric et al. 2016). Within the nucleolus, immiscibility between DFC and GC components maintains sub-compartmental organization. However, most insights into nucleolar phase behavior arise from in vitro reconstitution, whereas in vivo nucleolar

organization occurs within a complex nuclear environment influenced by chromatin, signaling pathways, and nuclear architecture.

Fibrillarin (FBL) is a conserved nucleolar protein enriched in the DFC and is best known as the catalytic component of box C/D snoRNPs responsible for site-specific 2′-O-methylation of rRNA, essential for translational fidelity (Tollervey et al. 1991). Emerging evidence suggests that fibrillarin also participates in non-canonical functions, including chromatin modification, nucleolar phase separation, and disease progression. Notably, fibrillarin is frequently dysregulated in cancers, yet its contribution to epithelial identity and tissue architecture remains poorly understood.

Epithelial homeostasis depends on the coordinated regulation of cell–cell adhesion, apico–basal polarity, and transcriptional programs that maintain epithelial identity. Loss of polarity and junctional integrity leads to epithelial–mesenchymal transition (EMT), a process central to cancer invasion and metastasis. While EMT has been extensively studied at the level of transcription factors and signaling pathways, the role of nucleolar organization and nucleolar proteins in regulating epithelial architecture remains largely unexplored.

In this thesis, I have investigated the role of fibrillarin as a regulator of epithelial architecture, chromatin organization, and epithelial plasticity, with a particular focus on its interaction with chromatin modifiers and polarity regulators.

Aims

1. To define how Fibrillarin regulates epithelial identity and junctional architecture through transcriptional and post-transcriptional control of polarity determinants
2. To elucidate the chromatin-based and spatial nuclear mechanisms by which Fibrillarin regulates the EZH2–Scribble axis to preserve epithelial polarity
3. To determine how Fibrillarin-mediated nucleolar–chromatin regulation governs epithelial cell migration, invasion, and metastatic dissemination

Aim 1: To define how Fibrillarin regulates epithelial identity and junctional architecture through transcriptional and post-transcriptional control of polarity determinants

Rationale and Background

Epithelial tissues rely on precise apico–basal polarity and stable cell–cell junctions to maintain tissue integrity and suppress malignant transformation. Loss of epithelial polarity is increasingly recognized as an early and permissive event in tumorigenesis, often preceding overt EMT or invasion. Central to this architecture are adherens junction components such as E-cadherin, tight junction proteins including ZO-1, and basolateral polarity regulators such as Scribble (SCRIB). Although Fibrillarin is classically regarded as a nucleolar rRNA methyltransferase, emerging evidence—including observations from this thesis—suggests that perturbation of nucleolar homeostasis can exert profound effects on epithelial organization. Preliminary findings indicate that depletion of FBL leads to mislocalization and internalization of E-cadherin, disruption of junctional continuity, and loss of epithelial morphology without globally impairing endocytosis. These observations point toward a selective and regulated mechanism, rather than a nonspecific trafficking defect. This aim is driven by the hypothesis that FBL functions as a higher-order regulator of epithelial identity, coordinating transcriptional programs and membrane trafficking processes that preserve junctional integrity.

Objectives and Experimental Logic

This aim seeks to systematically dissect the role of FBL in maintaining epithelial architecture by addressing three interrelated questions:

Does FBL depletion compromise epithelial polarity and junctional organization?

Using well-established epithelial models (DLD-1 and MCF10A-derived systems), this aim evaluates morphological changes, junctional continuity, and subcellular localization of E-cadherin, ZO-1, and polarity proteins following loss of FBL. High-resolution immunofluorescence and quantitative image analysis are used to distinguish between transcriptional downregulation and post-transcriptional mislocalization.

Is E-cadherin mislocalization driven by altered endocytic trafficking or selective internalization pathways?

To uncouple global endocytic defects from cargo-specific trafficking, transferrin uptake assays and pharmacological inhibition of dynamin-dependent endocytosis are employed. These

experiments directly test whether FBL loss selectively enhances clathrin-mediated internalization of E-cadherin while sparing bulk endocytosis.

Does FBL regulate epithelial identity at the transcriptional level?

RNA-sequencing analyses are leveraged to identify transcriptional changes in polarity and junctional gene networks. Integration of transcriptomic data with protein localization studies enables discrimination between primary transcriptional repression and secondary effects arising from architectural collapse.

Expected Outcomes and Significance

This aim establishes FBL as a non-canonical regulator of epithelial integrity, linking nucleolar function to membrane organization and polarity maintenance. By demonstrating that FBL loss induces selective junctional destabilization rather than generalized cellular dysfunction, this aim reframes nucleolar proteins as architectural gatekeepers of epithelial identity. Importantly, these findings provide the conceptual foundation for subsequent aims by positioning epithelial polarity loss as a downstream consequence of nucleolar dysregulation, rather than a passive byproduct of transformation.

Aim 2: To elucidate the chromatin-based and spatial nuclear mechanisms by which Fibrillarin regulates the EZH2–Scribble axis to preserve epithelial polarity

Rationale and Conceptual Framework

The maintenance of epithelial identity requires not only intact junctional complexes at the plasma membrane but also sustained transcription of polarity and adhesion genes. Findings from Aim 1 demonstrate that depletion of Fibrillarin (FBL) leads to profound disruption of epithelial architecture, including E-cadherin mislocalization and polarity loss. However, these phenotypic alterations cannot be fully explained by defects in protein trafficking alone. Transcriptomic analyses revealed that several polarity-associated genes, most notably SCRIB, are transcriptionally downregulated upon FBL depletion, indicating that epithelial collapse is accompanied by active gene repression rather than passive structural failure. SCRIB encodes a core basolateral polarity scaffold protein that functions as a tumor suppressor and a key antagonist of epithelial–mesenchymal transition (EMT). Its loss has been shown to promote junctional instability, aberrant activation of oncogenic signaling pathways, and enhanced migratory capacity across multiple epithelial cancer types. Importantly, SCRIB expression is

known to be tightly regulated at the chromatin level, and analysis of public epigenomic datasets indicates that the SCRIB promoter exhibits a bivalent chromatin configuration, characterized by the coexistence of active (H3K4me3) and repressive (H3K27me3) histone marks. Such promoters are poised for rapid transcriptional switching and are particularly vulnerable to perturbations in chromatin regulatory mechanisms. The repressive H3K27me3 mark is catalyzed by EZH2, the enzymatic subunit of Polycomb Repressive Complex 2 (PRC2), a master epigenetic regulator implicated in epithelial gene silencing, EMT induction, and metastatic progression. EZH2 is frequently overexpressed in epithelial cancers and has been shown to repress E-cadherin, polarity genes, and differentiation programs. However, EZH2 activity is not governed solely by expression levels; its subnuclear localization and accessibility to chromatin are emerging as critical determinants of its functional output. This aim is founded on the central hypothesis that FBL constrains EZH2 through nucleolar sequestration and spatial buffering, thereby limiting its access to chromatin targets such as the SCRIB promoter. Loss of FBL disrupts this spatial control, leading to aberrant redistribution of EZH2, increased H3K27me3 deposition, and stable repression of epithelial polarity genes.

Specific Objectives and Experimental Strategy

This aim addresses the molecular mechanism linking nucleolar integrity to chromatin-mediated transcriptional repression through three interdependent lines of investigation:

1. To determine whether FBL regulates the subnuclear localization and chromatin accessibility of EZH2

Although EZH2 is classically viewed as a chromatin-associated enzyme, accumulating evidence suggests that a fraction of EZH2 localizes to the nucleolus or perinucleolar regions, where its activity may be spatially restrained. This aim investigates whether FBL contributes to such spatial compartmentalization.

Using high-resolution immunofluorescence microscopy and quantitative image analysis, the localization of EZH2 is examined under control and FBL-depleted conditions. Emphasis is placed on distinguishing nucleolar, perinucleolar, and nucleoplasmic pools of EZH2. Complementary biochemical fractionation approaches further assess whether loss of FBL leads to a redistribution of EZH2 toward chromatin-enriched fractions.

These experiments test the hypothesis that FBL functions as a spatial regulator of EZH2, and that nucleolar disorganization following FBL depletion releases EZH2 from a constrained compartment, increasing its effective concentration in the nucleoplasm.

2. To establish whether EZH2 directly mediates transcriptional repression of SCRIB following FBL depletion

Having identified SCRIB as a transcriptionally downregulated polarity gene, this objective interrogates the chromatin-level mechanism underlying its repression. Chromatin immunoprecipitation (ChIP) assays are used to assess EZH2 occupancy and H3K27me3 enrichment at the SCRIB promoter in control versus FBL-depleted cells. These experiments determine whether loss of FBL correlates with enhanced PRC2 recruitment and increased deposition of repressive histone marks at this locus. To establish causality, pharmacological inhibition of EZH2 catalytic activity is employed to test whether repression of SCRIB is reversible. Restoration of SCRIB transcript levels and rescue of epithelial features upon EZH2 inhibition would provide strong evidence that SCRIB repression is PRC2-dependent and downstream of FBL loss. This objective therefore positions SCRIB as a critical chromatin-regulated effector linking nucleolar perturbation to epithelial polarity collapse.

3. To test the nucleolus as a regulatory buffer for chromatin-modifying enzymes

Beyond SCRIB alone, this aim explores a broader conceptual model in which the nucleolus functions as a regulatory sink or buffering compartment for chromatin modifiers. The nucleolus is increasingly recognized as a dynamic hub that sequesters regulatory proteins, thereby limiting their access to chromatin and fine-tuning nuclear signaling pathways. Within this framework, FBL is proposed to maintain nucleolar architecture and phase-separated environments that restrict EZH2 mobility. Disruption of FBL compromises this buffering capacity, allowing EZH2 to engage ectopic chromatin targets and initiate widespread epigenetic reprogramming. By integrating localization studies, chromatin occupancy analyses, and transcriptional outputs, this objective reframes FBL not merely as a nucleolar enzyme, but as a guardian of nuclear spatial organization with epigenetic consequences.

Aim 3: To determine how Fibrillarin-mediated nucleolar–chromatin regulation governs epithelial cell migration, invasion, and metastatic dissemination

Rationale and Conceptual Framework

Metastasis represents the culmination of a multistep biological process in which epithelial cells acquire the ability to detach, migrate, invade surrounding tissues, survive in circulation, and colonize distant organs. Central to this process is epithelial plasticity, characterized by loss of polarity, weakening of cell–cell adhesion, and transcriptional reprogramming toward a motile state. While classical EMT frameworks emphasize transcription factors such as SNAIL, ZEB, and TWIST, it is increasingly evident that upstream architectural and epigenetic perturbations can license migratory behavior even in the absence of full EMT. Findings from Aims 1 and 2 establish that depletion of Fibrillarin (FBL) leads to (i) disruption of epithelial junctional integrity and polarity, and (ii) chromatin-mediated repression of polarity genes, particularly SCRIB, via deregulated EZH2 activity. These alterations are predicted to lower the threshold for cell motility by simultaneously weakening physical constraints at cell–cell junctions and reprogramming transcriptional networks that suppress migration. This aim is based on the central hypothesis that FBL functions as a suppressor of epithelial cell migration and metastatic competence, and that its loss promotes migratory and invasive behavior through a nucleolar–chromatin–polarity axis. Importantly, this aim tests whether the molecular and architectural changes described in earlier aims translate into functional consequences relevant to cancer progression, both in vitro and in vivo.

Specific Objectives and Experimental Strategy

This aim interrogates the functional output of FBL depletion at three interconnected biological levels: collective cell migration, polarity-dependent motility control, and metastatic colonization.

1. To assess whether loss of FBL enhances epithelial cell migration and wound closure dynamics

The first objective examines whether FBL depletion directly alters migratory behavior in epithelial cells. Scratch wound–healing assays are employed as a quantitative and visual measure of collective cell migration in confluent monolayers. This assay is particularly well suited to epithelial systems, as it preserves cell–cell contacts and allows assessment of migration in a context where polarity cues remain relevant.

By comparing control and FBL-depleted cells, this objective evaluates both the rate and mode of wound closure, distinguishing between coordinated epithelial sheet migration and disorganized, individual cell movement. Time-resolved imaging and quantitative analysis provide insight into whether FBL loss accelerates migration kinetics and disrupts directional persistence. Importantly, these assays allow correlation of migratory behavior with junctional integrity and polarity status established in Aim 1, thereby directly linking architectural destabilization to functional motility.

2. To determine whether SCRIB repression is functionally required for FBL-dependent migratory phenotypes

While Aim 2 establishes SCRIB as a chromatin-repressed target downstream of FBL loss, these objective tests whether SCRIB repression is causally linked to enhanced migration.

This is achieved through two complementary approaches:

- Phenocopy experiments, in which SCRIB depletion alone is assessed for its ability to recapitulate the migratory phenotype observed upon FBL loss
- Rescue experiments, in which re-expression of SCRIB in an FBL-depleted background is used to determine whether restoring polarity signaling suppresses migration
- By integrating these strategies, this objective distinguishes whether SCRIB repression is merely correlated with migration or is a functional driver of the observed phenotype.

This approach is critical because it anchors the nucleolar–chromatin pathway to a specific polarity effector, strengthening the mechanistic coherence of the thesis. Demonstrating that SCRIB restoration can restrain migration despite nucleolar perturbation underscores the importance of polarity gene repression as a decisive step in epithelial plasticity.

3. To evaluate the impact of FBL depletion on metastatic dissemination in vivo

While in vitro assays provide valuable mechanistic insight, metastatic competence must ultimately be validated in an in vivo context. The final objective therefore extends the analysis to animal models to determine whether FBL depletion enhances metastatic colonization. Using inducible shRNA-based depletion of FBL in epithelial cancer cells, tail vein injection models are employed to assess lung colonization efficiency. This experimental system specifically interrogates late steps of metastasis, including survival in circulation, extravasation, and colonization of a secondary organ. Histological analysis of lung sections enables quantitative assessment of metastatic burden, including number, size, and distribution of metastatic lesions.

Comparison between FBL-depleted and control groups directly tests whether loss of nucleolar integrity confers a selective advantage during metastatic outgrowth. Importantly, this objective provides in vivo validation that nucleolar deregulation is not merely a cell-intrinsic defect but a driver of malignant progression.

Expected Outcomes and Significance:

Completion of this aim is expected to demonstrate that FBL acts as a multilevel suppressor of epithelial motility and metastasis, integrating nuclear organization, chromatin regulation, and cell behavior. Specifically, this aim will establish that:

- FBL depletion enhances epithelial migration in vitro
- SCRIB repression is a critical mediator of FBL-dependent motility
- Loss of FBL promotes metastatic colonization in vivo

Conceptually, this aim advances a unifying model in which nucleolar integrity restrains epithelial plasticity by preserving polarity gene expression and limiting chromatin-mediated reprogramming. By positioning FBL as a barrier to metastasis, this work broadens the biological significance of nucleolar proteins beyond ribosome biogenesis and highlights the nucleolus as a previously underappreciated regulator of cancer cell behavior.

Together with Aims 1 and 2, this aim completes a coherent mechanistic trajectory: from nucleolar perturbation → chromatin repression → polarity loss → migration → metastasis, providing a comprehensive framework for understanding how nuclear architecture governs epithelial fate and disease progression.

References

1. Brangwynne, Clifford P, Timothy J Mitchison, and Anthony A Hyman. 2011. “Active Liquid-like Behavior of Nucleoli Determines Their Size and Shape in Xenopus Laevis Oocytes.” *Proceedings of the National Academy of Sciences of the United States of America* 108 (11): 4334–39. https://doi.org/10.1073/pnas.1017150108.
2. Chen, Danyang, and Sui Huang. 2001. “Nucleolar Components Involved in Ribosome Biogenesis Cycle between the Nucleolus and Nucleoplasm in Interphase Cells.” *Journal of Cell Biology* 153 (1): 169–76. https://doi.org/10.1083/jcb.153.1.169.
3. Feric, Marina, Nilesh Vaidya, Tyler S Harmon, et al. 2016. “Coexisting Liquid Phases Underlie Nucleolar Subcompartments.” *Cell* 165 (7): 1686–97. https://doi.org/10.1016/j.cell.2016.04.047.
4. Handwerger, Korie E., and Joseph G. Gall. 2006. “Subnuclear Organelles: New Insights into Form and Function.” *Trends in Cell Biology* 16 (1): 19–26. https://doi.org/10.1016/j.tcb.2005.11.005.
5. James, Allison, Yubo Wang, Himanshu Raje, Raphyel Rosby, and Patrick DiMario. 2014. “Nucleolar Stress with and without P53.” *Nucleus* 5 (5): 402–26. https://doi.org/10.4161/nucl.32235.
6. Kurki, Sari, Karita Peltonen, and Marikki Laiho. 2004. “Nucleophosmin, HDM2 and P53: Players in UV Damage Incited Nucleolar Stress Response.” *Cell Cycle* 3 (8): 974–77. https://doi.org/10.4161/cc.3.8.1015.
7. Lallemand-Breitenbach, Valérie, and Hugues de Thé. 2010. “PML Nuclear Bodies.” *Cold Spring Harbor Perspectives in Biology* 2 (5): a000661. https://doi.org/10.1101/cshperspect.a000661.
8. Misteli, Tom. 2010. “Higher-Order Genome Organization in Human Disease.” *Cold Spring Harbor Perspectives in Biology* 2 (8): a000794. https://doi.org/10.1101/cshperspect.a000794.
9. Pederson, Thoru. 2011. “The Nucleolus.” *Cold Spring Harbor Perspectives in Biology* 3 (3). https://doi.org/10.1101/cshperspect.a000638.
10. Scheer, Ulrich, and Robert Hock. 1999. “Structure and Function of the Nucleolus.” *Current Opinion in Cell Biology* 11 (3): 385–90. https://doi.org/10.1016/S0955-0674(99)80054-4.
11. Shav-Tal, Yaron, Janna Blechman, Xavier Darzacq, et al. 2005. “Dynamic Sorting of Nuclear Components into Distinct Nucleolar Caps during Transcriptional Inhibition.” *Molecular Biology of the Cell* 16 (5): 2395–413. https://doi.org/10.1091/mbc.E04-11-0992.
12. Sirri, Valentina, Silvio Urcuqui-Inchima, Pascal Roussel, and Danièle Hernandez-Verdun. 2008. “Nucleolus: The Fascinating Nuclear Body.” *Histochemistry and Cell Biology* 129 (1): 13–31. https://doi.org/10.1007/s00418-007-0359-6.

13. Sleeman, Judith E, and Laura Trinkle-Mulcahy. 2014. “Nuclear Bodies: New Insights into Assembly/Dynamics and Disease Relevance.” *Current Opinion in Cell Biology*, Cell nucleus, vol. 28 (June): 76–83. https://doi.org/10.1016/j.ceb.2014.03.004.

14. Tollervey, D, H Lehtonen, M Carmo-Fonseca, and E C Hurt. 1991. “The Small Nucleolar RNP Protein NOP1 (Fibrillarin) Is Required for Pre-rRNA Processing in Yeast.” *The EMBO Journal* 10 (3): 573–83. https://doi.org/10.1002/j.1460-2075.1991.tb07984.x.

Essential Abbreviations

FBL - Fibrillarin

EZH2 - Enhancer of Zeste Homolog 2

PRC2 - Polycomb Repressive Complex 2

EMT - Epithelial-Mesenchymal Transition

DFC - Dense Fibrillar Component

FC - Fibrillar Center

GC - Granular Component

rDNA - Ribosomal DNA

rRNA - Ribosomal RNA

snoRNP - Small Nucleolar Ribonucleoprotein

LLPS - Liquid-Liquid Phase Separation

SCRIB - Scribble (cell polarity protein)

H3K27me3 - Trimethylation of Histone H3 at Lysine 27

H3K9me3 - Trimethylation of Histone H3 at Lysine 9

ChIP - Chromatin Immunoprecipitation

RNA-seq - RNA Sequencing

RT-qPCR - Reverse Transcription Quantitative Polymerase Chain Reaction

IF – Immunofluorescence

FACS - Fluorescence-Activated Cell Sorting

NCL - Nucleolin

NPM1 - Nucleophosmin 1

UBF - Upstream Binding Factor

Pol I - RNA Polymerase I

Pol II - RNA Polymerase II

NOR - Nucleolar Organizer Region

PNB - Pre-nucleolar Body

shRNA - Short Hairpin RNA

siRNA - Small Interfering RNA

WT - Wild Type

Chapter 1:
Introduction and Review of Literature

1.1.1. Overview of Nucleolar Architecture

The nucleolus, a dense, non-membranous organelle within the nucleus, plays a central role in ribosome biogenesis. It emerges around clusters of ribosomal DNA (rDNA) known as nucleolar organizing regions (NORs), which encode the 45S pre-rRNA precursor transcribed by RNA polymerase I. The assembly of the nucleolus is a self-organizing process driven by the transcription and co-transcriptional processing of rRNA, as well as by the interaction of ribonucleoprotein complexes that scaffold nucleolar compartments.[1,2]

Morphologically, the nucleolus is organized into three concentric subdomains that reflect its functional stages in ribosome production:

- *Fibrillar Center (FC)*: Typically hypodense under electron microscopy, the FC harbors inactive or poised rDNA and is enriched in upstream binding factor (UBF), a component-of-the-RNA-Pol-I-pre-initiation-complex.

- *Dense Fibrillar Component (DFC)*: Surrounds the FC and is the site of early rRNA processing and modification. It contains a high concentration of fibrillarin and snoRNPs (Fig. 1.2.).

- *Granular Component (GC)*: Occupies the peripheral and largest area of the nucleolus. It is the site of late rRNA processing, ribosomal protein assembly, and pre-ribosome maturation.

These regions are not membrane-bound but arise through liquid–liquid phase separation (LLPS) of proteins and RNAs into coexisting but dynamic compartments. Proteins like nucleophosmin (NPM1) and fibrillarin contribute to LLPS due to their intrinsically disordered regions (IDRs) and multivalent interactions with RNA. The organization of the nucleolus is closely linked to cellular physiology. In proliferating cells, nucleoli are large and highly active, while in quiescent or stressed cells, nucleoli may fragment or shrink. Disruption of nucleolar architecture is often observed in diseases such as cancer, viral infection, and neurodegenerative disorders (Boisvert et al. 2007; Pederson 2011).

A

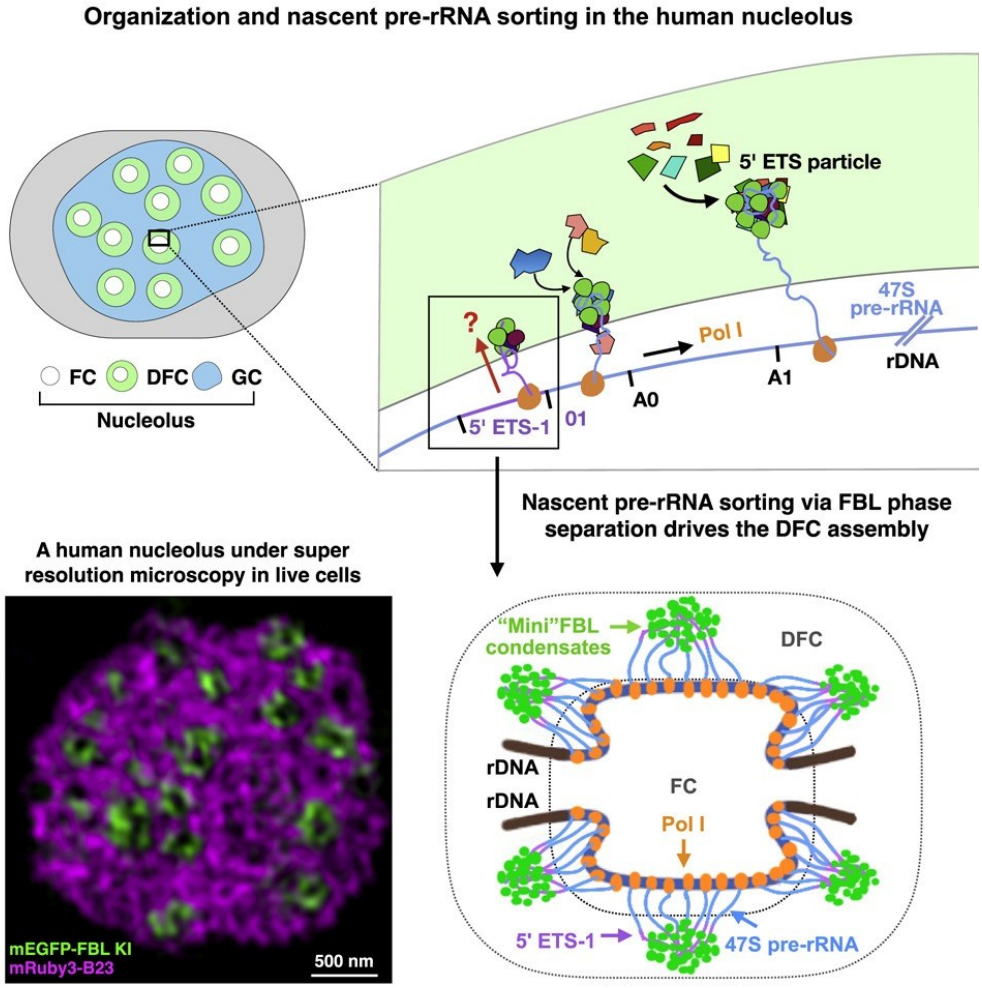
Organization and nascent pre-rRNA sorting in the human nucleolus
FC
DFC
GC
Nucleolus
5' ETS particle
47S pre-rRNA
Pol I
rDNA
A0
A1
5' ETS-1
01
?
Nascent pre-rRNA sorting via FBL phase separation drives the DFC assembly
A human nucleolus under super resolution microscopy in live cells
mEGFP-FBL KI
mRuby3-B23
500 nm
"Mini"FBL condensates
DFC
rDNA
rDNA
FC
Pol I
5' ETS-1
47S pre-rRNA

B

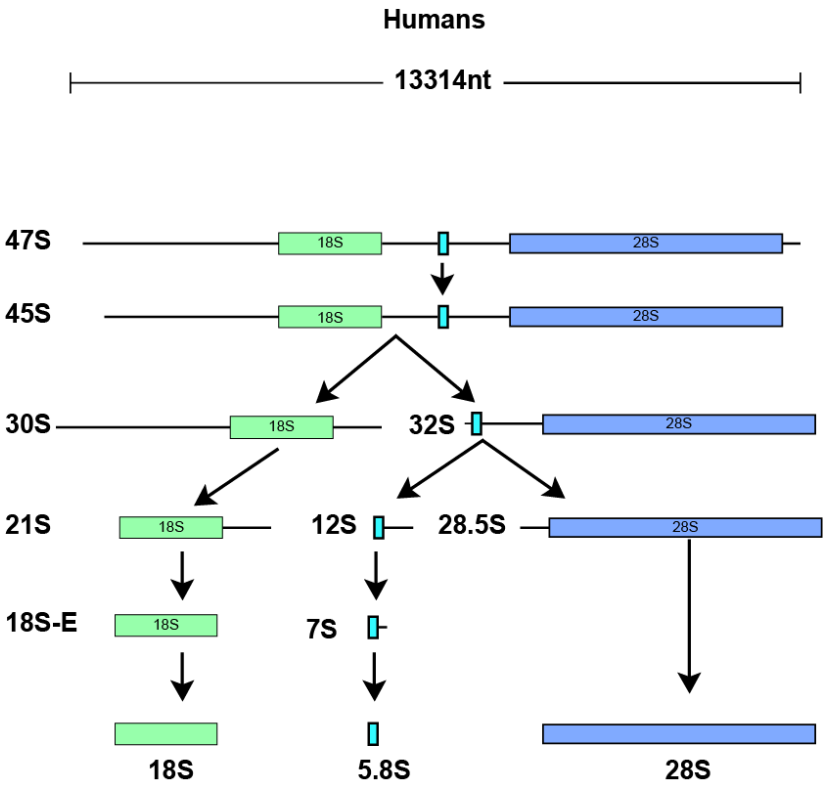
Humans
13314nt
47S
45S
30S
32S
21S
12S
28.5S
18S-E
7S
18S
28S
5.8S

Fig. 1.1. Organization of the human nucleolus and model of nascent pre-rRNA sorting mediated by Fibrillarin (FBL) and processing of rRNA

(A) Schematic representation of nucleolar subcompartments, highlighting the fibrillar center (FC), dense fibrillar component (DFC), and granular component (GC). (Top right) Newly synthesized 47S pre-rRNA emerges from RNA polymerase I (Pol I) at rDNA loci and undergoes early processing at the 5′ ETS region (A0, 01, A1 sites). The 5′ ETS-1 containing particles associate with FBL, facilitating sorting of nascent transcripts. Phase separation of FBL promotes coalescence of these pre-rRNA–bound complexes and contributes to DFC assembly. (Bottom left) Super-resolution live-cell imaging of a human nucleolus showing mEGFP-tagged FBL (green) enriched in DFC regions and mRuby3-tagged B23/NPM1 (magenta) marking GC. Scale bar: 500 nm. (Bottom right) Proposed model illustrating how "mini" FBL condensates form around nascent transcripts at rDNA transcription sites within the FC, driving accumulation of processing machinery and organizing the DFC. Through LLPS-mediated recruitment, pre-rRNA transitions from FC to DFC for early maturation and subsequent processing. **(B)** Human rRNAs are transcribed as long polycistronic precursor molecules that undergo sequential cleavage and modification to produce the mature rRNAs. For clarity, only the major processing route is shown, and minor alternative pathways have been omitted. Adapted from (Ojha et al. 2020; Yao et al. 2019)

1.1.2. Evolution of the Tripartite Structure of the Nucleolus

The nucleolus is a highly conserved nuclear sub-region dedicated primarily to ribosome biogenesis; however, its organisation is not static in evolution. Comparative cell-biological and ultrastructural studies show that the canonical tripartite architecture of the nucleolus - the fibrillar centre (FC), dense fibrillar component (DFC), and granular component (GC) – (Fig. 1.1.A.) represents an evolutionary refinement rather than the ancestral state, and arose in parallel with increased complexity in rDNA organisation, ribosome assembly pathways and protein synthesis demands in higher eukaryotes (Pederson 2011; Thiry and Lafontaine 2005).

In early eukaryotes and many unicellular organisms, including protists and yeast, the nucleolus typically exhibits a bipartite organisation, comprising a fibrillar zone and a granular zone. In these systems, transcription of rDNA and early rRNA processing are not spatially segregated, and instead occur within a unified fibrillar compartment that functionally incorporates what later evolved into FC and DFC(Thiry and Lafontaine 2005). During

vertebrate evolution — particularly at the transition from anamniotes to amniotes — the fibrillar compartment is thought to have split into two distinct subdomains, FC and DFC, thereby generating the tripartite configuration characteristic of mammals, birds, and reptiles (Thiry and Lafontaine 2005; Lafontaine 2023).

This transition coincided with major genomic and regulatory changes. Notably, intergenic spacer regions within rDNA loci expanded substantially in amniotes, adding regulatory modules that recruit chromatin remodellers and Pol I transcription factors. As a result, the FC emerged as a domain enriched in inactive or transcription-ready rDNA repeats and RNA polymerase I machinery, whereas the surrounding DFC became specialised for co-transcriptional rRNA modification and early processing, mediated by dense accumulation of snoRNPs including fibrillarin. The GC, already present in more primitive nucleoli, continued to function as the primary compartment for late rRNA processing and pre-ribosomal subunit maturation (Pederson 2011).

More recent work has reframed nucleolar architecture through the lens of multiphase biomolecular condensates, in which FC, DFC and GC constitute coexisting liquid-like phases driven by differential macromolecular interactions (Feric et al. 2016; Yao et al. 2019). Within this framework, the emergence of the third nucleolar subphase can be viewed as a biophysical optimisation, enabling sequential ribosome-biogenesis (Riback et al. 2023; Yao et al. 2019).

In higher eukaryotes, the nucleolus has additionally acquired functions beyond ribosome production, including regulation of cell-cycle progression, genome stability, senescence, and stress responses (Pederson 2011; Boulon et al. 2010). The increased modularity and spatial stratification granted by the tripartite structure facilitates expansion of functional repertoire (Boulon et al. 2010). Conversely, this refined structural organisation also introduces vulnerability to deregulation, as perturbations in intra-nucleolar compartmentalisation are a hallmark of nucleolar stress (Boulon et al. 2010; Pederson 2011).

Collectively, evolutionary studies suggest a continuous trend toward greater structural and functional specialization, culminating in the recent FC–DFC–GC architecture. This framework emphasises that nucleolar proteins such as fibrillarin — a defining component of the DFC — operate within a highly evolved spatial system designed to coordinate hierarchical steps of ribosome biogenesis and other nucleus-wide regulatory processes.

1.2.1. Fibrillarin as a Pivotal regulator of the nucleolus

Fibrillarin (FBL) is a 34-kDa nucleolar protein best known for its role as a hallmark autoantigen in systemic autoimmune diseases, initially discovered in the sera of scleroderma patients (Vaughan 1987). However, beyond its immunological significance, FBL has emerged as a multifunctional and evolutionarily conserved regulator that operates at the intersection of RNA metabolism, chromatin dynamics, phase separation, and cellular stress responses. Structurally, FBL is a S-adenosylmethionine (SAM)-dependent methyltransferase that localizes predominantly to the Dense Fibrillar Component (DFC) of the nucleolus—a specialized, membrane-less subcompartment responsible for early stages of pre-rRNA processing. Within this domain, FBL functions as the catalytic core of the box C/D small nucleolar ribonucleoprotein (snoRNP) complex, which mediates 2′-O-methylation of ribosomal RNA (rRNA) at over 100 specific nucleotide positions. These modifications enhance rRNA folding, structural stability, and translation fidelity, and are essential for assembling functional 40S and 60S ribosomal subunits (Erales et al. 2017; Tollervey et al. 1991).

As part of the snoRNP complex, FBL works in coordination with NOP56, NOP58, SNU13, and box C/D snoRNAs, ensuring high specificity in targeting rRNA methylation. These methylations occur at defined ribose positions guided by antisense snoRNA elements, fine-tuning ribosome architecture and promoting cellular proteostasis. Disruption of FBL function or methylation activity leads to-

- *Defective ribosome assembly*: FBL directly controls the levels of methylations on rRNA, which can alter the proportions of cap-dependent and cap-independent translation (Erales et al. 2017; Lacerda et al. 2017; Marcel et al. 2013).

- *Altered protein synthesis*: Certain cancer-associated proteins - MYC, FGF1, FGF2, and VEGFA have Internal Ribosome Entry Site (IRES) sequence in their transcripts, therefore modulating FBL levels and activity can alter the levels of cap-dependent and cap-independent translation (Marcel et al. 2013).

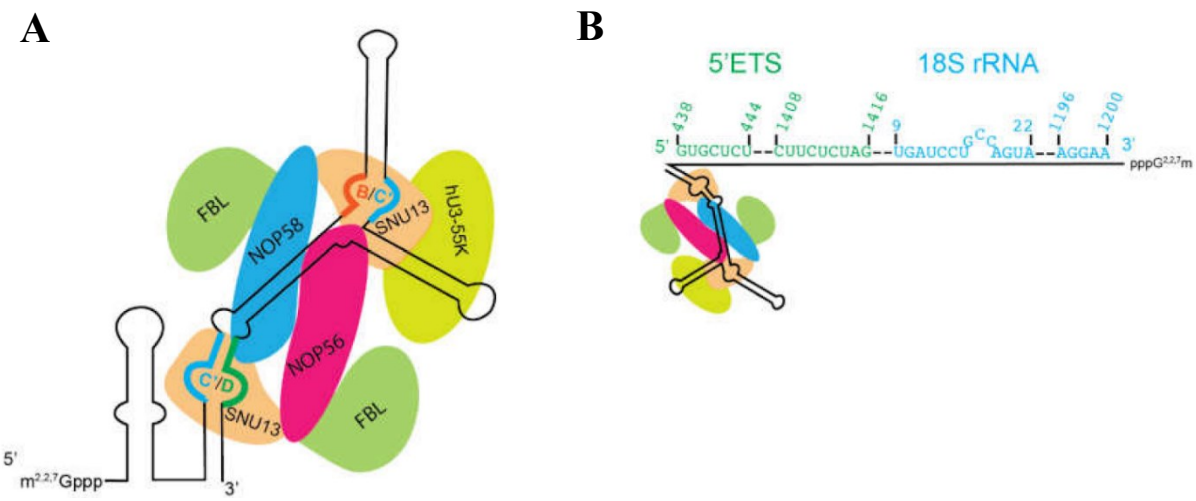

Fig. 1.2. Schematic structure of U3 snoRNP

(A) Predicted secondary structure of U3 snoRNA with associated protein components. SNU13 remains bound to k-turn elements formed by Box C′ (blue)–Box D (green) and Box C′ (blue)–Box B (red). Due to the unique architecture of U3, FBL is not positioned appropriately to perform 2′-O-methylation. **(B)** The 5′ extension of U3 establishes multiple base-pairing interactions with the pre-rRNA, contacting distinct regions within the 5′ ETS (green) and 18S rRNA (blue). Looped-out segments of rRNA are shown as dashed regions. Numbering corresponds to positions within 47S pre-rRNA (green) or 18S rRNA (blue). This diagram is simplified and does not fully reflect all looping. Secondary structure adapted from snoRNABase predictions. Schematic has been adapted from (Ojha et al. 2020).

1.2.2. Expanding Horizons: Multifunctionality Beyond rRNA Methylation

While traditionally confined to its role in ribosome biogenesis, emerging studies have substantially broadened the functional scope of FBL. Advanced techniques such as cryo-electron microscopy (cryo-EM) and live-cell imaging of phase-separated condensates have shed light on the role of FBL in nucleolar organization, chromatin remodeling, RNA cleavage, and cellular stress responses. For instance, FBL exhibits ribonuclease activity stimulated by nuclear phosphoinositides, implicating it in early rRNA cleavage events, potentially independent of its canonical methyltransferase function (Guillen-Chable et al. 2020).

Moreover, FBL functions beyond the nucleolus in influencing epigenetic landscapes, most notably through methylation of histone H2A at glutamine 104 (H2AQ104me), which

promotes RNA polymerase I (Pol I) recruitment and transcription of rDNA. This link between nucleolar chromatin status and rRNA gene activity underscores the role of FBL as both a transcriptional regulator and an epigenetic effector (Tessarz et al. 2014).

1.2.3. Phase separation in FBL

FBL has an intrinsically disordered N-terminal Glycine-Arginine rich GAR domain (8-80aa) facilitates liquid–liquid phase separation (LLPS), driving condensates of nucleolar compartments and enabling dynamic assembly of snoRNPs at rRNA transcription sites. This behavior is modulated by post-translational modifications such as arginine methylation, which alter the physico-chemical properties of FBL condensates and influence its partitioning between nuclear compartments- FC and GC. Disruption of LLPS—through substitutions in Phenylalanine-to-serine of the phenylalanine-glycine repeats in the GAR domain of FBL—mislocalizes FBL, destabilizes nucleolar architecture, and impairs ribosome biogenesis (Fig. 1.3. (A-C)) (Kim and Kwon 2021).

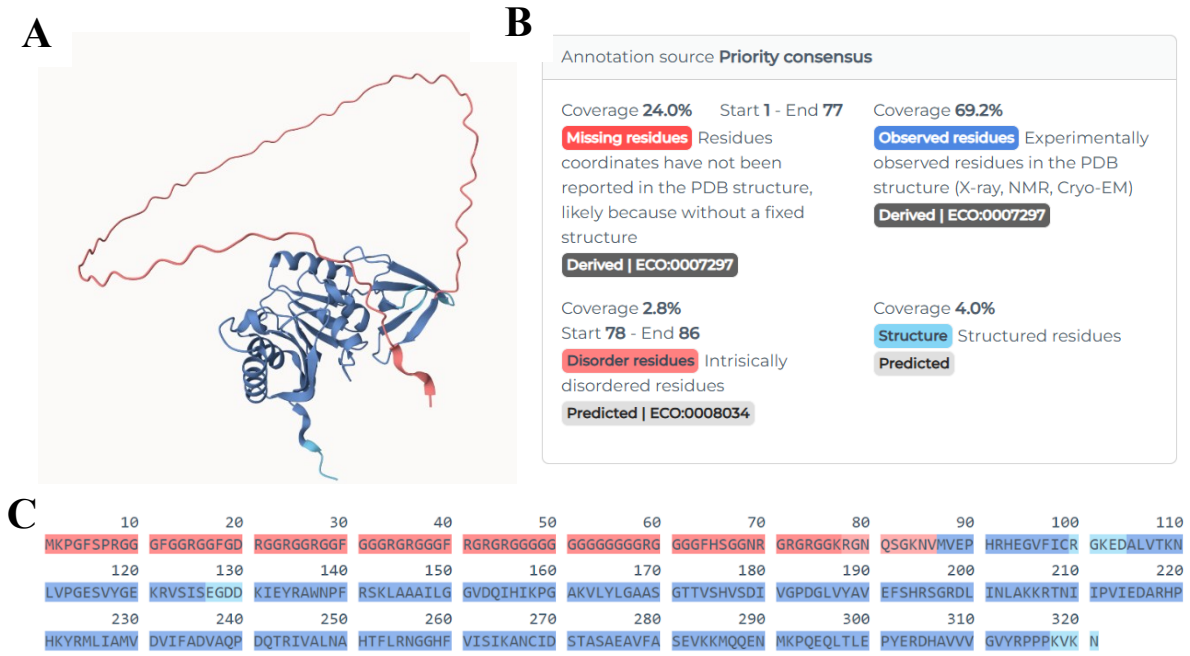

Fig. 1.3. Intrinsically disordered regions (IDRs) within human Fibrillarin (FBL). **(A)** AlphaFold-predicted 3D structure of human FBL showing structured regions (blue) and the extended N-terminal tail that lacks resolved conformation (red), characteristic of an intrinsically disordered region (IDR), which fails to fold into defined structure. **(B)** Structural annotation summary highlighting residue coverage from experimental and

predicted models. Approximately 69.2% of the protein corresponds to experimentally resolved structured domains (blue), whereas 24.0% of the N-terminal region lacks coordinates in PDB entries, suggesting intrinsic disorder. An additional 2.8% of residues (positions 78–86) are predicted to be disordered, and ~4.0% are predicted structured residues. **(C)** Primary amino acid sequence of FBL mapped with disorder predictions. Red-highlighted stretches represent disordered regions enriched in glycine-arginine (GAR) repeats, corresponding to the IDR located at the N-terminus. Blue-shaded regions denote structured residues within the core methyltransferase domain. The GAR-rich IDR is known to mediate protein-RNA interactions, phase separation, and snoRNP assembly. Acquired from (Piovesan et al. 2025).

1.2.4. Disease Connections: FBL at the crossroads of Pathophysiology

In viral infections, FBL antagonises the ISG (Interferon Stimulated Gene) expression through IFN-I signaling (Li et al. 2022). In autoimmune disorders, particularly systemic sclerosis, FBL becomes an autoantigen, with circulating anti-U3 RNP antibodies serving as clinical biomarkers of disease severity (Arnett et al. 1996). Cleavage of FBL during heavy metal exposure e.g., mercury produces neoantigens, potentially triggering immune responses (Pollard et al. 1997).

Most significantly, FBL has emerged as a pro-oncogenic factor. It is frequently overexpressed in aggressive tumors, contributing to ribosomal hyperactivation, oncogene translation, and p53 suppression through nucleolar stress pathways (Lohrum et al. 2003; James et al. 2014; Marcel et al. 2013). Targeting FBL or its interacting pathways has shown promise in sensitizing cancer cells to DNA-damaging agents, highlighting its potential as a therapeutic target (Sun et al. 2023; Stępiński 2018; Wu et al. 2025; Saffarian et al. 2025).

1.2.5. Toward a Systems View of FBL Function

As research continues to unravel the molecular grammar of nucleolar biology, FBL stands out as a central integrator of nucleic acid chemistry, nuclear architecture, and stress signaling. Its conservation across domains of life and integration of RNA, protein, and chromatin interactions make it an ideal factor for understanding eukaryotic gene expression, organelle dynamics, and disease transformation (Bouffard et al. 2018).

This chapter synthesizes two decades of research in understanding FBL, combining insights from structural biology, cell biology, immunology, and cancer research to portray FBL not simply as a methyltransferase, but as a multifunctional node in the regulatory network that sustains nuclear and cellular function. Through its canonical and non-canonical roles, FBL exemplifies the plasticity of nucleolar proteins and highlights the nucleolus as a central stress-sensing hub, with profound implications for development, immunity, aging, and disease (Bouffard et al. 2018; Decle-Carrasco et al. 2023; Tiku et al. 2018).

1.2.6. Domain Architecture of Fibrillarin

Fibrillarin (FBL), a 321-amino acid nucleolar protein, exhibits a modular architecture comprising functionally distinct domains that cooperate to mediate its roles in rRNA processing, chromatin modification, and phase-separated compartment formation (Feric et al. 2016; Shubina et al. 2016; Saha et al. 2025). These domains reflect a finely tuned evolutionary strategy to adapt a core methyltransferase enzyme to the spatial, structural, and regulatory complexity of eukaryotic nuclei.

1.2.7. GAR Domain (8–80 aa): A Eukaryotic Innovation for Phase Separation and Regulation

The glycine–arginine-rich (GAR) domain, occupying the N-terminal portion of FBL, is an intrinsically disordered region (IDR) composed of repeated RGG (Arg-Gly-Gly) and FG (Phe-Gly) motifs. This domain is unique to eukaryotic FBL, with no equivalent present in archaeal homologs—suggesting a key innovation that accompanied the evolution of nuclear compartmentalization and increased RNA processing complexity (Rodriguez-Corona et al. 2015).

1.2.8. Functionality of GAR Domain in FBL

Phase separation: Through weak multivalent interactions—particularly π–π and cation–π interactions involving phenylalanine and arginine residues—the GAR domain drives liquid–liquid phase separation (LLPS) (Patel et al. 2015; Kato et al. 2012). This promotes condensates of FBL into the dense fibrillar component (DFC) of the nucleolus, allowing dynamic compartmentalization of early rRNA processing (Tang et al. 1998; Lin et al. 2002).

Post-translational regulation: The arginine residues within the GAR domain are substrates for protein arginine methyltransferases (PRMTs), including PRMT1 and PRMT3. These

modifications modulate nuclear import, RNA-binding affinity, and possibly the material properties of condensates, influencing both localization and enzymatic activity of FBL.

- *Functional parallels*: GAR domains are conserved in other nucleolar and nuclear proteins—such as nucleolin, coilin, and hnRNPs—which also undergo phase separation, emphasizing the evolutionary conservation of GAR-mediated interactions in the assembly of membraneless organelles (Dreyfuss et al. 1993).
- *Methyltransferase Domain (133–306 aa):* The Catalytic Core for RNA and chromatin modification (Shubina et al. 2016). The C-terminal region of FBL harbors its SAM-dependent methyltransferase domain, which is structurally conserved from archaea to humans. This domain mediates the catalytic transfer of methyl groups to RNA or protein substrates and comprises multiple functionally specialized subregions:

- *RNA-binding subdomain (133–222 aa):* This region facilitates stable interaction with box C/D small nucleolar RNAs (snoRNAs) and pre-rRNA substrates. Electrostatic and base-stacking interactions ensure specificity for target nucleotide positioning during 2′-O-methylation (Shubina et al. 2016; Yi et al. 2021).

- *SAM-binding pocket (274–306 aa):* Composed predominantly of α-helices, this subregion forms a conserved structural motif that binds S-adenosylmethionine (SAM), the universal methyl donor. The spatial orientation of SAM in the catalytic cleft positions its methyl group in proximity to the 2′-OH group of the ribose, allowing efficient catalysis (Deng et al. 2004; Watkins and Bohnsack 2012).

- *Spacer regions (Sp1 and Sp2):* These interspersed linker regions, though less conserved, contribute to subnuclear localization and may act as flexible hinges that support conformational adaptability. They also interact with snoRNP assembly factors, such as NOP56 and NOP58, and may modulate complex formation and trafficking (Snaar et al. 2000).

1.2.9. Post-Translational Regulation

Fibrillarin (FBL), as a multifunctional nucleolar protein involved in rRNA modification, chromatin regulation, and phase separation, is tightly regulated at the post-translational level

to ensure spatial and temporal precision in its actions. These modifications allow FBL to alternate between active and repressed states, regulate subnuclear localization, and respond to cues such as nutrient availability, stress, or the cell cycle phase.

1.3.7. Arginine Methylation: Modulating RNA Binding and Nucleolar Localization

The glycine–arginine-rich (GAR) domain of FBL contains multiple arginine residues that are targets for asymmetric dimethylation (aDMA) by protein arginine methyltransferases PRMT1 (Tang et al. 1998; Bedford and Clarke 2009). This modification constitutes a regulatory switch that impacts several key aspects of FBL function:

- RNA-binding affinity: Methylation alters the electrostatic charge of the individual amino acid and hydrophobicity of the GAR domain, influencing its interaction with pre-rRNA, snoRNAs, and other nucleolar RNAs. In many cases, methylation enhances affinity of FBL for structured RNAs and facilitates the formation of functional box C/D snoRNPs.

- Phase separation dynamics: Methylation can fine-tune the biophysical behavior of FBL by modulating cation–π and electrostatic interactions involved in LLPS (McIntyre et al. 2025; Qamar et al. 2018). This affects the material properties of nucleolar condensates, potentially altering visco-elastic properties of FBL in response to changing cellular demands.

Importantly, these modifications can be manipulatable to cellular signaling, making them effective tools for rapid adaptation of FBL activity during development, stress, or transformation.

1.2.10. Acetylation and Deacetylation: Tuning Histone Methylation and rDNA Transcription

Another critical layer of regulation is lysine acetylation, which modulates non-canonical role of FBL as a histone methyltransferase for H2A glutamine 104 (H2AQ104). This function is tightly coupled to the cell cycle and is orchestrated by the NAD^+-dependent deacetylase SIRT7, a key epigenetic regulator localized to the nucleolus.

- During interphase, SIRT7 is enzymatically active and maintains FBL in a deacetylated state, which is essential for its methyltransferase activity. This promotes H2AQ104me, a modification that enhances RNA polymerase I (Pol I) recruitment and rDNA transcription (Iyer-Bierhoff et al. 2018).

- In contrast, during mitosis, SIRT7 is inactivated (via post-translational modifications or sequestration), leading to the accumulation of acetylated FBL, which exhibits reduced enzymatic activity. This results in a transient loss of H2AQ104me and an effective silencing of rRNA transcription, aligning with the global shutdown of transcription during mitosis (Iyer-Bierhoff et al. 2018).

This acetylation–deacetylation cycle ensures that rRNA production is coordinated with the cell cycle, rapidly resuming biosynthetic activity upon mitotic exit.

1.2.11. Functional Integration and Crosstalk

Arginine methylation and lysine acetylation represent two orthogonal regulatory systems that modulate distinct but interconnected aspects of FBL function. There could be a probable crosstalk between these pathways. For instance, lysine acetylation (K102, K121, K205, and K20) (Iyer-Bierhoff et al. 2018) could influence GAR domain accessibility. This interplay may be particularly relevant under stress conditions, such as nutrient deprivation or DNA damage, where nucleolar reprogramming is critical for survival.

1.2.12. Clinical and Pathological Implications

- *Cancer*: Dysregulation of SIRT7 and PRMT1 have both been implicated in cancer, leading to aberrant FBL localization, enhanced rRNA synthesis, and nucleolar hypertrophy—hallmarks of aggressive tumors (Geng et al. 2015; Wei et al. 2017; Shen et al. 2024; Yan et al. 2024; Ku et al. 2024; F. Wang et al. 2023; Deng et al. 2015).

- *Aging and senescence:* Loss of SIRT7 activity with age results in persistently acetylated FBL, impaired rRNA production, and nucleolar dysfunction, contributing to senescence-associated phenotypes (Liu et al. 2020).

- *Therapeutic targeting:* Modulators of SIRT7 (Nicotinamide) activity could indirectly influence FBL function and serve as nucleolar-targeted therapies in oncology or age-related disorders (Hendrickson-Rebizant et al. 2024), (Iyer-Bierhoff et al. 2018).

1.2.13. Evolutionary Perspective

The evolutionary divergence between archaeal and eukaryotic FBL highlights the functional repertoire required to accommodate cellular complexity:

- Archaeal homologs perform 2′-O-methylation using small guide RNAs but lack the GAR domain, and phase separation is absent or rudimentary in Archaea (Shubina et al. 2016).
- The emergence of the GAR domain in eukaryotes likely coincided with the expansion of the nucleolus, specialization of ribosome biogenesis, and integration of RNA processing with nuclear organization (Shubina et al. 2020) (Fig. 1.4.).
- This structural modularity exemplifies the concept of domain accretion, where a conserved catalytic core acquires additional domains to expand its regulatory capacity, reflecting evolutionary adaptation to compartmentalized gene expression.

1.2.14. Functional Integration

Taken together, these domains confer a dual identity on FBL:

- As a catalytic enzyme, performing site-specific methylation of rRNA and histones.
- As a scaffolding and regulatory factor, enabling dynamic assembly of snoRNPs and nucleolar sub-compartments via LLPS.

This architectural integration of structure, interaction potential, and catalytic function underpins the ability of FBL to respond to stress, transcriptional demands and cell cycle cues—positioning it as a central regulator of nucleolar physiology and a target for disease intervention.

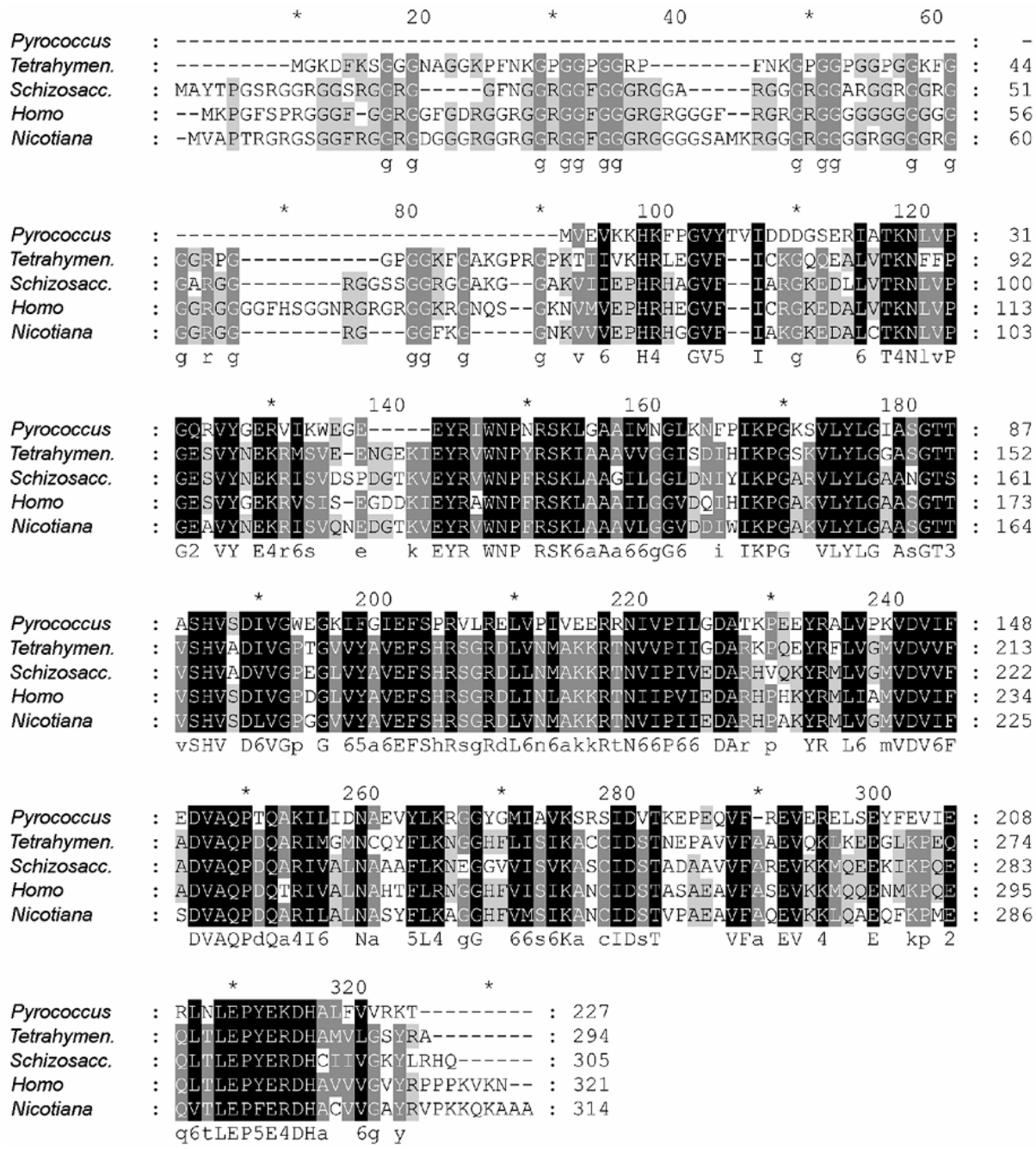

Fig. 1.4. Multiple sequence alignment of FBL

A multiple sequence alignment of fibrillarin proteins from diverse taxa—including the archaeon *Pyrococcus horikoshii*, the ciliate *Tetrahymena thermophila*, the yeast *Schizosaccharomyces pombe*, humans (*Homo sapiens*), and tobacco (*Nicotiana benthamiana*)—reveals that the RNA-binding region and α-helical core domains are highly conserved. In contrast, the glycine- and arginine-rich (GAR) domain shows substantial divergence among eukaryotes and is completely missing in archaeal fibrillarins. Adapted from (Shubina et al. 2016).

1.2.15. 2′-O-Methylation via Box C/D snoRNPs

The site-specific 2′-O-ribose methylation of pre-ribosomal RNA (pre-rRNA) - a key step in ribosome biogenesis is highly conserved. This reaction is catalyzed within a specialized ribonucleoprotein complex - box C/D small nucleolar ribonucleoprotein (snoRNP), which comprises four core proteins—FBL, NOP56, NOP58, and SNU13—along with a small nucleolar RNA (snoRNA) that provides substrate specificity.

1.2.15.1. Molecular Mechanism of Targeting and Catalysis

Each box C/D snoRNA harbours two conserved sequence motifs—box C (RUGAUGA) and box D (CUGA)—that form the structural scaffold for snoRNP assembly. The snoRNA also contains antisense elements that base-pair with complementary regions in the nascent pre-rRNA, typically spanning 10–20 nucleotides. This pairing aligns the target ribose nucleotide exactly five bases upstream of the D (or D′) box, positioning it in the active site of FBL (Erales et al. 2017).

FBL catalyzes the methyl transfer reaction, using S-adenosylmethionine (SAM) as the methyl donor, to convert the 2′-hydroxyl of the ribose sugar into a 2′-O-methyl group. This modification is non-reversible, energetically favourable, and does not alter base-pairing properties—allowing it to fine-tune rRNA structure and function without impacting the coding sequence.

Structural studies suggest that the catalytic site of FBL adopts a Rossmann-like fold, typical of Class I methyltransferases, and is evolutionarily conserved across eukaryotes and archaea. Notably, while archaeal FBL homologs perform the same function, their targeting relies on standalone guide RNAs, reflecting the conserved yet adaptable nature of this epitranscriptomic system (Wang et al. 2000; Ye et al. 2009).

1.2.15.2. Biological Consequences of 2′-O-Methylation

2′-O-methylation plays a pivotal role in rRNA maturation, folding, and function. More than 100 such modifications are introduced across the 18S, 5.8S, and 28S rRNA species in humans, with the majority concentrated in functionally critical regions such as the peptidyl transferase center (PTC) (in 28S) and the decoding site (18S) of the ribosome.

These modifications confer several advantages:

- Structural stabilization: Methylated riboses enhance the thermodynamic stability of rRNA secondary and tertiary structures by reducing the flexibility of the sugar-phosphate backbone.
- Folding efficiency: Proper folding of pre-rRNA is necessary for hierarchical assembly of ribosomal subunits. Methylation helps avoid kinetic traps and misfolded intermediates (Davis and Williamson 2017),(Woodson 2000).
- Translation fidelity: Methylation improves the accuracy of codon–anticodon pairing and reduces the risk of translational errors such as frameshifting or premature termination (Baxter-Roshek et al. 2007; Jack et al. 2011; Sloan et al. 2016; Baudin-Baillieu et al. 2009).

Disruption of FBL-mediated methylation has dramatic effects on ribosome assembly and cell viability. Previous study showed that depletion of FBL results in defective cleavage of pre-rRNA intermediates, particularly those required for generating 18S (small subunit) and 28S (large subunit) rRNAs. This leads to an imbalance in the subunit pools of 40S and 60S, severely compromising the global translation landscape and impairing cell growth (Tollervey et al. 1991).

1.2.15.3. Functional Heterogeneity and Selective Translation

Recent advances in RiboMeth-seq and Nanopore direct RNA sequencing have uncovered that 2′-O-methylation patterns are heterogeneous and context-specific. Certain methylation sites display plasticity in response to stress, differentiation signals, or oncogenic cues, suggesting that FBL can regulate specialization of ribosomal function and protein synthesis. Pervious study has demonstrated that FBL depletion mediated changes in methylation, disrupted 2′-O-methyl marks were predominantly found in translation-related regions of the ribosome, particularly surrounding the A- and P-sites, the connecting bridges between subunits, and near the peptide exit pathway (Erales et al. 2017). This dynamic regulation opens new perspectives on epitranscriptomic control of gene expression and positions FBL as a key regulator of ribosome functional diversity.

1.2.16. Ribonuclease Activity

While Fibrillarin (FBL) is traditionally recognized for its methyltransferase activity within box C/D snoRNP complexes, emerging evidence suggests it may also possess intrinsic

ribonuclease (RNase) activity, offering a dual enzymatic function in ribosome biogenesis. This unexpected finding adds a new layer to the multifunctionality of FBL in rRNA processing.

- **PI5P-Stimulated Ribonuclease Activity**

Earlier study has reported that phosphatidylinositol 5-phosphate (PI5P), a nuclear signaling lipid known to regulate chromatin structure and nucleolar stress responses, stimulates ribonuclease activity of FBL by interacting with the glycine–arginine-rich (GAR) domain. This activity was shown to promote site-specific cleavage of pre-rRNA at regions such as the 5′ external transcribed spacer (5′ ETS) - a key step in early pre-rRNA processing (Guillen-Chable et al. 2020). PI5P-mediated regulation suggests that lipid signaling pathways converge on the nucleolus, modulating the enzymatic behavior of resident factors like FBL. The GAR domain, traditionally viewed as a scaffold for phase separation and methylation targeting, thus assumes a direct catalytic role under specific cellular conditions (Rodriguez-Corona et al. 2017).

- **Regulation by U3 snoRNA: A Feedback Mechanism**

U3 snoRNA forms an extensive base-pairing interaction with the 5′ external transcribed spacer (ETS) of pre-rRNA and recruits fibrillarin as part of the box C/D snoRNP during early ribosome biogenesis. While U3 itself does not function as a methylation guide, its stable association with fibrillarin positions FBL within early processing complexes. This has led to the proposal that snoRNA binding may modulate the functional state of FBL, potentially restrict non-canonical activities while favoring its role in rRNA modification. Such functional plasticity would be consistent with the spatiotemporal coordination required for ribosomal subunit maturation (Beltrame and Tollervey 1995; Dragon et al. 2002).

- **Implications in Cellular Physiology**

This discovery provides insights into non-canonical roles of FBL in the nucleolus and reinforces the view of the nucleolus as a dynamic organelle where RNA processing, lipid signaling, and phase transitions converge. Dysregulation of RNase activity of FBL could lead to improper rRNA maturation, contributing to nucleolar stress, impaired ribosome biogenesis, and potentially to diseases such as cancer or ribosomopathies.

1.2.17. Histone Methylation

Beyond its functions in rRNA processing, FBL plays a surprising and impactful role in chromatin modification, bridging the traditionally distinct processes of epigenetic regulation and ribosome biogenesis. This is exemplified by its capacity to methylate histone H2A at glutamine 104 (H2AQ104), a unique and relatively rare post-translational modification with profound implications for nucleolar transcriptional activity.

1.2.17.1. H2AQ104 Methylation and rDNA Transcription

Previously it has been demonstrated that FBL specifically catalyzes H2AQ104me, a mark enriched at ribosomal DNA (rDNA) promoters and correlated with active transcription by RNA polymerase I (Pol I). This modification creates a chromatin environment conducive to rDNA accessibility, Pol I recruitment, and efficient transcription of 47S pre-rRNA.

This activity links FBL directly to epigenetic control of ribosome production, positioning it not only as an RNA-modifying enzyme but also as an epigenetic writer. It highlights how nucleolar proteins can modify histones to regulate nuclear architecture and transcriptional output (Tessarz et al. 2014).

1.2.17.2. Cell Cycle–Dependent Regulation via SIRT7

The methylation of H2AQ104 is tightly regulated by SIRT7, a nucleolar NAD^+-dependent deacetylase. During interphase, SIRT7 is active, maintaining FBL in a deacetylated, catalytically active state, thereby sustaining H2AQ104me and rDNA transcription. However, during mitosis, SIRT7 is inactivated, leading to hyperacetylation of FBL. This acetylated form of FBL exhibits reduced methyltransferase activity, resulting in the loss of H2AQ104me and a temporary shutdown of rDNA transcription (Tessarz et al. 2014).

This mechanism functions as a cell cycle checkpoint, ensuring that rRNA synthesis is silenced during mitosis when chromatin is condensed and nucleolar function is suspended. Post-mitotically, as SIRT7 is reactivated, FBL is deacetylated and H2AQ104me is reestablished, allowing for nucleolar reassembly and transcriptional reactivation.

1.2.17.3. Broader Implications for Chromatin and Transcription

The discovery of H2AQ104me challenges conventional paradigms of chromatin regulation, as it introduces a non-lysine methylation site on histones that links nucleolar function with the broader nuclear epigenetic landscape. It also illustrates the emerging theme of multifunctionality in nucleolar proteins, which do not merely execute structural or processing roles but actively participate in gene expression control.

Given the importance of rRNA synthesis in supporting cell growth and protein production, dysregulation histone methylation activity of FBL could impact proliferative capacity, and may contribute to oncogenesis, particularly in tumors with nucleolar hypertrophy or SIRT7 overexpression.

1.2.18. GAR Domain-Driven Liquid–Liquid Phase Separation (LLPS)

Fibrillarin (FBL) is a critical component of the dense fibrillar component (DFC) of the nucleolus, where it orchestrates early pre-rRNA processing and ribonucleoprotein assembly. A key feature enabling this function is its glycine–arginine-rich (GAR) domain, an intrinsically disordered region (IDR) unique to the FBL found in eukaryotic, which facilitates liquid–liquid phase separation (LLPS)—a biophysical mechanism by which biomolecules demix from the nucleoplasm to form membraneless organelles, such as the nucleolus (Kim and Kwon 2021), (Shubina et al. 2020), (Y.-C. Wang et al. 2023)

1.2.18.1. Multivalent Interactions via Aromatic Residues

The GAR domain of fibrillarin is enriched in RGG repeats interspersed with aromatic residues, including phenylalanine. In other RGG-containing RNA-binding proteins, such aromatic residues act as ‘stickers’ that mediate weak π–π and cation–π interactions, which are critical for multivalent self-association and liquid–liquid phase separation. Based on these principles, phenylalanine residues within the FBL GAR domain are likely to contribute to its condensate-forming potential, although direct mutational analyses in fibrillarin remain to be performed (Kim and Kwon 2021; Thandapani et al. 2013; Alberti et al. 2019; Calinsky and Levy 2024).

This suggests that condensates of FBL are not merely a passive consequence of its concentration in the nucleolus, but an active, sequence-encoded phenomenon, finely tuned by evolutionary pressure to support compartmentalized ribosome biogenesis.

1.4.2. RNA Scaffolding and Directional Condensation

In addition to protein–protein interactions, RNA molecules act as critical scaffolds for phase separation. Earlier study has showed that nascent pre-rRNA, transcribed from rDNA loci by RNA polymerase I, interacts with the GAR domain and templates nucleolar condensate formation. These RNAs serve as "valency enhancers," increasing interaction sites and enabling directional recruitment of FBL to sites of active rRNA synthesis (Yao et al. 2019).

Liquid–liquid phase separation (LLPS) underlies the multiphase organization of the nucleolus into the fibrillar center (FC), dense fibrillar component (DFC) and granular component (GC). In this architecture, fibrillarin (FBL) is highly enriched in the DFC at the FC/DFC border, spatially coupling rDNA transcription in the FC to co-transcriptional pre-rRNA modification and early processing within the DFC, before later assembly steps in the GC (Feric et al. 2016)'(Guillen-Chable et al. 2020). Biomolecular condensates formed by LLPS behave as selective compartments or 'molecular sieves' that enrich specific RNAs and processing enzymes while excluding non-clients or inhibitory factors, and the nucleolus is a canonical example of such selective partitioning (Altmeyer et al. 2015; Banani et al. 2017; Correll et al. 2019; Li et al. 2023).

1.2.18.2. LLPS as a Therapeutic Target

Understanding the phase behavior and interpretations of the biophysical basis of FBL opens avenues for novel therapeutic interventions. Small molecules or peptides that modulate LLPS—either by stabilizing or disrupting FBL condensates—could serve as targeted treatments in cancers or viral infections that exploit nucleolar dysfunction. Moreover, post-translational modifications such as arginine methylation by PRMTs may act as modulators of LLPS, offering another axis for intervention.

1.2.19. Mitotic Reorganization

As cells progress through the cell cycle, particularly during mitosis, the nucleolus disassembles and its components undergo dynamic relocalization. Unlike membranous

organelles, the nucleolus is a phase-separated condensate, and its disassembly is not mediated by vesicular fragmentation but rather by the dissolution and redistribution of its molecular constituents. Fibrillarin (FBL), a core nucleolar protein, plays a crucial role in nucleolar reassembly after mitosis and participates in the transient reorganization of nucleolar structures during cell division.

1.2.20. Association of FBL with Perichromosomal Layers

During prophase and metaphase, transcription ceases and chromatin condenses, FBL redistributes from the Dense Fibrillar Component (DFC) to form a layer surrounding mitotic chromosomes - perichromosomal layer. This structure acts as a scaffold for nucleolar proteins, ribosomal RNAs, and processing factors. FBL colocalizes with key components such as nucleophosmin (NPM1) and nuclear matrix proteins, including Ki-67, which collectively protect chromatin integrity and ensure the faithful transmission of epigenetic and ribosome biogenesis machinery to daughter cells (Bekers et al. 1986; Dubois and Boisvert 2016; Hernandez-Verdun 2011; Dundr et al. 2000; Savino et al. 2001).

Early studies demonstrated that fibrillarin, together with other rRNA processing factors, redistributes to coat metaphase chromosomes in a distinct perichromosomal layer that is enzymatically inactive during mitosis but strategically positioned for rapid post-mitotic nucleologenesis (Gautier et al. 1992; Van Hooser et al. 2005).

1.2.21. Formation of Nucleolus-Derived Foci (NDFs)

As cells transition into anaphase and telophase, FBL is detected in Nucleolus-Derived Foci (NDFs)—small, punctate structures dispersed in the cytoplasm and nuclear periphery. These foci store and protect nucleolar components until the nuclear envelope reforms and transcription resumes. NDFs act as precursors to pre-nucleolar bodies (PNBs), which later merge at rDNA loci to reconstitute a functional nucleolus in early G1 phase [78,81,83].

This stepwise reassembly involves:

- Re-engagement of RNA Polymerase I at rDNA loci
- Reformation of the fibrillar center (FC), dense fibrillar component (DFC), and granular component (GC)

- Sequential recruitment of nucleolar proteins, with FBL among the earliest to relocalize.

1.2.22. Functional Significance and Regulatory Mechanisms

The mitotic cycling of FBL is tightly regulated and reflects its essential role in cellular recovery post-division (Hernandez-Verdun 2011). By remaining associated with chromosomal surfaces and forming NDFs, FBL ensures:

- Rapid resumption of rRNA transcription
- Efficient assembly of snoRNP complexes
- Restoration of ribosome production capacity, which is critical for cell growth and proliferation

Disruptions in this dynamic behavior—such as mutations impairing LLPS or improper post-translational modification—can delay or prevent nucleolar reassembly, resulting in cell cycle arrest, nucleolar stress, or transcriptional silencing of rDNA (Leung et al. 2004).

Furthermore, the temporal and spatial choreography of FBL during mitosis is conserved across species, underscoring its evolutionarily stable role in coordinating nucleolar continuity through successive generations.

1.2.23. Implications in Disease and Therapeutic Targeting

Given the importance of mitotic nucleolar reorganization in maintaining genomic stability and protein synthesis, defects in this process have been implicated in cancer and aging-related disorders. For example:

- Cancer cells often exhibit nucleolar hypertrophy and aberrant mitotic nucleolar dynamics.
- Targeting redistribution of FBL or reassembly function could sensitize dividing tumor cells to anti-mitotic agents or rRNA synthesis inhibitors.
- Future studies examining how post-translational modifications (e.g., phosphorylation or acetylation) govern the mitotic transition of FBL may provide new therapeutic insights into cell-cycle–specific drug targeting.

1.2.24. Viral Pathogenesis

FBL has emerged as a key host factor that is hijacked by various viruses to support their replication, protein synthesis, and subcellular trafficking. Its involvement in ribosome biogenesis, nucleolar structure, and RNA processing makes it an attractive target for viral manipulation.

Henipaviruses (HeV and NiV)

Genome-wide RNA interference (RNAi) screens in mammalian cells infected with Henipaviruses, including Hendra virus (HeV) and Nipah virus (NiV), have identified FBL as an essential host factor required for viral replication (Deffrasnes et al. 2016). These paramyxoviruses depend on host machinery to replicate their negative-sense single-stranded RNA genome, and the study revealed that FBL knockdown severely impairs viral RNA synthesis. The mechanistic basis appears to involve interaction of FBL with viral RNA polymerase complexes or its contribution to host translational machinery, which may be co-opted for selective translation of viral mRNAs (Hiscox 2007; Emmott and Hiscox 2009).

Moreover, nucleolar proteins like FBL may act as scaffolds for assembling viral ribonucleoprotein complexes, facilitating efficient nuclear-cytoplasmic transport of viral RNA or proteins. Given the high pathogenicity and zoonotic potential of Henipaviruses, targeting host factors like FBL offers a novel avenue for antiviral intervention (Salvetti and Greco 2014).

SARS-CoV-2

During the COVID-19 pandemic, emerging research has highlighted a potential interaction between FBL and the SARS-CoV-2 nucleocapsid (N) protein, which localizes to the nucleolus in infected cells. The N protein is a multifunctional RNA-binding protein involved in viral genome packaging, replication, and host manipulation. Studies suggest that N protein binds to nucleolar proteins including FBL, possibly sequestering or dysregulating it, thereby interfering with rRNA processing and ribosome production (Li et al. 2022; Decle-Carrasco et al. 2023; Yerlici et al. 2024).

Disruption of nucleolar homeostasis by SARS-CoV-2 may serve to reprogram host translation in favor of viral protein synthesis while attenuating host stress responses and antiviral immunity. Given centrality of FBL in nucleolar function, its interaction with viral components such as N protein could be a critical node in the SARS-CoV-2 replication cycle (Thoms et al. 2020).

Plant Viruses: PVX and RSV

The role of FBL in viral pathogenesis also extends to the plant kingdom. Potato virus X (PVX) and Rice stripe virus (RSV) encode viral movement proteins (MPs) that directly interact with the GAR domain of FBL, enabling their intercellular transport through plasmodesmata (Chang et al. 2016)·(Zhang et al. 2024)·(Kim et al. 2007). This interaction facilitates the assembly of viral movement complexes that leverage host nuclear and nucleolar machinery for long-distance trafficking of viral RNAs (Wang et al. 2010).

These findings underscore the evolutionarily conserved strategy of targeting FBL by both animal and plant viruses. The reliance on LLPS properties of FBL and RNA-binding capacity highlights its function as a molecular "hub" for diverse host-pathogen interactions. It also raises the possibility that FBL-targeted interventions may offer broad-spectrum antiviral strategies.

1.2.25. Role of FBL in Cancer

FBL is frequently upregulated in a variety of malignancies, including breast, colorectal, prostate, and pancreatic cancers, and its expression often correlates with poor prognosis, increased tumor grade, and enhanced metastatic potential. Mechanistically, FBL contributes to cancer development and progression through multiple interconnected pathways.

1.2.25.1. Ribosome Hyperactivation and Oncogenic Translation

FBL overexpression leads to ribosome biogenesis hyperactivation, a hallmark of rapidly proliferating cancer cells. Earlier it was demonstrated that elevated FBL levels enhance the 2′-O-methylation landscape of rRNA, altering ribosome specificity and fidelity (Zhang et al. 2024). This results in a selective advantage for the translation of structured 5′UTR-containing mRNAs, notably those encoding oncogenes with internal ribosome entry sites (IRESs) such

as MYC, VEGFA, and PIK3CA (Marcel et al. 2013). These IRES-dependent transcripts are typically repressed under normal growth conditions, but FBL-driven ribosome reprogramming permits their sustained translation even during cellular stress, supporting malignant transformation and growth. Moreover, polysome profiling and ribosome footprinting analyses in FBL-overexpressing cancer models revealed a preferential translation of pro-proliferative and anti-apoptotic factors, reinforcing the concept that FBL can fine-tune the translatome to favor tumorigenesis (Wu et al. 2025).

1.2.25.2. Nucleolar Stress and p53 Suppression

Under normal conditions, nucleolar perturbation induces nucleolar stress, leading to the stabilization of p53 via the ribosomal protein (RPL5/RPL11)–MDM2 axis. Marcel et al. (2013) showed that silencing FBL triggers such nucleolar stress by disrupting pre-rRNA processing and snoRNP function, which in turn results in the accumulation of free ribosomal proteins (Marcel et al. 2013). These proteins bind and inhibit MDM2, preventing it from targeting p53 for degradation.

In cancer cells with wild-type TP53, the FBL-dependent pathway is critical: high FBL expression suppresses the p53 checkpoint, promoting unchecked proliferation. Conversely, FBL knockdown reactivates p53 signaling, resulting in cell cycle arrest, senescence, or apoptosis, depending on the TP53 genetic and epigenetic background. This function links ribosome biogenesis directly to the tumor suppressor network provides a mechanistic explanation for why nucleolar proteins like FBL are tightly regulated in normal cells but deregulated in cancer [1–3](Marcel et al. 2013).

1.2.25.3. Therapeutic Vulnerability and Chemosensitization

Given its integral role in ribosome assembly and tumor growth, fibrillarin has emerged as a potential therapeutic vulnerability within the ribosome biogenesis pathway. Studies in pancreatic ductal adenocarcinoma models have shown that inhibition of ribosome biogenesis and nucleolar function—particularly through targeting RNA polymerase I transcription—synergizes with DNA-damaging chemotherapeutics such as gemcitabine and oxaliplatin. Because fibrillarin operates at the core of rRNA synthesis and nucleolar organization, disruption of FBL-dependent processes is likely to contribute to the nucleolar stress responses that sensitize tumor cells to genotoxic therapy, although direct targeting of FBL itself remains to be explored. This synergy arises from the induction of nucleolar stress, which not only

slows ribosome biogenesis but also reactivates p53-mediated DNA damage responses. In addition, tumors with upregulated FBL show increased dependency on nucleolar homeostasis, making them selectively vulnerable to nucleolar disruption. This "non-oncogene addiction" offers a promising therapeutic window where normal cells are spared, but cancer cells undergo catastrophic failure due to their reliance on hyperactive ribosome production (Boulon et al. 2010; Bywater et al. 2012, 53).

1.2.25.4. Domain-wise analysis of FBL in cancer

The analysis of FBL (fibrillarin) mutations through the lollipop plot and accompanying mutation table reveals critical insights into the molecular alterations of this essential ribosome biogenesis factor across multiple cancer types. The lollipop plot demonstrates distinct mutational hotspots clustered in functionally significant domains, with recurrent N-terminal mutations (R24C, G26S, G25*) (Fig. 1.5.) prevalent in cutaneous melanoma that likely disrupt the RNA-binding domain crucial for rRNA processing. Meanwhile, central domain mutations (P212L, D216N, R218Q) in melanoma and breast cancer localize near the methyltransferase active site, potentially impairing enzymatic activity, while C-terminal variants (K320N) may interfere with protein-protein interactions or nucleolar localization. Notably, truncating mutations (I132Lfs*13, R15*) in colorectal and lung cancers generate premature stop codons predicted to trigger nonsense-mediated decay, representing complete loss-of-function events. The mutation spectrum varies significantly by tissue type, with melanoma showing a predominance of N-terminal missense mutations, colorectal cancers exhibiting diverse frameshift and nonsense mutations, and breast cancer displaying specific substitutions (R218Q) adjacent to nuclear localization signals. These mutational patterns correlate with multifaceted roles of FBL in ribosomal RNA methylation, nucleolar integrity maintenance, and cellular stress responses. These findings position FBL as both a potential biomarker for specific cancer subtypes and a candidate therapeutic target, particularly for tumors harboring methyltransferase domain mutations that might sensitize cells to ribosome-directed therapies or nucleolar stress-inducing agents. Future studies will functionally characterize these mutants to determine their impact on ribosome assembly kinetics, interactions with oncogenic signaling pathways, and potential as predictors of response to emerging RNA-modulating therapeutics. The mutational landscape presented here underscores the importance of considering both domain-specific effects and tissue context when evaluating the clinical relevance of ribosome biogenesis factors in cancer pathogenesis.

A

Sample ID	Cancer Type	Cancer Type Detailed	Protein Change
MO_1146	Melanoma	Cutaneous Melanoma	R24C
CR1509_T	Melanoma	Cutaneous Melanoma	G26S
MEL-IPI_Pat110-Tumor-SM-4CU6X	Melanoma	Cutaneous Melanoma	P212L
SP9433	Breast Cancer	Breast Invasive Ductal Carcinoma	R218Q
SP19215	Colorectal Cancer	Colorectal Adenocarcinoma	I132Lfs*13
SP20993	Colorectal Cancer	Colorectal Adenocarcinoma	G32R
SP18121	Colorectal Cancer	Colorectal Adenocarcinoma	R15*
SP17905	Colorectal Cancer	Mucinous Adenocarcinoma of the Colon and Rectum	K320N
SP124334	Melanoma	Melanoma	D216N
SP53810	Lung Cancer	Lung Adenocarcinoma	G25*

B

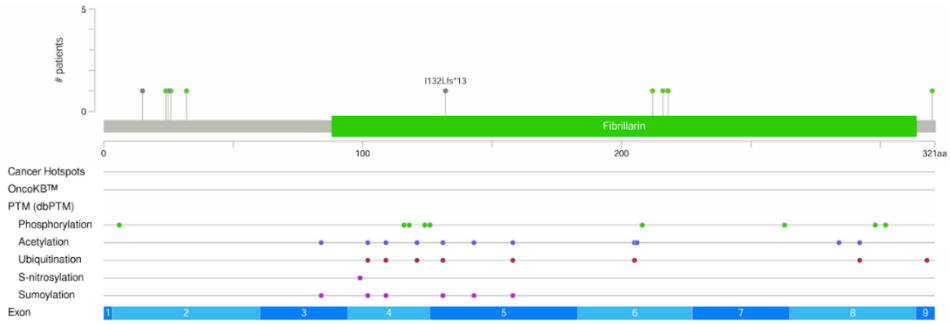

Fig. 1.5. Somatic mutations and post-translational modifications (PTMs) associated with human Fibrillarin (FBL) in cancer

(A) Table summarizing cancer patient samples harboring FBL alterations, including cancer type, specific subtype, and corresponding protein-level changes. **(B)** Lollipop plot displaying the distribution of FBL mutations across the protein sequence. Each dot represents the number of patients in which a specific mutation was identified. Most mutations are dispersed along the coding region, including within the conserved catalytic domain. Mapping of experimentally validated and predicted post-translational modifications (PTMs) on FBL, including phosphorylation (green), acetylation (blue), ubiquitination (red), S-nitrosylation (purple), and sumoylation (pink). Exon structure is shown at the bottom for reference, with exons 1–9 color-coded. The domain architecture highlights the core fibrillarin methyltransferase region, with mutation sites and PTMs positioned relative to residue number (Cerami et al. 2012; Gao et al. 2013; de Bruijn et al. 2023).

1.2.26. Functional study of FBL interactors

The functional enrichment analysis of biological processes from the interactors of FBL on ShinyGO (Ge et al. 2020) and BioGRID (Oughtred et al. 2021), revealed a strong association

with chromosome organization, cell cycle regulation, and metabolic control mechanisms (Fig. 1.6.). Highly significant terms included negative regulation of cellular biosynthetic processes and protein modification pathways, with exceptionally low false discovery rates (FDR < 1e-30). These findings suggest the studied gene set plays a central role in maintaining genomic stability and controlling fundamental cellular processes. The prominence of protein metabolic regulation and macromolecule modification highlights potential connections to disease mechanisms, particularly in conditions like cancer where these pathways are frequently dysregulated.

Analysis of cellular components demonstrated significant enrichment in nuclear structures, particularly the nucleolus and ribonucleoprotein complexes. The methyltransferase complex showed particularly high fold enrichment, supported by robust statistical significance (-log10(FDR) ≈ 50). Other notable components included ubiquitin ligase complexes and chromosomal binding factors, indicating important roles in epigenetic regulation and protein degradation pathways. These results align well with known cellular functions in RNA processing and genome maintenance, suggesting these cellular locales as potential hotspots for further mechanistic studies.

Molecular function analysis identified RNA binding and nucleic acid interactions as the most enriched categories, with transcription factor binding and enzyme regulatory activities also showing strong statistical support. The presence of specific binding functions like kinase binding and ubiquitin-like protein ligase binding points to intricate involvement in signal transduction and protein turnover networks. The high significance of these terms (up to -log10(FDR) ≈ 35) underscores their biological relevance and potential as intervention points for therapeutic development.

KEGG pathway analysis revealed significant enrichment in cancer-related pathways, with ubiquitin-mediated proteolysis and ribosome biogenesis emerging as top hits (Fig. 1.6.A.). Multiple cancer-specific pathways showed notable representation, including breast cancer, glioma, and transcriptional mis-regulation in cancer, all with highly significant FDR values ($< 10^{-8}$). The concurrent enrichment of spliceosome and ErbB signaling pathways suggests potential interplay between RNA processing and oncogenic signaling networks. These pathway associations provide compelling evidence for the studied involvement of gene set in malignant transformation and progression.

Taken together, these enrichment analyses paint a coherent picture of biological systems centered on genome regulation, protein homeostasis, and cancer pathogenesis. The consistent appearance of ribosome biogenesis components across multiple categories suggests it may represent a critical node in the studied biological context. Similarly, the recurring theme of ubiquitin-related processes in both molecular functions and pathways indicate their potential as high-value therapeutic targets. These findings provide a strong foundation for further mechanistic investigations into these fundamental biological processes and their disease associations.

A

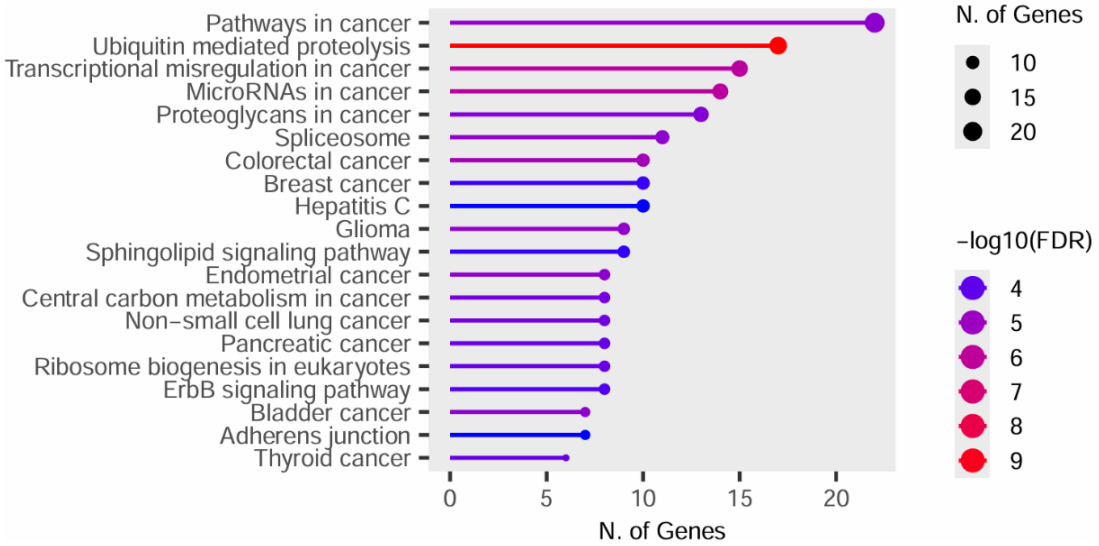
Pathways in cancer
Ubiquitin mediated proteolysis
Transcriptional misregulation in cancer
MicroRNAs in cancer
Proteoglycans in cancer
Spliceosome
Colorectal cancer
Breast cancer
Hepatitis C
Glioma
Sphingolipid signaling pathway
Endometrial cancer
Central carbon metabolism in cancer
Non−small cell lung cancer
Pancreatic cancer
Ribosome biogenesis in eukaryotes
ErbB signaling pathway
Bladder cancer
Adherens junction
Thyroid cancer
0
5
10
15
20
N. of Genes
N. of Genes
10
15
20
−log10(FDR)
4
5
6
7
8
9

B

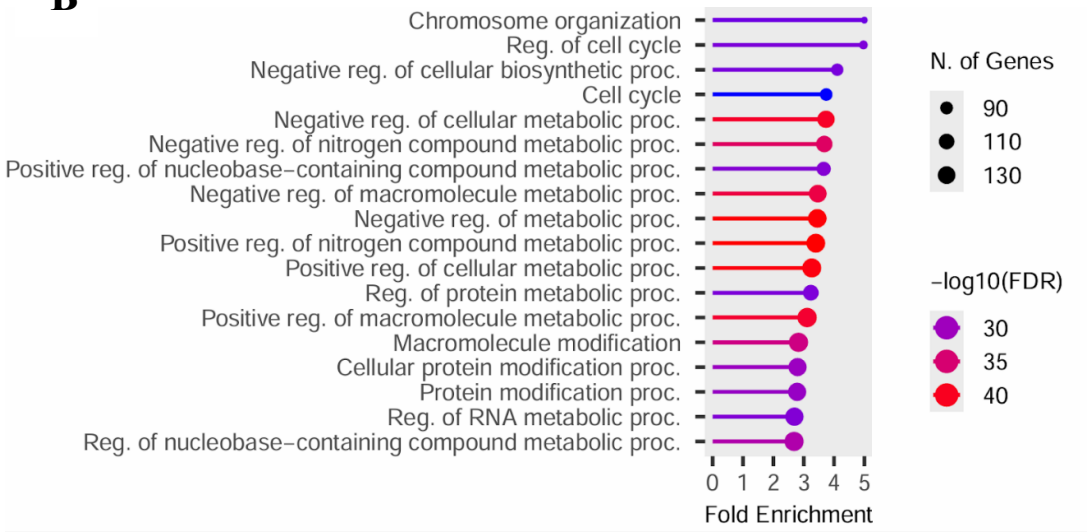
Chromosome organization
Reg. of cell cycle
Negative reg. of cellular biosynthetic proc.
Cell cycle
Negative reg. of cellular metabolic proc.
Negative reg. of nitrogen compound metabolic proc.
Positive reg. of nucleobase−containing compound metabolic proc.
Negative reg. of macromolecule metabolic proc.
Negative reg. of metabolic proc.
Positive reg. of nitrogen compound metabolic proc.
Positive reg. of cellular metabolic proc.
Reg. of protein metabolic proc.
Positive reg. of macromolecule metabolic proc.
Macromolecule modification
Cellular protein modification proc.
Protein modification proc.
Reg. of RNA metabolic proc.
Reg. of nucleobase−containing compound metabolic proc.
0
1
2
3
4
5
Fold Enrichment
N. of Genes
90
110
130
−log10(FDR)
30
35
40

C

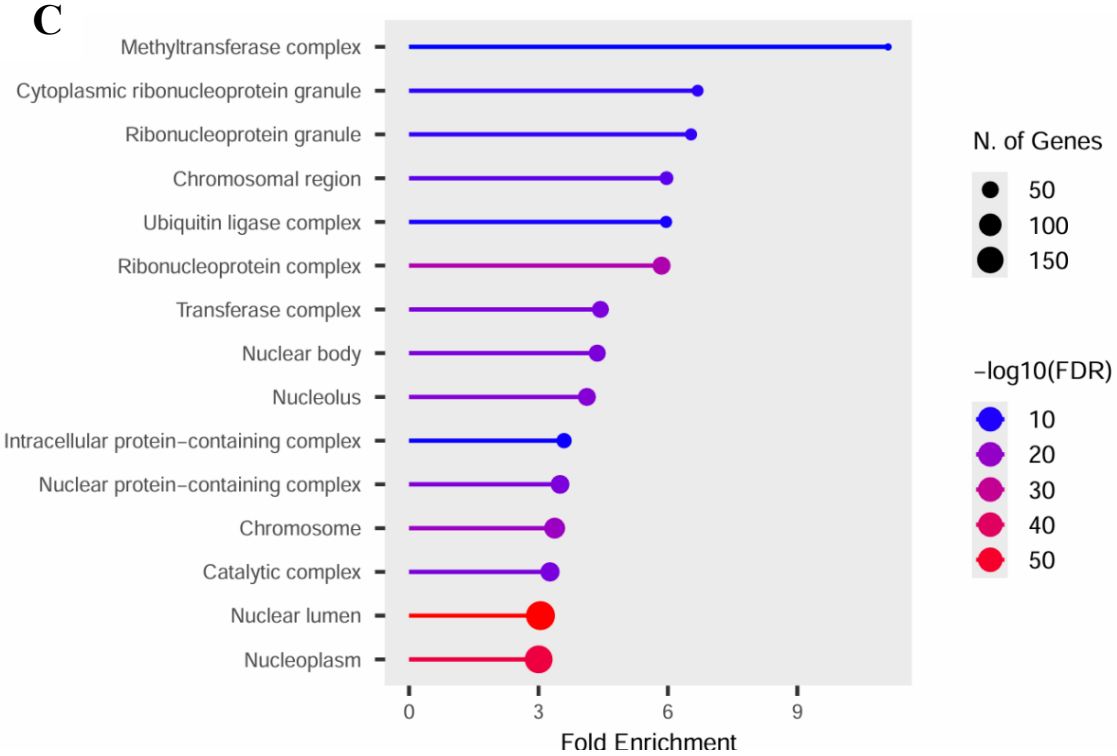
Methyltransferase complex
Cytoplasmic ribonucleoprotein granule
Ribonucleoprotein granule
Chromosomal region
Ubiquitin ligase complex
Ribonucleoprotein complex
Transferase complex
Nuclear body
Nucleolus
Intracellular protein−containing complex
Nuclear protein−containing complex
Chromosome
Catalytic complex
Nuclear lumen
Nucleoplasm
0
3
6
9
Fold Enrichment
N. of Genes
50
100
150
−log10(FDR)
10
20
30
40
50

D

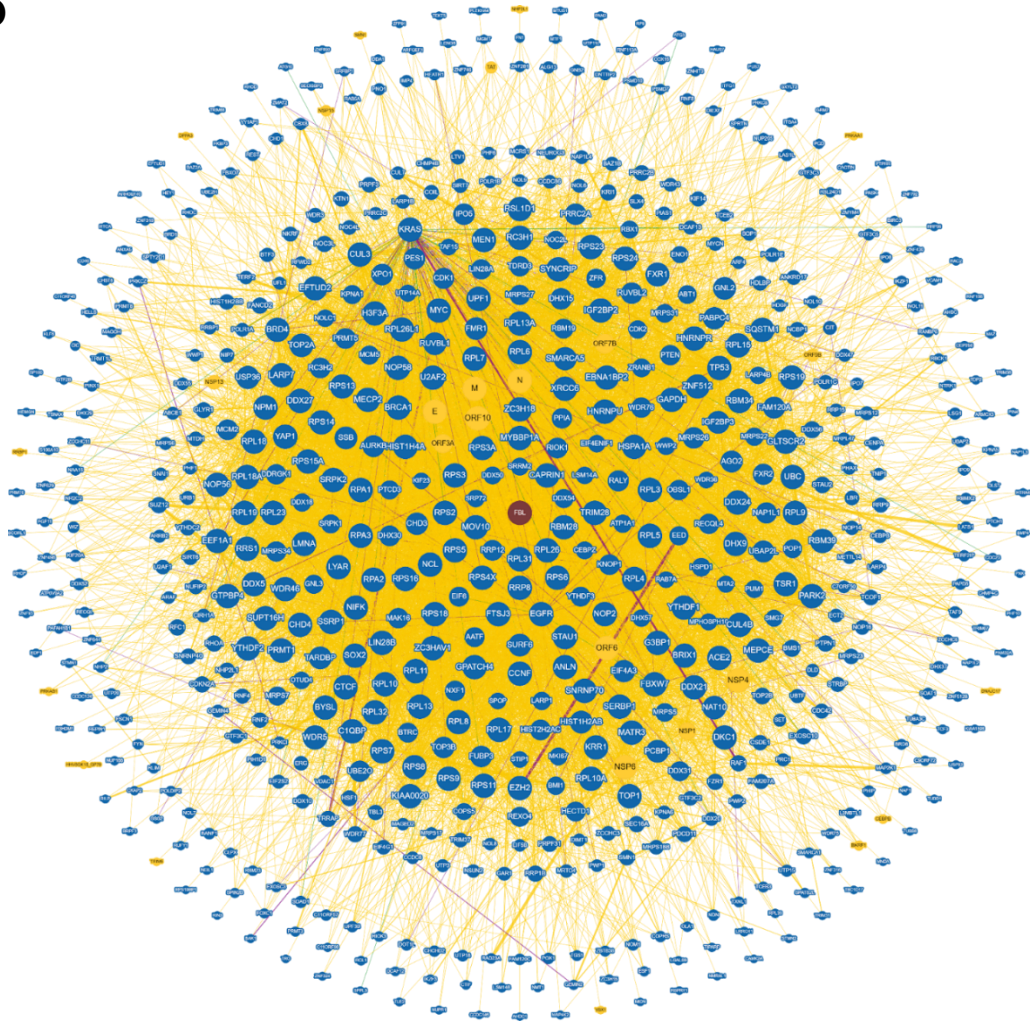

Fig. 1.6. Functional enrichment analysis of the differentially expressed gene set

(A) KEGG pathway enrichment highlighting major cancer-related pathways. Bubble size represents the number of genes and color indicates significance (–log10 FDR). Enriched pathways predominantly include cell cycle–associated, chromatin regulatory, metabolic and biosynthetic processes relevant to tumorbiology. **(B)** GO Cellular Component (CC) enrichment showing over-represented structural compartments such as methyltransferase and ribonucleoprotein complexes, nucleolus/nuclear body, chromosomal regions, and nucleoplasm, consistent with strong nuclear/chromatin involvement. **(C)** GO Molecular Function (MF) enrichment illustrating dominant functional categories including nucleic acid/RNA binding, enzyme and chromatin binding, transcription factor/co-regulator activity, kinase/transferase interactions, and other regulatory protein functions. In all panels, bubble size corresponds to gene count, and color scale represents enrichment significance (–log10 FDR). **(D)** Protein–protein interaction network centered around Fibrillarin (FBL) generated using BioGRID. Nodes represent proteins and edges indicate reported physical interactions with FBL or between FBL-associated proteins. The dense core highlights highly interconnected partners involved in ribosome biogenesis, RNA processing, nucleolar function, chromatin regulation, and transcriptional control, indicating interaction of FBL within the nucleus. Peripheral nodes represent lower-degree interactors linked to diverse regulatory pathways.

1.2.27. FBL as cancer biomarker

Fibrillarin (FBL; ENSG00000105202) represents a critical ribosome biogenesis factor whose dysregulation has been implicated in oncogenesis. Analysis of The Cancer Genome Atlas (TCGA) data for kidney renal clear cell carcinoma (KIRC) through the Human Protein Atlas (Uhlén et al. 2015) reveals significant alterations in FBL expression patterns between malignant and normal renal tissues. The dataset demonstrates a statistically significant ($p<0.05$) overexpression of FBL mRNA in KIRC specimens compared to adjacent normal tissue, suggesting a potential role in renal carcinogenesis. Kaplan-Meier survival analysis on GEPIA2 (Tang et al. 2019) indicates that elevated FBL expression correlates with reduced overall survival (log-rank $p=0.01$; HR=1.4, 95% CI 1.1-1.8), establishing its prognostic value in this malignancy (Fig. 1.7.B-C). Immunohistochemical validation confirms predominant nucleolar localization of FBL protein in tumor cells, with staining intensity positively associated with advanced tumor stage ($p=0.003$) and higher histological grade ($p=0.007$).

These clinical observations align with the molecular function of FBL in ribosomal RNA processing and its recently recognized role in stabilizing oncogenic protein synthesis machinery. The consistent overexpression across 85% of KIRC cases (n=537) and significant correlation with poor clinical outcomes position FBL as both a potential diagnostic biomarker and therapeutic target in renal cell carcinoma. These findings contribute to the growing understanding of nucleolar stress responses in cancer biology and suggest that targeting ribosome biogenesis pathways may represent a viable therapeutic strategy for KIRC patients with FBL-overexpressing tumors. Further investigation is warranted to elucidate the precise mechanisms by which FBL contributes to renal cancer progression and to evaluate its utility in clinical decision-making.

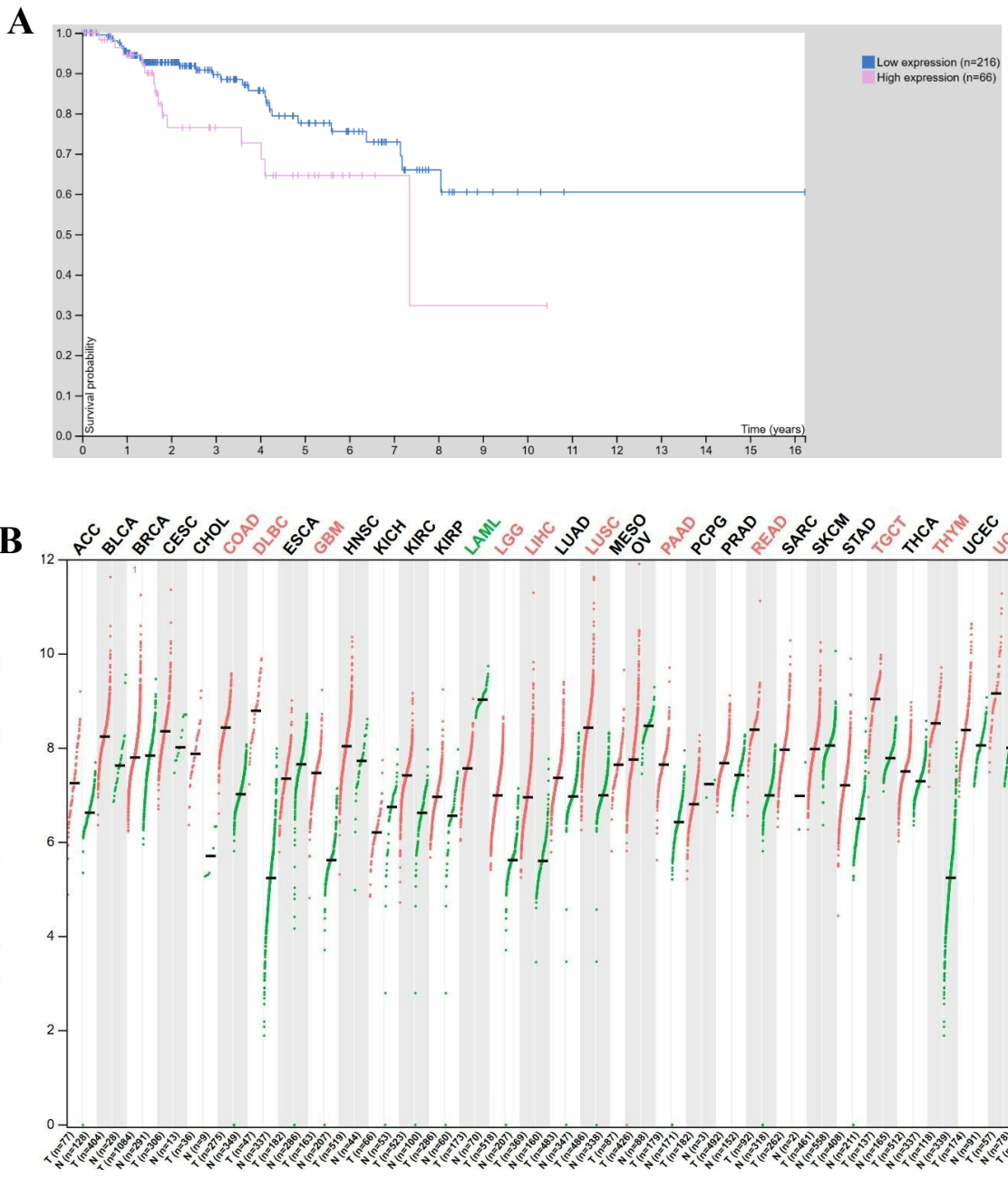

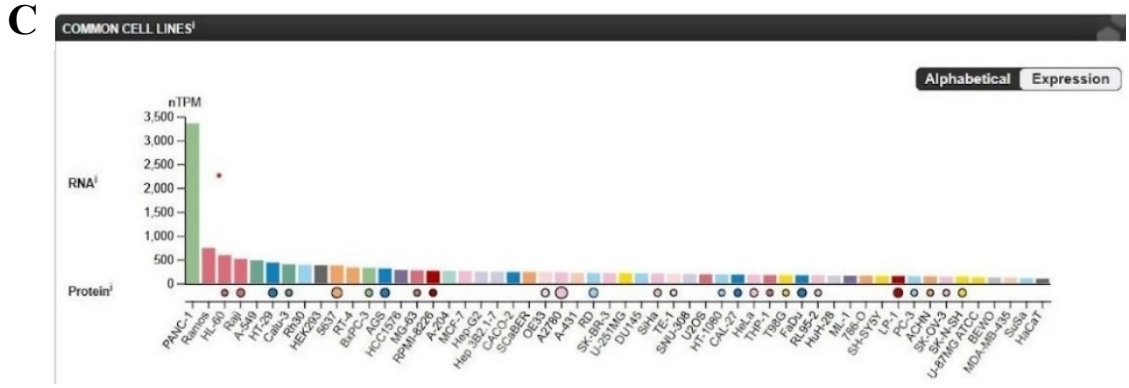

Fig. 1.7. Clinical relevance and expression landscape of FBL across cancers and cell lines **(A)** Kaplan–Meier curves comparing overall survival between high FBL expression (n=66) and low FBL expression (n=216) groups. Patients with high FBL expression show significantly reduced survival probability over time relative to the low-expression group, indicating that FBL upregulation correlates with poorer clinical outcome. Tick marks indicate censored events. **(B)** Dot plot representing FBL expression (TPM) in tumor (red) and corresponding normal tissues (green) across multiple cancer types. Each dot denotes an individual sample, with horizontal bars indicating mean ± variability. FBL is consistently upregulated in several tumor types compared to normal tissues, suggesting its potential oncogenic relevance across cancers. **(C)** Histogram plot showing RNA expression levels (TPM) of FBL across multiple human cell lines obtained from the Human Protein Atlas (HPA). FBL shows broad and high expression across diverse cell line types, with particularly elevated levels in select cancer-derived lines, reflecting its essential role in ribosome biogenesis and nucleolar function.

1.2.28. FBL expression across tissues

The pan-tissue analysis of fibrillarin (FBL) expression, quantified through normalized transcripts per million (nTPM), demonstrates a conserved yet variable expression profile across human tissues, reflecting its fundamental role in ribosome biogenesis (Uhlén et al. 2015). Tissues with high proliferative capacity and metabolic demand—including liver, hematopoietic cells, and glandular epithelia- exhibit robust FBL expression (nTPM range: 150–250), consistent with elevated ribosomal requirements (Sloan et al. 2016)(Fig. 1.8). In contrast, terminally differentiated tissues such as skeletal muscle and neurons show markedly

lower expression (nTPM < 50), aligning with their reduced protein synthesis activity. Notably, tissues prone to oncogenic transformation (e.g., colorectal and breast epithelia) display intermediate to high baseline FBL levels, suggesting a potential permissive role for FBL dysregulation in tumorigenesis (Marcel et al. 2013). The observed heterogeneity implies tissue-specific regulatory mechanisms, possibly mediated by MYC-driven transcription (van Riggelen et al. 2010), which may influence susceptibility to FBL-targeted therapies. These findings underscore the importance of contextualizing oncogenic contributions of FBL within the framework of native expression patterns, as both overexpression and haploinsufficiency could drive distinct pathogenic mechanisms depending on the tissue of origin (Pelletier et al. 2018). The ubiquitous but variable nature of FBL expression further highlights its dual role as both a housekeeping gene and a context-dependent modulator of cellular proliferation (Penzo et al. 2019).

The disease-free survival (DFS) analysis comparing low and high FBL (Fibrillarin) TPM (Transcripts Per Million) expression groups revealed no significant difference in outcomes, as demonstrated by nearly identical survival curves (log-rank p=0.58) and a hazard ratio of 1 (p=0.58) for the high-FBL group (Fig 1.7.A). This suggests that in this particular cohort, FBL transcript levels alone do not predict disease recurrence. However, these findings contrast with results from (Nguyen Van Long et al. 2022), which identified low fibrillarin protein expression as an independent poor prognostic marker in breast cancer. This discrepancy may arise from key biological and methodological differences: (1) protein versus RNA-level measurements of FBL, as post-transcriptional regulation may critically impact role of fibrillarin (2) distinct clinical endpoints (overall survival versus disease-free survival); or (3) differences in cohort characteristics such as cancer subtypes or treatment regimens. Previous study specifically highlights role of fibrillarin in ribosome biogenesis and its potential as a therapeutic target in aggressive breast cancer subtypes (Nguyen Van Long et al. 2022). These divergent results underscore the complexity of biomarker validation across molecular layers (RNA/protein) and clinical contexts. Future studies should investigate whether integrating FBL transcript levels with protein expression data or specific genetic backgrounds could yield more robust prognostic models, particularly in defined breast cancer subgroups. The current analysis, while negative, provides an important counterpoint that emphasizes the need for standardized biomarker assessment protocols in translational research. The subsequent sections focus on the non-canonical functions of FBL in maintaining epithelial architecture.

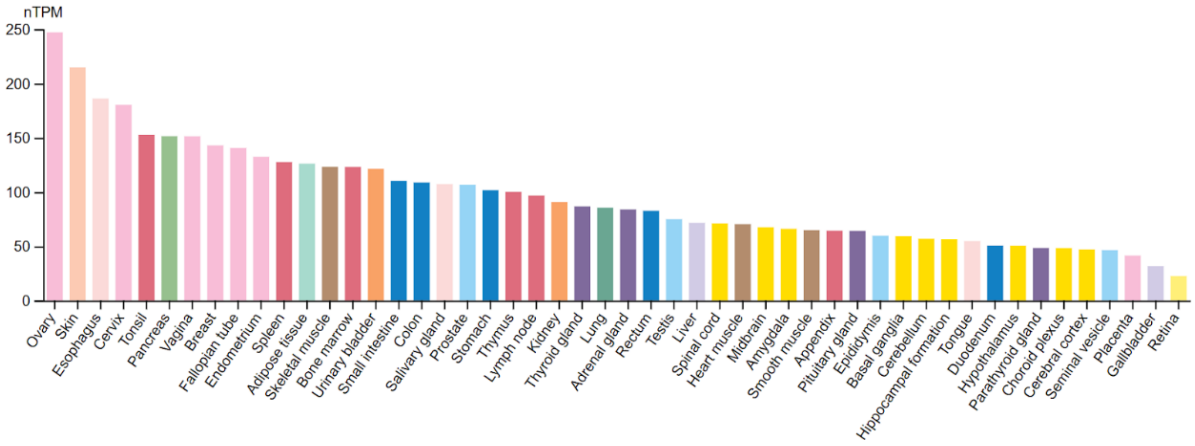

Fig. 1.8. Tissue-wide expression of FBL in normal human organs

Bar graph showing normalized RNA expression (nTPM) of FBL across multiple normal human tissues. Data obtained from the Human Protein Atlas. FBL is ubiquitously expressed, with highest expression observed in ovary, skin, esophageal, and cervical tissues, reflecting its essential role in ribosome biogenesis and cellular proliferation.

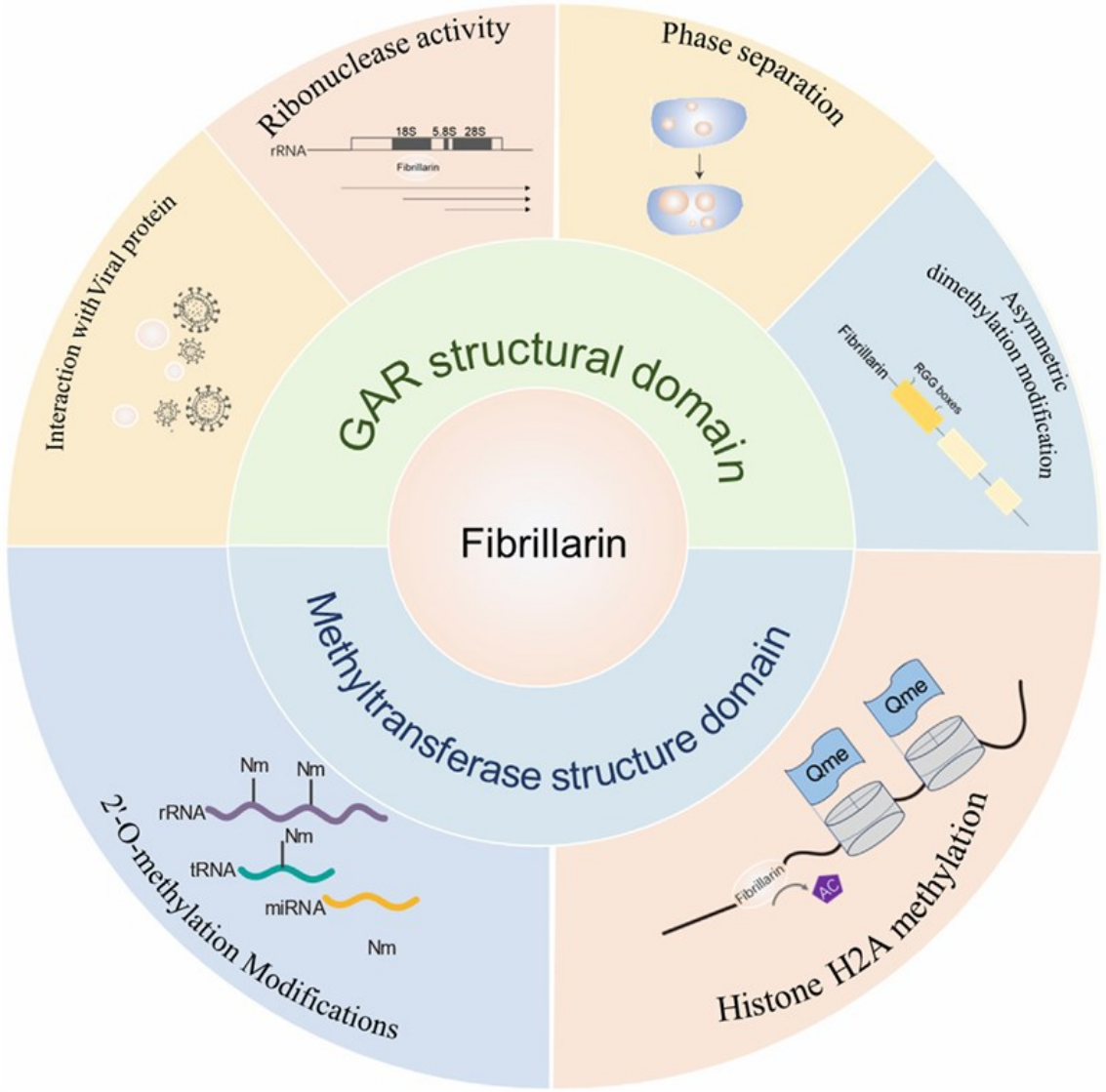

Fig. 1.9. Summary schematic of FBL domains and functions

The diagram illustrates the structural domains of fibrillarin (FBL) and their associated functions. The N-terminal GAR domain is implicated in interactions with viral proteins, ribonuclease-related activities, liquid–liquid phase separation, and arginine dimethylation. In contrast, the C-terminal methyltransferase domain mediates the canonical 2′-O-methylation of rRNA and contributes to methylation of histone H2A. Image has been used from (Zhang et al. 2024).

1.3. Importance of Epithelial Architecture and Polarity

Epithelial tissues serve as critical structural and functional barriers that line the outer surfaces and internal cavities of organs, including the gastrointestinal tract, respiratory system, urogenital tract, and exocrine glands (Mostov et al. 2003). These tissues are characterized by a tightly organized monolayer of epithelial cells exhibiting apical-basal polarity, which is vital for their barrier, absorptive, and secretory functions. This polarity is not merely a spatial orientation; it is a fundamental feature underpinning the architecture, homeostasis, and functionality of epithelial organs (Rodriguez-Boulan and Nelson 1989).

At the core of epithelial polarity is the asymmetric distribution of proteins, lipids, and organelles, allowing cells to distinguish their apical surface from the basolateral domain (McCaffrey and Macara 2011). The apical membrane faces the lumen or external environment and is enriched in proteins involved in absorption and secretion (e.g., transporters, channels, microvilli), whereas the basolateral membrane interfaces with the extracellular matrix (ECM) and adjacent cells, containing integrins, signaling receptors, and cell-cell adhesion molecules. These domains are separated by specialized intercellular junctions- tight junctions (TJs), adherens junctions (AJs), and desmosomes- collectively forming the apical junctional complex (AJC) (Nelson 2003; St Johnston and Sanson 2011).

Polarity Complexes and Polarity Establishment

The establishment and maintenance of epithelial polarity are orchestrated by three highly conserved polarity complexes:

- Crumbs complex (Crumbs/PALS1/PATJ) localized apically (Roh et al. 2002).
- Par complex (Par3/Par6/aPKC) that coordinates with tight junctions (Tunggal et al. 2005).
- Scribble complex (Scribble/Lgl/Dlg) localized to the basolateral membrane (W. Su et al. 2012).

These complexes exhibit mutual antagonism to maintain distinct apical and basolateral domains, supported by the underlying actin and microtubule cytoskeletons (Rodriguez-Boulan and Macara 2014). Polarity cues also emerge from cell–cell junctions, cell–ECM interactions, and intracellular trafficking pathways (Bryant and Mostov 2008; Datta et al. 2011). Epithelial cells require apical-basal plasma membrane polarity to carry out crucial vectorial transport

functions and cytoplasmic polarity to generate different cell progenies for tissue morphogenesis (Mostov et al. 2003; St Johnston and Sanson 2011). The establishment and maintenance of a polarized epithelial cell with apical, basolateral, and ciliary surface domains is guided by an epithelial polarity programme (EPP) that is controlled by a network of protein and lipid regulators (Bryant and Mostov 2008; Nelson 2009). The EPP is organized in response to extracellular cues and is executed through the establishment of an apical-basal axis, intercellular junctions, epithelial-specific cytoskeletal rearrangements and a polarized trafficking machinery. Recent studies have provided insight into the interactions of the EPP with the polarized trafficking machinery and how these regulate epithelial polarization and depolarization. Disruption in any of these complexes often leads to polarity loss, a frequent event in cancer and developmental defects (Datta et al. 2011; Apodaca et al. 2012).

1.3.1. Functional Significance of Epithelial Polarity

1. Barrier formation and homeostasis:

The most immediate function of epithelial polarity is to maintain barrier integrity, regulating the paracellular and transcellular passage of ions, nutrients, and signaling molecules [120]. TJs at the apical domain provide a selective seal, maintaining compartmentalization between the lumen and interstitium. This is vital in organs such as the intestine, where nutrient uptake occurs apically while immune surveillance occurs basolaterally [121].

2. Vectorial transport and organ function:

Epithelial polarity enables vectorial transport, essential for absorptive and secretory functions (Rodriguez-Boulan and Macara 2014). In kidney tubules, for instance, the apical localization of aquaporins and sodium channels (ENaC) is critical for fluid reabsorption, while basolateral Na^+/K^+ ATPases facilitate ion gradients (Edemir et al. 2011). Similarly, in the liver, hepatocytes use tight junctions to separate bile from blood flow, underscoring the physiological necessity of maintained polarity (Treyer and Müsch 2013).

3. Polarity during cell division and morphogenesis:

Polarity complexes regulate oriented cell division, ensuring proper daughter cell positioning during tissue expansion (Goldstein and Macara 2007). In the intestinal crypts, for example, stem cells divide along the polarity axis, balancing self-renewal and differentiation. This is tightly controlled by interactions between polarity proteins (e.g., Par3) and the mitotic spindle (Knoblich 2008).

4. Immune surveillance and pathogen defense:

Polarized distribution of pattern recognition receptors (e.g., TLRs) ensures context-specific immune responses (Abreu 2010). TLR5 is expressed apically in the gut epithelium to sense flagellated pathogens in the lumen, while basolateral TLR9 senses invasive microbes. Loss of this polarity may result in chronic inflammation, as seen in inflammatory bowel disease (Yu and Gao 2015).

1.3.2. Loss of Polarity and Disease Onset

Polarity is not only critical for physiological functions but also serves as a tumor-suppressive barrier. Cells that lose polarity often exhibit dedifferentiation, acquire migratory characteristics, and undergo epithelial–mesenchymal transition (EMT) (Royer and Lu 2011). This is especially evident in cancers of epithelial origin (carcinomas), where early stages of transformation are marked by the mislocalization or downregulation of polarity and junctional proteins (Coradini et al. 2011). A meta-analysis of cancer progression revealed consistent downregulation of polarity genes across multiple cancer types, including breast, colon, and pancreatic cancers (Aparicio et al. 2015; Yeung and Yang 2017).

The relevance of polarity loss is underscored in 3D culture systems, where normal epithelial cells form hollow cysts with correctly localized polarity markers. However, upon oncogenic transformation or polarity disruption (e.g., via Scribble knockdown), these cysts become filled or multilayered and lose proper apical-basal orientation (Muthuswamy and Xue 2012; Peglion and Etienne-Manneville 2023).

1.3.3. Roles of E-cadherin, ZO-1, and Scribble in Maintaining Junction Integrity

The structural and functional integrity of epithelial tissues is critically dependent on cell–cell junctions, which physically connect neighboring cells and coordinate intracellular signaling, polarity cues, and tissue homeostasis. Three key proteins- E-cadherin, ZO-1, and Scribble- are central components of the apical junctional complex and polarity architecture, and their functional interplay ensures the maintenance of epithelial cohesion(Gumbiner 1996; Niessen 2007). Perturbations in their expression or localization can lead to epithelial disintegration, enhanced cellular plasticity, and disease states, especially cancer (McCaffrey and Macara 2011; Royer and Lu 2011).

1.3.4. E-cadherin: The Central Adhesion Molecule of Adherens Junctions

E-cadherin (epithelial cadherin) is a calcium-dependent transmembrane glycoprotein that forms the backbone of adherens junctions (AJs). It mediates homophilic cell–cell adhesion by binding to E-cadherin molecules on adjacent cells through its extracellular domain. Its cytoplasmic tail binds to β-catenin and p120-catenin, which in turn link E-cadherin to the actin cytoskeleton via α-catenin, forming a dynamic but stable adhesion complex (Takeichi 1991).

Role of E-cadherin extends beyond mere adhesion. It participates in:

- Mechanotransduction: Transmits and resists mechanical tension across the epithelial sheet (Lecuit and Yap 2015).
- Cell signaling: Sequesters β-catenin at the membrane, thus regulating Wnt/β-catenin signaling; loss of E-cadherin enables β-catenin translocation to the nucleus, driving oncogenic transcription (Nelson and Nusse 2004; Halbleib and Nelson 2006).
- Junctional maturation: E-cadherin initiates the assembly of junctions and cooperates with tight junction proteins in establishing epithelial polarity (Izaguirre et al. 2010).

E-cadherin loss is considered a hallmark of epithelial–mesenchymal transition (EMT) (Serrano-Gomez et al. 2016; Fan et al. 2019). Downregulation is observed in various cancers, often driven by promoter methylation, mutations in the CDH1 gene (encoding E-cadherin), or repression by EMT transcription factors such as Snail, Zeb, and Twist (Tan et al. 2015). In lobular breast carcinoma, for instance, CDH1 mutations lead to complete loss of E-cadherin expression, resulting in discohesive, infiltrative tumor cells with high metastatic potential (McCart Reed et al. 2021).

1.3.5. ZO-1: The Scaffolding Protein of Tight Junctions

Zonula occludens-1 (ZO-1) is a multidomain cytoplasmic scaffolding protein localized at tight junctions (TJs), where it anchors transmembrane components such as claudins, occludins, and JAMs (junctional adhesion molecules) to the actin cytoskeleton. ZO-1 belongs to the membrane-associated guanylate kinase (MAGUK) family and contains PDZ, SH3, and GUK domains that facilitate interactions with a wide array of proteins involved in junction formation and signal regulation (Van Itallie et al. 2009; Fanning et al. 2012; Heinemann et al. 2019).

Key functions of ZO-1 include:

- TJ assembly and stabilization: Acts as an adaptor linking TJ proteins to actin filaments, stabilizing the paracellular seal (Belardi et al. 2020).
- Barrier regulation: Regulates transepithelial resistance (TER) and paracellular flux in various epithelia (Umeda et al. 2006).
- Polarity signaling: Coordinates with Par3/Par6/aPKC to align TJ assembly with apical–basal polarity cues (Hapak et al. 2018).

Loss or redistribution of ZO-1 impairs TJ integrity and enhances permeability, as observed in inflammatory bowel disease (IBD) and various cancers. In breast cancer cell lines, ZO-1 is often internalized or mislocalized, correlating with a mesenchymal-like morphology (Martin et al. 2004). Experimental knockdown of ZO-1 in MDCK cells leads to disorganized junctions, loss of polarity, and enhanced motility, indicating its direct role in epithelial cohesion (McNeil et al. 2006).

1.3.6. Scribble: A Master Regulator of Basolateral Polarity and Tumor Suppression

Scribble is a large multi-PDZ domain scaffold protein that forms the Scribble polarity complex with Dlg (Discs large) and Lgl (Lethal giant larvae). It localizes to the basolateral membrane and is crucial for the establishment and maintenance of apical–basal polarity. Scribble antagonizes the Par3/Par6/aPKC and Crumbs complexes, helping to define basolateral membrane identity (Pieczynski and Margolis 2011; Bilder 2004) (Fig. 1.10).

Role of Scribble span multiple dimensions:

- Polarity maintenance: Prevents apical protein invasion into the basolateral domain and ensures correct spatial organization (Yamanaka 2008).
- Junctional integrity: Stabilizes AJs through interactions with E-cadherin–catenin complexes; required for efficient reassembly of TJs after calcium switch assays (Yamanaka 2008; Ivanov et al. 2010; Zhan et al. 2008).
- Tumor suppression: Functions as a polarity-dependent tumor suppressor; mutations or mislocalization of Scribble cooperate with oncogenic Ras and Myc to drive neoplastic transformation in both Drosophila and mammals (Zhan et al. 2008).

Mechanistically, Scribble also acts as a signaling hub:

- It binds and sequesters PHLPP1, a phosphatase that negatively regulates Akt, thereby inhibiting EMT (Li et al. 2011).
- It forms complexes with Hippo pathway components (LATS1/2, MST1/2) to inhibit TAZ and YAP, transcriptional coactivators that drive EMT and cancer stemness (Cordenonsi et al. 2011).

Loss of Scribble has been observed in colorectal, breast, prostate, and lung cancers, often coinciding with poor prognosis and increased invasiveness. In mouse models, Scribble

knockdown causes mammary gland disorganization and hyperplasia, which become invasive when combined with oncogene activation (Zhan et al. 2008). Furthermore, Scribble loss is tightly linked to early disruption of junctional complexes, even before overt transformation, highlighting its importance in tumor initiation.

The functions of E-cadherin, ZO-1, and Scribble are highly interconnected:

- Scribble promotes E-cadherin junctional retention and polarity stabilization (Lohia et al. 2012).
- E-cadherin adhesion supports ZO-1 recruitment and TJ maturation (Qiao et al. 2014).
- ZO-1 scaffolds signaling molecules (e.g., ZONAB, ZO-1–associated nucleic acid-binding protein) that also affect cell proliferation and polarity (Lima et al. 2010).

Together, these proteins form a core polarity–adhesion axis, the disruption of which facilitates junctional disassembly, loss of apical–basal polarity, and initiation of EMT.

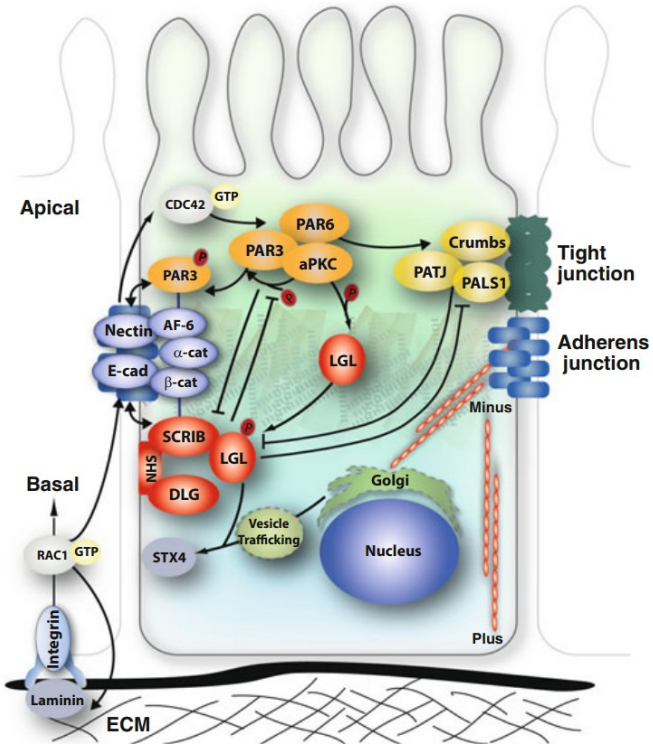

Fig. 1.10. Schematic representation of epithelial cell polarity complexes and junctional organization

Diagram illustrating the spatial organization and functional interplay of the apical PAR (PAR3–PAR6–aPKC), Crumbs (Crumbs–PALS1–PATJ), and basolateral Scribble (SCRIB–

DLG–LGL) polarity complexes in a polarized epithelial cell. Tight junctions and adherens junctions demarcate the apico–basal axis, with E-cadherin–based adherens junctions linking neighboring cells to the actin cytoskeleton. The polarity complexes coordinate with small GTPases, cytoskeletal elements, vesicular trafficking pathways, and signaling hubs to maintain epithelial architecture, junction integrity, and directional organization relative to the basement membrane and extracellular matrix (ECM). Adapted from (Humbert et al. 2015).

1.3.7. Consequences of Disrupted Polarity in Disease

The disruption of epithelial polarity represents a critical early event in the pathogenesis of numerous diseases, including carcinomas, chronic inflammatory disorders, and fibrotic diseases (Thiery 2002). The loss of organized apical–basal polarity destabilizes epithelial barrier integrity, triggers misregulation of signaling pathways, and enables epithelial cells to acquire mesenchymal and invasive properties (Ozdamar et al. 2005). This transition from a polarized, quiescent state to a migratory, proliferative phenotype is commonly referred to as epithelial–mesenchymal transition (EMT) and is a hallmark of cancer progression, metastasis, and resistance to therapy (W.-H. Su et al. 2012; Zeisberg et al. 2007).

1.3.8. Polarity Disruption and Carcinoma Progression

In epithelial-derived cancers, polarity defects precede and potentiate tumorigenesis. Normal epithelial cells are anchored in a structured monolayer through polarity complexes and cell–cell junctions. Oncogenic transformation is often accompanied by the mislocalization or degradation of polarity proteins, such as E-cadherin, Scribble, or Par3, resulting in disorganized tissue architecture.

- Experimental evidence strongly supports this paradigm:
- In 3D organoid models, oncogene-transformed mammary epithelial cells that lose Scribble or E-cadherin form filled, invasive acini lacking lumen and polarity, as opposed to normal hollow cysts (Debnath et al. 2003).
- Conditional Scribble deletion in mouse mammary glands leads to tissue hyperplasia and, in the presence of oncogenic Ras, results in aggressive, invasive carcinomas (Zhan et al. 2008).

- In colorectal cancer, loss of E-cadherin and nuclear localization of β-catenin correlate with higher histological grade, invasion depth, and nodal metastasis (Conacci-Sorrell et al. 2003).

Polarity loss also compromises contact inhibition, a property that prevents overproliferation. This loss is mediated in part by ZO-1 and E-cadherin–mediated junctional signaling, which sequester proliferative cues (e.g., β-catenin, YAP/TAZ). Once polarity is disrupted, these cues are unleashed, further promoting uncontrolled proliferation and dedifferentiation (Orsulic et al. 1999; Balda et al. 2003; Rodriguez et al. 2012; Kim and Gumbiner 2015; Varelas et al. 2010; Balda and Matter 2000).

1.3.9. Polarity and Epithelial–Mesenchymal Transition (EMT)

Disruption of polarity is both a cause and consequence of EMT. EMT involves transcriptional, structural, and functional reprogramming, where epithelial cells:

- Downregulate epithelial markers (e.g., E-cadherin, ZO-1)(Batlle et al. 2000; Wheelock et al. 2008)
- Upregulate mesenchymal markers (e.g., Vimentin, N-cadherin, Fibronectin) (Backhaus et al. 2004; Kalluri and Weinberg 2009)
- Acquire increased motility, invasiveness, and resistance to apoptosis (Thiery and Sleeman 2006).

Polarity regulators such as Scribble, Par3, and Crumbs act as gatekeepers against EMT. Their loss or mislocalization enables activation of EMT-driving transcription factors (TFs), such as Snail, Slug, Twist, and ZEB1/2 (Kohanski et al. 2008; Wu et al. 2013; Venkatraman Girija et al. 2013; Nieto et al. 2016). These TFs repress CDH1 (E-cadherin) transcription and activate mesenchymal gene programs.

For instance:

- Snail binds to E-box elements in the CDH1 promoter and represses E-cadherin transcription (Batlle et al. 2000).
- Scribble loss potentiates TAZ and Akt activation, which in turn stabilize Snail and enhance EMT progression (Cordenonsi et al. 2011).

- ZO-1 depletion results in cytoskeletal remodeling and TJ disassembly, facilitating the physical detachment necessary for EMT (McNeil et al. 2006).

In essence, loss of junctional and polarity integrity removes both mechanical constraints and transcriptional suppression of mesenchymal programs, rendering the epithelium susceptible to invasion and metastasis.

1.3.10. Clinical Correlates: EMT and Poor Prognosis

Numerous studies have demonstrated that polarity disruption and EMT are linked to poor clinical outcomes:

- In breast cancer, low E-cadherin and Scribble levels correlate with higher tumor grade, lymph node positivity, and reduced survival (Zhan et al. 2008; Harigopal et al. 2005).
- In lung adenocarcinoma, high levels of ZEB1 and reduced ZO-1 are associated with EMT phenotypes and resistance to EGFR inhibitors (Dongre and Weinberg 2019).
- In pancreatic cancer, EMT markers including vimentin and Snail are predictive of metastatic spread and chemoresistance (Rhim et al. 2012; Jakobsen et al. 2016; Gaianigo et al. 2017).
- The EMT process also imparts stem-like properties to cancer cells, increasing their ability to seed metastatic sites and survive in foreign microenvironments. This contributes to the formation of circulating tumor cells (CTCs), some of which retain partial EMT features, aiding in immune evasion and colonization (Roy et al. 2021; Saxena et al. 2020).

1.3.11. Polarity Disruption in Non-Malignant Diseases

Beyond cancer, loss of epithelial polarity contributes to chronic and degenerative diseases:

- In inflammatory bowel disease (IBD), disruption of TJ proteins (e.g., ZO-1, claudins) compromises barrier function, permitting microbial translocation and sustained inflammation (Zeissig et al. 2007).
- In renal fibrosis, TGF-β–induced EMT of tubular epithelial cells involves downregulation of E-cadherin and loss of apical–basal polarity, contributing to extracellular matrix deposition (Liu 2010).

- In chronic obstructive pulmonary disease (COPD), smoking-induced EMT leads to airway remodeling and fibrosis, involving loss of E-cadherin and ZO-1 in bronchial epithelia (Sohal et al. 2011).
- These examples reinforce the concept that epithelial polarity is a unifying principle of tissue integrity, and its disruption leads to functional deterioration across disease contexts.

1.3.12. Molecular Mechanisms Driving Polarity Breakdown

Several upstream signals drive polarity disruption:

- Oncogenic Ras and Myc promote degradation of polarity proteins and bypass junctional checkpoints (Pylayeva-Gupta et al. 2011; Leung and Brugge 2012).
- TGF-β signaling induces EMT through Smad-dependent transcription of EMT TFs and repression of polarity genes (Xu et al. 2009; Massagué 2012).
- Hypoxia and inflammation destabilize junctional complexes via HIF-1α and NF-κB–mediated pathways (Huang et al. 2025; Huber et al. 2004).
- Mechanical stress and matrix stiffness alter actomyosin contractility, destabilizing AJ and TJ integrity (Wozniak and Chen 2009).
- Additionally, polarity proteins themselves regulate feedback loops:
    - Loss of Scribble leads to hyperactivation of Akt, promoting EMT and survival (Zhan et al. 2008).
    - Mislocalized Par3 affects the orientation of mitosis and drives basal extrusion and invasion (McCaffrey et al. 2012).

Thus, polarity breakdown is both a signal and substrate for malignant transformation and progression.

1.3.13. Possible Influence of FBL on EMT through Chromatin Remodeling and Polarity Loss

Emerging evidence suggests that nucleolar proteins, long considered primarily involved in ribosome biogenesis, can participate in broader nuclear functions, including epigenetic regulation, chromatin remodeling, and transcriptional control. Among these, Fibrillarin (FBL) has garnered increasing attention for its non-canonical role in chromatin architecture and gene regulation, particularly in the context of epithelial plasticity and EMT.

While canonical EMT pathways have focused on transcription factors such as Snail, Zeb1/2, and Twist, it is now evident that EMT can also be induced by epigenetic reprogramming, which leads to the stable silencing of epithelial genes and activation of mesenchymal networks. This layer of regulation involves histone modifications, chromatin remodelers, and long-range chromatin looping — processes in which FBL may play a crucial regulatory or scaffolding role.

1.3.14. FBL and Epigenetic Regulation: Bridging the Nucleolus and Chromatin

Although FBL is classically localized to the dense fibrillar component (DFC) of the nucleolus, a subset of FBL has been reported to associate with perinucleolar chromatin and transcriptionally repressive nuclear compartments (Sirri et al. 2008). FBL has been shown to physically interact with chromatin-associated proteins, including histone methyltransferases, and may influence histone modification landscapes.

Key studies indicate that:

- FBL can methylate histone H2A in vitro, and may also scaffold chromatin-modifying complexes at specific gene loci (Loza-Muller et al. 2015).
- FBL interacts with nucleophosmin (NPM1) and other nucleolar proteins that modulate chromatin accessibility and polycomb repressor complex 2 (PRC2) activity (Sirri et al. 2008).
- Nucleolar stress caused by FBL imbalance has been linked to alterations in H3K27me3 distribution, potentially modifying the transcriptional activity of epithelial and EMT genes (Boulon et al. 2010).

This raises the hypothesis that FBL may contribute to chromatin-based silencing of epithelial polarity genes, thus favoring EMT, particularly in contexts where canonical EMT signals (e.g., TGF-β) are reinforced by epigenetic repression.

1.3.15. EZH2: A Central Epigenetic Regulator of EMT and Polarity

Enhancer of Zeste Homolog 2 (EZH2), the catalytic component of the PRC2 complex, mediates the trimethylation of histone H3 on lysine 27 (H3K27me3), a repressive chromatin marks that silences gene expression. EZH2 is overexpressed in various epithelial cancers, and its activity is closely tied to loss of cell polarity, EMT, and metastatic progression.

The seminal study by Y. Yi et al. (2021, *Nat Cell Biol*) demonstrated that:

- EZH2 directly represses the SCRIB gene, encoding Scribble, a key polarity determinant (Yi et al. 2021).
- EZH2 inhibition restores Scribble expression, enhances E-cadherin localization, and reduces metastatic dissemination in CRC models (Saha et al. 2025).

Mechanistically, EZH2 was shown to occupy the SCRIB promoter, deposit H3K27me3, and prevent transcription factor access. This silencing was independent of DNA methylation and was reversible upon EZH2 depletion or pharmacological inhibition (e.g., with GSK126).

This study establishes a direct link between epigenetic repression of polarity genes and EMT induction. Moreover, it provides a model where chromatin remodeling, rather than transcription factor binding alone, controls epithelial integrity.

1.3.16. FBL–EZH2 Axis: A Potential Intersection

Although direct physical interaction between FBL and EZH2 has not been fully established in the literature, the overlap in their nuclear localization, association with repressive chromatin, and roles in EMT suggests a functional convergence. Several hypotheses emerge:

- FBL may scaffold PRC2 components to specific nuclear compartments (e.g., perinucleolar heterochromatin) where polarity and epithelial genes are sequestered and repressed.
- Given that nucleolar proteins can modulate RNA Pol II transcription, FBL could indirectly influence EZH2 target gene expression through non-coding RNA processing or local chromatin compaction.
- FBL dysfunction may perturb histone methylation balance, favoring a shift toward H3K27me3 enrichment at epithelial gene loci — including CDH1, SCRIB, CRB3, and PAR3 — thereby tipping the epigenetic balance toward EMT.

In addition, studies on nucleolar sequestration of chromatin suggest that gene positioning within the nucleus—not just promoter methylation—can control gene expression. FBL may thus influence nuclear architecture in a way that favors gene silencing.

1.3.17. Epigenetic Silencing of Polarity Complex Genes in Cancer

Beyond SCRIB, many other genes encoding epithelial polarity components are epigenetically repressed in cancers:

- PAR3 and LGL2, two key basolateral polarity proteins, are silenced in EMT-positive tumors (McCaffrey et al. 2012).
- In gastric and esophageal cancers, E-cadherin is transcriptionally repressed by PRC2 recruitment to the CDH1 promoter (Fujii and Ochiai 2008).

These epigenetic modifications are often reversible, underscoring the therapeutic potential of targeting PRC2 and chromatin regulators in EMT-driven metastasis.

1.3.18. Future Directions and Therapeutic Implications

The integration of FBL and EZH2 biology opens up new lines of inquiry:

- Can modulation of FBL levels alter PRC2 localization or activity?
- Are there epigenomic signatures (e.g., histone modification maps) that reflect FBL status in tumors?
- Could targeting FBL in specific contexts sensitize tumors to EZH2 inhibitors, particularly in EMT-high cancers?

Ultimately, this intersection reflects a broader shift in understanding how nuclear compartmentalization, chromatin state, and epithelial plasticity are coordinated in health and disease.

1.4: Chromatin Dynamics and Nuclear Architecture

1.4.1. Basics of Chromatin Structure and Key Histone Modifications

Chromatin is a dynamic macromolecular complex composed of DNA and histone proteins that packages the eukaryotic genome within the nucleus while maintaining regulated accessibility for transcription, replication, recombination, and repair (Jenuwein and Allis 2001). The fundamental repeating unit of chromatin is the nucleosome, comprising ~146 base pairs of DNA wrapped around an octamer of histones—two copies each of H2A, H2B, H3, and H4 (Luger et al. 1997). These nucleosomes are further folded into higher-order structures regulated by linker histone H1 and chromatin-associated proteins.

The histone tails extending from the nucleosome core are subject to extensive post-translational modifications (PTMs), including methylation, acetylation, phosphorylation, and ubiquitination, collectively referred to as the "histone code" (Bannister and Kouzarides 2011). Acetylation neutralizes the positive charge lysine, weakening histone–DNA interaction and promoting a transcriptionally active chromatin state. Histone acetyltransferases (HATs) and deacetylases (HDACs) dynamically regulate these modifications (Hong et al. 1993; Grunstein 1997; Yang and Seto 2007; Hebbes et al. 1988).

Histone methylation, depending on the context, may either activate or repress gene expression. For instance, H3K4me3 is linked to active promoters, whereas H3K9me3 and H3K27me3 are associated with transcriptional repression (Bannister and Kouzarides 2005; Santos-Rosa et al. 2002; Peters et al. 2001; Cao and Zhang 2004). These PTMs are interpreted by 'reader' proteins that influence chromatin compaction and gene activity, underpinning the epigenetic control of cell identity and development (Taverna et al. 2007).

1.4.2. Functional Roles of Heterochromatin and Euchromatin Histone Marks

Chromatin exists in a dynamic continuum between transcriptionally active (euchromatin) and transcriptionally repressive (heterochromatin) states, marked by distinct histone post-translational modifications (PTMs), DNA methylation, chromatin accessibility, and spatial positioning within the nucleus. These chromatin states are critical for cellular identity, genome stability, and appropriate gene expression programs (Taverna et al. 2007; Allshire and Madhani 2018).

Heterochromatin: Gene Silencing and Structural Integrity

Heterochromatin is further divided into two types- constitutive heterochromatin, which is stably repressed across cell types and generations, and facultative heterochromatin, which is reversibly silenced depending on developmental or environmental contexts (Grewal and Jia 2007; Trojer and Reinberg 2007).

H3K9me3 and Constitutive Heterochromatin

H3K9me3, catalyzed by histone methyltransferases SUV39H1/2, is a key mark of constitutive heterochromatin. This mark is found at pericentromeric and telomeric regions and is essential for silencing transposable elements and maintaining genomic integrity (Peters et al. 2001). The binding of heterochromatin protein 1 (HP1) to H3K9me3-marked chromatin facilitates chromatin compaction and recruits additional chromatin modifiers such as DNMTs and HDACs (Maison and Almouzni 2004). HP1α and HP1β dimerization allow for higher-order chromatin organization, supporting large heterochromatin domains (Bannister et al. 2001; Lomberk et al. 2006).

Mutations in SUV39H1 or HP1 cause chromosomal instability, abnormal nuclear morphology, and derepression of satellite repeats—features often seen in cancer cells (Elsässer et al., 2015). The integrity of heterochromatin is also critical for centromere function, kinetochore assembly, and proper chromosome segregation during mitosis (Grewal and Jia 2007).

H4K20me3 in Heterochromatin Maintenance

Another key repressive mark, H4K20me3, deposited by SUV420H1/H2, is enriched in constitutive heterochromatin and often co-localizes with H3K9me3. It stabilizes chromatin compaction and contributes to genome stability (Schotta et al. 2004). H4K20me3 is also involved in DNA double-strand break repair and has been linked to lamina-associated domains (LADs) (van Steensel and Belmont 2017; Guelen et al. 2008).

H3K27me3 and Facultative Heterochromatin

Facultative heterochromatin is marked by H3K27me3, catalyzed by EZH2, the catalytic component of Polycomb Repressive Complex 2 (PRC2). H3K27me3 is highly dynamic and silences lineage-specific genes during development, maintaining cell identity (Margueron and

Reinberg 2011). Genome-wide mapping in embryonic stem cells shows that many developmentally important genes harbor bivalent domains marked by both H3K4me3 and H3K27me3, keeping them in a poised transcriptional state (Bernstein et al. 2006).

PRC2-mediated repression is stabilized by recruitment of PRC1, which ubiquitinates H2AK119 and contributes to chromatin compaction (Blackledge et al. 2014). Dysregulation of PRC2 components has been linked to developmental disorders, neurodegeneration, and various cancers (Laugesen and Helin 2014; Comet et al. 2016). Moreover, recent studies have identified noncanonical PRC1 complexes that mediate chromatin looping and long-range gene silencing independently of H3K27me3 (Kundu et al. 2017).

Interplay Between DNA Methylation and Histone Repression

DNA methylation at CpG dinucleotides often works in tandem with histone repressive marks. H3K9me3 facilitates recruitment of DNA methyltransferases (DNMT1, DNMT3A/B) via UHRF1, resulting in stable silencing of retrotransposons and imprinted genes (Bostick et al. 2007). Conversely, methyl-CpG-binding proteins like MeCP2 can recruit HDACs and histone methyltransferases, reinforcing heterochromatin architecture (Nan et al. 1998).

1.4.3. Euchromatin: Transcriptionally Active Domains

Euchromatin is characterized by a loose nucleosomal arrangement, high transcriptional activity, and the presence of activating histone marks such as H3K4me3, H3K9Ac, H3K27Ac, and H3K36me3.

H3K4me3 at Promoters

H3K4me3, deposited by MLL/SET1 complexes, is enriched at transcription start sites of actively transcribed genes. This mark facilitates recruitment of the general transcription machinery, including TFIID and chromatin remodelers like CHD1 (Miller et al. 2001; Vermeulen et al. 2007, 4; Sims et al. 2005).

H3K9Ac and H3K27Ac: Enhancer and Promoter Activation

Acetylation at H3K9 and H3K27, catalyzed by CBP/p300, correlates with transcriptional activation at enhancers and promoters (Visel et al. 2009). H3K27Ac distinguishes active enhancers from poised enhancers (Creyghton et al. 2010). These acetylation marks are read

by bromodomain proteins such as BRD4, which help recruit Mediator and P-TEFb complexes for RNA polymerase II elongation (Sabari et al. 2018).

Super-enhancers—clusters of H3K27Ac-rich enhancers—drive high-level expression of cell identity genes and are especially sensitive to perturbations in chromatin regulators (Hnisz et al. 2013). Loss of H3K27Ac at these regions is associated with dedifferentiation and cancer progression.

H3K36me3 and Transcriptional Elongation

H3K36me3, enriched in the bodies of transcribed genes, is catalyzed by SETD2 and supports transcriptional elongation. It recruits histone deacetylases to prevent aberrant initiation and maintains exon–intron architecture (Kolasinska-Zwierz et al. 2009; Li et al. 2013). H3K36me3 also antagonizes PRC2 recruitment, preventing ectopic deposition of H3K27me3 in active genes (Yuan et al. 2011).

1.4.4. Crosstalk Between histone Marks and Chromatin Readers

Histone marks do not function in isolation. Instead, their combinatorial readout by protein complexes determines chromatin states. For instance, the BAF (SWI/SNF) complex antagonizes PRC2 to maintain open chromatin, while NuRD coordinates deacetylation and nucleosome repositioning to repress transcription (Kadoch et al. 2013; Xue et al. 1998).

Additionally, nucleosome remodeling and histone variants (e.g., H2A.Z, H3.3) contribute to the dynamic nature of euchromatin and its accessibility (Henikoff and Smith 2015).

1.4.5. Chromatin State and Nuclear Morphology

The structural state of chromatin—ranging from open, transcriptionally active euchromatin to compact, transcriptionally repressive heterochromatin—plays a fundamental role in shaping the biophysical and spatial properties of the nucleus. While nuclear shape and organization were historically attributed largely to the nuclear lamina and associated structural proteins, it is now evident that chromatin compaction itself exerts intrinsic mechanical forces that influence nuclear rigidity, morphology, and integrity (Stephens et al. 2017; Nava et al. 2020).

1.4.6. Chromatin as a Structural Scaffold of the Nucleus

Studies using isolated nuclei or micropipette aspiration have shown that chromatin contributes significantly to nuclear stiffness. For instance, manipulating chromatin compaction through pharmacological inhibitors—such as histone deacetylase inhibitors (HDACis), which increase acetylation and decondense chromatin—results in more deformable nuclei and increased nuclear blebbing (Stephens et al. 2017). Conversely, enhancing heterochromatin content using lysine methyltransferase overexpression increases nuclear rigidity (Heo et al. 2016).

Importantly, these mechanical changes are independent of nuclear lamins, demonstrating that chromatin can function as a major internal determinant of nuclear biomechanics. For example, in cells lacking lamin A/C, chromatin compaction via H3K9me3 or H3K27me3 partially restores nuclear integrity (Stephens et al. 2017). This has implications in diseases such as laminopathies, where chromatin remodeling could potentially compensate for defects in the lamina.

1.4.7. Heterochromatin and Nuclear Shape Maintenance

Heterochromatin is typically concentrated at the nuclear periphery (in lamina-associated domains or LADs) and around the nucleolus (in nucleolus-associated domains or NADs), forming large repressive compartments that contribute to nuclear shape. These zones of condensed chromatin act as structural 'scaffolds' that reinforce nuclear geometry (van Steensel and Belmont 2017). Loss of heterochromatin—either through deletion of H3K9 methyltransferases or inhibition of PRC2-leads to a more rounded, deformed, and less mechanically stable nucleus (Attar et al. 2025).

Additionally, the tethering of chromatin to the nuclear lamina is essential for spatial organization. Proteins like the lamin B receptor (LBR) and lamin A/C interact with methylated histone tails (e.g., H3K9me2/3, H4K20me2/3) to anchor repressive chromatin at the periphery (Solovei et al. 2013). Disruption of these tethering mechanisms leads to chromatin reorganization and nuclear shape abnormalities, as seen in neutrophils and some cancer cells.

1.4.8. Chromatin Acetylation and Nuclear Softening

Hyperacetylated chromatin is associated with a euchromatic, transcriptionally permissive state. This state results in less dense chromatin packing and greater nuclear pliability. Inhibiting histone deacetylases (e.g., with TSA or SAHA) results in nuclear softening, often

visible as blebs, invaginations, or irregular nuclear contours under fluorescence microscopy (Bustin and Misteli 2016).

Previous study showed that chromatin decompaction, independent of lamina changes, is sufficient to drive nuclear rupture under mechanical stress, especially in three-dimensional matrices (Nava et al. 2020; Denais and Lammerding 2014). In addition, decondensed chromatin facilitates increased nuclear envelope fluctuations, which may promote the mislocalization of nuclear envelope proteins and genomic instability.

1.4.9. Chromatin Mechanics During Migration and Confinement

During cell migration, especially in confined environments like 3D collagen matrices or micropores, the nucleus is the largest and stiffest organelle and often represents the rate-limiting barrier for movement (Harada et al. 2014). Chromatin state modulates how easily the nucleus deforms through narrow spaces. Cells with more euchromatin (e.g., treated with HDACis) show greater nuclear plasticity and enhanced migration through tight constrictions, while those enriched in heterochromatin are more rigid and resist deformation (Maizels et al. 2017).

Interestingly, transient nuclear envelope rupture occurs more frequently during migration in cells with soft nuclei, leading to DNA damage and increased mutagenesis—a phenomenon observed in invasive cancer cells and immune cells [256].

1.4.10. Chromatin and Nuclear Morphology in Development

During differentiation, chromatin undergoes global reprogramming that directly affects nuclear shape. For instance, in embryonic stem cells, chromatin is mostly euchromatic and the nuclei are large and spherical. Upon differentiation, heterochromatin increases, the nuclear volume reduces, and nuclear architecture becomes more structured (Meshorer et al. 2006).

Previously it has been demonstrated that in rod photoreceptors of nocturnal mammals, nuclear architecture is inverted: heterochromatin is centrally localized and euchromatin is peripheral (Solovei et al. 2009). This arrangement is achieved by specific loss of LBR and helps optimize light transmission. These findings highlight that nuclear morphology is not only structurally regulated but can be adapted functionally during evolution.

1.4.11. Chromatin Dysregulation and Nuclear Aberrations in Disease

Abnormal chromatin states contribute to altered nuclear morphology in cancer, where nuclear atypia (e.g., nuclear enlargement, lobulation, hyperchromasia) is a diagnostic hallmark. Many cancer cells exhibit global loss of heterochromatin (e.g., loss of H3K9me3, H4K20me3), leading to softer nuclei, nuclear shape irregularities, and genomic instability (Chen et al. 2024).

Furthermore, epigenetic regulators such as EZH2, ATRX, and FBL influence both chromatin state and nuclear architecture. Loss of EZH2 causes decreased H3K27me3 and results in nuclear rounding and increased fragility (Margueron et al. 2008). Similarly, ATRX, which deposits the histone variant H3.3 at heterochromatin, is essential for pericentromeric chromatin integrity; ATRX mutations lead to nuclear blebbing and chromosomal aberrations (Teng et al. 2021).

Integration of Nuclear Lamina and Chromatin in Morphogenesis

While chromatin contributes intrinsic stiffness, the nuclear lamina provides extrinsic structural support. Cross-talk between these systems is essential. For example, loss of lamins (as seen in laminopathies such as Hutchinson-Gilford Progeria Syndrome) is often accompanied by altered chromatin distribution and nuclear morphology (Xue et al. 1998; Stephens et al. 2018; Goldman et al. 2004).

Importantly, the balance between euchromatin and heterochromatin, modulated by chromatin remodeling enzymes (e.g., CHD4, BRG1) and histone-modifying enzymes (e.g., EZH2, G9a, HDACs), influences nuclear morphology during both normal physiology and disease.

1.5. Role of EZH2 and PRC2 in Transcriptional Repression via H3K27me3

Overview of Polycomb Group Proteins

The Polycomb group (PcG) proteins are a family of transcriptional repressors critical for maintaining cell identity and regulating developmental gene expression programs. Originally identified in *Drosophila melanogaster* for their role in repressing Hox genes (Lewis, 1978), PcG proteins function as part of multi-subunit complexes that silence target genes via histone modification and chromatin compaction. The two major Polycomb repressive complexes, PRC1 and PRC2, act in a coordinated manner to establish and maintain facultative heterochromatin.

PRC2 catalyzes the trimethylation of lysine 27 on histone H3 (H3K27me3), a well-characterized repressive mark. This histone modification is critical for gene silencing in embryogenesis, X-chromosome inactivation, lineage commitment, and oncogenesis (Margueron and Reinberg 2011; Schuettengruber et al. 2017).

EZH2: The Catalytic Core of PRC2

EZH2 (Enhancer of Zeste Homolog 2) is the catalytic subunit of PRC2 and is responsible for the methylation of H3K27. It functions within a core complex that includes SUZ12, EED, and RbAp46/48, which stabilize EZH2, facilitate its chromatin recruitment, and allosterically activate its methyltransferase activity (Margueron et al. 2008; Cao et al. 2002) (Fig. 1.11). EZH2 contains a SET domain responsible for catalyzing mono-, di-, and trimethylation of H3K27, with H3K27me3 being the primary repressive signal (Cao and Zhang 2004).

The deposition of H3K27me3 by PRC2 facilitates the recruitment of PRC1, which ubiquitinates histone H2A at lysine 119 (H2AK119ub), leading to chromatin compaction and stable transcriptional repression (Blackledge et al. 2014).

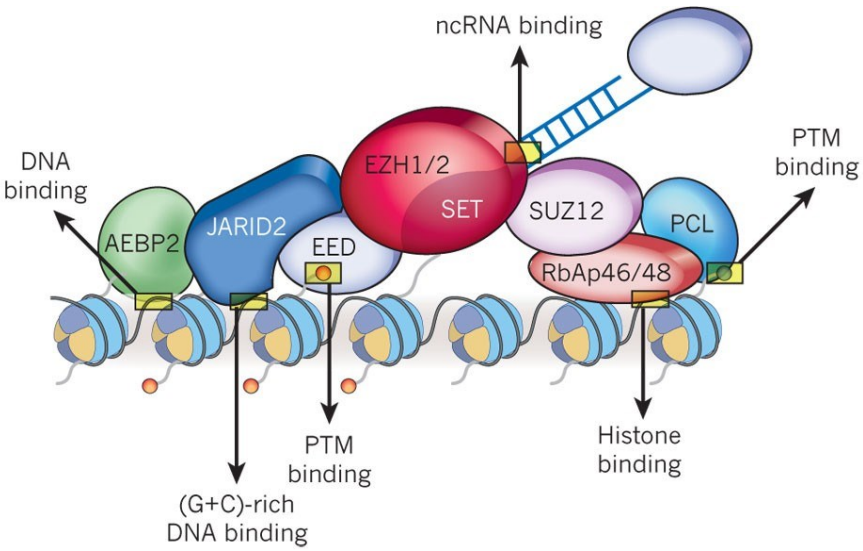

Fig. 1.11. PRC2 holoenzyme

Schematic depiction of the PRC2 holoenzyme associated with chromatin, highlighting proposed interactions with DNA and histone substrates that may underlie mechanisms of PRC2 recruitment. Adapted from (Margueron and Reinberg 2011).

–PRC2 in Developmental Gene Regulation

During embryonic development, PRC2 plays a critical role in establishing lineage-specific gene expression by silencing genes inappropriate for a given cell type. This is most evident in pluripotent stem cells, where PRC2 marks developmental regulators with bivalent domains—regions simultaneously marked by H3K4me3 (activation) and H3K27me3 (repression), allowing genes to remain transcriptionally silent but poised for activation upon differentiation (Bernstein et al. 2006).

Disruption of PRC2 function in mice results in embryonic lethality and derepression of developmental transcription factors, leading to failed lineage specification (Pasini et al. 2007; Shen et al. 2008). Similarly, EZH2-deficient embryonic stem cells fail to silence lineage-inappropriate genes, emphasizing its central role in developmental gene silencing (O'Carroll et al. 2001).

EZH2 and PRC2 in Cancer: A Double-Edged Sword

Although essential for normal development, dysregulation of EZH2 is implicated in a wide array of cancers. EZH2 often acts as an oncogene, particularly in epithelial-derived cancers, by repressing tumor suppressor genes and promoting epigenetic reprogramming conducive to proliferation, migration, and immune evasion (Kim and Roberts 2016).

1.5.1. Gain-of-Function and Oncogenic Mutations

In hematologic malignancies such as diffuse large B-cell lymphoma (DLBCL) and follicular lymphoma, EZH2 mutations at Y641 (Tyr641) in the SET domain increase H3K27 trimethylation activity, leading to hyper-repression of tumor suppressor genes (Morin et al. 2010). These mutations result in a gain-of-function phenotype and have become actionable targets for EZH2 inhibitors such as tazemetostat (FDA-approved in 2020 for epithelioid sarcoma and relapsed/refractory follicular lymphoma) (Italiano et al. 2018).

1.5.2. EZH2 and EMT

EZH2 promotes epithelial–mesenchymal transition (EMT) by silencing epithelial markers and activating mesenchymal programs. During EMT, transcription factors such as Snail, Slug, ZEB1, and Twist recruit PRC2 to epithelial gene promoters (e.g., CDH1), depositing

H3K27me3 and leading to transcriptional repression (Herranz et al. 2008). This facilitates loss of polarity, disruption of junctional complexes, and enhanced migration and invasion.

Emerging studies have shown that TAZ/YAP, effectors of the Hippo pathway, can cooperate with EZH2 to suppress epithelial genes and promote a stem-like, mesenchymal phenotype in cancers (Kim et al. 2017).

1.5.3. Context-Dependent Roles and Noncanonical Functions

Interestingly, in certain contexts such as leukemia and neurodevelopmental disorders, EZH2 acts as a tumor suppressor, highlighting its context-dependent functionality. For instance, in T-cell acute lymphoblastic leukemia, loss-of-function mutations in EZH2 lead to derepression of NOTCH target genes and enhanced tumorigenesis (Ntziachristos et al. 2012).

PRC2 also exerts noncanonical functions independent of its methyltransferase activity. For example, EZH2 can act as a transcriptional co-activator in prostate cancer, cooperating with androgen receptor (AR) signaling to activate genes involved in proliferation and survival (Xu et al. 2012). Such dual roles complicate therapeutic strategies and require cell-type–specific profiling of EZH2 function.

1.5.4. Regulation of PRC2 Activity

PRC2 recruitment is regulated by several factors:

- Non-coding RNAs (e.g., Xist, HOTAIR) guide PRC2 to specific genomic loci, especially in X-chromosome inactivation and metastasis-associated gene silencing (Rinn et al. 2007).
- Histone modifications such as H3K36me3 and H3K4me3 antagonize PRC2 binding, reinforcing mutually exclusive active and repressive chromatin domains (Yuan et al. 2011).
- Histone variants, such as H2A.Z, can influence PRC2 targeting to bivalent domains in stem cells (Hu et al. 2013).
- ATRX, a chromatin remodeler, facilitates the incorporation of histone H3.3 into telomeric and pericentromeric regions. Its cooperation with EZH2 in maintaining heterochromatin domains has been implicated in neurodevelopment and glioma (Lovejoy et al. 2012).

1.5.5. Therapeutic Targeting of EZH2

EZH2 is now a promising therapeutic target. Multiple EZH2 inhibitors, including tazemetostat, valemetostat, and GSK126, are in clinical trials for hematologic malignancies and solid tumors. These inhibitors show efficacy in EZH2-mutant cancers, as well as tumors with SWI/SNF mutations (which antagonize PRC2), such as malignant rhabdoid tumors and synovial sarcoma (Wilson et al. 2010; McCabe et al. 2012; Fujita et al. 2018; Morschhauser et al. 2020; Knutson et al. 2014).

Combination therapies, such as EZH2 inhibition plus immune checkpoint blockade or HDAC inhibition, are being explored to enhance anti-tumor responses by reactivating silenced immune genes and increasing chromatin accessibility.

Chapter 2:
Materials and Methods

2.1. Cell Culture and Treatment

DLD-1 human colorectal carcinoma cells, a pseudo-diploid model (Fig. 2.1), were cultured in RPMI-1640 medium supplemented with 10% fetal bovine serum (FBS), 2 mM L-glutamine, and 1% penicillin-streptomycin (100 U/mL penicillin and 100 µg/mL streptomycin) to prevent microbial contamination. The cells were maintained in a humidified incubator at 37°C with 5%-CO_2.

MCF10A human mammary epithelial cells were cultured in a 1:1 mixture of DMEM and F-12 medium, supplemented with 5% horse serum, 20 ng/mL epidermal growth factor (EGF), 0.5 µg/mL hydrocortisone, 100 ng/mL cholera toxin, and 10 µg/mL insulin. Antibiotic protection was provided by the addition of 1% penicillin-streptomycin. All cultures were maintained at 37°C in a humidified atmosphere containing 5% CO_2.

Component	DLD-1 Medium	MCF10A Medium
Basal Medium	RPMI-1640	DMEM/F-12 (1:1)
Serum Supplement	10% Fetal Bovine Serum (FBS)	5% Horse Serum
L-Glutamine	2 mM	—
Epidermal Growth Factor (EGF)	—	20 ng/mL
Hydrocortisone	—	0.5 µg/mL
Cholera Toxin	—	100 ng/mL
Insulin	—	10 µg/mL
Antibiotics	1% Penicillin-Streptomycin	1% Penicillin-Streptomycin
Incubation Conditions	37 °C, 5% CO_2, humidified incubator	37 °C, 5% CO_2, humidified incubator

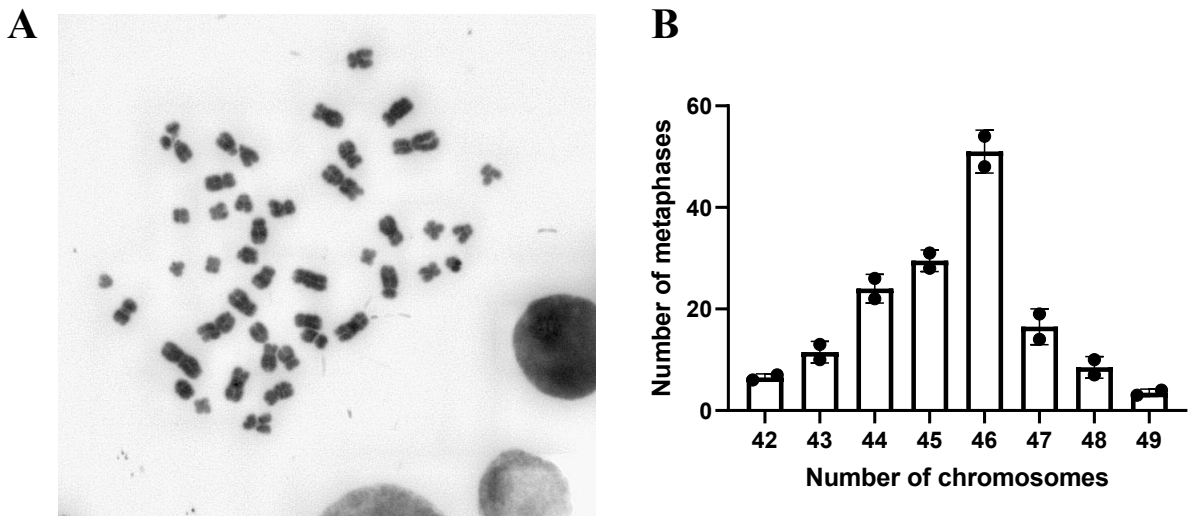

Fig. 2.1. Karyotype of the DLD-1 colorectal cancer cell line

(A) Representative metaphase spread showing the pseudodiploid karyotype characteristic of the DLD-1 cell line. Metaphase chromosome analysis confirms that DLD-1 cells exhibit a near-diploid karyotype, with modal number enriched at 46 (N=3, n=306). The representative inverted DAPI–stained metaphase spread. **(B)** A total of 306 metaphases were analyzed across three independent biological replicates.

2.2. Generation of Constructs

To functionally investigate the role of Fibrillarin (FBL) and its associated molecular interactions in regulating epithelial homeostasis, EMT, and chromatin remodeling, a suite of expression and knockdown constructs was generated using classical molecular cloning techniques. These included constructs for siRNA-resistant FBL, proximity-labeling vectors, overexpression plasmids for EZH2 and Scribble, and inducible shRNA expression systems for gene silencing.

2.2.1. Generation of siRNA-Resistant FBL Expression Constructs

The full-length coding sequence (CDS) of human *FBL* was initially obtained from a pEGFP-C1-Fibrillarin plasmid (gifted by Sui Huang, Northwestern University). To enable re-expression of FBL in knockdown experiments, we introduced silent mutations within the siRNA seed region of FBL without altering the amino acid sequence, thereby rendering the transcript resistant to siRNA-mediated degradation. Site-directed mutagenesis was performed using high-fidelity PCR amplification with partially overlapping primers designed to

incorporate the desired nucleotide substitutions, using Quikchange method (Liu and Naismith 2008).

Post-amplification, the PCR products were treated with DpnI (20 units, 3 hours at 37°C) to digest the methylated parental template plasmid. The digested product was then transformed into *E. coli* DH5α competent cells (Fig. 2.2). Single colonies were screened by colony PCR and validated by Sanger sequencing to confirm the incorporation of silent mutations. The resulting construct is hereafter referred to as GFP-FBL (siRes).

To subclone GFP-FBL (siRes) into a lentiviral expression vector, the mutated insert was PCR-amplified using primers flanked with BamHI and SalI restriction sites. After purification, the PCR product was double-digested with BamHI and SalI and ligated into the corresponding sites of the pLKO-MCS lentiviral backbone (Addgene #185594). The ligation reaction was incubated overnight at 16°C using 350 U of T4 DNA Ligase. Ligation products were transformed into *E. coli* DH5α, and positive clones were verified by sequencing.

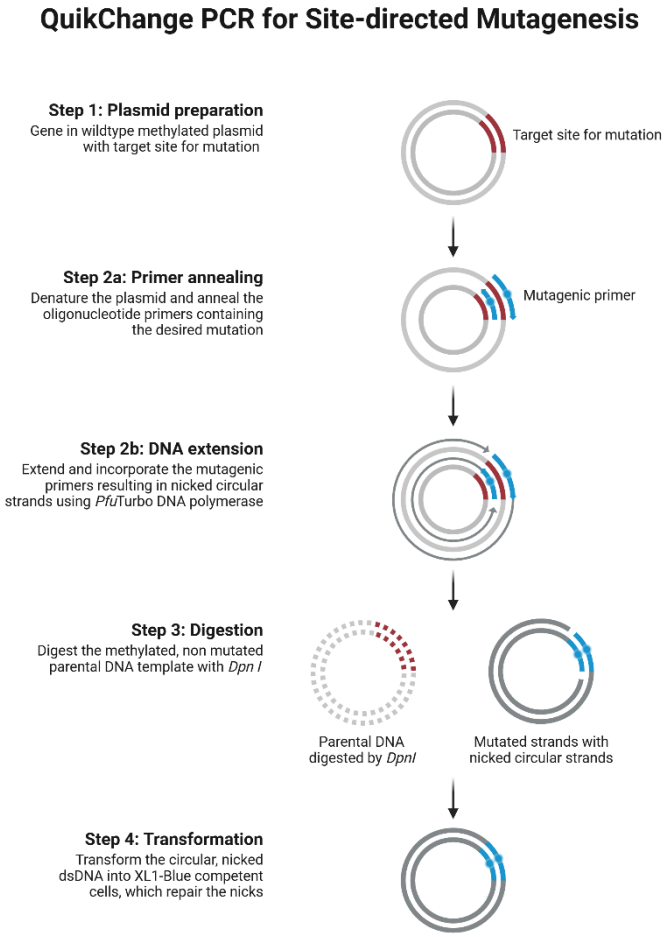

Fig. 2.2. Diagram illustrating the QuikChange PCR method for site-directed mutagenesis

A methylated plasmid containing the target site is denatured, followed by annealing of mutagenic primers carrying the intended nucleotide change. Primer extension by a high-fidelity polymerase generates nicked, circular mutant plasmids. The parental methylated DNA is then selectively digested using DpnI, and the resulting mutant plasmid is transformed into competent cells for repair and propagation. Adapted from (Braman et al. 1996).

2.2.2. Cloning of Wild-Type FBL into BioID2 Vector

To facilitate proximity-dependent biotin identification (BioID) experiments, wild-type FBL (FBL^{WT}) was cloned into the MCS-BioID2-HA pBabe-puro vector (Addgene #120308). The FBL CDS was amplified from the original pEGFP-C1-FBL plasmid with primers incorporating BamHI and EcoRI sites. The amplified product was gel-purified, digested, and ligated into the digested pBabe vector using standard ligation conditions. Positive clones were confirmed via restriction digestion and sequencing.

2.2.3. Generation of EZH2 Overexpression Constructs

To study the role of EZH2 in the epigenetic regulation of EMT targets and its interaction with FBL, a Flag-tagged EZH2 CDS was amplified from the MSCVhygro-F-EZH2 plasmid (Addgene #24926). The amplified product was engineered with NheI and EcoRI restriction sites and cloned into the doxycycline-inducible pCW57.1-GFP-tTA expression vector (Addgene #107551). Post-ligation, transformation, and selection were performed as described, and plasmids were validated by Sanger sequencing.

2.2.4. Cloning of SCRIB Expression Constructs

Since the CDS of human *SCRIB* is approximately 4.8 kb in length, a modified protocol for reverse transcription was adopted to avoid fragmentation during cDNA synthesis. Total RNA was extracted from DLD-1 cells using TRIzol reagent and converted to cDNA using SuperScript™ II Reverse Transcriptase. Oligo(dT)12-18 primers were used to ensure full-length cDNA synthesis. To prevent RNA degradation, which is often exacerbated by excess free Mg^{2+}, the reaction was supplemented with a final concentration of 4 mM dNTPs, limiting the availability of free Mg^{2+} and thereby stabilizing the RNA template during the reverse transcription process.

After completion of the cDNA synthesis and heat inactivation of the reverse transcriptase, full-length *SCRIB* CDS was PCR amplified using primers incorporating BamHI and EcoRI sites. The product was gel-purified, double-digested, and cloned into the pBABE-puro retroviral backbone (Addgene #21836). Ligation and transformation into *E. coli* DH5α were followed by colony screening and Sanger sequencing to confirm the correct orientation and integrity of the insert.

2.2.5. shRNA Constructs for FBL and SCRIB

To achieve conditional knockdown of *FBL* and *SCRIB*, shRNA sequences corresponding to validated siRNA regions were designed and synthesized as complementary oligonucleotides. The oligos were annealed in the presence of T4 Polynucleotide Kinase (10 U) at 37°C for 45 minutes, followed by thermal denaturation at 95°C and gradual cooling to 25°C. This ensured simultaneous 5′ phosphorylation and annealing of the strands to create cohesive ends compatible with AgeI and EcoRI digested sites of the Tet-pLKO-puro inducible vector (Addgene #21915).

Ligation reactions were set up using 5 µL of the annealed oligo duplex and 30 ng of the digested Tet-pLKO-puro vector with 350 U of T4 DNA ligase, incubated at 16°C overnight. The resulting constructs were transformed into *E. coli* DH5α and screened by XhoI digestion and sequencing to verify shRNA insertion.

2.3. siRNA-Mediated Gene Knockdown

Gene silencing via small interfering RNA (siRNA) was employed to deplete target transcripts in both DLD-1 and MCF10A(p53DN) epithelial cell lines. Custom-designed siRNA oligonucleotides targeting FBL (sense: AGGAGAACATGAAGCCGCA) were procured from Dharmacon (USA). For each experiment, approximately 0.2×10^6 cells were seeded into six-well plates 24 hours prior to transfection, allowing the cultures to reach 50–60% confluency.

Transfection was carried out using RNAiMAX transfection reagent (Invitrogen) according to the manufacturer's protocol. The siRNA-lipid complexes were prepared in Opti-MEM, a reduced-serum medium (Gibco), with a final siRNA concentration of 75 nM. Cells were incubated with the transfection mixture for 6 hours, following which the medium was replaced with their respective complete growth media (RPMI for DLD-1 and DMEM/F-12 for MCF10A).

MCF10A(p53DN) cells were harvested at 36- and 72-hours post-transfection for subsequent RNA isolation, immunofluorescence staining, or immunoblot analysis. DLD-1 cells were processed at 48- or 72-hours post-transfection, depending on the experimental endpoint. A non-targeting siRNA directed against LacZ (sense: CGUACGCGGAAUACUUCGAdTdT) served as the negative control for all RNAi experiments.

2.4. Immunofluorescence Assay

Approximately 0.2 million cells were seeded onto sterile 22 mm × 22 mm glass coverslips and allowed to adhere. After 24 hours, cells were gently washed twice with 1× phosphate-buffered saline (PBS, pH 7.4) for 5 minutes each. For general antigen detection, cells were fixed with 4% paraformaldehyde (PFA) prepared in PBS. For nuclear antigen staining, cells were first pre-permeabilized with ice-cold cytoskeleton (CSK) buffer containing 100 mM NaCl, 300 mM sucrose, 3 mM $MgCl_2$, 10 mM PIPES (pH 7.4), and 0.5% Triton X-100 for 4 minutes on ice, followed by PFA fixation (10 minutes) at RT.

Post-fixation, permeabilization was carried out using 0.5% Triton X-100 in 1X PBS for 10 minutes at RT. Non-specific binding was minimized by blocking the cells in 1% Bovine Serum Albumin (BSA) in 1X PBS for 30 minutes at room temperature. Coverslips were then incubated with primary antibodies diluted in blocking buffer for 2 hours, followed by fluorescently conjugated secondary antibodies for 1 hour. Nuclei were counterstained using

0.05 µg/mL DAPI for 2 minutes. After final 1X PBS washes, coverslips were mounted using SlowFade Gold Antifade reagent and stored at 4°C until imaging.
Fluorescence images were captured using Zeiss LSM 710 or LSM 780 confocal microscopes, equipped with a 63× Plan-Apochromat 1.4 NA oil immersion objective. Images were acquired with a zoom factor between 1.0 and 2.0, voxel dimensions of 0.07 µm × 0.07 µm × 0.34 µm, and a frame size of 1912 × 1912 pixels at 8-bit resolution. Line averaging was set to 4, and multi-channel acquisition was performed in sequential scanning mode (three or four channels).

2.5. Immunoblotting

For immunoblot analysis, total cell lysates were prepared using RIPA buffer (50 mM Tris-HCl (pH 7.4), 150 mM NaCl, 1% NP-40 or Triton X-100, 0.5% sodium deoxycholate, and 0.1% SDS, supplemented with 1Xprotease and 1Xphosphatase inhibitor cocktails), and protein concentrations were determined using the Bicinchoninic Acid (BCA) assay. Protein samples were denatured in 5× Laemmli buffer and resolved by SDS-PAGE on either 12.5% or 15% acrylamide-bisacrylamide gels, depending on the molecular weight of the target protein.

Following electrophoresis, proteins were transferred onto PVDF membranes (0.45µm) using a constant voltage of 80 V for 3 hours. Membranes were blocked for 1 hour at room temperature with 5% non-fat dry milk in 1× TBST (Tris-buffered saline with 0.1% Tween-20) to reduce non-specific binding. Primary and HRP-conjugated secondary antibodies were diluted in 0.5% milk in 1× TBST and incubated for 2 hours and 1 hour, respectively.
Protein bands were visualized using enhanced chemiluminescence (ECL) substrate (BioRad Clarity Western ECL), and images were acquired using the LAS4000 imaging system at 10-second exposure increments. Molecular weight was estimated using Precision Plus Protein Dual Color Standards ranging from 10 to 250 kDa.

2.6. Quantitative Real-Time PCR (RT-qPCR)

Total RNA was isolated from cultured cells using TRIzol reagent, and the RNA integrity was confirmed by spectrophotometric analysis and agarose gel electrophoresis. For cDNA synthesis, 1 µg of DNase-treated total RNA was reverse transcribed using the PrimeScript™

RT Reagent Kit (Takara, RR037A) according to the manufacturer's instructions. The reaction was carried out in a total volume of 20 µL, using a mixture of random hexamers and oligo(dT) primers to ensure comprehensive reverse transcription of all RNA species. The reverse transcription program included incubation at 37°C for 15 minutes for cDNA synthesis, followed by enzyme inactivation at 85°C for 5 seconds.

Subsequently, the synthesized cDNA was used as a template for quantitative real-time PCR, which was performed using TB Green® Premix Ex Taq™ (Takara, Cat# RR420A) on the Bio-Rad CFX96 Touch Real-Time PCR Detection System. Each reaction consisted of 10 µL of TB Green Premix, 0.4 µL each of forward and reverse primers (10 µM), 2 µL of diluted cDNA (typically 1:5), and nuclease-free water to a final volume of 20 µL. Thermal cycling conditions were set as follows: an initial denaturation at 95°C for 30 seconds, followed by 40 amplification cycles of 95°C for 5 seconds and 60°C for 30 seconds. Melt curve analysis was performed immediately after amplification to confirm primer specificity and the absence of primer-dimers or nonspecific amplification.

All reactions were conducted in technical triplicates, and each experiment was performed with at least three independent biological replicates. The relative gene expression levels were calculated using the ΔΔCt method, with GAPDH or 18S rRNA used as internal normalization controls, depending on experimental context. Primer efficiency was validated beforehand using a standard dilution curve, and only those primer sets with efficiencies between 90–100% were used for quantification.

2.7. Generation and Transduction of Viral Particles

Lentiviral and retroviral transductions were employed to stably express or knock down genes of interest in DLD-1 and MCF10A(p53DN) cells. Lentiviral particles were generated by transiently transfecting HEK293T cells with a lentiviral transfer plasmid and second-generation packaging plasmids psPAX2 and pMD2.G (in a 4:3:1 molar ratio). A total of 20 µg plasmid DNA was transfected into 100 mm dishes at ~65% confluency using standard transfection reagents. Seventy-two hours post-transfection, the viral supernatant was harvested, filtered, and supplemented with 12 µg/mL Polybrene to enhance transduction efficiency. Target epithelial cell lines were infected with the virus-containing media and subsequently subjected to selection using puromycin (4 µg/mL) or flow cytometry-based

sorting, depending on whether the construct carried a resistance gene or fluorescent tag. Successful transduction and expression were confirmed by immunoblotting or RT-PCR. For inducible shRNA-mediated knockdowns, doxycycline was added at a final concentration of 1200 ng/mL for FBL and 1000 ng/mL for SCRIB, with induction maintained for 48 hours across all experiments unless specified otherwise.

Retroviral transduction was similarly performed using HEK293T packaging cells co-transfected with the retroviral expression construct, pBS-CMV-gagpol, and pCAG-VSVG envelope plasmids (again in a 4:3:1 ratio), with a total DNA input of 20 µg per 100 mm dish. The transfection was carried out at ~65% confluency. Viral supernatants were collected 72 hours post-transfection, filtered, and supplemented with Polybrene (10 µg/mL) before being applied to the target cells. Post-infection, cells were selected using either puromycin (4 µg/mL) or hygromycin (50 µg/mL), depending on the antibiotic resistance cassette encoded by the viral vector. Expression of the gene of interest was verified by RT-PCR or western blot analysis.

2.8. Surface Sensing of Translation (SUnSET) Assay

To assess global protein synthesis upon FBL depletion, we utilized the Surface Sensing of Translation (SUnSET) assay, which monitors nascent polypeptide synthesis through the incorporation of puromycin into elongating chains during translation (Schmidt et al. 2009).

~0.2 million cells were transfected with either siLacZ (control) or siFBL. At 72 hours post-transfection, cells were pulsed with puromycin (1 µg/mL final concentration) for 15 minutes at 37 °C to allow incorporation into actively elongating peptides. Following the pulse, cells were immediately washed with ice-cold PBS and harvested.

To ensure accurate and unbiased comparison between control and FBL-depleted conditions, equal numbers of live cells from each condition were obtained by FACS-based sorting. This step ensured normalization based on cell count, rather than relying on total protein quantification.

Following sorting, cells were lysed in RIPA buffer supplemented with protease inhibitors (without quantification by protein estimation kits), and lysates were directly processed for SDS-PAGE. Equal volumes of lysates (from equivalent numbers of sorted cells) were resolved on polyacrylamide gels and transferred onto PVDF membranes using standard western blotting protocols.

Membranes were probed with a monoclonal anti-puromycin antibody (clone 12D10, Millipore) to detect puromycin-labeled nascent peptides. Chemiluminescent detection was performed using the Clarity ECL substrate (Bio-Rad), and images were acquired at multiple exposure times to ensure linear range of detection.

This assay enabled a direct comparison of translational output between siLacZ and siFBL-treated cells. Comparable levels of puromycin incorporation between conditions indicated that FBL depletion does not impair global protein synthesis, suggesting that the observed cellular phenotypes arise independently of changes in translational capacity.

2.9. EGTA-Mediated Calcium Chelation Assay for E-Cadherin Internalization

To evaluate the stability and membrane retention of E-cadherin under calcium-depleted conditions, a calcium chelation assay was performed using EGTA, a specific calcium chelator that disrupts calcium-dependent adherens junctions. This approach allowed for the assessment of E-cadherin internalization dynamics in both control and FBL-depleted cells (Tria et al. 2013).

DLD-1 cells transfected with siLacZ (control) or siFBL were cultured on 22 mm × 22 mm coverslips to approximately 60–70% confluency. After 72 hours of transfection, cells were washed once with 1× PBS (pH 7.4) and incubated in serum-free medium supplemented with 3 mM EGTA for 1 hour at 37 °C. This treatment chelates extracellular calcium and induces the disassembly of calcium-dependent E-cadherin-mediated cell-cell contacts, thereby facilitating internalization of E-cadherin from the plasma membrane. Following the EGTA incubation, cells were immediately washed with ice-cold PBS and fixed with 4% paraformaldehyde (PFA) in PBS for 15 minutes at room temperature. Cells were then permeabilized using 0.5% Triton X-100 in PBS for 10 minutes, blocked with 1% BSA for 30 minutes, and subjected to immunofluorescence staining for E-cadherin. E-cadherin localization was visualized using a primary antibody against E-cadherin followed by fluorescently conjugated secondary antibodies. Nuclei were counterstained with DAPI (0.05 μg/mL). Slides were mounted using SlowFade™ Gold Antifade and stored at 4 °C until imaging.

Images were acquired using a Zeiss LSM 710/780 confocal microscope with a 63× Plan-Apochromat oil objective. A consistent imaging protocol was followed for all experimental groups to allow quantitative comparison.

2.10. Transferrin Uptake Assay for Monitoring Clathrin-Mediated Endocytosis

To assess the efficiency of clathrin-mediated endocytosis in control and FBL-depleted cells, a transferrin internalization assay was performed using Alexa Fluor-conjugated human transferrin. This assay exploits the rapid, receptor-mediated endocytosis of transferrin through the transferrin receptor (TfR), a classical cargo of the clathrin-coated vesicle pathway (Khurana et al. 2023).

Cell Preparation

DLD-1 or MCF10A(p53DN) cells transfected with either siLacZ (control) or siFBL were seeded onto sterile 22 mm × 22 mm coverslips and allowed to grow to approximately 60–70% confluency. At 72 hours post-transfection, cells were serum-starved for 30 minutes at 37°C in serum-free RPMI (for DLD-1) or DMEM/F-12 (for MCF10A) to deplete endogenous transferrin and increase surface transferrin receptor availability.

Transferrin Uptake

Following serum deprivation, DLD-1 cells were incubated with Alexa Fluor 568–conjugated human transferrin (Thermo Fisher Scientific) at a final concentration of 25 µg/mL in pre-warmed serum-free medium for 15 minutes at 37°C to allow endocytosis to proceed.

Termination and Fixation

After the incubation, cells were incubated on ice to arrest further internalization and were washed quickly three times with ice-cold PBS to remove unbound transferrin. To remove transferrin bound to the cell surface but not internalized, cells were washed briefly with acidic buffer (0.2 M acetic acid, 0.5 M NaCl, pH 3.0) for 1–2 minutes on ice, followed by a PBS wash.

Cells were then fixed with 4% paraformaldehyde (PFA) in PBS for 15 minutes at room temperature. Post-fixation, cells were washed with PBS and counterstained with DAPI (0.05 µg/mL) for nuclear visualization. Coverslips were mounted with SlowFade Gold Antifade Mountant and stored at 4 °C until imaging.

Imaging and Analysis

Images were acquired using a Zeiss LSM 710/780 confocal microscope with consistent laser and gain settings across experimental groups (Fig. 2.3). For quantification, mean fluorescence intensity (MFI) of internalized transferrin per cell was calculated using FIJI/ImageJ by drawing a region of interest (ROI) around each cell, excluding the nucleus.

This assay enabled a comparative evaluation of endocytic trafficking under FBL-depleted conditions, providing insights into whether nucleolar dysfunction alters clathrin-mediated internalization, which may contribute to observed defects in membrane protein trafficking (e.g., E-cadherin internalization).

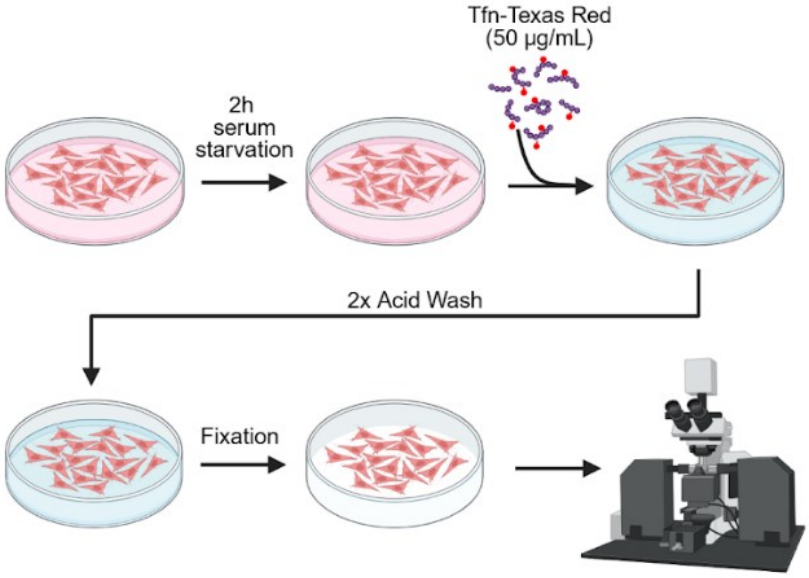

Fig. 2.3. Schematic representation of the transferrin uptake assay

Cells were serum-starved for 2 hours to deplete endogenous transferrin, followed by incubation with Texas Red–conjugated transferrin (50 µg/mL) to allow internalization. After incubation, cells underwent two acid washes to remove surface-bound transferrin, then were fixed and imaged by fluorescence microscopy to assess transferrin uptake.

2.11. RNA Sequencing and Transcriptomic Analysis

To delineate the transcriptional landscape altered by Fibrillarin (FBL) depletion, we performed high-throughput RNA sequencing in DLD-1 colorectal carcinoma cells. Approximately 0.6 million DLD-1 cells were seeded and transfected with either control (siLacZ) or siRNA targeting FBL (siFBL). Following 72 hours of incubation, total RNA was extracted using the RNeasy Mini Kit (Qiagen) according to the manufacturer's protocol, ensuring high-quality RNA suitable for sequencing applications.

The integrity and concentration of isolated RNA were verified using a NanoDrop spectrophotometer and agarose gel electrophoresis, and samples with RNA integrity number (RIN) values >8 were selected for library preparation. Poly-A enriched, strand-specific libraries were constructed using the NEBNext® Ultra™ II Directional RNA Library Prep Kit for Illumina (New England Biolabs), following the vendor's recommended workflow. The libraries were sequenced on the Illumina platform to generate paired-end 51 bp reads, yielding high-quality transcriptomic data for downstream analysis. The complete RNA-Seq dataset is publicly available via the Gene Expression Omnibus (GEO) under the accession number GSE289801.

Data Processing and Differential Expression Analysis

Raw sequencing reads were subjected to an initial quality assessment using FastQC to evaluate per-base quality scores, GC content, and sequence duplication levels. Adapter sequences and low-quality bases were trimmed using Trimmomatic (Bolger et al. 2014), ensuring high-fidelity data for alignment. Cleaned reads were then aligned to the human reference genome (GRCh38/hg38) using HISAT2 (Kim et al. 2015), a splice-aware aligner optimized for RNA-Seq datasets, implemented via the Galaxy bioinformatics platform.

Aligned reads were assembled and quantified using StringTie (Pertea et al. 2015), which estimated transcript abundance and normalized expression values using the FPKM (Fragments Per Kilobase of transcript per Million mapped reads) method. For statistical analysis of differential gene expression, raw read counts obtained from StringTie were analyzed using DESeq2 (Love et al. 2014), an R-based statistical package. Genes with adjusted p-values (Benjamini-Hochberg correction) below 0.05 were considered significantly differentially expressed (Fig. 2.4). A $\log_2$ fold change threshold was applied to define upregulated genes ($\log_2FC > 1$) and downregulated genes (log2FC < -1) between siLacZ and siFBL conditions.

Pathway and Functional Enrichment Analysis

To functionally interpret the transcriptomic changes upon FBL knockdown, we conducted Gene Ontology (GO) enrichment and Gene Set Enrichment Analysis (GSEA). GSEA was carried out using the GSEA desktop software (Broad Institute), using curated gene sets from the Molecular Signatures Database (MSigDB). Gene sets with Normalized Enrichment Score (NES) values and FDR q-values below 0.05 were considered significantly enriched. Enrichment plots were generated for key gene sets to visualize the distribution and significance of enrichment.

Additionally, GO enrichment analyses were performed for three major categories—Cellular Components, Molecular Functions, and Biological Processes—to identify functionally enriched annotations among differentially expressed genes. These analyses were conducted using ShinyGO (Ge et al. 2020) and SR Plot (Tang et al. 2023), applying a false discovery rate (FDR) cutoff of 0.05. Significantly enriched terms and pathways were further visualized through bubble plots and network diagrams.

Together, these analyses provided insights into FBL-mediated regulatory networks and highlighted pathways linked to ribosome biogenesis, cell polarity, and epithelial-to-mesenchymal transition (EMT), thus establishing a genome-wide framework of FBL-dependent transcriptional control.

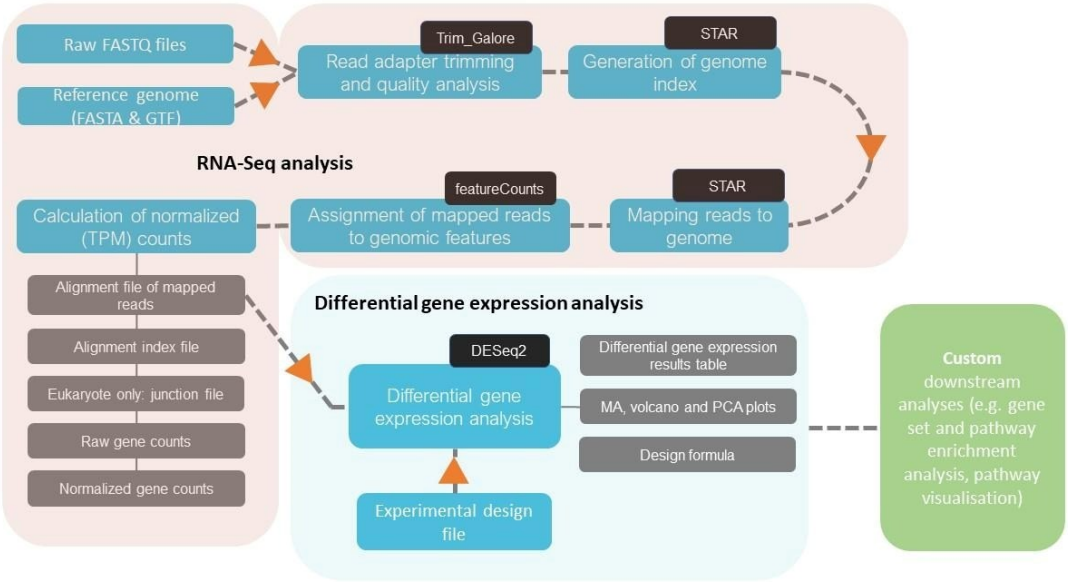

Fig. 2.4. Workflow for RNA-seq data processing and differential gene expression analysis

Overview of the analysis pipeline used for processing RNA-seq data. Raw FASTQ reads were subjected to adapter trimming and quality control using Trim_Galore, followed by genome index generation and read alignment with STAR. Mapped reads were then assigned to genomic features and normalized (TPM) using featureCounts. Differential gene expression analysis was performed in DESeq2, incorporating the experimental design matrix to generate statistical outputs including volcano, MA, and PCA plots. Final outputs were used for custom downstream analyses, including gene set and pathway enrichment analysis and data visualization.

2.12. Chromatin Immunoprecipitation Followed by PCR (ChIP-PCR)

Chromatin Crosslinking and Cell Harvesting

For chromatin immunoprecipitation, DLD-1 and MCF10A(p53DN) cells were cultured until they reached approximately 80% confluency. To preserve protein-DNA interactions, cells were fixed with 1% formaldehyde for 10 minutes at room temperature. The crosslinking reaction was subsequently quenched by adding 0.125 M glycine, followed by gentle mixing and incubation at room temperature for 5 minutes. Cells were then rinsed twice with ice-cold 1× phosphate-buffered saline (PBS, pH 7.4) and harvested by scraping. The cell suspension was centrifuged at 1,000 × g for 5 minutes at 4°C, and the resulting pellet was resuspended in ice-cold lysis buffer supplemented with protease inhibitors. The suspension was incubated on ice for 10 minutes to facilitate nuclear lysis and release of chromatin, as mentioned in (Saha et al. 2025; Labade et al. 2016).

Chromatin Shearing

Chromatin was fragmented by focused ultrasonication to achieve an optimal DNA fragment size of 100–500 bp. For DLD-1 cells, lysates were prepared in 130 µL lysis buffer and transferred into Covaris microTUBEs. Sonication was performed using a Covaris M220 system under the following settings: 75 W peak incident power, 60% duty factor, and 200

cycles per burst, for 30 minutes total, applied as 30 seconds on/off pulses, while maintaining the sample temperature at 6°C–7°C using an integrated chiller.

For MCF10A(p53DN) cells, the sonication conditions were similar, with a reduced sonication duration of 25 minutes under identical pulse and power parameters. Post-sonication, lysates were centrifuged at 16,000 × g for 10 minutes at 4°C, and the clear supernatant containing fragmented chromatin was collected for immunoprecipitation. The efficiency of chromatin fragmentation was assessed by agarose gel electrophoresis, and only those preparations showing a majority of fragments within the 100–500 bp range were processed further.

Immunoprecipitation of Chromatin

Fragmented chromatin was first pre-cleared using Protein A/G Dynabeads to reduce nonspecific interactions. This was carried out by incubating the chromatin with the beads for 1 hour at 4°C under gentle rotation. The pre-cleared chromatin was then incubated overnight at 4°C with target-specific antibodies. A total of 2 µg antibody was used for histone modifications and 5 µg for transcriptional regulators such as EZH2. An equivalent amount of IgG was used as a negative control to monitor background binding.

The next day, fresh Protein A/G Dynabeads were added to the antibody-chromatin complexes and incubated for an additional 1–2 hours at 4°C to capture immune complexes. Bead-bound chromatin was sequentially washed using the following buffers to minimize nonspecific binding:

- Low-salt buffer (0.1% SDS, 1% Triton X-100, 2 mM EDTA, 20 mM Tris-HCl pH 8.0, 150 mM NaCl)
- High-salt buffer (0.1% SDS, 1% Triton X-100, 2 mM EDTA, 20 mM Tris-HCl pH 8.0, 500 mM NaCl)
- LiCl buffer (0.25 M LiCl, 1% NP-40, 1% sodium deoxycholate, 1 mM EDTA, 10 mM Tris-HCl pH 8.0)
- TE buffer (10 mM Tris-HCl pH 8.0, 1 mM EDTA)

Each wash step was performed with constant rotation at 4°C.

Elution and Reverse Crosslinking

To release chromatin from the beads, immunoprecipitated complexes were incubated in an elution buffer containing 1% SDS and proteinase K (200 µg/mL). Crosslinks were reversed by incubating the samples at 65°C for 4–6 hours, ensuring complete dissociation of protein-DNA interactions. The released DNA was purified either by phenol-chloroform extraction followed by ethanol precipitation or using a commercial DNA purification kit (Qiagen). The final DNA pellet was resuspended in nuclease-free water and stored at −20°C until further analysis.

PCR Amplification and Detection

Purified DNA from ChIP was subjected to polymerase chain reaction (PCR) to amplify specific genomic loci. Each reaction was carried out in a total volume of 10 µL using 5 ng of ChIP DNA, 2X TB Green Taq polymerase master mix (Takara), and 0.3 µM of gene-specific primers. Thermal cycling conditions were optimized based on the melting temperatures of the primers and the expected amplicon size (Fig. 2.5).

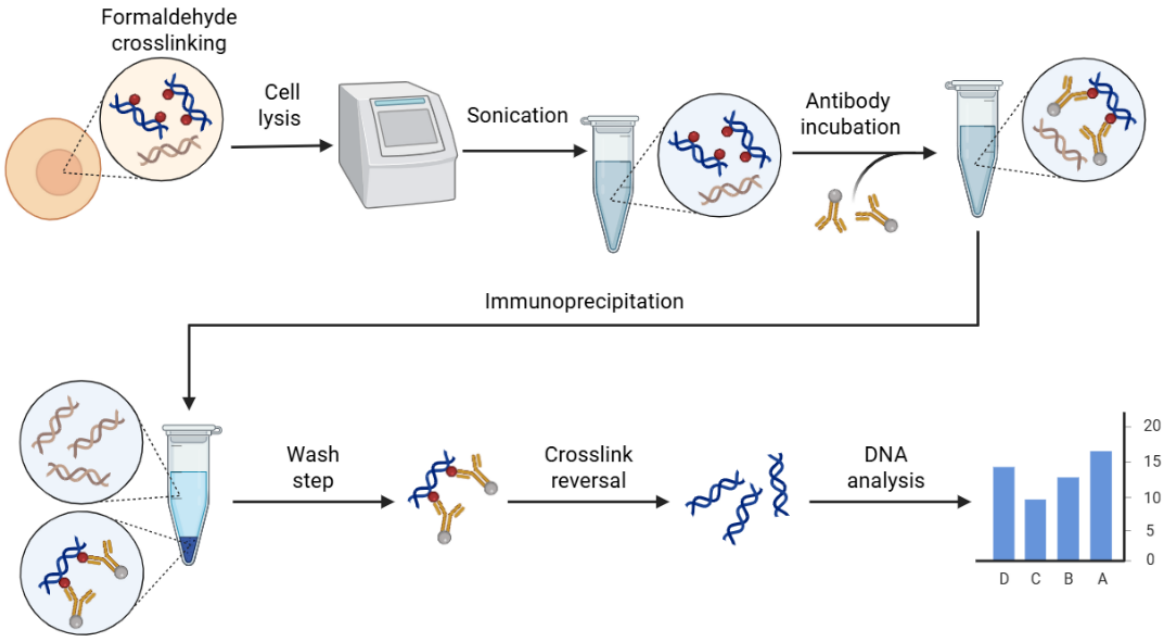

Fig. 2.5. Schematic representation of the ChIP–RT-qPCR workflow

Cells were crosslinked with formaldehyde to preserve protein–DNA interactions, followed by cell lysis and chromatin fragmentation by sonication. The sheared chromatin was incubated with specific antibodies to immunoprecipitate target protein–DNA complexes. After

sequential washing and crosslink reversal, DNA was purified and analyzed by RT-qPCR to quantify enrichment at selected genomic regions.

2.13. BioID2-Mediated Chromatin Immunoprecipitation and PCR (BioID2-ChIP-PCR)

To identify chromatin regions associated with Fibrillarin (FBL) proximity using the BioID2 system, we employed a proximity-dependent chromatin immunoprecipitation strategy in DLD-1 cells constitutively expressing either wild-type FBL fused to BirA* (FBL-WT-BioID2) or an empty vector (EV) control. Approximately 4 million cells were seeded into 100 mm tissue culture dishes and allowed to adhere overnight. Cells were treated with 50 µM Biotin for a minimum of 16 hours to facilitate in vivo biotinylation of FBL-proximal proteins and chromatin complexes (Fig. 2.6).

Following biotin incubation, cells were transfected with siLacZ (control) or siFBL at a final concentration of 75 nM, using standard RNAi protocols. After 36 hours, cells were harvested and immediately subjected to crosslinking with 1% formaldehyde for 10 minutes at room temperature, preserving protein–DNA interactions. The reaction was quenched with 0.125 M glycine and incubated for an additional 5 minutes to neutralize residual formaldehyde. Cells were rinsed twice with ice-cold PBS (pH 7.4) and detached by gentle scraping. Pelleted cells were lysed in a buffer composed of 50 mM HEPES-KOH (pH 7.5), 140 mM NaCl, 1 mM EDTA (pH 8.0), 1% Triton X-100, 0.1% SDS, and 0.1% sodium deoxycholate, supplemented with a protease inhibitor cocktail. The suspension was incubated on ice for 10 minutes to facilitate nuclear lysis (Kim et al. 2016).

Chromatin Shearing

Chromatin was fragmented using optimized sonication conditions to generate DNA fragments within the 200–600 bp range. Sonication was carefully performed to ensure retention of protein-DNA complexes, and the extent of fragmentation was validated by agarose gel electrophoresis.

Streptavidin-Based Chromatin Pull-Down

Following chromatin preparation, 100 µL of Streptavidin-coated Dynabeads were added to each lysate, and the suspension was incubated overnight at 4°C with constant rotation to enrich

for biotinylated chromatin fragments associated with FBL-BirA*. After incubation, the beads were collected using a magnetic stand and subjected to a series of stringent washes to eliminate nonspecific interactions. The sequential wash protocol included:

- Two washes with 2% SDS (w/v) to remove unbound proteins.
- A high-stringency buffer containing 0.1% sodium deoxycholate, 1% Triton X-100, 500 mM NaCl, 1 mM EDTA, and 50 mM HEPES-KOH (pH 7.5).
- Additional sequential washes with:
    - Low-salt buffer: 0.1% SDS, 1% Triton X-100, 2 mM EDTA (pH 8.0), 20 mM Tris-HCl (pH 8.0), 150 mM NaCl.
    - High-salt buffer: 0.1% SDS, 1% Triton X-100, 2 mM EDTA (pH 8.0), 20 mM Tris-HCl (pH 8.0), 500 mM NaCl.
    - LiCl buffer: 0.25 M LiCl, 1% NP-40, 1% sodium deoxycholate, 1 mM EDTA (pH 8.0), 10 mM Tris-HCl (pH 8.0).
    - TE buffer (pH 8.0) for final rinse and cleanup.

Elution and DNA Purification

Protein-DNA complexes were eluted from the beads using a buffer containing 1% SDS and 200 µg/mL proteinase K, followed by incubation at 65°C for 4–6 hours to reverse the crosslinks. DNA was then purified using a Qiagen DNA purification kit, and the final elution was carried out in nuclease-free water. The purified DNA was stored at –20°C until further analysis.

PCR Amplification of Target Regions

To evaluate chromatin enrichment at specific loci, 5 ng of BioID2-ChIP-derived DNA was used as a template for PCR amplification. Reactions were prepared in 10 µL volumes containing 2X TB Green Taq DNA Polymerase Master Mix (Takara) and 0.3 µM gene-specific primers. Thermal cycling conditions were optimized based on the amplicon characteristics and primer melting temperatures.

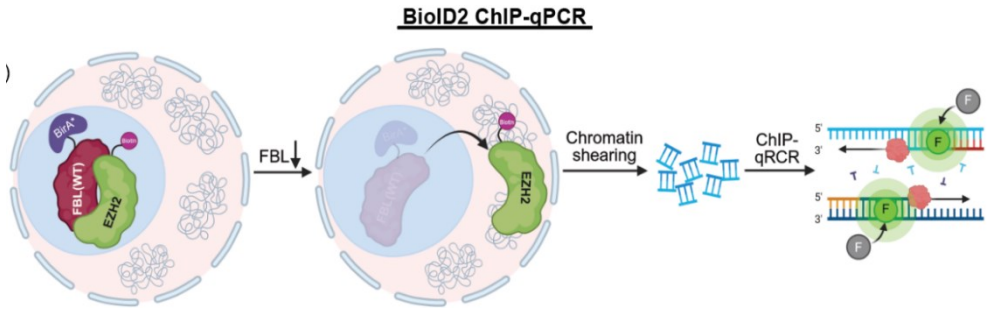

Fig. 2.6. Schematic representation of BioID2 ChIP-qPCR workflow to examine EZH2 chromatin association upon FBL depletion

Cells expressing BioID2-tagged EZH2 were subjected to FBL knockdown, followed by chromatin shearing and immunoprecipitation of biotinylated chromatin-associated proteins. Recovered DNA was subsequently analyzed by ChIP–qPCR to quantify EZH2 occupancy at specific genomic loci, enabling assessment of chromatin binding changes in response to FBL modulation.

2.14. Subcellular Fractionation: Isolation of Cytoplasmic, Nuclear, and Nucleolar Fractions

Cytoplasmic and Nuclear Fractionation

To assess the subcellular localization of specific proteins, cytoplasmic and nuclear fractions were isolated from DLD-1 and MCF10A(p53DN) cells. Approximately 10 million cells were processed per condition. Cells were initially washed thoroughly with ice-cold phosphate-buffered saline (PBS, pH 7.4) to remove any residual media components. Using a pre-chilled cell scraper, cells were detached on ice and collected into 1.5 mL microcentrifuge tubes containing 1 mL ice-cold PBS. The suspension was briefly centrifuged at 7,500 rpm for 10 seconds, after which the supernatant was carefully discarded.

The resulting cell pellets were gently resuspended in 900 µL of 0.1% NP-40 in PBS (ice-cold) and mixed by pipetting up and down five times using a P1000 micropipette to ensure efficient lysis of the plasma membrane while keeping the nuclear envelope intact. From this homogenate, 300 µL was removed and mixed with 100 µL of 5× Laemmli sample buffer,

designated as the whole cell lysate, and kept on ice until further processing (Suzuki et al. 2010).

The remaining 600 µL of lysate was subjected to another brief centrifugation for 10 seconds, allowing separation of the cytosolic and nuclear components. The supernatant (300 µL), representing the cytosolic fraction, was carefully aspirated and mixed with 100 µL of 5× Laemmli buffer, then immediately boiled for 1 minute to denature proteins.

To recover the nuclear pellet, the residual supernatant was discarded, and the pellet was resuspended in 1 mL of 0.1% NP-40 in PBS. A second brief centrifugation (10 seconds) was performed, after which the supernatant was discarded. The final nuclear pellet (~20 µL) was resuspended thoroughly in 180 µL of 1× Laemmli sample buffer.

Both the whole cell lysate and nuclear fraction were subjected to sonication using a microprobe sonicator (level 2 power setting) for two cycles of 5 seconds, to ensure DNA shearing and lysate homogenization. All samples were subsequently boiled for 1 minute before downstream analysis. Equal volumes from each fraction—10 µL of whole cell lysate, 10 µL of cytoplasmic fraction, and 5 µL of nuclear fraction—were loaded onto SDS-PAGE gels and transferred to nitrocellulose membranes for immunoblotting and marker validation.

Nucleolar Fraction Isolation

For nucleolar fractionation, a modified density-based centrifugation method was used to enrich for nucleoli from DLD-1 and MCF10A(p53DN) cells. Approximately 10 million cells per sample were processed. Cells were initially rinsed thoroughly with ice-cold PBS, and harvested in 0.5 mL of Sucrose Buffer I containing 0.5 M sucrose, 3 mM $MgCl_2$, and a 1× protease inhibitor cocktail (PIC) to protect labile proteins during lysis.

The cell suspension was subjected to mechanical disruption via sonication using a Sonics Vibracell probe sonicator. Sonication was performed on ice, using five cycles of 10 seconds ON and 10 seconds OFF at 50% amplitude, to ensure selective disruption of the nuclear membrane while maintaining nucleolar integrity.

The crude lysate was carefully layered over 0.7 mL of Sucrose Buffer II (composed of 1.0 M sucrose and 3 mM $MgCl_2$) to create a discontinuous sucrose gradient. The samples were centrifuged at 1,800 × g for 5 minutes at 4°C. Post-centrifugation, the supernatant containing soluble nuclear proteins was gently discarded without disturbing the pellet. The resulting nucleolar pellet was carefully resuspended in Radio Immunoprecipitation Assay (RIPA)

buffer for protein extraction and subsequent immunoblot analysis (Sen Gupta and Sengupta 2017).

This fractionation strategy enabled effective biochemical separation of the cytoplasmic, nuclear, and nucleolar compartments, which was critical for investigating subcellular protein localization, especially under FBL-depleted conditions.

2.15. Co-Immunoprecipitation (co-IP)

Co-immunoprecipitation (co-IP) was employed to investigate endogenous and exogenous protein–protein interactions under native conditions. This technique was particularly useful to validate interactions involving Fibrillarin (FBL), EZH2, and other candidate partners identified in prior screenings. All reagents were prepared fresh and maintained at 4°C throughout the procedure to preserve labile protein complexes.

Cell Harvesting and Lysis

DLD-1 and MCF10A(p53DN) cells were grown to ~80% confluency in 100 mm tissue culture dishes. Cells were washed twice with ice-cold phosphate-buffered saline (PBS, pH 7.4) to remove residual serum and media components, which can interfere with downstream interactions. The cells were harvested by scraping on ice, transferred to pre-chilled 1.5 mL microcentrifuge tubes, and pelleted by centrifugation at 1,000 × g for 5 minutes at 4°C.

The resulting cell pellet was resuspended in 1 mL of freshly prepared, ice-cold NP-40 lysis buffer, composed of the following:

- 50 mM Tris-HCl, pH 7.5
- 150 mM NaCl
- 1% NP-40 (non-ionic detergent)
- 1 mM EDTA
- 10% glycerol
- 1× protease inhibitor cocktail (Roche)
- 1×phosphatase inhibitor cocktail

The cell suspension was gently mixed and incubated on ice for 30 minutes with periodic inversion every 5 minutes. NP-40 was used as a mild detergent to solubilize membranes without disrupting native protein complexes. After lysis, cellular debris and insoluble aggregates were removed by centrifugation at 16,000 × g for 15 minutes at 4°C, and the clarified supernatant containing total cellular protein was transferred to fresh tubes, as mentioned in (Pradhan et al. 2018).

Protein Quantification and Pre-clearing

Although BCA estimation was not performed in this case, cell lysates were prepared from equal numbers of siLacZ (control) and siFBL (treated) cells (as determined by FACS-based cell counting) to ensure uniform input across samples. Pre-clearing was performed by incubating the lysate with 30–40 µL of Protein A/G magnetic beads (pre-equilibrated in lysis buffer) for 1 hour at 4°C under gentle end-over-end rotation. This step reduces non-specific binding of proteins or nucleic acids to the beads or antibodies in the subsequent IP steps. After pre-clearing, beads were separated using a magnetic stand, and the lysate was transferred to new, chilled tubes.

Antibody Incubation and Complex Capture

For each IP reaction, 500–800 µg of total protein lysate was incubated with 2–5 µg of primary antibody (specific to the bait protein) overnight at 4°C with continuous rotation. An equivalent amount of species- and isotype-matched IgG was included as a negative control for non-specific immunoglobulin interactions.
Following overnight incubation, 30–50 µL of Protein A/G agarose or magnetic beads (washed thrice in lysis buffer) were added to each reaction and incubated for 2–4 hours at 4°C to allow efficient capture of antibody–antigen complexes.

Bead Washing

To minimize non-specific protein binding, beads were washed 4–5 times with ice-cold lysis buffer. Each wash consisted of a 5-minute rotation followed by magnetic separation or gentle centrifugation (1,000 × g for 1 minute at 4°C). Wash buffers were as follows:

- Standard wash buffer (same as lysis buffer)

- Optional: High-salt buffer (500 mM NaCl) for increased stringency
- Optional: DNase/RNase treatment (if excluding nucleic acid-mediated interactions)
- Care was taken to avoid over-agitation, which could disrupt weak or transient interactions.

Elution and Sample Preparation for SDS-PAGE

After the final wash, the beads were resuspended in 40–50 µL of 2× Laemmli sample buffer supplemented with 5% β-mercaptoethanol or 100 mM DTT and heated at 95°C for 5–10 minutes to denature and release bound proteins.
Beads were pelleted by centrifugation or magnetically separated, and the supernatants were collected for electrophoresis.
Immunoblotting

Eluted proteins were resolved by SDS-PAGE (10–12% gel) and transferred onto nitrocellulose or PVDF membranes. Immunoblotting was carried out using appropriate primary and HRP-conjugated secondary antibodies. Detection was performed using enhanced chemiluminescence (ECL) substrates, and signals were captured using the LAS4000 imaging system or equivalent.

Control blots included:
- Input lysates (5–10% of starting material)
- IgG IP control
- Post-IP supernatants (optional, to assess depletion)
- Signal specificity and enrichment of prey proteins in bait IP lanes compared to IgG controls confirmed the presence of stable or transient protein–protein interactions.

2.16. Subcutaneous Xenograft Assay in NOD-SCID Mice

To evaluate the tumorigenic consequences of Fibrillarin (FBL) depletion, we established a subcutaneous xenograft model using NOD-SCID (NOD.CB17-Prkdc$^{scid/NcrCrl}$) immunodeficient mice, which lack mature T and B lymphocytes, enabling efficient engraftment of human tumor cells. All animal procedures were performed in compliance with

institutional ethical guidelines and were approved by the Institutional Animal Ethics Committee (IAEC, IISER_Pune/IAEC/2022_01/01).

Cell Preparation and Injection

Human colorectal carcinoma DLD-1 cells stably expressing shFBL under a Tet-ON inducible promoter were expanded in culture under standard conditions. At ~70–80% confluency, cells were harvested by trypsinization and washed thoroughly with sterile 1× PBS to remove serum components. Cells were resuspended in a 1:1 mixture of ice-cold PBS and Matrigel (Corning, Cat. No. 354234), and adjusted to a final density of 1×10^7 cells/mL. Each mouse received a subcutaneous injection of 100 µL of the prepared cell suspension (equivalent to 1×10^6 cells) into the right flank using a 26-gauge insulin syringe. Injections were performed aseptically on mildly restrained or briefly anesthetized animals. Mice were monitored post-injection for any signs of improper delivery or leakage.

Induction of FBL Knockdown

To achieve sustained knockdown of FBL, doxycycline (Dox) was administered via drinking water at a concentration of 2 mg/mL, supplemented with 5% sucrose to mask bitterness. Water bottles were protected from light and replaced every 72 hours throughout the experiment. Control mice received sucrose water alone (−Dox condition).

Monitoring and Endpoint Criteria

Mice were monitored biweekly for tumor appearance, growth kinetics, weight changes, and overall health. Tumor dimensions were measured using digital calipers, and tumor volume was calculated using the formula:

$$\text{Tumor Volume } (mm^3) = 21 \times (\text{Length} \times \text{Width}/2)$$

The experiment was terminated 35 days post-injection, at which point tumors were excised and analyzed.

Tumor Analysis and Molecular Characterization

At the experimental endpoint, tumors from both +Dox and −Dox groups were surgically excised and subjected to volume and weight measurements. Dox-treated mice (+Dox) exhibited significantly larger tumors in terms of both volume and weight compared to controls (−Dox), confirming that FBL depletion enhances tumorigenic potential in vivo.

Tumors were bisected: one half was snap-frozen in liquid nitrogen for immunoblot and nucleic acid extraction; the other was fixed in 10% neutral-buffered formalin for paraffin embedding and histological analysis.

2.17. Tail Vein Injection in NOD-SCID Mice to Assess Metastatic Potential

To evaluate the impact of FBL depletion on metastatic dissemination in vivo, a tail vein injection model was employed using NOD-SCID mice (NOD.CB17-Prkdc$^{scid/NcrCrl}$), which lack functional T and B lymphocytes, enabling efficient human tumor cell engraftment. All animal procedures were performed in accordance with the institutional animal care and use committee (IACUC) guidelines and were approved by the Institutional Animal Ethics Committee (IAEC).

Preparation of DLD-1 Cells Expressing Tet-ON shFBL

DLD-1 colorectal carcinoma cells stably expressing shFBL under a Tet-ON inducible promoter were cultured under standard conditions in RPMI-1640 medium supplemented with 10% FBS and antibiotics. Upon reaching ~70–80% confluence, cells were harvested using 0.25% trypsin-EDTA, followed by two washes in sterile, ice-cold 1× phosphate-buffered saline (PBS, pH 7.4) to remove residual serum and enzymes.
Cells were filtered through a 40 µm strainer to eliminate clumps and counted using a hemocytometer. The final cell suspension was adjusted to 1×10^7 cells/mL in sterile 1× PBS. A total of 1×10^6 cells (in 100 µL) was prepared per mouse for injection.

Tail Vein Injection

Mice were restrained gently in a pre-warmed restraining device to dilate the tail veins. Using a 30G insulin syringe, 100 µL of the cell suspension containing 1×10^6 DLD-1-shFBL cells was injected into the lateral tail vein of each mouse. Injections were performed slowly over 5–10 seconds to avoid vessel rupture or leakage. Mice were monitored closely for any immediate signs of injection-related complications and returned to their cages under observation.

Induction of FBL Depletion

To induce stable FBL knockdown in vivo, mice were randomly assigned to two groups:

- +Dox group: Received 2 mg/mL doxycycline in drinking water supplemented with 5% sucrose to enhance palatability. The solution was protected from light and replaced every 72 hours.
- −Dox group: Received 5% sucrose water without doxycycline as a control.
- Doxycycline administration was started 24 hours post-injection and continued throughout the duration of the experiment to ensure sustained shRNA expression.

Monitoring and Endpoint Analysis

Animals were monitored thrice weekly for changes in body weight, behavior, respiratory function, and overall health. Mice exhibiting signs of systemic distress, rapid weight loss, or labored breathing were flagged for humane euthanasia. The experiment was terminated 60 days post-injection. Mice were euthanized by CO_2 asphyxiation, and lungs were harvested for metastatic burden assessment. Lungs were inflated with 10% neutral-buffered formalin and fixed overnight.

2.18. Histological and Quantitative Assessment of Metastases

Formalin-fixed lung tissues were embedded in paraffin, sectioned, and subjected to hematoxylin and eosin (H&E) staining. Slides were imaged using a brightfield microscope to identify metastatic foci. To quantify lung metastatic burden, digital images were analyzed using FIJI (ImageJ). The metastatic score was calculated using the formula:

Metastatic Score = (Total lung area/Total metastatic area) ×100

Mice from the +Dox group displayed a significantly higher metastatic score compared to controls, indicating that FBL depletion enhances metastatic colonization in vivo.

Hematoxylin and Eosin (H&E) Staining of Paraffin-Embedded Lung and Tumor Tissues

To assess tissue morphology and metastatic infiltration, formalin-fixed, paraffin-embedded (FFPE) lung and tumor sections were subjected to standard Hematoxylin and Eosin (H&E) staining, a routinely employed histological technique for visualizing cellular and tissue architecture.

Tissue Fixation and Embedding

Lungs and subcutaneous tumors harvested from euthanized NOD-SCID mice were rinsed in phosphate-buffered saline (PBS) and fixed in 10% neutral-buffered formalin (NBF) for 24–48 hours at room temperature. Tissues were then dehydrated through a graded ethanol series (70%, 80%, 95%, and 100%) and cleared in xylene before being embedded in paraffin wax using a tissue processor. Tissue blocks were solidified and stored at room temperature until sectioning.

Sectioning

FFPE blocks were trimmed and sectioned at 4–5 μm thickness using a rotary microtome. Sections were floated on a 42°C water bath and mounted onto positively charged glass slides. The slides were then air-dried and incubated at 60°C for 1 hour to enhance tissue adherence.

Deparaffinization and Rehydration

Prior to staining, slides were deparaffinized and rehydrated as follows:

- Xylene: 2 changes, 5 minutes each
- 100% Ethanol: 2 changes, 3 minutes each
- 95% Ethanol: 1 change, 3 minutes
- 70% Ethanol: 1 change, 3 minutes
- Running Tap Water: 5 minutes

This step removes paraffin and gradually rehydrates the tissue, preparing it for aqueous staining solutions.

Hematoxylin Staining

Slides were immersed in Harris hematoxylin (or Mayer's hematoxylin, depending on lab preference) for 4–5 minutes at room temperature to stain nuclear chromatin.

- Rinse in running tap water for 5 minutes

- Differentiate in 0.3% acid alcohol (1% HCl in 70% ethanol) for 10–15 seconds to remove excess hematoxylin
- Rinse in running tap water for 5 minutes
- Bluing in 0.1% ammonia water or Scott's tap water substitute for 1 minute
- Rinse in running tap water for 2 minutes
- This sequence sharpens nuclear contrast and fixes hematoxylin to chromatin.

Eosin Staining

Slides were incubated in 0.5–1% eosin Y solution (in 95% ethanol) for 1–2 minutes to stain cytoplasmic and extracellular components.

- Rinse briefly in 95% ethanol to remove excess eosin
- Dehydrate through increasing ethanol concentrations:
- 95% ethanol: 1 minute
- 100% ethanol: 2 changes, 2 minutes each
- Clear in xylene: 2 changes, 5 minutes each

Mounting and Imaging

After clearing, slides were mounted using a permanent mounting medium (e.g., DPX or Permount) and covered with a glass coverslip. Slides were allowed to cure and stored at room temperature.

2.19. Scratch Wound Healing Assay

To investigate the migratory behavior of epithelial cells upon gene knockdown or pharmacological treatment, a scratch wound healing assay was performed. This assay enables the assessment of two-dimensional (2D) collective cell migration, which mimics wound closure in epithelial tissues and is a commonly used method to evaluate epithelial plasticity, particularly in the context of epithelial-to-mesenchymal transition (EMT).

DLD-1 and MCF10A(p53DN) cells were initially cultured in RPMI-1640 and DMEM-F12, respectively, under standard conditions (37°C, 5% CO_2) following siRNA-mediated

knockdown or drug administration. Approximately 12 hours post-transfection, cells were gently trypsinized, counted, and seeded into 24-well tissue culture plates at a density optimized to achieve confluence within the next 12–16 hours. Achieving a uniform monolayer is critical for minimizing variability in the wound area and ensuring consistency across replicates.

Once a confluent monolayer was established (typically 24 hours post-seeding), a straight linear wound was created in the center of each well using a sterile 200 μL pipette tip. The pipette tip was held perpendicular to the bottom of the plate and drawn steadily across the cell layer to avoid creating jagged or uneven wound edges. Care was taken to apply consistent pressure during scratch formation to ensure reproducibility across wells and experimental conditions.

Immediately after wounding, detached cells were removed by gently washing each well twice with sterile 1X phosphate-buffered saline (PBS). After washing, fresh assay medium appropriate for each cell line was added. For DLD-1 cells, RPMI containing 0.5% FBS was used to suppress cell proliferation and isolate the migratory component of wound closure. For MCF10A(p53DN) cells, EGF-free DMEM-F12 or Assay Medium was used for the same purpose.

Plates were then returned to the incubator and maintained under standard conditions for 48 hours, unless a shorter or longer observation period was necessitated by specific experimental requirements. At designated time points (typically t = 0 and t = 48 hours), wound closure was documented using a phase-contrast microscope at a fixed magnification. Multiple fields along the length of the wound were imaged to ensure adequate sampling and statistical validity (Fig. 2.7).

Quantification of wound closure was carried out using T-Stratch software. The wound area at each time point was measured, and the percentage of wound closure was calculated using the following formula:

Where:

Wound Closure (%) = (Initial Wound Area-Final Wound Area) ×100

Initial Wound Area refers to the open gap measured immediately after scratching (t = 0).

Final Wound Area refers to the remaining gap at the assay endpoint.

This quantitative measurement allowed for direct comparison of migration rates across various treatments and conditions, enabling functional insights into how specific gene perturbations, such as FBL or SCRIB depletion, influence epithelial sheet motility.

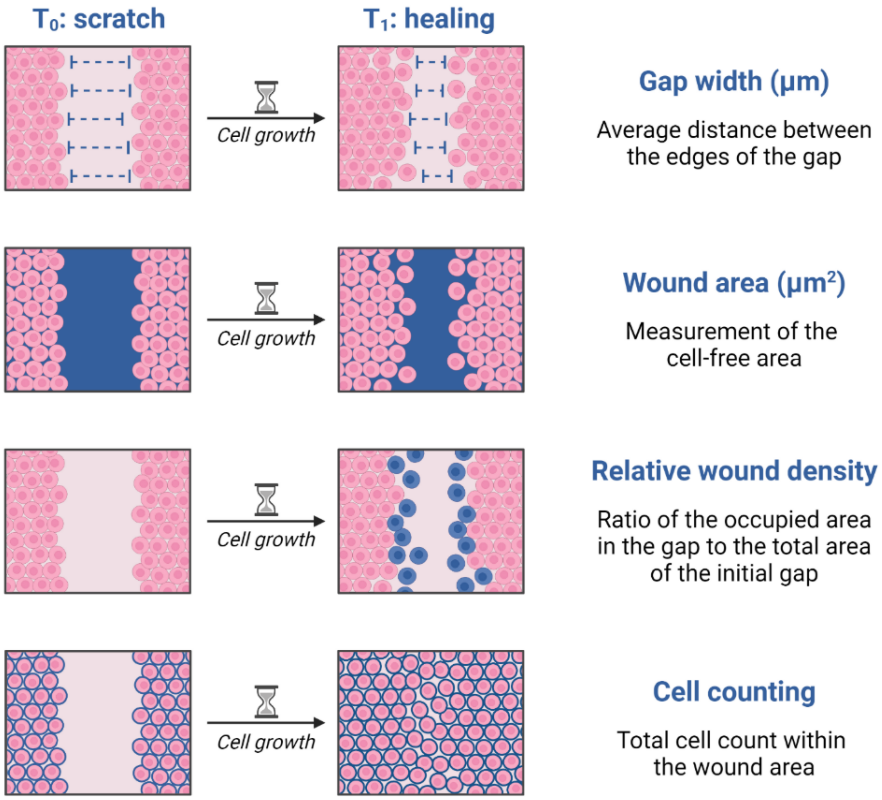

Fig. 2.7. Schematic representation of the scratch wound healing assay and quantification parameters

A scratch was introduced in a confluent cell monolayer (T_0) and wound closure was monitored during cell migration and proliferation (T_1: healing). Wound recovery was quantified using multiple metrics: gap width (µm) — average distance between wound edges; wound area (µm²) — remaining cell-free region; relative wound density — proportion of newly occupied area relative to initial wound space; and cell counting — number of cells migrated into the wound area.

2.20. Transwell Invasion Assay

To complement the findings of the wound healing assay and further assess the invasive properties of cells in response to genetic or pharmacological perturbations, a Transwell invasion assay was employed. This technique enables the study of chemotactic migration, in which cells move in response to a chemoattractant gradient through a porous membrane.

Transwell inserts with 8 μm pore-sized polycarbonate membranes (Corning) were used without Matrigel coating to specifically measure non-invasive cell migration rather than invasion through extracellular matrix (ECM) components. Approximately 36 hours post-siRNA transfection, cells were trypsinized, counted using a hemocytometer or automated counter, and resuspended in serum-free media to eliminate the influence of growth factors during the assay.

A total of 5×10^4 cells in 100–150 μL of serum-free RPMI or DMEM-F12 were seeded into the upper chambers of the inserts, which had been placed into corresponding wells of a 24-well plate. The lower chambers were filled with 600 μL of complete media containing 10% FBS for DLD-1 cells or 5% horse serum for MCF10A(p53DN) cells. These conditions were optimized to act as a chemoattractant and induce directional migration.
The plates were incubated at 37°C in a humidified CO_2 incubator for 36 hours, allowing cells to migrate through the pores toward the chemoattractant. After incubation, non-migrated cells on the upper surface of the membrane were carefully removed using a cotton swab, taking care not to disturb the lower surface. Migrated cells on the underside of the membrane were fixed with 4% paraformaldehyde (PFA) for 10 minutes at room temperature and then stained with DAPI to visualize nuclei.

Stained membranes were imaged using a fluorescence microscope, and five to seven random fields per insert were captured at 20× magnification. Quantification was performed using either manual counting or automated cell counting modules in ImageJ, allowing for statistical comparison of migratory behavior across conditions.

This assay provided an orthogonal measure of mesenchymal-like migration, capturing phenotypic outcomes relevant to EMT and metastatic potential. The ability to compare

Transwell migration with wound healing responses enabled a comprehensive evaluation of the role of FBL and SCRIB in epithelial cell motility.

Chapter 3:

Fibrillarin Controls Epithelial Architecture and Nuclear Organization

3.1. Introduction

Fibrillarin (FBL), a nucleolar methyltransferase required for 2′-O-methylation and processing of precursor rRNA, is canonically known for its essential role in ribosome biogenesis and cellular homeostasis (Newton et al. 2003; Tollervey et al. 1993). However, recent studies have identified nucleolar proteins as critical regulators of nuclear structure, chromatin dynamics, and cellular behavior under stress conditions (González-Arzola 2024; Yang et al. 2018). In the context of epithelial cells, which require tightly regulated junctional complexes and cytoskeletal integrity to maintain monolayer organization, the role of FBL remains poorly understood.

Loss of FBL in epithelial systems resulted in profound disruption of epithelial integrity and nuclear architecture. In both DLD-1 and MCF10A(p53DN) cells, FBL depletion led to a transition from the typical polygonal, cobblestone morphology to an elongated, spindle-like form, indicative of partial Epithelial-to-Mesenchymal Transition (EMT). Quantitative image analysis revealed a significant increase in aspect ratio upon FBL depletion, reflecting increased cellular elongation. These morphological alterations were accompanied by cytoplasmic redistribution of adherens and tight junction components—E-cadherin and ZO-1, respectively—suggesting impaired polarity and intercellular adhesion.

Intriguingly, the internalized E-cadherin co-localized with the Golgi marker GM130 (Lohia et al. 2012), suggesting a retention defect rather than a degradation event. Rescue experiments with Dynasore, a dynamin GTPase inhibitor, restored the membrane localization of E-cadherin, implicating clathrin-mediated endocytosis in the phenotype. Such trafficking alterations may underlie the adhesive defects observed following FBL loss.

In parallel, FBL depletion also elicited pronounced nuclear morphological changes, with decreased sphericity, increased surface area, and formation of micronuclei and nuclear blebs. These alterations occurred independently of Lamin A/C and B-type lamin levels, suggesting a chromatin-driven mechanism. Elevated deposition of heterochromatin-associated marks—H3K27me3 and H3K9me3—was observed in FBL-depleted cells at both the single-cell and population levels, suggesting global chromatin compaction. These findings are in contrast with classical models where chromatin decompaction contributes to nuclear softening; rather,

the data support a compensatory upregulation of repressive histone marks to stabilize nuclear architecture under nucleolar stress.

We further observed that FBL-depleted cells upregulated the inner nuclear envelope protein Emerin (Fig. 3.8(A-C)), which binds to repressive chromatin and recruits histone-modifying enzymes such as HDAC3, G9a, and EZH2 (Demmerle et al. 2012; Marano and Holaska 2022). Given the concurrent increase in H3K9me3 and Emerin levels, it is plausible that Emerin upregulation serves as a structural adaptation to nuclear deformation, consistent with previous studies linking Emerin to nuclear stiffness and heterochromatin organization (Dubińska-Magiera et al. 2019).

Interestingly, while both H3K9me3 and H3K27me3 were elevated, only the reduction of H3K27me3—via pharmacological inhibition of EZH2—was sufficient to rescue the enhanced migration phenotype associated with FBL loss. Genetic knockdown of SUV39H1, the H3K9 methyltransferase, failed to elicit a similar rescue, reinforcing a functional distinction between these heterochromatin marks. These findings align with prior studies linking EZH2-mediated H3K27me3 deposition to enhanced cancer cell plasticity and metastasis (Xu et al. 2012; McCabe et al. 2012).

Together, these results uncover a critical and previously unappreciated role for Fibrillarin in regulating epithelial morphology, junctional stability, nuclear shape, and epigenetic identity. By integrating mechanical and chromatin-based responses, FBL emerges as a central node in the maintenance of epithelial architecture, with potential implications for understanding nucleolar stress responses, chromatin remodeling, and early events in tumor progression.

FBL Depletion Perturbs Cell Morphology Independently of Protein Translation

Fibrillarin (FBL) depletion resulted in a striking disruption of classical epithelial morphology, characterized by the loss of the uniform, tightly packed cobblestone appearance that is typically observed in healthy epithelial monolayers. This morphological transformation was evident upon microscopic examination, as illustrated in (Fig. 3.1(A-B)). To address if the depletion of FBL manifests in a cell type independent manner, we independently silenced FBL in two distinct epithelial cell lines: DLD-1 (a colorectal carcinoma cell line) and MCF10A (a non-tumorigenic mammary epithelial line expressing a dominant-negative form of p53, referred to as p53DN). In both cell types, FBL knockdown induced a prominent morphological shift from a polygonal to an elongated, spindle-shaped form, suggestive of a partial epithelial-to-mesenchymal transition (EMT)-like phenotype.

Quantitative analysis of cellular morphology confirmed this visual observation. Measurement of the aspect ratio—a geometric descriptor representing the ratio of cell length to width—revealed a statistically significant increase following FBL depletion. Specifically, DLD-1 cells exhibited an approximate 5.8-fold increase (±1.0), whereas MCF10A(p53DN) cells demonstrated a 2.35-fold increase (±0.5) in aspect ratio compared to their respective control counterparts, as shown in Fig. 3.1B. These data collectively underscore the critical role of FBL in maintaining epithelial morphology and suppressing aberrant cell elongation.

Fibrillarin (FBL) is a nucleolar protein essential for the biogenesis and chemical modification of ribosomal RNA (rRNA), particularly in the processing of precursor 45S rRNA into mature 18S, 5.8S, and 28S rRNA species. Given its fundamental role in ribosome assembly and function, perturbation of FBL levels has the potential to influence both rRNA maturation and overall protein synthesis. To investigate whether depletion of FBL compromises global protein synthesis, we employed the Surface Sensing of Translation (SUnSET) assay, a non-radioactive method that allows quantification of nascent protein synthesis by puromycin incorporation. Interestingly, FBL-depleted cells did not exhibit a significant reduction in protein synthesis as measured by this assay (Fig. 3.2 I); S.D. = 0.26 (For 45S rRNA), indicating that global translation rates remained largely unaffected despite the knockdown.

This unexpected result led us to hypothesize that the residual FBL levels remaining after depletion may still be functionally sufficient to support critical steps in ribosome biogenesis, particularly the early processing of the 45S rRNA precursor. To explore this possibility, we analyzed the abundance of mature rRNA species following FBL knockdown. Notably, no substantial alterations were observed in the levels of 28S and 18S rRNA (Fig. 3.2H), suggesting that rRNA maturation proceeds relatively normally in the presence of low FBL levels. These findings imply that a threshold level of FBL activity is maintained even after siRNA-mediated depletion, which may be adequate to sustain essential nucleolar functions, thereby preserving basal translational output. Collectively, these observations highlight the robustness of the ribosome biogenesis machinery and suggest that FBL must be reduced beyond a critical threshold to significantly impair global protein synthesis.

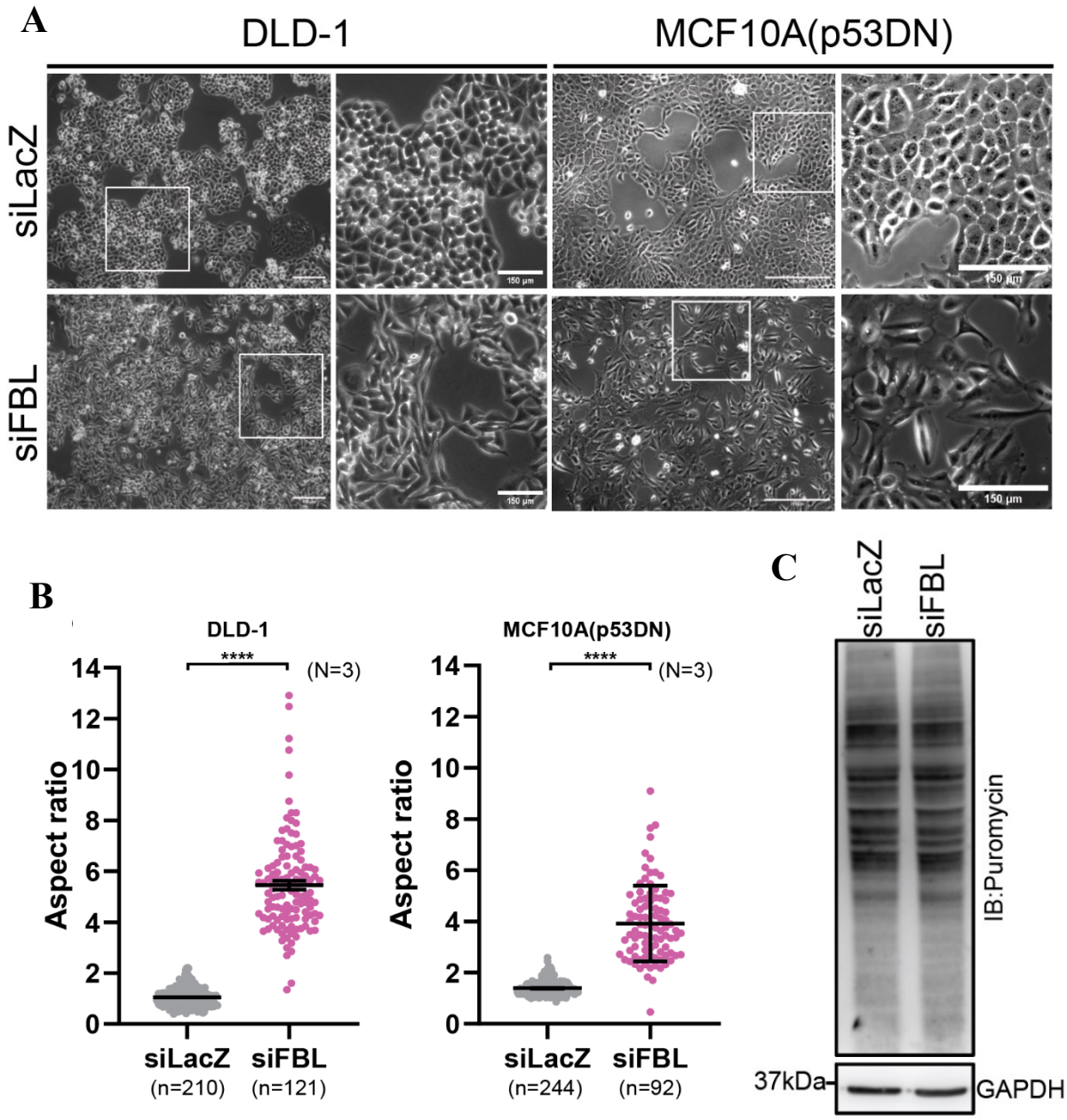

Fig. 3.1. FBL is required for maintenance of epithelial morphology and protein synthesis **(A)** Phase-contrast micrographs of siLacZ (control) and siFBL-treated DLD-1 and MCF10A(p53DN) cells at approximately 48 h and 36 h post-transfection, respectively. FBL depletion results in an elongated, spindle-like morphology accompanied by disruption of the characteristic epithelial cobblestone appearance. Scale bar, ~150 µm; inset scale bar, 150 µm (N = 3). (B) Quantitative analysis of cellular aspect ratio following FBL knockdown in DLD-1 and MCF10A(p53DN) cells at ~48 h post-transfection. Statistical significance was determined using an unpaired t-test. Measurements were pooled from 331 DLD-1 cells and 336 MCF10A(p53DN) cells across three independent biological replicates (N = 3) **(C)** SUnSET assay assessing global protein synthesis in siLacZ- and siFBL-transfected DLD-1

cells at approximately 48 h post-transfection. Puromycin-labeled nascent polypeptides were detected by immunoblotting, with GAPDH serving as a loading control (N = 2).

3.2.1. Internalization of E-Cadherin and ZO-1 Upon Loss of FBL

Fibrillarin (FBL) depletion led to a marked alteration in epithelial cell morphology, disrupting the characteristic cobblestone-like arrangement of tightly packed cells. This loss of structural uniformity indicates a breakdown in epithelial organization.

FBL depletion showed striking alterations in the subcellular localization of key epithelial adhesion molecules, most notably E-cadherin. Under normal physiological conditions, E-cadherin is predominantly localized at the plasma membrane, where it plays a central role in forming adherens junctions and maintaining epithelial integrity. However, upon knockdown of FBL, a substantial redistribution of E-cadherin was observed. Instead of localizing to the cell membrane, E-cadherin accumulated within the cytoplasmic compartment in ~72.5% (±12.5%) of cells, as shown in (Fig. 3.2A, D). This internalization was associated with a pronounced loss of cell-cell adhesion, suggesting that the adhesive architecture of the epithelial sheet was significantly compromised. Despite this altered localization, total cellular levels of E-cadherin protein remained largely unchanged, as confirmed by immunoblot analysis (Fig. 3.2(F-G); S.D.= 0.26). This indicates that the loss of membrane-associated E-cadherin was not due to downregulation or degradation, but rather due to dysregulated trafficking or increased internalization, possibly through an endocytic mechanism.

Notably, the mislocalization of adhesion proteins upon FBL depletion was not restricted to E-cadherin alone. ZO-1, a tight junction-associated scaffolding protein that normally localizes at the apical-most region of epithelial cell-cell contacts, also exhibited aberrant localization. In FBL-depleted cells, ZO-1 was found to be redistributed away from the plasma membrane and internalized into the cytoplasm, as shown in (Fig. 3.2 B, E) ~58.6% (±9.2%). This parallel mislocalization of both E-cadherin and ZO-1 strongly suggests a coordinated breakdown of intercellular junctional complexes following loss of FBL. Given that adherens junctions and tight junctions function cooperatively to establish and maintain epithelial barrier integrity, the simultaneous disruption of these structures implies a fundamental role of FBL in preserving epithelial architecture.

As we observed co-internalization of E-cadherin and ZO-1, to further dissect whether E-cadherin internalization is triggering ZO1 internalization, we performed EGTA mediated Ca^{2+} chelation assay. Upon incubating DLD-1 cells with EGTA(3mM) for 1 h, the E-cadherin stability on the cell membrane was compromised, as a result, E-cadherin was internalized into

cytoplasm along with ZO-1, as observed in a previous study (Tria et al. 2013) (Fig. 3.2C). Therefore, in an FBL depletion independent way we confirmed that E-cadherin internalization is leading to the internalization of ZO-1 in DLD-1, an observation that overlaps with the FBL depletion mediated co-internalization of E-cadherin and ZO-1.

To test whether E-cadherin internalization upon FBL depletion reflects altered endocytic trafficking, we assessed global endocytosis using a transferrin uptake assay. Transferrin internalization was unchanged following FBL knockdown (Fig. 3.2H), indicating that E-cadherin internalization is not due to a global increase in endocytosis.

Together, these findings indicate that FBL is essential for maintaining proper subcellular localization of major junctional proteins, and by extension, for the structural and functional integrity of epithelial monolayers. The internalization of E-cadherin and ZO-1 following FBL knockdown may reflect broader perturbations in membrane trafficking pathways or cytoskeletal organization, positioning FBL as a potential upstream regulator of junctional homeostasis. Further investigations are warranted to delineate the molecular mechanisms through which FBL influences adhesion protein localization, and whether this effect is mediated via direct interactions, epigenetic regulation, or alterations in intracellular transport dynamics.

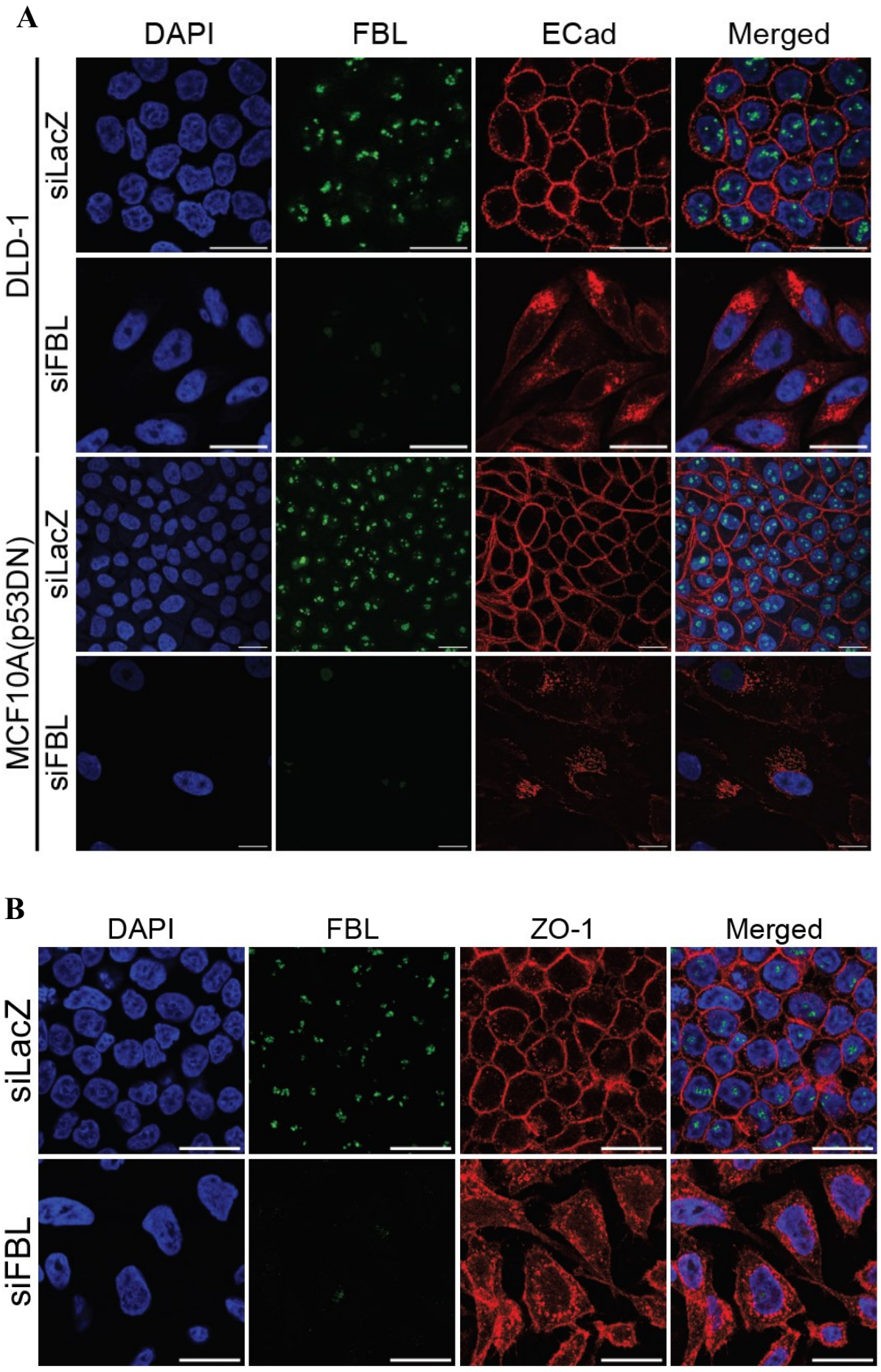
A
DAPI
FBL
ECad
Merged
DLD-1
siLacZ
siFBL
MCF10A(p53DN)
siLacZ
siFBL
B
DAPI
FBL
ZO-1
Merged
siLacZ
siFBL

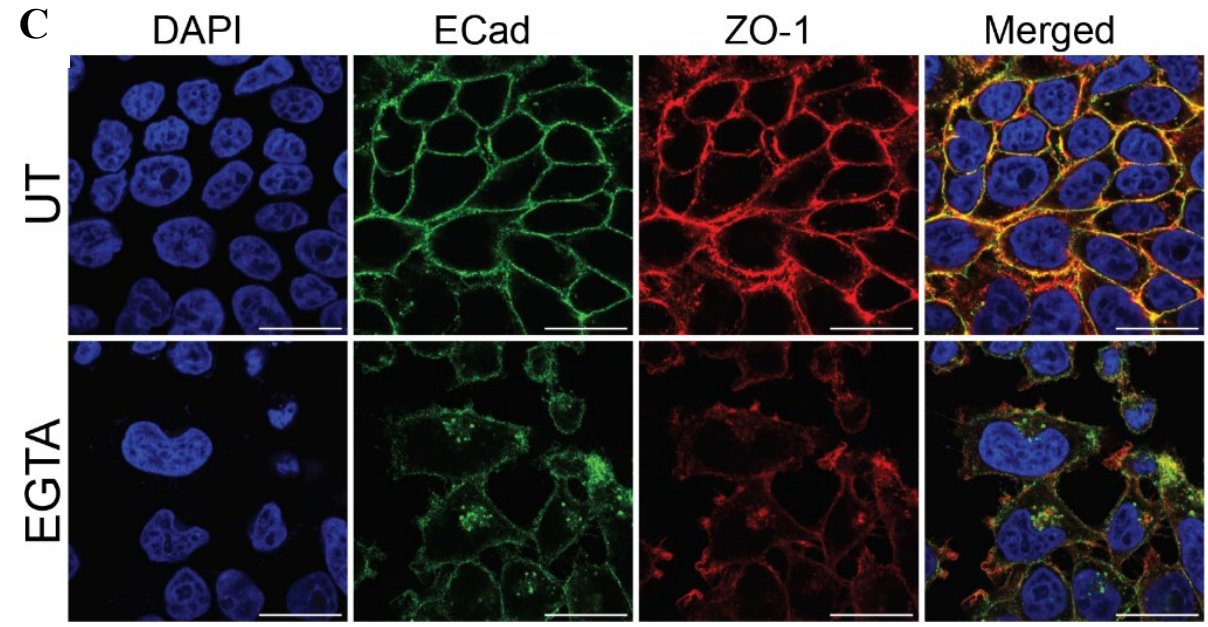
C
DAPI
ECad
ZO-1
Merged
UT
EGTA

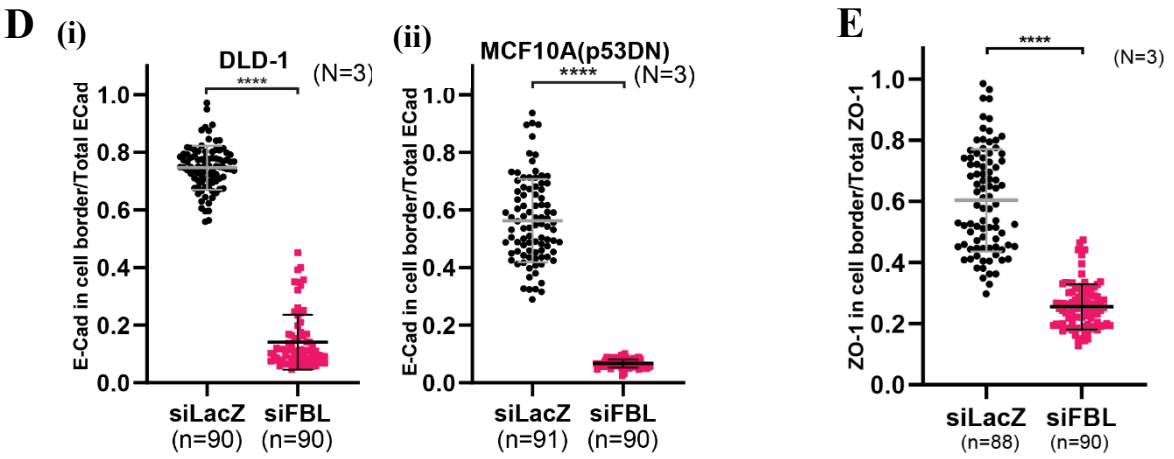
D
(i)
DLD-1
(N=3)
****
E-Cad in cell border/Total ECad
1.0
0.8
0.6
0.4
0.2
0.0
siLacZ
(n=90)
siFBL
(n=90)
(ii)
MCF10A(p53DN)
(N=3)
****
E-Cad in cell border/Total ECad
siLacZ
(n=91)
siFBL
(n=90)
E
****
(N=3)
ZO-1 in cell border/Total ZO-1
siLacZ
(n=88)
siFBL
(n=90)

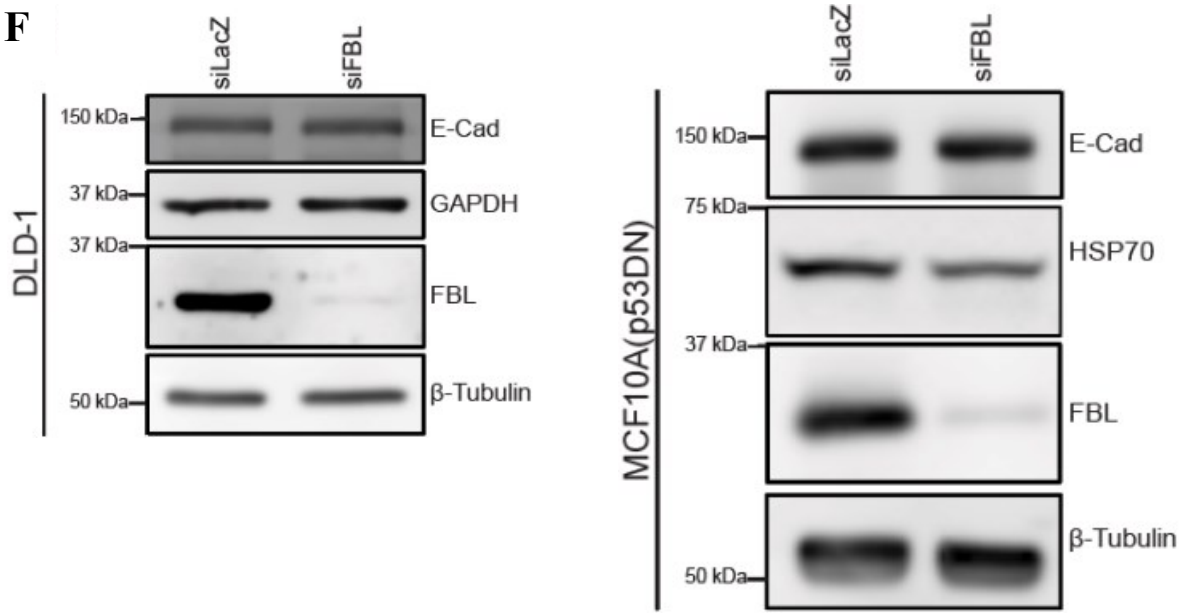
F
siLacZ
siFBL
DLD-1
150 kDa
E-Cad
37 kDa
GAPDH
37 kDa
FBL
50 kDa
β-Tubulin
MCF10A(p53DN)
150 kDa
E-Cad
75 kDa
HSP70
37 kDa
FBL
50 kDa
β-Tubulin

G (i)

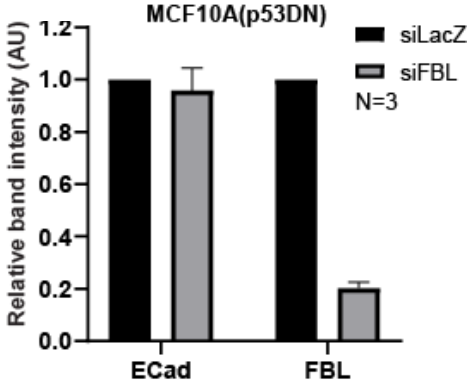
MCF10A(p53DN)
Relative band intensity (AU)
1.2
1.0
0.8
0.6
0.4
0.2
0.0
siLacZ
siFBL
N=3
ECad
FBL

(ii)

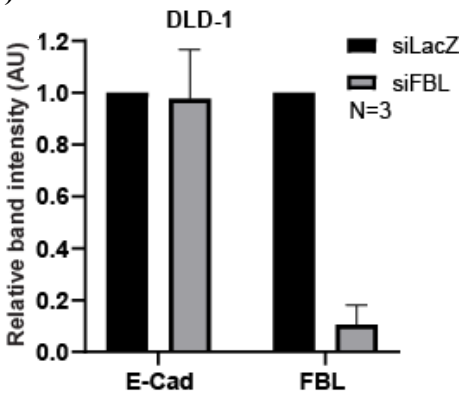
DLD-1
Relative band intensity (AU)
1.2
1.0
0.8
0.6
0.4
0.2
0.0
siLacZ
siFBL
N=3
E-Cad
FBL

H

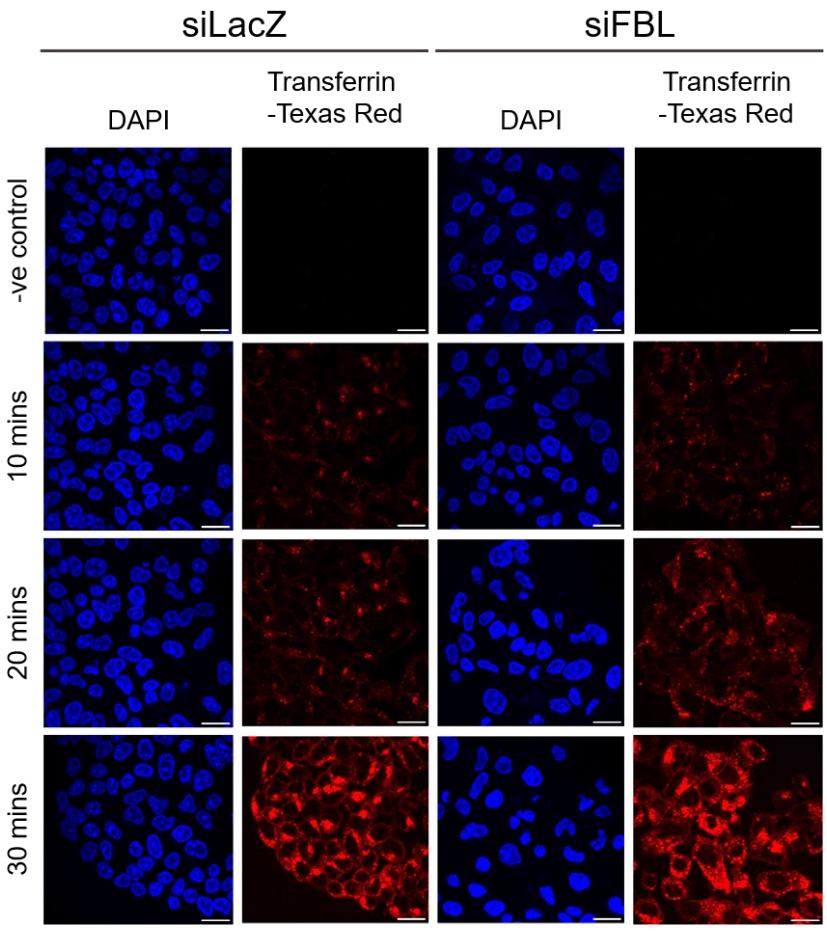
siLacZ
siFBL
DAPI
Transferrin
-Texas Red
DAPI
Transferrin
-Texas Red
-ve control
10 mins
20 mins
30 mins

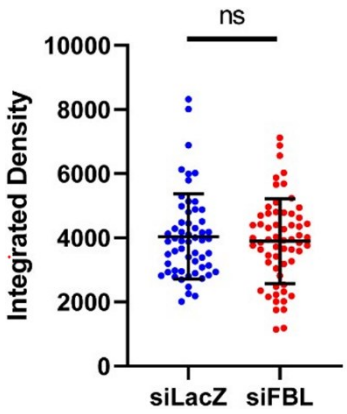
ns
Integrated Density
10000
8000
6000
4000
2000
0
siLacZ
siFBL

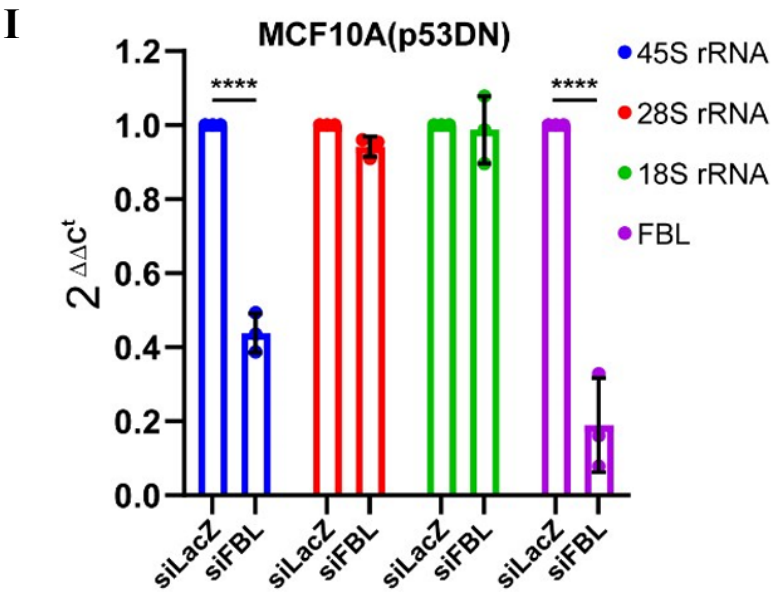

Fig. 3.2. FBL depletion disrupts junctional localization of epithelial polarity proteins

(A) Representative immunofluorescence micrographs depicting FBL (green), E-cadherin (red), and nuclei (DAPI; blue) in DLD-1 and MCF10A(p53DN) cells following FBL knockdown for approximately 48 h and 36 h, respectively. Depletion of FBL results in a marked redistribution of E-cadherin. Quantitative analyses were pooled from ≥90 cells per condition, comprising 180 DLD-1 and 181 MCF10A(p53DN) cells across three independent biological replicates (N = 3). Scale bar, ~20 µm. **(B)** Representative immunofluorescence images showing E-cadherin (green) and ZO-1 (red) localization in DLD-1 cells treated with or without EGTA (3 mM, 1 h). Data were collected from ≥60 cells per condition and pooled from two independent biological replicates (N = 2). Scale bar, ~20 µm. **(C)** Quantification of E-cadherin internalization in (i) DLD-1 and (ii) MCF10A(p53DN) cells, expressed as the ratio of E-cadherin fluorescence intensity at the cell–cell junctions to that of the entire cell. Statistical significance was determined using an unpaired t-test. Measurements were pooled from 180 DLD-1 and 181 MCF10A(p53DN) cells across three independent biological replicates (N = 3). **(D)** Quantitative analysis of ZO-1 internalization in DLD-1 cells, calculated as the ratio of junctional ZO-1 fluorescence intensity to total cellular fluorescence. Data represent measurements from 178 cells pooled from two independent biological replicates (N = 2). Statistical significance was assessed using an unpaired t-test. **(E)** Representative immunoblots showing E-cadherin and FBL protein levels, with GAPDH and β-tubulin serving as loading controls, in DLD-1 and MCF10A(p53DN) cells transfected with control siRNA (siLacZ) or FBL-targeting siRNA (siFBL) for approximately 48 h and 36 h, respectively. **(F)** Densitometric analysis of immunoblots showing relative levels of E-cadherin and FBL in (i) DLD-1 and (ii)

MCF10A(p53DN) cells, corresponding to Fig. S1B. Quantifications were pooled from three independent biological replicates (N = 3). **(G)** Representative confocal images of DLD-1 cells transfected with control siRNA (siLacZ) or FBL-targeting siRNA (siFBL) for approximately 48 h and stained for nuclei (DAPI; blue) and Transferrin–Texas Red (red). Transferrin uptake was monitored at 10-min intervals. Scale bar, 20 μm. (H) RT-qPCR analysis was performed to quantify rRNA precursor and mature rRNA species in MCF10A(p53DN) cells transfected with control siRNA (siLacZ) or FBL-targeting siRNA (siFBL) for approximately 36 h. Transcript levels of 45S pre-rRNA, 28S rRNA, 18S rRNA, and FBL mRNA were normalized to GAPDH and expressed as relative abundance using the 2^ΔΔCt method, with siLacZ-treated cells serving as the reference. Knockdown of FBL resulted in a marked decrease in 45S pre-rRNA and FBL transcript levels, whereas the levels of mature 28S and 18S rRNAs were largely unaffected. Data represent the mean ± SEM of biological replicates. Statistical significance was determined using an unpaired Student's t-test (****, $p < 0.0001$). **(J)**(i) Representative channel-separated images showing Dynasore treatment under FBL-depleted conditions, corresponding to Fig. 1D. (ii) Quantitative analysis of E-cadherin internalization in DLD-1 cells, expressed as the ratio of E-cadherin (green) fluorescence intensity at the cell periphery to that within the entire cell, as shown in Fig. 1D. Data were pooled from n = 339 cells across N = 3 independent biological replicates. Scale bar, ~20 μm.

3.2.2. E-Cadherin accumulation in Golgi

In addition to disrupting the membrane localization of E-cadherin, Fibrillarin (FBL) depletion resulted in its intracellular accumulation, particularly within the Golgi apparatus. This was evidenced by the colocalization of E-cadherin with GM130, a well-established marker of the Golgi complex. Under normal physiological conditions, E-cadherin is stabilized at the plasma membrane through a finely regulated mechanism involving its cytoplasmic domain. Specifically, the cytoplasmic tail of E-cadherin contains a ubiquitination site that marks it for internalization and degradation. This site is protected by the p120 catenin protein, which binds to E-cadherin and shields it from ubiquitin ligases, thereby maintaining its stability and surface localization.

Importantly, the apical-basal polarity protein Scribble plays a crucial role in reinforcing this stabilization. Scribble facilitates the interaction between E-cadherin and p120 catenin, further securing E-cadherin at adherens junctions and promoting junctional integrity. Given that FBL

depletion leads to mislocalization and Golgi accumulation of E-cadherin, it is plausible that FBL influences the expression of Scribble, either directly or indirectly. The disruption of this regulatory axis could impair the protective interaction between E-cadherin and p120, rendering E-cadherin susceptible to internalization and rerouting to intracellular compartments such as the Golgi.

Interestingly, in FBL-depleted cells E-cadherin colocalized with Golgi apparatus and the Golgi apparatus itself appeared fragmented and disorganized (Fig. 3.3(A-C)). Colocalization of E-cadherin with Golgi-marker GM130 is indicative of altered levels of Scribble upon FBL depletion. Such structural alterations of the Golgi may be indicative of broader cytoskeletal remodeling events (Khuntia et al. 2022). We speculate that the observed Golgi fragmentation may not be a direct consequence of FBL loss but rather a secondary effect resulting from cytoskeletal rearrangements, particularly actin remodeling, that occur during the cell shape changes associated with FBL knockdown. Given that FBL-depleted cells exhibit an elongated morphology and disrupted epithelial architecture, the reorganization of actin filaments may exert mechanical stress on Golgi positioning and integrity.

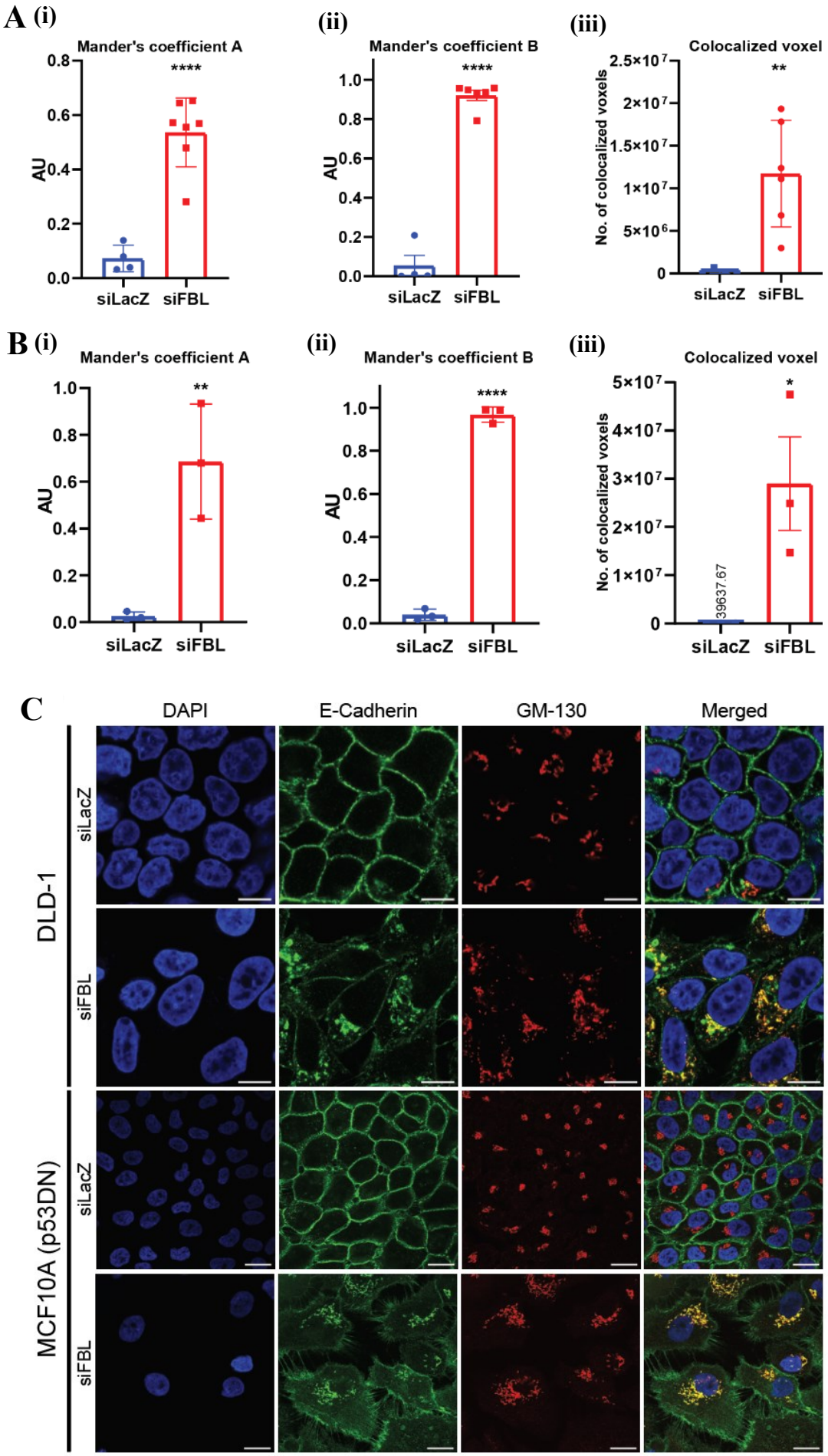
A (i)
Mander's coefficient A
AU
0.8
0.6
0.4
0.2
0.0
****
siLacZ
siFBL
(ii)
Mander's coefficient B
AU
1.0
0.8
0.6
0.4
0.2
0.0
****
siLacZ
siFBL
(iii)
Colocalized voxel
No. of colocalized voxels
2.5×10^7
2×10^7
1.5×10^7
1×10^7
5×10^6
0
**
siLacZ
siFBL
B (i)
Mander's coefficient A
AU
1.0
0.8
0.6
0.4
0.2
0.0
**
siLacZ
siFBL
(ii)
Mander's coefficient B
AU
1.0
0.8
0.6
0.4
0.2
0.0
****
siLacZ
siFBL
(iii)
Colocalized voxel
No. of colocalized voxels
5×10^7
4×10^7
3×10^7
2×10^7
1×10^7
0
39637.67
*
siLacZ
siFBL
C
DAPI
E-Cadherin
GM-130
Merged
DLD-1
siLacZ
siFBL
MCF10A (p53DN)
siLacZ
siFBL

Fig. 3.3. Loss of FBL promotes E-cadherin accumulation at the Golgi apparatus

(A)(i-iii) Quantitative colocalization analysis of E-cadherin and the cis-Golgi marker GM130 in DLD-1 cells transfected with control siRNA (siLacZ) or FBL-targeting siRNA (siFBL). Mander's coefficient A, Mander's coefficient B, and colocalized voxel volume were calculated using Imaris software. Statistical significance was assessed using an unpaired t-test. Data were pooled from three independent biological replicates (N = 3). **(B)(i-iii)** The same colocalization parameters were quantified for E-cadherin and GM130 in MCF10A(p53DN) cells using Imaris. Fixed threshold values were applied uniformly across replicates (DLD-1: threshold A = 11.930, threshold B = 11.920; MCF10A(p53DN): threshold A = 1.320, threshold B = 11.920). Statistical analysis was performed using an unpaired t-test, with data derived from three independent biological replicates (N = 3). **(C)** Representative immunofluorescence micrographs showing E-cadherin (green), GM130 (red), and nuclei (DAPI; blue) in DLD-1 and MCF10A(p53DN) cells transfected with siLacZ or siFBL for approximately 48 h. Images are representative of three independent biological replicates (N = 3). In siLacZ-transfected cells, the E-cadherin and GM130 panels correspond to different optical sections from the same confocal z-stack. Scale bar, ~20 μm.

3.2.3. Rescue of E-Cadherin Internalization by Dynasore

To gain mechanistic insight into the process of E-cadherin internalization observed upon Fibrillarin (FBL) depletion, we employed a pharmacological approach using Dynasore—a well-characterized, cell-permeable inhibitor of the GTPase activity of Dynamin. Dynamin is a critical component of the clathrin-mediated endocytic machinery, where it facilitates the scission of nascent clathrin-coated vesicles from the plasma membrane. Inhibiting Dynamin activity effectively halts the internalization of numerous membrane-bound receptors and adhesion molecules, including E-cadherin, thereby serving as a useful tool to probe the involvement of clathrin-dependent endocytosis in cellular trafficking events.

To assess whether the internalization of E-cadherin following FBL depletion was dependent on clathrin-mediated endocytosis, DLD-1 cells were treated with Dynasore under FBL knockdown conditions. Remarkably, Dynasore treatment resulted in a substantial rescue of E-cadherin membrane localization, with a marked reduction in its cytoplasmic accumulation (Fig. 3.4). These observations strongly indicate that the mislocalization of E-cadherin induced

by FBL depletion is mediated through a Dynamin-dependent internalization pathway. The ability of Dynasore to restore E-cadherin at the cell membrane highlights the functional relevance of clathrin-mediated endocytosis in this context. It suggests that FBL plays an upstream regulatory role in stabilizing membrane-bound E-cadherin by modulating endocytic trafficking.

This experiment not only validated our earlier observations regarding E-cadherin internalization but also established a direct link between FBL function and endocytic regulation. The observed rescue by Dynasore suggests that therapeutic modulation of endocytosis could potentially counteract adhesion defects arising from nucleolar or epigenetic dysregulation, such as that induced by FBL loss. Together, these findings position FBL as a novel upstream modulator of adhesion protein trafficking in epithelial cells.

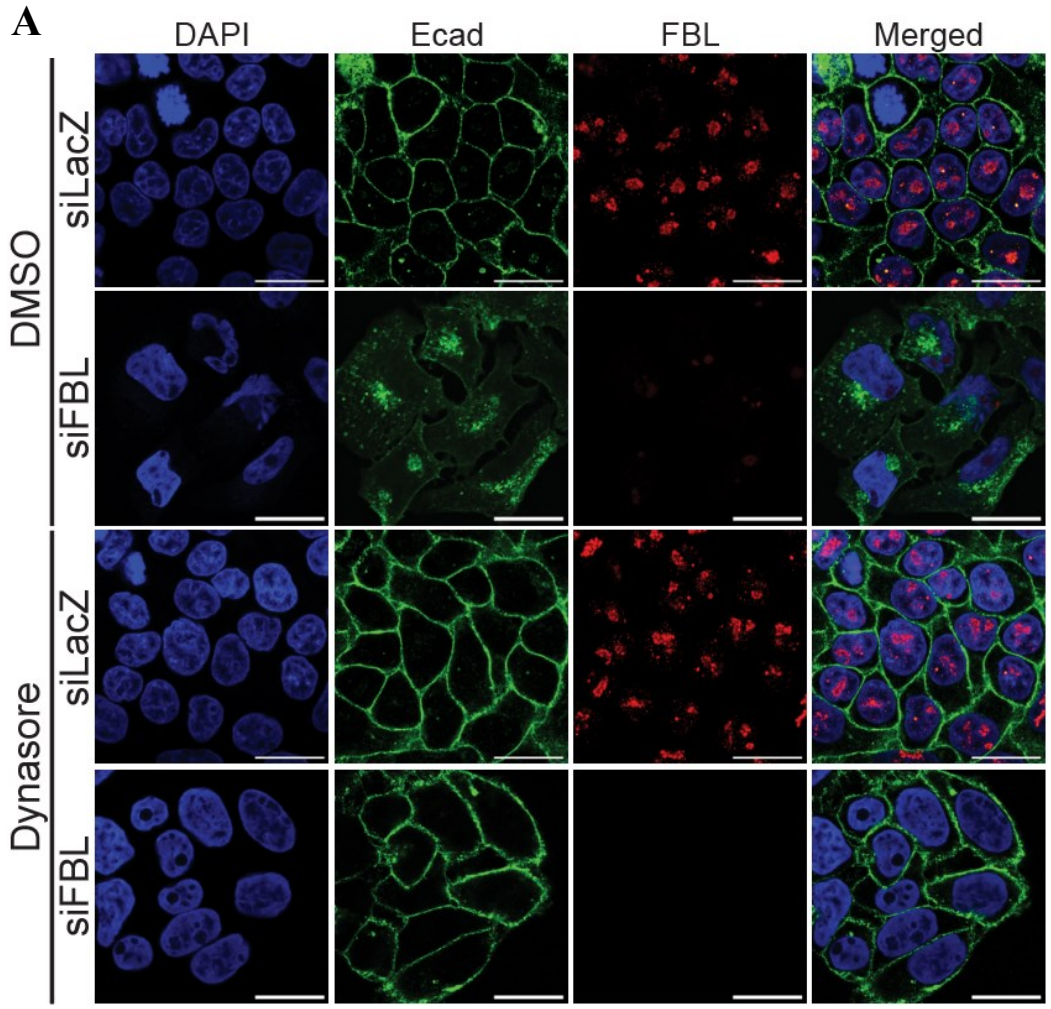
A
DAPI
Ecad
FBL
Merged
DMSO
siLacZ
siFBL
Dynasore
siLacZ
siFBL

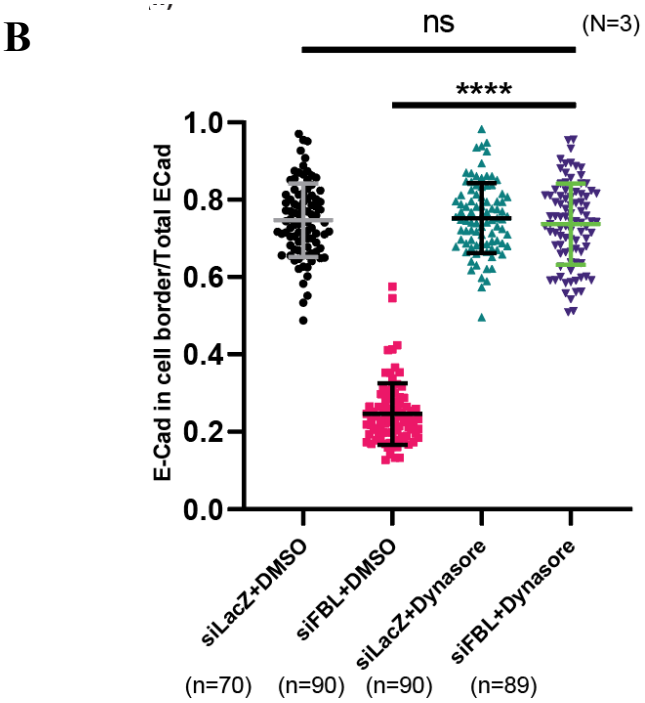
B
ns
(N=3)
****
E-Cad in cell border/Total ECad
1.0
0.8
0.6
0.4
0.2
0.0
siLacZ+DMSO
siFBL+DMSO
siLacZ+Dynasore
siFBL+Dynasore
(n=70)
(n=90)
(n=90)
(n=89)

Fig. 3.4. Dynasore Treatment Enhances E-cadherin Internalization in FBL-Depleted DLD-1 Cells

(A) Channel-separated fluorescence images showing Dynasore treatment under FBL-depleted conditions **(B)** Quantitative analysis of E-cadherin internalization in DLD-1 cells, expressed as the ratio of E-cadherin (green) fluorescence intensity at the cell periphery to that of the whole cell. Data were pooled from 339 cells across three independent biological replicates (N = 3). Scale bar, ~20 μm.

3.2.4. Increased Cell Migration Upon FBL Depletion

Fibrillarin (FBL) depletion was found to markedly enhance both the migratory properties of epithelial cells, highlighting its potential role in regulating cellular behaviours associated with tissue remodelling and cancer metastasis. To investigate the effect of FBL knockdown on cell migration, we performed a scratch wound healing assay, a well-established in vitro methodology used to monitor the collective migration of adherent cell monolayers. In this assay, a linear wound or "scratch" is introduced across a confluent monolayer of cells, maintained in serum depleted media (1% serum), and the rate of wound closure is quantified over time as an indicator of migratory capacity. Compared to control cells, FBL-depleted cells exhibited a pronounced increase in migration, with ~80% (±10%) wound closure observed over the same time-period (Fig. 3.5(A-B)). This significant enhancement in collective migration suggests that loss of FBL disrupts normal epithelial behavior, possibly through weakening of cell-cell junctions or cytoskeletal reorganization, thereby enabling cells to more freely mobilize as a sheet.

To assess whether this increased motility extended to invasive behavior—an essential characteristic of malignant progression—we employed the Boyden chamber (transwell) assay. This method enables the quantification of the ability of cells to invade through a porous polycarbonate membrane, typically coated with extracellular matrix (ECM) components such as collagen or Matrigel, to mimic the basement membrane. In this setup, cells must not only migrate but also degrade and pass through the ECM barrier and the membrane's pores (8 μm in diameter), simulating the process of tissue invasion in vivo. FBL-depleted cells showed a substantial increase in invasive potential, as evidenced by a ~2.65-fold increase in the number of cells successfully invading through the membrane compared to control cells (Fig. 3.5(C-D)).

The observed enhancement in both two-dimensional (scratch assay) and three-dimensional (Boyden chamber) migration strongly supports a role for FBL in restraining pro-migratory and pro-invasive cellular programs. These phenotypic changes are likely a consequence of disrupted epithelial architecture, altered adhesion protein trafficking (e.g., E-cadherin internalization), and potential cytoskeletal remodeling—all of which can contribute to a mesenchymal-like, invasive phenotype. Collectively, these findings implicate FBL as a critical regulator of epithelial stability, whose loss may promote cellular behaviors associated with epithelial-to-mesenchymal transition (EMT), tumor progression, and metastatic dissemination.

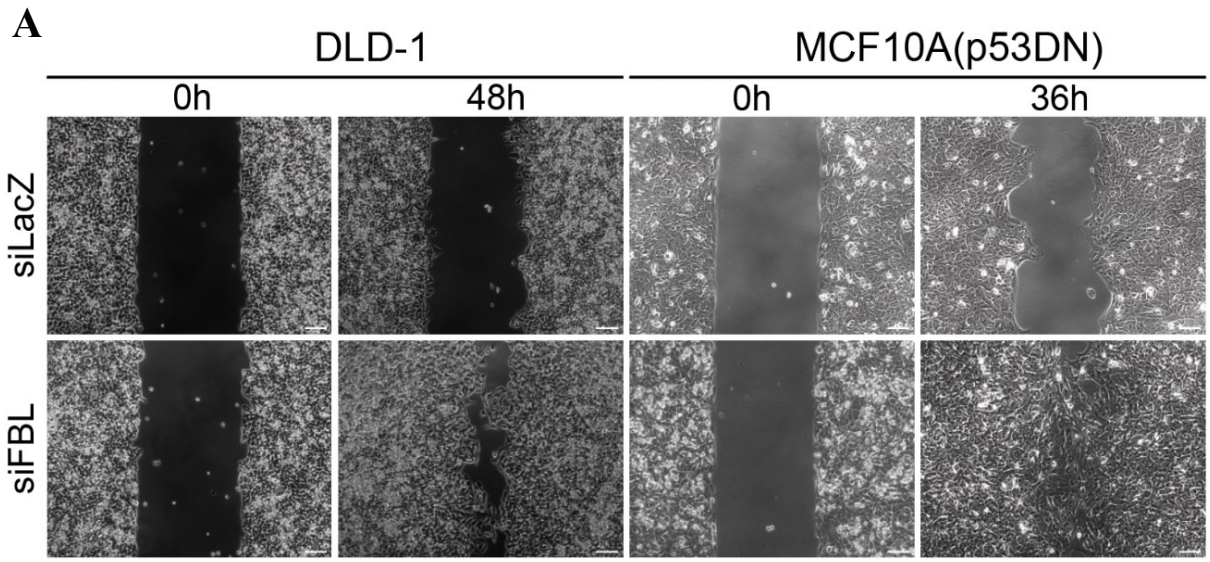

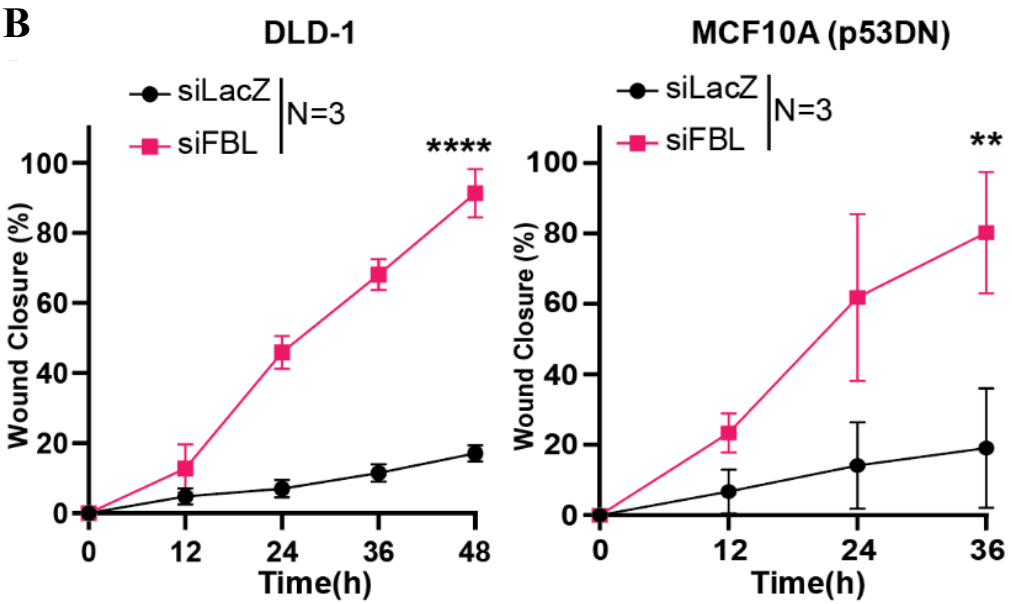

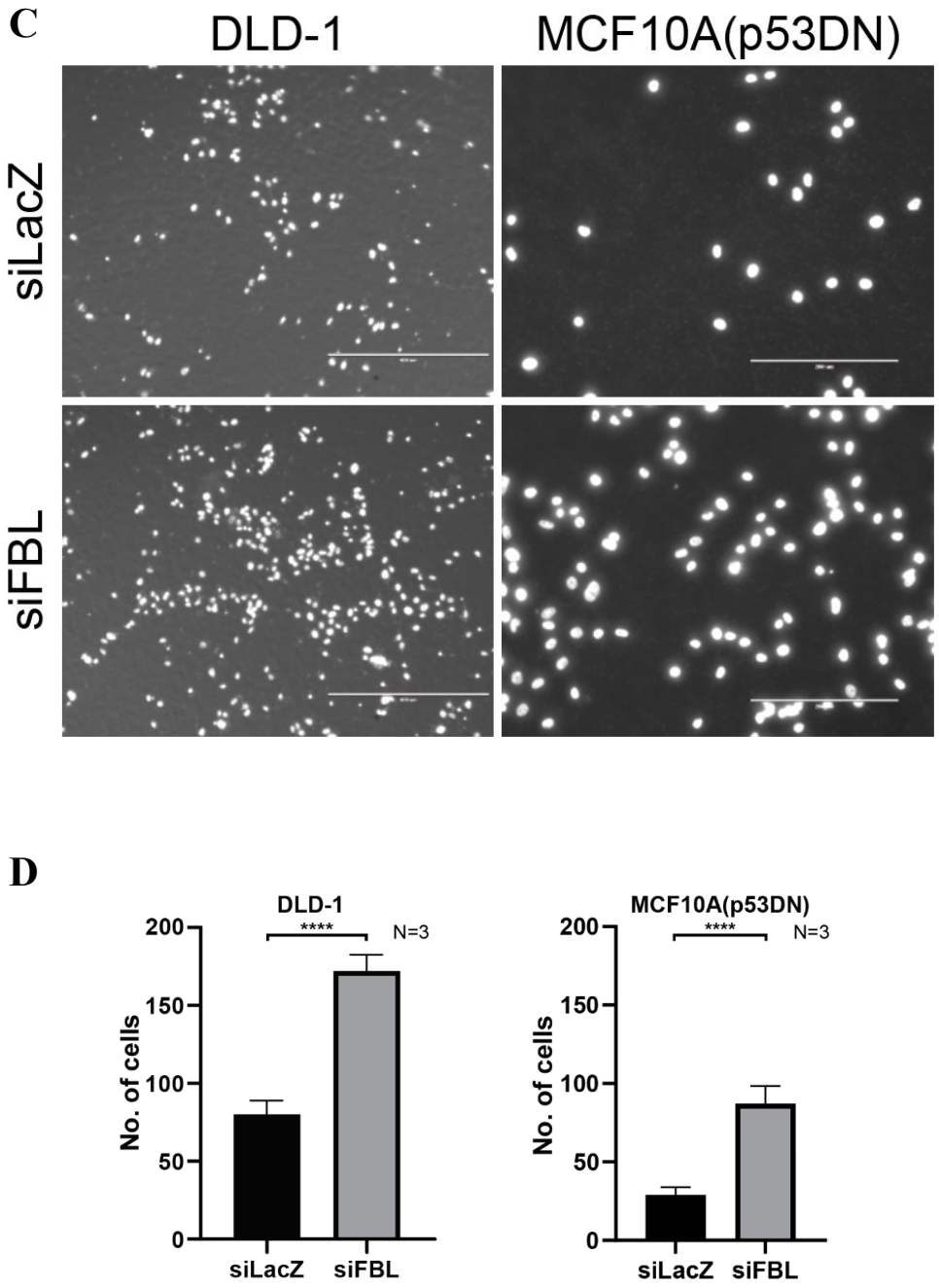

Fig. 3.5. Effect of FBL depletion on epithelial cell migration and invasion

(A) Representative phase-contrast micrographs of scratch wound–healing assays performed in DLD-1 and MCF10A(p53DN) cells transfected with control siRNA (siLacZ) or FBL-targeting siRNA (siFBL). Images are representative of three independent biological replicates (N = 3). Scale bar, ~100 μm. **(B)** Quantitative analysis of wound reveals a significant enhancement in migratory capacity following FBL depletion in both DLD-1 and MCF10A(p53DN) cells. Statistical significance was determined using an unpaired t-test. **(C)** Representative images of Boyden chamber invasion assays (pore size, ~8 μm) performed in DLD-1 and

MCF10A(p53DN) cells transfected with control siRNA (siLacZ) or FBL-targeting siRNA (siFBL). Images are representative of three independent biological replicates (N = 3). Scale bars, ~400 μm for DLD-1 and ~200 μm for MCF10A(p53DN). **(D)** Quantitative analysis of the invasion assays demonstrating a significant increase in invasive capacity upon FBL depletion in both DLD-1 and MCF10A(p53DN) cells. Data were pooled from three independent biological replicates (N = 3).

3.2.5. Altered Nuclear Topology

To further investigate the impact of Fibrillarin (FBL) depletion on nuclear architecture, we independently silenced FBL in two epithelial cell lines: DLD-1 (a colorectal cancer cell line) and MCF10A(p53DN) (a non-tumorigenic mammary epithelial line expressing a dominant-negative variant of p53). Quantitative image analysis following FBL knockdown revealed significant morphological changes to the nucleus, characterized by a marked reduction in nuclear sphericity. Specifically, both cell lines exhibited approximately an 18% (±7.2%) decrease in nuclear roundness, suggesting increased nuclear deformation or irregularity. This observation was accompanied by an increase in nuclear surface area of roughly 22% (±9%), further supporting the notion of altered nuclear contour and envelope integrity (Fig. 3.6(A-B)).

Interestingly, despite these pronounced changes in nuclear shape and surface geometry, the overall nuclear volume remained largely unchanged. This indicates that the observed phenotypic alterations reflect a remodeling of nuclear architecture rather than simple swelling or shrinkage of the nucleus. These shape changes may represent increased nuclear pliability or tension, possibly resulting from alterations in cytoskeletal-nuclear coupling or nuclear lamina organization.

To determine whether these morphological changes were associated with modifications to nuclear lamina components, we examined the levels of key nuclear envelope proteins, including Lamin A/C, Lamin B1, and Lamin B2. Immunoblot analyses showed that the total expression levels of these lamins remained unchanged upon FBL depletion (Fig. 3.6(C-G)). This is consistent with previous reports, which demonstrated that FBL knockdown does not significantly affect Lamin A/C abundance. Therefore, the alterations in nuclear shape observed here are unlikely to be driven by gross changes in nuclear lamina protein levels.

Together, these findings suggest that FBL plays a role in maintaining nuclear morphology and mechanical integrity, potentially through epigenetic regulation or chromatin structural dynamics rather than direct modulation of nuclear envelope proteins. The preservation of nuclear volume amidst increased surface area and loss of sphericity hints at underlying changes in nuclear rigidity or chromatin organization that warrant further investigation. Given the growing recognition of nuclear morphology as a functional readout of cellular health, differentiation state, and malignancy, the ability of FBL to modulate nuclear shape may have implications for its role in tumor progression and cellular plasticity.

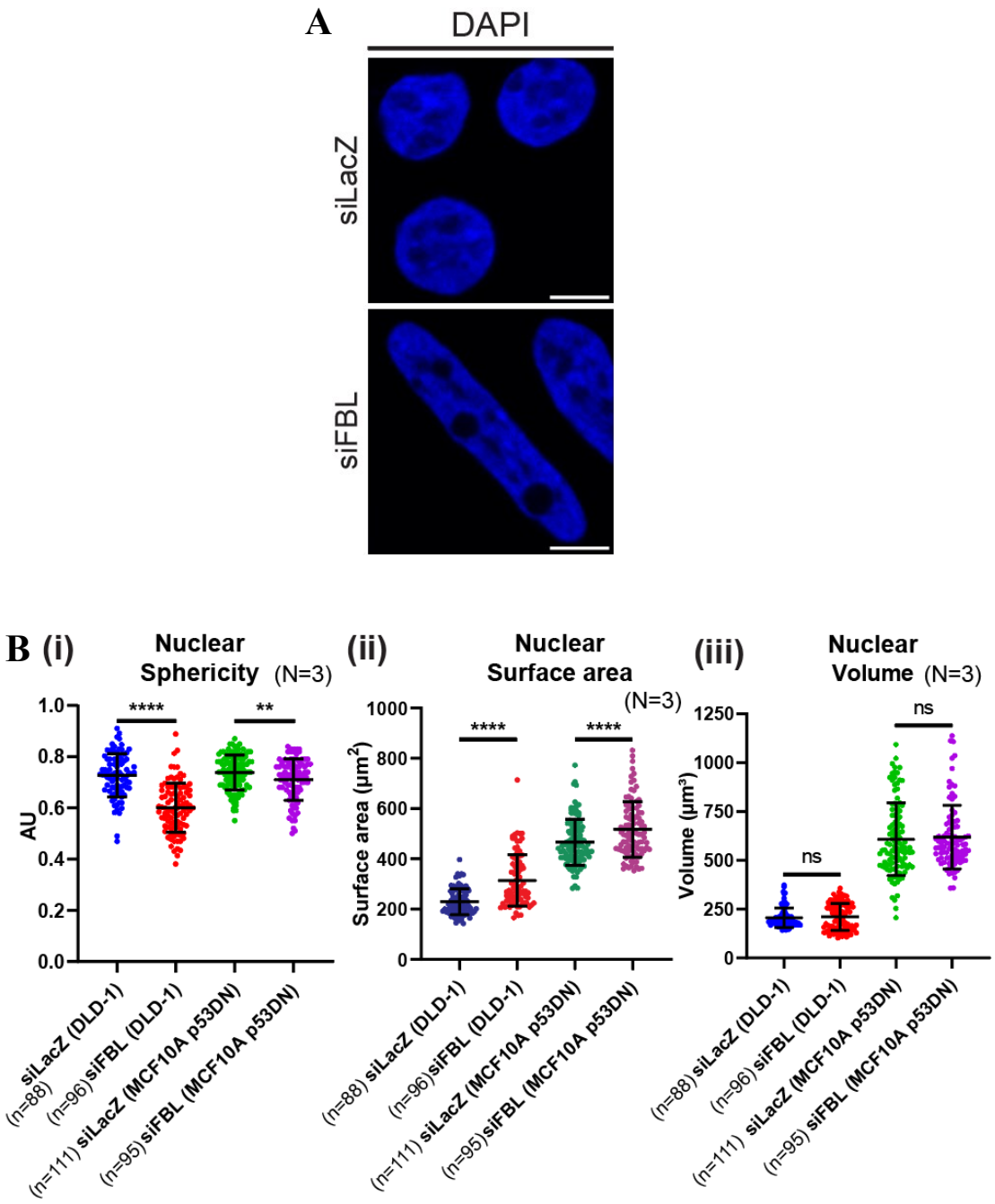

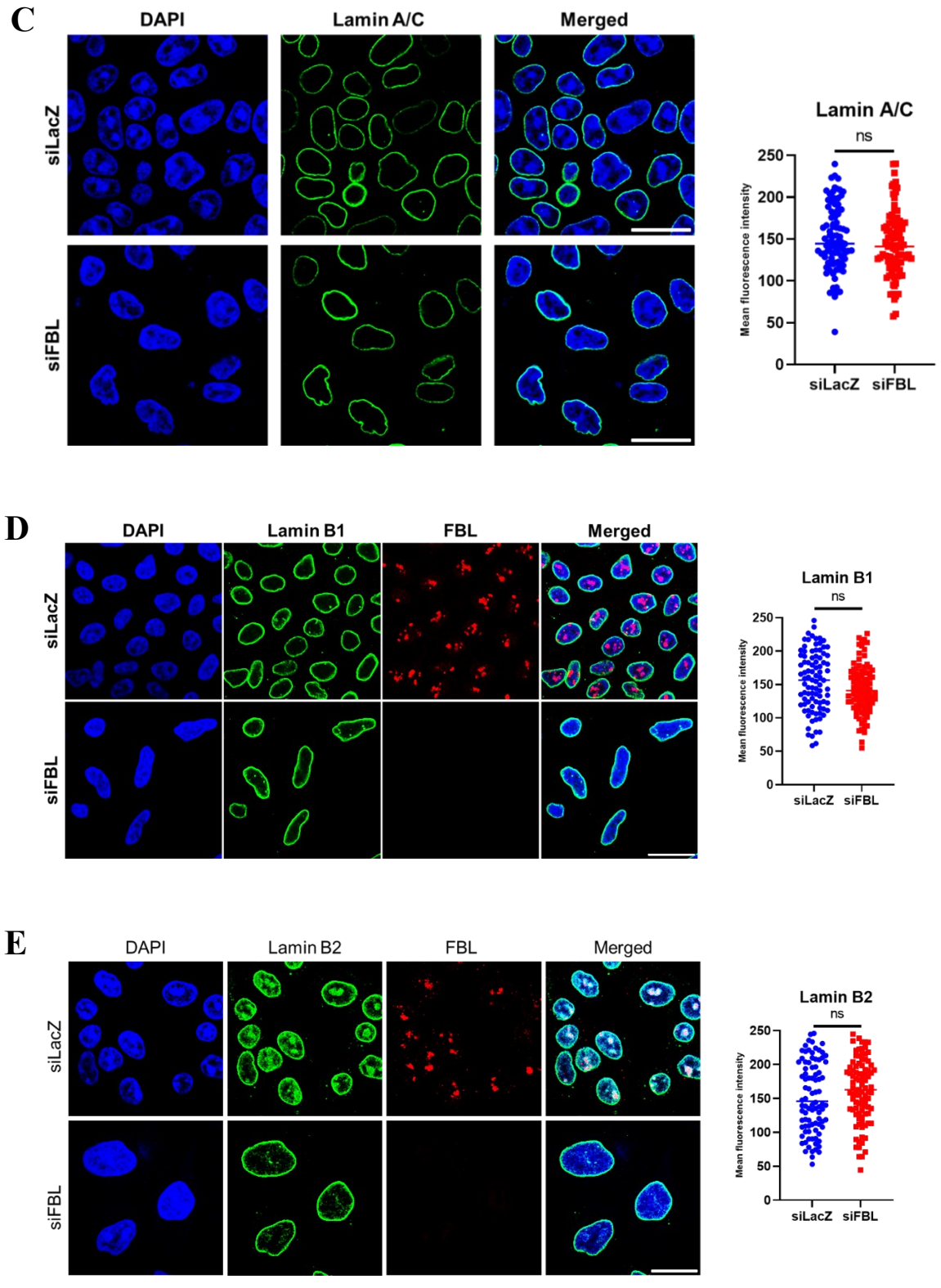
C
DAPI
Lamin A/C
Merged
siLacZ
siFBL
Lamin A/C
ns
Mean fluorescence intensity
250
200
150
100
50
0
siLacZ
siFBL
D
DAPI
Lamin B1
FBL
Merged
siLacZ
siFBL
Lamin B1
ns
Mean fluorescence intensity
250
200
150
100
50
0
siLacZ
siFBL
E
DAPI
Lamin B2
FBL
Merged
siLacZ
siFBL
Lamin B2
ns
Mean fluorescence intensity
250
200
150
100
50
0
siLacZ
siFBL

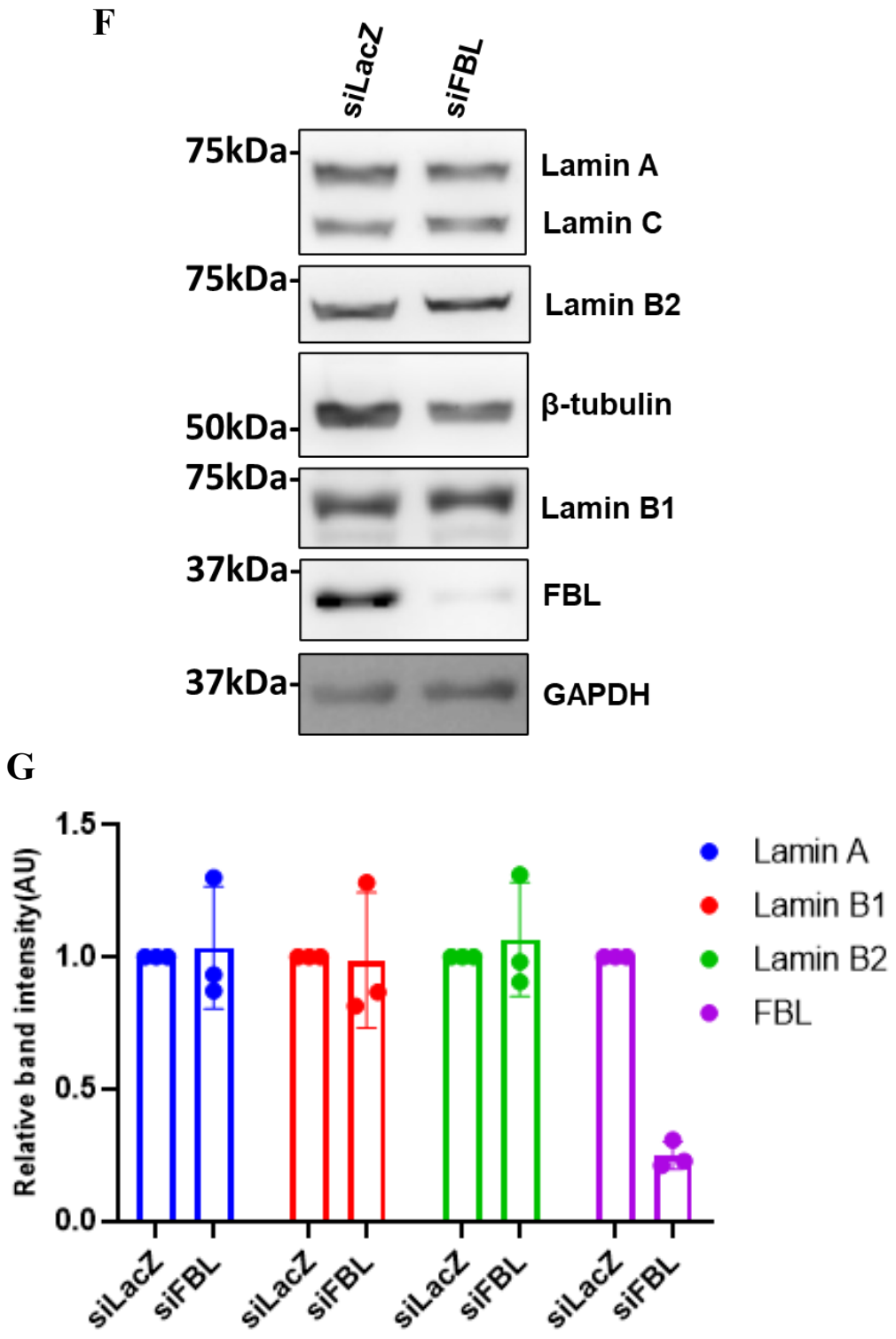

Fig. 3.6. FBL depletion alters nuclear morphology and nuclear lamina organization (A) Representative images showing nuclei stained with DAPI (blue) in control (siLacZ) and FBL-depleted (siFBL) cells, highlighting pronounced changes in nuclear shape following

FBL knockdown. Lower panels show immunofluorescence staining for the indicated nuclear envelope and chromatin-associated markers (green/red), along with merged images. Scale bars as indicated. (B) Scatter dot plots on the right represent quantitative analyses of nuclear morphology parameters (including nuclear area, aspect ratio, and/or circularity) comparing siLacZ (blue) and siFBL (red) conditions. Each dot represents an individual cell, with data pooled from multiple fields across independent biological replicates. Statistical significance was assessed using an unpaired t-test. (C) Representative immunoblots showing protein levels of Lamin A, Lamin B1, Lamin B2, and FBL in cells transfected with control siRNA (siLacZ) or FBL-targeting siRNA (siFBL). A housekeeping protein was used as a loading control. (D)The bar graph below shows densitometric quantification of Lamin A (blue), Lamin B1 (red), Lamin B2 (green), and FBL (purple) normalized to the loading control and expressed relative to the siLacZ condition. Each dot represents an independent biological replicate, and bars indicate mean ± SD. Data were pooled from independent experiments, and statistical significance was assessed using an unpaired t-test.

3.2.6. FBL Loss Enhances H3K9me3 and H3K27me3 Levels

Proper nuclear morphology is a tightly regulated feature of healthy cells and is often maintained through balanced interactions between the nuclear lamina, chromatin organization, and cytoskeletal forces. Disruption of this balance can result in aberrant nuclear structures such as blebs, micronuclei, and irregular shapes, which are frequently observed in cancer and other pathological states. Notably, previous studies have highlighted that a reduction in heterochromatin content—particularly histone modifications such as H3K9me3 and H3K27me3—can compromise nuclear rigidity and contribute to nuclear deformation (Stephens et al. 2018). These histone marks are associated with the formation of transcriptionally repressive chromatin, which not only regulates gene expression but also contributes to the mechanical properties of the nucleus by compacting chromatin and promoting structural stability.

Motivated by this connection, we investigated whether FBL depletion, which we previously found to disrupt nuclear morphology, also impacts global levels of key heterochromatin marks. In FBL-depleted DLD-1 and MCF10A(p53DN) cells, we consistently observed a decrease in nuclear sphericity and an increase in nuclear surface area, accompanied by a higher incidence of nuclear aberrations including nuclear blebbing and micronucleus formation. Interestingly, these nuclear morphological changes occurred despite the total levels of nuclear

lamina proteins—Lamin A/C, Lamin B1, and Lamin B2—remaining unchanged. This suggested that the defects in nuclear architecture might stem from changes in chromatin organization rather than lamina disruption.

To test this hypothesis, we examined the status of heterochromatin-associated histone modifications, specifically H3K9me3 and H3K27me3. Surprisingly, rather than observing a decrease in these marks (which would be expected if chromatin compaction were compromised), we found a significant increase in both modifications in FBL-depleted cells. Immunofluorescence assays at the single-cell level revealed enhanced staining intensity for H3K9me3 and H3K27me3, indicating elevated heterochromatin deposition (Fig. 3.7 (A-F)). This finding was further corroborated by immunoblotting analyses at the population level, which showed a robust increase in global levels of these repressive histone marks.

In particular, H3K27me3 levels were markedly upregulated upon FBL depletion, exhibiting nearly a six-fold increase in signal intensity in immunofluorescence assays, and approximately a 60% (±10%) increase in overall abundance in immunoblotting experiments. These data collectively suggest that loss of FBL not only disrupts nuclear morphology but is also associated with an unexpected elevation in heterochromatin levels. The observed increase in chromatin compaction marks may represent a compensatory response to mechanical stress or reflect a broader epigenetic reprogramming triggered by nucleolar dysfunction.

Taken together, these results uncover a novel link between FBL depletion and epigenetic remodeling, wherein the architectural abnormalities of the nucleus are accompanied by a paradoxical increase in heterochromatin deposition. This finding challenges the conventional view that nuclear deformation is always associated with chromatin decompaction, and raises the possibility that FBL may exert its regulatory effects on nuclear structure and gene silencing through complex, context-dependent chromatin interactions.

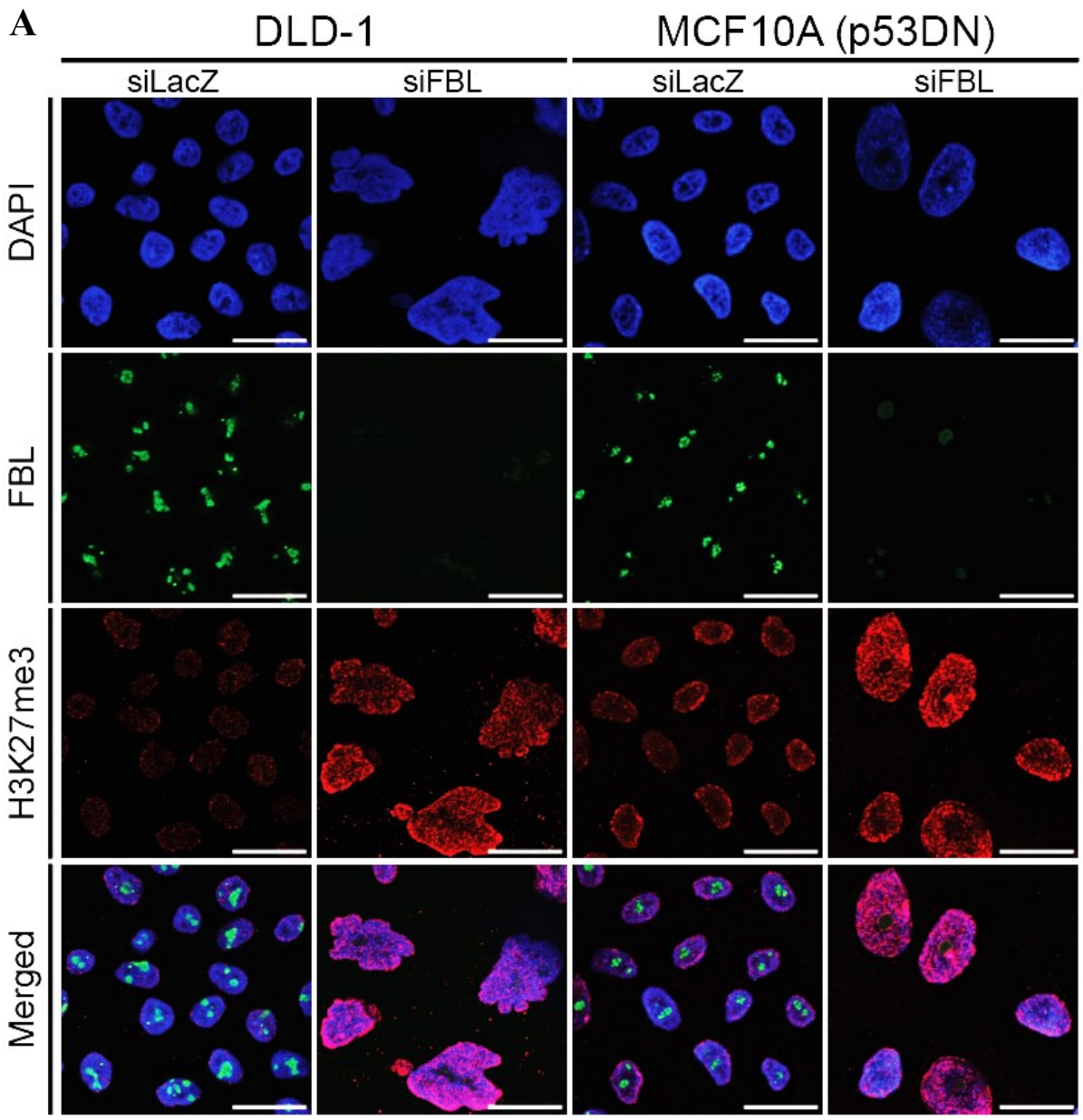
A
DLD-1
MCF10A (p53DN)
siLacZ
siFBL
siLacZ
siFBL
DAPI
FBL
H3K27me3
Merged

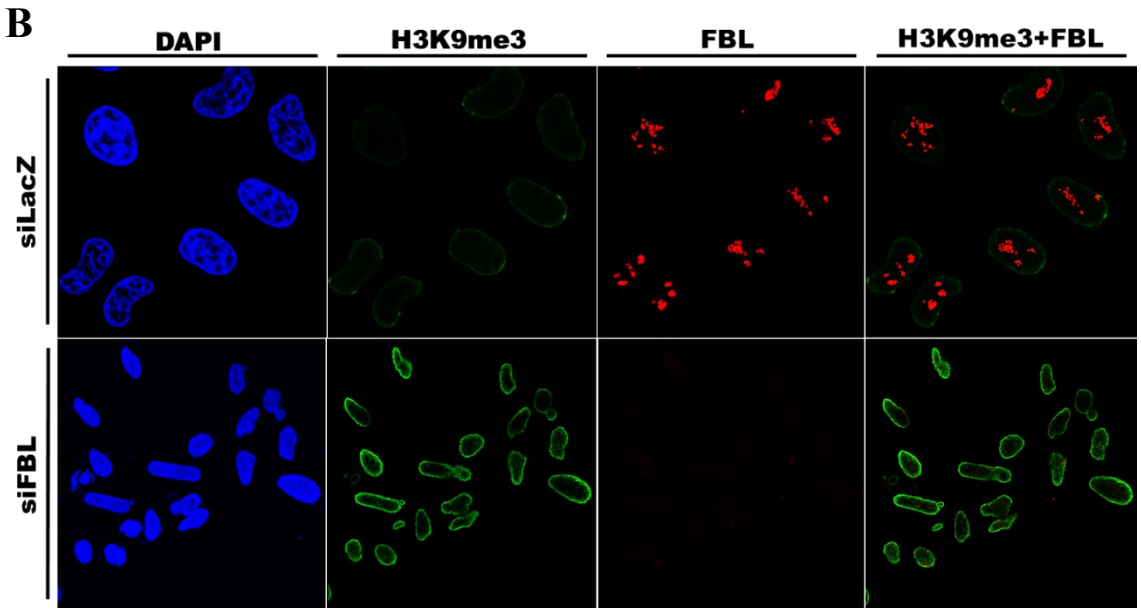
B
DAPI
H3K9me3
FBL
H3K9me3+FBL
siLacZ
siFBL

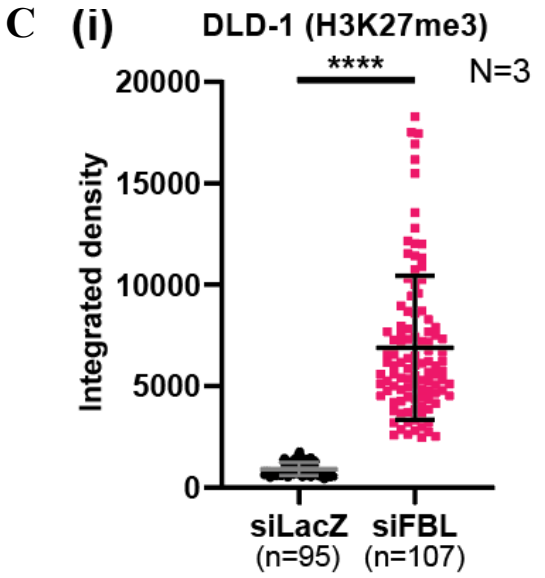
C (i)
DLD-1 (H3K27me3)
****
N=3
Integrated density
20000
15000
10000
5000
0
siLacZ
(n=95)
siFBL
(n=107)

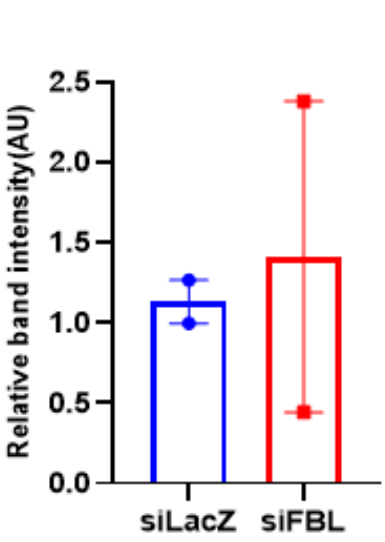
D
Relative band intensity(AU)
2.5
2.0
1.5
1.0
0.5
0.0
siLacZ
siFBL

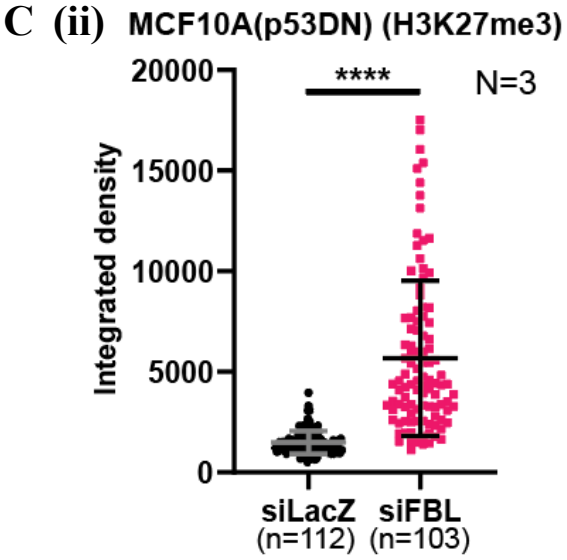
C (ii)
MCF10A(p53DN) (H3K27me3)
****
N=3
Integrated density
20000
15000
10000
5000
0
siLacZ
(n=112)
siFBL
(n=103)

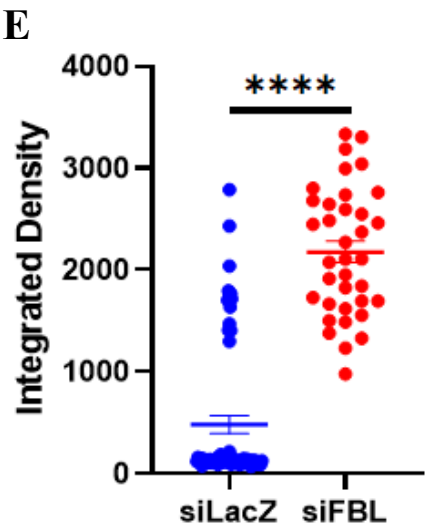
E
****
Integrated Density
4000
3000
2000
1000
0
siLacZ
siFBL

()

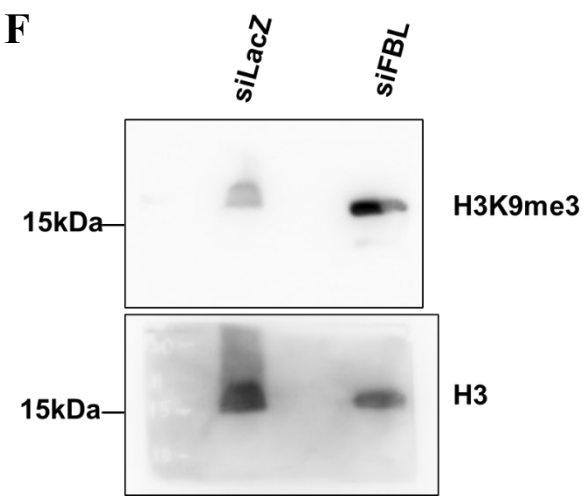

Fig. 3.7. FBL Depletion Promotes Global Increases in Repressive Histone Marks H3K9me3 and H3K27me3 in Epithelial Cells

(A) Representative immunofluorescence images showing FBL (green) and H3K9me3 (red) staining in MCF10A(p53DN) and DLD-1 cells transfected with control siRNA (siLacZ) or FBL-targeting siRNA (siFBL) for ~48 h and ~36 h, respectively. Data were acquired from three independent biological replicates (N = 3). Statistical significance was determined using an unpaired t-test. Scale bar, ~20 μm. **(B)(i-ii)** Representative channel-separated and merged immunofluorescence images showing FBL (green) and H3K9me3 (red) localization in control (siLacZ) and FBL-depleted (siFBL) MCF10A(p53DN) and DLD-1 cells. Nuclear DNA is counterstained with DAPI (blue). **(C)** Quantitative analysis of H3K27me3 levels in DLD-1 and MCF10A(p53DN) cells corresponding to panel A. Measurements were pooled from 202 DLD-1 cells and 225 MCF10A(p53DN) cells across three independent biological replicates (N = 3). An unpaired t-test was used to calculate p-values. **(D)** Bar graph showing relative H3K9me3 relative band intensity upon FBL depletion cmpared to control conditions. Data are represented as mean ± SD from three independent biological replicates. **(E)** Scatter dot plot depicting single-cell integrated density measurements of H3K9me3 fluorescence in siLacZ and siFBL conditions, highlighting a significant increase in H3K9me3 levels following FBL knockdown (****$p < 0.0001$, unpaired t-test). **(F)** Representative immunoblot showing H3K9me3 levels in control and FBL-depleted cells, with corresponding histone/loading controls shown below.

3.2.7. Increased H3K9me3 correlated with elevated levels of Emerin

Fibrillarin (FBL) depletion in epithelial cells led not only to nuclear morphological abnormalities but also to a notable upregulation of the inner nuclear envelope protein Emerin, along with a concomitant increase in the heterochromatin mark H3K9me3. These observations suggest a functional interplay between nuclear envelope dynamics and chromatin organization, particularly in the context of nuclear stress.

Emerin, encoded by the EMD gene, is a key component of the inner nuclear membrane and is known to tether chromatin to the nuclear periphery. It plays a crucial role in organizing perinuclear heterochromatin through direct interactions with chromatin-modifying complexes. For instance, Emerin recruits HDAC3 and associates with histone methyltransferases such as G9a and EZH2, thereby facilitating the formation and maintenance of repressive chromatin domains marked by H3K9me3 and H3K27me3 (Demmerle et al. 2012).

In our experimental setting, FBL-depleted cells exhibited a significant increase in the protein levels of Emerin (Fig. 3.8(A-E)). This increase was paralleled by elevated H3K9me3 levels, as evidenced by both immunofluorescence and immunoblotting. This strongly implies a global remodeling of heterochromatin architecture upon FBL loss, likely in part mediated by the nuclear envelope.

Previous studies have shown that loss of Emerin disrupts heterochromatin anchoring at the nuclear lamina, leading to nuclear instability and impaired gene silencing (Yorifuji et al. 1997; Marano and Holaska 2022). Our findings suggest increased Emerin may act as a compensatory mechanism to restore nuclear rigidity and structural integrity in the face of nucleolar stress induced by FBL depletion.

Furthermore, H3K9me3-enriched heterochromatin has been shown to reinforce nuclear shape by increasing chromatin compaction and stiffness (Stephens et al. 2017). Given that FBL-depleted cells display reduced nuclear sphericity and increased surface area—hallmarks of mechanical nuclear stress- it is plausible that the upregulation of Emerin and the corresponding increase in H3K9me3 deposition serve to buffer nuclear architecture against further deformation.

In summary, our data suggest a novel adaptive pathway where FBL depletion → Emerin upregulation → recruitment of H3K9-methyltransferases → enhanced H3K9me3 deposition, which may function to stabilize nuclear morphology through the expansion of repressive chromatin domains. This underscores the interdependence between nucleolar function,

nuclear envelope composition, and epigenetic regulation in maintaining epithelial nuclear integrity under stress conditions.

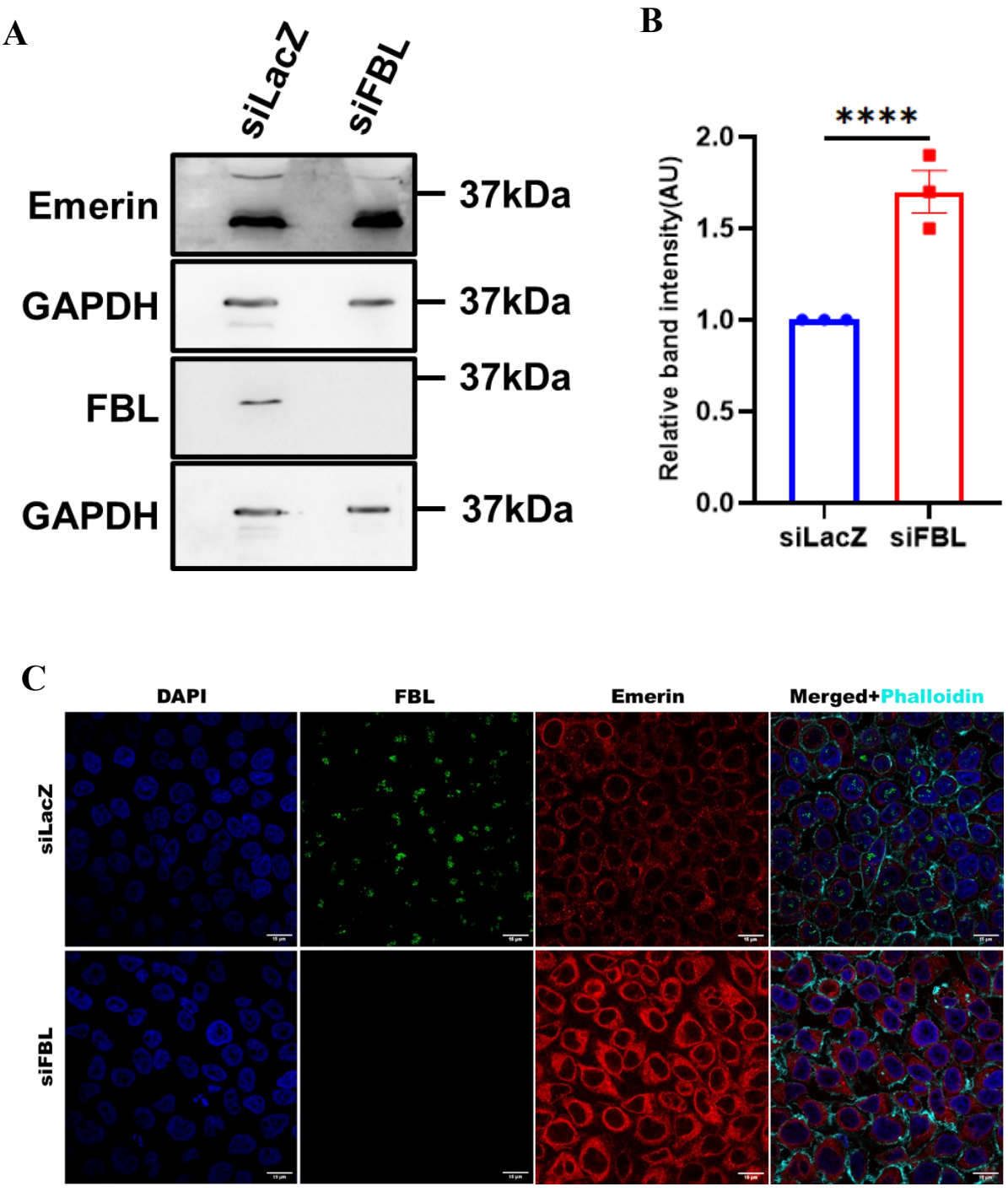

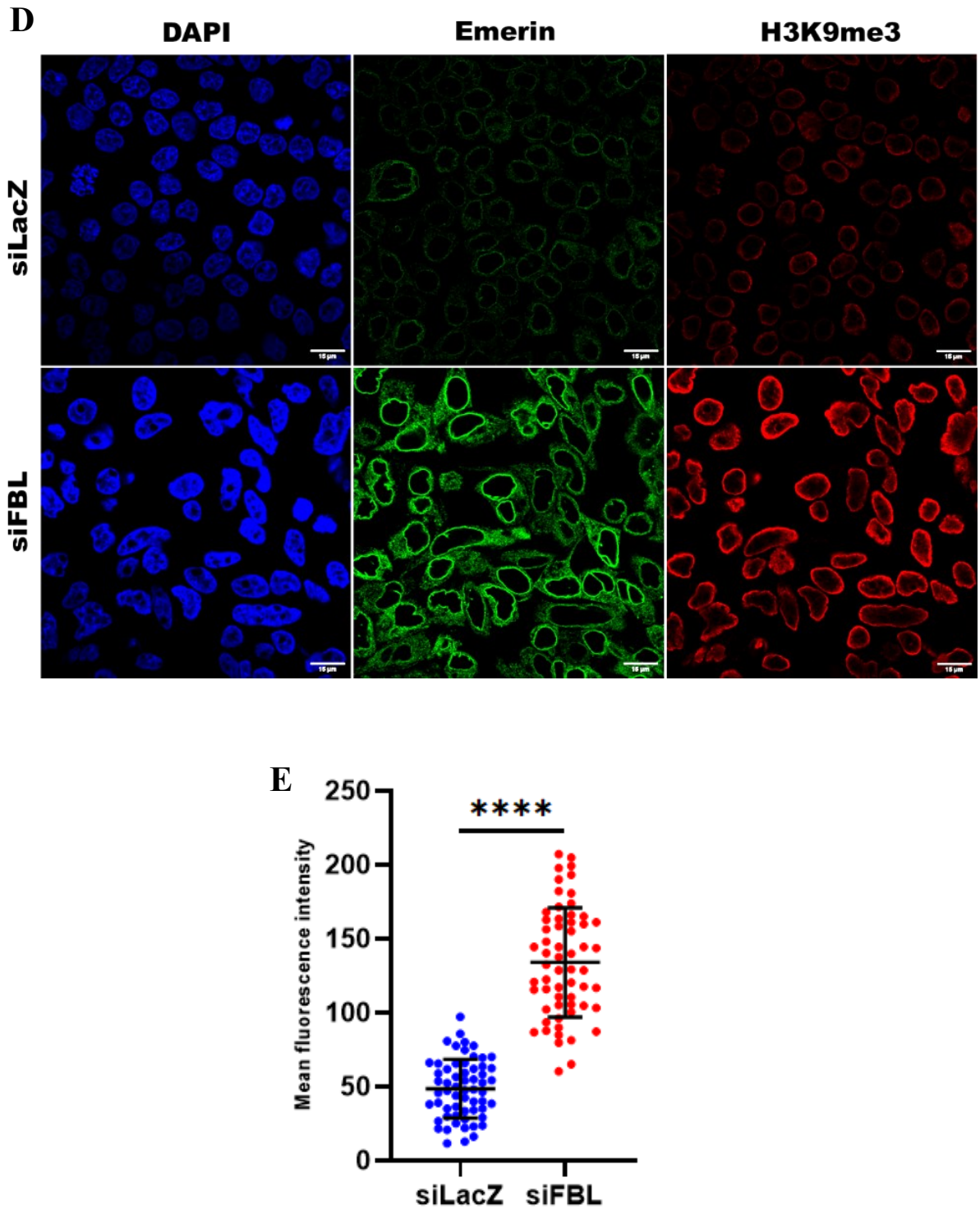

Fig. 3.8. FBL Depletion Upregulates Emerin Expression and Enhances Its Nuclear Envelope Localization

(A) Representative immunoblot analysis showing levels of Emerin in control (siLacZ) and FBL-depleted (siFBL) cells.GAPDH has been used as loading control. Blots are representative of three independent biological replicates, demonstrating increased enrichment of Emerin upon FBL knockdown. **(B)** Representative densitometric analysis showing levels Emerin in control

(siLacZ) and FBL-depleted (siFBL) cells. **(C)** Representative immunofluorescence images showing Emerin (red), FBL (Green), in control (siLacZ) and FBL-depleted (siFBL) cells. Nuclear DNA is stained with DAPI (blue), and F-actin is visualized using phalloidin (cyan). Merged images illustrate changes in Emerin signal intensity FBL knockdown. Images are representative of two independent biological replicates. Scale bar, ~20 μm. **(D)** Representative channel-separated immunofluorescence images showing nuclear DNA (DAPI, blue), Emerin (green), and H3K9me3 staining (red) in control (siLacZ) and FBL-depleted (siFBL) cells. Images illustrate enhanced Emerin signal intensity and altered nuclear morphology following FBL knockdown. Scale bar, ~15 μm. **(E)** Scatter dot plot showing single-cell quantification of mean Emerin fluorescence intensity in control (siLacZ) and FBL-depleted (siFBL) cells. Each dot represents an individual cell, with horizontal bars indicating the mean ± SD. Data were pooled from three independent biological replicates (N =2). Statistical significance was determined using an unpaired t-test (****$p < 0.0001$).

3.2.8. Reduction in Active Chromatin Marks H3K9Ac and H3K27Ac

Histone acetylation is a hallmark of open and transcriptionally active chromatin, with H3K9ac and H3K27ac being two well-characterized marks enriched at promoters and enhancers of actively transcribed genes. These acetylation marks neutralize the positive charge on histone tails, weakening histone-DNA interactions and facilitating access of the transcriptional machinery to chromatin. The dynamic balance between histone acetylation and methylation is a key regulatory mechanism that governs chromatin accessibility and gene expression.

Upon depletion of Fibrillarin (FBL), we observed a pronounced downregulation of both H3K9ac and H3K27ac, as determined by immunoblotting and immunofluorescence assays. This reduction in active histone marks indicates a global shift toward transcriptional repression. Importantly, this effect occurs concomitantly with an increase in repressive histone methylation marks-namely H3K9me3 and H3K27me3-which occupy the same lysine residues on histone H3 and are mutually exclusive with their acetylated counterparts (Kouzarides 2007; Wang et al. 2008). The reciprocal changes in acetylation and methylation suggest an active chromatin remodeling response following FBL depletion. Previous studies have demonstrated that decreased acetylation of H3K27 and H3K9 often precedes or facilitates the recruitment of repressive complexes such as PRC2 (for H3K27me3) and SUV39H1/G9a (for H3K9me3), reinforcing the establishment of heterochromatin and gene silencing (Tie et al. 2009; Padeken

et al. 2022). In our system, the loss of H3K9ac and H3K27ac upon FBL depletion (Fig. 3.9(A-D)) likely reflects either a reduction in histone acetyltransferase (HAT) activity or an increase in histone deacetylase (HDAC) activity in the absence of FBL. This aligns with the observed upregulation of H3K27me3 and H3K9me3, further confirming a coordinated epigenetic reprogramming toward chromatin compaction and gene repression. These alterations in chromatin state may be part of a broader nuclear stress response triggered by FBL loss. As FBL depletion is known to affect nuclear morphology and chromatin organization, the observed loss of acetylation could represent a mechanism to enhance chromatin rigidity and maintain structural integrity. Indeed, prior reports have demonstrated that reductions in active chromatin marks and increases in heterochromatin can help counterbalance mechanical perturbations to the nucleus (Nava et al. 2020).

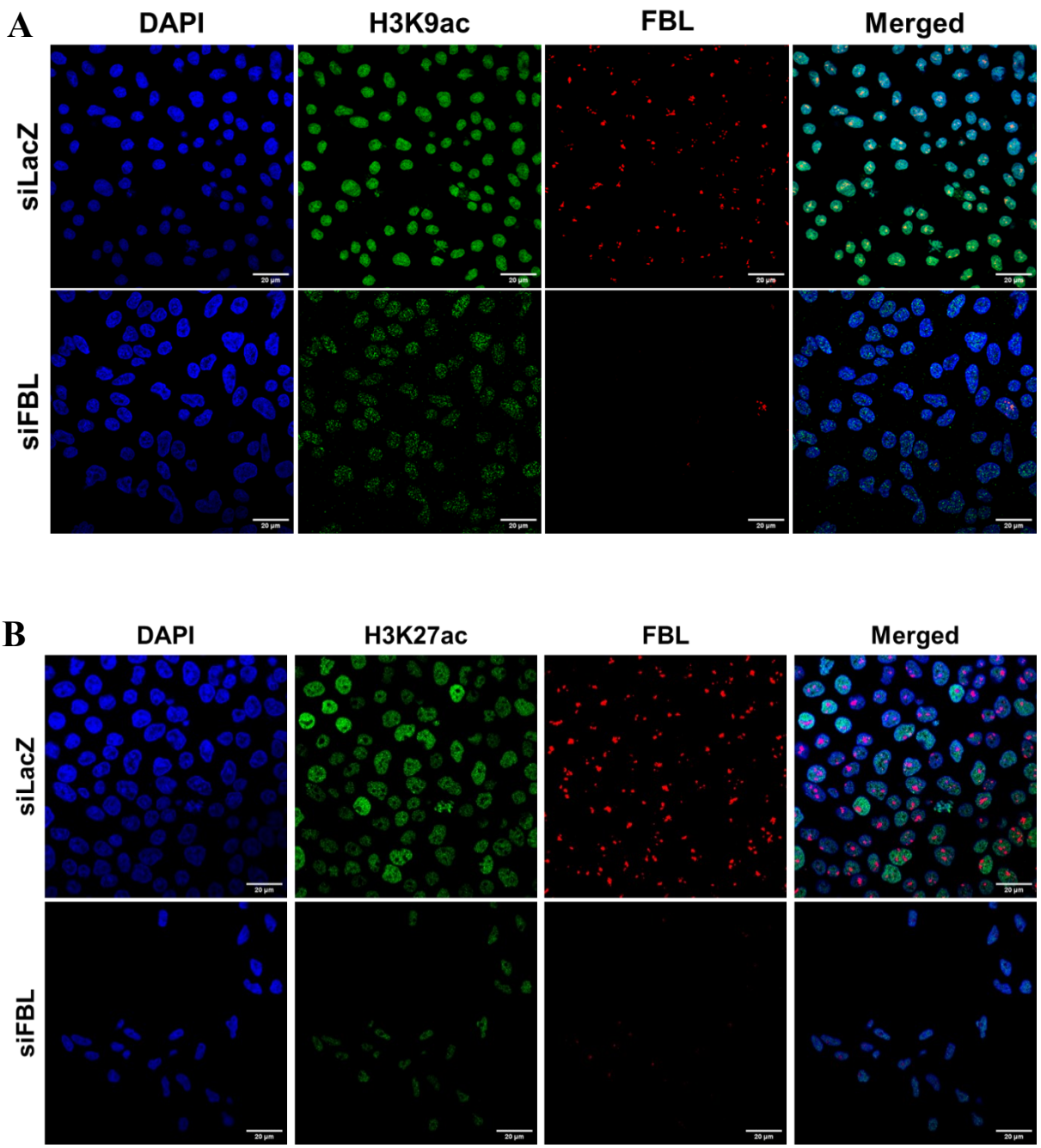
A
DAPI
H3K9ac
FBL
Merged
siLacZ
siFBL
B
DAPI
H3K27ac
FBL
Merged
siLacZ
siFBL
C
****
Mean fluorescence intensity
250
200
150
100
50
0
siLacZ
siFBL
D
****
Mean fluorescence intensity
200
150
100
50
0
siLacZ
siFBL

Fig. 3.9. FBL depletion causes reduced deposition of histone acetylation marks- H3K27 and H3K9ac

(A) Representative channel-separated and merged immunofluorescence images showing nuclear DNA (DAPI, blue), H3K9ac (green), and FBL (red) staining in control (siLacZ) and FBL-depleted (siFBL) cells. Merged images illustrate pronounced changes in nuclear morphology, redistribution of FBL, and enhanced accumulation of the repressive chromatin mark H3K9ac upon FBL knockdown. Images are representative of independent biological replicates. Scale bar, ~20 μm. **(B)** Representative immunofluorescence images showing nuclear DNA (DAPI, blue), H3K27ac (green), and FBL (red) in control (siLacZ; top row) and FBL-depleted (siFBL; bottom row) cells. The rightmost panels show merged images illustrating increased H3K27ac signal and altered nuclear morphology upon FBL knockdown, accompanied by redistribution and reduction of nucleolar FBL staining. Images are representative of independent biological replicates. Scale bar, ~20 μm. **(C)** Scatter dot plot showing single-cell measurements of mean H3K9ac fluorescence intensity in control (siLacZ) and FBL-depleted (siFBL) cells. Each dot represents an individual cell, with horizontal bars indicating the mean ± SD. Data were pooled from independent biological replicates. Statistical significance was assessed using an unpaired t-test (****$p < 0.0001$). **(D)** Scatter dot plot depicting single-cell quantification of average H3K27ac fluorescence intensity in control (siLacZ) and FBL-depleted (siFBL) DLD-1 cells. Each point corresponds to an individual cell, with bars representing the mean ± SD. Data were combined from N=2 independent biological replicates; n>60, and statistical significance was evaluated using an unpaired t-test (****$p < 0.0001$).

3.2.9. Reduction in H3K9me3 is insufficient in rescuing FBL loss mediated enhanced migration

To dissect the epigenetic underpinnings of the enhanced migratory phenotype observed upon FBL depletion, we focused on two major transcriptionally repressive histone marks: H3K9me3, deposited by SUV39H1, and H3K27me3, catalyzed by the Polycomb Repressive Complex 2 (PRC2) component EZH2. We first attempted to reduce H3K9me3 levels pharmacologically using Chaetocin, a known SUV39H1/2 inhibitor. However, Chaetocin was ineffective under our conditions due to its poor specificity and cytotoxicity, prompting us to adopt a genetic approach. We used siRNA-mediated knockdown of SUV39H1 and compared four experimental conditions in a scratch wound assay: siLacZ (control), siFBL, siLacZ + siSUV39H1, and siFBL + siSUV39H1. While SUV39H1 knockdown efficiently reduced H3K9me3 levels, it failed to reverse the enhanced migration phenotype induced by FBL loss, suggesting that H3K9me3 is not a critical effector in this context. In contrast, inhibition of EZH2 using GSK126 (10 μM for 48 hours) markedly reduced H3K27me3 levels and resulted in a significant attenuation of cell migration, even in an FBL-depleted background (Fig. 4.3B). These findings were confirmed by scratch wound closure assays, which showed a substantial decrease in wound closure rates following EZH2 inhibition. Together, these results indicate that while both H3K9me3 and H3K27me3 are elevated upon FBL depletion, only H3K27me3 is functionally linked to the acquisition of a migratory phenotype. The inability of SUV39H1 knockdown to rescue the migratory phenotype, coupled with the efficacy of EZH2 inhibition, positions H3K27me3 as the key epigenetic driver of FBL loss–associated epithelial plasticity and-motility.

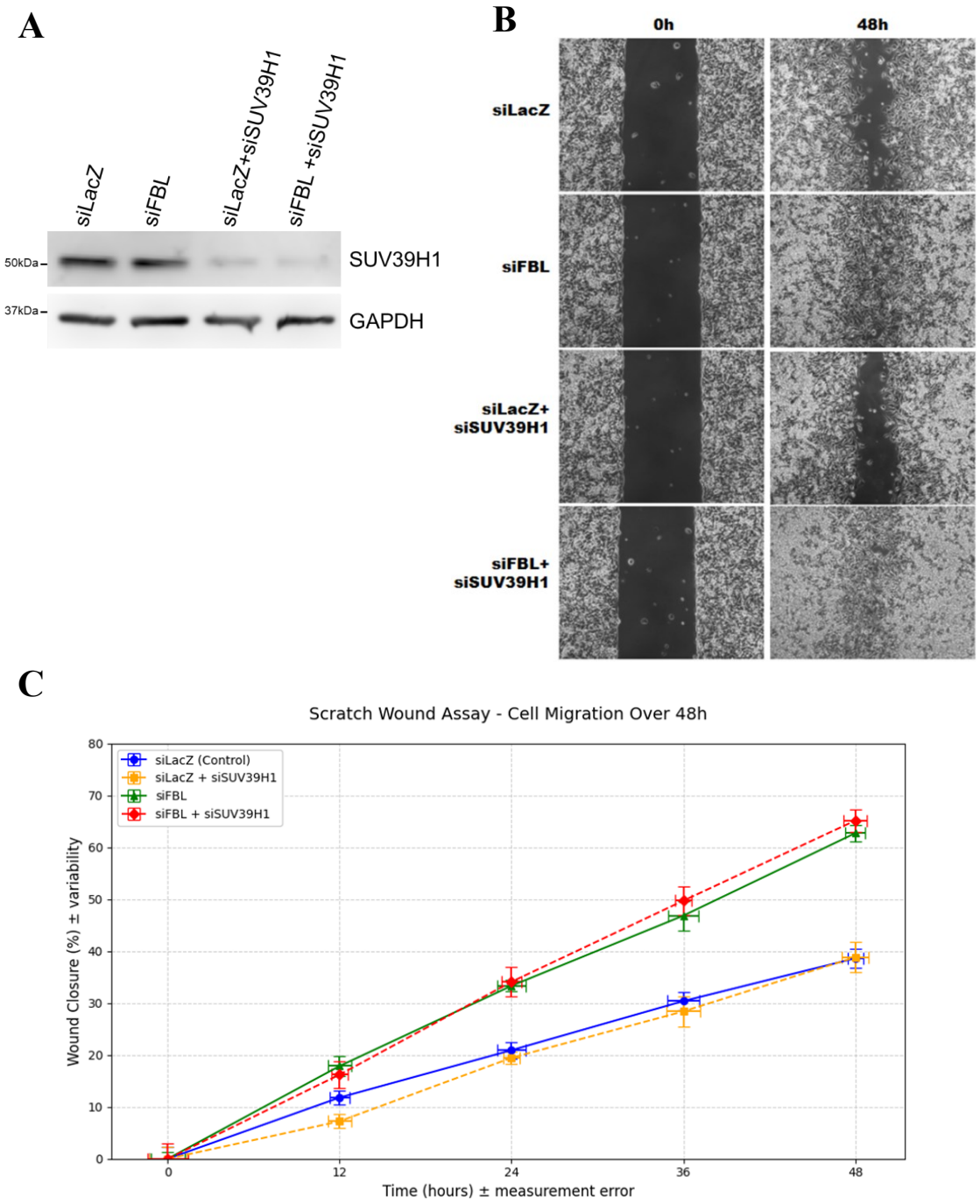

Fig. 3.10. Enhanced H3K9me3 levels are not responsible for FBL depletion mediated enhanced cell migration

(A) Immunoblot analysis depicting H3K9me3 protein levels in cells transfected with control siRNA (siLacZ) or FBL-targeting siRNA (siFBL). GAPDH is shown below to confirm equal protein loading. Blots are representative of independent biological replicates. **(B)** Representative phase-contrast images from scratch-wound (wound-healing) assays performed in control (siLacZ), FBL-depleted (siFBL), siLacZ + siSUV39H1, and siFBL + siSUV39H1 cells. Images were acquired immediately after wound generation (0 h) and further images

acquisition was done at the interval of every 12h till 48 h. Accelerated wound closure is observed upon FBL depletion, which is not attenuated following co-depletion of the H3K9 methyltransferase SUV39H1, indicating a role for H3K9me3-dependent chromatin regulation in FBL-mediated cell migration. Images are representative of independent biological replicates. **(C)** Line graph showing percentage wound closure measured at 0, 12, 24, 36, and 48 h in control (siLacZ), siLacZ + siSUV39H1, siFBL, and siFBL + siSUV39H1 cells. Data are presented as mean ± variability/error from independent biological replicates. FBL depletion accelerates wound closure compared to control, while co-depletion of SUV39H1 attenuates the enhanced migratory response, indicating involvement of SUV39H1-dependent H3K9 methylation in FBL-mediated cell migration.

3.3. Discussion

The current study identifies Fibrillarin (FBL) as a multifaceted regulator of epithelial identity, nuclear architecture, and chromatin organization. While canonical role of FBL in ribosome biogenesis has been extensively studied, its contribution to cellular homeostasis beyond the nucleolus remains underexplored. Here, we report that depletion of FBL in epithelial cell models results in widespread morphological alterations that are not merely a consequence of impaired ribosome function but reflect broader structural and epigenetic reprogramming. A hallmark observation in this study is the loss of epithelial morphology upon FBL knockdown, accompanied by the redistribution of E-cadherin and ZO-1 from the membrane to intracellular compartments. The internalization of E-cadherin and its accumulation in the Golgi—coupled with its rescue by Dynasore—strongly implicates a disruption in clathrin-mediated endocytosis. Such observations are reminiscent of similar trafficking defects seen in EMT-like transitions and may represent an early step toward phenotypic plasticity. Importantly, total protein levels of E-cadherin remained unaltered, indicating that the mislocalization arises not from degradation but from trafficking imbalances. This highlights a novel role for FBL in membrane protein localization and intercellular adhesion maintenance.

In parallel, FBL depletion disrupted nuclear morphology, resulting in decreased nuclear sphericity and increased surface area, despite unchanged Lamin A/C and B levels. These changes suggest an uncoupling between nuclear lamina structure and chromatin architecture. Supporting this, we observed upregulation of the repressive histone marks H3K9me3 and H3K27me3, along with increased Emerin levels. Previous work has established Emerin as a tether for perinuclear heterochromatin, stabilizing nuclear shape under mechanical stress (Pradhan et al. 2018; Marano and Holaska 2022). Our data suggest that FBL loss activates such compensatory pathways, potentially through nucleolar stress-mediated chromatin remodeling.

Interestingly, while both H3K9me3 and H3K27me3 were elevated upon FBL depletion, only H3K27me3 depletion via EZH2 inhibition could rescue the migration phenotype. In contrast, SUV39H1 knockdown, which reduces H3K9me3, did not mitigate cell motility. This functional divergence is in line with existing literature that implicates EZH2 in promoting invasive phenotypes in a variety of epithelial cancers (Varambally et al. 2002; Cao et al. 2008). Furthermore, the inability of Chaetocin to yield a reproducible reduction in H3K9me3 levels underscores the technical challenges in targeting heterochromatin pathways, necessitating

precise genetic tools. An unexpected finding of this study is the increase—not decrease—of heterochromatin following FBL loss, despite nuclear deformation. This contrasts with the classical notion that reduced chromatin compaction contributes to nuclear softening. However, similar observations have been reported wherein chromatin compaction increases in response to mechanical stress as a protective mechanism (Nava et al. 2020). The upregulation of Emerin and repressive histone marks in our model supports such a compensatory model, wherein nuclear stiffening acts to stabilize a deformed architecture.

Together, these results position FBL as a central node in integrating nucleolar function, chromatin regulation, and epithelial structure. Its depletion not only compromises ribosomal integrity but also activates broader architectural and epigenetic responses. Future work should explore the precise molecular intermediates through which FBL interfaces with the endocytic machinery and chromatin remodelers. In addition, given the role of EZH2 in regulating plasticity, targeting FBL-EZH2 interactions could offer therapeutic strategies in malignancies characterized by aberrant nucleolar activity and epithelial dedifferentiation.

Chapter 4:
Epigenetic Regulation of Polarity by FBL Through EZH2-Scribble Axis

4.1. Introduction

The structural and functional integrity of epithelial tissues depends on the maintenance of cell polarity, junctional organization, and transcriptional identity. These processes are tightly governed by a network of cytoskeletal regulators, cell adhesion molecules, and epigenetic modifiers. Disruption of these regulatory modules contributes to epithelial plasticity, which, while essential during developmental transitions such as gastrulation and wound repair, also underpins pathological conditions including fibrosis and tumorigenesis (Thiery et al. 2009; Zeisberg and Neilson 2009). A pivotal event in this transformation is the epithelial-to-mesenchymal transition (EMT), characterized by loss of adherens junctions, apical–basal polarity, and acquisition of migratory behavior. While numerous transcription factors such as Snail, Twist, and Zeb mediate EMT at the transcriptional level, increasingly, the contribution of chromatin regulators and subnuclear structures such as the nucleolus is being recognized (Nieto et al. 2016; Aiello and Kang 2019). Recent work, however, has expanded its functional portfolio to include roles in chromatin organization, genome stability, and nuclear architecture (Misteli 2007; Groth et al. 2007; Allshire and Madhani 2018). The nucleolus itself is emerging as a non-membranous compartment that coordinates both ribosomal synthesis and the sequestration of epigenetic and regulatory proteins under stress and developmental cues. Yet, whether FBL participates in direct regulation of gene expression and cellular plasticity beyond its canonical ribosomal roles remains insufficiently explored.

Our previous observations showed that FBL depletion alters epithelial cell morphology, disrupts E-cadherin localization, and enhances migratory behavior, hallmarks of an early EMT-like state. To investigate the molecular underpinnings of these phenotypes, we performed RNA-sequencing and found that the expression of Scribble (SCRIB), a critical scaffolding protein involved in maintaining epithelial polarity, was significantly downregulated upon FBL depletion. SCRIB is a member of the Scribble polarity complex and plays a central role in anchoring adherens junction proteins such as E-cadherin to the basolateral membrane, thereby restricting inappropriate cell migration and proliferation (Lohia et al. 2012). Loss of Scribble has been associated with increased EMT, tumorigenesis, and metastatic potential in multiple cancers including breast, colorectal, and cervical carcinomas (Humbert et al. 2008).

Given that SCRIB downregulation occurred at the transcript level, we hypothesized a transcriptional repression mechanism involving chromatin remodeling. Analysis of public

ChIP-seq data from colorectal and breast epithelial cells revealed that the SCRIB promoter is marked by a bivalent chromatin state—simultaneously harboring active (H3K4me3) and repressive (H3K27me3) histone modifications—suggesting its expression is subject to tight epigenetic control. H3K27me3 is deposited by EZH2, the methyltransferase component of the Polycomb Repressive Complex 2 (PRC2), which functions as a central epigenetic silencer of differentiation and lineage-specific genes (Mohn et al. 2008; Teschendorff et al. 2010). Notably, PRC2-mediated repression has been shown to drive EMT and stemness by silencing epithelial genes including E-cadherin and miR-200 family members (Nourmohammadi et al. 2022).

To elucidate whether FBL modulates PRC2 function, we examined the chromatin occupancy of EZH2 and H3K27me3 at the SCRIB promoter and found both to be significantly enriched upon FBL knockdown. However, total EZH2 protein levels remained unchanged, suggesting a redistribution rather than upregulation of PRC2 activity. Subsequent subcellular analyses revealed that FBL depletion causes EZH2 to exit the nucleolus and accumulate in the nucleoplasm. Previous studies have shown that nucleolar sequestration of regulatory proteins can serve as a buffering mechanism, restricting their access to chromatin until needed (Boisvert et al. 2007; Rubbi and Milner 2003; Lohrum et al. 2003; Audas et al. 2012). In our system, the interaction between FBL and EZH2 via the RNA-binding domain of FBL appears essential for EZH2 nucleolar localization, raising the possibility that FBL functions as a spatial regulator of PRC2.

To confirm the functional relevance of this interaction, we expressed an RNA-binding-deficient mutant of FBL in a knockdown background. This disrupted the FBL–EZH2 interaction, promoted EZH2 nucleoplasmic accumulation, and recapitulated the enhanced migration and E-cadherin internalization observed in FBL-depleted cells. Furthermore, pharmacological inhibition of EZH2 using GSK126 restored SCRIB expression, reduced H3K27me3 levels, and reversed the pro-migratory phenotype. These findings strongly suggest that FBL restricts the transcriptional repression of epithelial genes by spatially regulating the subnuclear distribution of PRC2 components.

In this chapter, we demonstrate that FBL governs epithelial identity by orchestrating the localization and function of EZH2 and modulating the epigenetic status of key polarity genes such as SCRIB. The FBL-EZH2-SCRIB regulatory axis represents a novel nucleolar–epigenetic interface that controls epithelial plasticity, with significant implications for understanding early events in carcinogenesis and metastasis.

4.2.1. GO and GSEA analysis from RNA-seq Data Reveal Downregulation of SCRIB Upon FBL Depletion

To gain mechanistic insights into the role of Fibrillarin (FBL) in epithelial cell homeostasis, we performed transcriptome-wide RNA sequencing (RNA-Seq) following FBL depletion in DLD-1 colorectal carcinoma cells. This approach aimed to systematically identify downstream genes and pathways affected by the loss of FBL. The transcriptomic data were analyzed using two complementary enrichment strategies: Gene Ontology (GO) enrichment analysis and Gene Set Enrichment Analysis (GSEA) (Subramanian et al. 2005). These analyses revealed widespread transcriptional deregulation involving key functional categories, notably genes associated with ribosome biogenesis and structural components of the ribosome, cell-cell adhesion complexes, components of the apical plasma membrane, and gene sets implicated in epithelial-to-mesenchymal transition (EMT). The enrichment of EMT-associated signatures pointed toward a broader role for FBL in regulating epithelial identity and suppressing mesenchymal transformation (Fig. 4.1(A,B,D, E)).

Within the pool of significantly downregulated genes, Scribble (SCRIB)- a well-characterized scaffolding protein involved in maintaining epithelial polarity- stood out as a key molecular target of FBL (Fig. 4.1B). Scribble is an apical-basal polarity determinant that plays a crucial role in stabilizing E-cadherin at the plasma membrane by facilitating its interaction with p120-catenin. This interaction prevents the internalization and degradation of E-cadherin and is essential for the maintenance of adherens junctions and overall epithelial integrity. The downregulation of Scribble mRNA upon FBL knockdown was further validated by independent quantitative RT-qPCR assays, confirming the transcriptional repression (Fig. 4.1H). In addition, immunoblot analysis demonstrated a corresponding decrease in Scribble protein levels (Fig. 4.1(G-H)), reinforcing the post-transcriptional consequences of FBL depletion on cell polarity regulators. Upon studying the correlation of transcript levels of SCRIB and FBL across tumor samples on GEPIA2, we observed a moderately positive correlation between the expression of FBL and SCRIB (Fig. 4.1F).

It is well established that E-cadherin stability and localization at the plasma membrane are regulated by a complex network of proteins, including Discs Large Homolog 5 (DLG5) (Liu et al. 2017), CTNND1 (Delta-catenin) (Nanes et al. 2012), Epsin 3 (EPN3) (Schiano Lomoriello et al. 2020), VANGL2 (Van Gogh-like 2) (Nagaoka et al. 2014), and Discoidin Domain Receptor 1 (DDR1) (Chen et al. 2016). Notably, previous studies have implicated the

depletion of DLG5 and DDR1 in the internalization and mislocalization of E-cadherin. However, our RNA-Seq analysis did not reveal any significant downregulation of DLG5 or DDR1 transcript levels in FBL-depleted DLD-1 cells. This suggests that the observed E-cadherin internalization in our model is unlikely to be mediated through changes in these regulators. Instead, the marked downregulation of Scribble emerged as the most plausible explanation for the destabilization of E-cadherin and the resulting loss of epithelial cohesion observed upon FBL knockdown.

Collectively, these findings reveal a novel and fundamental mechanistic link between the nucleolar protein FBL and the polarity scaffolding protein Scribble in preserving epithelial architecture. Through the transcriptional regulation of Scribble, FBL indirectly governs the localization and stability of E-cadherin at the cell surface, thereby maintaining the structural and functional integrity of epithelial junctions. Disruption of this axis by FBL depletion results in compromised cell polarity, internalization of adhesion proteins, and increased cellular motility—hallmarks of epithelial destabilization and early events in tumor progression. These insights establish FBL as a critical upstream regulator of epithelial polarity and highlight its potential role in modulating key cellular behaviors that underpin malignancy.

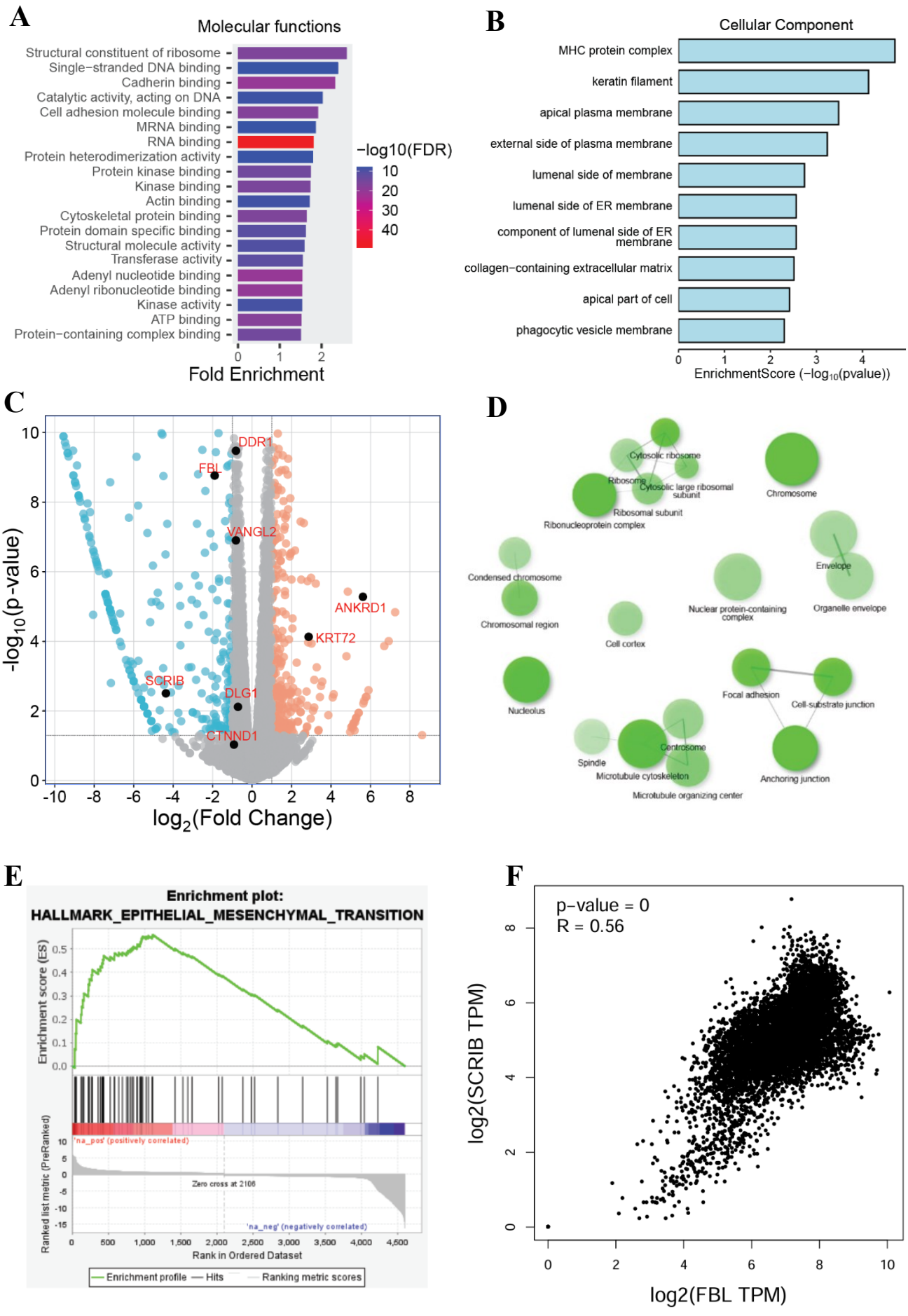
A
Molecular functions
Structural constituent of ribosome
Single−stranded DNA binding
Cadherin binding
Catalytic activity, acting on DNA
Cell adhesion molecule binding
MRNA binding
RNA binding
Protein heterodimerization activity
Protein kinase binding
Kinase binding
Actin binding
Cytoskeletal protein binding
Protein domain specific binding
Structural molecule activity
Transferase activity
Adenyl nucleotide binding
Adenyl ribonucleotide binding
Kinase activity
ATP binding
Protein−containing complex binding
−log10(FDR)
10
20
30
40
0
1
2
Fold Enrichment
B
Cellular Component
MHC protein complex
keratin filament
apical plasma membrane
external side of plasma membrane
lumenal side of membrane
lumenal side of ER membrane
component of lumenal side of ER membrane
collagen−containing extracellular matrix
apical part of cell
phagocytic vesicle membrane
0
1
2
3
4
EnrichmentScore (−log10(pvalue))
C
DDR1
FBL
VANGL2
ANKRD1
KRT72
SCRIB
DLG1
CTNND1
10
8
6
4
2
0
-10
-8
-6
-4
-2
0
2
4
6
8
-log10(p-value)
log2(Fold Change)
D
Cytosolic ribosome
Ribosome
Cytosolic large ribosomal subunit
Ribosomal subunit
Ribonucleoprotein complex
Chromosome
Condensed chromosome
Chromosomal region
Envelope
Organelle envelope
Nuclear protein-containing complex
Cell cortex
Nucleolus
Focal adhesion
Cell-substrate junction
Spindle
Centrosome
Microtubule cytoskeleton
Microtubule organizing center
Anchoring junction
E
Enrichment plot:
HALLMARK_EPITHELIAL_MESENCHYMAL_TRANSITION
Enrichment score (ES)
0.5
0.4
0.3
0.2
0.1
0.0
'na_pos' (positively correlated)
Zero cross at 2106
'na_neg' (negatively correlated)
Ranked list metric (PreRanked)
0
500
1,000
1,500
2,000
2,500
3,000
3,500
4,000
4,500
Rank in Ordered Dataset
Enrichment profile
Hits
Ranking metric scores
F
p-value = 0
R = 0.56
log2(SCRIB TPM)
log2(FBL TPM)
0
2
4
6
8
10

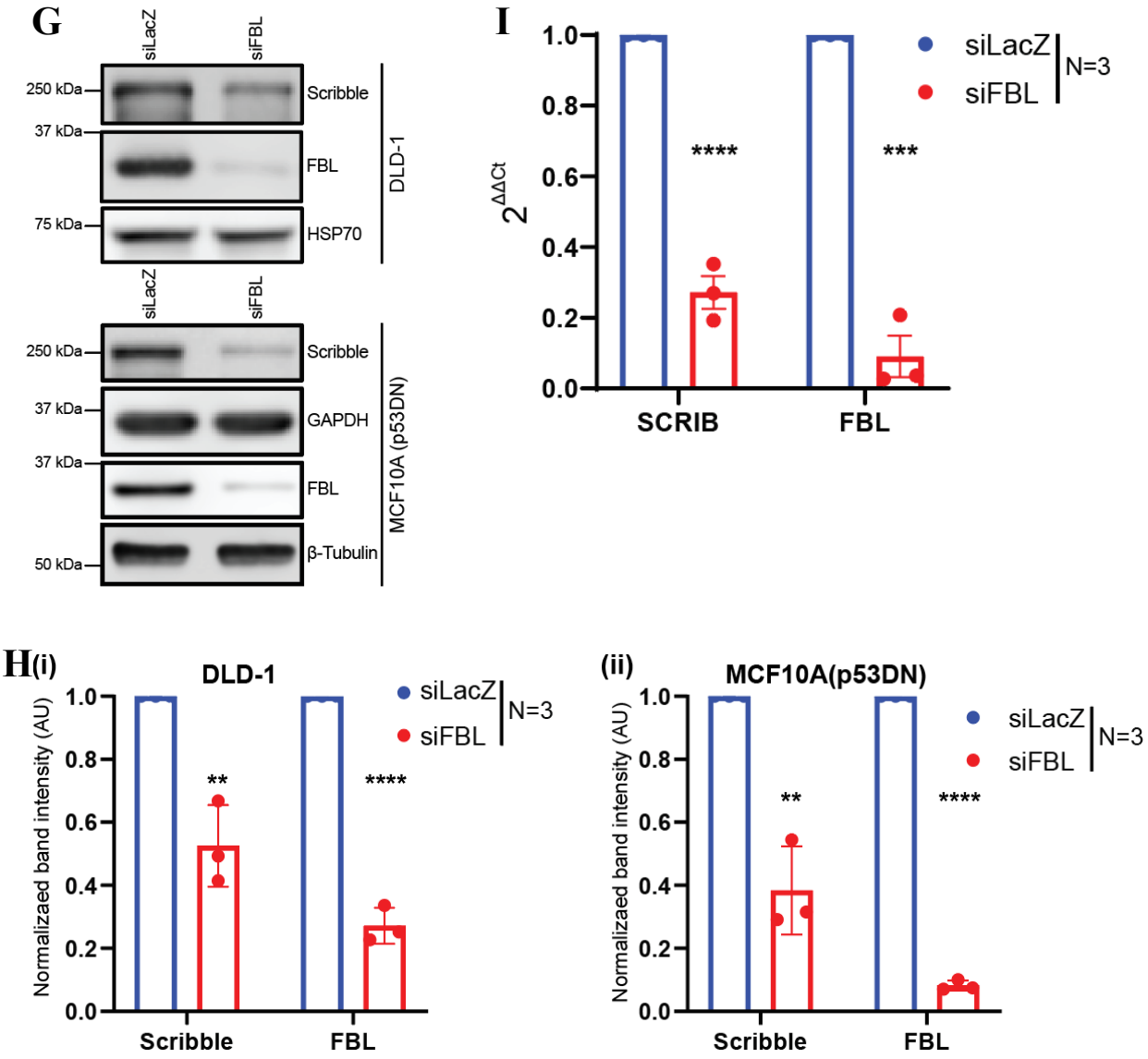

Fig. 4.1. Transcriptomic Profiling Reveals FBL-Dependent Regulation of SCRIB Expression

(A) Bar graph illustrating the most significantly deregulated molecular function categories identified by Gene Ontology (GO) analysis of RNA-seq data from FBL-depleted DLD-1 cells (~72 h). Bar height denotes the number of associated genes; FDR cutoff = 0.05. **(B)(i-ii)** Bar graph depicting the top deregulated cellular component categories obtained from GO analysis of the same RNA-seq dataset. Bar height represents the number of genes within each category; FDR cutoff = 0.05. **(C)** Volcano plots displaying differentially expressed genes identified by RNA-seq analysis of cells transfected with control siRNA (siLacZ) or FBL-targeting siRNA (siFBL) for ~72 h. Downregulated genes are shown in blue, upregulated genes in orange, and non-significant genes in gray. Thresholds were set at $\log_2$(fold change) = 2.0 and $-\log_{10}$(p

value) = 2. Data were pooled from two independent biological replicates (N = 2). **(D)** Network representation of major dysregulated cellular pathways identified from RNA-seq analysis following FBL depletion in DLD-1 cells. An edge cutoff of 0.3 was applied to define pathway interactions. **(E)** Gene Set Enrichment Analysis (GSEA) enrichment plot derived from RNA-seq data, highlighting significant enrichment of epithelial-to-mesenchymal transition (EMT)–associated gene signatures. The analysis yielded an FDR of 0 and a normalized enrichment score (NES) of 3.33. **(F)** Scatter plot showing the correlation between FBL and SCRIB transcript abundance, plotted as $\log_2$-transformed TPM values. Each dot represents an individual sample. A positive correlation is observed between FBL and SCRIB expression (Pearson correlation coefficient R = 0.56; p value = 0), indicating coordinated expression across the dataset. **(G)** Representative immunoblot analyses showing reduced Scribble levels along with corresponding FBL expression in DLD-1 and MCF10A(p53DN) cells transfected with control siRNA (siLacZ) or FBL-targeting siRNA (siFBL) for ~48 h and ~36 h, respectively. GAPDH, β-tubulin, and HSP70 were used as loading controls. Data are representative of three independent biological replicates (N = 3). **(H)** Densitometric quantification of immunoblot analyses showing Scribble protein levels in DLD-1 and MCF10A(p53DN) cells. Statistical significance was assessed using an unpaired t-test. Data were obtained from three independent biological replicates (N = 3). **(I)** Relative mRNA expression levels of SCRIB and FBL following FBL knockdown in DLD-1 cells for ~48 h. p-values were calculated using an unpaired t-test. Data represent three independent biological replicates (N = 3), with error bars indicating standard deviation (SD). Statistical significance is denoted as *p < 0.05, **p < 0.01, and ****p < 0.0001.

4.2.2. Reduced Scribble Expression Impacts Cell Migration

Interestingly, functional studies further confirmed the role of Scribble in regulating cell migration. Depletion of Scribble alone, independent of FBL knockdown, led to a substantial increase in migratory capacity, as assessed by the scratch wound healing assay. In this assay, cells lacking Scribble displayed significantly enhanced wound closure, with approximately 65% (±5%) of the wound area covered within the observation period. This increase in collective migration is consistent with established role of Scribble as a key negative regulator of cell motility and polarity. The loss of Scribble disrupts the maintenance of tight epithelial junctions and cell polarity cues, which normally act to constrain migratory behavior.

Scribble functions as a crucial component of the basolateral polarity complex and has been implicated in tumor suppression by restricting inappropriate cell movement and maintaining epithelial architecture. Prior studies, have shown that Scribble depletion leads to aberrant activation of signaling pathways such as MAPK/ERK, which are known to drive cell motility and proliferation (Qin et al. 2005). Moreover, loss of Scribble impairs front-rear polarity and directional persistence, resulting in increased but disorganized migration. These mechanisms are particularly relevant in the context of epithelial plasticity and cancer progression, where deregulation of polarity complexes contributes to invasive behavior (Fig. 4.2A, C).

Conversely, enforced overexpression of Scribble in FBL-depleted cells led to a marked reduction in cell migration (Fig. 4.2B, D, E). Reintroducing Scribble restored, at least in part, the polarity and adhesion landscape disrupted by FBL knockdown, resulting in slower wound closure and reduced cellular motility. This phenotypic rescue further supports the hypothesis that FBL regulates epithelial behavior through modulation of Scribble expression and activity. The ability of Scribble to counteract the migratory phenotype induced by FBL depletion highlights its critical role in maintaining epithelial restraint and preventing the transition to a more motile, mesenchymal-like state.

Together, these findings provide compelling evidence that Scribble functions downstream of FBL and plays a central role in controlling epithelial cell migration. Through this axis, FBL acts to stabilize epithelial polarity and junctional organization, thereby suppressing aberrant migratory responses. Disruption of this regulatory pathway, as observed in FBL-deficient cells, may facilitate early events in tumorigenesis, including loss of polarity, weakened cell-cell adhesion, and enhanced invasiveness. These insights align with the broader understanding

of Scribble as a tumor suppressor and polarity regulator, reinforcing its importance in the maintenance of epithelial tissue integrity.

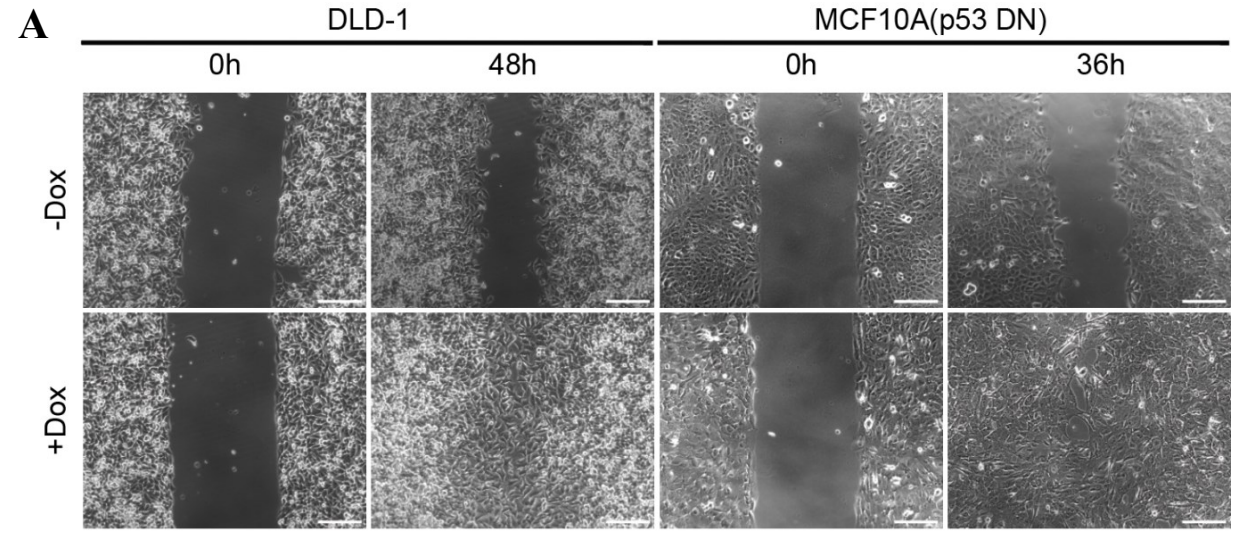

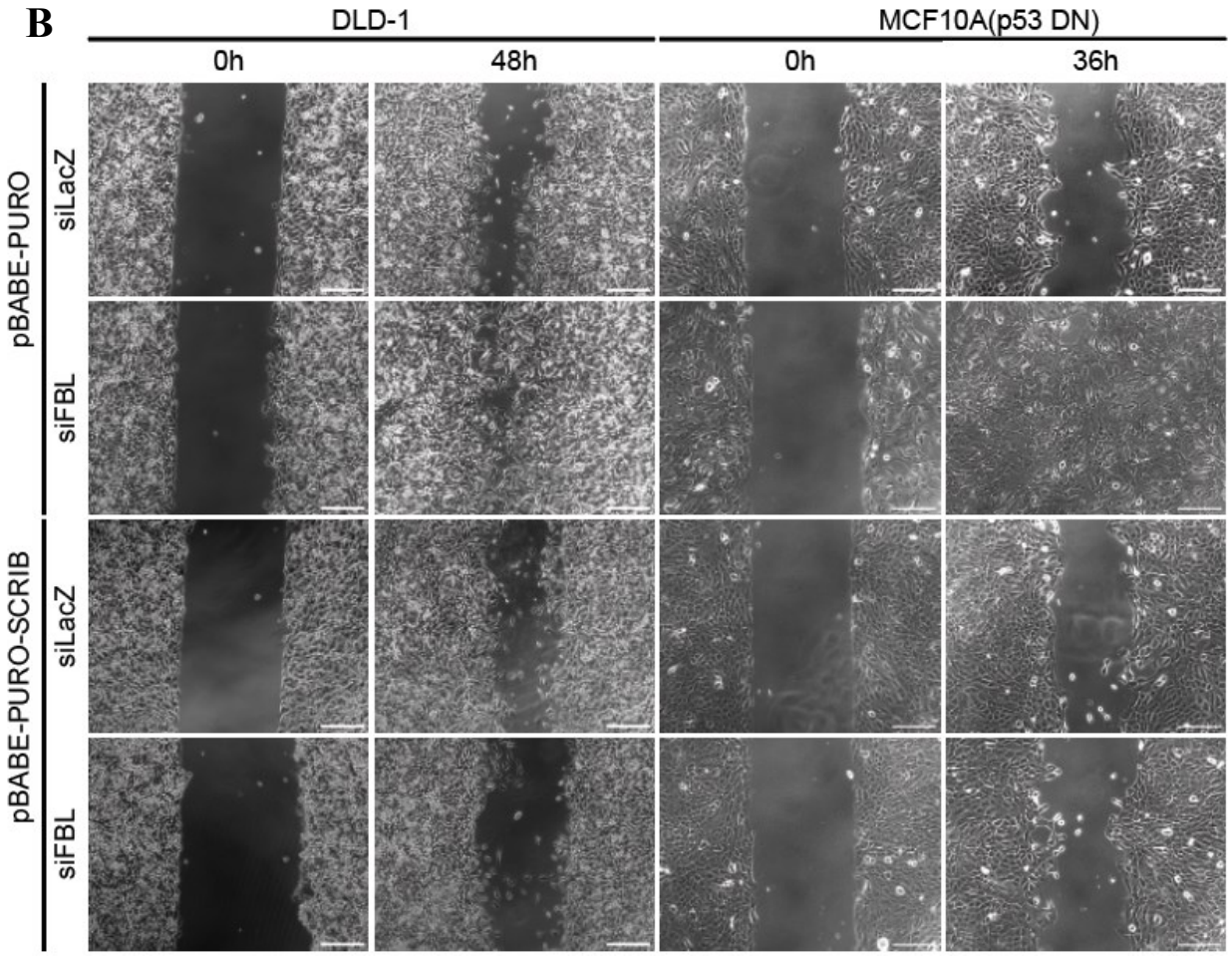

C

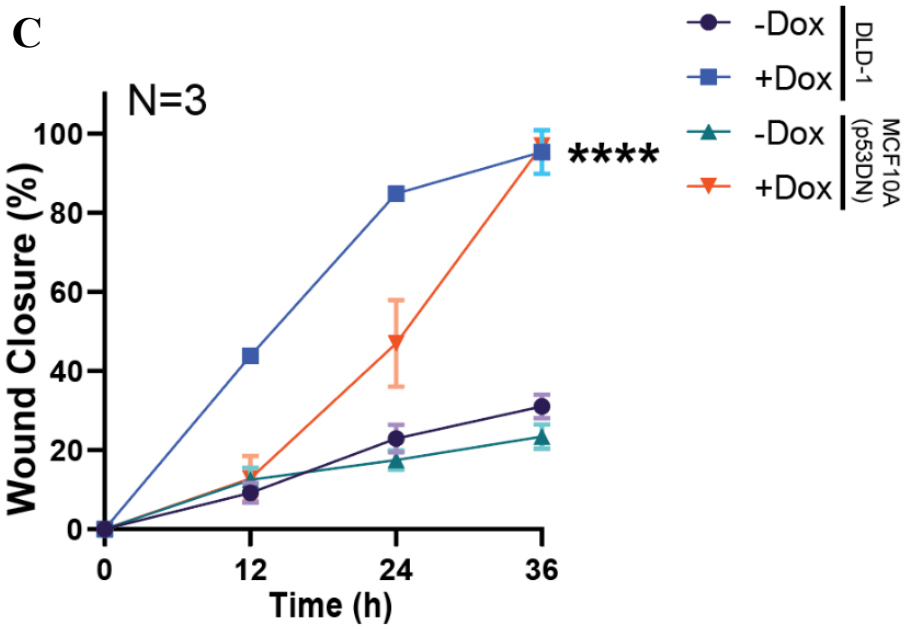
N=3
****
-Dox
+Dox
-Dox
+Dox
DLD-1
MCF10A (p53DN)
Wound Closure (%)
Time (h)
0
20
40
60
80
100
0
12
24
36

D

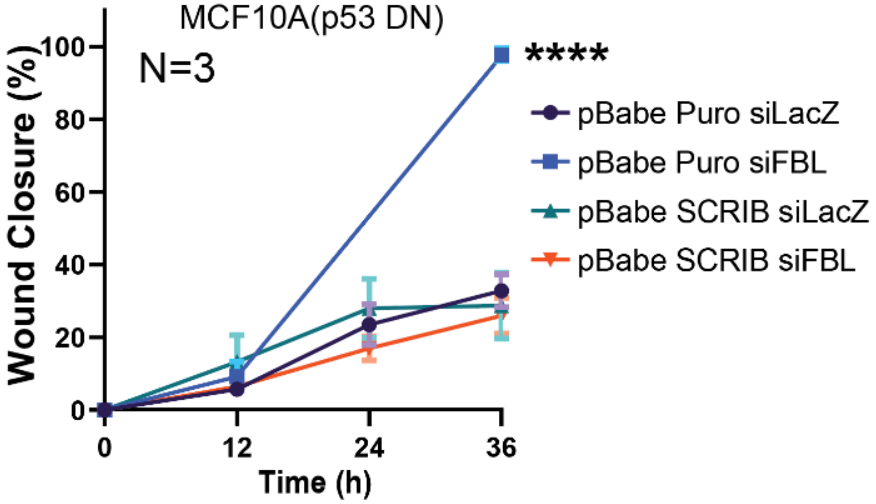
MCF10A(p53 DN)
N=3
****
pBabe Puro siLacZ
pBabe Puro siFBL
pBabe SCRIB siLacZ
pBabe SCRIB siFBL
Wound Closure (%)
Time (h)
0
20
40
60
80
100
0
12
24
36

E

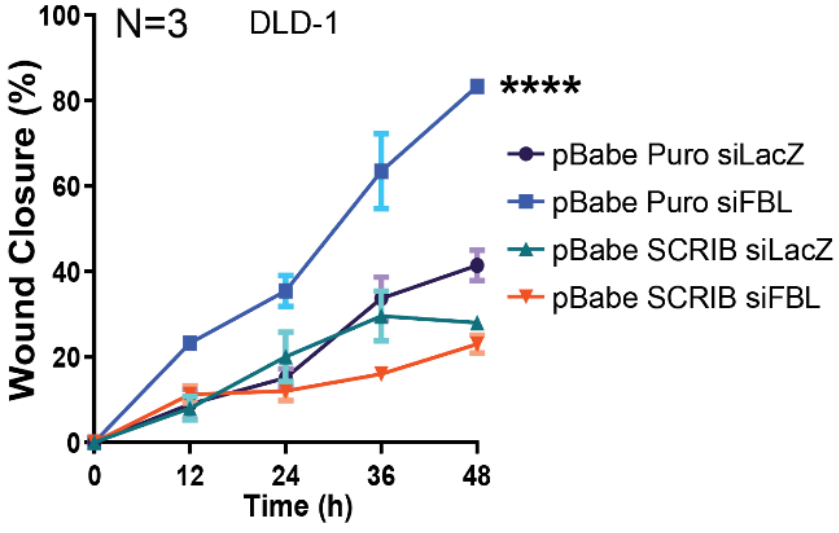
N=3
DLD-1
****
pBabe Puro siLacZ
pBabe Puro siFBL
pBabe SCRIB siLacZ
pBabe SCRIB siFBL
Wound Closure (%)
Time (h)
0
20
40
60
80
100
0
12
24
36
48

Fig. 4.2. SCRIB overexpression rescues FBL depletion mediated enhanced cell migration

(A) Representative phase-contrast images from scratch-wound assays conducted independently in DLD-1 and MCF10A(p53DN) cells following SCRIB depletion via doxycycline-induced shSCRIB expression, under −Dox and +Dox conditions. **(B)** Representative scratch-wound assay images of DLD-1 and MCF10A(p53DN) cells transduced with pBabe-Puro or pBabe-SCRIB in siLacZ- or siFBL-transfected conditions. Data are representative of three independent biological replicates (N = 3). **(C)** Line graph showing percentage wound closure over time (0, 12, 24, and 36 h) in DLD-1 and MCF10A(p53DN) cells expressing inducible shSCRIB under −Dox and +Dox conditions. Doxycycline treatment induces SCRIB knockdown and results in significantly accelerated wound closure compared to −Dox controls. Data represent mean ± SD from three independent biological replicates (N = 3). Statistical significance was assessed using an unpaired t-test (****$p < 0.0001$). **(D)** Line graph showing quantification of wound closure (%) over time following scratch-wound assay in DLD-1 cells stably expressing control vector (pBabe-Puro) or SCRIB (pBabe-SCRIB), transfected with control siRNA (siLacZ) or FBL-targeting siRNA (siFBL). Wound closure was measured at the indicated time points and expressed relative to the initial wound area (0 h). Data represent mean ± SEM from three independent biological replicates (N = 3). Statistical significance was determined by two-way ANOVA with appropriate post-hoc testing; **** denotes $p < 0.0001$. **(E)** Line graph depicting wound closure (%) over time following scratch-wound assay in MCF10A(p53DN) cells expressing control vector (pBabe-Puro) or SCRIB (pBabe-SCRIB), transfected with control siRNA (siLacZ) or FBL-targeting siRNA (siFBL). Wound closure was quantified at the indicated time points and normalized to the initial wound area at 0 h. Data are shown as mean ± SEM from three independent biological replicates (N = 3). Statistical significance was assessed using two-way ANOVA with appropriate post-hoc analysis; **** indicates $p < 0.0001$.

4.2.3. EZH2 Mediates Scribble Downregulation Upon FBL Loss

Having observed that Scribble expression was significantly downregulated upon FBL depletion, we sought to investigate whether this regulation occurred at the transcriptional level. To this end, we analyzed publicly available chromatin immunoprecipitation sequencing (ChIP-seq) datasets to explore the chromatin landscape at the SCRIB promoter.

Using the ChIP-ATLAS platform (Oki et al. 2018), we specifically examined the occupancy profiles of various histone modifications in DLD-1 colorectal cancer cells. Intriguingly, this analysis revealed a complex epigenetic environment at the SCRIB promoter region, located approximately 1 kilobase upstream of the transcription start site (TSS). Enrichment of repressive (H3K27me3) histone marks was detected at this locus (Fig. 4.3A).

To determine whether this regulatory pattern is conserved across other cell types, we extended our analysis to include additional datasets. Similar enrichment of the repressive histone modification H3K27me3 at the SCRIB promoter was observed in several epithelial and stem cell systems, including breast epithelial cells (MCF10A), human embryonic stem cells (hESCs), and breast cancer cell lines (MCF-7 and T-47D) (Fig. 4.3A). This widespread presence of repressive histone marks suggests that the transcriptional regulation of SCRIB is subject to polycomb-mediated silencing in diverse cellular contexts.

Given the established role of H3K27me3 as a hallmark of Polycomb Repressive Complex 2 (PRC2) activity, we next sought to experimentally examine the occupancy of PRC2 components on the SCRIB promoter in the context of FBL depletion. Chromatin immunoprecipitation followed by quantitative PCR (ChIP-qPCR) was employed to assess the enrichment of EZH2- the catalytic subunit of PRC2- and the H3K27me3 mark at the SCRIB promoter in FBL-depleted DLD-1 cells. This analysis revealed a clear increase in both EZH2 binding and H3K27me3 deposition at a site approximately 500 base pairs upstream of the SCRIB TSS following FBL knockdown. Notably, despite this enhanced chromatin occupancy, the total protein levels of EZH2 remained unchanged, indicating that FBL depletion likely promotes the redistribution or enhanced recruitment of EZH2 to specific genomic loci rather than affecting its overall abundance.

To functionally validate whether the increased repressive histone deposition at the SCRIB promoter was responsible for its transcriptional downregulation, we employed a pharmacological approach. DLD-1 cells were treated with GSK126, a selective inhibitor of EZH2 enzymatic activity, at a concentration of 10 μM for 48 hours (Al-Hasani et al. 2022). This treatment resulted in a marked reduction in H3K27me3 levels and a concomitant restoration of SCRIB expression, even in the background of FBL depletion (Fig. 4.3(D, G)). These findings strongly implicate EZH2-mediated repression as a key mechanism through which FBL regulates Scribble transcription.

In addition to rescuing SCRIB expression, inhibition of EZH2 activity had functional consequences on epithelial cell behavior. Scratch wound healing assays demonstrated a significant decrease in cell migration following GSK126 treatment (Fig. 4.3(B-C)), suggesting that the derepression of SCRIB may restore polarity and restrain motility. To further understand the phenotypic impact of EZH2 inhibition, we examined the subcellular distribution of E-cadherin using immunofluorescence. In stark contrast to the internalized pattern of E-cadherin observed in FBL-depleted cells, GSK126-treated cells exhibited a marked reduction in E-cadherin internalization, with restored membrane localization (Fig. 4.3(H, J)). These results indicate that EZH2 activity indirectly regulates E-cadherin trafficking, potentially through its influence on Scribble expression.

To reinforce this connection, we next investigated the effects of EZH2 overexpression in epithelial cells. Overexpression of EZH2 resulted in pronounced internalization of E-cadherin into the cytoplasm, mimicking the phenotype observed in FBL-depleted cells (Fig. 4.3 J, L). Furthermore, cells overexpressing EZH2 exhibited significantly elevated migratory behavior in wound healing assays, further supporting the role of EZH2 in promoting a motile, less adherent phenotype (Fig. 4.3 I, K). Consistent with these functional changes, immunoblotting analysis revealed that overexpression of EZH2 led to a substantial downregulation of Scribble protein levels (Fig. 4.3 N, O).

To assess whether EZH2 and H3K27me3 recruitment following FBL depletion represents a global effect or is confined to specific loci, we selected ten candidate genes exhibiting varying degrees of transcriptional deregulation in the RNA-seq dataset and examined EZH2 and H3K27me3 occupancy by ChIP-qPCR. Increased enrichment of both EZH2 and H3K27me3 was observed at promoter regions (within 1 kb upstream of the TSS) of downregulated genes, whereas no significant changes were detected at the promoters of upregulated genes (Fig. 4.3 (P-A4)). These results indicate that enhanced EZH2 recruitment upon FBL depletion is not restricted to the SCRIB promoter. Additional integrative analyses revealed that the downregulated genes were already enriched for H3K27me3, consistent with pre-existing PRC2 occupancy. This suggests that relocalized EZH2 is preferentially recruited to promoters bearing established H3K27me3 marks, supporting a model of PRC2-mediated epigenetic memory.

Taken together, these findings establish a direct epigenetic regulatory axis wherein FBL loss enhances the recruitment of EZH2 and H3K27me3 to the SCRIB promoter, resulting in transcriptional repression of Scribble. This repression disrupts epithelial polarity and adhesion by promoting E-cadherin internalization and increasing cell migration. Conversely, inhibition of EZH2 restores SCRIB expression and epithelial organization, while EZH2 overexpression exacerbates polarity loss. These observations suggest that FBL serves as a critical upstream modulator of PRC2 activity at the SCRIB locus, linking nucleolar function to chromatin-mediated regulation of epithelial integrity and migratory behavior. This FBL–EZH2–Scribble axis thus represents a novel epigenetic pathway with potential implications in epithelial plasticity, tumor progression, and metastasis.

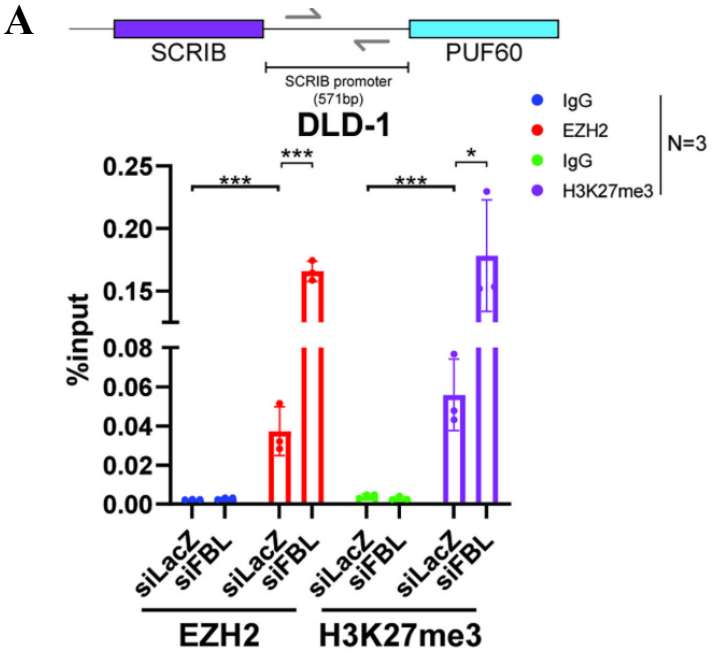
A
SCRIB
PUF60
SCRIB promoter
(571bp)
DLD-1
IgG
EZH2
IgG
H3K27me3
N=3
***
***
***
*
0.25
0.20
0.15
0.08
0.06
0.04
0.02
0.00
%input
siLacZ
siFBL
siLacZ
siFBL
siLacZ
siFBL
siLacZ
siFBL
EZH2
H3K27me3

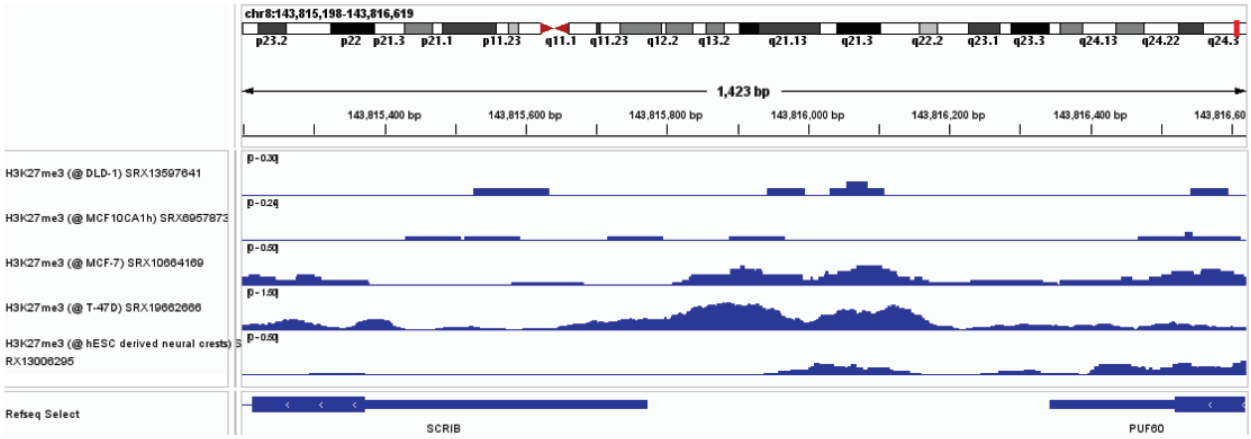
chr8:143,815,198-143,816,619
1,423 bp
143,815,400 bp
143,815,600 bp
143,815,800 bp
143,816,000 bp
143,816,200 bp
143,816,400 bp
H3K27me3 (@ DLD-1) SRX13597641
H3K27me3 (@ MCF10CA1h) SRX6957873
H3K27me3 (@ MCF-7) SRX10664169
H3K27me3 (@ T-47D) SRX19662666
H3K27me3 (@ hESC derived neural crests)
RX13006295
Refseq Select
SCRIB
PUF60

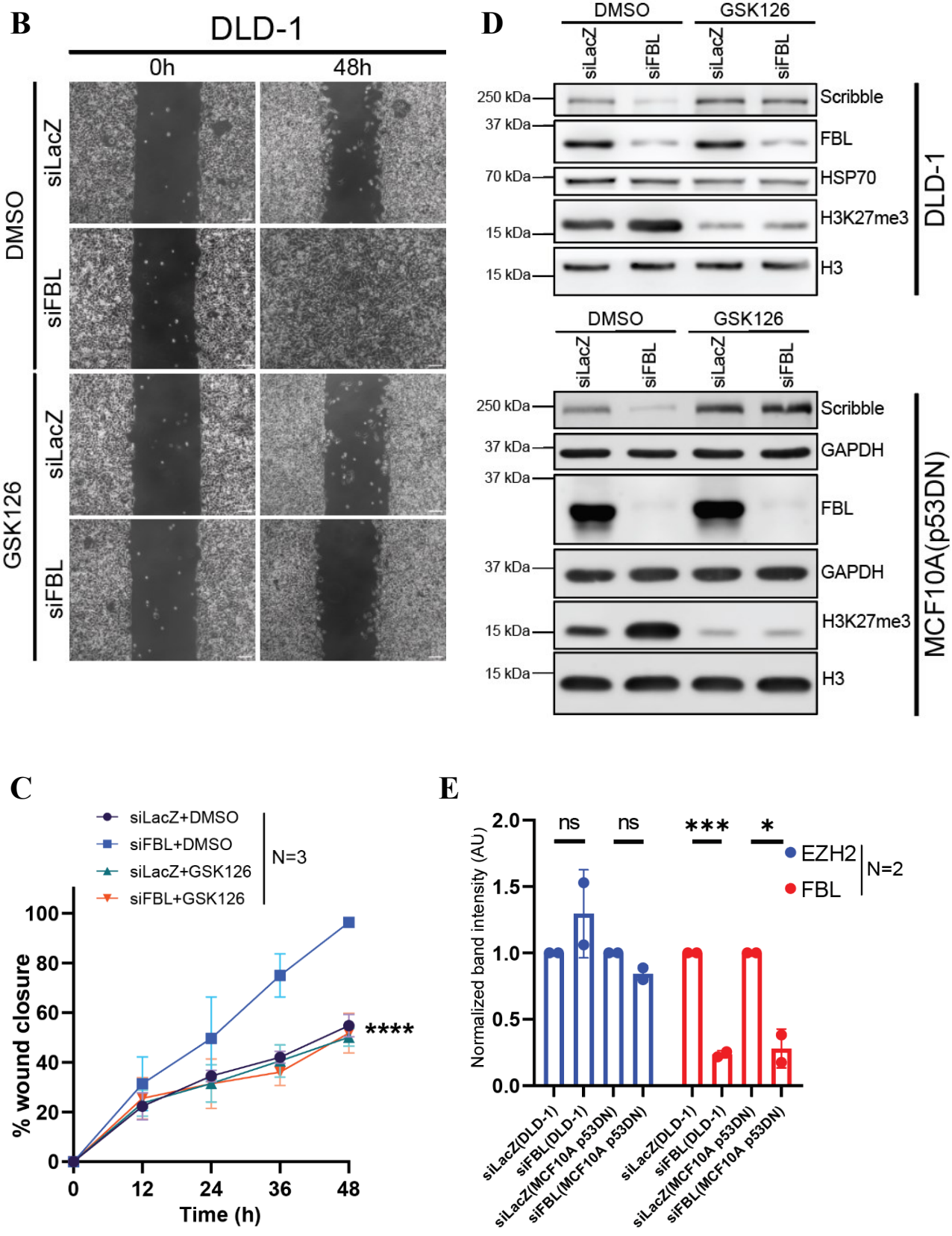
B
DLD-1
0h
48h
DMSO
GSK126
siLacZ
siFBL
D
DMSO
GSK126
siLacZ
siFBL
250 kDa
37 kDa
70 kDa
15 kDa
Scribble
FBL
HSP70
H3K27me3
H3
DLD-1
GAPDH
MCF10A(p53DN)
C
siLacZ+DMSO
siFBL+DMSO
siLacZ+GSK126
siFBL+GSK126
N=3
% wound closure
Time (h)
****
E
Normalized band intensity (AU)
ns
***
*
EZH2
FBL
N=2
siLacZ(DLD-1)
siFBL(DLD-1)
siLacZ(MCF10A p53DN)
siFBL(MCF10A p53DN)

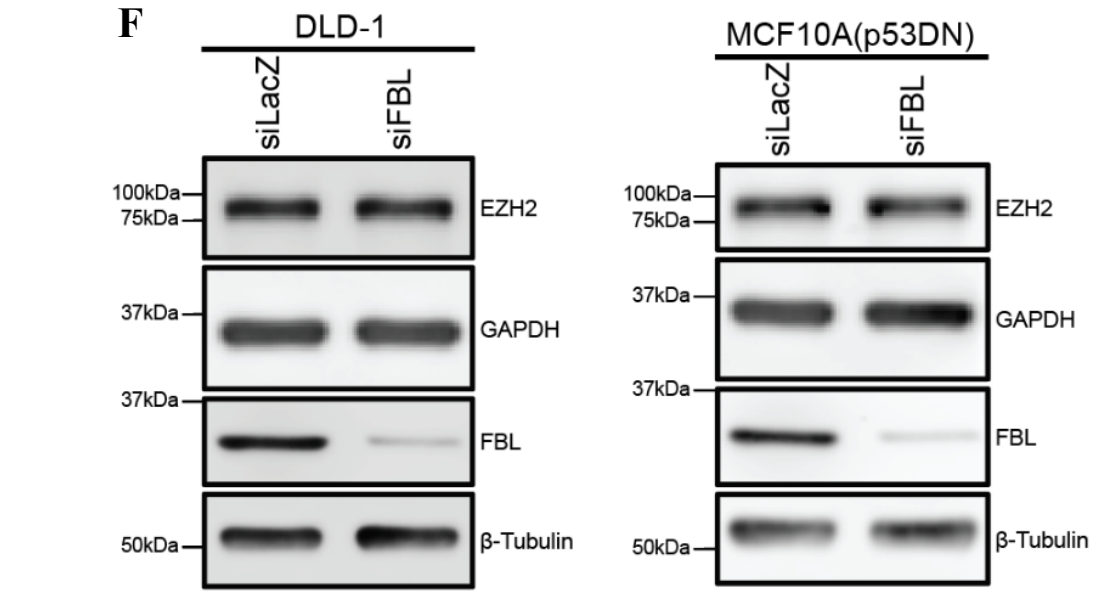
F
DLD-1
siLacZ
siFBL
100kDa
75kDa
EZH2
37kDa
GAPDH
37kDa
FBL
50kDa
β-Tubulin
MCF10A(p53DN)
siLacZ
siFBL
100kDa
75kDa
EZH2
37kDa
GAPDH
37kDa
FBL
50kDa
β-Tubulin

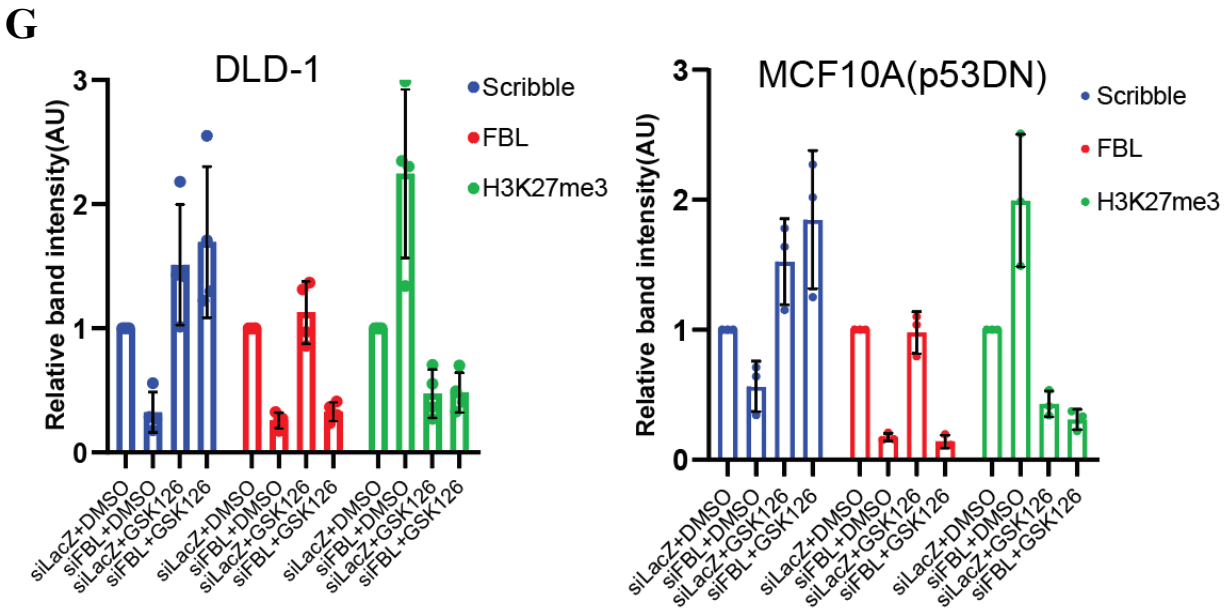
G
DLD-1
Relative band intensity(AU)
Scribble
FBL
H3K27me3
siLacZ+DMSO
siFBL+DMSO
siLacZ+GSK126
siFBL+GSK126
MCF10A(p53DN)
Relative band intensity(AU)
Scribble
FBL
H3K27me3
siLacZ+DMSO
siFBL+DMSO
siLacZ+GSK126
siFBL+GSK126

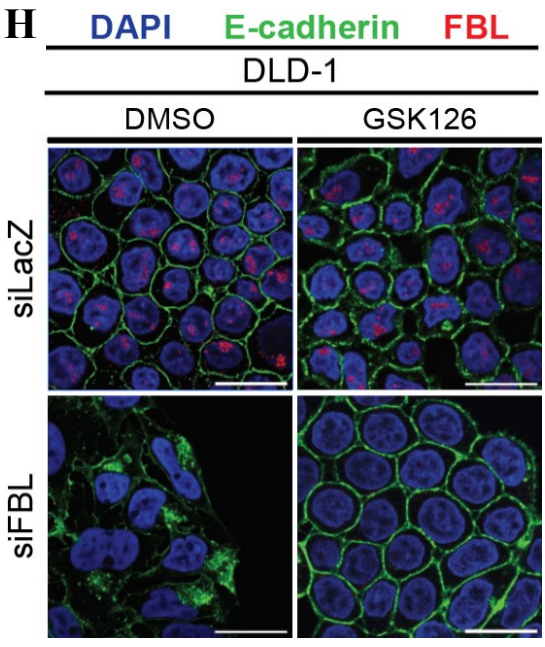
H
DAPI
E-cadherin
FBL
DLD-1
DMSO
GSK126
siLacZ
siFBL

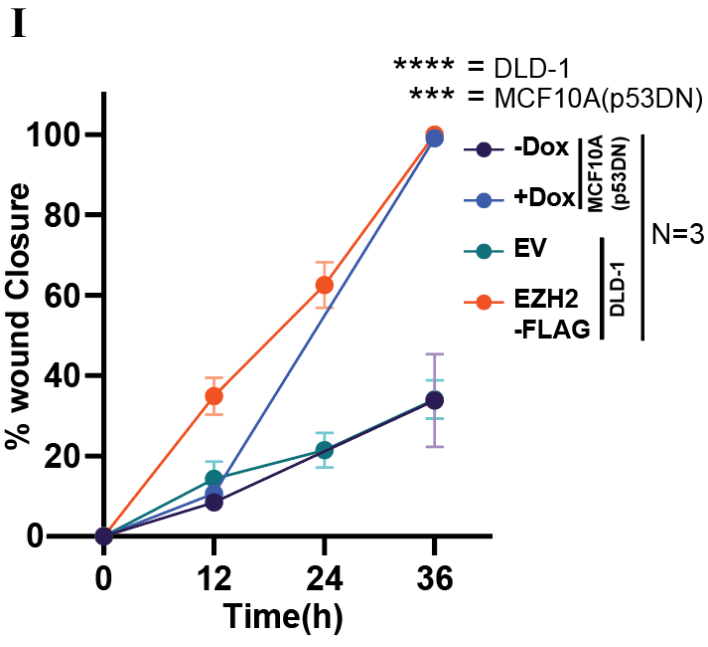
I
**** = DLD-1
*** = MCF10A(p53DN)
% wound Closure
Time(h)
-Dox
+Dox
EV
EZH2
-FLAG
MCF10A (p53DN)
DLD-1
N=3

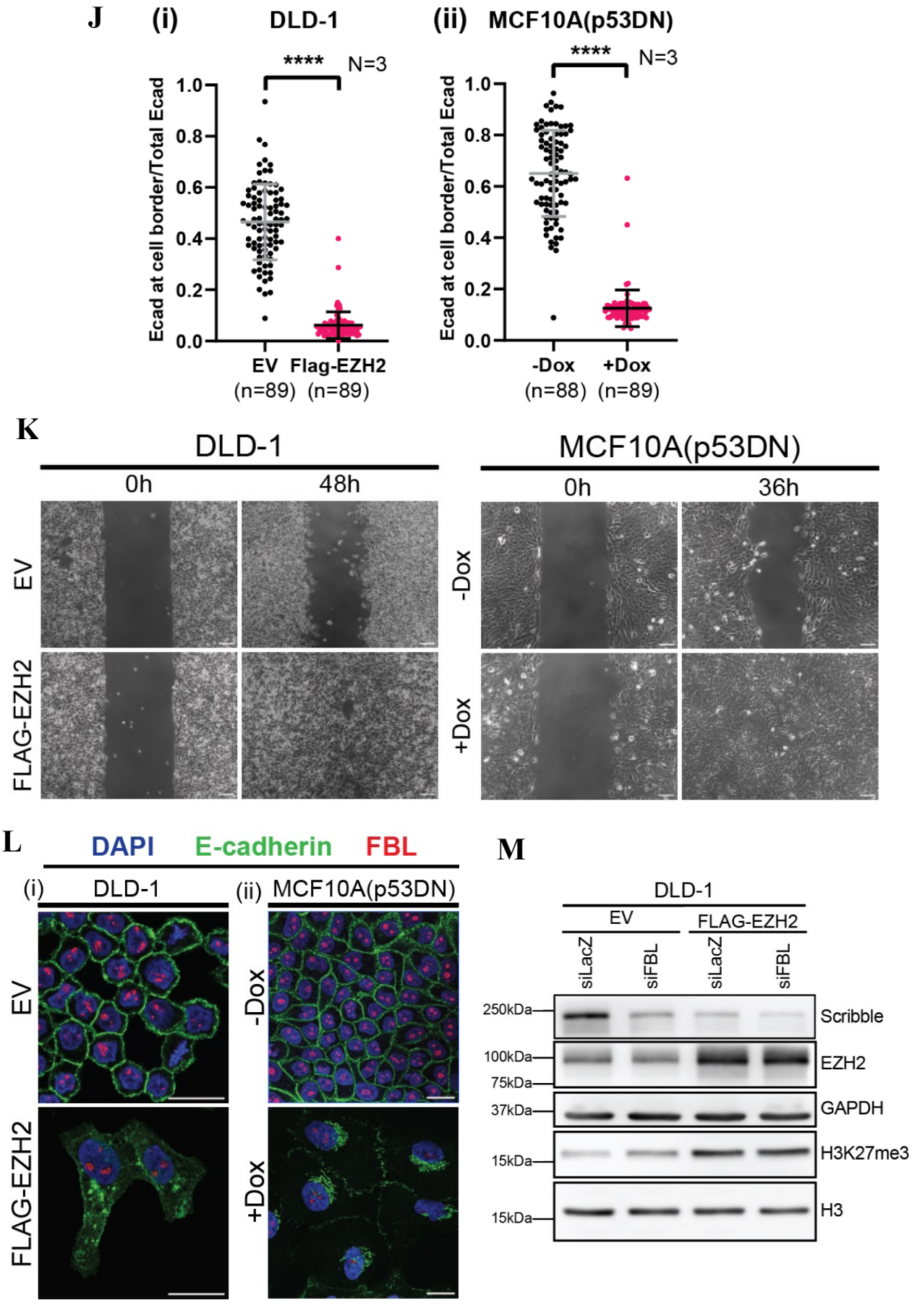
J
(i) DLD-1
(ii) MCF10A(p53DN)
****
N=3
Ecad at cell border/Total Ecad
1.0
0.8
0.6
0.4
0.2
0.0
EV
Flag-EZH2
(n=89) (n=89)
-Dox
+Dox
(n=88) (n=89)
K
DLD-1
MCF10A(p53DN)
0h
48h
36h
EV
FLAG-EZH2
-Dox
+Dox
L
DAPI
E-cadherin
FBL
(i) DLD-1
(ii) MCF10A(p53DN)
M
DLD-1
EV
FLAG-EZH2
siLacZ
siFBL
250kDa
100kDa
75kDa
37kDa
15kDa
Scribble
EZH2
GAPDH
H3K27me3
H3

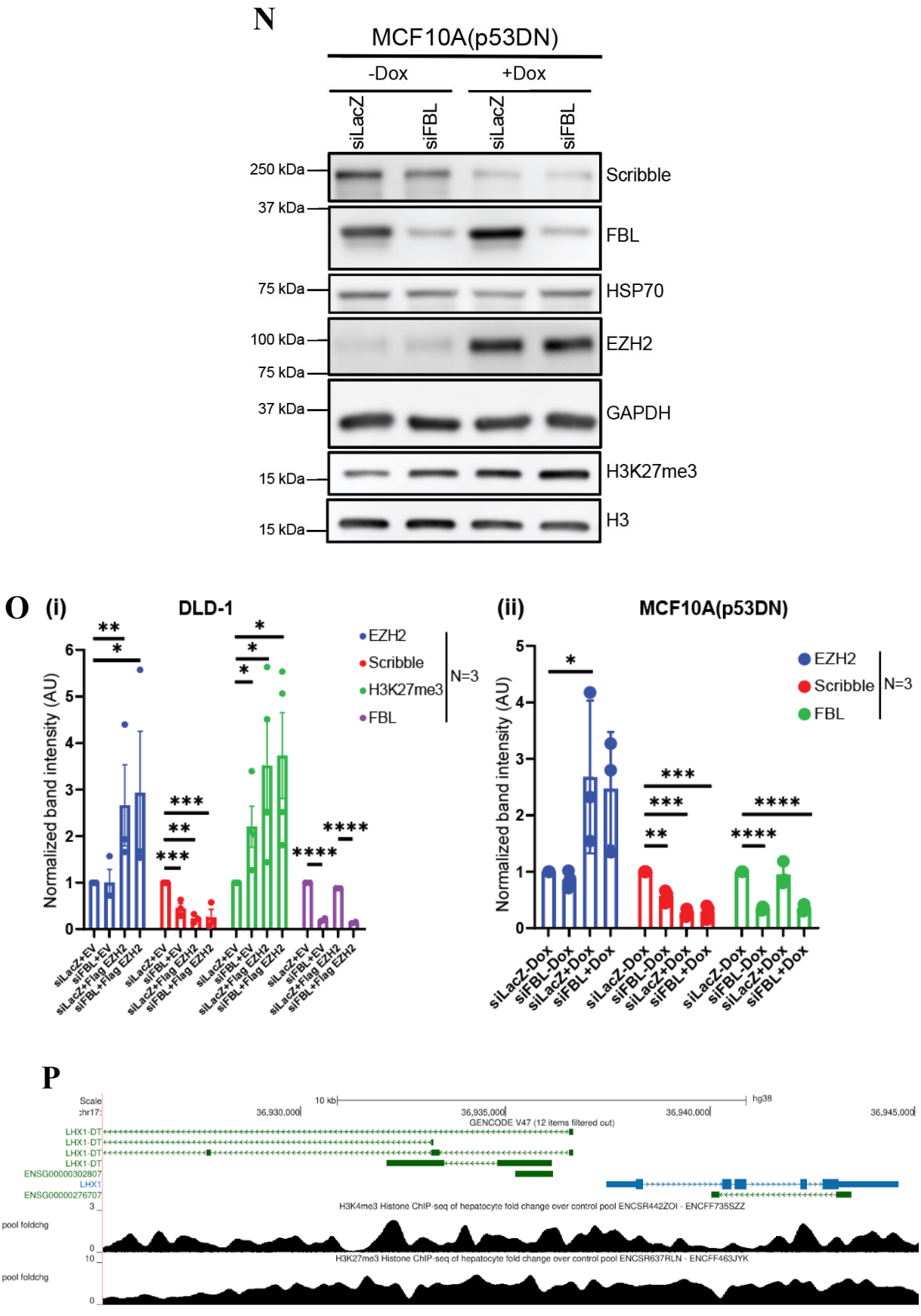
N
MCF10A(p53DN)
-Dox
+Dox
siLacZ
siFBL
siLacZ
siFBL
250 kDa
Scribble
37 kDa
FBL
75 kDa
HSP70
100 kDa
EZH2
75 kDa
37 kDa
GAPDH
15 kDa
H3K27me3
15 kDa
H3
O
(i)
DLD-1
Normalized band intensity (AU)
EZH2
Scribble
H3K27me3
FBL
N=3
siLacZ+EV
siFBL+EV
siLacZ+Flag EZH2
siFBL+Flag EZH2
(ii)
MCF10A(p53DN)
Normalized band intensity (AU)
EZH2
Scribble
FBL
N=3
siLacZ-Dox
siFBL-Dox
siLacZ+Dox
siFBL+Dox
P
Scale
10 kb
hg38
chr17:
36,930,000
36,935,000
36,940,000
36,945,000
GENCODE V47 (12 items filtered out)
LHX1-DT
LHX1-DT
LHX1-DT
LHX1-DT
ENSG00000302807
LHX1
ENSG00000276707
H3K4me3 Histone ChIP-seq of hepatocyte fold change over control pool ENCSR442ZOI - ENCFF735SZZ
pool foldchg
H3K27me3 Histone ChIP-seq of hepatocyte fold change over control pool ENCSR637RLN - ENCFF463JYK
pool foldchg

Q

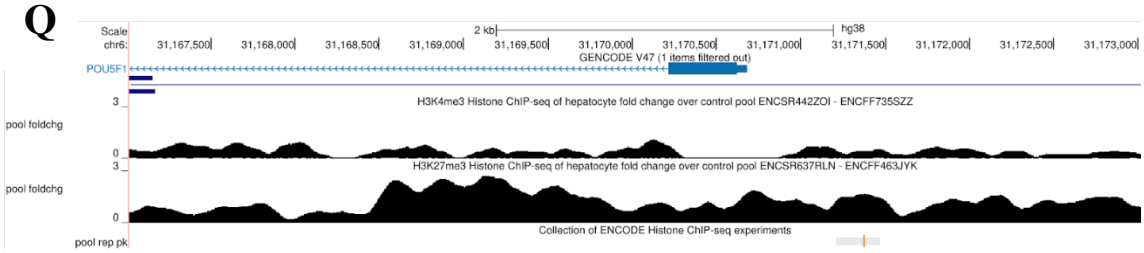
Scale
chr6:
2 kb
hg38
31,167,500
31,168,000
31,168,500
31,169,000
31,169,500
31,170,000
31,170,500
31,171,000
31,171,500
31,172,000
31,172,500
31,173,000
GENCODE V47 (1 items filtered out)
POU5F1
H3K4me3 Histone ChIP-seq of hepatocyte fold change over control pool ENCSR442ZOI - ENCFF735SZZ
pool foldchg
H3K27me3 Histone ChIP-seq of hepatocyte fold change over control pool ENCSR637RLN - ENCFF463JYK
pool foldchg
Collection of ENCODE Histone ChIP-seq experiments
pool rep pk

R

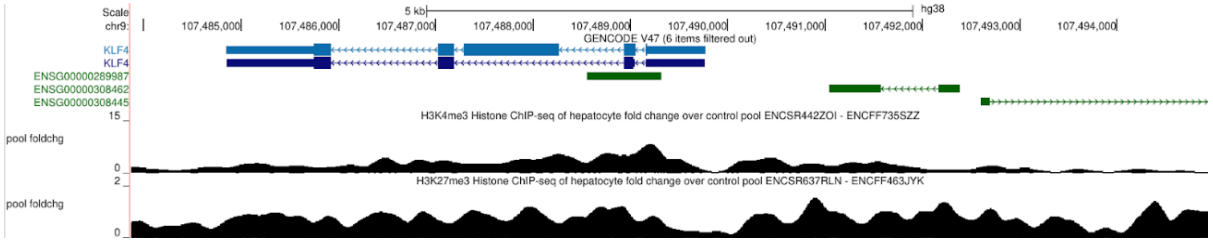
Scale
chr9:
5 kb
hg38
107,485,000
107,486,000
107,487,000
107,488,000
107,489,000
107,490,000
107,491,000
107,492,000
107,493,000
107,494,000
GENCODE V47 (6 items filtered out)
KLF4
KLF4
ENSG00000289987
ENSG00000308462
ENSG00000308445
H3K4me3 Histone ChIP-seq of hepatocyte fold change over control pool ENCSR442ZOI - ENCFF735SZZ
pool foldchg
H3K27me3 Histone ChIP-seq of hepatocyte fold change over control pool ENCSR637RLN - ENCFF463JYK
pool foldchg

S

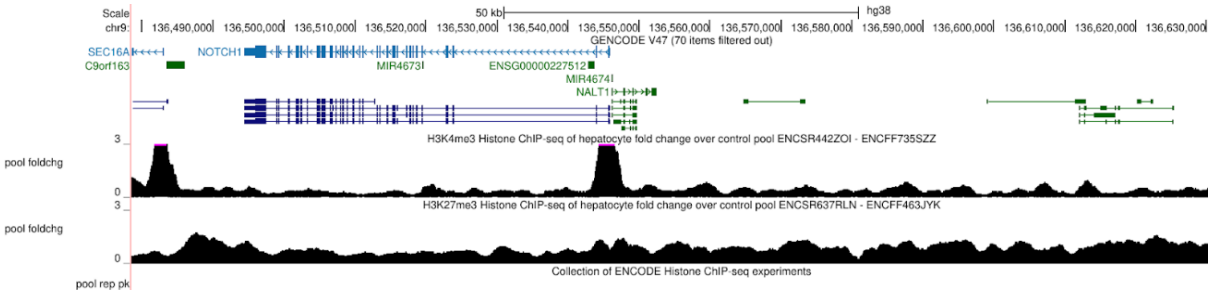
Scale
chr9:
50 kb
hg38
136,490,000
136,500,000
136,510,000
136,520,000
136,530,000
136,540,000
136,550,000
136,560,000
136,570,000
136,580,000
136,590,000
136,600,000
136,610,000
136,620,000
136,630,000
GENCODE V47 (70 items filtered out)
SEC16A
NOTCH1
C9orf163
MIR4673
ENSG00000227512
MIR4674
NALT1
H3K4me3 Histone ChIP-seq of hepatocyte fold change over control pool ENCSR442ZOI - ENCFF735SZZ
pool foldchg
H3K27me3 Histone ChIP-seq of hepatocyte fold change over control pool ENCSR637RLN - ENCFF463JYK
pool foldchg
Collection of ENCODE Histone ChIP-seq experiments
pool rep pk

T

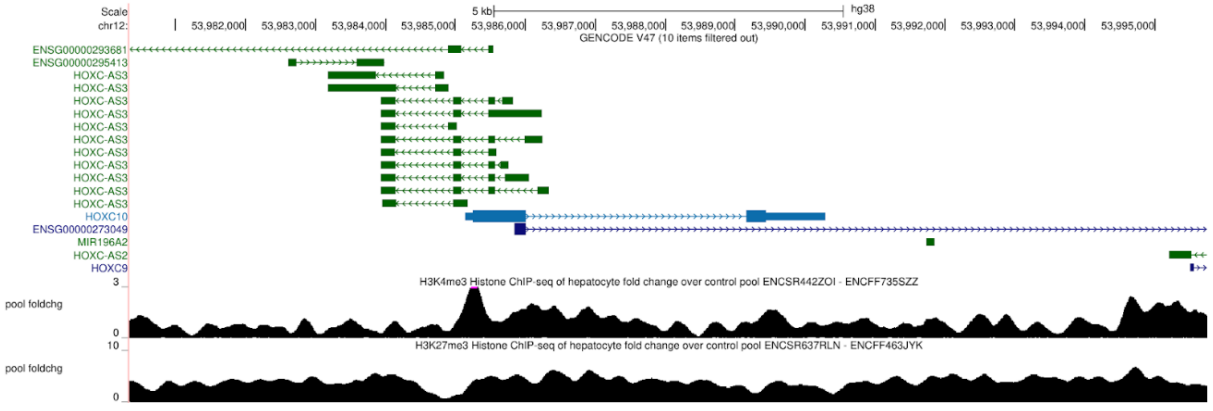
Scale
chr12:
5 kb
hg38
53,982,000
53,983,000
53,984,000
53,985,000
53,986,000
53,987,000
53,988,000
53,989,000
53,990,000
53,991,000
53,992,000
53,993,000
53,994,000
53,995,000
GENCODE V47 (10 items filtered out)
ENSG00000293681
ENSG00000295413
HOXC-AS3
HOXC10
ENSG00000273049
MIR196A2
HOXC-AS2
HOXC9
H3K4me3 Histone ChIP-seq of hepatocyte fold change over control pool ENCSR442ZOI - ENCFF735SZZ
pool foldchg
H3K27me3 Histone ChIP-seq of hepatocyte fold change over control pool ENCSR637RLN - ENCFF463JYK
pool foldchg

U

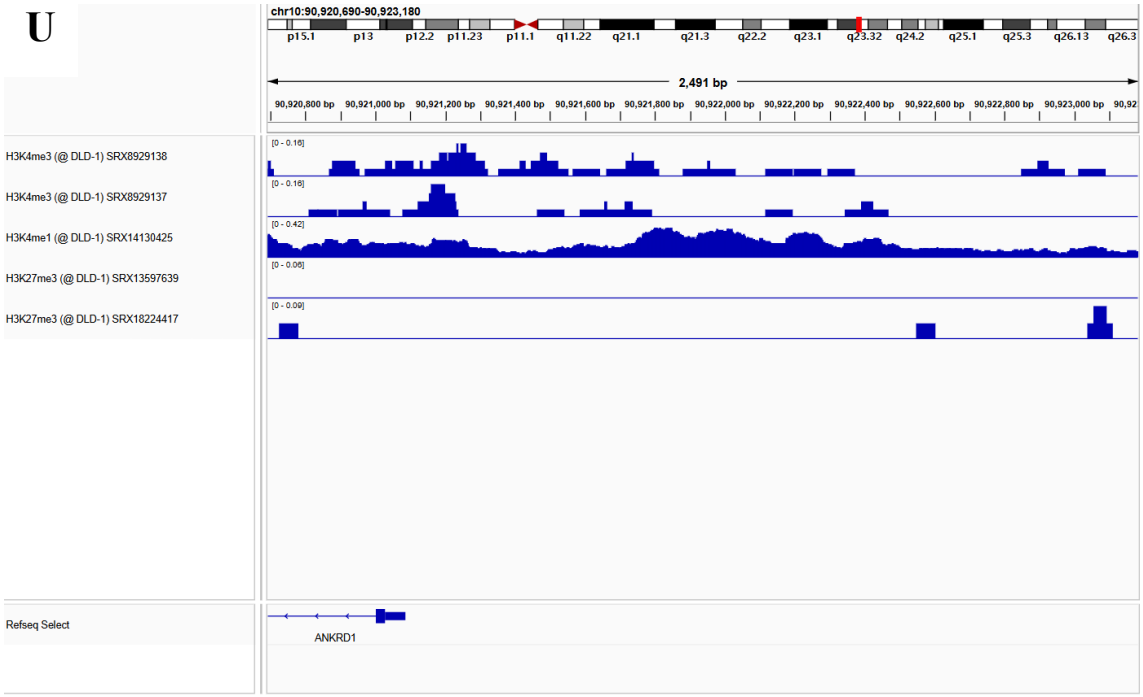
chr10:90,920,690-90,923,180
p15.1 p13 p12.2 p11.23 p11.1 q11.22 q21.1 q21.3 q22.2 q23.1 q23.32 q24.2 q25.1 q25.3 q26.13 q26.3
2,491 bp
90,920,800 bp 90,921,000 bp 90,921,200 bp 90,921,400 bp 90,921,600 bp 90,921,800 bp 90,922,000 bp 90,922,200 bp 90,922,400 bp 90,922,600 bp 90,922,800 bp 90,923,000 bp
H3K4me3 (@ DLD-1) SRX8929138
H3K4me3 (@ DLD-1) SRX8929137
H3K4me1 (@ DLD-1) SRX14130425
H3K27me3 (@ DLD-1) SRX13597639
H3K27me3 (@ DLD-1) SRX18224417
[0 - 0.16]
[0 - 0.16]
[0 - 0.42]
[0 - 0.06]
[0 - 0.09]
Refseq Select
ANKRD1

V

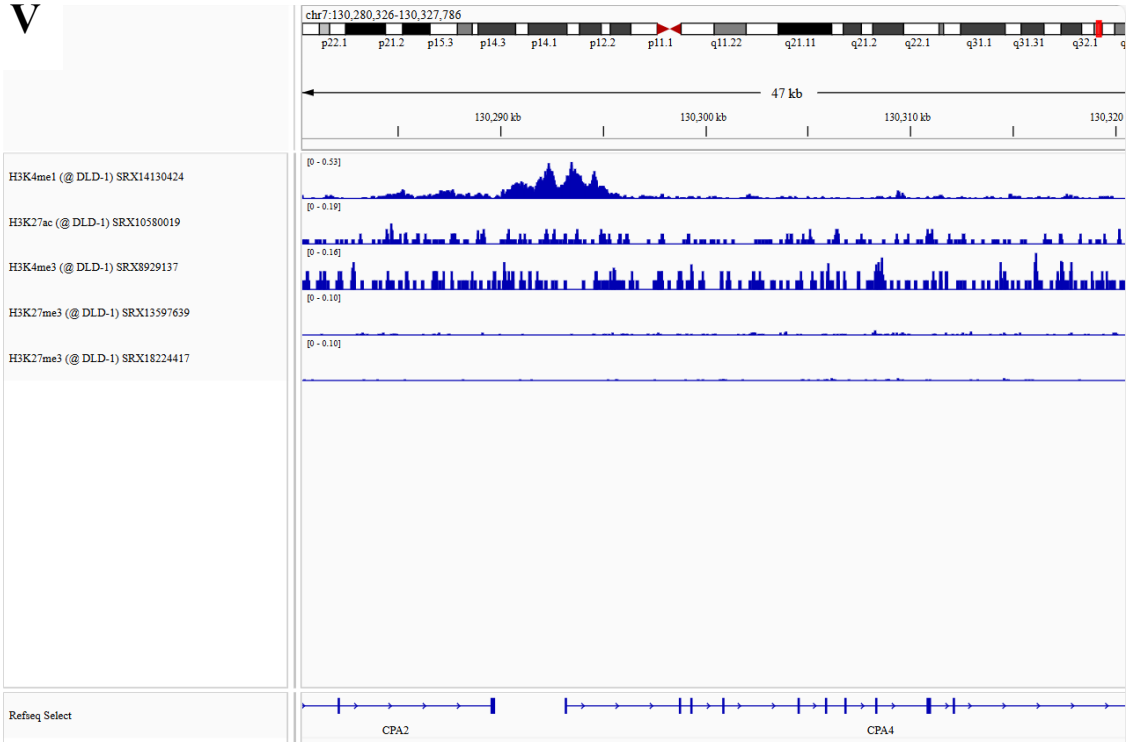
chr7:130,280,326-130,327,786
p22.1 p21.2 p15.3 p14.3 p14.1 p12.2 p11.1 q11.22 q21.11 q21.2 q22.1 q31.1 q31.31 q32.1
47 kb
130,290 kb 130,300 kb 130,310 kb 130,320
H3K4me1 (@ DLD-1) SRX14130424
H3K27ac (@ DLD-1) SRX10580019
H3K4me3 (@ DLD-1) SRX8929137
H3K27me3 (@ DLD-1) SRX13597639
H3K27me3 (@ DLD-1) SRX18224417
[0 - 0.53]
[0 - 0.19]
[0 - 0.16]
[0 - 0.10]
[0 - 0.10]
Refseq Select
CPA2
CPA4

X

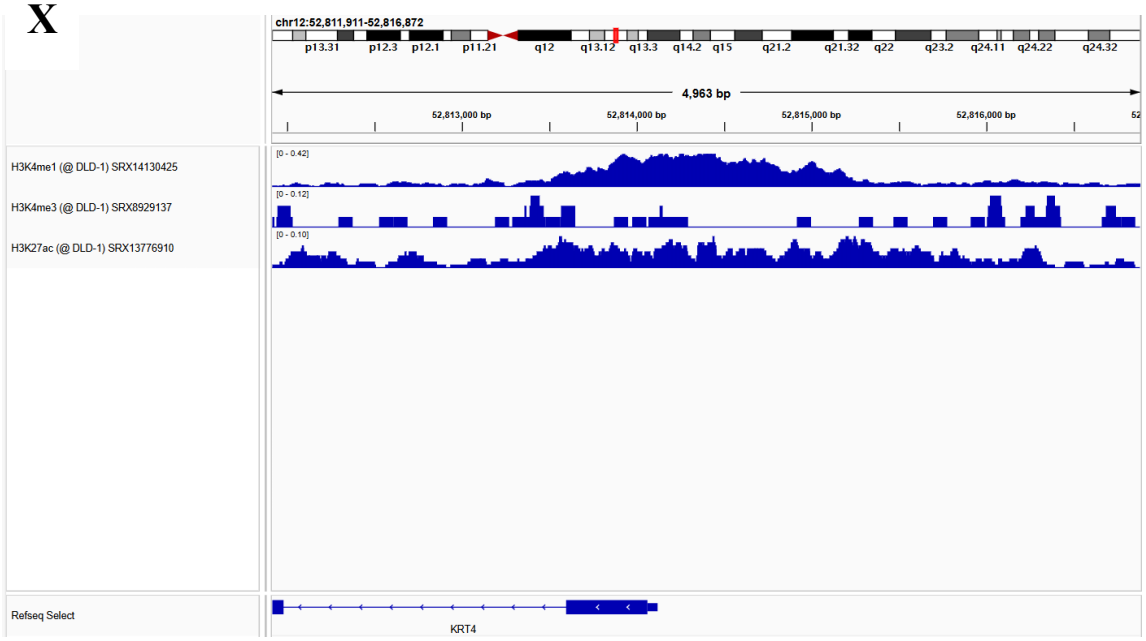
chr12:52,811,911-52,816,872
p13.31 p12.3 p12.1 p11.21 q12 q13.12 q13.3 q14.2 q15 q21.2 q21.32 q22 q23.2 q24.11 q24.22 q24.32
4,963 bp
52,813,000 bp
52,814,000 bp
52,815,000 bp
52,816,000 bp
H3K4me1 (@ DLD-1) SRX14130425
H3K4me3 (@ DLD-1) SRX8929137
H3K27ac (@ DLD-1) SRX13776910
[0 - 0.42]
[0 - 0.12]
[0 - 0.10]
Refseq Select
KRT4

Y

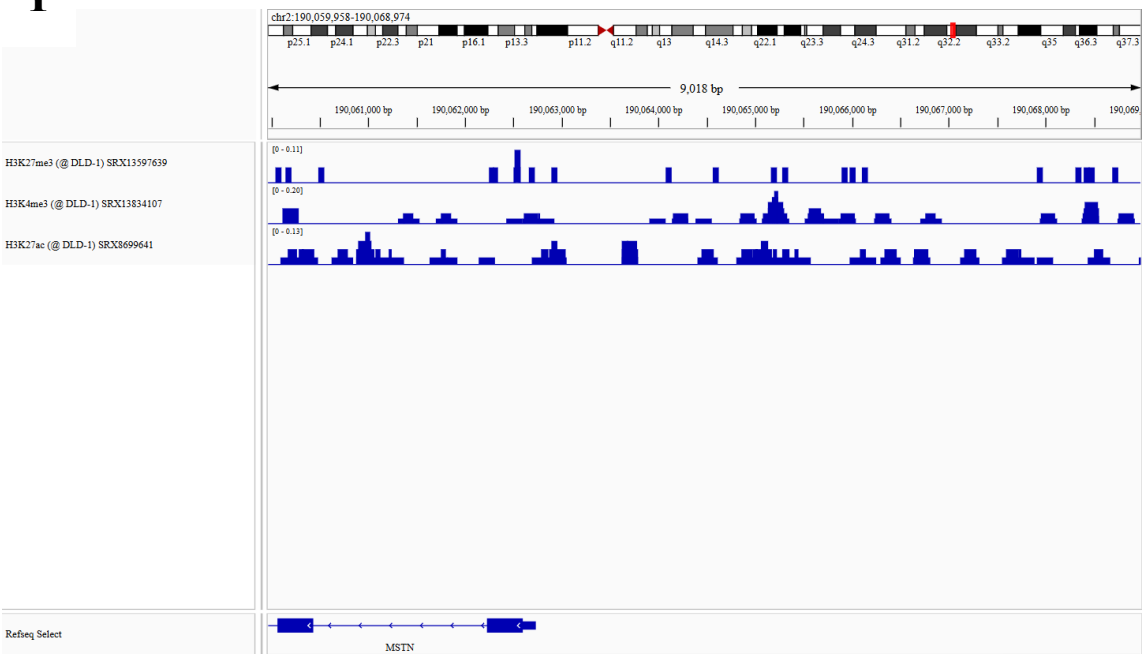
chr2:190,059,958-190,068,974
p25.1 p24.1 p22.3 p21 p16.1 p13.3 p11.2 q11.2 q13 q14.3 q22.1 q23.3 q24.3 q31.2 q32.2 q33.2 q35 q36.3 q37.3
9,018 bp
190,061,000 bp
190,062,000 bp
190,063,000 bp
190,064,000 bp
190,065,000 bp
190,066,000 bp
190,067,000 bp
190,068,000 bp
H3K27me3 (@ DLD-1) SRX13597639
H3K4me3 (@ DLD-1) SRX13834107
H3K27ac (@ DLD-1) SRX8699641
[0 - 0.11]
[0 - 0.20]
[0 - 0.13]
Refseq Select
MSTN

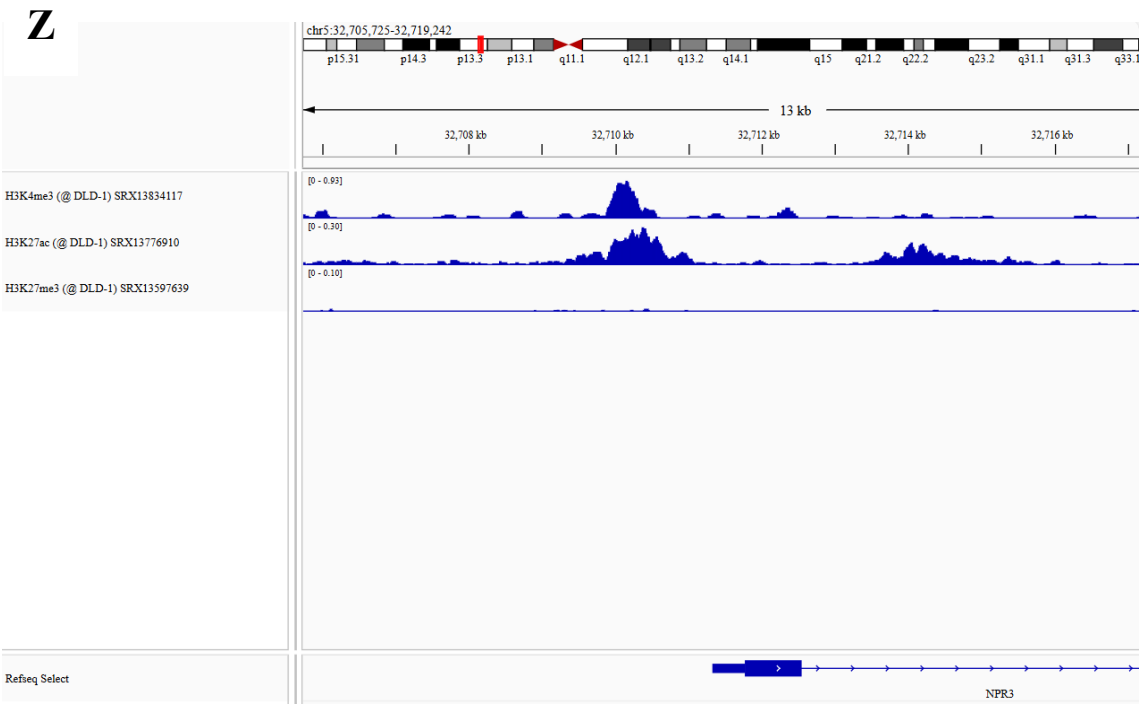
Z
chr5:32,705,725-32,719,242
p15.31
p14.3
p13.3
p13.1
q11.1
q12.1
q13.2
q14.1
q15
q21.2
q22.2
q23.2
q31.1
q31.3
q33.1
13 kb
32,708 kb
32,710 kb
32,712 kb
32,714 kb
32,716 kb
H3K4me3 (@ DLD-1) SRX13834117
H3K27ac (@ DLD-1) SRX13776910
H3K27me3 (@ DLD-1) SRX13597639
[0 - 0.93]
[0 - 0.30]
[0 - 0.10]
Refseq Select
NPR3

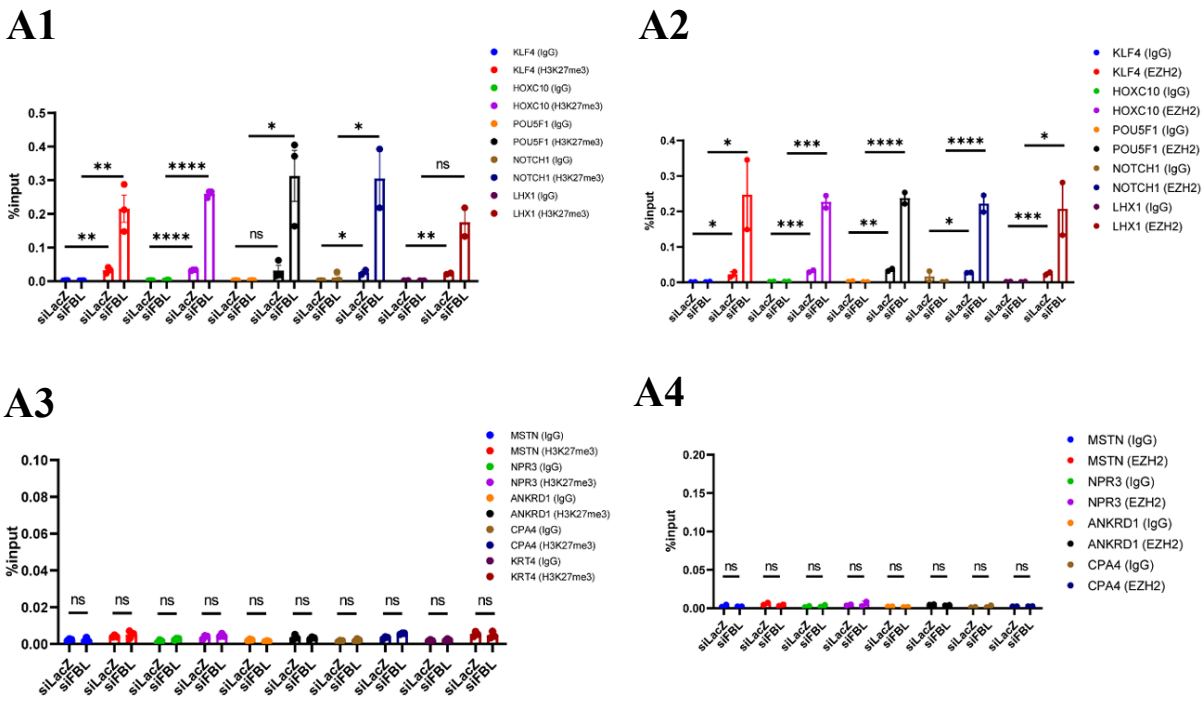
A1
%input
KLF4 (IgG)
KLF4 (H3K27me3)
HOXC10 (IgG)
HOXC10 (H3K27me3)
POU5F1 (IgG)
POU5F1 (H3K27me3)
NOTCH1 (IgG)
NOTCH1 (H3K27me3)
LHX1 (IgG)
LHX1 (H3K27me3)
siLacZ
siFBL

A2
%input
KLF4 (IgG)
KLF4 (EZH2)
HOXC10 (IgG)
HOXC10 (EZH2)
POU5F1 (IgG)
POU5F1 (EZH2)
NOTCH1 (IgG)
NOTCH1 (EZH2)
LHX1 (IgG)
LHX1 (EZH2)
siLacZ
siFBL

A3
%input
MSTN (IgG)
MSTN (H3K27me3)
NPR3 (IgG)
NPR3 (H3K27me3)
ANKRD1 (IgG)
ANKRD1 (H3K27me3)
CPA4 (IgG)
CPA4 (H3K27me3)
KRT4 (IgG)
KRT4 (H3K27me3)
siLacZ
siFBL

A4
%input
MSTN (IgG)
MSTN (EZH2)
NPR3 (IgG)
NPR3 (EZH2)
ANKRD1 (IgG)
ANKRD1 (EZH2)
CPA4 (IgG)
CPA4 (EZH2)
siLacZ
siFBL

Fig. 4.3. FBL depletion leads to increased enrichment of the repressive histone mark H3K27me3 at the Scribble promoter

(A) Schematic of the SCRIB promoter region indicating primer binding sites. Quantitative analysis of chromatin immunoprecipitation data demonstrates a significant enrichment of both EZH2 and the repressive histone mark H3K27me3 at the SCRIB promoter in DLD-1 cells. This enrichment is shown under control conditions (siLacZ) and following a ~48-hour depletion of FBL. Results are presented as the mean ± SEM from three independent biological replicates. Statistical significance was determined using unpaired t-tests. **(B)** Representative phase-contrast images from scratch-wound assays performed in DLD-1 cells following EZH2 inhibition by GSK126 treatment in control (siLacZ) and FBL-depleted (siFBL) conditions. Images are representative of three independent biological replicates (N = 3). Scale bar, ~100 μm. **(C)** Quantitative assessment of scratch-wound assays following GSK126 treatment in DLD-1 cells transfected with control siRNA (siLacZ) or FBL-targeting siRNA (siFBL). Statistical significance was determined using an unpaired t-test. **(D)** Immunoblotting performed after ~48 h of FBL knockdown and EZH2 inhibition with GSK126 reveals a recovery of Scribble protein expression. HSP70, histone H3, and GAPDH served as loading controls. Results are derived from three independent biological replicates (N=3). **(E)** Densitometric analysis of Western blot data. Statistical significance was evaluated using unpaired t-tests. **(F)** Representative immunoblots of EZH2 and FBL indicating no significant change in EZH2 protein levels in control (siLacZ) and FBL-depleted (siFBL) DLD-1 and MCF10A(p53DN) cells. GAPDH and β-tubulin were used as loading controls. Cells were analyzed ~48 h (DLD-1) and ~36 h [MCF10A(p53DN)] post-transfection. Data are representative of two independent biological replicates (N = 2). **(G)** Densitometric analysis of immunoblots following GSK126 treatment, with DMSO serving as the vehicle control, in DLD-1 and MCF10A(p53DN) cells transfected with control siRNA (siLacZ) or FBL-targeting siRNA (siFBL). **(H)** Immunofluorescence analysis demonstrating restoration of E-cadherin localization at the cell–cell borders following EZH2 inhibition with GSK126. E-cadherin (green), FBL (red), and nuclei (DAPI; blue) are shown in GSK126-treated cells (10 μM, 48 h) as well as in control (siLacZ) and FBL-depleted cells (~48 h). Data are representative of three independent biological replicates (N = 3). Scale bar, ~20 μm. **(I)** Quantitative evaluation of scratch-wound assays conducted in DLD-1 and MCF10A(p53DN) cells overexpressing Flag-EZH2 and EZH2, respectively. Statistical significance was assessed using unpaired t-tests for both DLD-1 and MCF10A(p53DN) datasets. **(J)** Quantitative assessment of E-cadherin internalization following EZH2 overexpression in DLD-1 and MCF10A(p53DN) cells,

expressed as the ratio of E-cadherin fluorescence intensity at the cell–cell borders to that of the whole cell. Measurements were obtained from n = 178 (DLD-1) and n = 177 [MCF10A(p53DN)] cells across three independent biological replicates (N = 3). Statistical significance was evaluated using unpaired t-tests. **(K)** Representative phase-contrast images from scratch-wound assays performed in DLD-1 cells transduced with control Flag or Flag-EZH2 overexpression constructs, and in MCF10A(p53DN) cells expressing EZH2 under a doxycycline-inducible promoter. Images are representative of three independent biological replicates (N = 3). Scale bar, ~100 μm. **(L)** Immunofluorescence analysis showing the localization of E-cadherin (green), FBL (red), and nuclei (DAPI; blue) in DLD-1 cells expressing control Flag or Flag-EZH2 constructs, and in MCF10A(p53DN) cells with doxycycline (Dox)–inducible EZH2 overexpression. Images are representative of three independent biological replicates (N = 3). Scale bar, ~20 μm. **(M)** Representative immunoblots illustrating the effects of EZH2 overexpression on EZH2, Scribble, H3K27me3, and FBL protein levels in DLD-1 cells transfected with control siRNA (siLacZ) or FBL-targeting siRNA (siFBL) and transduced with MSCV-Flag or MSCV-Flag–EZH2 constructs. HSP70, histone H3, and GAPDH were used as loading controls. Data are representative of three independent biological replicates (N = 3). **(N)** Representative immunoblots demonstrating that EZH2 overexpression reduces Scribble protein levels in MCF10A(p53DN) cells expressing EZH2 under a doxycycline-inducible promoter, transfected with control siRNA (siLacZ) or FBL-targeting siRNA (siFBL) (~36 h). HSP70, GAPDH, and histone H3 were used as loading controls. Data are representative of three independent biological replicates (N = 3). **(O)** Densitometric quantification of immunoblots assessing the impact of EZH2 overexpression on Scribble expression. Data were obtained from three independent biological replicates (N = 3). Statistical significance was evaluated using one-way ANOVA followed by Sidak's multiple-comparison test. **(P)** UCSC Genome Browser snapshot of the LHX1 locus on chromosome 17 displaying ChIP-seq fold-change tracks in hepatocytes relative to control samples. Enrichment of H3K4me3 (upper track) is confined to the promoter region, whereas H3K27me3 (lower track) shows a broader distribution across the gene locus. **(Q)** UCSC Genome Browser snapshot of the POU5F1 locus on chromosome 6 showing ChIP-seq fold-change tracks in hepatocytes relative to control samples. H3K4me3 enrichment (upper track) is concentrated at the promoter region, whereas H3K27me3 enrichment (lower track) extends across broader regions of the locus, indicating the coexistence of active and repressive chromatin marks. **(R)** UCSC Genome Browser snapshot of the KLF4 locus on chromosome 9 displaying ChIP-seq fold-change tracks in hepatocytes relative to control samples. Enrichment of H3K4me3 (upper

track) is restricted to the promoter region, whereas H3K27me3 (lower track) extends across broader regions of the gene locus. **(T)** UCSC Genome Browser snapshot of the NOTCH1 locus on chromosome 9 showing ChIP-seq fold-change tracks in hepatocytes relative to control samples. H3K4me3 enrichment (upper track) is concentrated at the promoter region, whereas H3K27me3 enrichment (lower track) is distributed across broader regions of the gene locus. **(U)** UCSC Genome Browser view of the HOXC10 locus on chromosome 12 showing ChIP-seq fold-change profiles in hepatocytes relative to control samples. H3K4me3 enrichment is focused at the promoter region, while H3K27me3 enrichment spans broader domains across the gene locus, indicating the coexistence of activating and repressive chromatin marks. **(V)** IGV genome browser (Robinson et al. 2011) tracks illustrating ChIP-seq enrichment of histone modifications across the ANKRD1 locus (chr10:90,920,680–90,923,160; hg38) in DLD-1 cells. Active histone marks H3K4me3, H3K9ac, and H3K4me1 exhibit prominent peaks at the promoter and within the gene body, whereas repressive marks H3K27me3 and H3K9me2 show broader enrichment across the locus, reflecting the chromatin landscape of the ANKRD1 gene region. **(X)** IGV genome browser view of ChIP-seq profiles for histone modifications across the CPA4 locus (chr7) in DLD-1 cells. Activating histone marks, including H3K4me3, H3K9ac, and H3K4me1, are enriched at the promoter and along the gene body, whereas the repressive mark H3K27me3 displays a broader distribution across the region, illustrating the chromatin organization at the CPA4 locus. **(Y)** IGV genome browser views showing ChIP-seq profiles of histone modifications across multiple gene loci in DLD-1 cells. At the KRT4 locus (chr10:90,920,680–90,923,160; hg38), activating histone marks (H3K4me3, H3K9ac, and H3K4me1) are enriched at the promoter and along the gene body, whereas repressive marks (H3K27me3 and H3K9me2) display broader distributions, reflecting the chromatin organization of this region. **(Z)** Genome browser tracks across the MSTN locus reveal prominent enrichment of active marks H3K4me3 and H3K27ac at the promoter and gene body, accompanied by broader enrichment of the repressive mark H3K27me3, illustrating the chromatin state of the MSTN gene region. **(A1)** IGV genome browser tracks of the NPR3 locus show similar patterns, with H3K4me3 and H3K27ac enriched around the promoter and gene body, and H3K27me3 exhibiting broader coverage across the locus, highlighting the chromatin landscape of the NPR3 gene region. **(A2)** ChIP–qPCR analysis of H3K27me3 enrichment at the promoters of *KLF4, HOXC10, POU5F1, NOTCH1,* and *LHX1* in DLD-1 cells transfected with control siRNA (siLacZ) or FBL-targeting siRNA (siFBL) for ~48 h. IgG served as a negative control. FBL depletion resulted in a significant increase in H3K27me3 occupancy at these promoters. Data are expressed as % input (mean ± SEM). $p < 0.05$; *$p < 0.01$; ***$p <$

0.0001; ns, not significant (unpaired Student's *t*-test). **(A3)** ChIP–qPCR assessment of EZH2 occupancy at the promoters of *KLF4, HOXC10, POU5F1, NOTCH1,* and *LHX1* in DLD-1 cells following transfection with siLacZ or siFBL for ~48 h. IgG was used as a negative control. Knockdown of FBL significantly enhanced EZH2 recruitment to these loci. Data are presented as % input (mean ± SEM). $p < 0.05$; *$p < 0.01$; ***$p < 0.0001$; ns, not significant (unpaired Student's *t*-test). **(A4)** ChIP–qPCR analysis of H3K27me3 occupancy at the promoters of *MSTN, NPR3, ANKRD1, CPA4,* and *KRT4* in DLD-1 cells transfected with siLacZ or siFBL for ~48 h. IgG served as a negative control. FBL depletion led to increased H3K27me3 enrichment at these loci. Data are shown as % input (mean ± SEM). ns, not significant (unpaired Student's *t*-test). (A5) ChIP–qPCR analysis of EZH2 binding at the promoters of *MSTN, NPR3, ANKRD1,* and *CPA4* in DLD-1 cells transfected with siLacZ or siFBL for ~48 h. IgG was used as a negative control. Loss of FBL resulted in elevated EZH2 occupancy at these promoters. Data are expressed as % input (mean ± SEM). ns, not significant (unpaired Student's *t*-test).

4.2.4. FBL Depletion Leads to EZH2 Exodus from Nucleoli and Increases H3K27me3 Deposition

To further understand how FBL regulates chromatin dynamics and gene expression, we investigated whether FBL depletion affects the genomic occupancy and subcellular localization of EZH2, the catalytic subunit of the Polycomb Repressive Complex 2 (PRC2). Our initial chromatin immunoprecipitation analyses revealed that upon FBL knockdown, there was a significant increase in the enrichment of EZH2 at the promoter region of the SCRIB gene. Despite this increase in promoter occupancy, the total levels of EZH2 protein within the cell remained unchanged. This observation suggested that FBL does not regulate EZH2 at the level of expression or stability, but rather influences its genomic targeting or spatial distribution within the nucleus.

To explore this hypothesis, we examined whether FBL depletion impacts the subcellular localization of EZH2, particularly its distribution between the nucleolus and the nucleoplasm. Two complementary approaches were employed: (i) biochemical subcellular fractionation to quantify EZH2 in nucleolar versus nucleoplasmic compartments, and (ii) immunofluorescence imaging at the single-cell level to visually assess EZH2 localization in both DLD-1 colorectal cancer cells and MCF10A(p53DN) breast epithelial cells. These analyses consistently showed that FBL depletion led to a striking reduction in EZH2 presence within the nucleolus. Instead, EZH2 accumulated in the nucleoplasm, with quantification indicating an approximate 16% (±2.4%) increase in the nucleoplasmic pool of EZH2 (Fig. 4.4 (A-C)).

Immunofluorescence staining further confirmed this redistribution. In control cells, a fraction of EZH2 localized to the nucleolus, identified through co-localization with Nucleolin (NCL), a well-established nucleolar marker. Upon FBL knockdown, this nucleolar enrichment of EZH2 was significantly diminished, and EZH2 was largely excluded from the nucleolar compartment (Fig. 4.4 (E-G)). Further analysis of immunofluorescence assay, we observed while the total EZH2 levels remain unaltered, significant ~26% of EZH2 translocated out of the nucleoli and nucleoplasm showed ~23% increase in EZH2 levels, suggesting translocation of EZH2 from nucleolus to the nucleoplasm (Fig. 4.4(H-J)). This observation strongly indicates that FBL plays a role in retaining a subpopulation of EZH2 within the nucleolus under normal conditions.

To probe the molecular basis of this interaction, we considered previous evidence suggesting that FBL directly interacts with EZH2 through its RNA-binding domain (RBD), while EZH2

mediates this interaction via its CXC domain (Yi et al. 2021). To test whether this interaction is essential for the nucleolar sequestration of EZH2, we generated a mutant version of FBL lacking the RNA-binding domain (FBLΔRBD), which was rendered resistant to siRNA-mediated knockdown. When this mutant was expressed in FBL-depleted cells, it failed to retain EZH2 within the nucleolus (Fig. 4.4(K-N)). Instead, EZH2 was displaced to the nucleoplasm, similar to the effect observed with complete FBL knockdown. Quantitative analysis of this redistribution revealed a substantial displacement of EZH2 from the nucleolus, with nearly 50% (±10%) of total EZH2 relocalizing to the nucleoplasm in the absence of the FBL-EZH2 interaction. We also performed co-IP experiment where we pulled-down FBL (Full length and ΔRBD mutant). We observed that the ΔRBD mutant of FBL was unable to co-precipitate EZH2 (Fig. 4.4P).

Consistent with the altered localization of EZH2, we observed a significant upregulation of the repressive histone mark H3K27me3 upon FBL depletion. Immunofluorescence analyses showed an approximately six-fold increase in global H3K27me3 levels, while immunoblotting confirmed this elevation with an estimated 60% (±7%) increase (Fig. 4.4 O, (Q-T)). This suggests that the redistribution of EZH2 from the nucleolus to the nucleoplasm leads to enhanced PRC2 activity on chromatin, particularly at genomic loci such as the SCRIB promoter.

Taken together, these results demonstrate that FBL, through its RNA-binding domain, physically interacts with EZH2 and plays a critical role in regulating its subnuclear localization. Under normal conditions, FBL appears to sequester a subset of EZH2 molecules within the nucleolus, thereby restricting their access to chromatin substrates in the nucleoplasm. Disruption of this interaction, either through FBL depletion or deletion of its RNA-binding domain, results in the release of EZH2 into the nucleoplasm, where it gains access to target gene promoters and increases the deposition of repressive H3K27me3 marks. This shift in EZH2 localization represents a key regulatory mechanism by which FBL modulates the epigenetic landscape of the cell. By limiting the availability of EZH2 in the nucleoplasm, FBL serves as a spatial regulator of PRC2 activity, ensuring that repression of critical epithelial regulators such as Scribble is tightly controlled. Loss of this spatial restraint leads to aberrant gene silencing, disrupted epithelial polarity, and enhanced cell motility—phenotypes associated with epithelial plasticity and early tumor progression. These findings thus define a novel nucleolar-epigenetic interface in which FBL regulates chromatin structure and gene expression through spatial sequestration of chromatin modifiers such as EZH2.

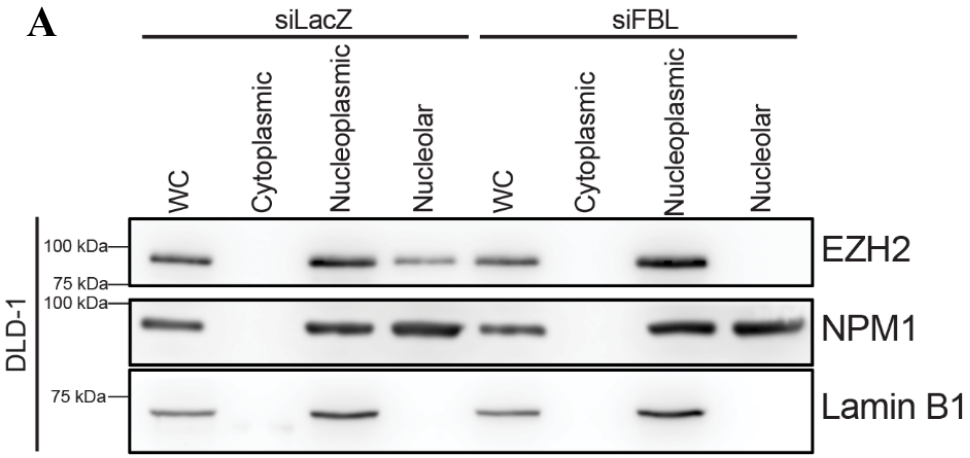
A
siLacZ
siFBL
WC
Cytoplasmic
Nucleoplasmic
Nucleolar
WC
Cytoplasmic
Nucleoplasmic
Nucleolar
DLD-1
100 kDa
75 kDa
100 kDa
75 kDa
EZH2
NPM1
Lamin B1

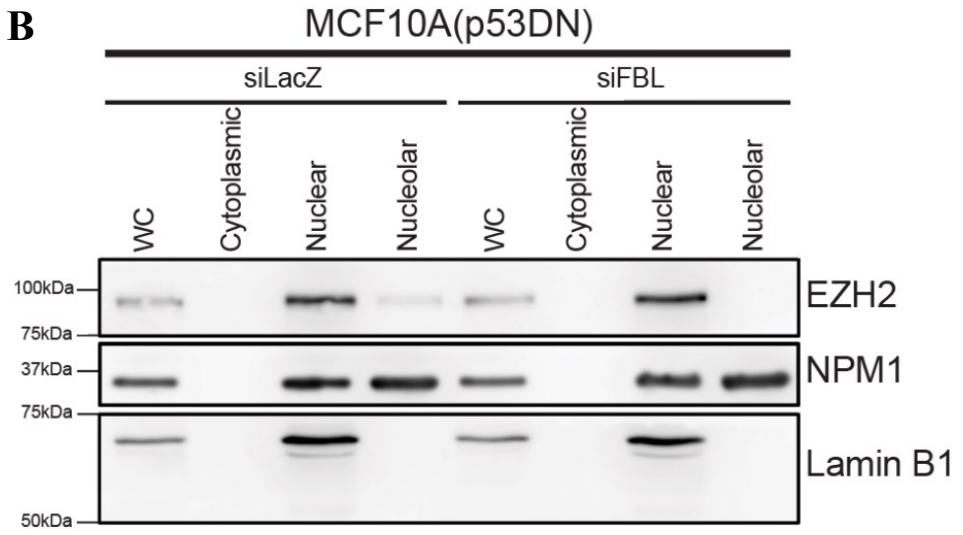
B
MCF10A(p53DN)
siLacZ
siFBL
WC
Cytoplasmic
Nuclear
Nucleolar
WC
Cytoplasmic
Nuclear
Nucleolar
100kDa
75kDa
37kDa
75kDa
50kDa
EZH2
NPM1
Lamin B1

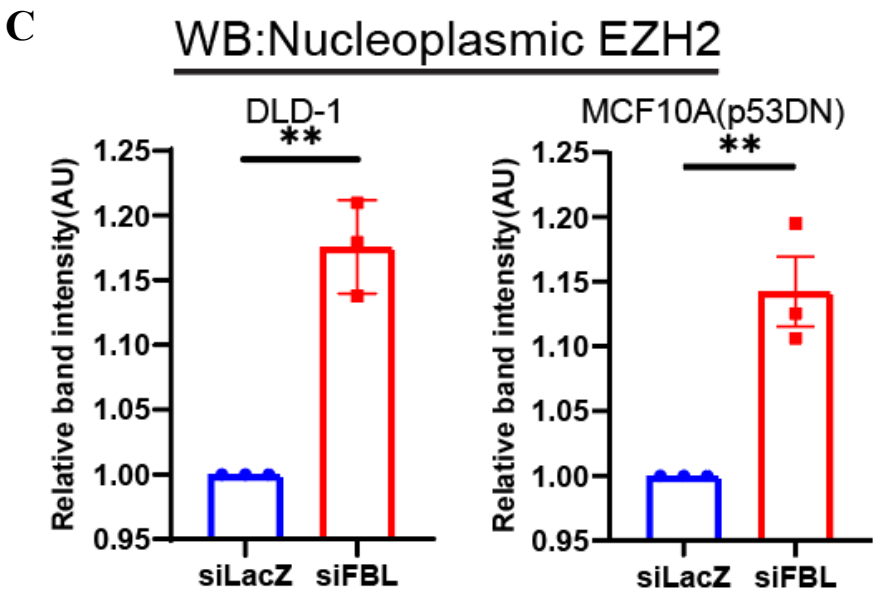
C
WB:Nucleoplasmic EZH2
DLD-1
MCF10A(p53DN)
**
**
Relative band intensity(AU)
1.25
1.20
1.15
1.10
1.05
1.00
0.95
siLacZ
siFBL

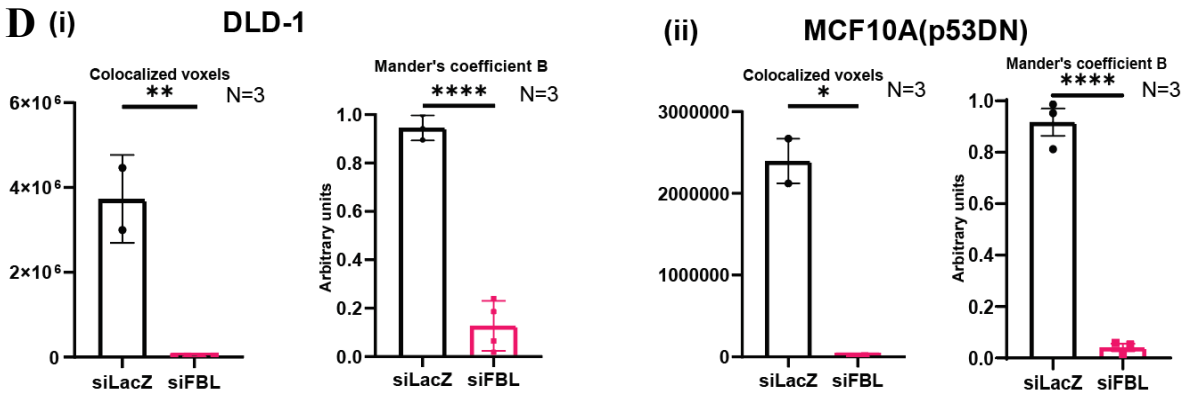
D (i)
DLD-1
Colocalized voxels
**
N=3
6×10⁶
4×10⁶
2×10⁶
0
siLacZ
siFBL
Mander's coefficient B
****
N=3
Arbitrary units
1.0
0.8
0.6
0.4
0.2
0.0
siLacZ
siFBL
(ii)
MCF10A(p53DN)
Colocalized voxels
*
N=3
3000000
2000000
1000000
0
siLacZ
siFBL
Mander's coefficient B
****
N=3
Arbitrary units
1.0
0.8
0.6
0.4
0.2
0.0
siLacZ
siFBL

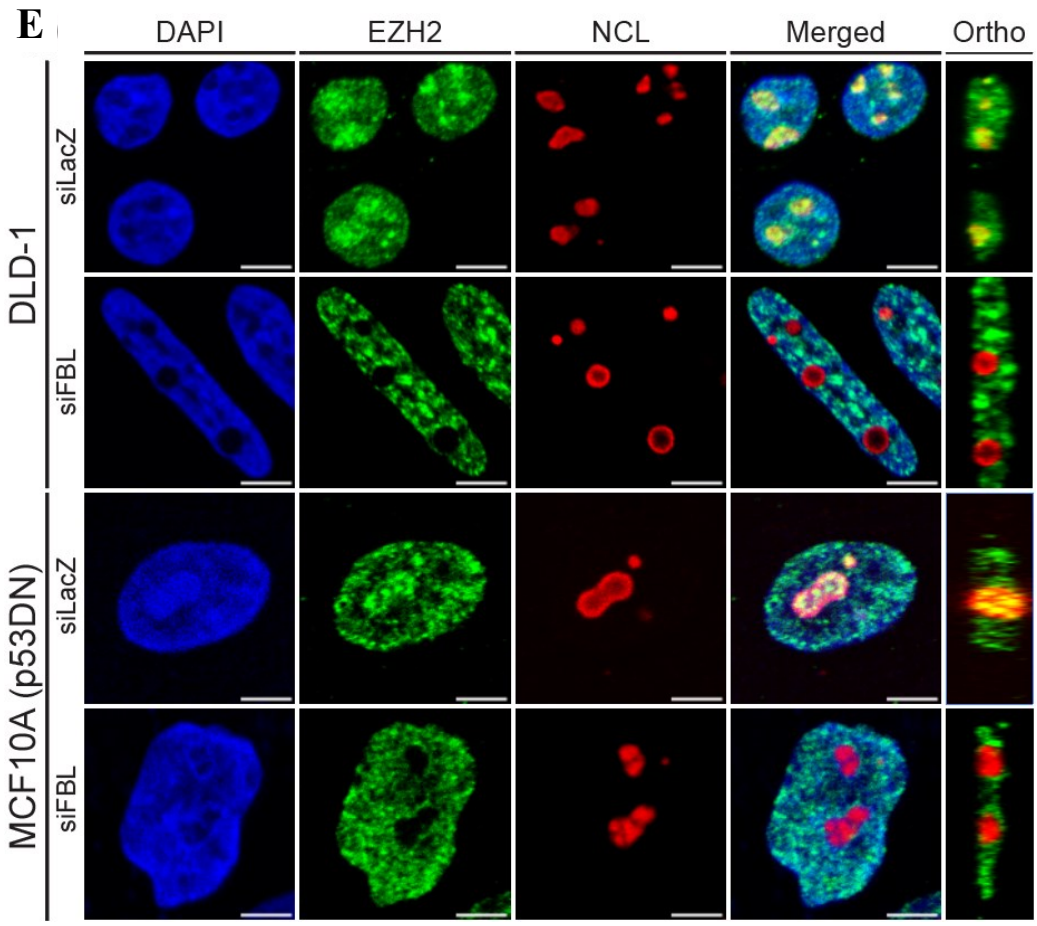
E
DAPI
EZH2
NCL
Merged
Ortho
DLD-1
siLacZ
siFBL
MCF10A (p53DN)
siLacZ
siFBL

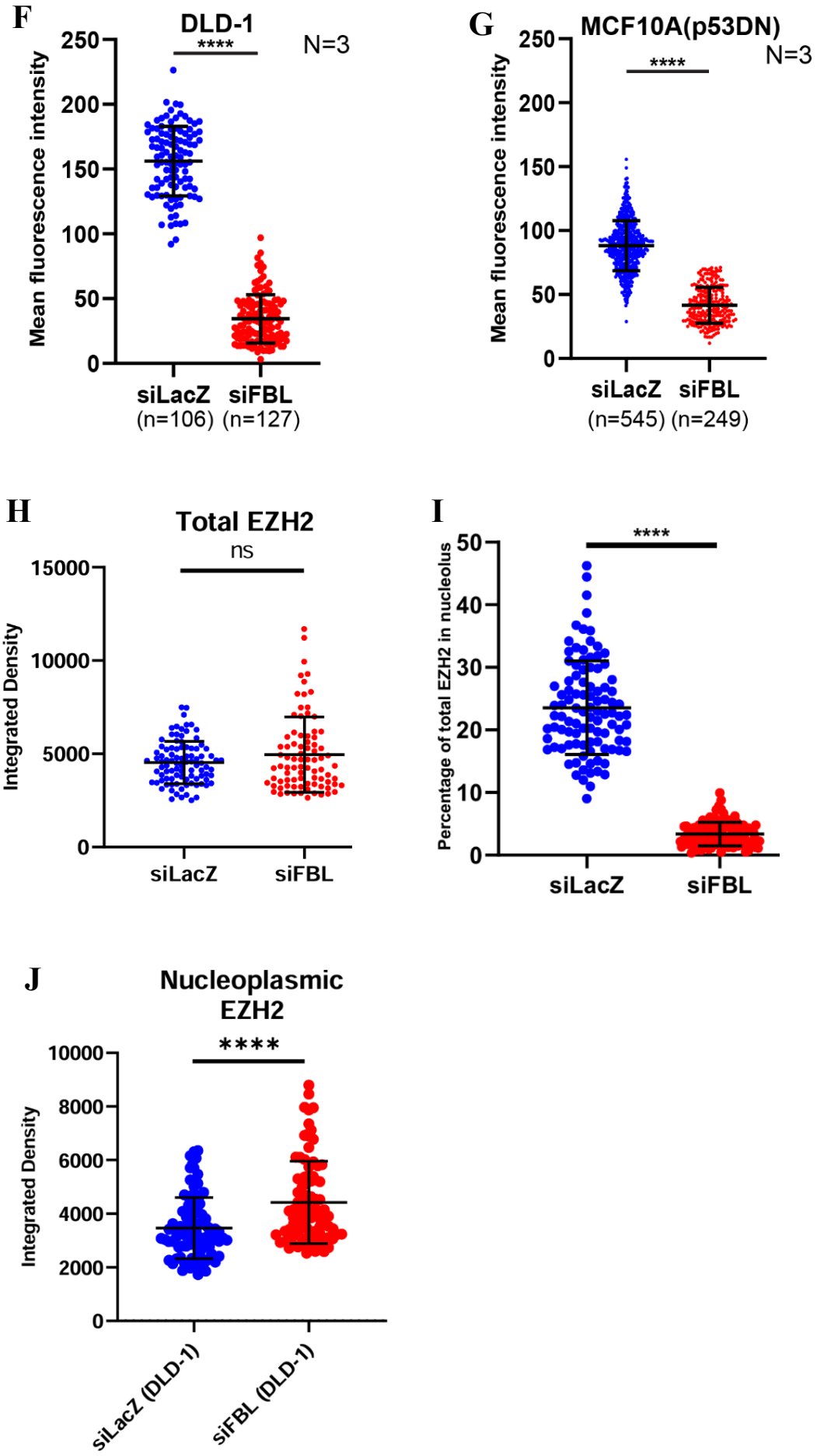
F
DLD-1
****
N=3
Mean fluorescence intensity
250
200
150
100
50
0
siLacZ
siFBL
(n=106) (n=127)
G
MCF10A(p53DN)
****
N=3
Mean fluorescence intensity
250
200
150
100
50
0
siLacZ
siFBL
(n=545) (n=249)
H
Total EZH2
ns
Integrated Density
15000
10000
5000
0
siLacZ
siFBL
I
****
Percentage of total EZH2 in nucleolus
50
40
30
20
10
0
siLacZ
siFBL
J
Nucleoplasmic EZH2
****
Integrated Density
10000
8000
6000
4000
2000
0
siLacZ (DLD-1)
siFBL (DLD-1)

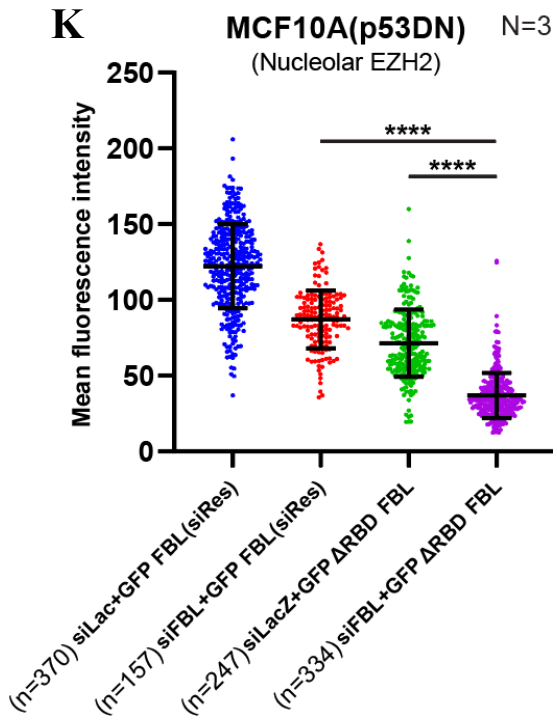
K
MCF10A(p53DN)
N=3
(Nucleolar EZH2)
Mean fluorescence intensity
250
200
150
100
50
0
****
****
(n=370) siLac+GFP FBL(siRes)
(n=157) siFBL+GFP FBL(siRes)
(n=247) siLacZ+GFP ΔRBD FBL
(n=334) siFBL+GFP ΔRBD FBL

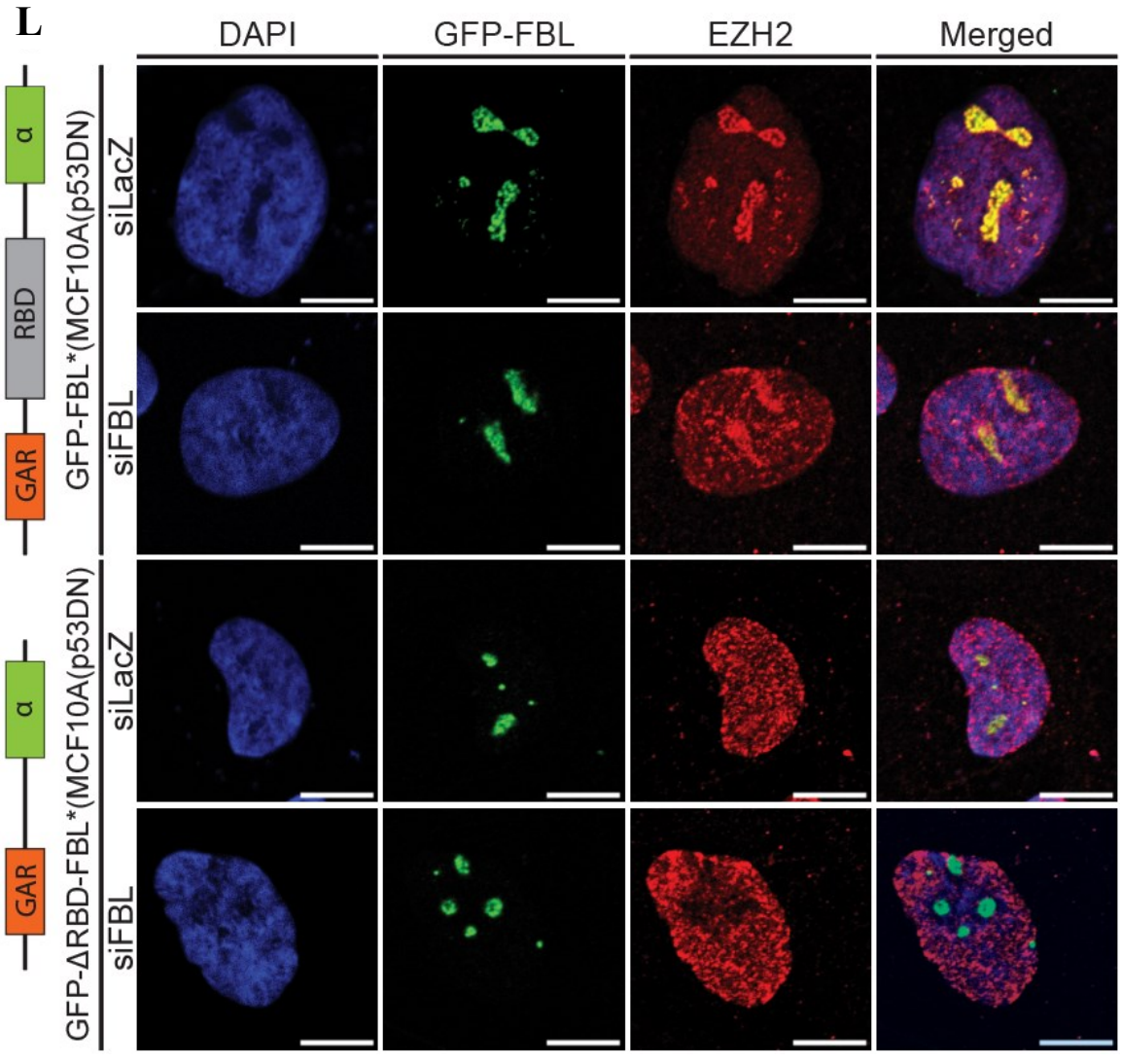
L
DAPI
GFP-FBL
EZH2
Merged
α
RBD
GAR
GFP-FBL*(MCF10A(p53DN)
siLacZ
siFBL
α
GAR
GFP-ΔRBD-FBL*(MCF10A(p53DN)
siLacZ
siFBL

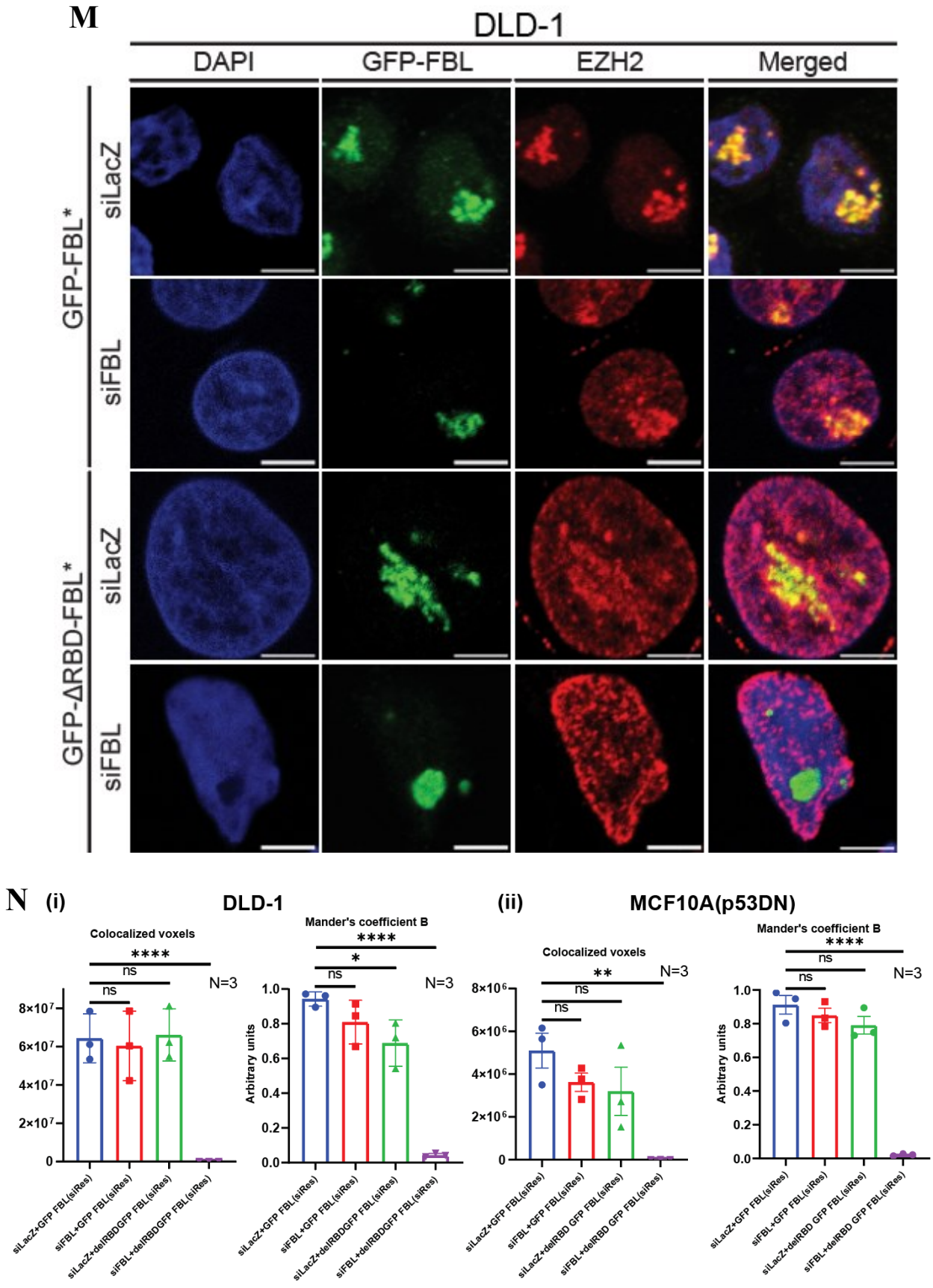
M
DLD-1
DAPI
GFP-FBL
EZH2
Merged
GFP-FBL*
siLacZ
siFBL
GFP-ΔRBD-FBL*
siLacZ
siFBL
N
(i)
DLD-1
Colocalized voxels
Mander's coefficient B
(ii)
MCF10A(p53DN)
Colocalized voxels
Mander's coefficient B
****
**
*
ns
N=3
Arbitrary units
siLacZ+GFP FBL(siRes)
siFBL+GFP FBL(siRes)
siLacZ+delRBDGFP FBL(siRes)
siFBL+delRBDGFP FBL(siRes)
siLacZ+delRBD GFP FBL(siRes)
siFBL+delRBD GFP FBL(siRes)

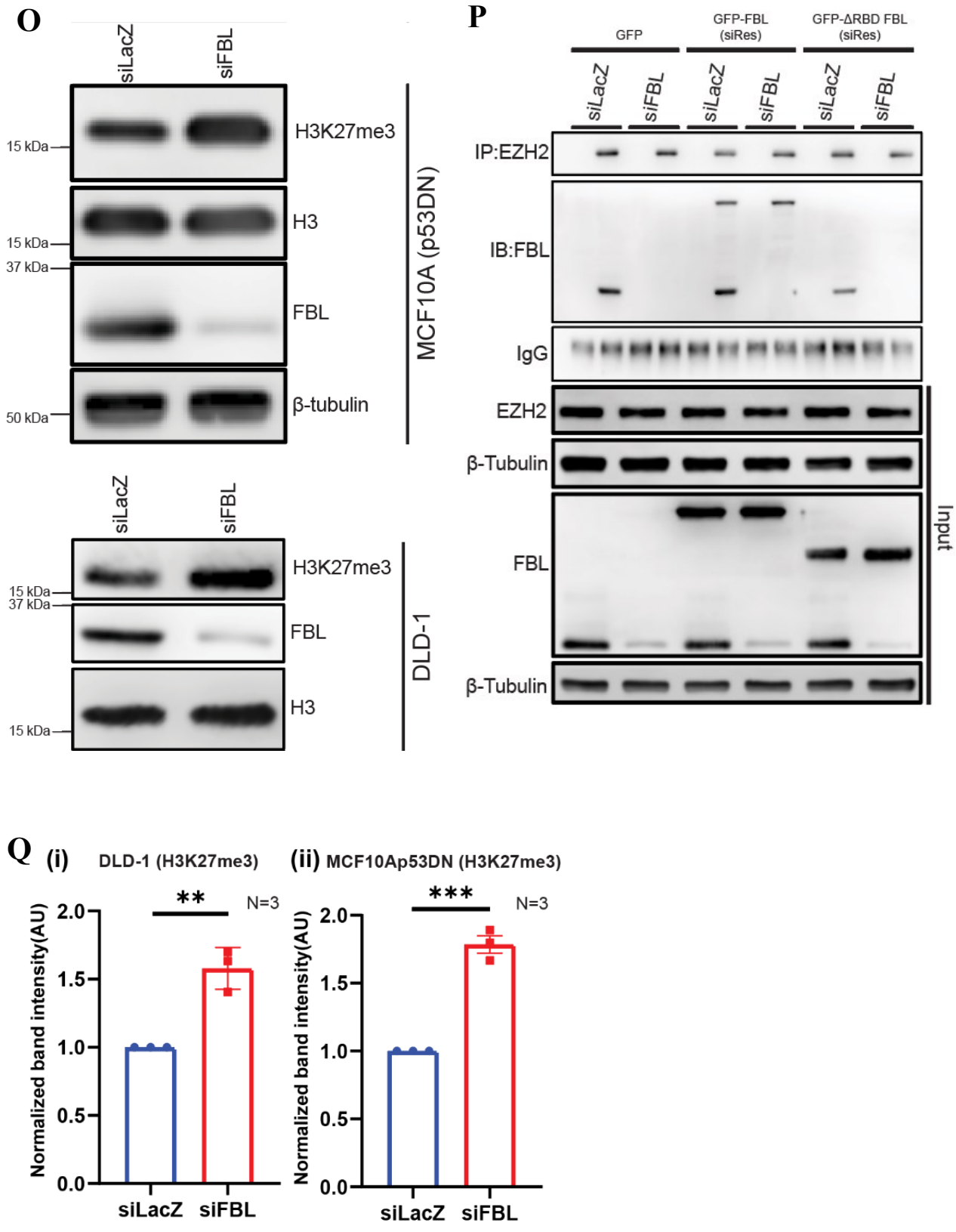
O
siLacZ
siFBL
15 kDa
H3K27me3
15 kDa
H3
37 kDa
FBL
50 kDa
β-tubulin
MCF10A (p53DN)
siLacZ
siFBL
15 kDa
37 kDa
H3K27me3
FBL
15 kDa
H3
DLD-1
P
GFP
GFP-FBL (siRes)
GFP-ΔRBD FBL (siRes)
siLacZ
siFBL
siLacZ
siFBL
siLacZ
siFBL
IP:EZH2
IB:FBL
IgG
EZH2
β-Tubulin
FBL
β-Tubulin
Input
Q
(i) DLD-1 (H3K27me3)
(ii) MCF10Ap53DN (H3K27me3)
**
N=3
***
N=3
Normalized band intensity(AU)
2.0
1.5
1.0
0.5
0.0
siLacZ
siFBL

R

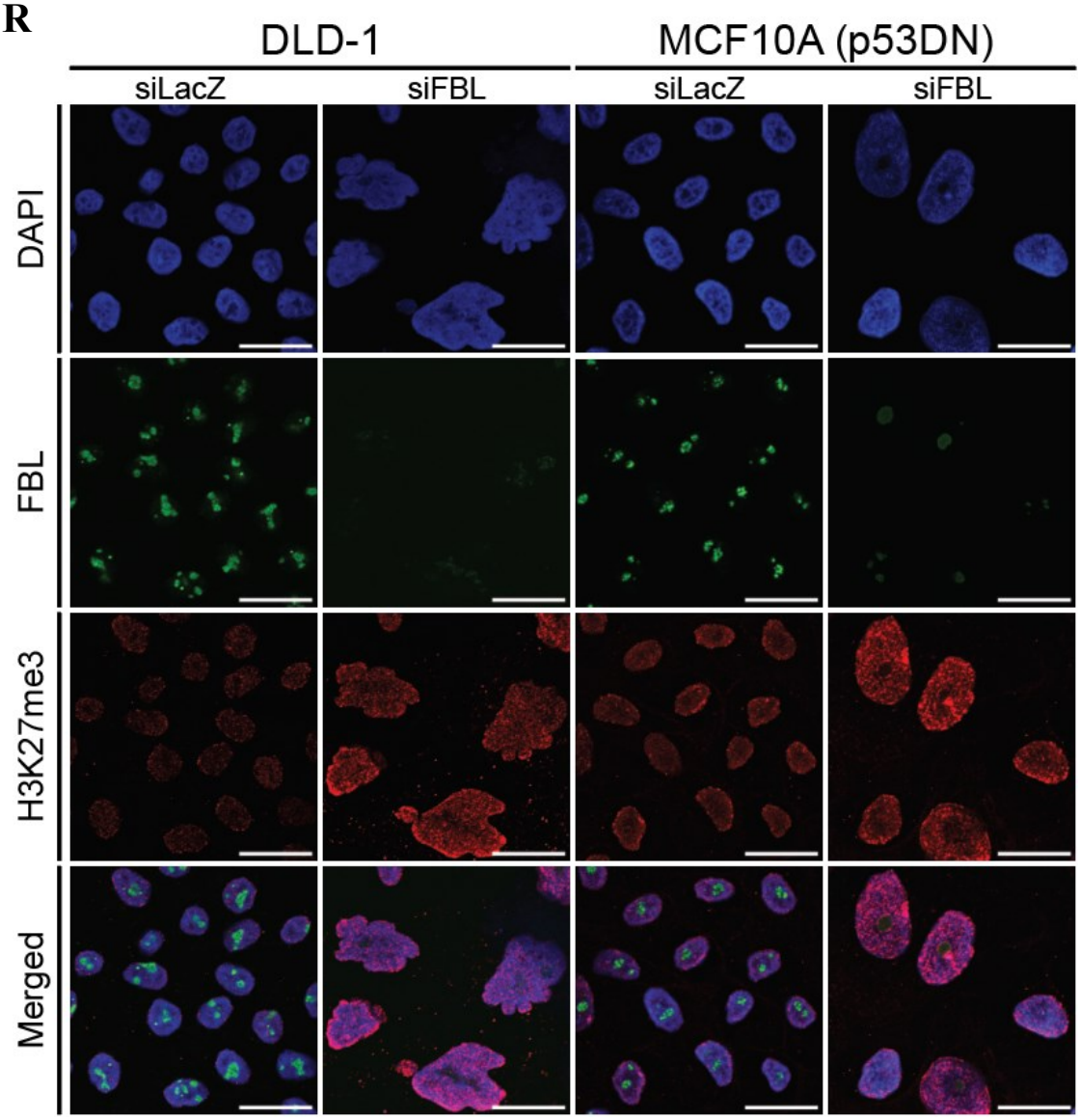
DLD-1
MCF10A (p53DN)
siLacZ
siFBL
siLacZ
siFBL
DAPI
FBL
H3K27me3
Merged

S

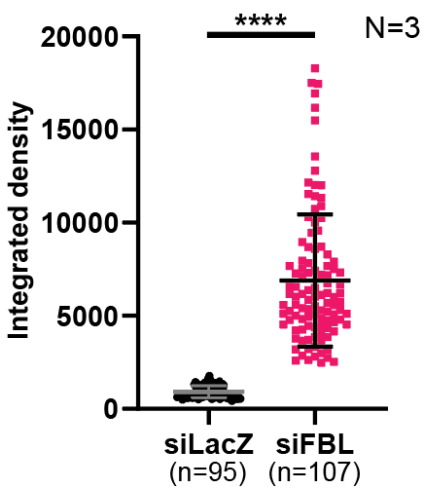
DLD-1 (H3K27me3)
****
N=3
Integrated density
20000
15000
10000
5000
0
siLacZ
(n=95)
siFBL
(n=107)

T

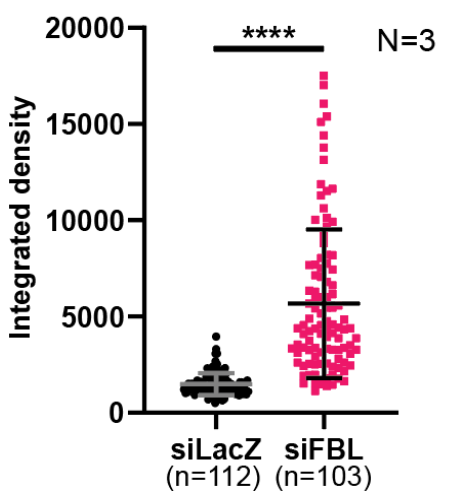
MCF10A(p53DN) (H3K27me3)
****
N=3
Integrated density
20000
15000
10000
5000
0
siLacZ
(n=112)
siFBL
(n=103)

Fig. 4.4. Abrogating FBL-EZH2 interaction leads to translocation of EZH2 from the nucleolus and increased deposition of H3K27me3 deposition

(A) Representative immunoblots of subcellular fractions obtained from DLD-1 cells transfected with control siRNA (siLacZ) or FBL-targeting siRNA (siFBL) for ~48 h, including whole-cell lysate (WC), cytoplasmic, nuclear, and nucleolar fractions. Lamin B1 and nucleophosmin 1 (NPM1) were used as markers for nuclear and nucleolar fractions, respectively. **(B)** Representative immunoblots of subcellular fractions obtained from MCF10A(p53DN) cells transfected with control siRNA (siLacZ) or FBL-targeting siRNA (siFBL) for ~36 h, including whole-cell lysate (WC), cytoplasmic, nuclear, and nucleolar fractions. Lamin B1 and nucleophosmin 1 (NPM1) were used as nuclear and nucleolar loading controls, respectively. Data are representative of three independent biological replicates (N = 3). **(C)** Quantitative analysis of immunoblot data from DLD-1 and MCF10A cells reveals a significant increase in nucleoplasmic EZH2 upon FBL depletion. Data are derived from three independent biological replicates (N = 3). Statistical significance was determined using an unpaired t-test. **(D)** Quantitative analysis of FBL and EZH2 colocalization using Mander's coefficient B and colocalized voxel measurements, calculated with Imaris, in DLD-1 and MCF10A(p53DN) cells. Thresholds applied were A = 19.820 and B = 54.500 for DLD-1, and A = 2.630 and B = 3.420 for MCF10A(p53DN), and were kept constant across all images and biological replicates. Data were derived from three independent biological replicates (N = 3). Statistical significance was assessed using an unpaired t-test. **(E)** Representative immunofluorescence images showing depletion of nucleolar EZH2, with nucleolin (NCL; red) marking the nucleolus relative to the nucleoplasm, in DLD-1 and MCF10A(p53DN) cells transfected with control siRNA (siLacZ) or FBL-targeting siRNA (siFBL) for ~48 h and ~36 h, respectively. EZH2 is shown in green and nuclei are counterstained with DAPI (blue). Images are representative of three independent biological replicates (N = 3). Scale bar, ~20 μm. **(F)** Scatter dot plot with overlaid mean showing a significant decrease in nucleolar EZH2 levels in DLD-1 cells following siFBL transfection compared with siLacZ control cells after ~48 h. Quantification was performed on a total of 233 nucleoli pooled from three independent biological replicates (N = 3). Statistical significance was assessed using an unpaired t-test. **(G)** Scatter dot plot with overlaid mean illustrating reduced nucleolar EZH2 levels in MCF10A(p53DN) cells transfected with siFBL for ~36 h relative to siLacZ-transfected control cells. Measurements were obtained from 794 nucleoli pooled across three independent

biological replicates (N = 3). Statistical significance was determined using an unpaired t-test. **(H)** Quantification of total EZH2 levels, expressed as integrated fluorescence intensity (integrated density), in DLD-1 cells transfected with siLacZ or siFBL. **(I)** Quantification of nucleoplasmic EZH2, calculated by subtracting the nucleolar EZH2 integrated fluorescence intensity from the total nuclear EZH2 integrated fluorescence intensity. **(J)** Quantification of the proportion of EZH2 localized to the nucleolus, determined by dividing the nucleolar EZH2 integrated fluorescence intensity by the total nuclear EZH2 integrated fluorescence intensity and multiplying by 100. Error bars represent SD. Statistical significance was assessed using an unpaired t-test; ****$p < 0.0001$, ns = not significant. **(K)** Quantification of nucleolar EZH2 mean fluorescence intensity in DLD-1 cells (N = 3). Error bars denote SD. Statistical significance was assessed using an unpaired t-test; ****$p < 0.0001$. **(L)** Representative immunofluorescence images showing EZH2 (red) and nuclei (DAPI; blue) in DLD-1 cells overexpressing GFP-FBL(siRes) or ΔRBD-GFP-FBL(siRes) following transfection with siLacZ or siFBL for ~48 h. Quantification was performed on ≥120 nucleoli, with data pooled from three independent biological replicates (N = 3). Scale bar, ~20 μm. **(M)** Channel-separated representative immunofluorescence images of EZH2 in MCF10A(p53DN) cells overexpressing GFP-FBL(siRes) or ΔRBD-GFP-FBL(siRes) following transfection with siLacZ or siFBL. Nuclei are visualized by DAPI staining, and EZH2 is shown in red. Scale bar, 10 μm. **(N)** Quantification of the colocalization between EZH2 and GFP-tagged FBL constructs using Mander's coefficient B and the percentage of colocalized voxels, as calculated with Imaris, in MCF10A(p53DN) and DLD-1 cells overexpressing GFP-FBL(siRes) or ΔRBD-GFP-FBL(siRes) and transfected with siLacZ. Data were pooled from three independent biological replicates (N = 3). Statistical significance was assessed using an unpaired t-test; *$p < 0.05$, **$p < 0.01$, ****$p < 0.0001$, ns = not significant. **(O)** Representative immunoblots demonstrating a marked increase in H3K27me3 levels in DLD-1 and MCF10A(p53DN) cells following transfection with siLacZ (control) or siFBL for ~48 h and ~36 h, respectively. Histone H3 and β-tubulin were used as loading controls in MCF10A(p53DN) cells transfected with siLacZ or siFBL. Data were pooled from three independent biological replicates (N = 3). **(P)** Representative co-immunoprecipitation immunoblots showing EZH2 pull-down from DLD-1 cells overexpressing GFP-FBL(siRes) or ΔRBD-GFP-FBL(siRes) following transfection with siLacZ or siFBL. Data were obtained from two independent biological replicates (N = 2). **(Q)** Densitometric quantification of immunoblots demonstrating increased H3K27me3 levels. Statistical significance was assessed using an unpaired t-test. **(R)** Representative immunofluorescence images showing FBL (green) and H3K27me3 (red) in

MCF10A(p53DN) and DLD-1 cells following transfection with siLacZ or siFBL for ~36 h and ~48 h, respectively. Data were pooled from three independent biological replicates (N = 3). Statistical significance was assessed using an unpaired t-test. Scale bar, ~20 μm. **(S)** Quantitative analysis of H3K27me3 levels in DLD-1 and MCF10A(p53DN) cells. Measurements were obtained from 202 DLD-1 cells and 225 **(T)** MCF10A(p53DN) cells, pooled across three independent biological replicates (N = 3). Statistical significance was assessed using an unpaired t-test.

4.2.5. Nucleoplasmic EZH2 Binds the SCRIB Promoter

It is well established that EZH2 exerts its transcriptional repression activity as part of the Polycomb Repressive Complex 2 (PRC2), interacting with its core partners SUZ12 and EED1 (McCart Reed et al. 2021; Pasini et al. 2007). Under normal conditions, a subset of cellular EZH2 localizes to the nucleolus. However, our findings revealed that depletion of FBL causes a relocalization of EZH2 from the nucleolus into the nucleoplasm, where it engages with PRC2 components and contributes to chromatin-mediated gene repression.

Given this observation, we sought to determine whether the nucleoplasmic EZH2 population released upon FBL depletion actively participates in the repression of SCRIB. To specifically trace the subset of EZH2 originally associated with the nucleolus, we employed a proximity-based chromatin immunoprecipitation approach using BioID2-tagged wild-type FBL (Kim et al. 2016). Cells stably expressing BioID2-FBL were cultured in the presence of biotin, enabling the biotinylation of proteins in the immediate vicinity of FBL. Following FBL knockdown, chromatin was isolated and sonicated, and streptavidin-conjugated magnetic beads were used to pull down the biotinylated chromatin-protein complexes (Fig. 4.5(A-C)). Western blot validation confirmed the presence of biotinylated EZH2 in the pulled-down chromatin. Subsequent ChIP-PCR analyses revealed a significant enrichment of this nucleolar-origin EZH2 at the SCRIB promoter specifically in the FBL-depleted condition. This finding strongly suggests that EZH2, once released from the nucleolus, can bind to target gene promoters in the nucleoplasm and contribute to their transcriptional repression.

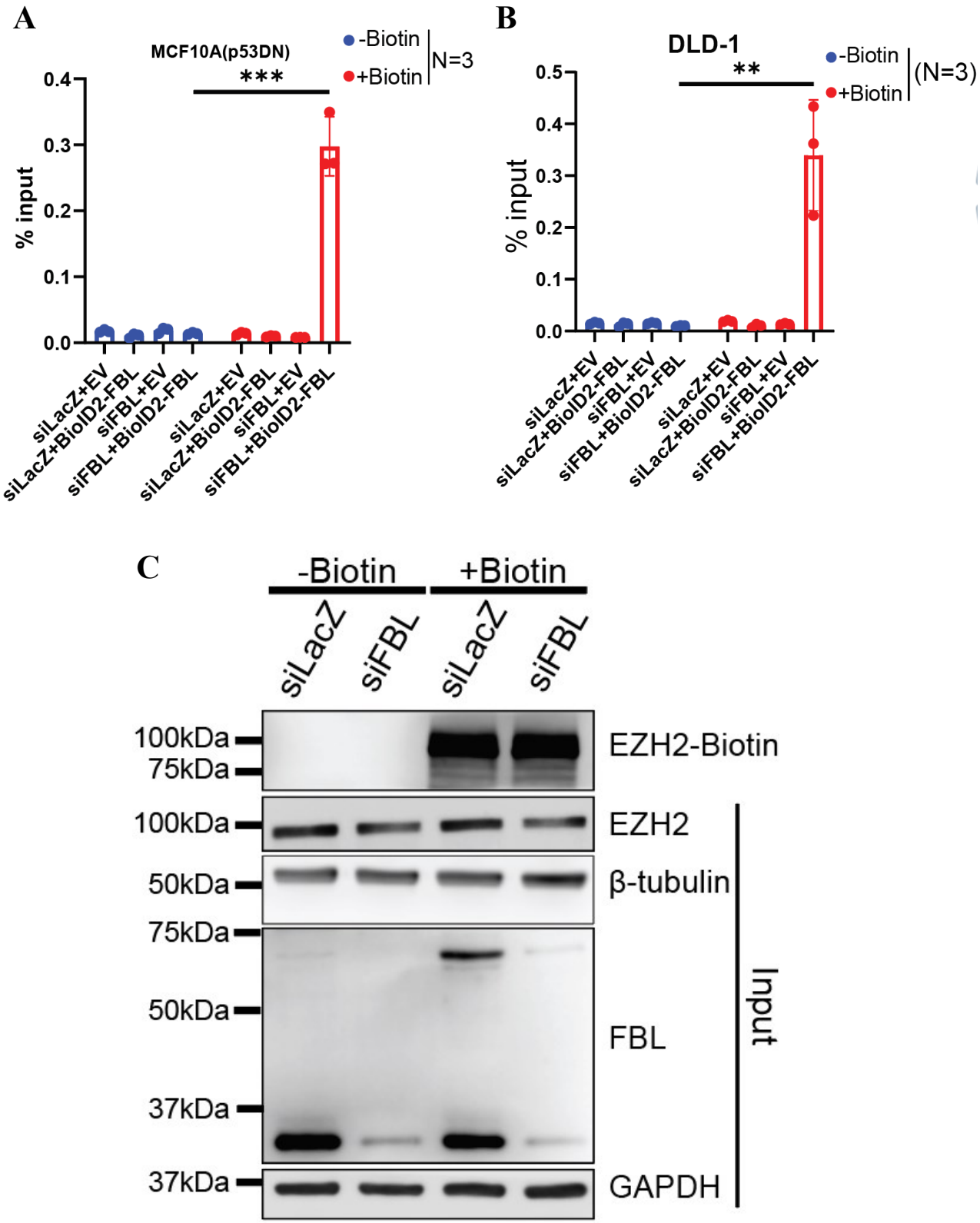
A
MCF10A(p53DN)
***
-Biotin
+Biotin
N=3
% input
0.4
0.3
0.2
0.1
0.0
siLacZ+EV
siLacZ+BioID2-FBL
siFBL+EV
siFBL+BioID2-FBL
siLacZ+EV
siLacZ+BioID2-FBL
siFBL+EV
siFBL+BioID2-FBL
B
DLD-1
**
-Biotin
+Biotin
(N=3)
% input
0.5
0.4
0.3
0.2
0.1
0.0
siLacZ+EV
siLacZ+BioID2-FBL
siFBL+EV
siFBL+BioID2-FBL
siLacZ+EV
siLacZ+BioID2-FBL
siFBL+EV
siFBL+BioID2-FBL
C
-Biotin
+Biotin
siLacZ
siFBL
siLacZ
siFBL
100kDa
75kDa
EZH2-Biotin
100kDa
EZH2
50kDa
β-tubulin
75kDa
50kDa
FBL
37kDa
37kDa
GAPDH
Input

Fig. 4.5. BioID2 ChIP-RT-qPCR reveals occupancy of nucleolar EZH2 on SCRIB promoter

(A) Bar plot representing BioID2-ChIP-qPCR enrichment of EZH2 (biotinylated and non-biotinylated) on the SCRIB promoter in MCF10A(p53DN) cells in siLacZ- and siFBL-transfected cells (N = 3) for ∼24h. p values derived from an unpaired t test. The schematic represents the steps involved in BioID2-ChIP-qPCR. **(B)** Bar graphs depicting BioID2–ChIP–qPCR enrichment of EZH2, including biotinylated and non-biotinylated fractions, at the SCRIB promoter in DLD-1 cells transfected with siLacZ or siFBL for ~24 h (N = 3). P values were calculated using an unpaired t-test. The schematic outlines the BioID2–ChIP–qPCR experimental workflow. **(C)** Representative immunoblots showing pull-down of biotinylated EZH2, probed for EZH2 and FBL, from pBP-FBL(WT)-BirA*-HA–overexpressing DLD-1 and MCF10A(p53DN) cells transfected with siLacZ or siFBL and treated with or without biotin. GAPDH was used as a loading control for input samples. Data were obtained from two independent biological replicates (N = 2).

4.2.6. Disruption of FBL-EZH2 Interaction Mimics FBL Loss Phenotype

To understand whether the physical interaction between FBL and EZH2 is necessary to maintain epithelial homeostasis, we next disrupted this interaction and assessed the resulting phenotypic consequences. FBL contains an RNA-binding domain (RBD) that is known to mediate its interaction with EZH2. To test the functional requirement of this domain, we used a siRNA-resistant FBL mutant lacking the RBD (FBLΔRBD) in FBL-depleted cells.

Immunofluorescence staining revealed that the disruption of the FBL–EZH2 interaction, either by FBL depletion or by expression of FBLΔRBD, resulted in marked internalization of E-cadherin from the plasma membrane to the cytoplasm, along with this we also observed increased aspect ratio upon abrogating FBL-EZH2 interaction (Fig. 4.6 (A-D)). This loss of junctional E-cadherin was accompanied by a reduction in Scribble protein levels, as confirmed by immunoblotting (Fig. 4.6 G). These observations indicate that disrupting the FBL–EZH2 interaction leads to phenotypes that closely mimic those observed upon complete FBL depletion.

Functionally, this disruption also led to a significant increase in cell motility (Fig. 4.6 (H-J)). Scratch wound healing assays showed that cells expressing GFP control or FBLΔRBD in an FBL-depleted background migrated more rapidly, covering the wound area faster than control cells. This suggests that FBL–EZH2 interaction restrains cell migration, likely by preserving the epithelial state. To explore the underlying epigenetic mechanism, we performed ChIP-qPCR to examine the occupancy of EZH2 and H3K27me3 on the SCRIB promoter under conditions where FBL–EZH2 interaction was disrupted (Fig. 4.6G). We found increased binding of both EZH2 and H3K27me3 to the SCRIB promoter, consistent with enhanced transcriptional repression of Scribble. The downregulation of Scribble was associated with mislocalization of E-cadherin and increased cell migration—hallmarks of an epithelial-to-mesenchymal-like transition.

Finally, to investigate whether these effects were sensitive to EZH2 dosage, we induced graded overexpression of EZH2 using a doxycycline-inducible system. A ~200% increase in EZH2 levels led to a ~25% reduction in Scribble expression, reinforcing the notion that elevated nucleoplasmic EZH2 levels are sufficient to downregulate SCRIB (Fig. 4.6 (L-M)).

In summary, disruption of the FBL–EZH2 interaction releases EZH2 from the nucleolus into the nucleoplasm, where it engages with PRC2 to deposit repressive H3K27me3 marks on the SCRIB promoter. This epigenetic silencing of Scribble leads to E-cadherin internalization and enhanced cell migration, collectively mimicking the morphological and functional

consequences of FBL loss. These results underscore the critical role of FBL in spatially restricting EZH2 activity and maintaining epithelial identity through transcriptional regulation of polarity and adhesion genes.

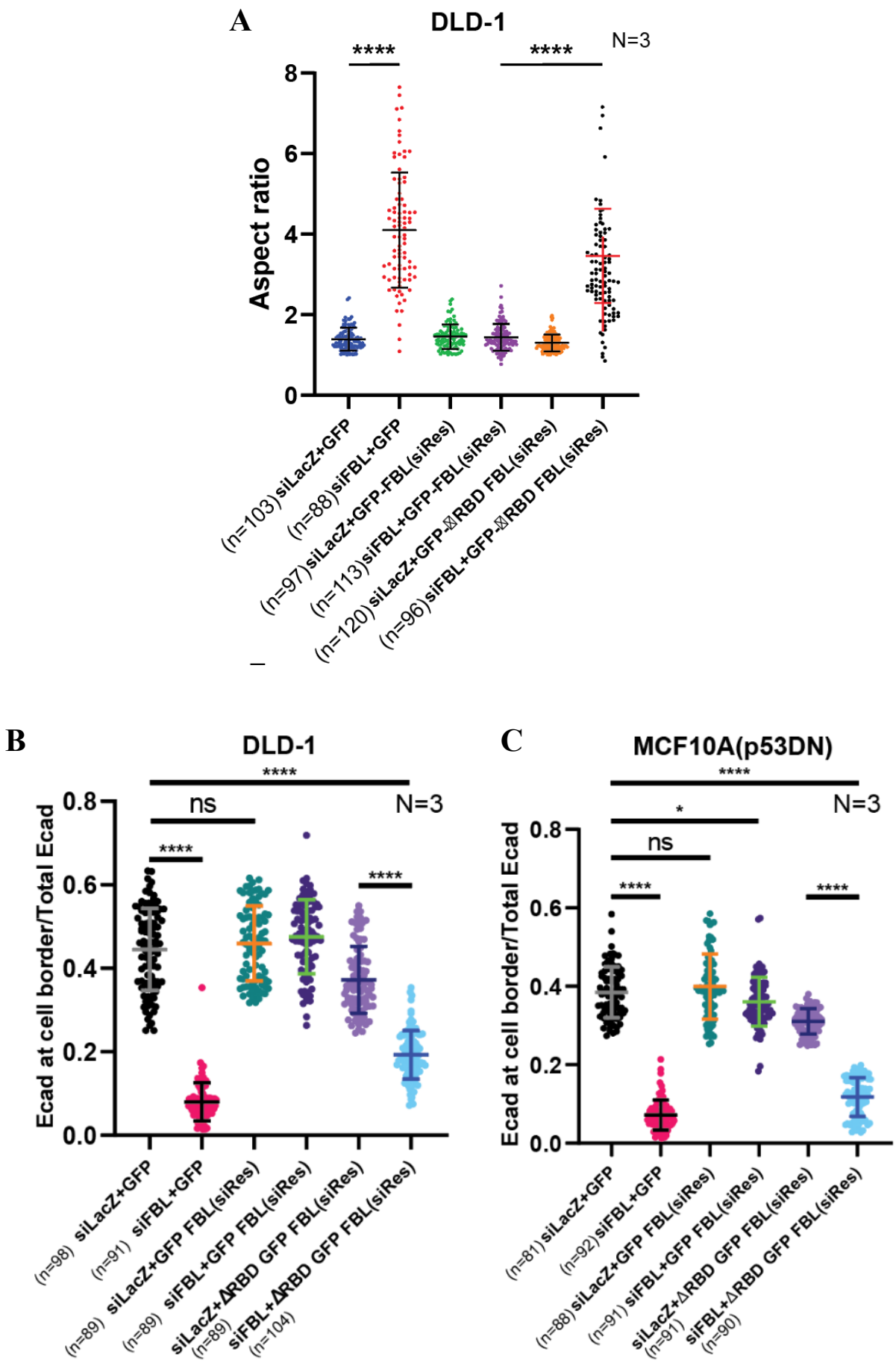
A
DLD-1
N=3
****
****
Aspect ratio
0
2
4
6
8
(n=103) siLacZ+GFP
(n=88) siFBL+GFP
(n=97) siLacZ+GFP-FBL(siRes)
(n=113) siFBL+GFP-FBL(siRes)
(n=120) siLacZ+GFP-ΔRBD FBL(siRes)
(n=96) siFBL+GFP-ΔRBD FBL(siRes)
B
DLD-1
****
ns
N=3
****
****
Ecad at cell border/Total Ecad
0.0
0.2
0.4
0.6
0.8
(n=98) siLacZ+GFP
(n=91) siFBL+GFP
(n=89) siLacZ+GFP FBL(siRes)
(n=89) siFBL+GFP FBL(siRes)
(n=89) siLacZ+ΔRBD GFP FBL(siRes)
(n=104) siFBL+ΔRBD GFP FBL(siRes)
C
MCF10A(p53DN)
****
*
ns
N=3
****
****
Ecad at cell border/Total Ecad
0.0
0.2
0.4
0.6
0.8
(n=81) siLacZ+GFP
(n=92) siFBL+GFP
(n=88) siLacZ+GFP FBL(siRes)
(n=91) siFBL+GFP FBL(siRes)
(n=91) siLacZ+ΔRBD GFP FBL(siRes)
(n=90) siFBL+ΔRBD GFP FBL(siRes)

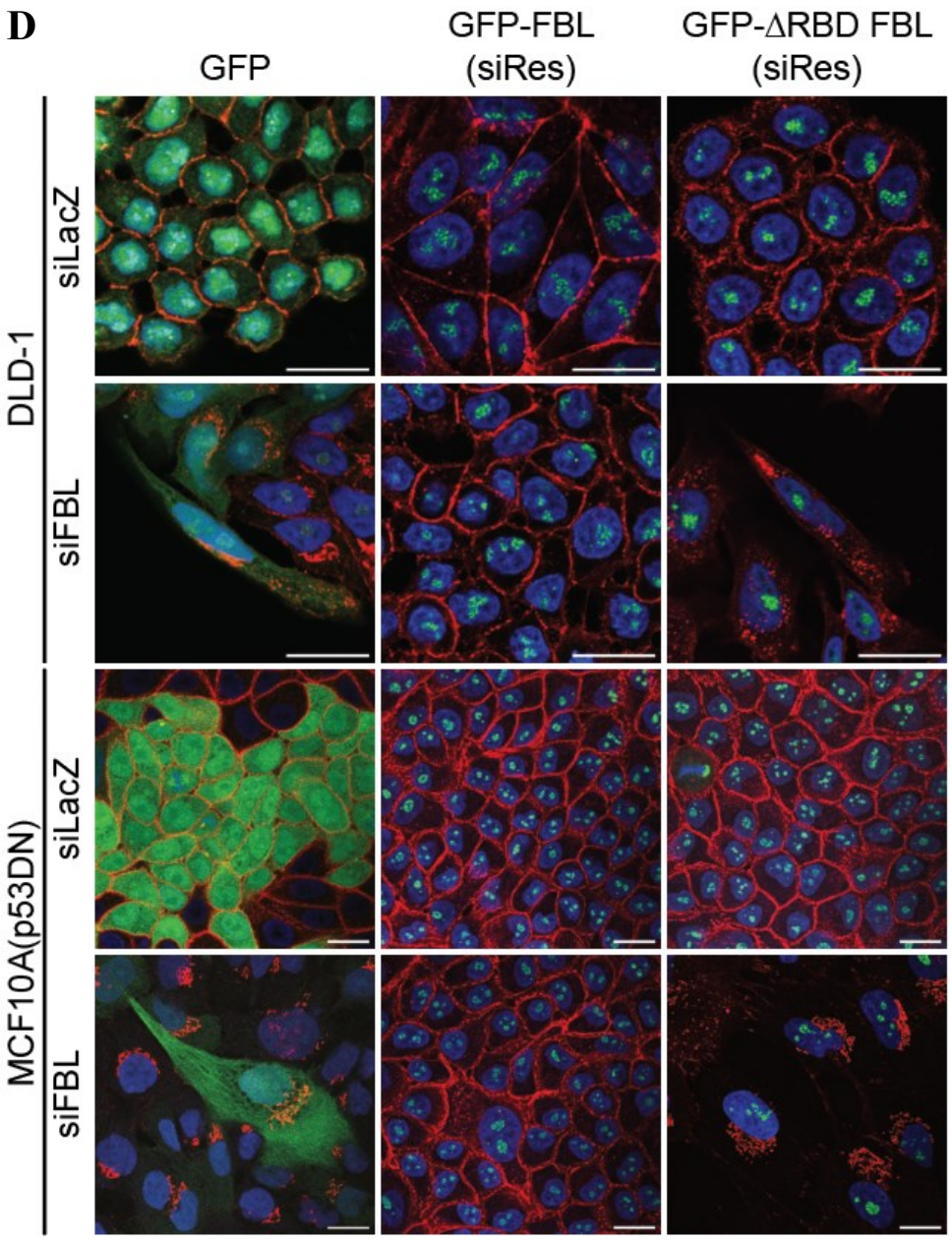
D
GFP
GFP-FBL (siRes)
GFP-ΔRBD FBL (siRes)
DLD-1
siLacZ
siFBL
MCF10A(p53DN)
siLacZ
siFBL

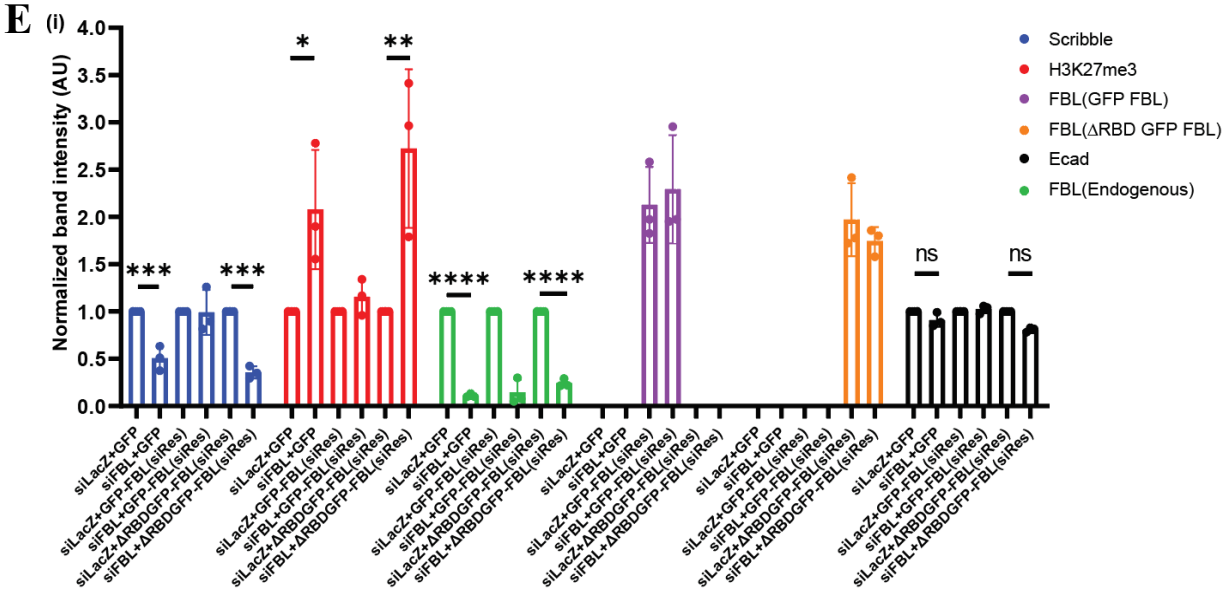
E
(i)
Normalized band intensity (AU)
4.0
3.5
3.0
2.5
2.0
1.5
1.0
0.5
0.0
***
***
*
**
****
****
ns
ns
Scribble
H3K27me3
FBL(GFP FBL)
FBL(ΔRBD GFP FBL)
Ecad
FBL(Endogenous)
siLacZ+GFP
siFBL+GFP
siLacZ+GFP-FBL(siRes)
siFBL+GFP-FBL(siRes)
siLacZ+ΔRBDGFP-FBL(siRes)
siFBL+ΔRBDGFP-FBL(siRes)

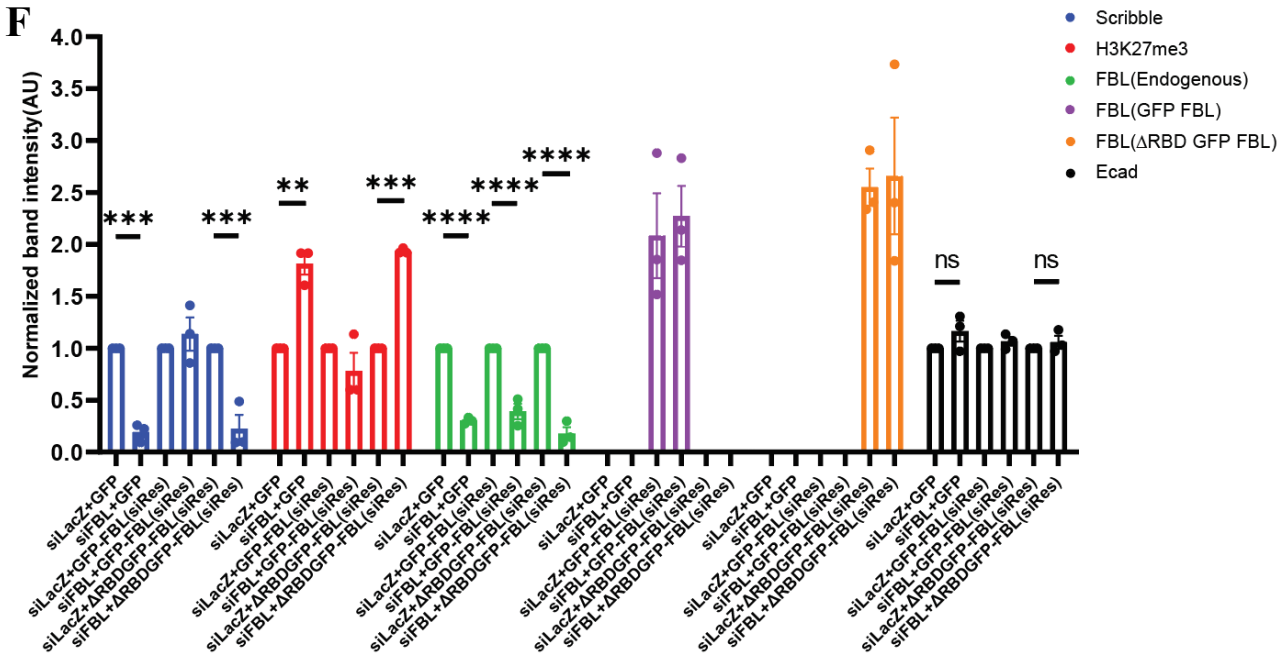
F
Normalized band intensity(AU)
4.0
3.5
3.0
2.5
2.0
1.5
1.0
0.5
0.0
***
***
**
***
****
****
****
ns
ns
Scribble
H3K27me3
FBL(Endogenous)
FBL(GFP FBL)
FBL(ΔRBD GFP FBL)
Ecad
siLacZ+GFP
siFBL+GFP
siLacZ+GFP-FBL(siRes)
siFBL+GFP-FBL(siRes)
siLacZ+ΔRBDGFP-FBL(siRes)
siFBL+ΔRBDGFP-FBL(siRes)

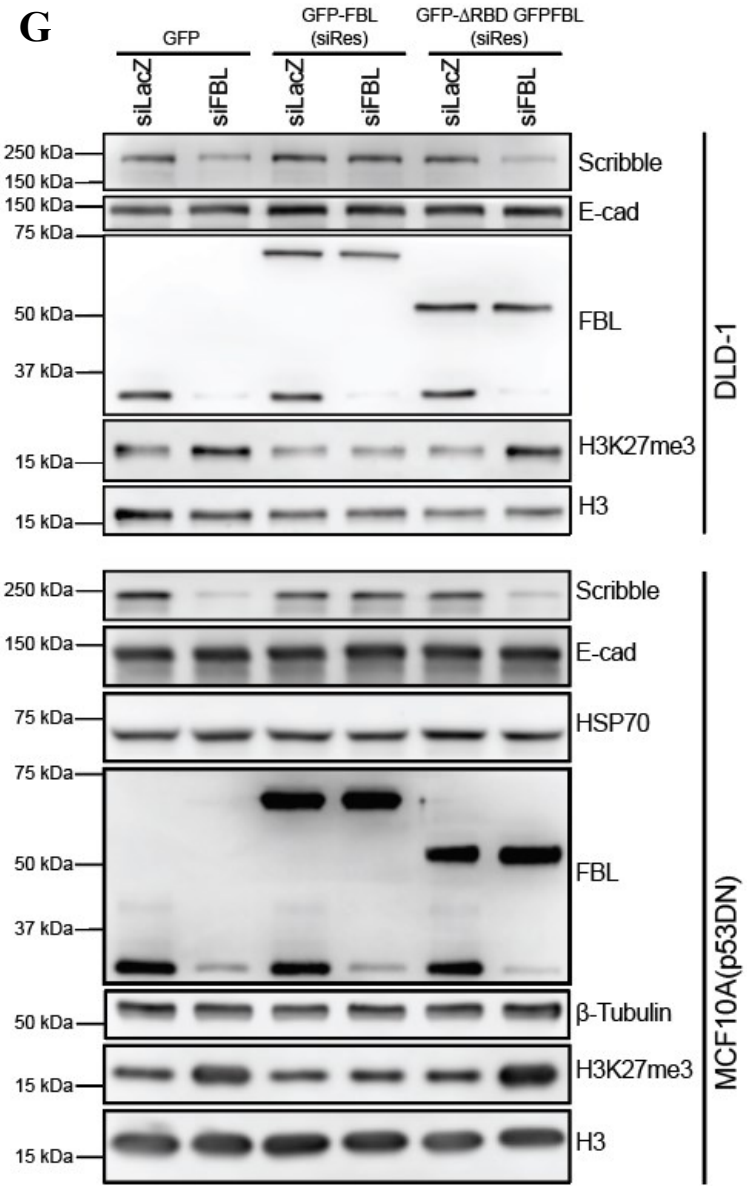
G
GFP
GFP-FBL (siRes)
GFP-ΔRBD GFPFBL (siRes)
siLacZ
siFBL
250 kDa
150 kDa
150 kDa
75 kDa
50 kDa
37 kDa
15 kDa
15 kDa
Scribble
E-cad
FBL
H3K27me3
H3
DLD-1
250 kDa
150 kDa
75 kDa
75 kDa
50 kDa
37 kDa
50 kDa
15 kDa
15 kDa
Scribble
E-cad
HSP70
FBL
β-Tubulin
H3K27me3
H3
MCF10A(p53DN)

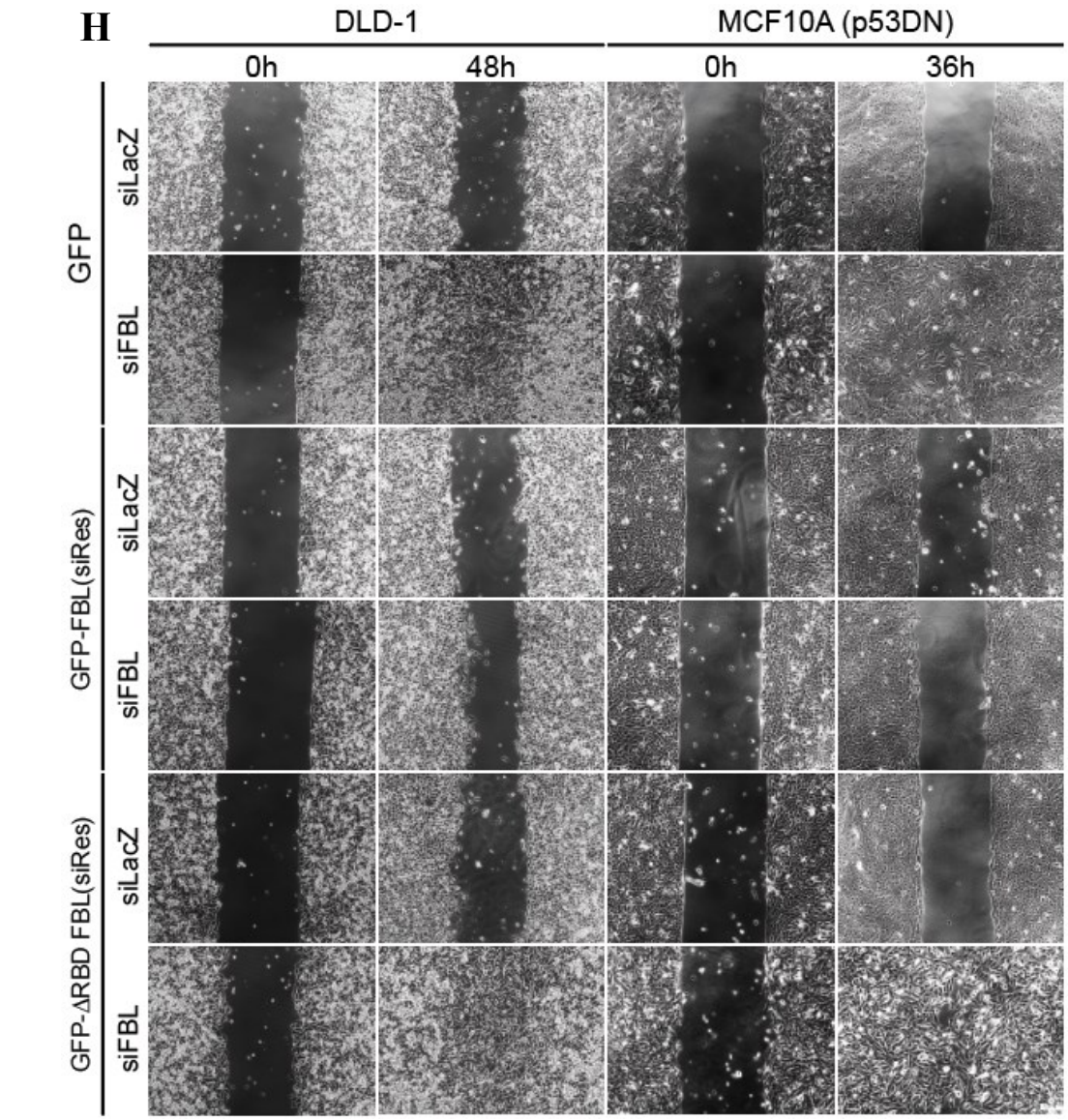
H
DLD-1
MCF10A (p53DN)
0h
48h
0h
36h
GFP
siLacZ
siFBL
GFP-FBL(siRes)
siLacZ
siFBL
GFP-ΔRBD FBL(siRes)
siLacZ
siFBL

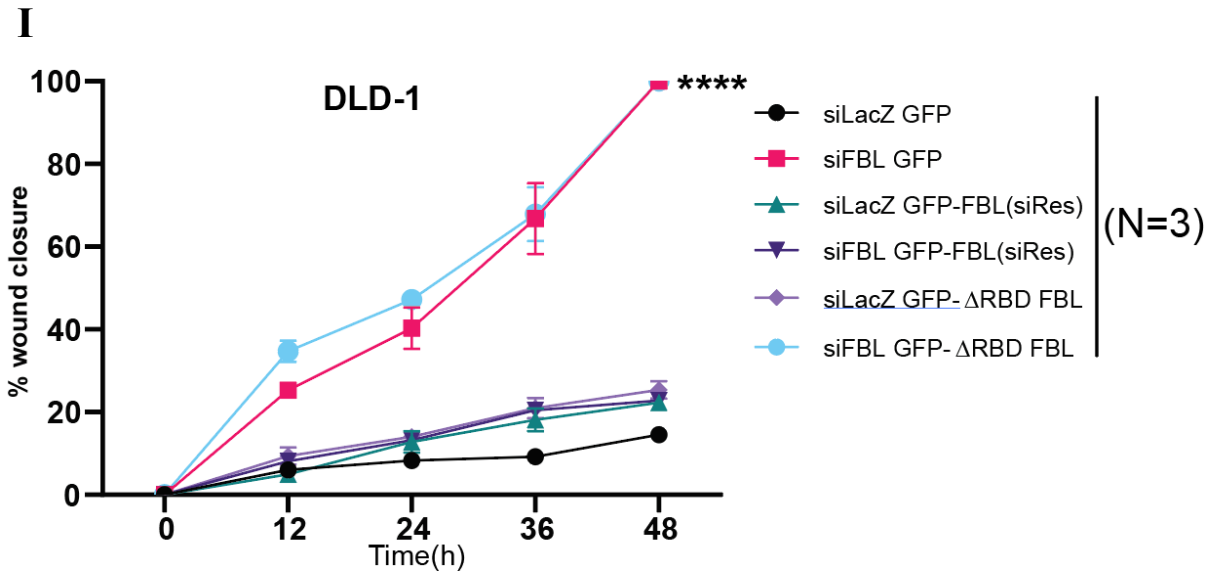
I
DLD-1
****
% wound closure
100
80
60
40
20
0
0
12
24
36
48
Time(h)
siLacZ GFP
siFBL GFP
siLacZ GFP-FBL(siRes)
siFBL GFP-FBL(siRes)
siLacZ GFP-ΔRBD FBL
siFBL GFP-ΔRBD FBL
(N=3)

J

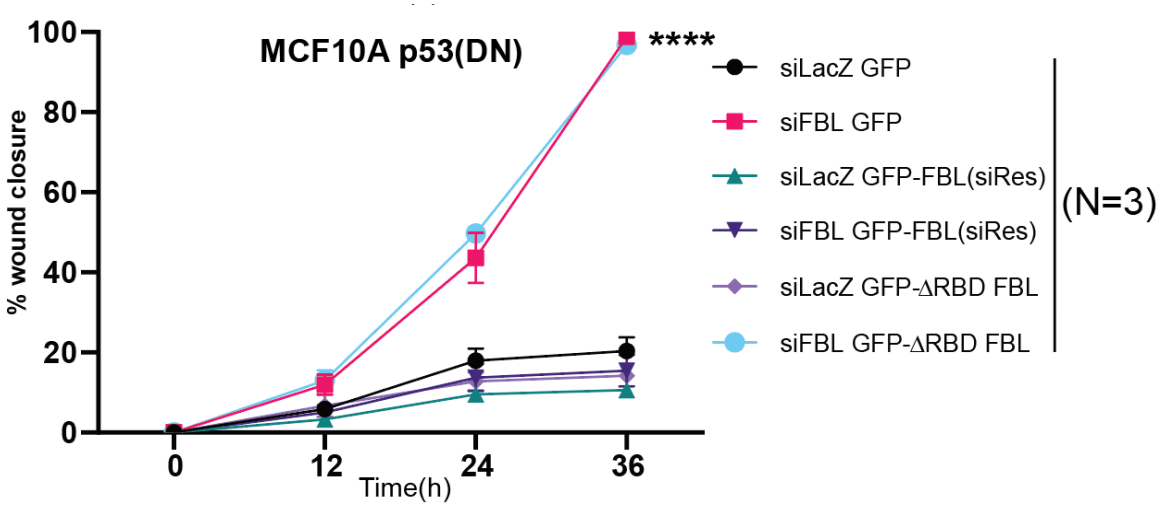
MCF10A p53(DN)
% wound closure
100
80
60
40
20
0
0
12
24
36
Time(h)
****
siLacZ GFP
siFBL GFP
siLacZ GFP-FBL(siRes)
siFBL GFP-FBL(siRes)
siLacZ GFP-ΔRBD FBL
siFBL GFP-ΔRBD FBL
(N=3)

K

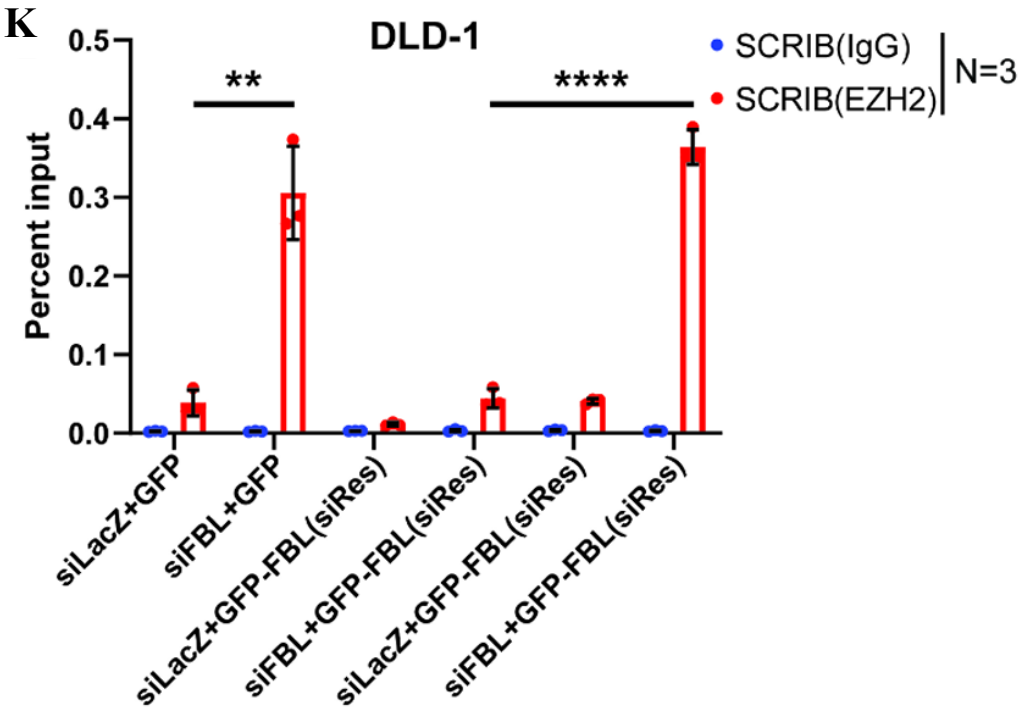
DLD-1
Percent input
0.5
0.4
0.3
0.2
0.1
0.0
**
****
SCRIB(IgG)
SCRIB(EZH2)
N=3
siLacZ+GFP
siFBL+GFP
siLacZ+GFP-FBL(siRes)
siFBL+GFP-FBL(siRes)
siLacZ+GFP-FBL(siRes)
siFBL+GFP-FBL(siRes)

L

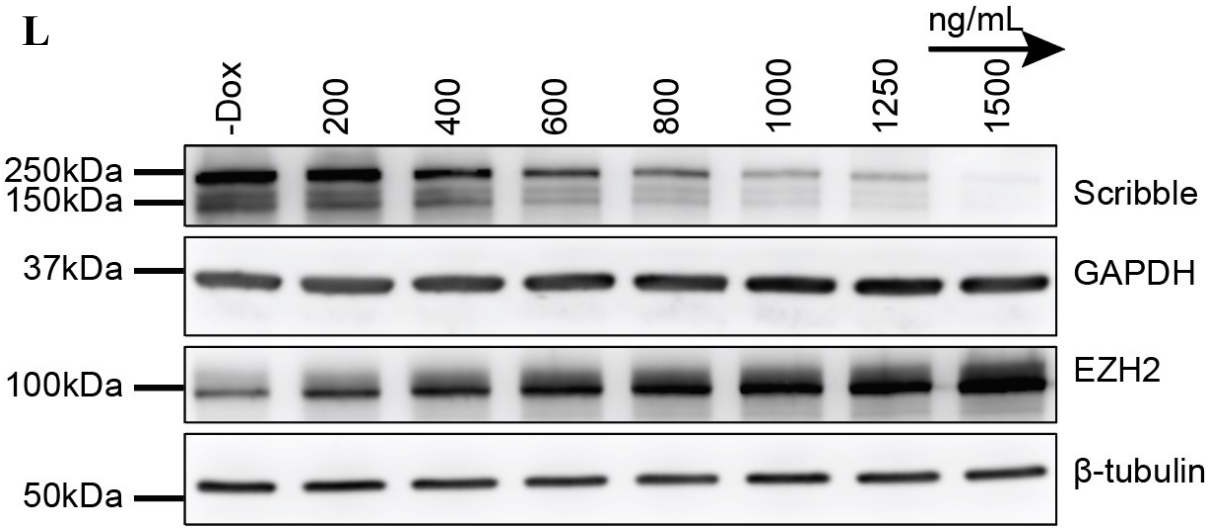
ng/mL
-Dox
200
400
600
800
1000
1250
1500
250kDa
150kDa
Scribble
37kDa
GAPDH
100kDa
EZH2
50kDa
β-tubulin

M

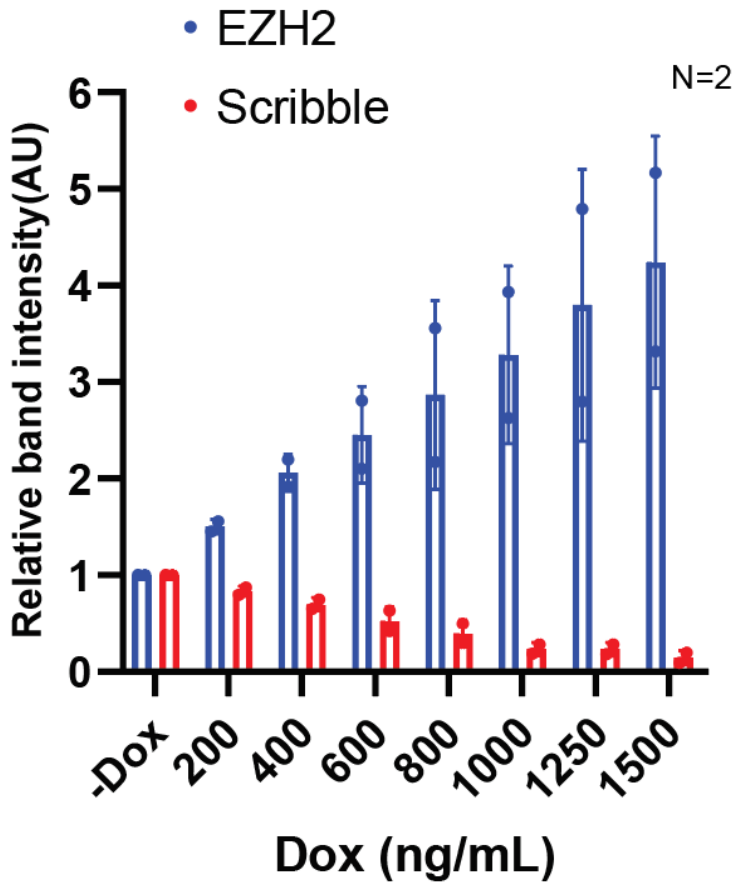
EZH2
Scribble
N=2
Relative band intensity(AU)
0
1
2
3
4
5
6
-Dox
200
400
600
800
1000
1250
1500
Dox (ng/mL)

Fig. 4.6. Disrupting FBL-EZH2 interaction downregulates SCRIB expression and increases cell migration

(A) Quantification of nuclear aspect ratio in DLD-1 cells overexpressing GFP, GFP-FBL(siRes), or ΔRBD-GFP-FBL(siRes) following transfection with siLacZ or siFBL for ~48 h. Measurements were obtained from 617 cells pooled across three independent biological replicates (N = 3). Error bars represent SD. Statistical significance was assessed using an unpaired t-test; ****$p < 0.0001$. **(B)** Quantification of E-cadherin internalization in DLD-1 cells, expressed as the ratio of E-cadherin fluorescence intensity at the cell border to that of the entire cell. **(C)** Quantification of E-cadherin internalization in MCF10A(p53DN) cells using the same border-to-total fluorescence intensity ratio. Measurements were obtained from 560 cells pooled across three independent biological replicates (N = 3). Statistical significance was assessed using one-way ANOVA and unpaired t-tests. **(D)** Representative immunofluorescence images showing E-cadherin (red) in DLD-1 and MCF10A(p53DN) cells overexpressing GFP, GFP-FBL(siRes), or ΔRBD-GFP-FBL(siRes) following transfection with siLacZ or siFBL for ~48 h and ~36 h, respectively. GFP or GFP-tagged constructs are shown in green, and nuclei are visualized by DAPI staining (blue). Data were pooled from three independent biological replicates (N = 3). Scale bar, ~20 μm. **(E)** Densitometric quantification of immunoblots shown in Fig. 5C for DLD-1 cells. Statistical significance was assessed using one-way ANOVA. **(F)** Densitometric quantification of immunoblots shown in Fig. 5C for MCF10A(p53DN) cells. Data were pooled from three independent biological replicates (N = 3), and statistical significance was determined using one-way ANOVA. **(G)** Representative immunoblots depicting Scribble, E-cadherin, FBL, and H3K27me3 protein levels in DLD-1 and MCF10A(p53DN) cells overexpressing GFP, GFP-FBL(siRes), or ΔRBD-GFP-FBL(siRes) following transfection with siLacZ or siFBL for ~48 h and ~36 h, respectively. HSP70, β-tubulin, histone H3, and GAPDH were used as loading controls. Data were pooled from three independent biological replicates (N = 3). **(H)** Representative phase-contrast images from scratch wound–healing assays performed in DLD-1 and MCF10A(p53DN) cells expressing GFP, GFP-FBL(siRes), or ΔRBD-GFP-FBL(siRes) following transfection with siLacZ or siFBL. Data were pooled from three independent biological replicates (N = 3). **(I)** Quantitative analysis of scratch wound–healing assays for DLD-1. Statistical significance was assessed using two-way ANOVA followed by Sidak's multiple-comparisons test. **(J)** Quantitative evaluation of the scratch wound–healing assay for MCF10A(p53DN). Statistical analysis was performed using two-way ANOVA with Sidak's multiple-comparisons test to determine p values. **(K)** Bar graph illustrating differential EZH2 occupancy at the SCRIB promoter in DLD-

1 cells transfected with control siRNA (siLacZ) or siFBL for ~48 h (N = 3). Error bars represent SD. Statistical significance was determined using an unpaired t-test; **p < 0.01 and ****p < 0.0001. **(L)** Representative immunoblots showing Scribble and EZH2 protein levels in cells transduced with a doxycycline-inducible EZH2 overexpression construct. GAPDH and βtubulin were used as loading controls. **(M)** Densitometric quantification of the immunoblots shown in Fig. 4.6.L.

4.3. Discussion

The results presented in this study establish Fibrillarin (FBL) as a critical upstream regulator of epithelial polarity, acting through transcriptional control of Scribble (SCRIB) and spatial modulation of EZH2 activity. Through a multi-tiered experimental framework involving transcriptomic analyses, chromatin profiling, functional rescue assays, and subcellular localization studies, we delineate a mechanistic model wherein FBL maintains epithelial architecture by spatially restricting PRC2 activity and ensuring transcriptional competence at key polarity gene loci.

RNA-seq and enrichment analyses revealed that FBL depletion results in significant downregulation of SCRIB, a known tumor suppressor and epithelial polarity scaffold. Scribble serves as a molecular anchor for E-cadherin by stabilizing its interaction with p120-catenin, thus maintaining adherens junctions and epithelial cohesion. The repression of SCRIB upon FBL loss was confirmed at both transcript and protein levels. Notably, other E-cadherin trafficking regulators such as DLG5 and DDR1 remained unaltered, reinforcing the central role of Scribble as a downstream effector of FBL.

ChIP-qPCR and publicly available ChIP-seq data provided compelling evidence that the SCRIB promoter exhibits a poised bivalent chromatin state, with concurrent enrichment of H3K4me3 and H3K27me3. This configuration allows for rapid gene activation or silencing in response to cellular stimuli. FBL depletion resulted in enhanced recruitment of EZH2 and accumulation of H3K27me3 at the SCRIB promoter without altering total EZH2 levels, suggesting a redistribution of EZH2 rather than its overexpression. Pharmacological inhibition of EZH2 using GSK126 led to derepression of SCRIB and a rescue of both E-cadherin localization and epithelial cell migration, establishing the functional relevance of EZH2-mediated repression.

A major mechanistic insight from this work is the role of FBL in sequestering EZH2 within the nucleolus. Using subcellular fractionation and immunofluorescence, we demonstrated that FBL depletion shifts EZH2 from the nucleolus to the nucleoplasm. This spatial redistribution increases the pool of chromatin-bound EZH2 available for H3K27me3 deposition. Importantly, a mutant form of FBL lacking the RNA-binding domain (FBLΔRBD) was unable to retain EZH2 in the nucleolus and phenocopied FBL knockdown with respect to E-cadherin mislocalization and enhanced cell migration. These findings suggest that the FBL–EZH2 interaction, likely RNA-dependent, is necessary for spatial regulation of PRC2 activity.

This spatial modulation of EZH2 by FBL parallels recent findings in nuclear architecture research, where subnuclear compartmentalization is increasingly recognized as a regulatory mechanism for chromatin modifiers. Similar to nucleophosmin and nucleolin, FBL appears to act as a nuclear sink for EZH2, buffering its availability and function. Loss of this sequestration mechanism results in inappropriate repression of key epithelial genes, thereby initiating a cascade of polarity loss and migratory activation.

Functional assays further highlighted the pivotal role of Scribble in epithelial homeostasis. Scribble knockdown alone was sufficient to recapitulate the migratory phenotype of FBL-depleted cells, while Scribble overexpression in an FBL-deficient background rescued cell polarity and restrained motility. These observations affirm the positioning of Scribble downstream of FBL and validate it as a primary effector in the maintenance of epithelial identity.

Taken together, this study defines a novel epigenetic axis whereby FBL controls epithelial polarity through spatial restriction of EZH2 and transcriptional maintenance of SCRIB. This mechanism provides a unifying explanation for the observed defects in junctional stability, E-cadherin trafficking, and enhanced migratory behavior upon FBL depletion. Given the recurrent loss of FBL and deregulation of PRC2 components in several cancers, these findings also open avenues for targeting the FBL–EZH2–Scribble axis in therapeutic strategies aimed at restoring epithelial integrity and suppressing metastatic progression. Importantly, these results contribute a new layer of understanding to nucleolar regulation in epithelial homeostasis, linking spatial chromatin control to cell polarity. Future investigations could explore how FBL-EZH2 dynamics are modulated under oncogenic stress or during epithelial plasticity transitions such as EMT, and whether pharmacological modulation of this axis offers clinical benefit in epithelial cancers marked by polarity disruption.

Chapter 5:
FBL Depletion Promotes EMT and Tumor Progression in Breast Epithelial Cells

5.1. Introduction

The transition from a stable epithelial state to a more plastic, migratory phenotype represents a critical step in carcinoma progression. This process, often governed by epithelial-to-mesenchymal transition (EMT), involves a coordinated suppression of epithelial markers and activation of mesenchymal programs, driven by alterations in transcriptional networks and signaling cascades. Among the key regulators of epithelial homeostasis are polarity determinants such as Scribble, signaling nodes including the PI3K-Akt and Hippo pathways, and chromatin-modifying enzymes like EZH2, the catalytic component of Polycomb Repressive Complex 2 (PRC2). However, the upstream mechanisms that simultaneously coordinate these diverse regulatory layers remain incompletely understood.

Recent data have suggested that nucleolar proteins may exert broader cellular influence beyond ribosome biogenesis, impacting chromatin dynamics, signaling integration, and stress responses (González-Arzola 2024; Leeke et al. 2025; Pederson and Tsai 2009; Böğürcü-Seidel et al. 2023). Fibrillarin (FBL), being a conserved nucleolar methyltransferase responsible for 2′-O-methylation of rRNA, has previously been implicated in maintaining nuclear morphology, and chromatin organization (Tessarz et al. 2014; Amin et al. 2007). Building on these observations, we explored whether FBL governs EMT-related signaling and tumorigenic behaviors in epithelial cancer models.

Transcriptomic and phenotypic analyses following FBL depletion revealed widespread dysregulation of polarity proteins and EMT drivers. Notably, loss of FBL led to a reduction in Scribble expression and its membrane localization, derepressing downstream pathways including PI3K-Akt and Hippo signaling. The resulting activation of Akt was accompanied by a loss of H3K27me3, consistent with previous reports showing that Akt-mediated phosphorylation of EZH2 impairs its catalytic activity (Cha et al. 2005a). Simultaneously, stabilization of TAZ, a Hippo pathway effector, was observed, further promoting the expression of key mesenchymal transcription factors such as Snail and FoxC2 (Lei et al. 2008). These transcriptional changes were validated at the protein level and were exacerbated upon disruption of the FBL–EZH2 interaction, establishing a mechanistic link between nucleolar regulation and EMT progression.

Importantly, pharmacological inhibition of Akt reversed the EMT phenotype and restored epithelial marker expression, highlighting Akt signaling as a critical mediator of the migratory behavior seen in FBL-depleted cells. These observations suggest that FBL acts as a signaling

integrator, modulating both membrane-associated and chromatin-based regulators of epithelial stability.

In vivo, FBL-depleted DLD-1 cells exhibited enhanced tumor growth and significantly increased metastatic colonization of the lungs in immunocompromised mice. These phenotypes were accompanied by nuclear displacement of EZH2, global elevation of H3K27me3, and persistent Scribble downregulation—an epigenetic shift that favors tumor plasticity and dissemination. Consistent with our findings, prior studies have shown that increased EZH2 expression promotes EMT and metastasis through repression of epithelial adhesion genes and activation of mesenchymal (Herranz et al. 2008; Chang et al. 2011).

These data collectively establish FBL as a crucial regulator of epithelial cell identity, integrating spatial control of EZH2, modulation of Akt and Hippo signaling, and maintenance of polarity determinants. Its depletion rewires the transcriptional and signaling landscape toward an EMT-like state, fueling tumor progression and metastatic competence.

5.2.1. FBL Depletion Activates Akt Signaling Pathways

Scribble, a well-characterized cell polarity regulator, plays a pivotal role in the suppression of oncogenic signaling pathways. One of its crucial functions is the inhibition of Akt activation via interaction with the phosphatase PHLPP1, which dephosphorylates and inactivates Akt. In our study, depletion of FBL led to a significant reduction in Scribble levels. This downregulation correlated with a marked increase in phosphorylated Akt (pAkt), indicating that FBL loss indirectly promotes Akt activation by disrupting the Scribble–PHLPP1 axis.

The elevated Akt activity observed upon FBL knockdown is particularly relevant given that Akt phosphorylates EZH2 at Ser21, a post-translational modification known to inhibit histone methyltransferase activity of EZH2. This can lead to a global reduction in the repressive H3K27me3 mark and a consequent shift in the chromatin landscape toward a more transcriptionally permissive state. In FBL-depleted MCF10A(p53DN) cells, we observed a clear decrease in global H3K27me3 levels concomitant with increased pAkt levels, confirming the activation of the Akt pathway.

To determine whether Akt activation directly contributes to epithelial-to-mesenchymal transition (EMT) in this context, we treated FBL-depleted cells with the Akt inhibitor GSK690693 at a concentration of 2 nM for 72 hours (Rhodes et al. 2008). Inhibition of Akt significantly reduced the expression of mesenchymal transcription factors including Snail, Twist, and Zeb1, and downregulated the cytoskeletal protein Vimentin. Simultaneously, epithelial markers such as E-cadherin and Occludin were restored (Fig. 5.1(A-C)). These results firmly establish that Akt activation is a critical downstream event following FBL loss, which facilitates EMT and contributes to loss of epithelial identity.

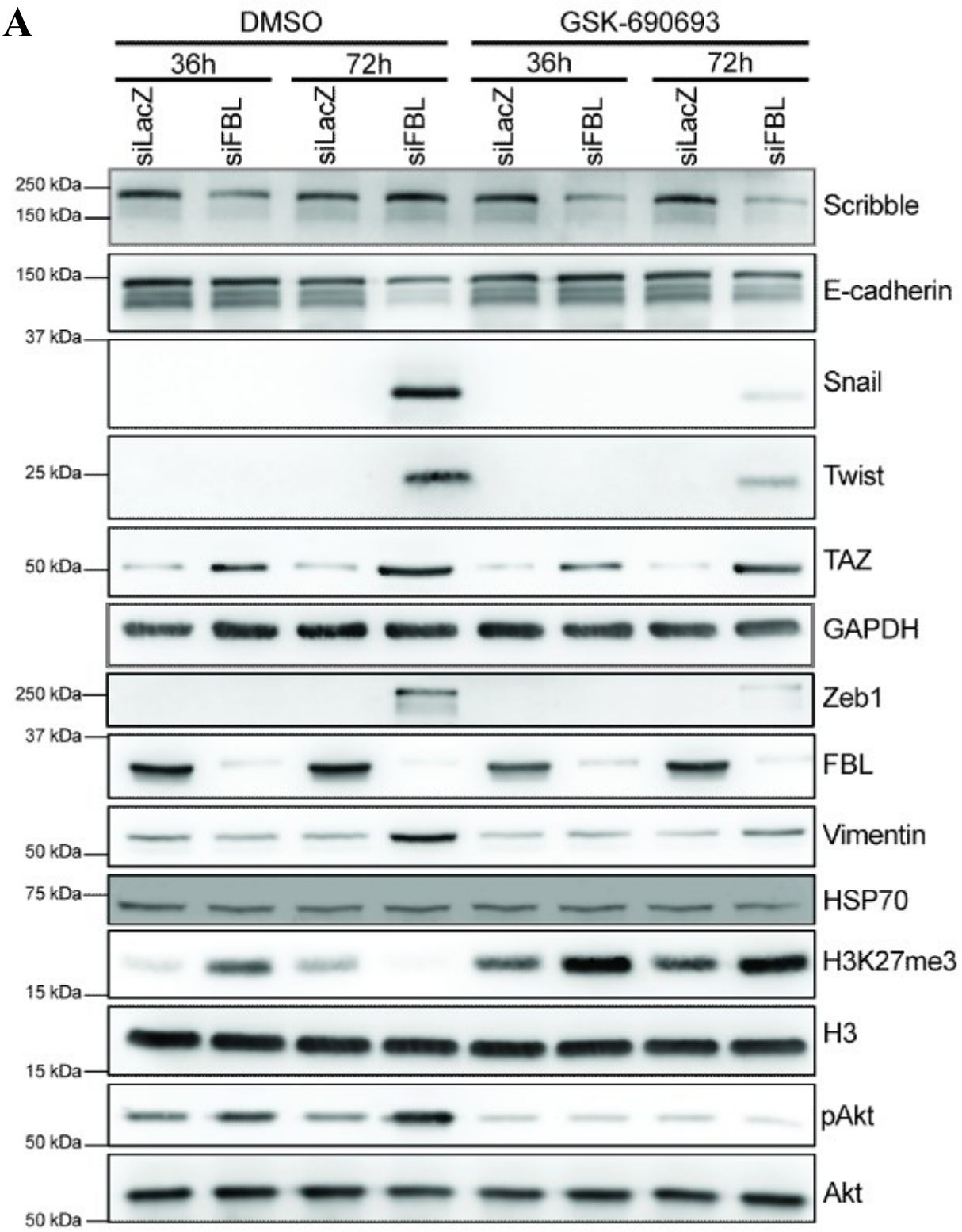
A
DMSO
GSK-690693
36h
72h
36h
72h
siLacZ
siFBL
siLacZ
siFBL
siLacZ
siFBL
siLacZ
siFBL
250 kDa
150 kDa
Scribble
150 kDa
E-cadherin
37 kDa
Snail
25 kDa
Twist
50 kDa
TAZ
GAPDH
250 kDa
Zeb1
37 kDa
FBL
50 kDa
Vimentin
75 kDa
HSP70
15 kDa
H3K27me3
15 kDa
H3
50 kDa
pAkt
50 kDa
Akt

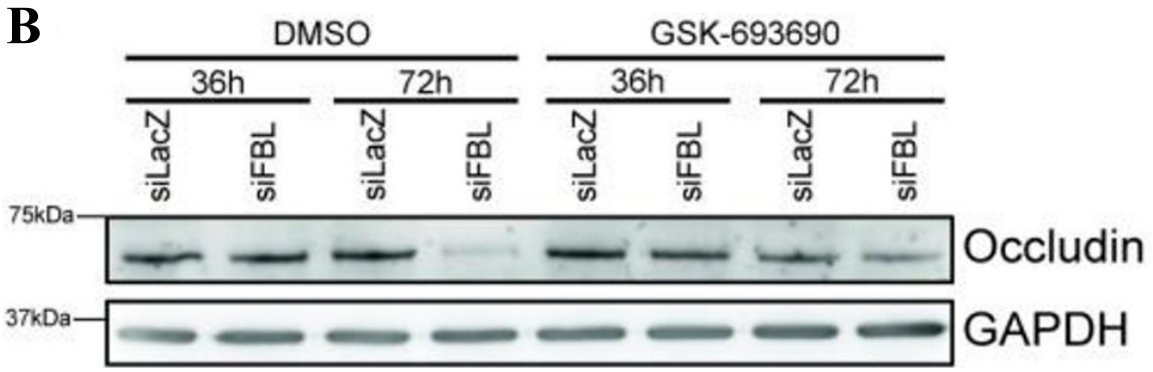
B
DMSO
GSK-693690
36h
72h
36h
72h
siLacZ
siFBL
siLacZ
siFBL
siLacZ
siFBL
siLacZ
siFBL
75kDa
Occludin
37kDa
GAPDH

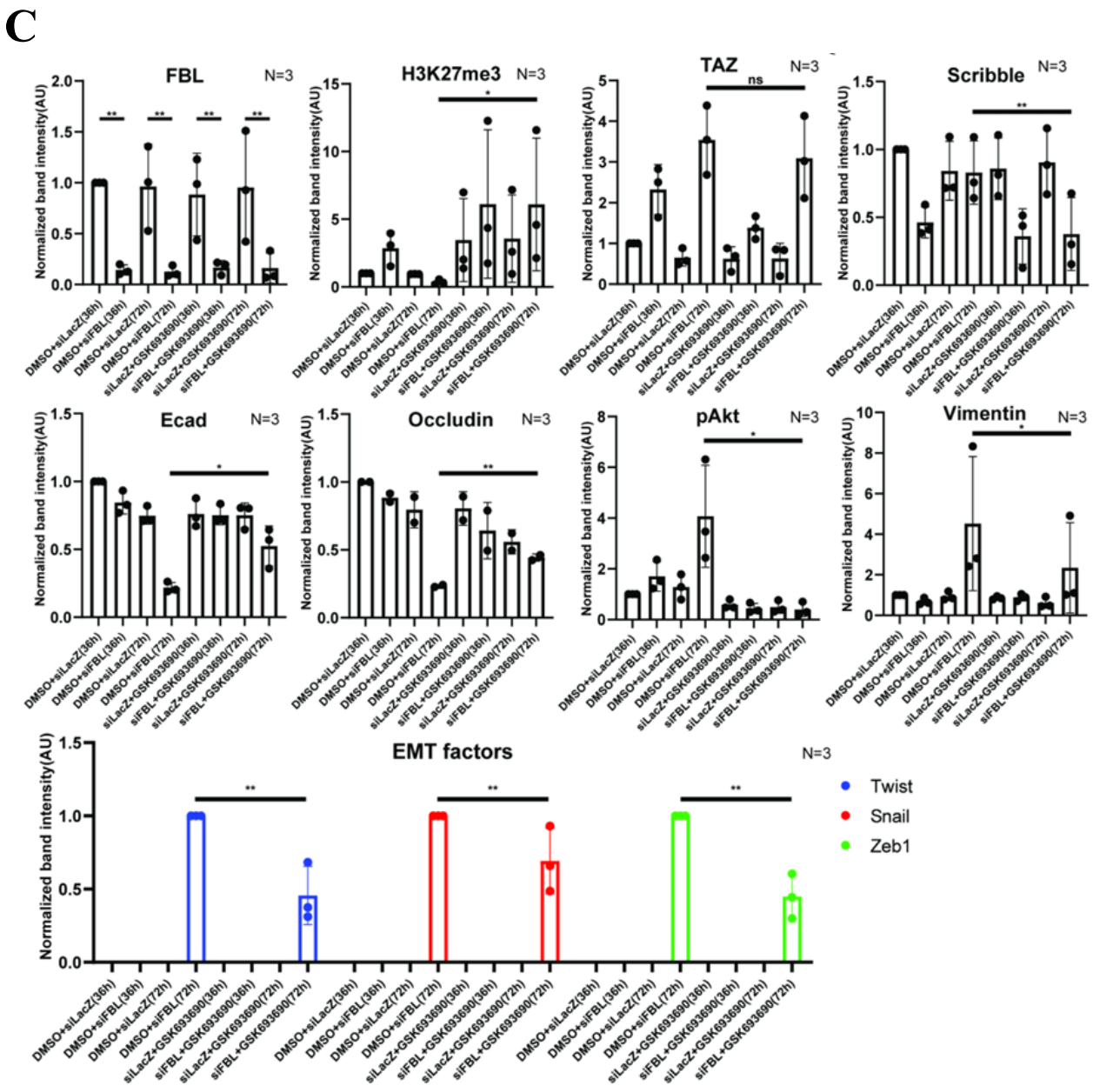
C
FBL
N=3
H3K27me3
N=3
TAZ
N=3
ns
Scribble
N=3
Ecad
N=3
Occludin
N=3
pAkt
N=3
Vimentin
N=3
EMT factors
N=3
Twist
Snail
Zeb1
Normalized band intensity(AU)
DMSO+siLacZ(36h)
DMSO+siFBL(36h)
DMSO+siLacZ(72h)
DMSO+siFBL(72h)
siLacZ+GSK693690(36h)
siFBL+GSK693690(36h)
siLacZ+GSK693690(72h)
siFBL+GSK693690(72h)

Fig. 5.1. Akt mitigates FBL depletion mediated EMT progression in MCF10A(p53DN)

(A) Representative immunoblots demonstrating rescue of EMT-associated phenotypes following Akt inhibition. Immunoblotting was performed for Scribble, E-cadherin, vimentin, Snail, Zeb1, Twist, pAkt, TAZ, FBL, and H3K27me3 in MCF10A(p53DN) cells transfected with siLacZ or siFBL for ~36 h and ~72 h, respectively, and treated with the Akt inhibitor GSK690693 (2 nM) or DMSO (control). HSP70, β-tubulin, histone H3, total Akt, and GAPDH were used as loading controls. Data were pooled from three independent biological replicates (N = 3). (B) Representative immunoblots showing Occludin protein levels in MCF10A(p53DN) cells transfected with siLacZ or siFBL for 36 h and 72 h and treated with the Akt inhibitor GSK690693 or DMSO (control). GAPDH was used as a loading control. Data were obtained from three independent biological replicates (N = 3). Statistical significance was assessed using an unpaired t-test. (C) Densitometric quantification of immunoblots demonstrating attenuation of EMT progression following treatment with GSK690693 in siLacZ- and siFBL-transfected MCF10A(p53DN) cells (Fig. 6E). Statistical significance was assessed using an unpaired t-test. Error bars represent SD; *$p < 0.05$, **$p < 0.01$.

5.2.2. Extended FBL Knockdown Stabilizes TAZ, a Key EMT Regulator

In addition to activating the Akt pathway, FBL depletion also impacted the Hippo signaling cascade, a major regulator of cellular proliferation and differentiation. Specifically, we observed that FBL knockdown resulted in the stabilization of TAZ, a transcriptional co-activator and downstream effector of the Hippo pathway. TAZ is known to drive EMT by enhancing the expression of Snail and Foxc2, both of which are potent inducers of mesenchymal traits.

In MCF10A(p53DN) cells, FBL depletion led to a progressive accumulation of TAZ, particularly upon extended knockdown or disruption of the FBL–EZH2 interaction through the expression of a mutant FBL construct (GFP-ΔRBD-FBL). This stabilization of TAZ was accompanied by the upregulation of EMT-related transcription factors such as Snail, Twist, and Zeb1, reinforcing the role of TAZ in mediating mesenchymal transformation (Fig. 5.3(F-I)). Taken together, these findings reveal that FBL loss promotes EMT not only through Akt activation but also via deregulation of Hippo signaling and stabilization of TAZ, amplifying the transcriptional program necessary for epithelial plasticity.

5.2.3. Scribble is Retained in the Cytoplasm Upon FBL Depletion

Although Scribble levels were initially reduced upon short-term FBL depletion (~36 hours), extended knockdown (~72 hours) resulted in a partial recovery of total protein levels. However, despite this recovery, Scribble remained mislocalized within the cytoplasm rather than at the plasma membrane where it typically functions to regulate polarity and suppress oncogenic signaling (Olmeda et al. 2007; Abedrabbo and Ravid 2020).

This mislocalization is likely driven by elevated levels of Snail, an EMT transcription factor known to facilitate the internalization and cytoplasmic retention of Scribble. Supporting this hypothesis, the aggressive and mesenchymal-like breast cancer cell line MDA-MB-231, which constitutively expresses Snail, also exhibits a predominantly cytoplasmic distribution of Scribble.

To interrogate the mechanistic link between FBL loss and Scribble mislocalization, we depleted FBL in MCF10A(p53DN) cells for ~72 h. We observed cytoplasmic retention of Scribble in the cytoplasm in FBL depleted cells (Fig. 5.2(A-B)). This was concomitant with the expression of Snail in FBL depleted cells upon prolonged FBL depletion (Fig. 5.3A).

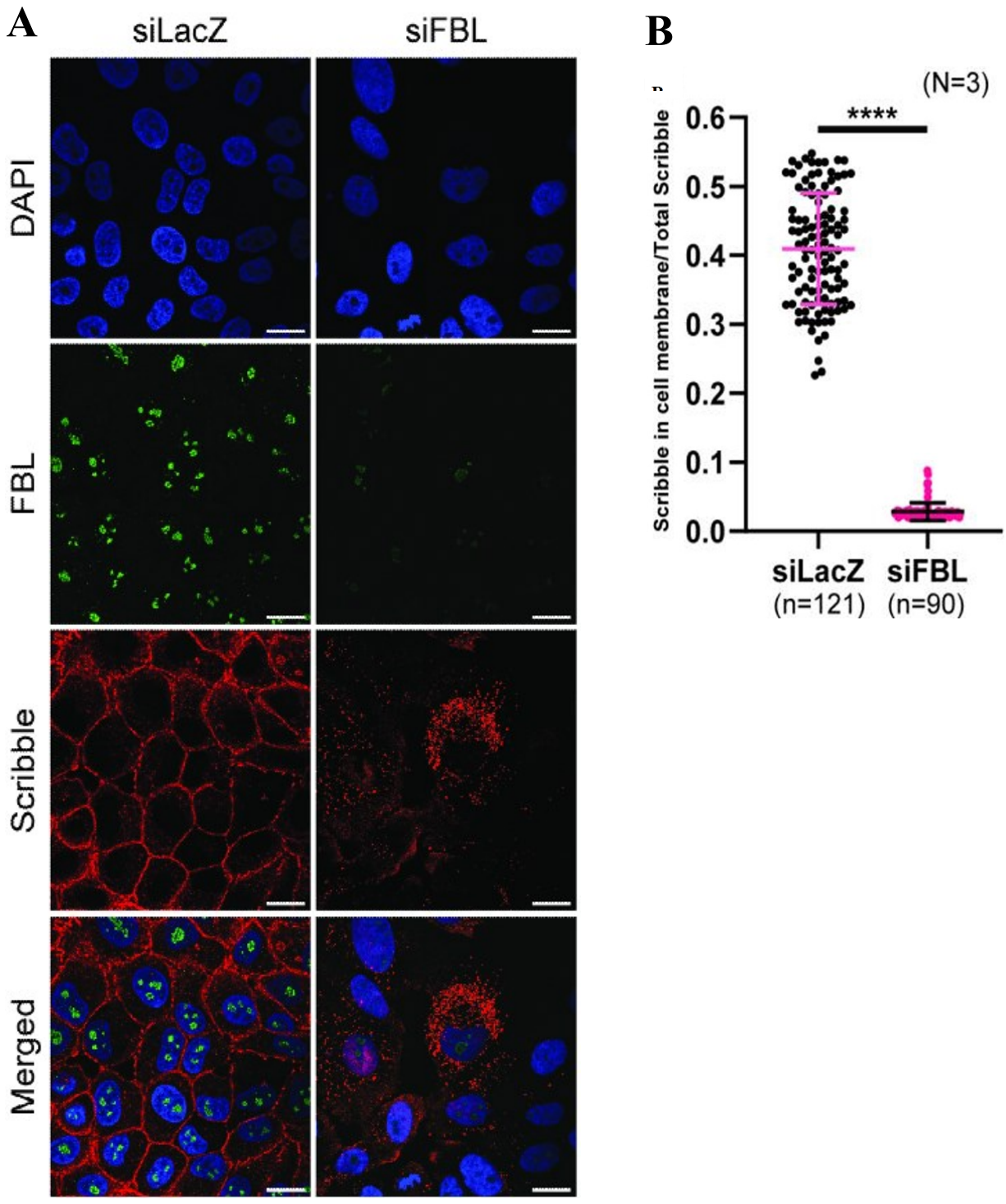

Fig. 5.2. FBL depletion causes cytoplasmic retention of Scribble

(A) Representative immunofluorescence images illustrating SCRIB internalization in cells transfected with siLacZ or siFBL for 72 h. Nuclei are visualized by DAPI staining, Scribble is shown in red, and FBL in green. Quantification was performed on 211 cells pooled from three independent biological replicates (N = 3). Scale bar, 20 μm. (B) Quantification of Scribble

internalization in MCF10A(p53DN) cells, expressed as the ratio of Scribble fluorescence intensity at the cell border to that of the entire cell. Measurements were obtained from 211 cells pooled across three independent biological replicates (N = 3).

5.2.4. Extended FBL Knockdown Increases Mesenchymal Markers and Reduces Epithelial Markers

Short-term FBL depletion had a negligible effect on EMT markers. However, upon prolonged knockdown (~72 hours), a robust induction of mesenchymal genes including Snail1, Twist1, and Zeb1 was observed. These changes were accompanied by a significant reduction in epithelial junction proteins such as E-cadherin and Occludin, indicating a full EMT response (Fig. 5.3 (A-C)).

Protein-level analysis using immunoblotting and immunofluorescence confirmed this transcriptional reprogramming. Vimentin levels increased markedly, while E-cadherin decreased. These EMT markers were further exaggerated in cells overexpressing GFP-ΔRBD-FBL in an FBL-depleted background, further highlighting the importance of the FBL–EZH2 interaction in maintaining epithelial identity (Fig. 5.3(F, G, I)).

To understand the dynamics of chromatin regulation during this process, we performed ChIP-PCR on the SCRIB promoter. Initially, elevated levels of EZH2 and H3K27me3 were detected, which suppressed Scribble expression. Interestingly, by 72 hours, both EZH2 and H3K27me3 enrichment at the SCRIB promoter declined, correlating with the partial recovery of Scribble protein observed earlier. This suggests a temporal reprogramming of chromatin modifications that accompanies extended FBL depletion and EMT progression (Fig. 5.3E).

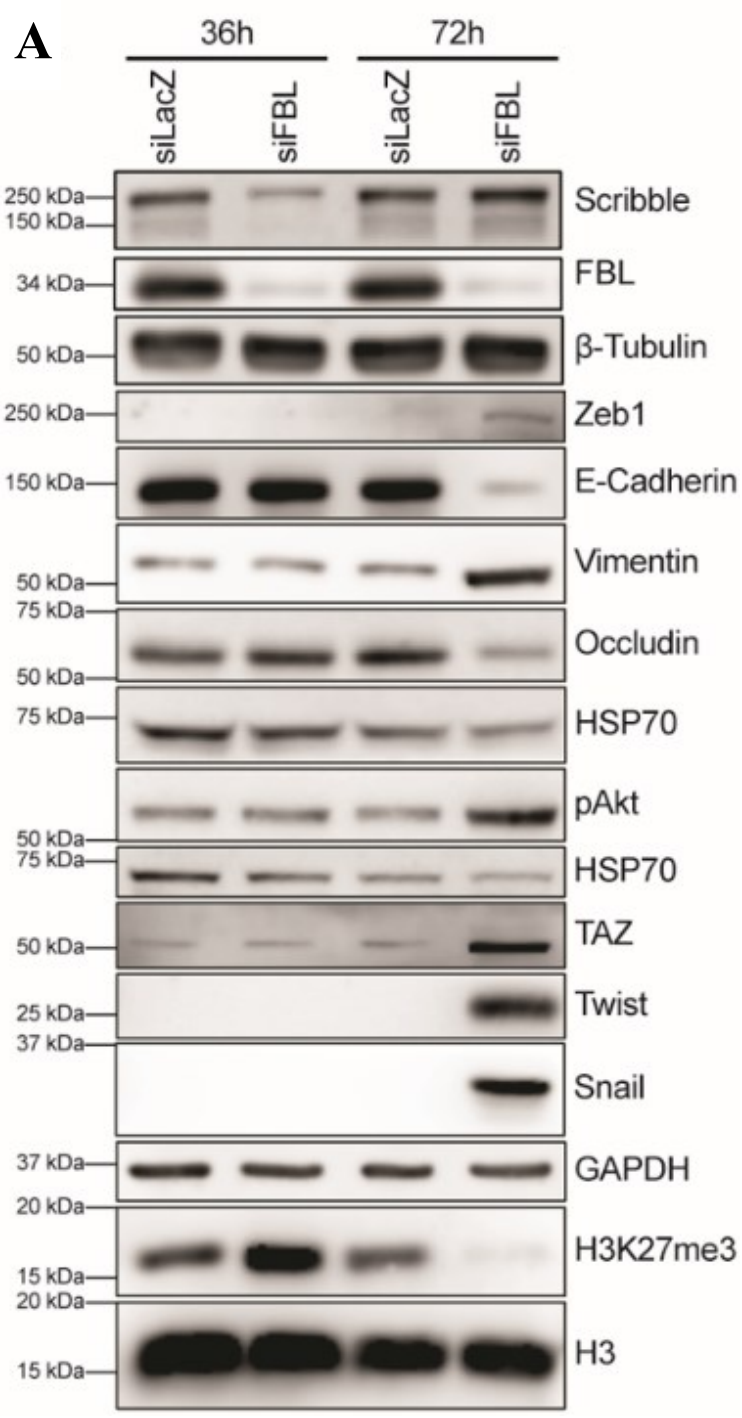
A
36h
72h
siLacZ
siFBL
siLacZ
siFBL
250 kDa
150 kDa
Scribble
34 kDa
FBL
50 kDa
β-Tubulin
250 kDa
Zeb1
150 kDa
E-Cadherin
50 kDa
Vimentin
75 kDa
Occludin
50 kDa
75 kDa
HSP70
50 kDa
pAkt
75 kDa
HSP70
50 kDa
TAZ
25 kDa
Twist
37 kDa
Snail
37 kDa
GAPDH
20 kDa
H3K27me3
15 kDa
20 kDa
H3
15 kDa

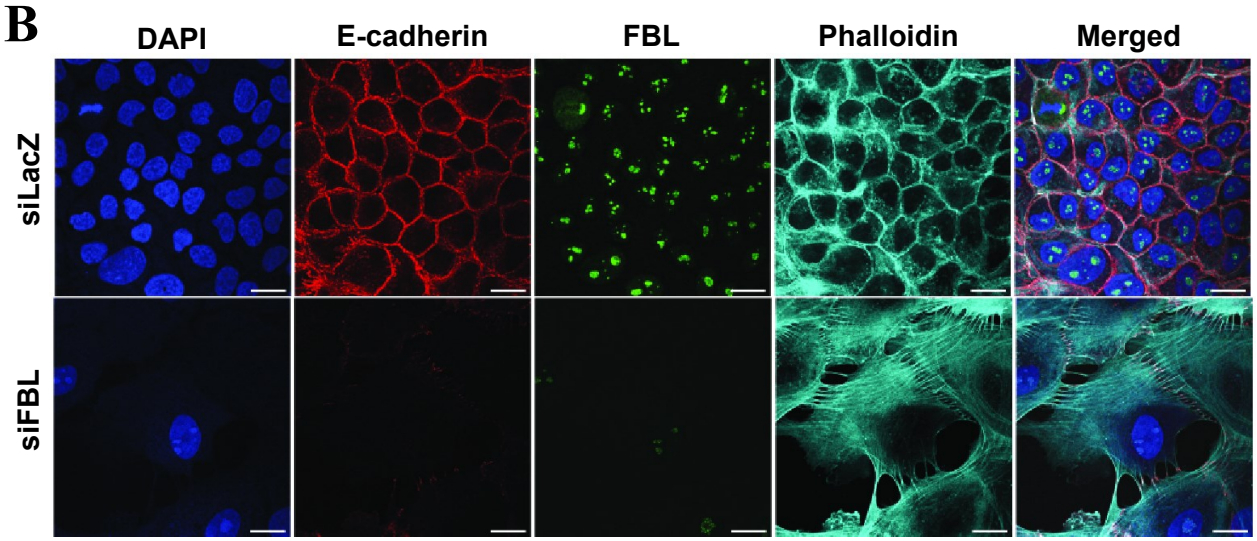
B
DAPI
E-cadherin
FBL
Phalloidin
Merged
siLacZ
siFBL

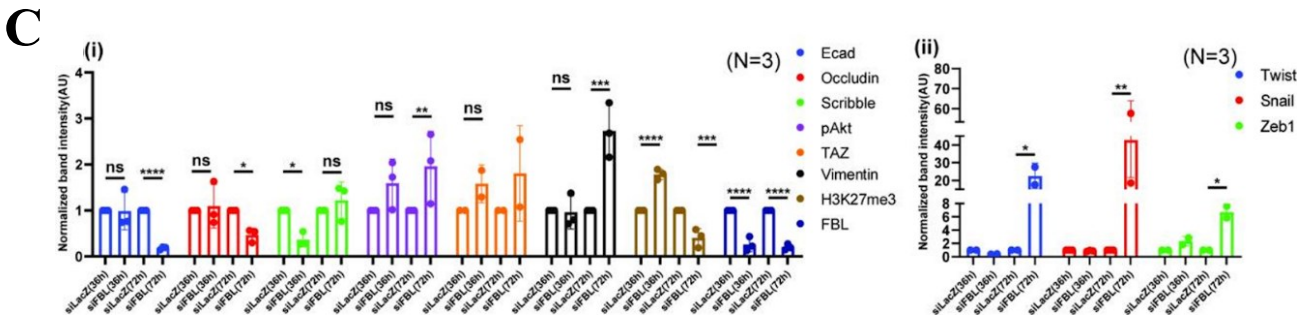
C
(i)
(N=3)
Normalized band intensity(AU)
Ecad
Occludin
Scribble
pAkt
TAZ
Vimentin
H3K27me3
FBL
(ii)
(N=3)
Twist
Snail
Zeb1

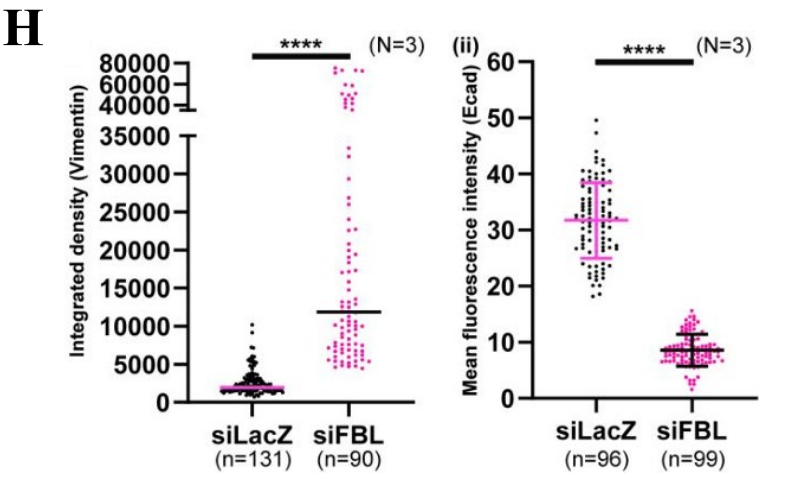
H
****
(N=3)
Integrated density (Vimentin)
siLacZ
(n=131)
siFBL
(n=90)
(ii)
Mean fluorescence intensity (Ecad)
siLacZ
(n=96)
siFBL
(n=99)

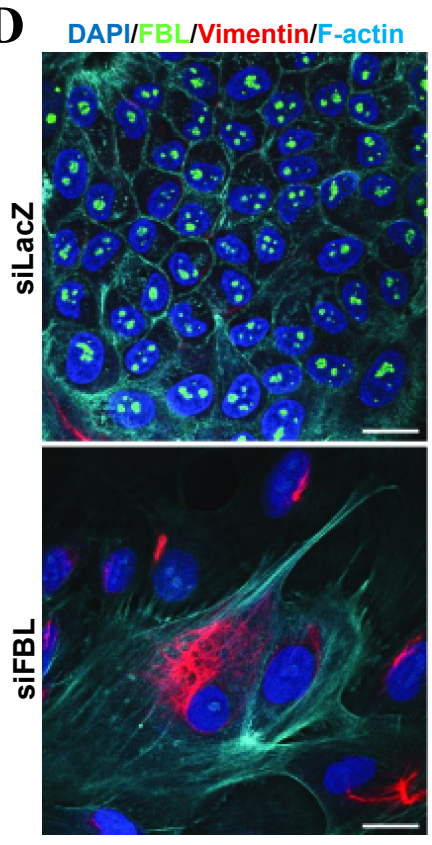
D
DAPI/FBL/Vimentin/F-actin
siLacZ
siFBL

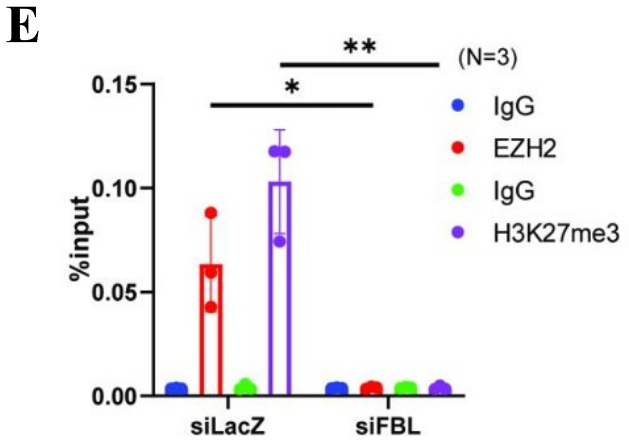
E
**
*
(N=3)
IgG
EZH2
IgG
H3K27me3
%input
siLacZ
siFBL

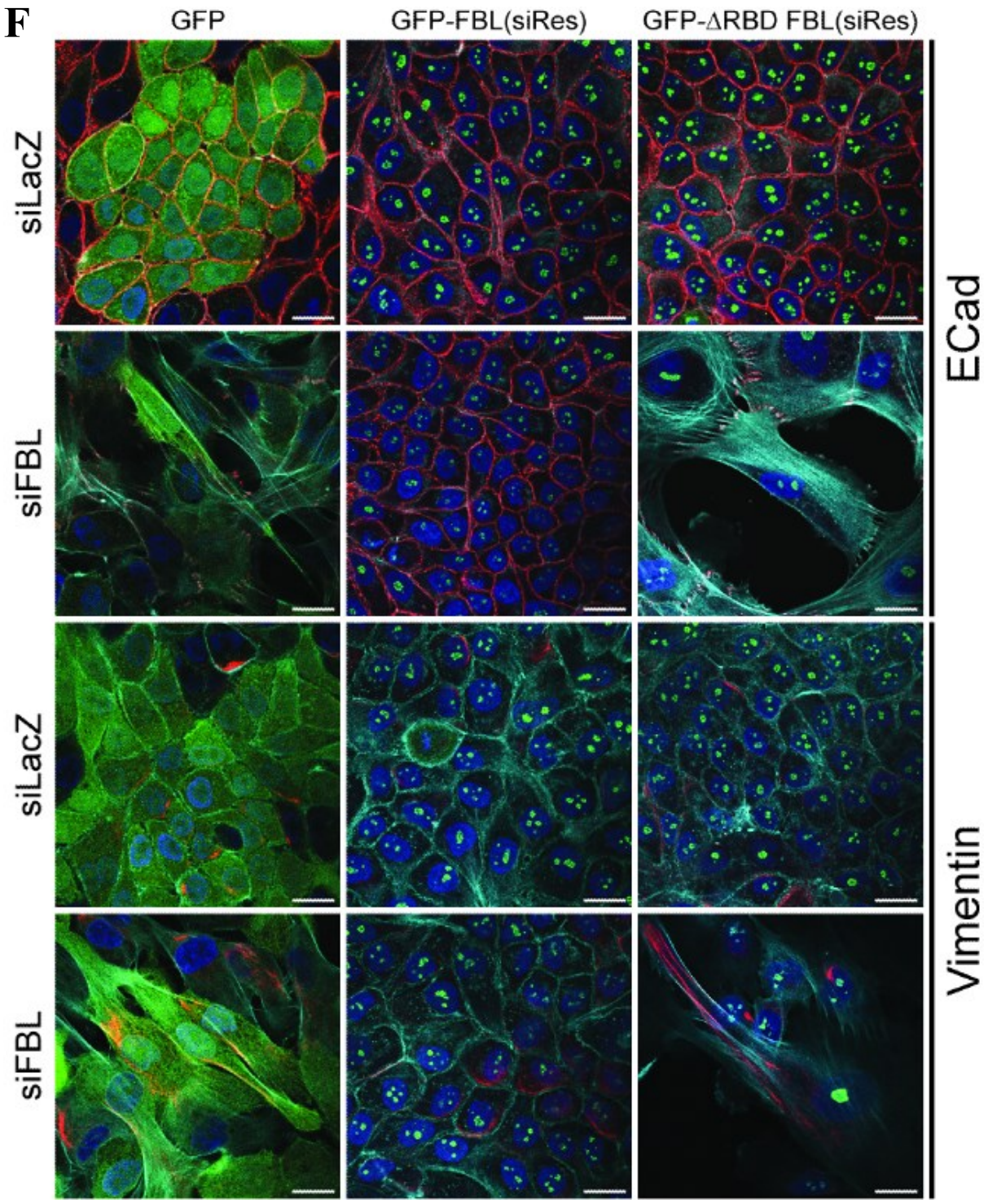
F
GFP
GFP-FBL(siRes)
GFP-ΔRBD FBL(siRes)
siLacZ
siFBL
siLacZ
siFBL
ECad
Vimentin

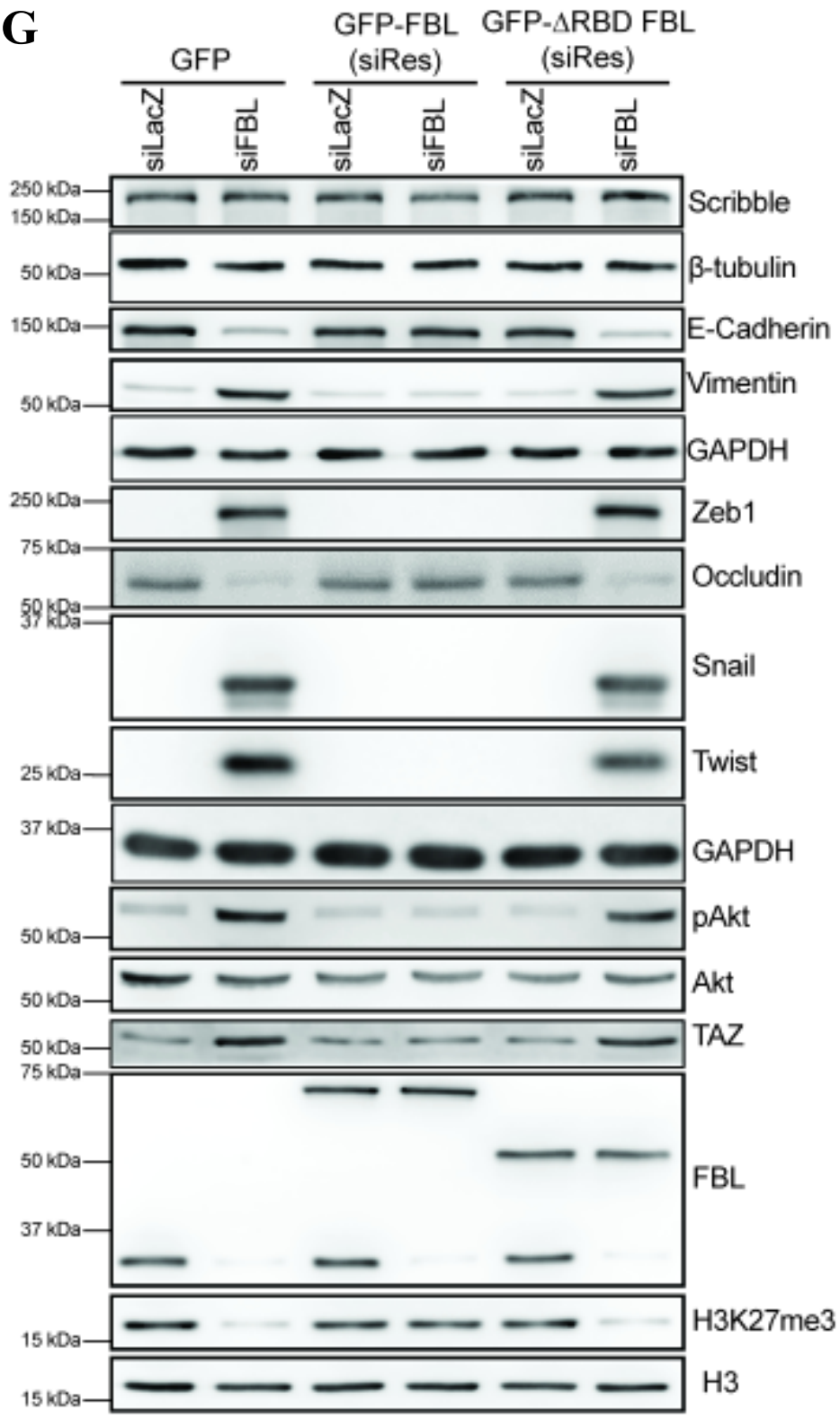
G
GFP
GFP-FBL (siRes)
GFP-ΔRBD FBL (siRes)
siLacZ
siFBL
siLacZ
siFBL
siLacZ
siFBL
250 kDa
150 kDa
Scribble
50 kDa
β-tubulin
150 kDa
E-Cadherin
Vimentin
50 kDa
GAPDH
250 kDa
Zeb1
75 kDa
Occludin
50 kDa
37 kDa
Snail
Twist
25 kDa
37 kDa
GAPDH
pAkt
50 kDa
Akt
50 kDa
TAZ
50 kDa
75 kDa
FBL
50 kDa
37 kDa
H3K27me3
15 kDa
H3
15 kDa

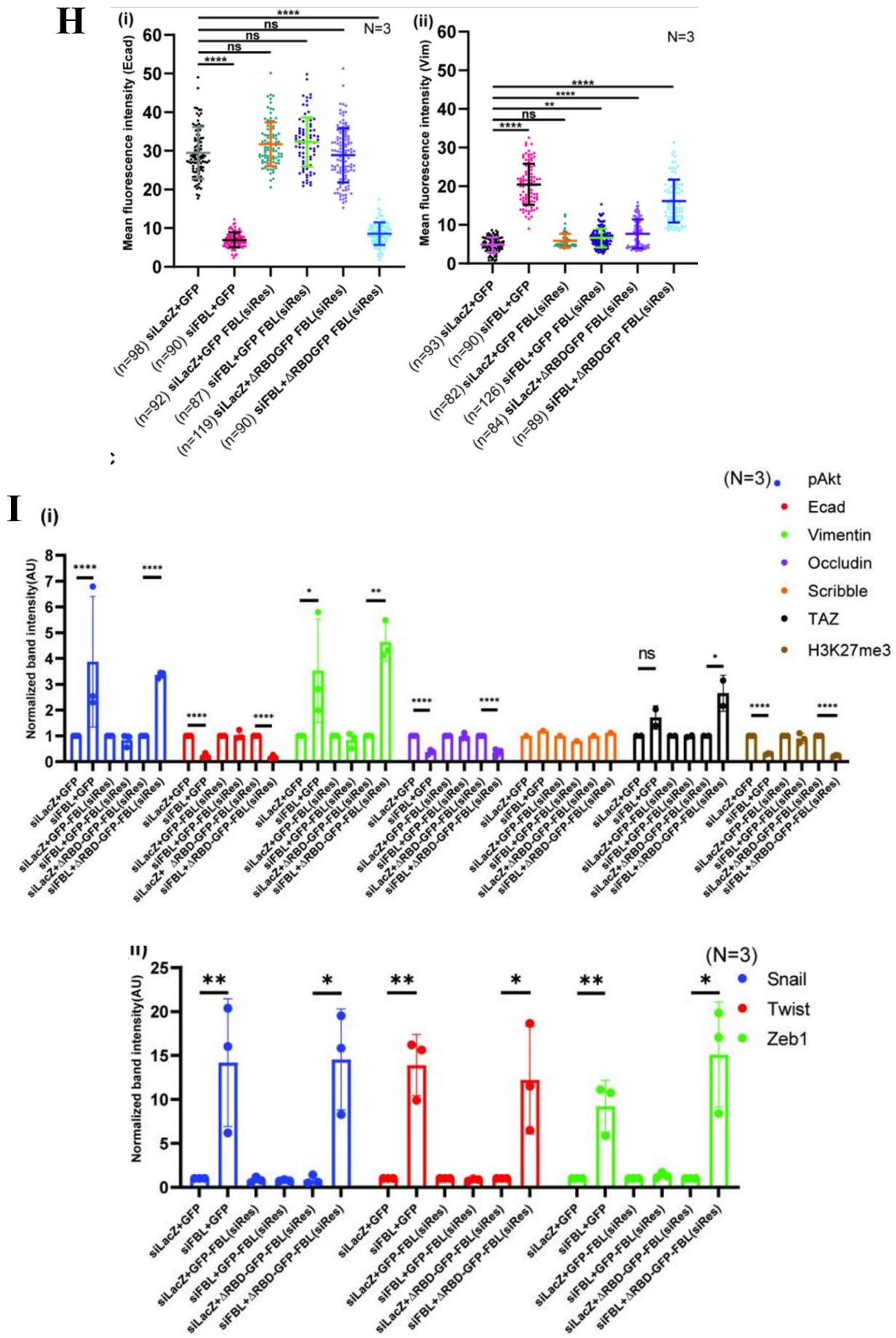
H
(i)
Mean fluorescence intensity (Ecad)
N=3
(ii)
Mean fluorescence intensity (Vim)
N=3
(n=98) siLacZ+GFP
(n=90) siFBL+GFP
(n=92) siLacZ+GFP FBL(siRes)
(n=87) siFBL+GFP FBL(siRes)
(n=119) siLacZ+ΔRBDGFP FBL(siRes)
(n=90) siFBL+ΔRBDGFP FBL(siRes)
(n=93) siLacZ+GFP
(n=90) siFBL+GFP
(n=82) siLacZ+GFP FBL(siRes)
(n=126) siFBL+GFP FBL(siRes)
(n=84) siLacZ+ΔRBDGFP FBL(siRes)
(n=89) siFBL+ΔRBDGFP FBL(siRes)
I
(i)
(N=3)
pAkt
Ecad
Vimentin
Occludin
Scribble
TAZ
H3K27me3
Normalized band intensity(AU)
siLacZ+GFP
siFBL+GFP
siLacZ+GFP-FBL(siRes)
siFBL+GFP-FBL(siRes)
siLacZ+ΔRBD-GFP-FBL(siRes)
siFBL+ΔRBD-GFP-FBL(siRes)
(ii)
(N=3)
Snail
Twist
Zeb1
Normalized band intensity(AU)

Fig. 5.3. Prolonged FBL depletion triggers EMT in MCF10A(p53DN)

(A) Representative immunoblots depicting Scribble, occludin, E-cadherin, vimentin, Snail, Zeb1, Twist, pAkt, TAZ, FBL, and H3K27me3 protein levels in MCF10A(p53DN) cells transfected with siLacZ or siFBL for 36 h and 72 h. The first HSP70 blot served as the loading control for Zeb1, E-cadherin, vimentin, and occludin, while the second HSP70 blot was used as the loading control for pAkt. β-tubulin, histone H3, and GAPDH were used as additional loading controls. Data were pooled from three independent biological replicates (N = 3). (B) Representative immunofluorescence images showing FBL (green), E-cadherin (red), F-actin (phalloidin; cyan), and nuclei (DAPI; blue) following FBL depletion for ~72 h, demonstrating reduced E-cadherin levels. Data were pooled from 416 cells across three independent biological replicates (N = 3). (C) Densitometric quantification of immunoblots demonstrating EMT induction upon FBL depletion (Fig. 6A). Data were obtained from three independent biological replicates (N = 3). Statistical significance was assessed using one-way ANOVA and unpaired t-tests. (D) Representative immunofluorescence images depicting FBL (green), Vimentin (red), F-actin (phalloidin; cyan), and nuclei (DAPI; blue) following ~72 h of FBL depletion, showing reduced E-cadherin levels accompanied by increased vimentin expression. Data were pooled from 416 cells across three independent biological replicates (N = 3). (E) Bar graphs depicting ChIP–qPCR enrichment of EZH2 and H3K27me3 at the SCRIB promoter in MCF10A(p53DN) cells transfected with siLacZ or siFBL for 72 h. Data were obtained from three independent biological replicates (N = 3). Statistical significance was assessed using unpaired t-tests. (F) Representative immunofluorescence images showing E-cadherin or vimentin (red), F-actin (phalloidin; cyan), and nuclei (DAPI; blue) in MCF10A(p53DN) cells overexpressing GFP, GFP-FBL(siRes), or ΔRBD-GFP-FBL(siRes) following transfection with siLacZ or siFBL for 72 h. Data were pooled from three independent biological replicates (N = 3). (G) Representative immunoblots demonstrating EMT induction following ~72 h of disruption of the FBL–EZH2 interaction in MCF10A(p53DN) cells overexpressing GFP, GFP-FBL(siRes), or ΔRBD-GFP-FBL(siRes) and transfected with siLacZ or siFBL. Immunoblotting was performed for Scribble, occludin, E-cadherin, vimentin, Snail, Zeb1, Twist, pAkt, TAZ, FBL, and H3K27me3, with HSP70, β-tubulin, histone H3, total Akt, and GAPDH used as loading controls. Data were obtained from three independent biological replicates (N = 3). (H) Quantitative analysis of mean fluorescence intensity of vimentin and E-cadherin in MCF10A(p53DN) cells expressing GFP, GFP-FBL(siRes), or GFP-RBD-FBL(siRes) and transfected with siLacZ or siFBL, as shown in Fig. 6F. Data were obtained from three independent biological experiments (N = 3). Statistical significance was assessed

using the Brown–Forsythe and Welch ANOVA tests. (I) Densitometric quantification of the immunoblots shown in Fig. 6D. Data were obtained from three independent biological replicates (N = 3). Statistical significance was assessed using unpaired t-tests.

5.2.5. FBL-Depleted Cells Exhibit Enhanced Tumorigenesis in Xenograft Models

To determine the in vivo relevance of our in vitro findings, we evaluated the tumorigenic potential of FBL-depleted cells using a xenograft model. DLD-1 colorectal cancer cells stably expressing shFBL under a Tet-ON promoter were subcutaneously injected into NOD-SCID mice. FBL knockdown was induced by doxycycline administration via drinking water, which was refreshed every 72 hours.

Compared to control animals, doxycycline-treated mice showed accelerated tumor growth, as evidenced by increased tumor volumes and higher final tumor weights by day 35 post-injection (Fig. 5.4(A-E)). These data underscore the tumor-suppressive role of FBL in colorectal cancer and highlight its importance in maintaining the balance between epithelial homeostasis and tumor progression.

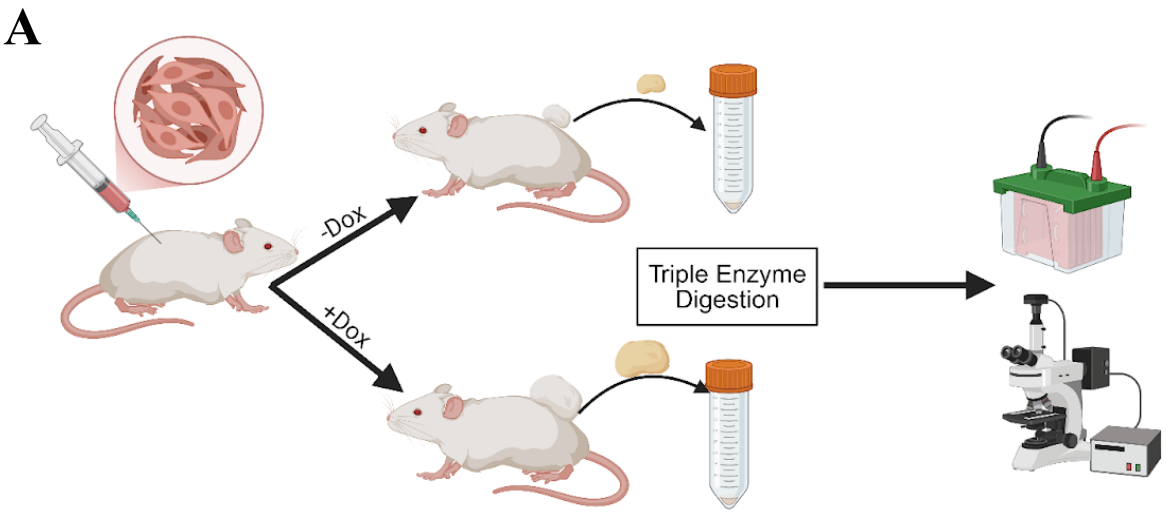
A
-Dox
+Dox
Triple Enzyme Digestion

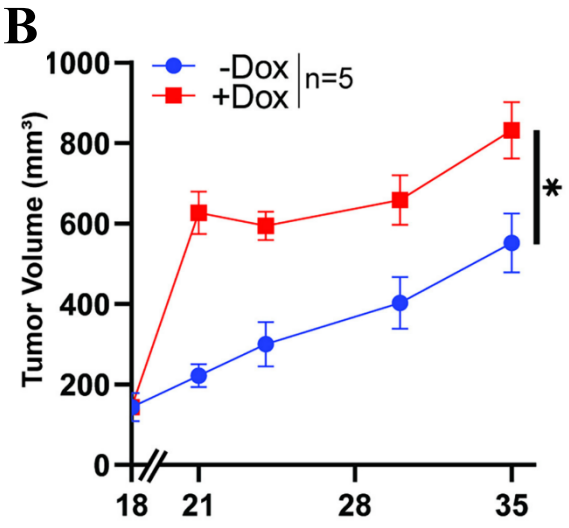
B
Tumor Volume (mm³)
1000
800
600
400
200
0
-Dox
+Dox
n=5
*
18
21
28
35

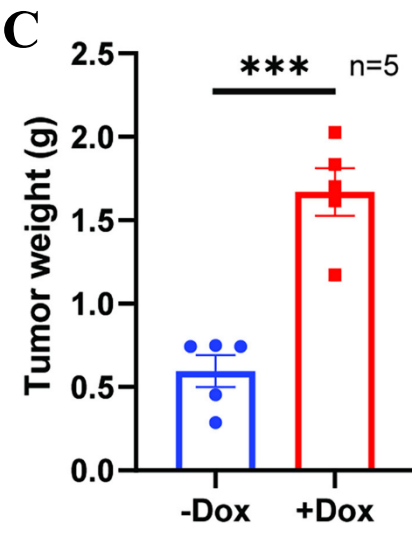
C
Tumor weight (g)
2.5
2.0
1.5
1.0
0.5
0.0
***
n=5
-Dox
+Dox

D

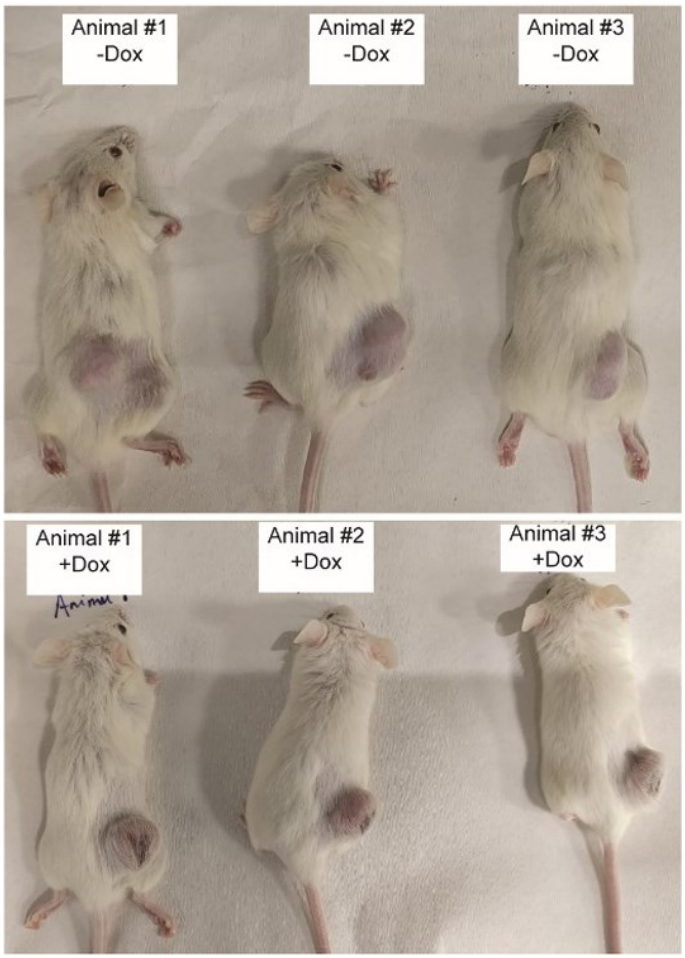
Animal #1
-Dox
Animal #2
-Dox
Animal #3
-Dox
Animal #1
+Dox
Animal #2
+Dox
Animal #3
+Dox

E

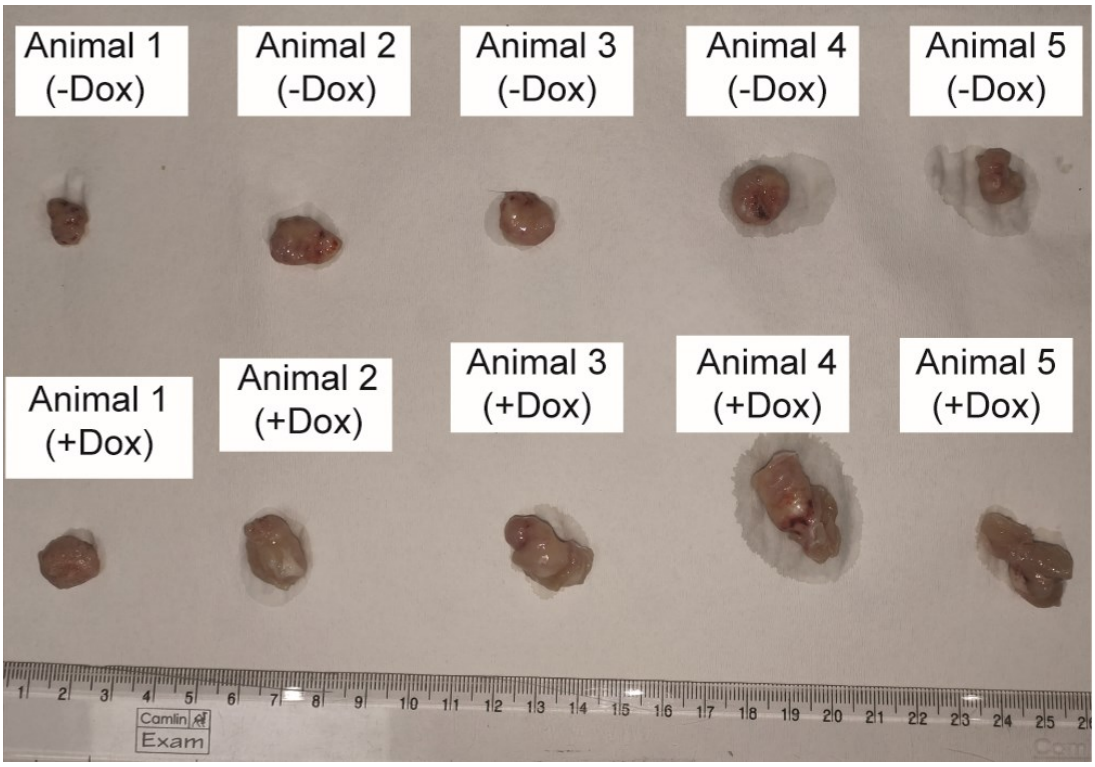
Animal 1
(-Dox)
Animal 2
(-Dox)
Animal 3
(-Dox)
Animal 4
(-Dox)
Animal 5
(-Dox)
Animal 1
(+Dox)
Animal 2
(+Dox)
Animal 3
(+Dox)
Animal 4
(+Dox)
Animal 5
(+Dox)

Fig. 5.4. FBL depletion promotes increased tumorigenic potential in xenograft models
(A) Schematic illustration of xenograft experiments conducted in NOD/SCID mice, outlining tumor establishment, tissue harvest, and subsequent processing for immunoblotting and immunofluorescence analyses. **(B)** Quantitative assessment of tumor growth over a 35-day period in mice with or without doxycycline (Dox) treatment (n = 5). Error bars represent SD; *p < 0.5. **(C)** Tumor weights measured after excision from mice (n = 5). Error bars represent SD; ***p < 0.001. **(D)** Representative images of NOD/SCID mice bearing subcutaneous tumors generated from DLD-1 cells expressing a doxycycline (Dox)–inducible shRNA targeting FBL (shFBL). Cells were injected into the right flank, and mice were maintained either without Dox (−Dox; top row) or with Dox (+Dox; bottom row) in the drinking water to induce shFBL expression. **(E)** Representative images of tumors excised from mice 35 days after injection (n = 5).

5.2.6 EZH2 Mislocalization Observed in FBL-Depleted Xenografts

Histological examination of xenograft tumors revealed a substantial reduction in nucleolar EZH2 localization in FBL-depleted tissues. Co-immunostaining with Nucleolin, a marker of the nucleolar granular component, confirmed that the majority of EZH2 was displaced from the nucleolus to the nucleoplasm upon FBL loss (Fig. 5.5(A-B)).
This observation mirrors our in vitro findings and suggests that FBL is essential for the nucleolar retention of a subset of EZH2 molecules. In its absence, EZH2 is redistributed to the nucleoplasm, where it may aberrantly engage in gene repression programs, including those targeting epithelial polarity genes such as Scribble.

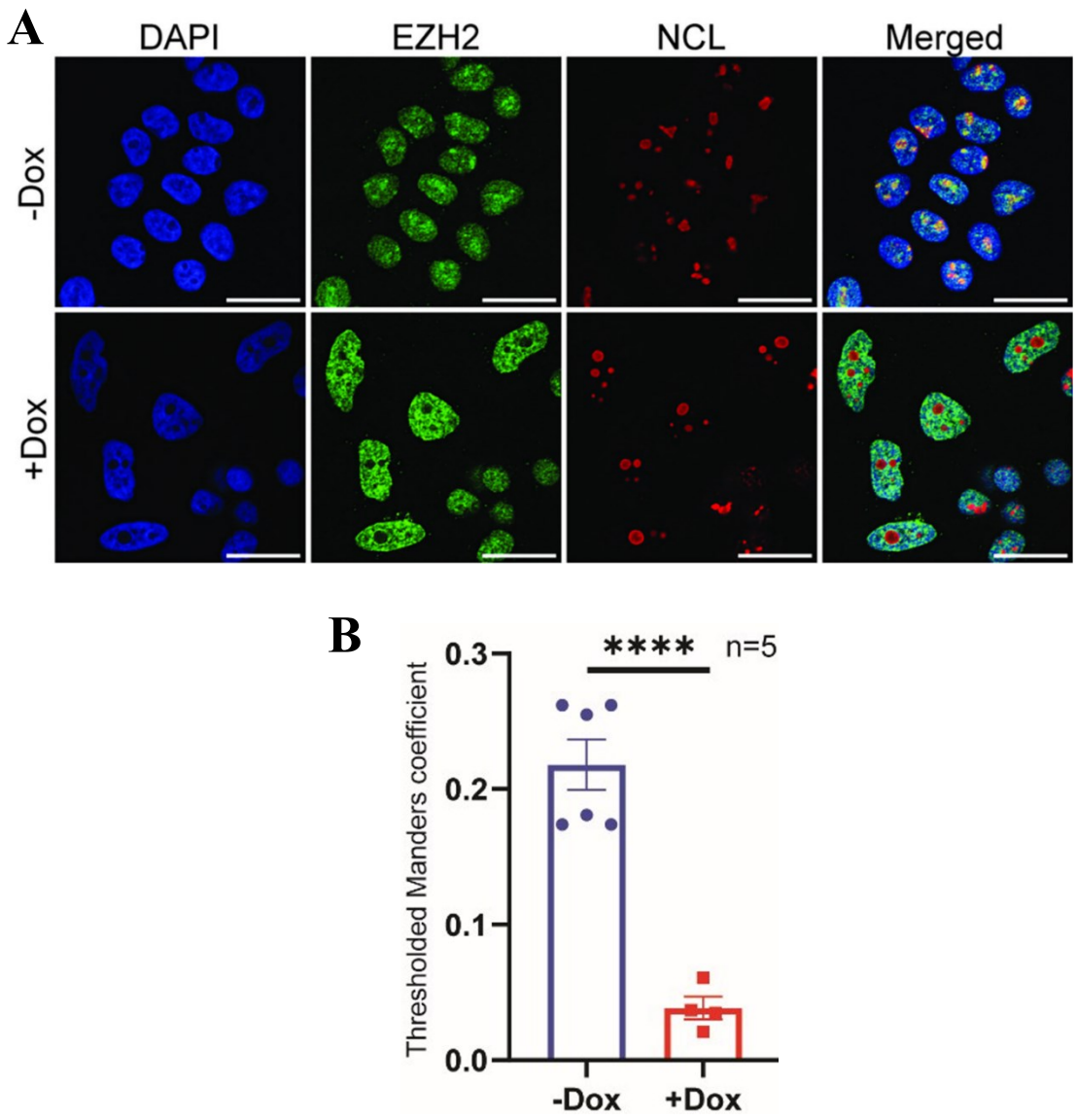

Fig. 5.5. EZH2 displays aberrant subcellular localization in FBL-depleted xenograft tumors

(A) Representative immunofluorescence images showing EZH2 and nucleolin (NCL) in MCF10A(p53DN) and DLD-1 cells transfected with siLacZ or siFBL. Nuclei are visualized by DAPI staining, EZH2 is shown in green, and NCL in red. Quantification was performed on ≥90 cells, with data pooled from three independent biological replicates (N = 3). Scale bar, 20 µm. **(B)** Colocalization analysis of EZH2 and nucleolin (NCL). Statistical significance was assessed using an unpaired t-test. Error bars represent SD; ****$p < 0.0001$.

5.2.7 Scribble Downregulation Confirmed in Tumor Tissues

Consistent with the changes observed in cultured cells, tumor lysates from FBL-depleted mice displayed markedly reduced Scribble protein levels. This downregulation correlated with an increase in global H3K27me3 levels, confirming the enhanced activity of the PRC2 complex in the absence of FBL (Fig. 5.6 (A-B)).

The coordinated reduction in Scribble, increased H3K27me3 deposition, and concurrent mislocalization of EZH2 collectively support a model wherein FBL orchestrates a chromatin-based mechanism to preserve epithelial integrity. Its depletion promotes a cascade of molecular events leading to EMT and tumor progression, reinforcing the significance of the FBL–EZH2–Scribble axis as a key regulatory module in epithelial biology and cancer.

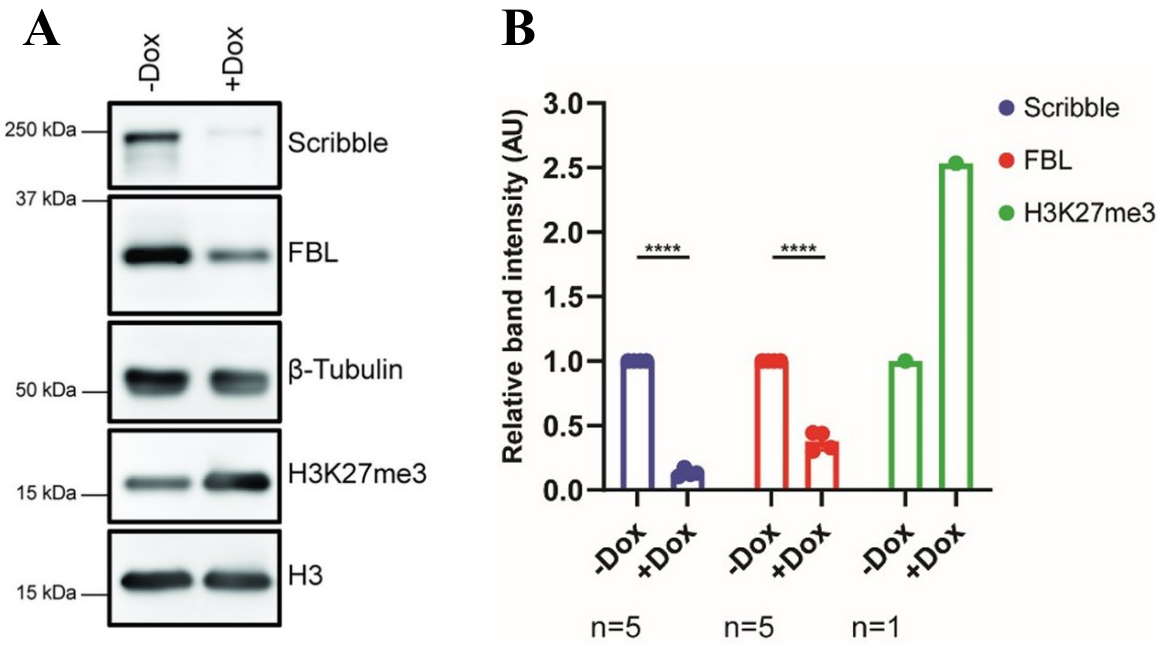

Fig. 5.6. Scribble downregulation and increased H3K27me3 enrichment are confirmed in tumor tissues

(A) Representative immunoblots showing Scribble, E-cadherin, FBL, and H3K27me3 protein levels in tumor-derived cells, with β-tubulin and histone H3 used as loading controls. **(B)** Densitometric quantification of the immunoblots shown in Fig. 5.6.A.

5.2.8 FBL-Depleted Cells Promote Lung Infiltration in Xenograft Mice

FBL knockdown leads to significantly enhanced tumor growth in vivo, as seen in subcutaneous xenograft models using Tet-inducible shFBL-expressing DLD-1 cells. Doxycycline (administered every 72 hours) sustained FBL depletion and resulted in markedly larger tumors, consistent with its role in maintaining epithelial homeostasis and suppressing tumor progression.

To assess the impact of FBL depletion on metastatic potential, we performed tail-vein injections in NOD-SCID mice with the same shFBL-expressing DLD-1 cells. Mice receiving Dox exhibited a substantial increase in metastatic lung colonization compared to controls. Histological analysis of H&E-stained lung sections revealed extensive metastatic foci, which correlated with progressive body weight loss—suggesting systemic disease burden. Importantly EZH2 histone methyltransferase known to promote epithelial-to-mesenchymal transition (EMT), invasion, and metastasis in multiple cancer models. EZH2 has been shown to directly repress E-cadherin (CDH1) and promote metastasis via its methyltransferase activity and PRC2 complex function (Cao et al. 2008; Fujii and Ochiai 2008).

Mechanistically, EZH2 overexpression has been implicated in silencing epithelial markers and upregulating mesenchymal programs across various tumor types. In breast and prostate cancers, elevated EZH2 expression correlates with poor prognosis and increased risk of metastasis (Chang et al. 2011; Kleer et al. 2003). EZH2 also promotes metastatic outgrowth by repressing metastasis suppressor genes such as RKIP and DAB2IP (Zong et al. 2020; Ren et al. 2012).

In our model, FBL depletion—by mislocalizing EZH2 to the nucleoplasm and increasing its chromatin-associated activity—likely contributes to a transcriptional reprogramming that favors metastatic dissemination. The observed increase in H3K27me3 levels in tumor and lung tissues supports enhanced PRC2 activity following FBL loss.

For quantitative analysis of lung metastases, metastatic burden was scored from H&E-stained lung sections using FIJI (ImageJ). The metastatic score was defined as:

Metastatic Score = (Total metastatic area / Total lung area) × 100

This scoring revealed a significant increase in metastatic infiltration in +Dox mice, providing strong evidence that FBL functions as a suppressor of metastasis, potentially through regulation of the EZH2-H3K27me3 axis.

A

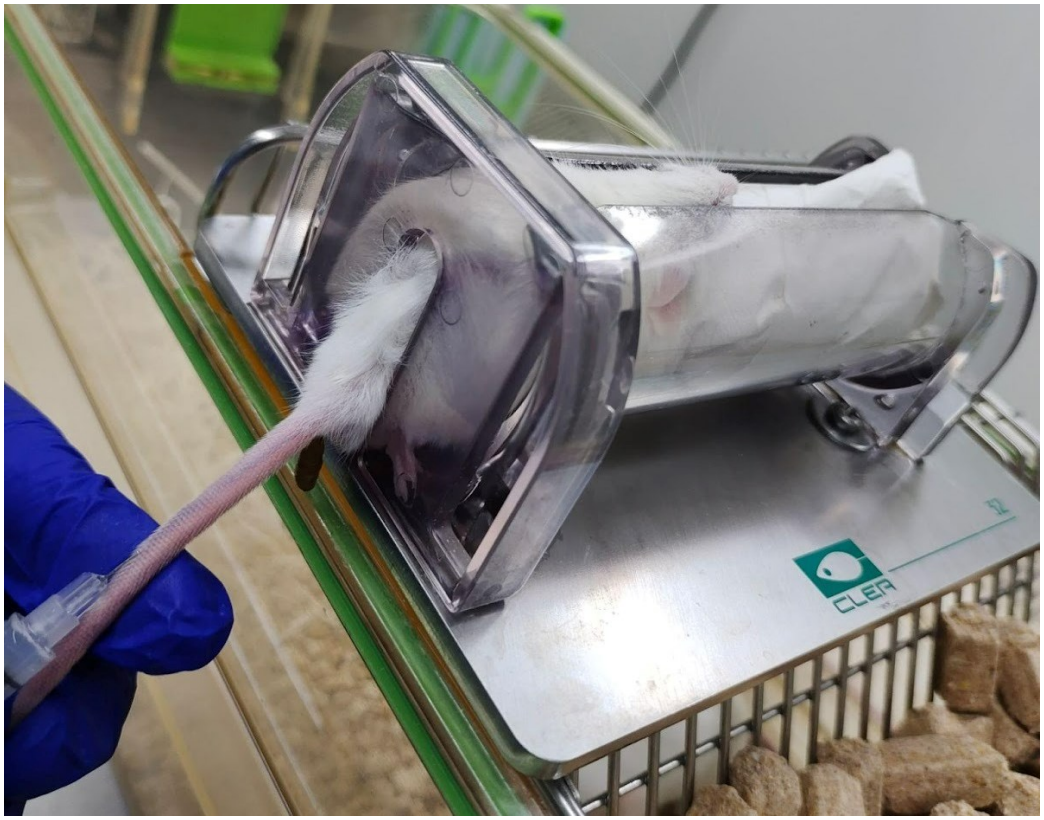

B

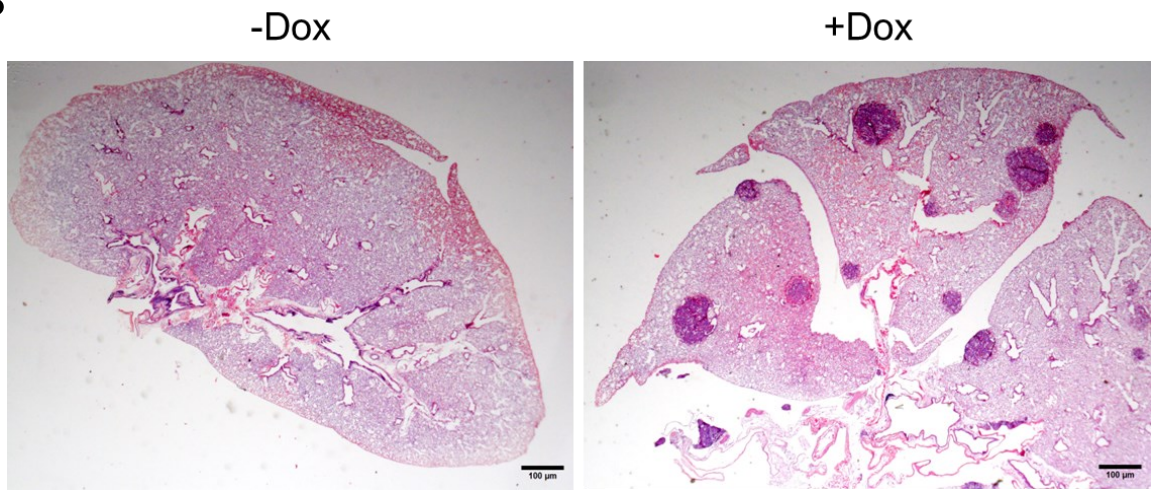

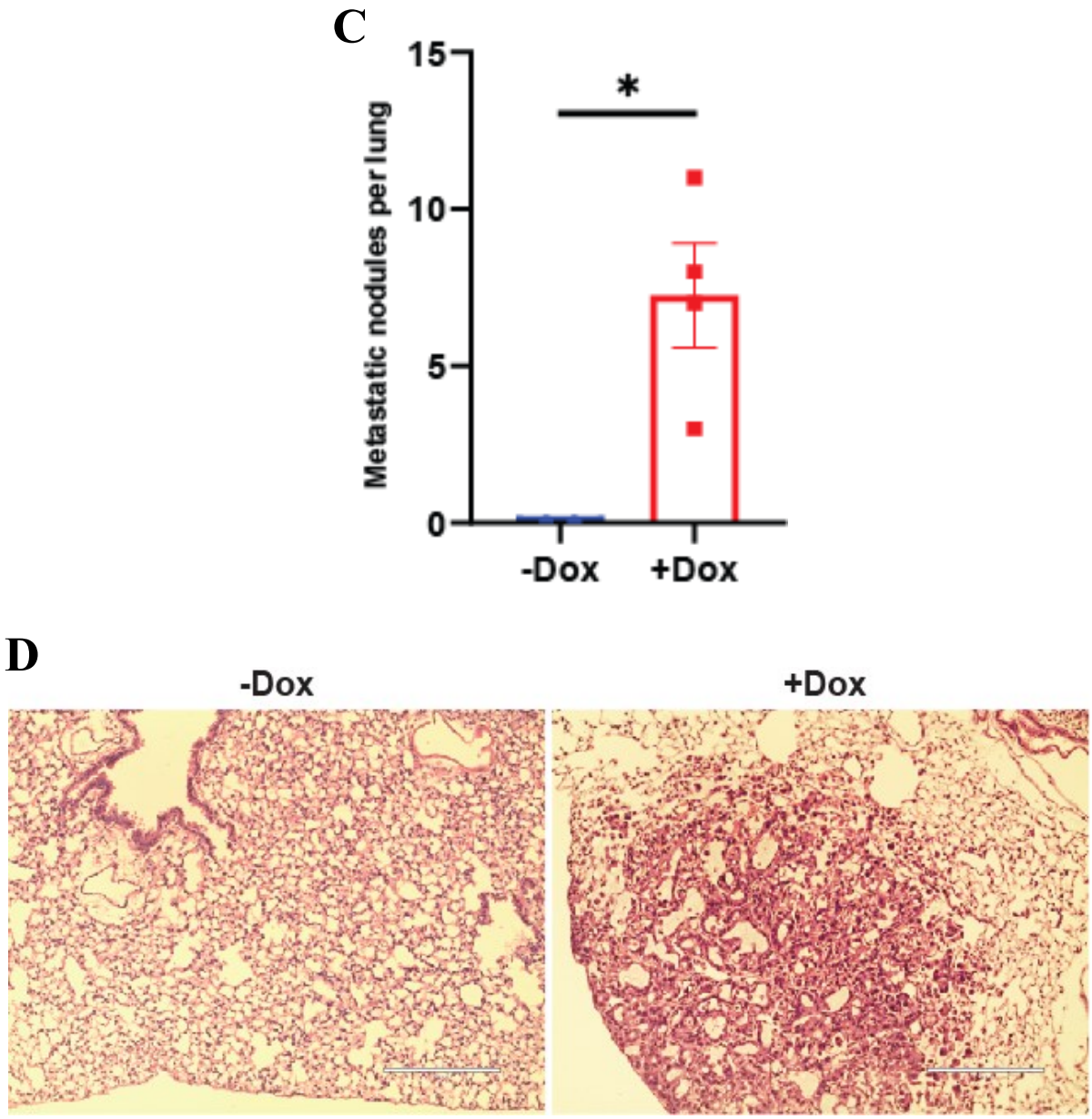

Fig. 5.7. FBL depletion triggers lung infiltration in DLD-1 cells in mice xenograft

(A) The animal is restrained in a mouse restrainer to immobilize the body and tail, allowing clear visualization of the lateral tail vein. shFBL DLD-1 stable cells are administered intravenously using a fine-gauge needle under aseptic conditions to ensure accurate systemic delivery. **(B)** Representative hematoxylin and eosin (H&E)–stained lung sections from NOD/SCID mice collected 60 days after tail vein injection of DLD-1 cells expressing a doxycycline (Dox)–inducible shRNA targeting FBL (shFBL). Lungs from Dox-treated (+Dox)

mice showed numerous, well-circumscribed metastatic nodules throughout the lung parenchyma, whereas lungs from mice without Dox treatment exhibited markedly fewer and smaller metastatic lesions. Scale bar, 100 μm. **(C)** Quantitative assessment of metastatic burden in the lungs of NOD/SCID mice following tail vein injection of DLD-1 cells expressing doxycycline (Dox)–inducible shFBL. Data are presented as mean ± SEM, with each dot representing an individual lung sample. **(D)** Magnified representative images corresponding to Fig. 5.7.B.

5.3. Discussion

This study identifies Fibrillarin (FBL), traditionally characterized as a nucleolar rRNA methyltransferase, as a pivotal regulator of epithelial integrity, chromatin organization, and tumor suppression. While canonical role of FBL in ribosome biogenesis is well established, emerging literature suggests that nucleolar proteins may participate in broader regulatory circuits beyond ribosomal processing, particularly those governing chromatin state (Tessarz et al. 2014; Iyer-Bierhoff et al. 2018). Our work extends this concept by demonstrating that FBL depletion disrupts key polarity pathways, activates oncogenic signaling, and drives epithelial plasticity, thereby promoting tumor progression and metastasis.

Mechanistically, FBL depletion led to marked downregulation and cytoplasmic mislocalization of Scribble, a core component of the basolateral polarity complex. The loss of membrane-bound Scribble disrupted the inhibitory axis that normally suppresses Akt signaling via PHLPP1 (Li et al. 2011). Consequently, we observed hyperactivation of Akt, a kinase that not only drives survival and motility but also phosphorylates and inactivates methyltransferase activity of EZH2 via Ser21 modification (Cha et al. 2005b). Interestingly, the activation of Akt in FBL-depleted cells was accompanied by a global reduction in H3K27me3, suggesting that the chromatin landscape is dynamically reprogrammed in response to altered polarity and signaling inputs. The reversal of these EMT features upon pharmacological inhibition of Akt underscores its role as a central effector in this regulatory axis.

In parallel, FBL loss stabilized TAZ, a Hippo pathway effector that functions as a transcriptional co-activator for EMT drivers such as Snail and Foxc2 (Lei et al. 2008). TAZ stabilization-especially under conditions of extended FBL knockdown or disruption of the FBL–EZH2 interaction- further amplified EMT transcriptional programs, reinforcing a mesenchymal phenotype. These findings indicate that FBL coordinates multiple signaling pathways-namely Akt and Hippo-to maintain epithelial identity, and that its depletion activates parallel mechanisms converging on EMT induction.

A striking observation in our study is the temporal uncoupling of Scribble expression and localization. While Scribble protein levels partially recovered at later time points post-FBL depletion, its mislocalization to the cytoplasm persisted. This spatial mislocalization, likely driven by sustained Snail expression, phenocopies mesenchymal-like cancer models such as MDA-MB-231, where high Snail levels correlate with cytoplasmic Scribble and impaired polarity (Abedrabbo and Ravid 2020b). Importantly, overexpression of an RNA-binding

deficient FBL mutant that cannot interact with EZH2 recapitulated these phenotypes, highlighting the critical role of the FBL–EZH2 interaction in regulating epithelial state.

Our in vivo data further validate the tumor suppressive role of FBL. DLD-1 cells with stable, doxycycline-inducible FBL knockdown exhibited significantly increased tumorigenicity and metastatic potential in xenograft and tail-vein injection models, respectively. Histological analysis of tumors and lung tissues confirmed the redistribution of EZH2 from the nucleolus to the nucleoplasm, increased H3K27me3 deposition, and marked downregulation of Scribble—all of which mirrored in vitro observations. These findings collectively implicate a spatial regulatory role of FBL in modulating PRC2 activity by restricting access of EZH2 to chromatin through nucleolar sequestration. Upon FBL loss, EZH2 becomes nucleoplasmic and transcriptionally active, repressing polarity determinants and enhancing migratory capacity.

The observed increase in lung metastases following tail-vein injections provides compelling evidence that FBL also serves as a suppressor of metastatic dissemination. Notably, EZH2 has been shown to promote EMT and metastasis through repression of epithelial and polarity genes such as CDH1, DAB2IP, and RKIP (Lv et al. 2019; Zong et al. 2020; Lachat et al. 2018). Our results position FBL upstream of this regulatory axis, suggesting that FBL loss not only relieves spatial constraints on EZH2 but also activates signaling circuits that collectively remodel the chromatin landscape to favor invasive phenotypes.

Importantly, the specificity of H3K27me3 in driving this phenotypic switch was demonstrated through selective inhibition of EZH2 using GSK126, which restored epithelial features and attenuated cell migration, even in the context of persistent FBL depletion. In contrast, reduction of H3K9me3 through SUV39H1 knockdown failed to rescue the migratory phenotype, reinforcing a unique functional role for H3K27me3 in mediating FBL-dependent epithelial regulation.

These findings offer several avenues for future investigation. First, the precise molecular mechanisms governing the FBL–EZH2 interaction and its modulation by nucleolar architecture warrant further exploration. Understanding whether FBL sequesters EZH2 via RNA scaffolding, phase separation, or ribonucleoprotein complex formation could reveal novel regulatory paradigms of subnuclear compartmentalization. Second, given the dual regulation of Akt and TAZ upon FBL loss, identifying potential crosstalk or convergence points between these pathways may uncover therapeutic vulnerabilities in tumors with nucleolar dysregulation. Third, our work highlights the potential of targeting chromatin modifiers—particularly EZH2—in cancers with impaired nucleolar integrity or FBL function.

Assessing FBL expression and EZH2 localization in clinical specimens may inform biomarker-driven stratification for epigenetic therapies.

In sum, this study establishes FBL as a central orchestrator of epithelial homeostasis, integrating nucleolar architecture, polarity signaling, and chromatin regulation. Its depletion triggers a complex network of signaling and epigenetic reprogramming that collectively disrupts cell polarity, enhances migration, and promotes tumor progression. These insights not only expand our understanding of nucleolar function but also position FBL–EZH2 axis as a promising target in epithelial cancers characterized by high plasticity and metastatic potential.

Chapter 6:
Discussion and Future Perspectives

6.1. Discussion

This study uncovers a previously unappreciated role for Fibrillarin (FBL), traditionally recognized for its functions in ribosome biogenesis, in orchestrating epithelial identity, nuclear integrity, and chromatin regulation. By integrating molecular, imaging, and in vivo approaches, we demonstrate that FBL functions beyond the nucleolus as a key regulator of subcellular localization, epigenetic state, and epithelial plasticity—properties essential in both tissue homeostasis and tumor progression.

One of the pivotal discoveries was the widespread phenotypic shift following FBL depletion, characterized by a breakdown of epithelial morphology and acquisition of mesenchymal-like traits. Loss of the cobblestone monolayer appearance, elongation of cell shape, and the internalization of E-cadherin and ZO-1 collectively suggested a destabilization of junctional complexes and induction of EMT. Notably, the accumulation of E-cadherin in the Golgi and its rescue upon Dynasore treatment pointed to enhanced clathrin-mediated endocytosis. These findings extend the regulatory reach of FBL into the domain of membrane trafficking—implicating nucleolar proteins in polarity protein localization and maintenance of epithelial integrity.

Concomitant with junctional defects, nuclear morphology was significantly perturbed. Cells exhibited reduced sphericity, increased surface area, and displayed nuclear anomalies such as blebs and micronuclei. Importantly, these defects were independent of alterations in Lamin A/C and B1/B2 levels, shifting attention to chromatin composition as a potential mediator. Supporting this, we observed a paradoxical upregulation of the repressive histone marks H3K27me3 and H3K9me3 upon FBL loss. This increase in chromatin compaction contradicts the classical view that nuclear deformation stems from chromatin relaxation, suggesting instead a compensatory stiffening mechanism under nucleolar stress, a phenomenon supported by previous work (Stephens et al. 2018; Amin et al. 2007).

Adding a new layer of complexity, we identified a marked upregulation of Emerin—an inner nuclear envelope protein implicated in heterochromatin tethering and nuclear shape stabilization. Emerin is known to recruit chromatin-modifying enzymes including HDAC3, G9a, and EZH2 (Demmerle et al. 2012; Marano and Holaska 2022), and has been implicated in reinforcing nuclear rigidity under stress (Yorifuji et al. 1997). The concurrent rise in

H3K9me3 and Emerin suggests a compensatory epigenetic scaffold activated in response to FBL depletion.

To dissect the contribution of specific histone modifications, we compared the impact of depleting SUV39H1 (H3K9me3 methyltransferase) versus EZH2 (H3K27me3 methyltransferase). Only EZH2 inhibition via GSK126 was able to reverse the enhanced migratory phenotype and restore epithelial markers, establishing H3K27me3 as a key functional driver in FBL-deficient cells. These findings align with literature demonstrating role of EZH2 in repressing CDH1 and promoting EMT in various cancer types (Lv et al. 2019).

Mechanistically, we show that FBL binds EZH2 via its RNA-binding domain and retains it in the nucleolus. Loss of FBL or expression of an RBD-deficient mutant disrupts this interaction, leading to release of EZH2 into the nucleoplasm, where it deposits H3K27me3 on target loci such as the SCRIB promoter. ChIP-PCR confirmed this enhanced enrichment of both EZH2 and H3K27me3 on the SCRIB promoter in FBL-depleted cells. This was accompanied by downregulation of Scribble protein, internalization of E-cadherin, and enhanced cell migration, mirroring canonical EMT features.

Transcriptome-wide RNA-seq further substantiated these findings, revealing Scribble among the top downregulated genes upon FBL depletion. Enrichment of EMT-related gene sets, apical polarity regulators, and adhesion molecules supports the broader relevance of FBL in epithelial maintenance. Functionally, the migratory phenotype observed upon FBL loss was recapitulated by Scribble knockdown and could be rescued by Scribble overexpression, establishing it as a downstream effector of regulatory axis of FBL.

The in vivo relevance of these mechanisms was demonstrated in xenograft and metastasis models. FBL-depleted DLD-1 tumors exhibited increased growth and elevated H3K27me3 levels. Histologically, EZH2 was mislocalized from the nucleolus to the nucleoplasm, paralleling in vitro observations. Tail-vein metastasis assays showed a significant increase in lung colonization upon FBL knockdown. Image-based quantification revealed elevated metastatic scores in +Dox mice, correlating with weight loss and systemic disease burden. Given prior reports linking EZH2 overexpression to increased metastasis and poor prognosis

(Varambally et al. 2002; Lachat et al. 2018), these results place the FBL–EZH2 axis at a critical juncture of metastasis regulation.

6.2. Future Perspectives

The discovery that Fibrillarin (FBL) functions beyond its canonical role in ribosome biogenesis to govern epithelial polarity, chromatin state, and tumor progression presents a paradigm shift in our understanding of nucleolar biology. This work positions FBL as a central node in coordinating epigenetic regulation, junctional stability, and nuclear organization—hallmarks of epithelial identity. The multifaceted effects observed upon FBL depletion not only illuminate new regulatory layers of epithelial maintenance but also raise compelling questions for future investigation.

A key future direction involves delineating the molecular mechanism by which FBL sequesters EZH2 in the nucleolus. While the current study identifies the RNA-binding domain (RBD) of FBL and the CXC domain of EZH2 as essential for this interaction, it remains unclear whether this complex requires RNA intermediates, additional cofactors, or nucleolar scaffold proteins for stabilization. Defining the molecular composition of the FBL–EZH2 complex through mass spectrometry and proximity labeling could reveal novel nucleolar regulators of chromatin modifiers.

Furthermore, understanding the genome-wide impact of EZH2 mislocalization is critical. Chromatin immunoprecipitation sequencing (ChIP-seq) for EZH2 and H3K27me3 in FBL-depleted versus control conditions would help map the redistribution of repressive chromatin domains. Integrating this with transcriptome profiling would clarify how FBL loss reprograms the transcriptional landscape. Additionally, it will be of interest to test whether nucleolar sequestration regulates the availability of other chromatin regulators, such as G9a, SUV39H1, or HDACs, thereby contributing to broader epigenetic shifts.

Given the observed upregulation of Emerin and heterochromatin marks upon FBL loss, another intriguing avenue is the mechanistic interplay between nucleolar stress, nuclear envelope remodeling, and chromatin state. Investigating whether FBL depletion activates nuclear mechanosensing pathways (such as YAP/TAZ or lamin-associated chromatin tethering) could connect mechanical and epigenetic regulation of epithelial fate. It would also be important to determine whether Emerin upregulation is a compensatory response to chromatin reorganization or a direct consequence of transcriptional derepression due to EZH2 relocalization.

From a translational perspective, the FBL–EZH2–Scribble axis emerges as a potential therapeutic target. Pharmacological disruption of this axis could restore epithelial traits and suppress invasive behavior in epithelial cancers. Small-molecule inhibitors of EZH2, such as GSK126, show promise in reversing EMT and restoring epithelial architecture. Future studies should assess the efficacy of these inhibitors in combination with FBL modulation across in vivo metastasis models and patient-derived organoids. Moreover, examining FBL and EZH2 expression levels in clinical tumor samples may establish their value as diagnostic or prognostic biomarkers, particularly in cancers with high EMT or metastatic signatures.

Finally, the broader implication of this study is the demonstration that the nucleolus can function as a compartmentalized reservoir for epigenetic regulators. This concept—of spatial regulation of chromatin-modifying enzymes by the nucleolus—invites deeper inquiry into the compartmentalization of transcriptional repression, its dynamic control under stress, and its impact on cell plasticity. It also prompts a reevaluation of other nucleolar proteins with possible dual functions in chromatin organization and transcriptional control, opening the door to a new dimension of nuclear regulation.

In conclusion, this work not only reveals a novel role for FBL in preserving epithelial structure through spatial epigenetic regulation but also paves the way for future studies that could redefine how nuclear architecture, chromatin dynamics, and cell identity are intertwined. Understanding these relationships holds significant promise for developing strategies to combat tumor progression, metastasis, and therapy resistance in epithelial cancers.

References

1. Abedrabbo, Maha, and Shoshana Ravid. 2020a. “Scribble, Lgl1, and Myosin II Form a Complex in Vivo to Promote Directed Cell Migration.” *Molecular Biology of the Cell* 31 (20): 2234–48. https://doi.org/10.1091/mbc.E19-11-0657.

2. Abedrabbo, Maha, and Shoshana Ravid. 2020b. “Scribble, Lgl1, and Myosin II Form a Complex in Vivo to Promote Directed Cell Migration.” *Molecular Biology of the Cell* 31 (20): 2234–48. https://doi.org/10.1091/mbc.E19-11-0657.

3. Abreu, Maria T. 2010. “Toll-like Receptor Signalling in the Intestinal Epithelium: How Bacterial Recognition Shapes Intestinal Function.” *Nature Reviews. Immunology* 10 (2): 131–44. https://doi.org/10.1038/nri2707.

4. Aiello, Nicole M, and Yibin Kang. 2019. “Context-Dependent EMT Programs in Cancer Metastasis.” *The Journal of Experimental Medicine* 216 (5): 1016–26. https://doi.org/10.1084/jem.20181827.

5. Alberti, Simon, Amy Gladfelter, and Tanja Mittag. 2019. “Considerations and Challenges in Studying Liquid-Liquid Phase Separation and Biomolecular Condensates.” *Cell* 176 (3): 419–34. https://doi.org/10.1016/j.cell.2018.12.035.

6. Al-Hasani, Keith, Ishant Khurana, Lina Mariana, et al. 2022. “Inhibition of Pancreatic EZH2 Restores Progenitor Insulin in T1D Donor.” *Signal Transduction and Targeted Therapy* 7 (1): 248. https://doi.org/10.1038/s41392-022-01034-7.

7. Allshire, Robin C., and Hiten D. Madhani. 2018. “Ten Principles of Heterochromatin Formation and Function.” *Nature Reviews. Molecular Cell Biology* 19 (4): 229–44. https://doi.org/10.1038/nrm.2017.119.

8. Altmeyer, Matthias, Kai J. Neelsen, Federico Teloni, et al. 2015. “Liquid Demixing of Intrinsically Disordered Proteins Is Seeded by Poly(ADP-Ribose).” *Nature Communications* 6 (1): 8088. https://doi.org/10.1038/ncomms9088.

9. Amin, Mohammed Abdullahel, Sachihiro Matsunaga, Nan Ma, et al. 2007. “Fibrillarin, a Nucleolar Protein, Is Required for Normal Nuclear Morphology and Cellular Growth in HeLa Cells.” *Biochemical and Biophysical Research Communications* 360 (2): 320–26. https://doi.org/10.1016/j.bbrc.2007.06.092.

10. Aparicio, Luis A., Moisés Blanco, Raquel Castosa, et al. 2015. “Clinical Implications of Epithelial Cell Plasticity in Cancer Progression.” *Cancer Letters* 366 (1): 1–10. https://doi.org/10.1016/j.canlet.2015.06.007.

11. Apodaca, Gerard, Luciana I. Gallo, and David M. Bryant. 2012. “Role of Membrane Traffic in the Generation of Epithelial Cell Asymmetry.” *Nature Cell Biology* 14 (12): 1235–43. https://doi.org/10.1038/ncb2635.

12. Arnett, Frank C., John D. Reveille, Rose Goldstein, et al. 1996. “Autoantibodies to Fibrillarin in Systemic Sclerosis (Scleroderma). An Immunogenetic, Serologic, and Clinical Analysis.” *Arthritis & Rheumatism* 39 (7): 1151–60. https://doi.org/10.1002/art.1780390712.

13. Attar, A. Goktug, Jaroslaw Paturej, Ozan S. Sariyer, Edward J. Banigan, and Aykut Erbas. 2025. “Peripheral Heterochromatin Tethering Is Required for Chromatin-Based Nuclear

Mechanical Response." Preprint, bioRxiv, February 16. https://doi.org/10.1101/2025.02.12.637704.

14. Audas, Timothy E., Mathieu D. Jacob, and Stephen Lee. 2012. "Immobilization of Proteins in the Nucleolus by Ribosomal Intergenic Spacer Noncoding RNA." *Molecular Cell* 45 (2): 147–57. https://doi.org/10.1016/j.molcel.2011.12.012.

15. Backhaus, Rafael, Christoph Zehe, Sabine Wegehingel, Angelika Kehlenbach, Blanche Schwappach, and Walter Nickel. 2004. "Unconventional Protein Secretion: Membrane Translocation of FGF-2 Does Not Require Protein Unfolding." *Journal of Cell Science* 117 (Pt 9): 1727–36. https://doi.org/10.1242/jcs.01027.

16. Balda, M. S., and K. Matter. 2000. "The Tight Junction Protein ZO-1 and an Interacting Transcription Factor Regulate ErbB-2 Expression." *The EMBO Journal* 19 (9): 2024–33. https://doi.org/10.1093/emboj/19.9.2024.

17. Balda, Maria S., Michelle D. Garrett, and Karl Matter. 2003. "The ZO-1-Associated Y-Box Factor ZONAB Regulates Epithelial Cell Proliferation and Cell Density." *The Journal of Cell Biology* 160 (3): 423–32. https://doi.org/10.1083/jcb.200210020.

18. Banani, Salman F, Hyun O Lee, Anthony A Hyman, and Michael K Rosen. 2017. "Biomolecular Condensates: Organizers of Cellular Biochemistry." *Nature Reviews. Molecular Cell Biology* 18 (5): 285–98. https://doi.org/10.1038/nrm.2017.7.

19. Bannister, A. J., P. Zegerman, J. F. Partridge, et al. 2001. "Selective Recognition of Methylated Lysine 9 on Histone H3 by the HP1 Chromo Domain." *Nature* 410 (6824): 120–24. https://doi.org/10.1038/35065138.

20. Bannister, Andrew J., and Tony Kouzarides. 2005. "Reversing Histone Methylation." *Nature* 436 (7054): 1103–6. https://doi.org/10.1038/nature04048.

21. Bannister, Andrew J., and Tony Kouzarides. 2011. "Regulation of Chromatin by Histone Modifications." *Cell Research* 21 (3): 381–95. https://doi.org/10.1038/cr.2011.22.

22. Batlle, E, E Sancho, C Francí, et al. 2000. "The Transcription Factor Snail Is a Repressor of E-Cadherin Gene Expression in Epithelial Tumour Cells." *Nature Cell Biology* 2 (2): 84–89. https://doi.org/10.1038/35000034.

23. Baudin-Baillieu, Agnès, Céline Fabret, Xue-hai Liang, Dorota Piekna-Przybylska, Maurille J. Fournier, and Jean-Pierre Rousset. 2009. "Nucleotide Modifications in Three Functionally Important Regions of the Saccharomyces Cerevisiae Ribosome Affect Translation Accuracy." *Nucleic Acids Research* 37 (22): 7665–77. https://doi.org/10.1093/nar/gkp816.

24. Baxter-Roshek, Jennifer L., Alexey N. Petrov, and Jonathan D. Dinman. 2007. "Optimization of Ribosome Structure and Function by rRNA Base Modification." *PLOS ONE* 2 (1): e174. https://doi.org/10.1371/journal.pone.0000174.

25. Bedford, Mark T., and Steven G. Clarke. 2009. "Protein Arginine Methylation in Mammals: Who, What, and Why." *Molecular Cell* 33 (1): 1–13. https://doi.org/10.1016/j.molcel.2008.12.013.

26. Bekers, AD G. M., Anna C. M. Pieck, Antonia A. M. Rijken, and Friedrich Wanka. 1986. "Evidence for the Persistence of a Decondensed Chromosome Scaffold in the Interphase Nucleus." *Journal of Cell Science* 86 (1): 155–71. https://doi.org/10.1242/jcs.86.1.155.

27. Belardi, Brian, Tiama Hamkins-Indik, Andrew R. Harris, Jeongmin Kim, Ke Xu, and Daniel A. Fletcher. 2020. “A Weak Link with Actin Organizes Tight Junctions to Control Epithelial Permeability.” *Developmental Cell* 54 (6): 792-804.e7. https://doi.org/10.1016/j.devcel.2020.07.022.

28. Beltrame, M., and D. Tollervey. 1995. “Base Pairing between U3 and the Pre-Ribosomal RNA Is Required for 18S rRNA Synthesis.” *The EMBO Journal* 14 (17): 4350–56. https://doi.org/10.1002/j.1460-2075.1995.tb00109.x.

29. Bernstein, Bradley E., Tarjei S. Mikkelsen, Xiaohui Xie, et al. 2006. “A Bivalent Chromatin Structure Marks Key Developmental Genes in Embryonic Stem Cells.” *Cell* 125 (2): 315–26. https://doi.org/10.1016/j.cell.2006.02.041.

30. Bilder, David. 2004. “Epithelial Polarity and Proliferation Control: Links from the Drosophila Neoplastic Tumor Suppressors.” *Genes & Development* 18 (16): 1909–25. https://doi.org/10.1101/gad.1211604.

31. Blackledge, Neil P., Anca M. Farcas, Takashi Kondo, et al. 2014. “Variant PRC1 Complex-Dependent H2A Ubiquitylation Drives PRC2 Recruitment and Polycomb Domain Formation.” *Cell* 157 (6): 1445–59. https://doi.org/10.1016/j.cell.2014.05.004.

32. Böğürcü-Seidel, Nuray, Nadja Ritschel, Till Acker, and Attila Németh. 2023. “Beyond Ribosome Biogenesis: Noncoding Nucleolar RNAs in Physiology and Tumor Biology.” *Nucleus* 14 (1): 2274655. https://doi.org/10.1080/19491034.2023.2274655.

33. Boisvert, François-Michel, Silvana van Koningsbruggen, Joaquín Navascués, and Angus I. Lamond. 2007. “The Multifunctional Nucleolus.” *Nature Reviews Molecular Cell Biology* 8 (7): 574–85. https://doi.org/10.1038/nrm2184.

34. Bolger, Anthony M., Marc Lohse, and Bjoern Usadel. 2014. “Trimmomatic: A Flexible Trimmer for Illumina Sequence Data.” *Bioinformatics (Oxford, England)* 30 (15): 2114–20. https://doi.org/10.1093/bioinformatics/btu170.

35. Bostick, Magnolia, Jong Kyong Kim, Pierre-Olivier Estève, Amander Clark, Sriharsa Pradhan, and Steven E. Jacobsen. 2007. “UHRF1 Plays a Role in Maintaining DNA Methylation in Mammalian Cells.” *Science (New York, N.Y.)* 317 (5845): 1760–64. https://doi.org/10.1126/science.1147939.

36. Bouffard, Stéphanie, Emilie Dambroise, Alessandro Brombin, et al. 2018. “Fibrillarin Is Essential for S-Phase Progression and Neuronal Differentiation in Zebrafish Dorsal Midbrain and Retina.” *Developmental Biology* 437 (1): 1–16. https://doi.org/10.1016/j.ydbio.2018.02.006.

37. Boulon, Séverine, Belinda J Westman, Saskia Hutten, François-Michel Boisvert, and Angus I Lamond. 2010. “The Nucleolus under Stress.” *Molecular Cell* 40 (2): 216–27. https://doi.org/10.1016/j.molcel.2010.09.024.

38. Braman, J., C. Papworth, and A. Greener. 1996. “Site-Directed Mutagenesis Using Double-Stranded Plasmid DNA Templates.” *Methods in Molecular Biology (Clifton, N.J.)* 57: 31–44. https://doi.org/10.1385/0-89603-332-5:31.

39. Bruijn, Ino de, Ritika Kundra, Brooke Mastrogiacomo, et al. 2023. “Analysis and Visualization of Longitudinal Genomic and Clinical Data from the AACR Project GENIE Biopharma Collaborative in cBioPortal.” *Cancer Research* 83 (23): 3861–67. https://doi.org/10.1158/0008-5472.CAN-23-0816.

40. Bryant, David M, and Keith E Mostov. 2008. “From Cells to Organs: Building Polarized Tissue.” *Nature Reviews Molecular Cell Biology* 9 (11): 887–901. https://doi.org/10.1038/nrm2523.

41. Bustin, Michael, and Tom Misteli. 2016. “Nongenetic Functions of the Genome.” *Science (New York, N.Y.)* 352 (6286): aad6933. https://doi.org/10.1126/science.aad6933.

42. Bywater, Megan J., Gretchen Poortinga, Elaine Sanij, et al. 2012. “Inhibition of RNA Polymerase I as a Therapeutic Strategy to Promote Cancer-Specific Activation of P53.” *Cancer Cell* 22 (1): 51–65. https://doi.org/10.1016/j.ccr.2012.05.019.

43. Calinsky, Rivka, and Yaakov Levy. 2024. “Aromatic Residues in Proteins: Re-Evaluating the Geometry and Energetics of π–π, Cation−π, and CH−π Interactions.” *The Journal of Physical Chemistry B* 128 (36): 8687–700. https://doi.org/10.1021/acs.jpcb.4c04774.

44. Cao, Q., J. Yu, S. M. Dhanasekaran, et al. 2008. “Repression of E-Cadherin by the Polycomb Group Protein EZH2 in Cancer.” *Oncogene* 27 (58): 7274–84. https://doi.org/10.1038/onc.2008.333.

45. Cao, Ru, Liangjun Wang, Hengbin Wang, et al. 2002. “Role of Histone H3 Lysine 27 Methylation in Polycomb-Group Silencing.” *Science* 298 (5595): 1039–43. https://doi.org/10.1126/science.1076997.

46. Cao, Ru, and Yi Zhang. 2004. “The Functions of E(Z)/EZH2-Mediated Methylation of Lysine 27 in Histone H3.” *Current Opinion in Genetics & Development* 14 (2): 155–64. https://doi.org/10.1016/j.gde.2004.02.001.

47. Cerami, Ethan, Jianjiong Gao, Ugur Dogrusoz, et al. 2012. “The cBio Cancer Genomics Portal: An Open Platform for Exploring Multidimensional Cancer Genomics Data.” *Cancer Discovery* 2 (5): 401–4. https://doi.org/10.1158/2159-8290.CD-12-0095.

48. Cha, Tai-Lung, Binhua P Zhou, Weiya Xia, et al. 2005a. “Akt-Mediated Phosphorylation of EZH2 Suppresses Methylation of Lysine 27 in Histone H3.” *Science* 310 (5746): 306–10. https://doi.org/10.1126/science.1118947.

49. Cha, Tai-Lung, Binhua P Zhou, Weiya Xia, et al. 2005b. “Akt-Mediated Phosphorylation of EZH2 Suppresses Methylation of Lysine 27 in Histone H3.” *Science* 310 (5746): 306–10. https://doi.org/10.1126/science.1118947.

50. Chang, Chih-Hao, Fu-Chen Hsu, Shu-Chuan Lee, et al. 2016. “The Nucleolar Fibrillarin Protein Is Required for Helper Virus-Independent Long-Distance Trafficking of a Subviral Satellite RNA in Plants.” *The Plant Cell* 28 (10): 2586–602. https://doi.org/10.1105/tpc.16.00071.

51. Chang, Chun-Ju, Jer-Yen Yang, Weiya Xia, et al. 2011. “EZH2 Promotes Expansion of Breast Tumor Initiating Cells through Activation of RAF1-β-Catenin Signaling.” *Cancer Cell* 19 (1): 86–100. https://doi.org/10.1016/j.ccr.2010.10.035.

52. Chen, Hong-Ru, Yi-Chun Yeh, Ching-Yi Liu, et al. 2016. “DDR1 Promotes E-Cadherin Stability via Inhibition of Integrin-\beta1-Src Activation-Mediated E-Cadherin Endocytosis.” *Scientific Reports* 6 (November): 36336. https://doi.org/10.1038/srep36336.

53. Chen, Ping, Guohong Li, and Wei Li. 2024. “Nucleosome Dynamics Derived at the Single-Molecule Level Bridges Its Structures and Functions.” *JACS Au* 4 (3): 866–76. https://doi.org/10.1021/jacsau.3c00658.

54. Comet, Itys, Eva M. Riising, Benjamin Leblanc, and Kristian Helin. 2016. “Maintaining Cell Identity: PRC2-Mediated Regulation of Transcription and Cancer.” *Nature Reviews. Cancer* 16 (12): 803–10. https://doi.org/10.1038/nrc.2016.83.

55. Conacci-Sorrell, Maralice, Inbal Simcha, Tamar Ben-Yedidia, Janna Blechman, Pierre Savagner, and Avri Ben-Ze’ev. 2003. “Autoregulation of E-Cadherin Expression by Cadherin–Cadherin Interactions.” *The Journal of Cell Biology* 163 (4): 847–57. https://doi.org/10.1083/jcb.200308162.

56. Coradini, Danila, Claudia Casarsa, and Saro Oriana. 2011. “Epithelial Cell Polarity and Tumorigenesis: New Perspectives for Cancer Detection and Treatment.” *Acta Pharmacologica Sinica* 32 (5): 552–64. https://doi.org/10.1038/aps.2011.20.

57. Cordenonsi, Michelangelo, Francesca Zanconato, Luca Azzolin, et al. 2011. “The Hippo Transducer TAZ Confers Cancer Stem Cell-Related Traits on Breast Cancer Cells.” *Cell* 147 (4): 759–72. https://doi.org/10.1016/j.cell.2011.09.048.

58. Correll, Carl C., Jiri Bartek, Miroslav Dundr, Carl C. Correll, Jiri Bartek, and Miroslav Dundr. 2019. “The Nucleolus: A Multiphase Condensate Balancing Ribosome Synthesis and Translational Capacity in Health, Aging and Ribosomopathies.” *Cells* 8 (8). https://doi.org/10.3390/cells8080869.

59. Creyghton, Menno P., Albert W. Cheng, G. Grant Welstead, et al. 2010. “Histone H3K27ac Separates Active from Poised Enhancers and Predicts Developmental State.” *Proceedings of the National Academy of Sciences of the United States of America* 107 (50): 21931–36. https://doi.org/10.1073/pnas.1016071107.

60. Datta, Anirban, David M. Bryant, and Keith E. Mostov. 2011. “Molecular Regulation of Lumen Morphogenesis.” *Current Biology* 21 (3): R126–36. https://doi.org/10.1016/j.cub.2010.12.003.

61. Davis, Joseph H., and James R. Williamson. 2017. “Structure and Dynamics of Bacterial Ribosome Biogenesis.” *Philosophical Transactions of the Royal Society B: Biological Sciences* 372 (1716): 20160181. https://doi.org/10.1098/rstb.2016.0181.

62. Debnath, Jayanta, Senthil K. Muthuswamy, and Joan S. Brugge. 2003. “Morphogenesis and Oncogenesis of MCF-10A Mammary Epithelial Acini Grown in Three-Dimensional Basement Membrane Cultures.” *Methods (San Diego, Calif.)* 30 (3): 256–68. https://doi.org/10.1016/s1046-2023(03)00032-x.

63. Decle-Carrasco, Stefano, Alma Laura Rodríguez-Piña, Luis Carlos Rodríguez-Zapata, and Enrique Castano. 2023. “Current Research on Viral Proteins That Interact with Fibrillarin.” *Molecular Biology Reports* 50 (5): 4631–43. https://doi.org/10.1007/s11033-023-08343-2.

64. Deffrasnes, Celine, Glenn A. Marsh, Chwan Hong Foo, et al. 2016. “Genome-Wide siRNA Screening at Biosafety Level 4 Reveals a Crucial Role for Fibrillarin in Henipavirus Infection.” *PLoS Pathogens* 12 (3): e1005478. https://doi.org/10.1371/journal.ppat.1005478.

65. Demmerle, Justin, Adam J Koch, and James M Holaska. 2012. “The Nuclear Envelope Protein Emerin Binds Directly to Histone Deacetylase 3 (HDAC3) and Activates HDAC3 Activity.” *The Journal of Biological Chemistry* 287 (26): 22080–88. https://doi.org/10.1074/jbc.M111.325308.

66. Denais, Celine, and Jan Lammerding. 2014. “Nuclear Mechanics in Cancer.” *Advances in Experimental Medicine and Biology* 773: 435–70. https://doi.org/10.1007/978-1-4899-8032-8_20.

67. Denais, Celine M, Rachel M Gilbert, Philipp Isermann, et al. 2016. “Nuclear Envelope Rupture and Repair during Cancer Cell Migration.” *Science* 352 (6283): 353–58. https://doi.org/10.1126/science.aad7297.

68. Deng, Lu, Natalia G. Starostina, Zhi-Jie Liu, et al. 2004. “Structure Determination of Fibrillarin from the Hyperthermophilic Archaeon *Pyrococcus Furiosus*.” *Biochemical and Biophysical Research Communications* 315 (3): 726–32. https://doi.org/10.1016/j.bbrc.2004.01.114.

69. Deng, Xiaolan, Gottfried Von Keudell, Takehiro Suzuki, et al. 2015. “PRMT1 Promotes Mitosis of Cancer Cells through Arginine Methylation of INCENP.” *Oncotarget* 6 (34): 35173–82. https://doi.org/10.18632/oncotarget.6050.

70. Dongre, Anushka, and Robert A. Weinberg. 2019. “New Insights into the Mechanisms of Epithelial-Mesenchymal Transition and Implications for Cancer.” *Nature Reviews. Molecular Cell Biology* 20 (2): 69–84. https://doi.org/10.1038/s41580-018-0080-4.

71. Dragon, François, Jennifer E. G. Gallagher, Patricia A. Compagnone-Post, et al. 2002. “A Large Nucleolar U3 Ribonucleoprotein Required for 18S Ribosomal RNA Biogenesis.” *Nature* 417 (6892): 967–70. https://doi.org/10.1038/nature00769.

72. Dreyfuss, G., M. J. Matunis, S. Piñol-Roma, and C. G. Burd. 1993. “hnRNP Proteins and the Biogenesis of mRNA.” *Annual Review of Biochemistry* 62: 289–321. https://doi.org/10.1146/annurev.bi.62.070193.001445.

73. Dubińska-Magiera, Magda, Katarzyna Kozioł, Magdalena Machowska, Katarzyna Piekarowicz, Daria Filipczak, and Ryszard Rzepecki. 2019. “Emerin Is Required for Proper Nucleus Reassembly after Mitosis: Implications for New Pathogenetic Mechanisms for Laminopathies Detected in EDMD1 Patients.” *Cells* 8 (3). https://doi.org/10.3390/cells8030240.

74. Dubois, Marie-Line, and François-Michel Boisvert. 2016. “The Nucleolus: Structure and Function.” *The Functional Nucleus*, April 23, 29–49. https://doi.org/10.1007/978-3-319-38882-3_2.

75. Dundr, Miroslav, Tom Misteli, and Mark O.J. Olson. 2000. “The Dynamics of Postmitotic Reassembly of the Nucleolus.” *Journal of Cell Biology* 150 (3): 433–46. https://doi.org/10.1083/jcb.150.3.433.

76. Edemir, Bayram, Hermann Pavenstädt, Eberhard Schlatter, and Thomas Weide. 2011. “Mechanisms of Cell Polarity and Aquaporin Sorting in the Nephron.” *Pflugers Archiv: European Journal of Physiology* 461 (6): 607–21. https://doi.org/10.1007/s00424-011-0928-3.

77. Emmott, Edward, and Julian A. Hiscox. 2009. “Nucleolar Targeting: The Hub of the Matter.” *The EMBO Reports* 10 (3): 231–38. https://doi.org/10.1038/embor.2009.14.

78. Erales, Jenny, Virginie Marchand, Baptiste Panthu, et al. 2017. “Evidence for rRNA 2’-O-Methylation Plasticity: Control of Intrinsic Translational Capabilities of Human Ribosomes.” *Proceedings of the National Academy of Sciences of the United States of America* 114 (49): 12934–39. https://doi.org/10.1073/pnas.1707674114.

79. Fan, Xiaoxiao, Shengxi Jin, Yirun Li, et al. 2019. “<p>Genetic And Epigenetic Regulation Of E-Cadherin Signaling In Human Hepatocellular Carcinoma</P>.” *Cancer Management and Research* 11 (October): 8947–63. https://doi.org/10.2147/CMAR.S225606.

80. Fanning, Alan S., Christina M. Van Itallie, and James M. Anderson. 2012. “Zonula Occludens-1 and -2 Regulate Apical Cell Structure and the Zonula Adherens Cytoskeleton in Polarized Epithelia.” *Molecular Biology of the Cell* 23 (4): 577–90. https://doi.org/10.1091/mbc.E11-09-0791.

81. Feric, Marina, Nilesh Vaidya, Tyler S Harmon, et al. 2016. “Coexisting Liquid Phases Underlie Nucleolar Subcompartments.” *Cell* 165 (7): 1686–97. https://doi.org/10.1016/j.cell.2016.04.047.

82. Fujii, Satoshi, and Atsushi Ochiai. 2008. “Enhancer of Zeste Homolog 2 Downregulates E-Cadherin by Mediating Histone H3 Methylation in Gastric Cancer Cells.” *Cancer Science* 99 (4): 738–46. https://doi.org/10.1111/j.1349-7006.2008.00743.x.

83. Fujita, S., D. Honma, N. Adachi, et al. 2018. “Dual Inhibition of EZH1/2 Breaks the Quiescence of Leukemia Stem Cells in Acute Myeloid Leukemia.” *Leukemia* 32 (4): 855–64. https://doi.org/10.1038/leu.2017.300.

84. Gaianigo, Nicola, Davide Melisi, and Carmine Carbone. 2017. “EMT and Treatment Resistance in Pancreatic Cancer.” *Cancers* 9 (9): 122. https://doi.org/10.3390/cancers9090122.

85. Gao, Jianjiong, Bülent Arman Aksoy, Ugur Dogrusoz, et al. 2013. “Integrative Analysis of Complex Cancer Genomics and Clinical Profiles Using the cBioPortal.” *Science Signaling* 6 (269): pl1. https://doi.org/10.1126/scisignal.2004088.

86. Gautier, T., M. Robert-Nicoud, M. N. Guilly, and D. Hernandez-Verdun. 1992. “Relocation of Nucleolar Proteins around Chromosomes at Mitosis. A Study by Confocal Laser Scanning Microscopy.” *Journal of Cell Science* 102 (Pt 4) (August): 729–37. https://doi.org/10.1242/jcs.102.4.729.

87. Ge, Steven Xijin, Dongmin Jung, and Runan Yao. 2020. “ShinyGO: A Graphical Gene-Set Enrichment Tool for Animals and Plants.” *Bioinformatics* 36 (8): 2628–29. https://doi.org/10.1093/bioinformatics/btz931.

88. Geng, Qian, Haoyu Peng, Fengsheng Chen, Rongcheng Luo, and Rong Li. 2015. “High Expression of Sirt7 Served as a Predictor of Adverse Outcome in Breast Cancer.” *International Journal of Clinical and Experimental Pathology* 8 (2): 1938–45.

89. Goldman, Robert D., Dale K. Shumaker, Michael R. Erdos, et al. 2004. “Accumulation of Mutant Lamin A Causes Progressive Changes in Nuclear Architecture in Hutchinson-Gilford Progeria Syndrome.” *Proceedings of the National Academy of Sciences of the United States of America* 101 (24): 8963–68. https://doi.org/10.1073/pnas.0402943101.

90. Goldstein, Bob, and Ian G. Macara. 2007. “The PAR Proteins: Fundamental Players in Animal Cell Polarization.” *Developmental Cell* 13 (5): 609–22. https://doi.org/10.1016/j.devcel.2007.10.007.

91. González-Arzola, Katiuska. 2024. “The Nucleolus: Coordinating Stress Response and Genomic Stability.” *Biochimica et Biophysica Acta (BBA) - Gene Regulatory Mechanisms* 1867 (2): 195029. https://doi.org/10.1016/j.bbagrm.2024.195029.

92. Grewal, Shiv I. S., and Songtao Jia. 2007. “Heterochromatin Revisited.” *Nature Reviews. Genetics* 8 (1): 35–46. https://doi.org/10.1038/nrg2008.

93. Groth, Anja, Walter Rocha, Alain Verreault, and Geneviève Almouzni. 2007. “Chromatin Challenges during DNA Replication and Repair.” *Cell* 128 (4): 721–33. https://doi.org/10.1016/j.cell.2007.01.030.

94. Grunstein, M. 1997. “Histone Acetylation in Chromatin Structure and Transcription.” *Nature* 389 (6649): 349–52. https://doi.org/10.1038/38664.

95. Guelen, Lars, Ludo Pagie, Emilie Brasset, et al. 2008. “Domain Organization of Human Chromosomes Revealed by Mapping of Nuclear Lamina Interactions.” *Nature* 453 (7197): 948–51. https://doi.org/10.1038/nature06947.

96. Guillen-Chable, Francisco, Ulises Rodríguez Corona, Alejandro Pereira-Santana, et al. 2020. “Fibrillarin Ribonuclease Activity Is Dependent on the GAR Domain and Modulated by Phospholipids.” *Cells* 9 (5). https://doi.org/10.3390/cells9051143.

97. Gumbiner, B. M. 1996. “Cell Adhesion: The Molecular Basis of Tissue Architecture and Morphogenesis.” *Cell* 84 (3): 345–57. https://doi.org/10.1016/s0092-8674(00)81279-9.

98. Halbleib, Jennifer M., and W. James Nelson. 2006. “Cadherins in Development: Cell Adhesion, Sorting, and Tissue Morphogenesis.” *Genes & Development* 20 (23): 3199–214. https://doi.org/10.1101/gad.1486806.

99. Hapak, Sophie M., Carla V. Rothlin, and Sourav Ghosh. 2018. “PAR3–PAR6–Atypical PKC Polarity Complex Proteins in Neuronal Polarization.” *Cellular and Molecular Life Sciences: CMLS* 75 (15): 2735–61. https://doi.org/10.1007/s00018-018-2828-6.

100. Harada, Takamasa, Joe Swift, Jerome Irianto, et al. 2014. “Nuclear Lamin Stiffness Is a Barrier to 3D Migration, but Softness Can Limit Survival.” *The Journal of Cell Biology* 204 (5): 669–82. https://doi.org/10.1083/jcb.201308029.

101. Harigopal, Malini, Aaron J. Berger, Robert L. Camp, David L. Rimm, and Harriet M. Kluger. 2005. “Automated Quantitative Analysis of E-Cadherin Expression in Lymph Node Metastases Is Predictive of Survival in Invasive Ductal Breast Cancer.” *Clinical Cancer Research: An Official Journal of the American Association for Cancer Research* 11 (11): 4083–89. https://doi.org/10.1158/1078-0432.CCR-04-2191.

102. Hebbes, T. R., A. W. Thorne, and C. Crane-Robinson. 1988. “A Direct Link between Core Histone Acetylation and Transcriptionally Active Chromatin.” *The EMBO Journal* 7 (5): 1395–402. https://doi.org/10.1002/j.1460-2075.1988.tb02956.x.

103. Heinemann, Udo, Anja Schuetz, Udo Heinemann, and Anja Schuetz. 2019. “Structural Features of Tight-Junction Proteins.” *International Journal of Molecular Sciences* 20 (23). https://doi.org/10.3390/ijms20236020.

104. Hendrickson-Rebizant, Thordur, Sadhana R. N. Sudhakar, Michael J. Rowley, Adam Frankel, James R. Davie, and Ted M. Lakowski. 2024. “Structure, Function, and Activity of Small Molecule and Peptide Inhibitors of Protein Arginine Methyltransferase 1.” *Journal of Medicinal Chemistry* 67 (18): 15931–46. https://doi.org/10.1021/acs.jmedchem.4c00490.

105. Henikoff, Steven, and M Mitchell Smith. 2015. “Histone Variants and Epigenetics.” *Cold Spring Harbor Perspectives in Biology* 7 (1): a019364. https://doi.org/10.1101/cshperspect.a019364.

106. Heo, Su-Jin, Tristan P. Driscoll, Stephen D. Thorpe, et al. 2016. “Differentiation Alters Stem Cell Nuclear Architecture, Mechanics, and Mechano-Sensitivity.” *eLife* 5 (November): e18207. https://doi.org/10.7554/eLife.18207.

107. Hernandez-Verdun, Danièle. 2011. “Assembly and Disassembly of the Nucleolus during the Cell Cycle.” *Nucleus (Austin, Tex.)* 2 (3): 189–94. https://doi.org/10.4161/nucl.2.3.16246.

108. Herranz, Nicolás, Diego Pasini, Víctor M. Díaz, et al. 2008. “Polycomb Complex 2 Is Required for E-Cadherin Repression by the Snail1 Transcription Factor.” *Molecular and Cellular Biology* 28 (15): 4772–81. https://doi.org/10.1128/MCB.00323-08.

109. Hiscox, Julian A. 2007. “RNA Viruses: Hijacking the Dynamic Nucleolus.” *Nature Reviews Microbiology* 5 (2): 119–27. https://doi.org/10.1038/nrmicro1597.

110. Hnisz, Denes, Brian J. Abraham, Tong Ihn Lee, et al. 2013. “Super-Enhancers in the Control of Cell Identity and Disease.” *Cell* 155 (4): 934–47. https://doi.org/10.1016/j.cell.2013.09.053.

111. Hong, L., G. P. Schroth, H. R. Matthews, P. Yau, and E. M. Bradbury. 1993. “Studies of the DNA Binding Properties of Histone H4 Amino Terminus. Thermal Denaturation Studies Reveal That Acetylation Markedly Reduces the Binding Constant of the H4 ‘Tail’ to DNA.” *The Journal of Biological Chemistry* 268 (1): 305–14.

112. Hu, Gangqing, Kairong Cui, Daniel Northrup, et al. 2013. “H2A.Z Facilitates Access of Active and Repressive Complexes to Chromatin in Embryonic Stem Cell Self-Renewal and Differentiation.” *Cell Stem Cell* 12 (2): 180–92. https://doi.org/10.1016/j.stem.2012.11.003.

113. Huang, Jianmin, Shan He, Qiuyun Zhang, Yunliang Liu, and Yongjing You. 2025. “Hypoxia Disrupts Human Bronchial Epithelial Barrier Integrity via Tight Junction Protein Remodeling and Enhanced Paracellular Leakage.” *European Journal of Medical Research* 30 (August): 794. https://doi.org/10.1186/s40001-025-03080-7.

114. Huber, Margit A., Ninel Azoitei, Bernd Baumann, et al. 2004. “NF-kappaB Is Essential for Epithelial-Mesenchymal Transition and Metastasis in a Model of Breast Cancer Progression.” *The Journal of Clinical Investigation* 114 (4): 569–81. https://doi.org/10.1172/JCI21358.

115. Humbert, P. O., N. A. Grzeschik, A. M. Brumby, R. Galea, I. Elsum, and H. E. Richardson. 2008. “Control of Tumourigenesis by the Scribble/Dlg/Lgl Polarity Module.” *Oncogene* 27 (55): 6888–907. https://doi.org/10.1038/onc.2008.341.

116. Humbert, Patrick O., Sarah M. Russell, Lorey Smith, and Helena E. Richardson. 2015. “The Scribble–Dlg–Lgl Module in Cell Polarity Regulation.” In *Cell Polarity 1: Biological Role and Basic Mechanisms*, edited by Klaus Ebnet. Springer International Publishing. https://doi.org/10.1007/978-3-319-14463-4_4.

117. Italiano, Antoine, Jean-Charles Soria, Maud Toulmonde, et al. 2018. “Tazemetostat, an EZH2 Inhibitor, in Relapsed or Refractory B-Cell Non-Hodgkin Lymphoma and Advanced Solid Tumours: A First-in-Human, Open-Label, Phase 1 Study.” *The Lancet. Oncology* 19 (5): 649–59. https://doi.org/10.1016/S1470-2045(18)30145-1.

118. Ivanov, Andrei I., Cheryl Young, Kyle Den Beste, et al. 2010. “Tumor Suppressor Scribble Regulates Assembly of Tight Junctions in the Intestinal Epithelium.” *The American Journal of Pathology* 176 (1): 134–45. https://doi.org/10.2353/ajpath.2010.090220.

119. Iyer-Bierhoff, Aishwarya, Nicolai Krogh, Peter Tessarz, Thomas Ruppert, Henrik Nielsen, and Ingrid Grummt. 2018. “SIRT7-Dependent Deacetylation of Fibrillarin Controls Histone H2A

Methylation and rRNA Synthesis during the Cell Cycle." *Cell Reports* 25 (11): 2946-2954.e5. https://doi.org/10.1016/j.celrep.2018.11.051.

120. Izaguirre, M. F., D. Larrea, J. F. Adur, et al. 2010. "Role of E-Cadherin in Epithelial Architecture Maintenance." *Cell Communication & Adhesion* 17 (1): 1–12. https://doi.org/10.3109/15419061003686938.

121. Jack, Karen, Cristian Bellodi, Dori M. Landry, et al. 2011. "rRNA Pseudouridylation Defects Affect Ribosomal Ligand Binding and Translational Fidelity from Yeast to Human Cells." *Molecular Cell* 44 (4): 660–66. https://doi.org/10.1016/j.molcel.2011.09.017.

122. Jakobsen, Kristine Raaby, Christina Demuth, Boe Sandahl Sorensen, and Anders Lade Nielsen. 2016. "The Role of Epithelial to Mesenchymal Transition in Resistance to Epidermal Growth Factor Receptor Tyrosine Kinase Inhibitors in Non-Small Cell Lung Cancer." *Translational Lung Cancer Research* 5 (2): 172–82. https://doi.org/10.21037/tlcr.2016.04.07.

123. James, Allison, Yubo Wang, Himanshu Raje, Raphyel Rosby, and Patrick DiMario. 2014. "Nucleolar Stress with and without P53." *Nucleus* 5 (5): 402–26. https://doi.org/10.4161/nucl.32235.

124. Jenuwein, T., and C. D. Allis. 2001. "Translating the Histone Code." *Science (New York, N.Y.)* 293 (5532): 1074–80. https://doi.org/10.1126/science.1063127.

125. Kadoch, Cigall, Diana C. Hargreaves, Courtney Hodges, et al. 2013. "Proteomic and Bioinformatic Analysis of Mammalian SWI/SNF Complexes Identifies Extensive Roles in Human Malignancy." *Nature Genetics* 45 (6): 592–601. https://doi.org/10.1038/ng.2628.

126. Kalluri, Raghu, and Robert A. Weinberg. 2009. "The Basics of Epithelial-Mesenchymal Transition." *The Journal of Clinical Investigation* 119 (6): 1420–28. https://doi.org/10.1172/JCI39104.

127. Kato, Masato, Tina W. Han, Shanhai Xie, et al. 2012. "Cell-Free Formation of RNA Granules: Low Complexity Sequence Domains Form Dynamic Fibers within Hydrogels." *Cell* 149 (4): 753–67. https://doi.org/10.1016/j.cell.2012.04.017.

128. Khuntia, Purnati, Simran Rawal, Rituraj Marwaha, and Tamal Das. 2022. "Actin-Driven Golgi Apparatus Dispersal during Collective Migration of Epithelial Cells." *Proceedings of the National Academy of Sciences of the United States of America* 119 (26): e2204808119. https://doi.org/10.1073/pnas.2204808119.

129. Khurana, Himani, Krishnakanth Baratam, Soumya Bhattacharyya, Anand Srivastava, and Thomas J. Pucadyil. 2023. "Mechanistic Analysis of a Novel Membrane-Interacting Variable Loop in the Pleckstrin-Homology Domain Critical for Dynamin Function." *Proceedings of the National Academy of Sciences* 120 (11): e2215250120. https://doi.org/10.1073/pnas.2215250120.

130. Kim, Dae In, Samuel C Jensen, Kyle A Noble, et al. 2016. "An Improved Smaller Biotin Ligase for BioID Proximity Labeling." *Molecular Biology of the Cell* 27 (8): 1188–96. https://doi.org/10.1091/mbc.E15-12-0844.

131. Kim, Daehwan, Ben Langmead, and Steven L. Salzberg. 2015. "HISAT: A Fast Spliced Aligner with Low Memory Requirements." *Nature Methods* 12 (4): 357–60. https://doi.org/10.1038/nmeth.3317.

132. Kim, Eunji, and Ilmin Kwon. 2021. “Phase Transition of Fibrillarin LC Domain Regulates Localization and Protein Interaction of Fibrillarin.” *The Biochemical Journal* 478 (4): 799–810. https://doi.org/10.1042/BCJ20200847.

133. Kim, Kimberly H, and Charles W M Roberts. 2016. “Targeting EZH2 in Cancer.” *Nature Medicine* 22 (2): 128–34. https://doi.org/10.1038/nm.4036.

134. Kim, Nam-Gyun, and Barry M. Gumbiner. 2015. “Adhesion to Fibronectin Regulates Hippo Signaling via the FAK–Src–PI3K Pathway.” *The Journal of Cell Biology* 210 (3): 503–15. https://doi.org/10.1083/jcb.201501025.

135. Kim, Sang Hyon, Stuart MacFarlane, Natalia O. Kalinina, et al. 2007. “Interaction of a Plant Virus-Encoded Protein with the Major Nucleolar Protein Fibrillarin Is Required for Systemic Virus Infection.” *Proceedings of the National Academy of Sciences* 104 (26): 11115–20. https://doi.org/10.1073/pnas.0704632104.

136. Kim, Wantae, Sanjoy Kumar Khan, Jelena Gvozdenovic-Jeremic, et al. 2017. “Hippo Signaling Interactions with Wnt/β-Catenin and Notch Signaling Repress Liver Tumorigenesis.” *The Journal of Clinical Investigation* 127 (1): 137–52. https://doi.org/10.1172/JCI88486.

137. Kleer, Celina G, Qi Cao, Sooryanarayana Varambally, et al. 2003. “EZH2 Is a Marker of Aggressive Breast Cancer and Promotes Neoplastic Transformation of Breast Epithelial Cells.” *Proceedings of the National Academy of Sciences of the United States of America* 100 (20): 11606–11. https://doi.org/10.1073/pnas.1933744100.

138. Knoblich, Juergen A. 2008. “Mechanisms of Asymmetric Stem Cell Division.” *Cell* 132 (4): 583–97. https://doi.org/10.1016/j.cell.2008.02.007.

139. Knutson, Sarah K., Satoshi Kawano, Yukinori Minoshima, et al. 2014. “Selective Inhibition of EZH2 by EPZ-6438 Leads to Potent Antitumor Activity in EZH2-Mutant Non-Hodgkin Lymphoma.” *Molecular Cancer Therapeutics* 13 (4): 842–54. https://doi.org/10.1158/1535-7163.MCT-13-0773.

140. Kohanski, Michael A., Daniel J. Dwyer, Jamey Wierzbowski, Guillaume Cottarel, and James J. Collins. 2008. “Mistranslation of Membrane Proteins and Two-Component System Activation Trigger Antibiotic-Mediated Cell Death.” *Cell* 135 (4): 679–90. https://doi.org/10.1016/j.cell.2008.09.038.

141. Kolasinska-Zwierz, Paulina, Thomas Down, Isabel Latorre, Tao Liu, X. Shirley Liu, and Julie Ahringer. 2009. “Differential Chromatin Marking of Introns and Expressed Exons by H3K36me3.” *Nature Genetics* 41 (3): 376–81. https://doi.org/10.1038/ng.322.

142. Kouzarides, Tony. 2007. “Chromatin Modifications and Their Function.” *Cell* 128 (4): 693–705. https://doi.org/10.1016/j.cell.2007.02.005.

143. Ku, Bomin, David Eisenbarth, Seonguk Baek, et al. 2024. “PRMT1 Promotes Pancreatic Cancer Development and Resistance to Chemotherapy.” *Cell Reports Medicine* 5 (3). https://doi.org/10.1016/j.xcrm.2024.101461.

144. Kundu, Sharmistha, Fei Ji, Hongjae Sunwoo, et al. 2017. “Polycomb Repressive Complex 1 Generates Discrete Compacted Domains That Change during Differentiation.” *Molecular Cell* 65 (3): 432-446.e5. https://doi.org/10.1016/j.molcel.2017.01.009.

145. Labade, Ajay S, Krishanpal Karmodiya, and Kundan Sengupta. 2016. “HOXA Repression Is Mediated by Nucleoporin Nup93 Assisted by Its Interactors Nup188 and Nup205.” *Epigenetics & Chromatin* 9 (December): 54. https://doi.org/10.1186/s13072-016-0106-0.

146. Lacerda, Rafaela, Juliane Menezes, and Luísa Romão. 2017. “More than Just Scanning: The Importance of Cap-Independent mRNA Translation Initiation for Cellular Stress Response and Cancer.” *Cellular and Molecular Life Sciences* 74 (9): 1659–80. https://doi.org/10.1007/s00018-016-2428-2.

147. Lachat, Camille, Michaël Boyer-Guittaut, Paul Peixoto, and Eric Hervouet. 2018. “Epigenetic Regulation of EMT (Epithelial to Mesenchymal Transition) and Tumor Aggressiveness: A View on Paradoxical Roles of KDM6B and EZH2.” *Epigenomes* 3 (1): 1. https://doi.org/10.3390/epigenomes3010001.

148. Lafontaine, Denis L. J. 2023. “When Two Became Three: Shaping the Nucleolus with *Treacle*.” *Cell Reports* 42 (9): 113060. https://doi.org/10.1016/j.celrep.2023.113060.

149. Laugesen, Anne, and Kristian Helin. 2014. “Chromatin Repressive Complexes in Stem Cells, Development, and Cancer.” *Cell Stem Cell* 14 (6): 735–51. https://doi.org/10.1016/j.stem.2014.05.006.

150. Lecuit, Thomas, and Alpha S. Yap. 2015. “E-Cadherin Junctions as Active Mechanical Integrators in Tissue Dynamics.” *Nature Cell Biology* 17 (5): 533–39. https://doi.org/10.1038/ncb3136.

151. Leeke, Bryony J., Imke Staffhorst, and Michelle Percharde. 2025. “Emerging Roles for the Nucleolus in Development and Stem Cells.” *Development (Cambridge, England)* 152 (9): dev204696. https://doi.org/10.1242/dev.204696.

152. Lei, Qun-Ying, Heng Zhang, Bin Zhao, et al. 2008. “TAZ Promotes Cell Proliferation and Epithelial-Mesenchymal Transition and Is Inhibited by the Hippo Pathway.” *Molecular and Cellular Biology* 28 (7): 2426–36. https://doi.org/10.1128/MCB.01874-07.

153. Leung, Anthony Kar Lun, Daniel Gerlich, Gail Miller, et al. 2004. “Quantitative Kinetic Analysis of Nucleolar Breakdown and Reassembly during Mitosis in Live Human Cells.” *The Journal of Cell Biology* 166 (6): 787–800. https://doi.org/10.1083/jcb.200405013.

154. Leung, Cheuk T., and Joan S. Brugge. 2012. “Outgrowth of Single Oncogene-Expressing Cells from Suppressive Epithelial Environments.” *Nature* 482 (7385): 410–13. https://doi.org/10.1038/nature10826.

155. Li, Dingfeng, Ran Cao, Qiaodan Li, et al. 2023. “Nucleolus Assembly Impairment Leads to Two-Cell Transcriptional Repression via NPM1-Mediated PRC2 Recruitment.” *Nature Structural & Molecular Biology* 30 (7): 914–25. https://doi.org/10.1038/s41594-023-01003-w.

156. Li, Feng, Guogen Mao, Dan Tong, et al. 2013. “The Histone Mark H3K36me3 Regulates Human DNA Mismatch Repair through Its Interaction with MutSα.” *Cell* 153 (3): 590–600. https://doi.org/10.1016/j.cell.2013.03.025.

157. Li, Panpan, Yang Liu, Renjie Song, et al. 2022. “RNA 2’-O-Methyltransferase Fibrillarin Facilitates Virus Entry Into Macrophages Through Inhibiting Type I Interferon Response.” *Frontiers in Immunology* 13 (April): 793582. https://doi.org/10.3389/fimmu.2022.793582.

158. Li, Xin, Haihua Yang, Jianyu Liu, Micheal D Schmidt, and Tianyan Gao. 2011. “Scribble-Mediated Membrane Targeting of PHLPP1 Is Required for Its Negative Regulation of Akt.” *EMBO Reports* 12 (8): 818–24. https://doi.org/10.1038/embor.2011.106.

159. Lima, Wânia R., Kleber S. Parreira, Olivier Devuyst, et al. 2010. “ZONAB Promotes Proliferation and Represses Differentiation of Proximal Tubule Epithelial Cells.” *Journal of the American Society of Nephrology : JASN* 21 (3): 478–88. https://doi.org/10.1681/ASN.2009070698.

160. Lin, Chia-Hui, Hung-Ming Huang, Mingli Hsieh, K. Michael Pollard, and Chuan Li. 2002. “Arginine Methylation of Recombinant Murine Fibrillarin by Protein Arginine Methyltransferase.” *Journal of Protein Chemistry* 21 (7): 447–53.

161. Liu, Huanting, and James H Naismith. 2008. “An Efficient One-Step Site-Directed Deletion, Insertion, Single and Multiple-Site Plasmid Mutagenesis Protocol.” *BMC Biotechnology* 8 (December): 91. https://doi.org/10.1186/1472-6750-8-91.

162. Liu, Jie, Juan Li, Pingping Li, et al. 2017. “Loss of DLG5 Promotes Breast Cancer Malignancy by Inhibiting the Hippo Signaling Pathway.” *Scientific Reports* 7 (1): 42125. https://doi.org/10.1038/srep42125.

163. Liu, Xiyang, Chengling Li, Qing Li, Hung-Chun Chang, and Yun-Chi Tang. 2020. “SIRT7 Facilitates CENP-A Nucleosome Assembly and Suppresses Intestinal Tumorigenesis.” *iScience* 23 (9): 101461. https://doi.org/10.1016/j.isci.2020.101461.

164. Liu, Youhua. 2010. “New Insights into Epithelial-Mesenchymal Transition in Kidney Fibrosis.” *Journal of the American Society of Nephrology: JASN* 21 (2): 212–22. https://doi.org/10.1681/ASN.2008121226.

165. Lohia, Madhura, Yi Qin, and Ian G Macara. 2012. “The Scribble Polarity Protein Stabilizes E-Cadherin/P120-Catenin Binding and Blocks Retrieval of E-Cadherin to the Golgi.” *Plos One* 7 (11): e51130. https://doi.org/10.1371/journal.pone.0051130.

166. Lohrum, Marion A. E., Robert L. Ludwig, Michael H. G. Kubbutat, Mary Hanlon, and Karen H. Vousden. 2003. “Regulation of HDM2 Activity by the Ribosomal Protein L11.” *Cancer Cell* 3 (6): 577–87. https://doi.org/10.1016/s1535-6108(03)00134-x.

167. Lomberk, Gwen, Lori Wallrath, and Raul Urrutia. 2006. “The Heterochromatin Protein 1 Family.” *Genome Biology* 7 (7): 228. https://doi.org/10.1186/gb-2006-7-7-228.

168. Love, Michael I, Wolfgang Huber, and Simon Anders. 2014. “Moderated Estimation of Fold Change and Dispersion for RNA-Seq Data with DESeq2.” *Genome Biology* 15 (12): 550–550. https://doi.org/10.1186/s13059-014-0550-8.

169. Lovejoy, Courtney A., Wendi Li, Steven Reisenweber, et al. 2012. “Loss of ATRX, Genome Instability, and an Altered DNA Damage Response Are Hallmarks of the Alternative Lengthening of Telomeres Pathway.” *PLoS Genetics* 8 (7): e1002772. https://doi.org/10.1371/journal.pgen.1002772.

170. Loza-Muller, Lloyd, Ulises Rodríguez-Corona, Margarita Sobol, Luis C. Rodríguez-Zapata, Pavel Hozak, and Enrique Castano. 2015. “Fibrillarin Methylates H2A in RNA Polymerase I Trans-Active Promoters in Brassica Oleracea.” *Frontiers in Plant Science* 6: 976. https://doi.org/10.3389/fpls.2015.00976.

171. Luger, K., A. W. Mäder, R. K. Richmond, D. F. Sargent, and T. J. Richmond. 1997. “Crystal Structure of the Nucleosome Core Particle at 2.8 A Resolution.” *Nature* 389 (6648): 251–60. https://doi.org/10.1038/38444.

172. Lv, Shijian, Na Wang, Hong Lv, et al. 2019. “The Attenuation of Trophoblast Invasion Caused by the Downregulation of EZH2 Is Involved in the Pathogenesis of Human Recurrent Miscarriage.” *Molecular Therapy Nucleic Acids* 14 (March): 377–87. https://doi.org/10.1016/j.omtn.2018.12.011.

173. Maison, Christèle, and Geneviève Almouzni. 2004. “HP1 and the Dynamics of Heterochromatin Maintenance.” *Nature Reviews. Molecular Cell Biology* 5 (4): 296–304. https://doi.org/10.1038/nrm1355.

174. Maizels, Yael, Adi Elbaz, Rosari Hernandez-Vicens, Oshrat Sandrusy, Anna Rosenberg, and Gabi Gerlitz. 2017. “Increased Chromatin Plasticity Supports Enhanced Metastatic Potential of Mouse Melanoma Cells.” *Experimental Cell Research* 357 (2): 282–90. https://doi.org/10.1016/j.yexcr.2017.05.025.

175. Marano, Nicholas, and James M. Holaska. 2022. “Emerin Interacts with Histone Methyltransferases to Regulate Repressive Chromatin at the Nuclear Periphery.” *Frontiers in Cell and Developmental Biology* 10 (October): 1007120. https://doi.org/10.3389/fcell.2022.1007120.

176. Marcel, Virginie, Sandra E Ghayad, Stéphane Belin, et al. 2013. “P53 Acts as a Safeguard of Translational Control by Regulating Fibrillarin and rRNA Methylation in Cancer.” *Cancer Cell* 24 (3): 318–30. https://doi.org/10.1016/j.ccr.2013.08.013.

177. Margueron, Raphael, Guohong Li, Kavitha Sarma, et al. 2008. “Ezh1 and Ezh2 Maintain Repressive Chromatin through Different Mechanisms.” *Molecular Cell* 32 (4): 503–18. https://doi.org/10.1016/j.molcel.2008.11.004.

178. Margueron, Raphaël, and Danny Reinberg. 2011. “The Polycomb Complex PRC2 and Its Mark in Life.” *Nature* 469 (7330): 343–49. https://doi.org/10.1038/nature09784.

179. Martin, Tracey A., Gareth Watkins, Robert E. Mansel, and Wen G. Jiang. 2004. “Loss of Tight Junction Plaque Molecules in Breast Cancer Tissues Is Associated with a Poor Prognosis in Patients with Breast Cancer.” *European Journal of Cancer (Oxford, England: 1990)* 40 (18): 2717–25. https://doi.org/10.1016/j.ejca.2004.08.008.

180. Massagué, Joan. 2012. “TGFβ Signalling in Context.” *Nature Reviews. Molecular Cell Biology* 13 (10): 616–30. https://doi.org/10.1038/nrm3434.

181. McCabe, Michael T, Heidi M Ott, Gopinath Ganji, et al. 2012. “EZH2 Inhibition as a Therapeutic Strategy for Lymphoma with EZH2-Activating Mutations.” *Nature* 492 (7427): 108–12. https://doi.org/10.1038/nature11606.

182. McCaffrey, Luke Martin, and Ian G. Macara. 2011. “Epithelial Organization, Cell Polarity and Tumorigenesis.” *Trends in Cell Biology* 21 (12): 727–35. https://doi.org/10.1016/j.tcb.2011.06.005.

183. McCaffrey, Luke Martin, JoAnne Montalbano, Constantina Mihai, and Ian G. Macara. 2012. “Loss of the Par3 Polarity Protein Promotes Breast Tumorigenesis and Metastasis.” *Cancer Cell* 22 (5): 601–14. https://doi.org/10.1016/j.ccr.2012.10.003.

184. McCart Reed, Amy E., Lauren Kalinowski, Peter T. Simpson, and Sunil R. Lakhani. 2021. “Invasive Lobular Carcinoma of the Breast: The Increasing Importance of This Special Subtype.” *Breast Cancer Research* 23 (1): 6. https://doi.org/10.1186/s13058-020-01384-6.

185. McIntyre, Alexa B. R., Adrian Beat Tschan, Katrina Meyer, et al. 2025. “Phosphorylation of a Nuclear Condensate Regulates Cohesion and mRNA Retention.” *Nature Communications* 16 (1): 390. https://doi.org/10.1038/s41467-024-55469-3.

186. McNeil, Elizabeth, Christopher T. Capaldo, and Ian G. Macara. 2006. “Zonula Occludens-1 Function in the Assembly of Tight Junctions in Madin-Darby Canine Kidney Epithelial Cells.” *Molecular Biology of the Cell* 17 (4): 1922–32. https://doi.org/10.1091/mbc.e05-07-0650.

187. Meshorer, Eran, Dhananjay Yellajoshula, Eric George, Peter J. Scambler, David T. Brown, and Tom Misteli. 2006. “Hyperdynamic Plasticity of Chromatin Proteins in Pluripotent Embryonic Stem Cells.” *Developmental Cell* 10 (1): 105–16. https://doi.org/10.1016/j.devcel.2005.10.017.

188. Miller, T., N. J. Krogan, J. Dover, et al. 2001. “COMPASS: A Complex of Proteins Associated with a Trithorax-Related SET Domain Protein.” *Proceedings of the National Academy of Sciences of the United States of America* 98 (23): 12902–7. https://doi.org/10.1073/pnas.231473398.

189. Misteli, Tom. 2007. “Beyond the Sequence: Cellular Organization of Genome Function.” *Cell* 128 (4): 787–800. https://doi.org/10.1016/j.cell.2007.01.028.

190. Mohn, Fabio, Michael Weber, Michael Rebhan, et al. 2008. “Lineage-Specific Polycomb Targets and de Novo DNA Methylation Define Restriction and Potential of Neuronal Progenitors.” *Molecular Cell* 30 (6): 755–66. https://doi.org/10.1016/j.molcel.2008.05.007.

191. Morin, Ryan D., Nathalie A. Johnson, Tesa M. Severson, et al. 2010. “Somatic Mutations Altering EZH2 (Tyr641) in Follicular and Diffuse Large B-Cell Lymphomas of Germinal-Center Origin.” *Nature Genetics* 42 (2): 181–85. https://doi.org/10.1038/ng.518.

192. Morschhauser, Franck, Hervé Tilly, Aristeidis Chaidos, et al. 2020. “Tazemetostat for Patients with Relapsed or Refractory Follicular Lymphoma: An Open-Label, Single-Arm, Multicentre, Phase 2 Trial.” *The Lancet. Oncology* 21 (11): 1433–42. https://doi.org/10.1016/S1470-2045(20)30441-1.

193. Mostov, Keith, Tao Su, and Martin ter Beest. 2003. “Polarized Epithelial Membrane Traffic: Conservation and Plasticity.” *Nature Cell Biology* 5 (4): 287–93. https://doi.org/10.1038/ncb0403-287.

194. Muthuswamy, Senthil K, and Bin Xue. 2012. “Cell Polarity as a Regulator of Cancer Cell Behavior Plasticity.” *Annual Review of Cell and Developmental Biology* 28 (January): 599–625. https://doi.org/10.1146/annurev-cellbio-092910-154244.

195. Nagaoka, Tadahiro, Ayumu Inutsuka, Khadiza Begum, Khandakar musabbir Bin hafiz, and Masashi Kishi. 2014. “Vangl2 Regulates E-Cadherin in Epithelial Cells.” *Scientific Reports* 4 (November): 6940. https://doi.org/10.1038/srep06940.

196. Nan, X., H. H. Ng, C. A. Johnson, et al. 1998. “Transcriptional Repression by the Methyl-CpG-Binding Protein MeCP2 Involves a Histone Deacetylase Complex.” *Nature* 393 (6683): 386–89. https://doi.org/10.1038/30764.

197. Nanes, Benjamin A, Christine Chiasson-MacKenzie, Anthony M Lowery, et al. 2012. “P120-Catenin Binding Masks an Endocytic Signal Conserved in Classical Cadherins.” *The Journal of Cell Biology* 199 (2): 365–80. https://doi.org/10.1083/jcb.201205029.

198. Nava, Michele M, Yekaterina A Miroshnikova, Leah C Biggs, et al. 2020. “Heterochromatin-Driven Nuclear Softening Protects the Genome against Mechanical Stress-Induced Damage.” *Cell* 181 (4): 800-817.e22. https://doi.org/10.1016/j.cell.2020.03.052.

199. Nelson, W. James. 2003. “Adaptation of Core Mechanisms to Generate Cell Polarity.” *Nature* 422 (6933): 766–74. https://doi.org/10.1038/nature01602.

200. Nelson, W. James. 2009. “Remodeling Epithelial Cell Organization: Transitions Between Front–Rear and Apical–Basal Polarity.” *Cold Spring Harbor Perspectives in Biology* 1 (1): a000513. https://doi.org/10.1101/cshperspect.a000513.

201. Nelson, W. James, and Roel Nusse. 2004. “Convergence of Wnt, β-Catenin, and Cadherin Pathways.” *Science (New York, N.y.)* 303 (5663): 1483–87. https://doi.org/10.1126/science.1094291.

202. Newton, Kathryn, Elisabeth Petfalski, David Tollervey, and Javier F Cáceres. 2003. “Fibrillarin Is Essential for Early Development and Required for Accumulation of an Intron-Encoded Small Nucleolar RNA in the Mouse.” *Molecular and Cellular Biology* 23 (23): 8519–27. https://doi.org/10.1128/MCB.23.23.8519-8527.2003.

203. Nguyen Van Long, Flora, Audrey Lardy-Cleaud, Dimitri Carène, et al. 2022. “Low Level of Fibrillarin, a Ribosome Biogenesis Factor, Is a New Independent Marker of Poor Outcome in Breast Cancer.” *BMC Cancer* 22 (1): 526. https://doi.org/10.1186/s12885-022-09552-x.

204. Niessen, Carien M. 2007. “Tight Junctions/Adherens Junctions: Basic Structure and Function.” *The Journal of Investigative Dermatology* 127 (11): 2525–32. https://doi.org/10.1038/sj.jid.5700865.

205. Nieto, M Angela, Ruby Yun-Ju Huang, Rebecca A Jackson, and Jean Paul Thiery. 2016. “EMT: 2016.” *Cell* 166 (1): 21–45. https://doi.org/10.1016/j.cell.2016.06.028.

206. Nourmohammadi, Fatemeh, Mohammad Mahdi Forghanifard, Mohammad Reza Abbaszadegan, and Vajiheh Zarrinpour. 2022. “EZH2 Regulates oncomiR-200c and EMT Markers in Esophageal Squamous Cell Carcinomas.” *Scientific Reports* 12 (October): 18290. https://doi.org/10.1038/s41598-022-23253-2.

207. Ntziachristos, Panagiotis, Aristotelis Tsirigos, Pieter Van Vlierberghe, et al. 2012. “Genetic Inactivation of the Polycomb Repressive Complex 2 in T Cell Acute Lymphoblastic Leukemia.” *Nature Medicine* 18 (2): 298–301. https://doi.org/10.1038/nm.2651.

208. O’Carroll, D., S. Erhardt, M. Pagani, S. C. Barton, M. A. Surani, and T. Jenuwein. 2001. “The Polycomb-Group Gene Ezh2 Is Required for Early Mouse Development.” *Molecular and Cellular Biology* 21 (13): 4330–36. https://doi.org/10.1128/MCB.21.13.4330-4336.2001.

209. Ojha, Sandeep, Sulochan Malla, Shawn M. Lyons, Sandeep Ojha, Sulochan Malla, and Shawn M. Lyons. 2020. “snoRNPs: Functions in Ribosome Biogenesis.” *Biomolecules* 10 (5). https://doi.org/10.3390/biom10050783.

210. Oki, Shinya, Tazro Ohta, Go Shioi, et al. 2018. “ChIP-Atlas: A Data-Mining Suite Powered by Full Integration of Public ChIP-Seq Data.” *EMBO Reports* 19 (12). https://doi.org/10.15252/embr.201846255.

211. Olmeda, David, Gema Moreno-Bueno, Juana M Flores, Angels Fabra, Francisco Portillo, and Amparo Cano. 2007. “SNAI1 Is Required for Tumor Growth and Lymph Node Metastasis of

Human Breast Carcinoma MDA-MB-231 Cells." *Cancer Research* 67 (24): 11721–31. https://doi.org/10.1158/0008-5472.CAN-07-2318.

212. Orsulic, S., O. Huber, H. Aberle, S. Arnold, and R. Kemler. 1999. "E-Cadherin Binding Prevents Beta-Catenin Nuclear Localization and Beta-Catenin/LEF-1-Mediated Transactivation." *Journal of Cell Science* 112 (Pt 8) (April): 1237–45. https://doi.org/10.1242/jcs.112.8.1237.

213. Oughtred, Rose, Jennifer Rust, Christie Chang, et al. 2021. "The BioGRID Database: A Comprehensive Biomedical Resource of Curated Protein, Genetic, and Chemical Interactions." *Protein Science* 30 (1): 187–200. https://doi.org/10.1002/pro.3978.

214. Ozdamar, Barish, Rohit Bose, Miriam Barrios-Rodiles, Hong-Rui Wang, Yue Zhang, and Jeffrey L. Wrana. 2005. "Regulation of the Polarity Protein Par6 by TGFbeta Receptors Controls Epithelial Cell Plasticity." *Science (New York, N.Y.)* 307 (5715): 1603–9. https://doi.org/10.1126/science.1105718.

215. Padeken, Jan, Stephen P Methot, and Susan M Gasser. 2022. "Establishment of H3K9-Methylated Heterochromatin and Its Functions in Tissue Differentiation and Maintenance." *Nature Reviews. Molecular Cell Biology* 23 (9): 623–40. https://doi.org/10.1038/s41580-022-00483-w.

216. Pasini, Diego, Adrian P. Bracken, Jacob B. Hansen, Manuela Capillo, and Kristian Helin. 2007. "The Polycomb Group Protein Suz12 Is Required for Embryonic Stem Cell Differentiation." *Molecular and Cellular Biology* 27 (10): 3769–79. https://doi.org/10.1128/MCB.01432-06.

217. Patel, Avinash, Hyun O. Lee, Louise Jawerth, et al. 2015. "A Liquid-to-Solid Phase Transition of the ALS Protein FUS Accelerated by Disease Mutation." *Cell* 162 (5): 1066–77. https://doi.org/10.1016/j.cell.2015.07.047.

218. Pederson, Thoru. 2011. "The Nucleolus." *Cold Spring Harbor Perspectives in Biology* 3 (3). https://doi.org/10.1101/cshperspect.a000638.

219. Pederson, Thoru, and Robert Y.L. Tsai. 2009. "In Search of Nonribosomal Nucleolar Protein Function and Regulation." *Journal of Cell Biology* 184 (6): 771–76. https://doi.org/10.1083/jcb.200812014.

220. Peglion, Florent, and Sandrine Etienne-Manneville. 2023. "Cell Polarity Changes in Cancer Initiation and Progression." *Journal of Cell Biology* 223 (1): e202308069. https://doi.org/10.1083/jcb.202308069.

221. Pelletier, Joffrey, George Thomas, and Siniša Volarević. 2018. "Ribosome Biogenesis in Cancer: New Players and Therapeutic Avenues." *Nature Reviews Cancer* 18 (1): 51–63. https://doi.org/10.1038/nrc.2017.104.

222. Penzo, Marianna, Lorenzo Montanaro, Davide Treré, et al. 2019. "The Ribosome Biogenesis—Cancer Connection." *Cells* 8 (1). https://doi.org/10.3390/cells8010055.

223. Pertea, Mihaela, Geo M. Pertea, Corina M. Antonescu, Tsung-Cheng Chang, Joshua T. Mendell, and Steven L. Salzberg. 2015. "StringTie Enables Improved Reconstruction of a Transcriptome from RNA-Seq Reads." *Nature Biotechnology* 33 (3): 290–95. https://doi.org/10.1038/nbt.3122.

224. Peters, A. H., D. O'Carroll, H. Scherthan, et al. 2001. "Loss of the Suv39h Histone Methyltransferases Impairs Mammalian Heterochromatin and Genome Stability." *Cell* 107 (3): 323–37. https://doi.org/10.1016/s0092-8674(01)00542-6.

225. Pieczynski, Jay, and Ben Margolis. 2011. “Protein Complexes That Control Renal Epithelial Polarity.” *American Journal of Physiology - Renal Physiology* 300 (3): F589–601. https://doi.org/10.1152/ajprenal.00615.2010.

226. Piovesan, Damiano, Alessio Del Conte, Mahta Mehdiabadi, et al. 2025. “MOBIDB in 2025: Integrating Ensemble Properties and Function Annotations for Intrinsically Disordered Proteins.” *Nucleic Acids Research* 53 (D1): D495–503. https://doi.org/10.1093/nar/gkae969.

227. Pollard, K M, D K Lee, C A Casiano, M Bluthner, M M Johnston, and E M Tan. 1997. “The Autoimmunity-Inducing Xenobiotic Mercury Interacts with the Autoantigen Fibrillarin and Modifies Its Molecular and Antigenic Properties.” *The Journal of Immunology* 158 (7): 3521–28. https://doi.org/10.4049/jimmunol.158.7.3521.

228. Pradhan, Roopali, Devika Ranade, and Kundan Sengupta. 2018. “Emerin Modulates Spatial Organization of Chromosome Territories in Cells on Softer Matrices.” *Nucleic Acids Research* 46 (11): 5561–86. https://doi.org/10.1093/nar/gky288.

229. Pylayeva-Gupta, Yuliya, Elda Grabocka, and Dafna Bar-Sagi. 2011. “RAS Oncogenes: Weaving a Tumorigenic Web.” *Nature Reviews. Cancer* 11 (11): 761–74. https://doi.org/10.1038/nrc3106.

230. Qamar, Seema, GuoZhen Wang, Suzanne J. Randle, et al. 2018. “FUS Phase Separation Is Modulated by a Molecular Chaperone and Methylation of Arginine Cation-π Interactions.” *Cell* 173 (3): 720-734.e15. https://doi.org/10.1016/j.cell.2018.03.056.

231. Qiao, Xiaomu, Isabelle Roth, Eric Féraille, and Udo Hasler. 2014. “Different Effects of ZO-1, ZO-2 and ZO-3 Silencing on Kidney Collecting Duct Principal Cell Proliferation and Adhesion.” *Cell Cycle* 13 (19): 3059–75. https://doi.org/10.4161/15384101.2014.949091.

232. Qin, Yi, Christopher Capaldo, Barry M Gumbiner, and Ian G Macara. 2005. “The Mammalian Scribble Polarity Protein Regulates Epithelial Cell Adhesion and Migration through E-Cadherin.” *The Journal of Cell Biology* 171 (6): 1061–71. https://doi.org/10.1083/jcb.200506094.

233. Ren, Gang, Stavroula Baritaki, Himangi Marathe, et al. 2012. “Polycomb Protein EZH2 Regulates Tumor Invasion via the Transcriptional Repression of the Metastasis Suppressor RKIP in Breast and Prostate Cancer.” *Cancer Research* 72 (12): 3091–104. https://doi.org/10.1158/0008-5472.CAN-11-3546.

234. Rhim, Andrew D., Emily T. Mirek, Nicole M. Aiello, et al. 2012. “EMT and Dissemination Precede Pancreatic Tumor Formation.” *Cell* 148 (1–2): 349–61. https://doi.org/10.1016/j.cell.2011.11.025.

235. Rhodes, Nelson, Dirk A Heerding, Derek R Duckett, et al. 2008. “Characterization of an Akt Kinase Inhibitor with Potent Pharmacodynamic and Antitumor Activity.” *Cancer Research* 68 (7): 2366–74. https://doi.org/10.1158/0008-5472.CAN-07-5783.

236. Riback, Joshua A., Jorine M. Eeftens, Daniel S. W. Lee, et al. 2023. “Viscoelasticity and Advective Flow of RNA Underlies Nucleolar Form and Function.” *Molecular Cell* 83 (17): 3095-3107.e9. https://doi.org/10.1016/j.molcel.2023.08.006.

237. Riggelen, Jan van, Alper Yetil, and Dean W Felsher. 2010. “MYC as a Regulator of Ribosome Biogenesis and Protein Synthesis.” *Nature Reviews Cancer* 10 (4): 301–9. https://doi.org/10.1038/nrc2819.

238. Rinn, John L., Michael Kertesz, Jordon K. Wang, et al. 2007. “Functional Demarcation of Active and Silent Chromatin Domains in Human HOX Loci by Noncoding RNAs.” *Cell* 129 (7): 1311–23. https://doi.org/10.1016/j.cell.2007.05.022.

239. Robinson, James T., Helga Thorvaldsdóttir, Wendy Winckler, et al. 2011. “Integrative Genomics Viewer.” *Nature Biotechnology* 29 (1): 24–26. https://doi.org/10.1038/nbt.1754.

240. Rodriguez, Fausto J., Laura J. Lewis-Tuffin, and Panos Z. Anastasiadis. 2012. “E-Cadherin’s Dark Side: Possible Role in Tumor Progression.” *Biochimica Et Biophysica Acta* 1826 (1): 23–31. https://doi.org/10.1016/j.bbcan.2012.03.002.

241. Rodriguez-Boulan, E., and W. J. Nelson. 1989. “Morphogenesis of the Polarized Epithelial Cell Phenotype.” *Science (New York, N.Y.)* 245 (4919): 718–25. https://doi.org/10.1126/science.2672330.

242. Rodriguez-Boulan, Enrique, and Ian G Macara. 2014. “Organization and Execution of the Epithelial Polarity Programme.” *Nature Reviews Molecular Cell Biology* 15 (4): 225–42. https://doi.org/10.1038/nrm3775.

243. Rodriguez-Corona, Ulises, Alejandro Pereira-Santana, Margarita Sobol, Luis C. Rodriguez-Zapata, Pavel Hozak, and Enrique Castano. 2017. “Novel Ribonuclease Activity Differs between Fibrillarins from Arabidopsis Thaliana.” *Frontiers in Plant Science* 8 (October). https://doi.org/10.3389/fpls.2017.01878.

244. Rodriguez-Corona, Ulises, Margarita Sobol, Luis Carlos Rodriguez-Zapata, Pavel Hozak, and Enrique Castano. 2015. “Fibrillarin from Archaea to Human.” *Biology of the Cell* 107 (6): 159–74. https://doi.org/10.1111/boc.201400077.

245. Roh, Michael H., Olga Makarova, Chia-Jen Liu, et al. 2002. “The Maguk Protein, Pals1, Functions as an Adapter, Linking Mammalian Homologues of Crumbs and Discs Lost.” *The Journal of Cell Biology* 157 (1): 161–72. https://doi.org/10.1083/jcb.200109010.

246. Roy, Sayoni, Raghava R. Sunkara, Manan Y. Parmar, Saima Shaikh, and Sanjeev K. Waghmare. 2021. “EMT Imparts Cancer Stemness and Plasticity: New Perspectives and Therapeutic Potential.” *Frontiers in Bioscience (Landmark Edition)* 26 (2): 238–65. https://doi.org/10.2741/4893.

247. Royer, C., and X. Lu. 2011. “Epithelial Cell Polarity: A Major Gatekeeper against Cancer?” *Cell Death & Differentiation* 18 (9): 1470–77. https://doi.org/10.1038/cdd.2011.60.

248. Rubbi, Carlos P, and Jo Milner. 2003. “Disruption of the Nucleolus Mediates Stabilization of P53 in Response to DNA Damage and Other Stresses.” *The EMBO Journal* 22 (22): 6068–77. https://doi.org/10.1093/emboj/cdg579.

249. Sabari, Benjamin R., Alessandra Dall’Agnese, Ann Boija, et al. 2018. “Coactivator Condensation at Super-Enhancers Links Phase Separation and Gene Control.” *Science (New York, N.Y.)* 361 (6400): eaar3958. https://doi.org/10.1126/science.aar3958.

250. Saffarian, Sarina, Ziwei Cai, Jordan Lam, Htoo Zarni Oo, and Syam Somasekharan. 2025. “Elevated NPM1 and FBL Expression Correlates with Prostate Cancer Aggressiveness and Progression.” *The Journal of Pathology* 267 (1): 56–68. https://doi.org/10.1002/path.6447.

251. Saha, Santam, Balaji A.K., Sweety Meel, Dimple Notani, and Kundan Sengupta. 2025. “Fibrillarin Regulates Epithelial Integrity via EZH2-Mediated Modulation of Scribble Expression.” *Cell Reports* 44 (12). https://doi.org/10.1016/j.celrep.2025.116608.

252. Salvetti, Anna, and Anna Greco. 2014. “Viruses and the Nucleolus: The Fatal Attraction.” *Biochimica Et Biophysica Acta* 1842 (6): 840–47. https://doi.org/10.1016/j.bbadis.2013.12.010.

253. Santos-Rosa, Helena, Robert Schneider, Andrew J. Bannister, et al. 2002. “Active Genes Are Tri-Methylated at K4 of Histone H3.” *Nature* 419 (6905): 407–11. https://doi.org/10.1038/nature01080.

254. Savino, Tulia Maria, Jeannine Gébrane-Younès, Jan De Mey, Jean-Baptiste Sibarita, and Danièle Hernandez-Verdun. 2001. “Nucleolar Assembly of the Rrna Processing Machinery in Living Cells.” *Journal of Cell Biology* 153 (5): 1097–110. https://doi.org/10.1083/jcb.153.5.1097.

255. Saxena, Kritika, Mohit Kumar Jolly, and Kuppusamy Balamurugan. 2020. “Hypoxia, Partial EMT and Collective Migration: Emerging Culprits in Metastasis.” *Translational Oncology* 13 (11): 100845. https://doi.org/10.1016/j.tranon.2020.100845.

256. Schiano Lomoriello, Irene, Giovanni Giangreco, Claudia Iavarone, et al. 2020. “A Self-Sustaining Endocytic-Based Loop Promotes Breast Cancer Plasticity Leading to Aggressiveness and pro-Metastatic Behavior.” *Nature Communications* 11 (1): 3020. https://doi.org/10.1038/s41467-020-16836-y.

257. Schmidt, Enrico K, Giovanna Clavarino, Maurizio Ceppi, and Philippe Pierre. 2009. “SUnSET, a Nonradioactive Method to Monitor Protein Synthesis.” *Nature Methods* 6 (4): 275–77. https://doi.org/10.1038/nmeth.1314.

258. Schotta, Gunnar, Monika Lachner, Kavitha Sarma, et al. 2004. “A Silencing Pathway to Induce H3-K9 and H4-K20 Trimethylation at Constitutive Heterochromatin.” *Genes & Development* 18 (11): 1251–62. https://doi.org/10.1101/gad.300704.

259. Schuettengruber, Bernd, Henri-Marc Bourbon, Luciano Di Croce, and Giacomo Cavalli. 2017. “Genome Regulation by Polycomb and Trithorax: 70 Years and Counting.” *Cell* 171 (1): 34–57. https://doi.org/10.1016/j.cell.2017.08.002.

260. Sen Gupta, Ayantika, and Kundan Sengupta. 2017. “Lamin B2 Modulates Nucleolar Morphology, Dynamics, and Function.” *Molecular and Cellular Biology* 37 (24). https://doi.org/10.1128/MCB.00274-17.

261. Serrano-Gomez, Silvia Juliana, Mazvita Maziveyi, and Suresh K. Alahari. 2016. “Regulation of Epithelial-Mesenchymal Transition through Epigenetic and Post-Translational Modifications.” *Molecular Cancer* 15 (February): 18. https://doi.org/10.1186/s12943-016-0502-x.

262. Shen, Shiquan, Honglong Zhou, Zongyu Xiao, et al. 2024. “PRMT1 in Human Neoplasm: Cancer Biology and Potential Therapeutic Target.” *Cell Communication and Signaling : CCS* 22 (February): 102. https://doi.org/10.1186/s12964-024-01506-z.

263. Shen, Xiaohua, Yingchun Liu, Yu-Jung Hsu, et al. 2008. “EZH1 Mediates Methylation on Histone H3 Lysine 27 and Complements EZH2 in Maintaining Stem Cell Identity and Executing Pluripotency.” *Molecular Cell* 32 (4): 491–502. https://doi.org/10.1016/j.molcel.2008.10.016.

264. Shubina, M Y, Y R Musinova, and E V Sheval. 2016. “Nucleolar Methyltransferase Fibrillarin: Evolution of Structure and Functions.” *Biochemistry. Biokhimiia* 81 (9): 941–50. https://doi.org/10.1134/S0006297916090030.

265. Shubina, Maria Y, Eugene A Arifulin, Dmitry V Sorokin, et al. 2020. “The GAR Domain Integrates Functions That Are Necessary for the Proper Localization of Fibrillarin (FBL) inside Eukaryotic Cells.” *PeerJ* 8 (April): e9029. https://doi.org/10.7717/peerj.9029.

266. Sims, Robert J., Chi-Fu Chen, Helena Santos-Rosa, Tony Kouzarides, Smita S. Patel, and Danny Reinberg. 2005. “Human but Not Yeast CHD1 Binds Directly and Selectively to Histone H3 Methylated at Lysine 4 via Its Tandem Chromodomains.” *The Journal of Biological Chemistry* 280 (51): 41789–92. https://doi.org/10.1074/jbc.C500395200.

267. Sirri, Valentina, Silvio Urcuqui-Inchima, Pascal Roussel, and Danièle Hernandez-Verdun. 2008. “Nucleolus: The Fascinating Nuclear Body.” *Histochemistry and Cell Biology* 129 (1): 13–31. https://doi.org/10.1007/s00418-007-0359-6.

268. Sloan, Katherine E., Ahmed S. Warda, Sunny Sharma, Karl-Dieter Entian, Denis L. J. Lafontaine, and Markus T. Bohnsack. 2016. “Tuning the Ribosome: The Influence of rRNA Modification on Eukaryotic Ribosome Biogenesis and Function.” *RNA Biology* 14 (9): 1138–52. https://doi.org/10.1080/15476286.2016.1259781.

269. Snaar, S, K Wiesmeijer, A G Jochemsen, H J Tanke, and R W Dirks. 2000. “Mutational Analysis of Fibrillarin and Its Mobility in Living Human Cells.” *The Journal of Cell Biology* 151 (3): 653–62. https://doi.org/10.1083/jcb.151.3.653.

270. Sohal, Sukhwinder S., David Reid, Amir Soltani, et al. 2011. “Evaluation of Epithelial Mesenchymal Transition in Patients with Chronic Obstructive Pulmonary Disease.” *Respiratory Research* 12 (1): 130. https://doi.org/10.1186/1465-9921-12-130.

271. Solovei, Irina, Moritz Kreysing, Christian Lanctôt, et al. 2009. “Nuclear Architecture of Rod Photoreceptor Cells Adapts to Vision in Mammalian Evolution.” *Cell* 137 (2): 356–68. https://doi.org/10.1016/j.cell.2009.01.052.

272. Solovei, Irina, Audrey S Wang, Katharina Thanisch, et al. 2013. “LBR and Lamin A/C Sequentially Tether Peripheral Heterochromatin and Inversely Regulate Differentiation.” *Cell* 152 (3): 584–98. https://doi.org/10.1016/j.cell.2013.01.009.

273. St Johnston, Daniel, and Bénédicte Sanson. 2011. “Epithelial Polarity and Morphogenesis.” *Current Opinion in Cell Biology* 23 (5): 540–46. https://doi.org/10.1016/j.ceb.2011.07.005.

274. Steensel, Bas van, and Andrew S Belmont. 2017. “Lamina-Associated Domains: Links with Chromosome Architecture, Heterochromatin, and Gene Repression.” *Cell* 169 (5): 780–91. https://doi.org/10.1016/j.cell.2017.04.022.

275. Stephens, Andrew D., Edward J. Banigan, Stephen A. Adam, Robert D. Goldman, and John F. Marko. 2017. “Chromatin and Lamin A Determine Two Different Mechanical Response Regimes of the Cell Nucleus.” *Molecular Biology of the Cell* 28 (14): 1984–96. https://doi.org/10.1091/mbc.E16-09-0653.

276. Stephens, Andrew D, Patrick Z Liu, Edward J Banigan, et al. 2018. “Chromatin Histone Modifications and Rigidity Affect Nuclear Morphology Independent of Lamins.” *Molecular Biology of the Cell* 29 (2): 220–33. https://doi.org/10.1091/mbc.E17-06-0410.

277. Stępiński, Dariusz. 2018. “The Nucleolus, an Ally, and an Enemy of Cancer Cells.” *Histochemistry and Cell Biology* 150 (6): 607–29. https://doi.org/10.1007/s00418-018-1706-5.

278. Su, Wen-Hui, Dolores D. Mruk, Elissa W.P. Wong, Wing-Yee Lui, and C. Yan Cheng. 2012. “Polarity Protein Complex Scribble/Lgl/Dlg and Epithelial Cell Barriers.” *Advances in Experimental Medicine and Biology* 763: 149–70. https://doi.org/10.1007/978-1-4614-4711-5_7.

279. Su, Wenhui, Elissa W. P. Wong, Dolores D. Mruk, and C. Yan Cheng. 2012. “The Scribble/Lgl/Dlg Polarity Protein Complex Is a Regulator of Blood-Testis Barrier Dynamics and

Spermatid Polarity during Spermatogenesis." *Endocrinology* 153 (12): 6041–53. https://doi.org/10.1210/en.2012-1670.

280. Subramanian, Aravind, Pablo Tamayo, Vamsi K Mootha, et al. 2005. "Gene Set Enrichment Analysis: A Knowledge-Based Approach for Interpreting Genome-Wide Expression Profiles." *Proceedings of the National Academy of Sciences of the United States of America* 102 (43): 15545–50. https://doi.org/10.1073/pnas.0506580102.

281. Sun, Xiaorui, Congwen Gao, Xin Xu, et al. 2023. "FBL Promotes Cancer Cell Resistance to DNA Damage and BRCA1 Transcription via YBX1." *EMBO Reports* 24 (9): e56230. https://doi.org/10.15252/embr.202256230.

282. Suzuki, Keiko, Pinaki Bose, Rebecca Yy Leong-Quong, Donald J Fujita, and Karl Riabowol. 2010. "REAP: A Two Minute Cell Fractionation Method." *BMC Research Notes* 3 (November): 294. https://doi.org/10.1186/1756-0500-3-294.

283. Takeichi, M. 1991. "Cadherin Cell Adhesion Receptors as a Morphogenetic Regulator." *Science* 251 (5000): 1451–55. https://doi.org/10.1126/science.2006419.

284. Tan, E-Jean, Kaoru Kahata, Oskar Idås, Sylvie Thuault, Carl-Henrik Heldin, and Aristidis Moustakas. 2015. "The High Mobility Group A2 Protein Epigenetically Silences the Cdh1 Gene during Epithelial-to-Mesenchymal Transition." *Nucleic Acids Research* 43 (1): 162–78. https://doi.org/10.1093/nar/gku1293.

285. Tang, Doudou, Mingjie Chen, Xinhua Huang, et al. 2023. "SRplot: A Free Online Platform for Data Visualization and Graphing." *PLOS ONE* 18 (11): e0294236. https://doi.org/10.1371/journal.pone.0294236.

286. Tang, Jie, Jonathan D. Gary, Steven Clarke, and Harvey R. Herschman. 1998. "PRMT 3, a Type I Protein Arginine *N*-Methyltransferase That Differs from PRMT1 in Its Oligomerization, Subcellular Localization, Substrate Specificity, and Regulation*." *Journal of Biological Chemistry* 273 (27): 16935–45. https://doi.org/10.1074/jbc.273.27.16935.

287. Tang, Zefang, Boxi Kang, Chenwei Li, Tianxiang Chen, and Zemin Zhang. 2019. "GEPIA2: An Enhanced Web Server for Large-Scale Expression Profiling and Interactive Analysis." *Nucleic Acids Research* 47 (W1): W556–60. https://doi.org/10.1093/nar/gkz430.

288. Taverna, Sean D., Haitao Li, Alexander J. Ruthenburg, C. David Allis, and Dinshaw J. Patel. 2007. "How Chromatin-Binding Modules Interpret Histone Modifications: Lessons from Professional Pocket Pickers." *Nature Structural & Molecular Biology* 14 (11): 1025–40. https://doi.org/10.1038/nsmb1338.

289. Teng, Yu-Ching, Aishwarya Sundaresan, Ryan O'Hara, et al. 2021. "ATRX Promotes Heterochromatin Formation to Protect Cells from G-Quadruplex DNA-Mediated Stress." *Nature Communications* 12 (1): 3887. https://doi.org/10.1038/s41467-021-24206-5.

290. Teschendorff, Andrew E., Usha Menon, Aleksandra Gentry-Maharaj, et al. 2010. "Age-Dependent DNA Methylation of Genes That Are Suppressed in Stem Cells Is a Hallmark of Cancer." *Genome Research* 20 (4): 440–46. https://doi.org/10.1101/gr.103606.109.

291. Tessarz, Peter, Helena Santos-Rosa, Sam C Robson, et al. 2014. "Glutamine Methylation in Histone H2A Is an RNA-Polymerase-I-Dedicated Modification." *Nature* 505 (7484): 564–68. https://doi.org/10.1038/nature12819.

292. Thandapani, Palaniraja, Timothy R. O'Connor, Timothy L. Bailey, and Stéphane Richard. 2013. "Defining the RGG/RG Motif." *Molecular Cell* 50 (5): 613–23. https://doi.org/10.1016/j.molcel.2013.05.021.

293. "The Role of the Nucleolus in Regulating the Cell Cycle and the DNA Damage Response." 2023. In *Advances in Protein Chemistry and Structural Biology*, vol. 135. Academic Press. https://doi.org/10.1016/bs.apcsb.2023.01.001.

294. Thiery, Jean Paul. 2002. "Epithelial-Mesenchymal Transitions in Tumour Progression." *Nature Reviews. Cancer* 2 (6): 442–54. https://doi.org/10.1038/nrc822.

295. Thiery, Jean Paul, Hervé Acloque, Ruby Y J Huang, and M Angela Nieto. 2009. "Epithelial-Mesenchymal Transitions in Development and Disease." *Cell* 139 (5): 871–90. https://doi.org/10.1016/j.cell.2009.11.007.

296. Thiery, Jean Paul, and Jonathan P. Sleeman. 2006. "Complex Networks Orchestrate Epithelial-Mesenchymal Transitions." *Nature Reviews. Molecular Cell Biology* 7 (2): 131–42. https://doi.org/10.1038/nrm1835.

297. Thiry, Marc, and Denis L. J. Lafontaine. 2005. "Birth of a Nucleolus: The Evolution of Nucleolar Compartments." *Trends in Cell Biology* 15 (4): 194–99. https://doi.org/10.1016/j.tcb.2005.02.007.

298. Thoms, Matthias, Robert Buschauer, Michael Ameismeier, et al. 2020. "Structural Basis for Translational Shutdown and Immune Evasion by the Nsp1 Protein of SARS-CoV-2." *Science* 369 (6508): 1249–55. https://doi.org/10.1126/science.abc8665.

299. Tie, Feng, Rakhee Banerjee, Carl A. Stratton, et al. 2009. "CBP-Mediated Acetylation of Histone H3 Lysine 27 Antagonizes Drosophila Polycomb Silencing." *Development (Cambridge, England)* 136 (18): 3131–41. https://doi.org/10.1242/dev.037127.

300. Tiku, Varnesh, Chun Kew, Parul Mehrotra, Raja Ganesan, Nirmal Robinson, and Adam Antebi. 2018. "Nucleolar Fibrillarin Is an Evolutionarily Conserved Regulator of Bacterial Pathogen Resistance." *Nature Communications* 9 (September): 3607. https://doi.org/10.1038/s41467-018-06051-1.

301. Tollervey, D, H Lehtonen, M Carmo-Fonseca, and E C Hurt. 1991. "The Small Nucleolar RNP Protein NOP1 (Fibrillarin) Is Required for Pre-rRNA Processing in Yeast." *The EMBO Journal* 10 (3): 573–83. https://doi.org/10.1002/j.1460-2075.1991.tb07984.x.

302. Tollervey, David, Hanna Lehtonen, Ralf Jansen, Hildegard Kern, and Eduard C. Hurt. 1993. "Temperature-Sensitive Mutations Demonstrate Roles for Yeast Fibrillarin in Pre-rRNA Processing, Pre-rRNA Methylation, and Ribosome Assembly." *Cell* 72 (3): 443–57.

303. Treyer, Aleksandr, and Anne Müsch. 2013. "Hepatocyte Polarity." *Comprehensive Physiology* 3 (January): 243–87. https://doi.org/10.1002/cphy.c120009.

304. Tria, Scherrine, Leslie H. Jimison, Adel Hama, Manuelle Bongo, and Róisín M. Owens. 2013. "Sensing of EGTA Mediated Barrier Tissue Disruption with an Organic Transistor." *Biosensors* 3 (1): 44–57. https://doi.org/10.3390/bios3010044.

305. Trojer, Patrick, and Danny Reinberg. 2007. "Facultative Heterochromatin: Is There a Distinctive Molecular Signature?" *Molecular Cell* 28 (1): 1–13. https://doi.org/10.1016/j.molcel.2007.09.011.

306. Tunggal, Judith A, Iris Helfrich, Annika Schmitz, et al. 2005. “E-Cadherin Is Essential for in Vivo Epidermal Barrier Function by Regulating Tight Junctions.” *The EMBO Journal* 24 (6): 1146–56. https://doi.org/10.1038/sj.emboj.7600605.

307. Turner, Jerrold R. 2009. “Intestinal Mucosal Barrier Function in Health and Disease.” *Nature Reviews. Immunology* 9 (11): 799–809. https://doi.org/10.1038/nri2653.

308. Uhlén, Mathias, Linn Fagerberg, Björn M. Hallström, et al. 2015. “Tissue-Based Map of the Human Proteome.” *Science* 347 (6220): 1260419. https://doi.org/10.1126/science.1260419.

309. Umeda, Kazuaki, Junichi Ikenouchi, Sayaka Katahira-Tayama, et al. 2006. “ZO-1 and ZO-2 Independently Determine Where Claudins Are Polymerized in Tight-Junction Strand Formation.” *Cell* 126 (4): 741–54. https://doi.org/10.1016/j.cell.2006.06.043.

310. Van Hooser, Aaron A., Patrick Yuh, and Rebecca Heald. 2005. “The Perichromosomal Layer.” *Chromosoma* 114 (6): 377–88. https://doi.org/10.1007/s00412-005-0021-9.

311. Van Itallie, Christina M., Alan S. Fanning, Arlene Bridges, and James M. Anderson. 2009. “ZO-1 Stabilizes the Tight Junction Solute Barrier through Coupling to the Perijunctional Cytoskeleton.” *Molecular Biology of the Cell* 20 (17): 3930–40. https://doi.org/10.1091/mbc.e09-04-0320.

312. Varambally, Sooryanarayana, Saravana M Dhanasekaran, Ming Zhou, et al. 2002. “The Polycomb Group Protein EZH2 Is Involved in Progression of Prostate Cancer.” *Nature* 419 (6907): 624–29. https://doi.org/10.1038/nature01075.

313. Varelas, Xaralabos, Bryan W. Miller, Richelle Sopko, et al. 2010. “The Hippo Pathway Regulates Wnt/Beta-Catenin Signaling.” *Developmental Cell* 18 (4): 579–91. https://doi.org/10.1016/j.devcel.2010.03.007.

314. Vaughan, M. A. 1987. “An Autoimmune Antibody from Scleroderma Patients Recognizes a Component of the Plant Cell Nucleolus.” *Histochemistry* 86 (5): 533–35. https://doi.org/10.1007/BF00500629.

315. Venkatraman Girija, Umakhanth, Alexandre R. Gingras, Jamie E. Marshall, et al. 2013. “Structural Basis of the C1q/C1s Interaction and Its Central Role in Assembly of the C1 Complex of Complement Activation.” *Proceedings of the National Academy of Sciences of the United States of America* 110 (34): 13916–20. https://doi.org/10.1073/pnas.1311113110.

316. Vermeulen, Michiel, Klaas W. Mulder, Sergei Denissov, et al. 2007. “Selective Anchoring of TFIID to Nucleosomes by Trimethylation of Histone H3 Lysine 4.” *Cell* 131 (1): 58–69. https://doi.org/10.1016/j.cell.2007.08.016.

317. Visel, Axel, Edward M. Rubin, and Len A. Pennacchio. 2009. “Genomic Views of Distant-Acting Enhancers.” *Nature* 461 (7261): 199–205. https://doi.org/10.1038/nature08451.

318. Wang, Feng, Shitong Chen, Shihan Peng, et al. 2023. “PRMT1 Promotes the Proliferation and Metastasis of Gastric Cancer Cells by Recruiting MLXIP for the Transcriptional Activation of the β-Catenin Pathway.” *Genes & Diseases* 10 (6): 2622–38. https://doi.org/10.1016/j.gendis.2023.02.006.

319. Wang, Hongming, David Boisvert, Kyeong Kyu Kim, Rosalind Kim, and Sung-Hou Kim. 2000. “Crystal Structure of a Fibrillarin Homologue from Methanococcus Jannaschii, a Hyperthermophile, at 1.6 Å Resolution.” *The EMBO Journal* 19 (3): 317–23. https://doi.org/10.1093/emboj/19.3.317.

320. Wang, Lei, Xiao-ming Ren, Jun-ji Xing, and Alan C. Zheng. 2010. “The Nucleolus and Viral Infection.” *Virologica Sinica* 25 (3): 151–57. https://doi.org/10.1007/s12250-010-3093-5.

321. Wang, Yi-Chun, Shang-Hsuan Huang, Chien-Ping Chang, et al. 2023. “Identification and Characterization of Glycine- and Arginine-Rich Motifs in Proteins by a Novel GAR Motif Finder Program.” *Genes* 14 (2). https://doi.org/10.3390/genes14020330.

322. Wang, Zhibin, Chongzhi Zang, Jeffrey A. Rosenfeld, et al. 2008. “Combinatorial Patterns of Histone Acetylations and Methylations in the Human Genome.” *Nature Genetics* 40 (7): 897–903. https://doi.org/10.1038/ng.154.

323. Watkins, Nicholas J, and Markus T Bohnsack. 2012. “The Box C/D and H/ACA snoRNPs: Key Players in the Modification, Processing and the Dynamic Folding of Ribosomal RNA.” *Wiley Interdisciplinary Reviews. RNA* 3 (3): 397–414. https://doi.org/10.1002/wrna.117.

324. Wei, Wang, Zhang Xiao Jing, Zheng Ke, and Pei Yi. 2017. “Sirtuin 7 Plays an Oncogenic Role in Human Osteosarcoma via Downregulating CDC4 Expression.” *American Journal of Cancer Research* 7 (9): 1788–803.

325. Wheelock, Margaret J., Yasushi Shintani, Masato Maeda, Yuri Fukumoto, and Keith R. Johnson. 2008. “Cadherin Switching.” *Journal of Cell Science* 121 (Pt 6): 727–35. https://doi.org/10.1242/jcs.000455.

326. Wilson, Boris G., Xi Wang, Xiaohua Shen, et al. 2010. “Epigenetic Antagonism between Polycomb and SWI/SNF Complexes during Oncogenic Transformation.” *Cancer Cell* 18 (4): 316–28. https://doi.org/10.1016/j.ccr.2010.09.006.

327. Woodson, S. A. 2000. “Recent Insights on RNA Folding Mechanisms from Catalytic RNA.” *Cellular and Molecular Life Sciences: CMLS* 57 (5): 796–808. https://doi.org/10.1007/s000180050042.

328. Wozniak, Michele A., and Christopher S. Chen. 2009. “Mechanotransduction in Development: A Growing Role for Contractility.” *Nature Reviews. Molecular Cell Biology* 10 (1): 34–43. https://doi.org/10.1038/nrm2592.

329. Wu, J., S.-W. Lee, X. Zhang, et al. 2013. “Foxo3a Transcription Factor Is a Negative Regulator of Skp2 and Skp2 SCF Complex.” *Oncogene* 32 (1): 78–85. https://doi.org/10.1038/onc.2012.26.

330. Wu, Ting, Mounira Chalabi-Dchar, Wei Xiong, et al. 2025. “Fibrillarin Contributes to the Oncogenic Characteristics of Colorectal Cancer Cells and Reduces Sensitivity to 5-Fluorouracil.” *Cancers* 17 (24). https://doi.org/10.3390/cancers17243900.

331. Xu, Jian, Samy Lamouille, and Rik Derynck. 2009. “TGF-Beta-Induced Epithelial to Mesenchymal Transition.” *Cell Research* 19 (2): 156–72. https://doi.org/10.1038/cr.2009.5.

332. Xu, Kexin, Zhenhua Jeremy Wu, Anna C. Groner, et al. 2012. “EZH2 Oncogenic Activity in Castration-Resistant Prostate Cancer Cells Is Polycomb-Independent.” *Science (New York, N.Y.)* 338 (6113): 1465–69. https://doi.org/10.1126/science.1227604.

333. Xue, Y., J. Wong, G. T. Moreno, M. K. Young, J. Côté, and W. Wang. 1998. “NURD, a Novel Complex with Both ATP-Dependent Chromatin-Remodeling and Histone Deacetylase Activities.” *Molecular Cell* 2 (6): 851–61. https://doi.org/10.1016/s1097-2765(00)80299-3.

334. Yamanaka, Tomoyuki. 2008. “Role of Lgl/Dlg/Scribble in the Regulation of Epithelial Junction, Polarity and Growth.” *Frontiers in Bioscience* Volume (13): 6693. https://doi.org/10.2741/3182.

335. Yan, Jia, Ke xin Li, Lei Yu, et al. 2024. “PRMT1 Integrates Immune Microenvironment and Fatty Acid Metabolism Response in Progression of Hepatocellular Carcinoma.” *Journal of Hepatocellular Carcinoma* 11 (January): 15–27. https://doi.org/10.2147/JHC.S443130.

336. Yang, Kai, Jie Yang, and Jing Yi. 2018. “Nucleolar Stress: Hallmarks, Sensing Mechanism and Diseases.” *Cell Stress* 2 (6): 125–40. https://doi.org/10.15698/cst2018.06.139.

337. Yang, X.-J., and E. Seto. 2007. “HATs and HDACs: From Structure, Function and Regulation to Novel Strategies for Therapy and Prevention.” *Oncogene* 26 (37): 5310–18. https://doi.org/10.1038/sj.onc.1210599.

338. Yao, Run-Wen, Guang Xu, Ying Wang, et al. 2019. “Nascent Pre-rRNA Sorting via Phase Separation Drives the Assembly of Dense Fibrillar Components in the Human Nucleolus.” *Molecular Cell* 76 (5): 767-783.e11. https://doi.org/10.1016/j.molcel.2019.08.014.

339. Ye, Keqiong, Ru Jia, Jinzhong Lin, et al. 2009. “Structural Organization of Box C/D RNA-Guided RNA Methyltransferase.” *Proceedings of the National Academy of Sciences of the United States of America* 106 (33): 13808–13. https://doi.org/10.1073/pnas.0905128106.

340. Yerlici, V. Talya, Audrey Astori, Nevraj S. Kejiou, et al. 2024. “SARS-CoV-2 Targets Ribosomal RNA Biogenesis.” *Cell Reports* 43 (3): 113891. https://doi.org/10.1016/j.celrep.2024.113891.

341. Yeung, Kay T., and Jing Yang. 2017. “Epithelial–Mesenchymal Transition in Tumor Metastasis.” *Molecular Oncology* 11 (1): 28–39. https://doi.org/10.1002/1878-0261.12017.

342. Yi, Yang, Yanqiang Li, Qingshu Meng, et al. 2021. “A PRC2-Independent Function for EZH2 in Regulating rRNA 2’-O Methylation and IRES-Dependent Translation.” *Nature Cell Biology* 23 (4): 341–54. https://doi.org/10.1038/s41556-021-00653-6.

343. Yorifuji, H., Y. Tadano, Y. Tsuchiya, et al. 1997. “Emerin, Deficiency of Which Causes Emery-Dreifuss Muscular Dystrophy, Is Localized at the Inner Nuclear Membrane.” *Neurogenetics* 1 (2): 135–40. https://doi.org/10.1007/s100480050020.

344. Yu, Shiyan, and Nan Gao. 2015. “Compartmentalizing Intestinal Epithelial Cell Toll-like Receptors for Immune Surveillance.” *Cellular and Molecular Life Sciences: CMLS* 72 (17): 3343–53. https://doi.org/10.1007/s00018-015-1931-1.

345. Yuan, Wen, Mo Xu, Chang Huang, Nan Liu, She Chen, and Bing Zhu. 2011. “H3K36 Methylation Antagonizes PRC2-Mediated H3K27 Methylation*.” *Journal of Biological Chemistry* 286 (10): 7983–89. https://doi.org/10.1074/jbc.M110.194027.

346. Zeisberg, Michael, and Eric G. Neilson. 2009. “Biomarkers for Epithelial-Mesenchymal Transitions.” *The Journal of Clinical Investigation* 119 (6): 1429–37. https://doi.org/10.1172/JCI36183.

347. Zeisberg, Michael, Changqing Yang, Margot Martino, et al. 2007. “Fibroblasts Derive from Hepatocytes in Liver Fibrosis via Epithelial to Mesenchymal Transition.” *The Journal of Biological Chemistry* 282 (32): 23337–47. https://doi.org/10.1074/jbc.M700194200.

348. Zeissig, S., N. Bürgel, D. Günzel, et al. 2007. “Changes in Expression and Distribution of Claudin 2, 5 and 8 Lead to Discontinuous Tight Junctions and Barrier Dysfunction in Active Crohn’s Disease.” Inflammatory Bowel Disease. *Gut* 56 (1): 61–72. https://doi.org/10.1136/gut.2006.094375.

349. Zhan, Lixing, Avi Rosenberg, Kenneth C Bergami, et al. 2008. “Deregulation of Scribble Promotes Mammary Tumorigenesis and Reveals a Role for Cell Polarity in Carcinoma.” *Cell* 135 (5): 865–78. https://doi.org/10.1016/j.cell.2008.09.045.

350. Zhang, Xue, Wenxin Li, Shulan Sun, and Yefu Liu. 2024. “Advances in the Structure and Function of the Nucleolar Protein Fibrillarin.” *Frontiers in Cell and Developmental Biology* 12 (November). https://doi.org/10.3389/fcell.2024.1494631.

351. Zong, Xingyue, Weini Wang, Ali Ozes, Fang Fang, George E. Sandusky, and Kenneth P. Nephew. 2020. “EZH2-Mediated Downregulation of the Tumor Suppressor DAB2IP Maintains Ovarian Cancer Stem Cells.” *Cancer Research* 80 (20): 4371–85. https://doi.org/10.1158/0008-5472.CAN-20-0458.

Appendix

REAGENT or RESOURCE	SOURCE	IDENTIFIER
Antibodies		
Mouse monoclonal anti-FBL(IB, IFA)	Abcam	Cat#ab4566
Rabbit polyclonal anti-FBL (IB, IFA)	Abcam	Cat#ab5821
Rabbit monoclonal anti-E-cadherin(IB)	Cell Signaling Technology	E-Cadherin (24E10) Rabbit mAb Cat#3195
Mouse monoclonal anti-E-cadherin(IB, IFA)	Abcam	Cat#ab1614(HECD-1)
Mouse monoclonal anti-E-cadherin(IB, IFA)	Abcam	Cat#ab11512 (DECMA-1)
Rabbit polyclonal Anti-ZO-1(IFA)	Abcam	Cat#ab597204
Mouse monoclonal anti-GM130 (IFA)	BD Biosciences	Cat#35/GM130
Mouse monoclonal anti-Scribble(IB)	SantaCruz	Cat#sc-55543
Rabbit monoclonal anti-Scribble(IB, IFA)	Cell Signaling Technology	Scribble Antibody #4475
Mouse monoclonal anti-HSP70(IB)	Abcam	Cat#ab47455
Mouse monoclonal anti-GAPDH(IB)	SantaCruz	Cat#sc-32233
Rabbit polyclonal anti-GAPDH(IB)	Merck	Cat#G9545
Rat monoclonal anti-Beta-tubulin(IB)	Abcam	Cat#[YOL1/34](ab6161)
Mouse monoclonal anti-Beta-tubulin(IB)	DHSB	Cat#E7
Rabbit polyclonal anti-H3K27me3(IB, IFA)	Merck	Cat#07-449
Rabbit polyclonal anti-H3(IB)	Abcam	Cat#ab1719
Rabbit monoclonal anti-EZH2(IB, IFA)	Cell Signaling Technology	Ezh2 (D2C9) XP® Rabbit mAb Cat#5246
Rabbit polyclonal anti-EZH2(IB)	Merck	Cat#07-1562
Rabbit polyclonal anti-Zeb1(IB)	Abcam	Cat#ab203829
Rabbit polyclonal anti-Vimentin(IB)	Abcam	Cat#ab92547 [EPR3776]
Rabbit polyclonal anti-Occludin(IB, IFA)	Abcam	Cat#ab216327 [EPR20992]
Rabbit monoclonal anti-pAkt(Ser473)(IB)	Cell Signaling Technology	Cat#9271
Rabbit monoclonal anti-Akt(IB)	Cell Signaling Technology	Cat#9272
Rabbit polyclonal anti-TAZ(IB)	Abcam	Cat#84927
Mouse monoclonal anti-Twist(IB)	Abcam	Cat#ab50887
Rabbit polyclonal anti-Snail(IB)	Abcam	Cat#ab85931
Rabbit monoclonal anti-Rab11(IFA)	Cell Signaling Technology	Cat#Rab11 (D4F5) XP® Rabbit mAb #5589
Mouse monoclonal anti-EEA-1(IFA)	BD Biosciences	Clone 14/EEA1 (RUO)
Mouse monoclonal anti-PTEN(IB)	BD Biosciences	Clone A2B1 (RUO)
Goat anti-Mouse IgG (H+L) Cross-Adsorbed Secondary Antibody, Alexa Fluor™ 488	Invitrogen	Cat#A-11029
Goat anti-Mouse IgG (H+L) Cross-Adsorbed Secondary Antibody, Alexa Fluor™ 568	Invitrogen	Cat#A-11004
Goat anti-Rabbit IgG (H+L) Cross-Adsorbed Secondary Antibody, Alexa Fluor™ 488	Invitrogen	Cat#A-11008

Goat anti-Rabbit IgG (H+L) Cross-Adsorbed Secondary Antibody, Alexa Fluor™ 568	Invitrogen	Cat#A-11011
Peroxidase AffiniPure® Goat Anti-Mouse IgG (H+L)	Jackson ImmunoResearch	Cat#115-035-003; RRID: AB_10015289
Peroxidase AffiniPure® Goat Anti-Rabbit IgG (H+L)	Jackson ImmunoResearch	Cat#111-035-003; RRID: AB_2313567
Goat anti-rat IgG H&L (HRP)	Abcam	Cat#ab97057
Bacterial and virus strains		
E.coli DH5α	Lab generated	N/A
Biological samples		
N/A	N/A	N/A
Chemicals, peptides, and recombinant proteins		
Protease inhibitor cocktail complete EDTA-free	Roche	Cat#4693132001
DynaBeads	Invitrogen	Cat#10002D
Streptavidin DynaBeads	Invitrogen	Cat#65801D
GSK-126	MedChemExpress	Cat#HY-13470
GSK-690693	MedChemExpress	Cat#HY-10249
Sodium Deoxycholate	SigmaAldrich	Cat#S1827
Nonidet P-40	SigmaAldrich	Cat#74385-1L
Tris free base	SigmaAldrich	Cat#T1503
Glycine	Thermo Fisher Scientific	Cat#Q24755
NaCl	SigmaAldrich	Cat#S7653
HEPES	SigmaAldrich	Cat#H3375
EDTA	SigmaAldrich	Cat#E9884
DTT	SigmaAldrich	Cat#D0632
Tween20	SigmaAldrich	Cat#P9416
SDS	SigmaAldrich	Cat#L3771
BSA	SigmaAldrich	Cat#A7906
MgCl2	SigmaAldrich	Cat#M1028
DMEM-F12	Invitrogen	Cat#11330-032
EGF	Peprotech	Cat#AF-100-15
Bovine Insulin	Sigma	Cat#I-1882
Cholera toxin	Sigma	Cat#C-8052
Hydrocortisone	Sigma	Cat#H-0888
Horse Serum	Invitrogen	Cat#16050-122
Pen/Strep	Invitrogen	Cat#15070-063
RPMI-1640	Invitrogen	Cat#31800-022
Fetal Bovine Serum (Brazil oragin)	Invitrogen	Cat#10270106
Texas Red® Conjugated Human Transferrin	Invitrogen	Cat#T2875; Lot# 1848488
Critical commercial assays		
PrimeScript™ 1st strand cDNA Synthesis Kit	Takara	6110B
Deposited data		
RNA-sequencing	This thesis	GSE289801

Experimental models: Cell lines		
DLD-1	ATCC	CCL-221
MCF10A	ATCC	CRL-10317
MCF10A(p53DN)	This thesis	N/A
A549(p53DN)	This thesis	N/A
HCT116	ATCC	CCL-247
SW480	ATCC	CCL-228
HEK293T	ATCC	CRL-3216
Experimental models: Organisms/strains		
NOD-SCID male/female mice syngeneic	Animal House facility, IISER, Pune, India	N/A
Recombinant DNA		
pLKOMCS-GFP	This thesis	N/A
pLKOMCS-GFP-FBL(siRes)	This thesis	N/A
pLKOMCS-GFP-ΔRBD FBL(siRes)	This thesis	N/A
pBabe-SCRIB-Puro	This thesis	N/A
pBABE-hygro p53 DD	Addgene	Addgene #9058
Tet-pLKO-shFBL-puro	This thesis	N/A
Tet-pLKO-shSCRIB-puro	This thesis	N/A
MSCVhygro-F-Ezh2	Addgene	Addgene #24926
pCW57.1 F-EZH2	This thesis	N/A
MSCV Puro SCRIB P305L	This thesis	N/A
MSCV Puro SCRIB C4S	This thesis	N/A
MSCV Puro SCRIB C10S	This thesis	N/A
FBL(WT)-BioID2-HA-pBabe puro		
Software and algorithms		
Graphpad prism V.8.0	N/A	https://www.graphstats.net/graphpad-prism
ImageJ	Schneider et al.	https://imagej.nih.gov/ij/
Galaxy	The Galaxy Community	https://doi.org/10.1093/nar/gkae410
T-scratch	Gebäck et al. (2018)	https://doi.org/10.2144/000113083
Imaris	N/A	RRID:SCR_007370

Oligonucleotides		
FBL to HABioID2 pBP w/BamHI_F	This thesis	AAAGGATCCATGAAGCCAGGATTCAGTCCCC
FBL to HABioID2 pBP w/EcoRI_R	This thesis	TCAGAATTCGTTCTTCACCTTGGGGGGTGGC
EZH2 to mycBioID2MCS w/BamHI_F	This thesis	AAAGGATCCGATGGGCCAGACTGGGAAG
EZH2 to MCS BioID2_GA_F	This thesis	CACACTGGACTAGTGATGGGCCAGACTGGGAAG
EZH2 to MCS BioID2_GA_R	This thesis	GTTTAAACTTAAGCTTCAAGGGATTTCCATTTCTCGTTCG
EZH2 to mycBioID2MCS (new)_F	This thesis	TCAGTCGACGATGGGCCAGACTGGGAAG
EZH2 to mycBioID2MCS (new)_R	This thesis	AATGGTACCTCAAGGGATTTCCATTTCTCGTTC
MCS BioID2 vector for GA_F	This thesis	AGCTTAAGTTTAAACCGCTGATC
MCS BioID2 vector for GA_R	This thesis	CACTAGTCCAGTGTGGTGG
BioID2_FBL to pLentiPuro new w/BamHI_F	This thesis	AAAGGATCCGCCACCATGGAACAAAAACTC
BioID2_FBL to pLentiPuro new w/AgeI_R	This thesis	CTGACCGGTTCAGTTCTTCACCTTGGGGG
FBL with EcoRI_F	This thesis	AAAGAATTCATGAAGCCAGGATTCAGTCC
FBL with BamH1_R	This thesis	GGTGGATCCTCAGTTCTTCACC
EZH2 to pcw57 w/NheI_F	This thesis	TCAGCTAGCATGGGCCAGACTGGGAAG
EZH2 to pCW57 w/BamHI_R	This thesis	ACTGGATCCTCAAGGGATTTCCATTTCTCGTTC
RBD del_F	This thesis	TACCGCATGCTCATCGCAATG
RBD del_R	This thesis	AATTTTGTCATCTCCTTCCGAAATCG
FBL with BamH1_F	This thesis	TCAGGATCCGCCACCATGGTGAGCAAG
FBL with SalI_R	This thesis	ACTGTCGACTCAGTTCTTCACCTTGGGGGG
FBL with EcoRI_R	This thesis	ACTGAATTCTCAGTTCTTCACCTTGGGGGG
EZH2_Fwd	This thesis	GGCATCTTTATCAAAGATCCTG
EZH2_Rev	This thesis	CTCTTCACCAGTCTGGATAGC
SCRIB_F2 (RTPCR)	This thesis	GCACGTGGAGTCGGTGGAC
SCRIB_R2 (RTPCR)	This thesis	CTCAGGGATATCGTTCCGGGAC
F_SCRIB to pBP_BamH1	This thesis	AATGGATCCATGCTCAAGTGCATCCCGC

R_SCRIB to pBP_EcoR1	This thesis	AATGAATTCCTAGGAGGGCACAGGGCC
SCRIB_ChIP_F1	This thesis	GAAACAAGGCGAGGAGGAGG
SCRIB_ChIP_R 1	This thesis	TCGTACACTTCAGCCACCAC
SCRIB_ChIP_F2	This thesis	ATAAAGGTGCGGATGCTGCT
SCRIB_ChIP_R 2	This thesis	ACAGGAAGCAGGTCCAGAGA
SCRIB_ChIP_F3	This thesis	CAGGGTGGTGCTGAGAGAAG
SCRIB_ChIP_R 3	This thesis	CTTAACGCACAGCCTCCTCC
SCRIB_ChIP_F4	This thesis	GGAGGAGGCTGTGCGTTAAG
SCRIB_ChIP_R 4	This thesis	GCGGGATATTGGGAGCTACA
ACTB_ChIP_F1	This thesis	CCCCAACACCACACTCTACC
ACTB_ChIP_R1	This thesis	TTGCCGACTTCAGAGCAACT
ACTB_ChIP_F2	This thesis	CCTCCAAGAGCTCCTTCTGC
ACTB_ChIP_R2	This thesis	ACATCTCTTGGGCACTGAGC
ACTB_ChIP_F3	This thesis	GGCGTGACTGTTACCCTCAA
ACTB_ChIP_R3	This thesis	GCCCGTGATGAAGGCTACAA
ACTB_ChIP_F4	This thesis	TTGTAGCCTTCATCACGGGC
ACTB_ChIP_R4	This thesis	GTAGAGTGTGGTGTTGGGGG
U6 snRNA ctrl_F	PMID-23542174	GCTTCGGCAGCACATATACTAAAAT
U6 snRNA ctrl_R	PMID-23542174	CGCTTCACGAATTTGCGTGTCAT
shSCRIB_F	This thesis	CCGGAGCACTTCAAGATCTCCAACTCGAGTTGGAGATC TTGAAGTGCTTTTTT
shSCRIB_R	This thesis	AATTAAAAAAGCACTTCAAGATCTCCAACTCGAGTTGG AGATCTTGAAGTGCT
EZH2_1F	This thesis	CCGGGACTCTGAATGCAGTTGCTCTCGAGAGCAACTGC ATTCAGAGTCTTTTT
EZH2_1R	This thesis	AATTAAAAAGACTCTGAATGCAGTTGCTCTCGAGAGCA ACTGCATTCAGAGTC
EZH2_2F	This thesis	CCGGCGGTGGGACTCAGAAGGCACTCGAGTGCCTTCT GAGTCCCACCGTTTTT
EZH2_2R	This thesis	AATTAAAAACGGTGGGACTCAGAAGGCACTCGAGTGC CTTCTGAGTCCCACCG
EZH2_3F	This thesis	CCGGGCACAAGTCATCCCGTTAAAGCTCGAGCTTTAAC GGGATGACTTGTGCTTTTTG
EZH2_3R	This thesis	AATTAAAAACGGTGGGACTCAGAAGGCACTCGAGTGC CTTCTGAGTCCCACCG
EZH2_3F_default	This thesis	CCGGGCACAAGTCATCCCGTTAAAGCTCGAGCTTTAAC GGGATGACTTGTGCTTTTT
EZH2_3R_default	This thesis	AATTAAAAACGGTGGGACTCAGAAGGCACTCGAGTGC CTTCTGAGTCCCACCG
shFBL4_F	This thesis	CCGGAGGAGAACATGAAGCCGCACTCGAGTGCGGCTT CATGTTCTCCTTTTT
shFBL4_R	This thesis	AATTAAAAAAGGAGAACATGAAGCCGCACTCGAGTGC GGCTTCATGTTCTCC
P305L_F (lig)	This thesis	CTTCGCTCCCTGGGAAAGCTG

P305L_R(lig)	This thesis	CAGGGCCATCAGCAGGTTC
SCRIB_C4S_F	This thesis	ATGCTCAAGTCCATCCCGCTG
SCRIB_C4S_R	This thesis	CAGCGGGATGGACTTGAGCAT
SCRIB_C10S F	This thesis	CTGTGGCGCTTCAACCGGCAC
SCRIB_C10S R	This thesis	GTGCCGGTTGAAGCGCCACAG
MYT1_ChIP_F	This thesis	AGCCATGTCTGAAGGCACTC
MYT1_ChIP_R	This thesis	TGCATTGGCTTTTTGGCCTT
siFBL_oligo#1	This thesis	AGGAGAACATGAAGCCGCAdTdT
siFBL_oligo#2	This thesis	GTCTTCATTTGTCGAGGAAAdTdT
siFBL_oligo#3	This thesis	TGGAGGACACTTTGTGATTTTdTdT
siLacZ	(Pradhan et al., 2020)	CGUACGCGGAAUACUUCGAdTdT

List of publications

- **Saha, S.**, A.K., B., Meel, S., Notani, D., & Sengupta, K. (2025). Fibrillarin regulates epithelial integrity via EZH2-mediated modulation of scribble expression. Cell Reports, 44(12), 116608.

- Balaji AK, **Santam Saha**, Kundan Sengupta; Phosphorylation-dependent modulation of the Lamin A/C–EZH2 complex regulates epithelial–mesenchymal plasticity; Nucleic acids research – 2026 Nucleic Acids Research, 2026, gkaf1464.

- Balaji AK, **Saha S**, Deshpande S, Poola D, Sengupta K. Nuclear envelope, chromatin organizers, histones, and DNA: The many achilles heels exploited across cancers. Front Cell Dev Biol. 2022 Dec 16;10:1068347.

Cell Reports

Article

Fibrillarin regulates epithelial integrity via EZH2-mediated modulation of scribble expression

Graphical abstract

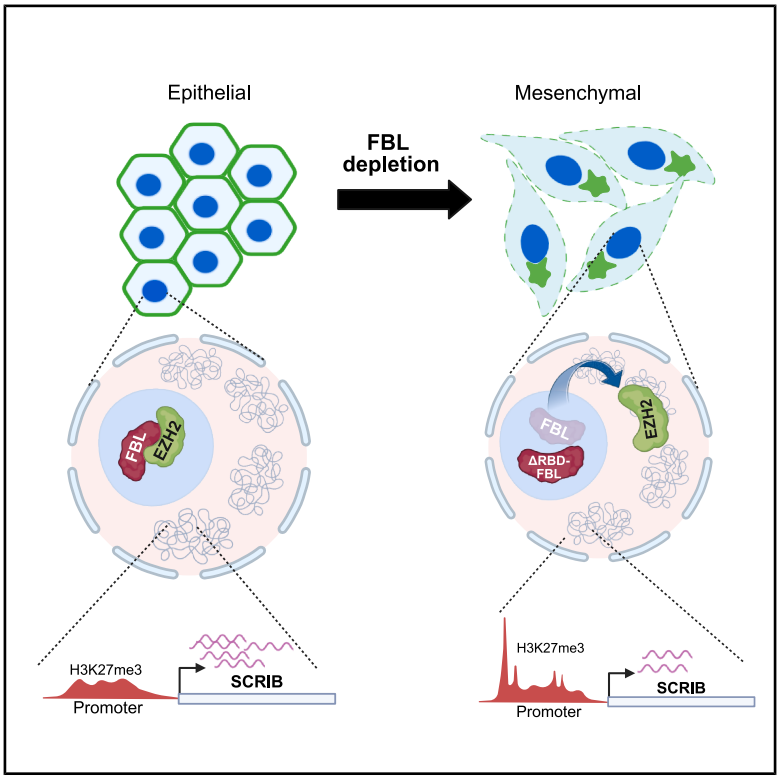

Authors

Santam Saha, Balaji A.K., Sweety Meel, Dimple Notani, Kundan Sengupta

Correspondence

kunsen@iiserpune.ac.in

In brief

Saha et al. reveal that fibrillarin, a nucleolar protein, safeguards epithelial integrity by preventing EZH2-driven repression of Scribble. Fibrillarin loss disrupts cell-cell junctions, induces epithelial-to-mesenchymal transition (EMT), and enhances cell migration, uncovering a crucial link between nucleolar function and cancer progression.

Highlights

- Fibrillarin maintains epithelial stability by regulating cell-cell adhesion
- FBL depletion shuttles EZH2 out of the nucleoli
- FBL loss drives EZH2 relocalization and repression of Scribble
- Prolonged FBL depletion promotes epithelial-to-mesenchymal transition (EMT) and metastasis

Saha et al., 2025, Cell Reports *44*, 116608
December 23, 2025
https://doi.org/10.1016/j.celrep.2025.116608

CellPress

Cell Reports

CellPress
OPEN ACCESS

Article

Fibrillarin regulates epithelial integrity via EZH2-mediated modulation of scribble expression

Santam Saha,[1] Balaji A.K.,[1] Sweety Meel,[2] Dimple Notani,[2] and Kundan Sengupta[1,3,*]
[1]B-216, Chromosome Biology Lab (CBL), Biology, Indian Institute of Science Education and Research (IISER), Dr. Homi Bhabha Road, Pashan, 411008 Pune, Maharashtra, India
[2]National Center for Biological Sciences (NCBS), Tata Institute of Fundamental Research (TIFR), 560065 Bangalore, Karnataka, India
[3]Lead contact
*Correspondence: kunsen@iiserpune.ac.in
https://doi.org/10.1016/j.celrep.2025.116608

SUMMARY

Fibrillarin (FBL) is a nucleolar protein critical for rRNA biogenesis. We show that FBL is essential for the maintenance of epithelial integrity through its regulation of cell-cell adhesion proteins. RNA-seq analyses upon FBL depletion revealed deregulation of adhesion- and apical membrane organization-associated pathways. FBL loss deregulates cell polarity via increased deposition of H3K27me3 on the SCRIB promoter, driven by the localization of a subpopulation of EZH2 from the nucleolus to the nucleoplasm. Disrupting the FBL-EZH2 interaction increases cell migration, underscoring a requirement for retaining EZH2 also in the nucleolus. Furthermore, FBL depletion induces EMT in breast epithelial cells, owing to increased levels of mesenchymal factors (Snail1, Twist1, and Zeb1) and activation of Akt. Since Scribble tethers PHLPP1 and PTEN to antagonize Akt, repression of Scribble induces EMT. In summary, FBL safeguards epithelial integrity, by regulating the expression of Scribble, uncovering an FBL-EZH2 axis in EMT and metastasis.

INTRODUCTION

The nucleolar protein fibrillarin (FBL) is a highly conserved 2′-*O*-methyltransferase involved in ribosomal RNA (rRNA) biogenesis.[1] As a core component of the C/D box small nucleolar ribonucleoprotein (snoRNP) complex, FBL catalyzes 2′-*O*-methylation of ribose in rRNA, which enhances ribosomal stability and function.[2,3] This modification occurs through the base pairing of C/D box snoRNAs with rRNA, positioning FBL at target sites, to transfer a methyl (-CH_3) group from S-adenosyl methionine (SAM) to the 2′-hydroxyl (-OH) of ribose.[4] Methylation imparts stability to rRNA, facilitating ribosome assembly while ensuring translational fidelity and adaptation to cellular stress.[5] FBL also methylates histone H2A (H2AQ104me) at glutamine residues. This H2AQme modification plays a role in epigenetic regulation, impacting the transcription of ribosomal DNA (rDNA) by altering its interaction with the FACT complex, which facilitates nucleosome reorganization at the rDNA promoter.[6] FBL also mediates 2′-*O*-methylation of peroxidasin (Pxdn) mRNAs, especially at the 5′ cap (Cap 0 to Cap 1/Cap 2), enhancing their stability.[7] Elevated FBL expression is implicated in aggressive cancers such as breast cancer, hepatocellular carcinoma, and colorectal cancer[8–10] where it drives aberrant ribosome biogenesis, correlating with enhanced cell proliferation and poor prognosis.[8] Mechanistically, elevated FBL levels enhance 2′-*O*-methylation of rRNA, which increases the efficiency of internal ribosome entry site (IRES)-mediated translation of oncogenic mRNAs FGF1, FGF2, MYC, and VEGFA.[8] In contrast, reduced levels of FBL are associated with poor prognosis of patients with early-stage breast cancer.[11]

Emerging evidence suggests that the oncogenic functions of FBL extend beyond ribosome biogenesis to influence gene expression programs that govern cell identity and behavior. One such critical process is the epithelial-to-mesenchymal transition (EMT), a cell state transition that reshapes epithelial identity and function, closely associated with cancer progression and metastasis. EMT is characterized by a gradual loss of epithelial morphology and the acquisition of mesenchymal properties, facilitating increased motility and invasiveness. The epithelial morphology is characterized by prominent cell-cell adhesion, apico-basal polarity, and the organization of cells into structured, functional sheets. Central to these functions are cell adhesion molecules and junctional complexes, particularly E-cadherin (epithelial cadherin, CDH1), tight junction complexes, and crucial polarity regulators such as Scribble, which function synergistically to maintain epithelial integrity. E-cadherin, a calcium-dependent transmembrane glycoprotein, mediates homophilic interactions between adjacent cells and forms a key component of adherens junctions. Its cytoplasmic domain binds to β-catenin and p120-catenin, anchoring the complex to F-actin (filamentous actin).[12,13] E-cadherin functions as a key determinant of epithelial organization, and its decrease or altered localization facilitates EMT. While type 1 EMT is associated with normal development, type 3 EMT is associated with cancer progression.[14,15] Complementing adherens junctions, tight junctions occupy the most apical position in the junctional complex. They are composed of transmembrane proteins such as claudins, occludin, and junctional adhesion molecules (JAMs). These proteins interact with scaffold proteins, including ZO-1, ZO-2, and ZO-3, which in turn connect the

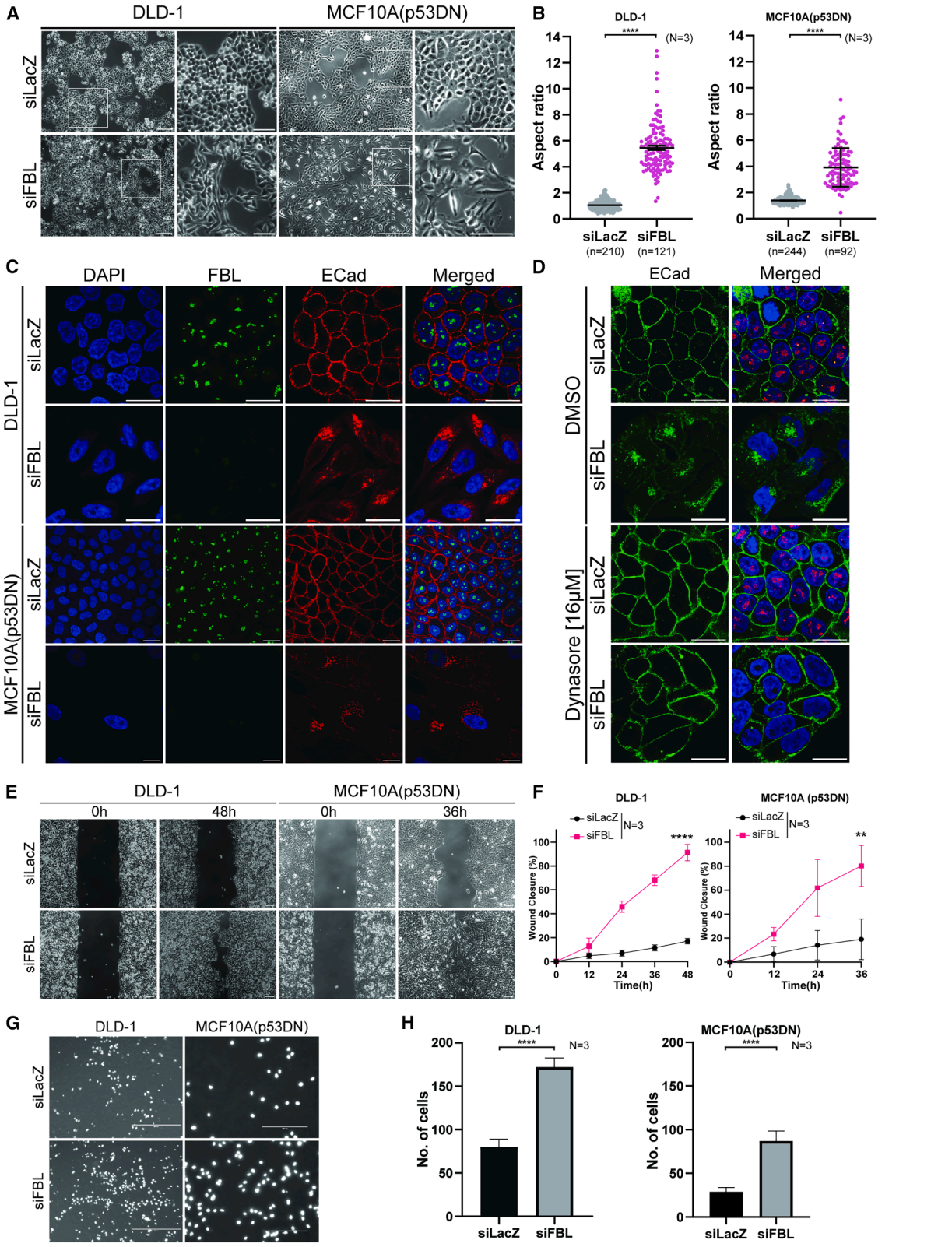

(legend on next page)

junctions to the actin cytoskeleton. These structures are crucial in establishing epithelial polarity and paracellular permeability. The key polarity protein Scribble, a keystone component of the Scribble-Lgl-Dlg complex, localizes to the basolateral membrane and is critical for maintaining epithelial architecture by suppressing apical polarity signals and promoting the formation of adherens and tight junctions.[16,17] Disruption of Scribble function results in the loss of polarity and induction of EMT. The physical and functional interplay between E-cadherin-mediated adherens junctions, tight junctions, and Scribble is critical for epithelial homeostasis, and their dysregulation is a common feature of tissue remodeling, inflammation, and tumorigenesis.[18,19]

Here, we have unraveled a novel role of FBL in the maintenance of epithelial integrity, thereby preventing cell migration and EMT. Our study uncovers a previously unrecognized role of FBL in the maintenance of epithelial homeostasis beyond its canonical function in ribosome biogenesis. We demonstrate that FBL depletion induces a striking loss of the classical cobblestone morphology of epithelial cells, characterized by the destabilization of adherens and tight junctions in two independent epithelial cell lines, namely, DLD-1 (colorectal cancer) and MCF10A (breast epithelial). This is driven by the mislocalization of E-cadherin via endocytosis, which disrupts cell-cell adhesion. Mechanistically, we uncover a direct link between FBL and the epigenetic regulation of cell adhesion genes. Loss of FBL transcriptionally represses Scribble expression (a key polarity protein) via enhanced deposition of the inactive histone mark (H3K27me3) on the SCRIB promoter. This is mediated by the translocation of a subpopulation of EZH2 from the nucleolus to the nucleoplasm. Notably, pharmacological inhibition of EZH2 rescues Scribble expression, restoring epithelial integrity and establishing FBL as a key regulator of epithelial stability. Concomitant with the loss of cell-cell adhesion, FBL depletion induces EMT, with the upregulation of Snail, Twist1, Zeb1, and pAkt. Strikingly, disruption of the FBL-EZH2 interaction for prolonged duration induces EMT in MCF10A(p53DN) breast cells, underscoring the functional significance of this interaction in retaining a nucleolar pool of EZH2 that safeguards epithelial integrity.

Taken together, these findings uncover a novel role of FBL in restraining EMT, preserving epithelial identity by maintaining cell-cell junction proteins. Our study, for the first time, highlights a novel function of FBL as a therapeutic target in cancers of epithelial origin, crucial for maintaining the integrity of epithelial cells and preventing metastasis.

RESULTS

FBL depletion disrupts cell-cell adhesion and alters cell morphology

FBL is a highly conserved nucleolar protein localized within the dense fibrillar compartment (DFC) of the nucleolus.[20] Increased levels of FBL enhance cell proliferation and chemoresistance in breast and colorectal cancer cells.[8,9] In contrast, reduced levels of FBL correlate with poor prognosis in breast cancers.[11]

We depleted FBL in two independent epithelial cell lines: colorectal cancer DLD-1 ($TP53^{WT/S241F}$) and breast epithelial MCF10A ($TP53^{WT/WT}$) cells. Since FBL is involved in rRNA biogenesis and maturation,[3,4] disrupting rRNA biogenesis stabilizes p53, enhancing cell death.[21–24] FBL depletion in MCF10A cells showed a significant increase in cell death (~60%), owing to the wild-type status of TP53 in MCF10A cells ($TP53^{WT/WT}$). We therefore created MCF10A cells stably expressing dominant-negative p53 (hereafter MCF10A(p53DN)) by transducing cells with a pBabe-Hygro-p53DD construct, which maintained cell viability of ~95%, upon FBL depletion (Figure S3B).[25–27]

Remarkably, FBL depletion caused a loss of the classical cobblestone morphology of epithelial cells (Figure 1A). Independent depletion of FBL showed a ~70%–80% knockdown in both epithelial cell types (Figure S1C(i–iii)), along with a significant increase in cell elongation, with an increased aspect ratio in both cell lines (DLD-1 [~5.8-fold ± 1.0] and MCF10A(p53DN) [~2.35-fold ± 0.5]; Figure 1B). Furthermore, FBL knockdown significantly altered the subcellular localization of the cell adhesion protein E-cadherin. Specifically, E-cadherin was internalized into the cytoplasm of cells (~72.5% ± 12.5%), resulting in loss of cell-cell adhesion (Figures 1C and S1A(i–ii); Videos S1

Figure 1. FBL depletion leads to loss of cell-cell junctions and enhanced cell migration

(A) Phase-contrast images of siLacZ (control) and siFBL-transfected DLD-1 and MCF10A(p53DN) cells for ~48 and ~36 h, respectively, showing elongated, spindle-shaped cells and loss of cobblestone morphology. Scale bar, ~150 μm. Scale bar for insets, 150 μm ($N = 3$).

(B) Quantification of the aspect ratio of cells upon FBL depletion in (1) DLD-1 (knockdown for ~48 h) and (2) MCF10A(p53DN) (knockdown for ~48 h) cells ($N = 3$). Unpaired t test was performed to calculate the p values. The data were pooled from $n = 331$ (DLD-1) and $n = 336$ (MCF10A(p53DN)) cells from $N = 3$ independent biological replicates.

(C) Representative images of immunofluorescence showing FBL (green), E-cadherin (red), and nucleus (DAPI; blue) in DLD-1 and MCF10A(p53DN) cells, respectively, upon FBL depletion ($n \geq 90$), for ~48 and 36 h, respectively. FBL depletion shows distinct relocalization of E-cadherin. The data were pooled from DLD-1 ($n = 180$) and MCF10A ($n = 181$) cells from $N = 3$ independent biological replicates. Scale bar, ~20 μm. Quantification in Figure S1A(i–ii).

(D) Representative immunofluorescence staining of E-cadherin (Ecad; green), FBL (red), and nucleus (DAPI; blue) in control and FBL-depleted cells (FBL depletion for ~48 h; $n \geq 339$), pooled from $N = 3$ independent biological replicates, with DMSO control and 16 μm Dynasore. Scale bar, ~20 μm. Quantification in Figure S1D(ii).

(E) Representative phase-contrast images showing scratch wound assays performed on DLD-1 and MCF10A(p53DN) cells in control (siLacZ) and FBL-depleted ($N = 3$) cells. Scale bar, ~100 μm.

(F) Quantification of Figure 1E showing a significant increase in wound closure upon FBL depletion in both DLD-1 and MCF10A(p53DN) cells. Unpaired t test was performed to calculate the p values.

(G) Invasion assays using Boyden chambers (pore size, ~8 μm) to quantify cell migration in DLD-1 and MCF10A(p53DN) cells in control (siLacZ) and FBL-depleted ($N = 3$) cells. Scale bars for DLD-1 (~400 μm) and MCF10A(p53DN) cells (~200 μm).

(H) Quantification of invasion assays for data in Figure 1G showing a significant increase in the number of migrated DLD-1 and MCF10A(p53DN) cells. The data were pooled from $N = 3$ biological replicates.

p values were computed from unpaired Student's t tests in (B), (F), and (G). Error bars indicate SD. *$p < 0.1$, **$p < 0.01$, ***$p < 0.001$, and ****$p < 0.0001$.

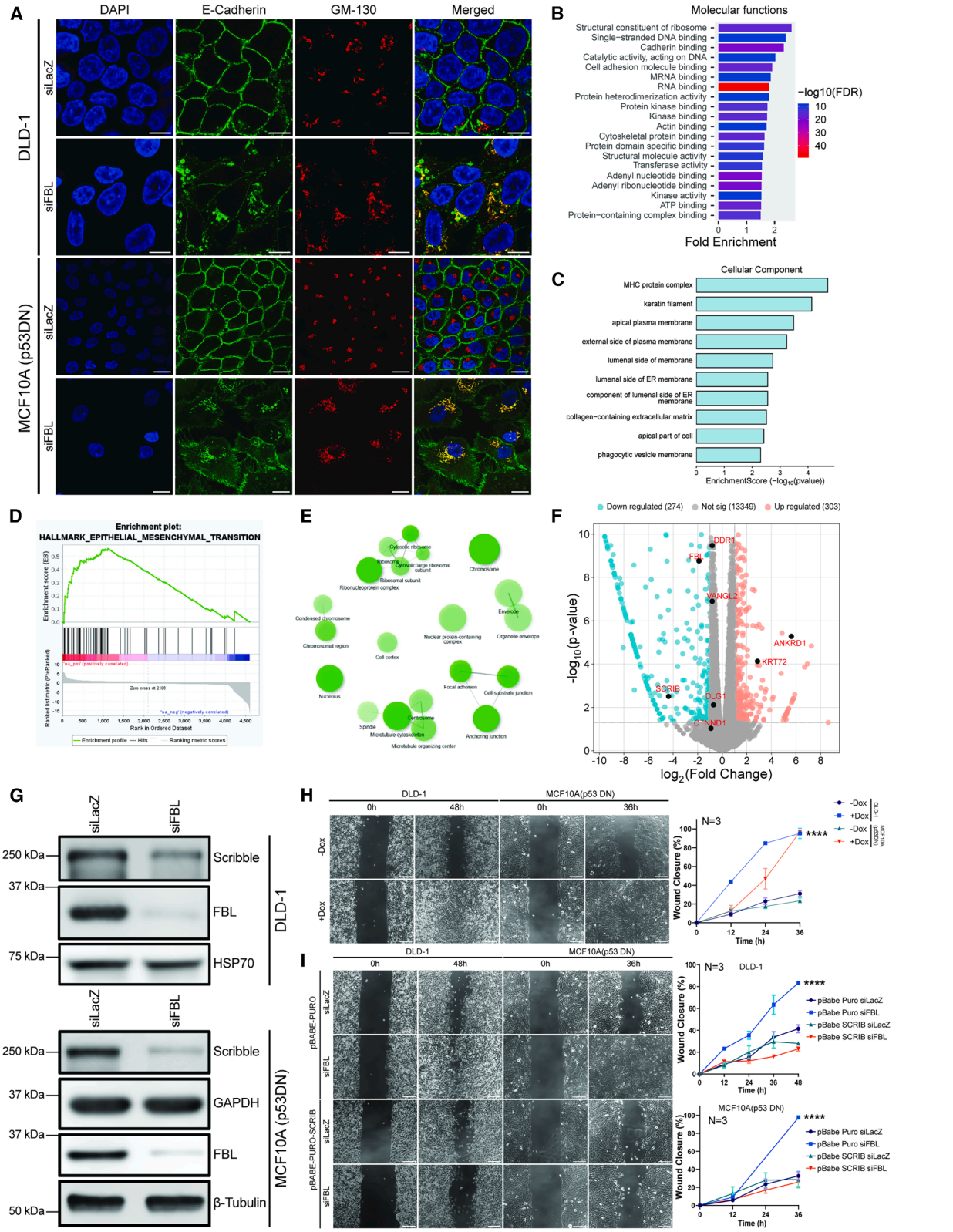

(legend on next page)

and S2). Notably, the total protein levels of E-cadherin remained unaltered (Figure S1C(i–iii)). To further ascertain the nature of the internalization of E-cadherin, we co-immunostained E-cadherin with two independent endosomal markers: EEA1 (early endosome antigen 1, an early endosome marker) and Rab11 (a recycling endosome marker).[28,29] Notably, E-cadherin showed a striking increase (∼8-fold) in its colocalization with both early (EEA-1) and recycling (Rab11) endosomes, corroborating the internalization of E-cadherin upon FBL depletion (Figures S4A(i–ii) and S4B(i–ii)). Collectively, these findings underscore an enhanced internalization and trafficking of E-cadherin upon the depletion of FBL.

To assess whether FBL depletion-mediated E-cadherin internalization is due to altered endocytic trafficking, we monitored alterations in global endocytosis using a transferrin uptake assay.[30] We did not detect a significant difference in the extent of transferrin uptake upon FBL depletion (Figure S3A(i–ii)), revealing that E-cadherin internalization is not a manifestation of alterations in overall endocytosis. We further determined if E-cadherin internalization can be rescued upon the inhibition of dynamin (a large GTPase critical for clathrin-mediated endocytosis).[31] We treated DLD-1 cells with Dynasore (an inhibitor of the GTPase domain of dynamin) in an FBL-depleted background. This showed a significant rescue of clathrin-mediated endocytosis of E-cadherin (Figures 1D and S1D(i–ii)),[32–34] suggesting a dynamin-dependent internalization of E-cadherin.

In addition to the adherens junction protein E-cadherin, FBL depletion perturbed the localization of tight junction proteins ZO-1 and occludin (Figures S2C (i–ii) and S3C(i–ii)), revealing a redistribution of key cell-cell adhesion proteins. To assess the effect of E-cadherin internalization on the integrity of tight junctions, we treated cells with EGTA (3 mM for 1 h), which showed internalization of E-cadherin and ZO-1 (Figure S2A).[35] Taken together, these results suggest that internalization of E-cadherin and ZO-1 collectively disrupts cell-cell junctions.

We next asked if the FBL depletion-mediated disruption of cell adhesion impacts cell migration. We performed scratch wound assays on a monolayer of cells to monitor cell migration, while we independently assessed the effect of FBL depletion on cell invasiveness, using the Boyden chamber assay. FBL depletion showed a significant increase in (1) cell migration (∼80% ± 10%) and (2) cell invasion (∼2.65-fold ± 0.3; Figures 1E and 1F). Furthermore, FBL depletion also increased cell invasion through relatively narrow pores (∼8 μm), as monitored by Boyden chamber assays (Figures 1G and 1H(i–ii)).

In summary, FBL maintains cell-cell adhesion by regulating the localization of adherens and tight junction proteins, such as E-cadherin, occludin, and ZO-1, respectively. FBL depletion disrupts cell-cell adhesion, facilitating enhanced cell migration and invasiveness, highlighting a novel and unreported function of FBL in the maintenance of the integrity and morphology of epithelial cells.

FBL depletion downregulates Scribble expression, enhancing cell migration

We next examined the pattern of E-cadherin internalization upon FBL depletion using immunofluorescence assays (IFAs). Interestingly, the internalized E-cadherin showed distinct co-localization with the Golgi marker GM130, establishing the association of E-cadherin with the Golgi (Figures 2A and S5A(i–iii) and S5B(i–iii)). This striking phenotype of E-cadherin internalization into the Golgi is consistent with the depletion of Scribble, a basolateral cell polarity protein.[36]

To address the molecular underpinnings of FBL function, we performed RNA sequencing (RNA-seq) upon FBL depletion in DLD-1 colorectal cancer cells. Analyses of the RNA-seq datasets using GO (Gene Ontology) enrichment and GSEA (Gene Set Enrichment Analysis)[37] revealed genes that were deregulated in cellular and molecular functions such as (1) structure of ribosome, (2) cell-cell adhesion, (3) apical plasma membrane,

Figure 2. Depletion of FBL shows a significant decrease in Scribble levels, which promotes cell migration

(A) Representative images of immunofluorescence assay performed for E-cadherin (green), GM130 (red), and nucleus (DAPI; blue) from DLD-1 and MCF10A(p53DN) cells transfected with siLacZ (control) and siFBL for ∼48 h from $N = 3$ independent biological replicates. The GM130 and E-cadherin panels in siLacZ-transfected cells are from different optical sections of the same confocal image stack. Scale bar, ∼20 μm. Quantification in Figures S5A(i–iii) and S5B(iii).

(B) Bar plot representing the top deregulated molecular functions obtained from Gene Ontology (GO) analysis of RNA-seq data from FBL-depleted DLD-1 cells (∼72 h). Bar height represents the number of genes; FDR cutoff = 0.05.

(C) Bar plot showing the top deregulated cellular components obtained from GO analysis of RNA-seq data. Bar height represents the number of genes; FDR cutoff = 0.05.

(D) Enrichment plot obtained from Gene Set Enrichment Analysis (GSEA) of RNA-seq data showing enrichment of genes involved in epithelial-to-mesenchymal transition (EMT); FDR = 0; normalized enrichment score (NES) = 3.33.

(E) Network analysis of the key dysregulated cellular pathways derived from RNA-seq data upon FBL depletion in DLD-1 cells. Edge cutoff = 0.3.

(F) Volcano plots for differentially expressed genes derived from RNA-seq analysis of cells transfected with siLacZ (control) and siFBL for ∼72 h. Blue, downregulated; orange, upregulated; gray, unchanged. Log_2(fold change cut-off) = 2.0; $-\log_{10}(p$ value) = 2. Data were pooled from $N = 2$ independent biological replicates; siLacZ (control).

(G) Representative western blots showing a decrease for Scribble along with expression levels of FBL in DLD-1 and MCF10A(p53DN) cells transfected with siLacZ (control) and siFBL for ∼48 and ∼36 h, respectively. Loading controls: GAPDH, β-tubulin, and HSP70. Data were pooled from $N = 3$ independent biological replicates. Quantifications shown in Figure S5C(i–ii).

(H) Representative phase-contrast images from scratch wound assays performed independently on DLD-1 and MCF10A(p53DN) cells upon SCRIB depletion using induced expression of shSCRIB, in −Dox and +Dox conditions, obtained from $N = 3$ biological replicates. Two-way ANOVA with Bonferroni correction was used to perform multiple comparisons. Scale bar, ∼100 μm.

(I) Representative images of scratch wound assay of DLD-1 and MCF10A(p53DN) cells transduced with pBabe-Puro and pBabe-SBRIB in siLacZ- and siFBL-transfected backgrounds ($N = 3$). Two-way and one-way ANOVA with Bonferroni correction were used to perform multiple comparisons for DLD-1 and MCF10A, respectively. Scale bar, ∼100 μm.

Error bars indicate SD. $^{*}p < 0.1$, $^{**}p < 0.01$, $^{***}p < 0.001$, and $^{****}p < 0.0001$.

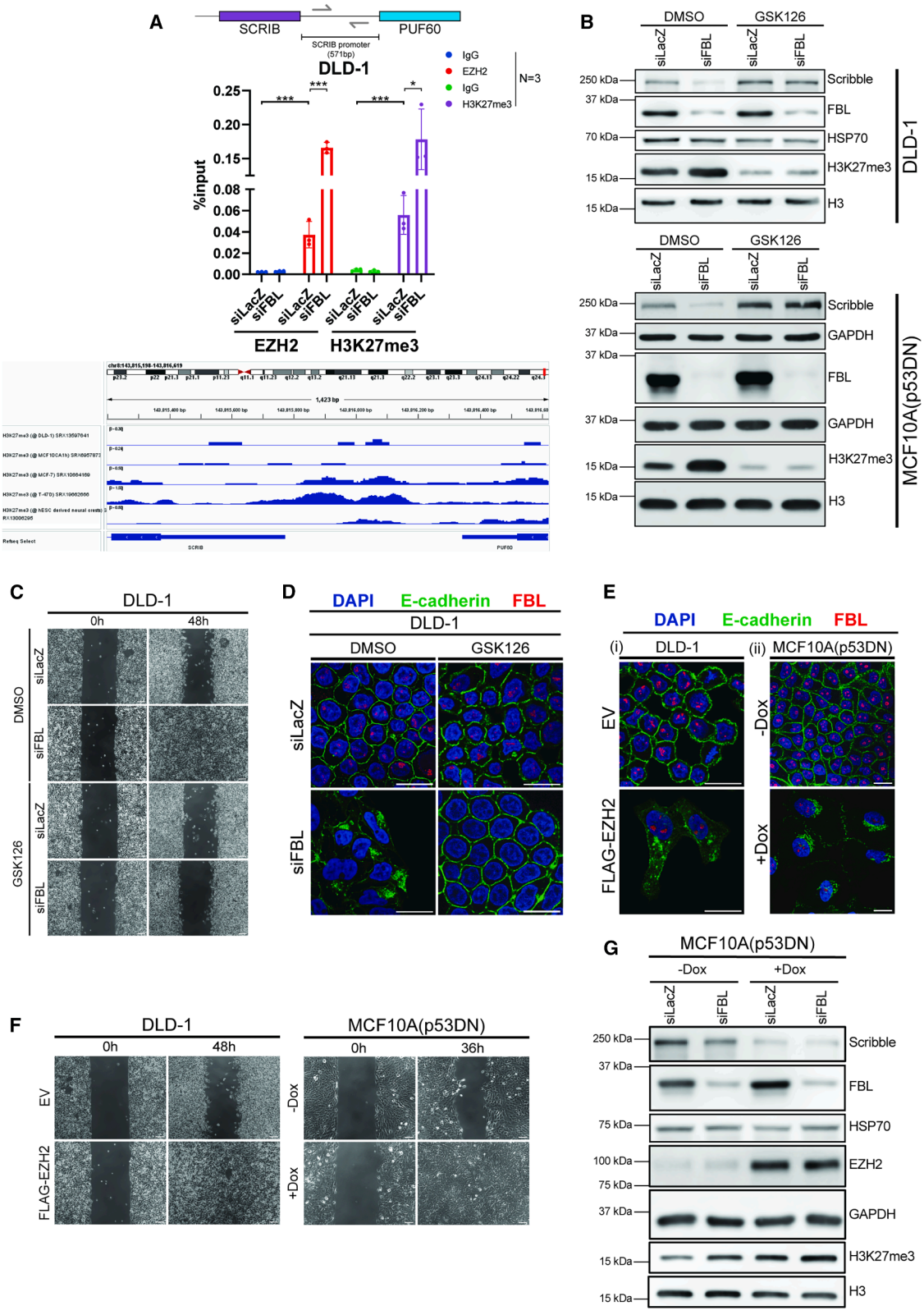

(legend on next page)

and (4) EMT, among others (Figures 2B–2E). Notably, Scribble showed a significant downregulation upon FBL depletion (Figure 2F), as corroborated by RT-qPCR (Figure S5D) and immunoblotting (Figures 2G and S5C(i–ii)). Interestingly, Scribble depletion also showed a significant increase in the extent of wound closure (~65% ± 5%), consistent with the role of Scribble depletion in promoting cell migration (Figure 2H).[38] In contrast, overexpression of Scribble in FBL-depleted cells decreased cell migration (Figure 2I). Taken together, these data implicate Scribble as a key molecular determinant of regulating cell migration upon FBL depletion.

FBL loss increases the occupancy of repressive histone marks (H3K27me3) on the Scribble promoter

We found that Scribble expression was transcriptionally downregulated upon FBL knockdown (Figure S5D). We therefore analyzed the occupancy profiles of histone modifications on the SCRIB promoter in DLD-1 colorectal cancer cells using publicly available data from ChIP-ATLAS.[39] Surprisingly, this analysis showed an enrichment of H3K4me3 (active), H3K27me3 (repressive) histone marks, and H2AK119Ub (repressive mark) upstream of the transcription start site (TSS; −0.5 kb). Similarly, inactive (H3K27me3) histone marks were enriched on the SCRIB promoter in (1) breast epithelial (MCF10A), (2) human embryonic stem cells (hESCs), and (3) breast cancer (MCF-7 and T-47D; Figure 3A).

We next examined the occupancy of H3K27me3 on the SCRIB promoter upon FBL depletion using ChIP-qPCR, since H3K27me3 is indicative of PRC2 occupancy.[40] ChIP-qPCR analyses showed increased enrichment of EZH2 and H3K27me3 on the SCRIB promoter upon FBL depletion (−500 bp from TSS; Figures 3A and S4A), although the total protein levels of EZH2 were unaltered (Figures S4B(i–ii) and S4D). To ascertain the effect of increased EZH2 and H3K27me3 deposition on the SCRIB promoter upon FBL depletion, we treated cells with the EZH2 inhibitor GSK126 (10 μM for 48 h).[41] This showed a significant reduction in the levels of the inactive histone mark H3K27me3 and a concomitant rescue of SCRIB levels even in the FBL-depleted background (Figures 3B and S6B(i–ii)). Remarkably, GSK126-treated cells showed a significant decrease in cell migration as quantified by scratch wound assays (Figures 3C and S7B). We next performed IFAs to monitor the localization of E-cadherin upon inhibition of EZH2 activity. Interestingly, in contrast to FBL depletion, GSK126 treatment showed a significant decrease in the extent of E-cadherin internalization in DLD-1 cells (Figure 3D). To further assess the impact of EZH2 on Scribble regulation, we overexpressed EZH2. Interestingly, EZH2 overexpression led to internalization of E-cadherin into the cytoplasm (Figures 3E and S7A(i–ii)). Furthermore, scratch wound assays showed increased cell migration rates upon EZH2 overexpression (Figures 3F and S7C). Consistent with these observations, immunoblotting revealed that EZH2 overexpression showed a significant decrease in the levels of Scribble (Figures 3G and S6D and S7A(i–ii)).

To determine whether EZH2/H3K27me3 recruitment upon FBL depletion is a general phenomenon or is restricted to specific gene promoters, we selected ten candidate genes showing varied extents of differential deregulation upon FBL depletion from the RNA-seq data and performed ChIP-qPCR to assess the occupancy of EZH2 and H3K27me3 on these genes. We detected increased occupancy of both EZH2 and H3K27me3 on the promoters (−1 kb of TSS) of the downregulated genes (log_2FC −3.0 to −7.0; Figures S10C and S10D). In contrast, no significant changes were detected on the promoters of the upregulated genes (log_2FC +3.0 to +10.0; Figures S10E and S10F). This indicates that enhanced EZH2 recruitment upon FBL depletion is not limited to the SCRIB promoter. ChIP-Atlas analyses further showed that the downregulated genes were pre-enriched for H3K27me3 (Figures S8A–S8D, S9A, S9C, S9D, and S10A and S10B), indicating the presence of PRC2, suggesting that the relocalized EZH2 was preferentially recruited to the promoters with pre-existing H3K27me3 marks, consistent with a potential epigenetic memory mediated by PRC2.[40]

In summary, FBL depletion downregulates Scribble by increasing EZH2/H3K27me3 occupancy on its promoter. EZH2 inhibition restores Scribble expression, reduces E-cadherin

Figure 3. FBL depletion increases the occupancy of the inactive histone mark H3K27me3 on the Scribble promoter

(A) Schematic representation of the SCRIB promoter with primer locations. Bar plot shows significant enrichment of EZH2 and H3K27me3 occupancy on the SCRIB promoter in DLD-1 cells in control (siLacZ) and FBL-depleted (~48 h) cells. Data from $N = 3$ independent biological replicates. Statistical analysis was performed using unpaired t tests.

(B) Immunoblotting performed upon FBL depletion (~48 h) and inhibition of EZH2 (using GSK126) shows rescue of Scribble levels. Loading controls: HSP70, H3, and GAPDH. Data pooled from $N = 3$ independent biological replicates. Quantification in Figure S6B(i–ii).

(C) Representative phase-contrast images of scratch wound assay from DLD-1 cells upon EZH2 inhibition after treatment with GSK126 in siLacZ (control) and siFBL-transfected cells. Data pooled from $N = 3$ independent biological replicates. Scale bar, ~100 μm. Quantification in Figure S7B.

(D) Immunofluorescence assay showing the rescue of E-cadherin localization to the cell border upon the inhibition of EZH2 using GSK126. E-cadherin (green), FBL (red), and nucleus (DAPI; blue) in GSK126-treated cells (10 μm, for 48 h) and control siLacZ and FBL-depleted cells (~48 h). Data were pooled from $N = 3$ independent biological replicates. Scale bar, ~20 μm. Quantification in Figure S7E.

(E) Immunofluorescence analysis displaying E-cadherin (green), FBL (red), and nucleus (DAPI; blue) localization in DLD-1 cells overexpressing either Flag or Flag-EZH2, as well as in EZH2-overexpressing MCF10A(p53DN) cells under a doxycycline (Dox)-inducible promoter. Data were pooled from $N = 3$ independent biological replicates. Scale bar, ~20 μm. Quantification in Figure S6F(i–ii).

(F) Representative phase-contrast images of scratch wound assays of DLD-1 cells transduced with Flag and Flag-EZH2 overexpression constructs and EZH2-overexpressing MCF10A(p53DN) cells under a Dox-inducible promoter. Data were pooled from $N = 3$ independent biological replicates. Scale bar, ~100 μm. Quantification in Figure S7C.

(G) Representative immunoblots showing EZH2 overexpression downregulates Scribble levels in EZH2-overexpressing MCF10A(p53DN) cells under a Dox-inducible promoter, with cells transfected with siLacZ and siFBL (~36 h). Loading controls: HSP70, GAPDH, and H3. Data were pooled from $N = 3$ independent biological replicates.

$^{*}p < 0.1$, $^{**}p < 0.01$, $^{***}p < 0.001$, and $^{****}p < 0.0001$. Quantification in Figure S7A(i–ii).

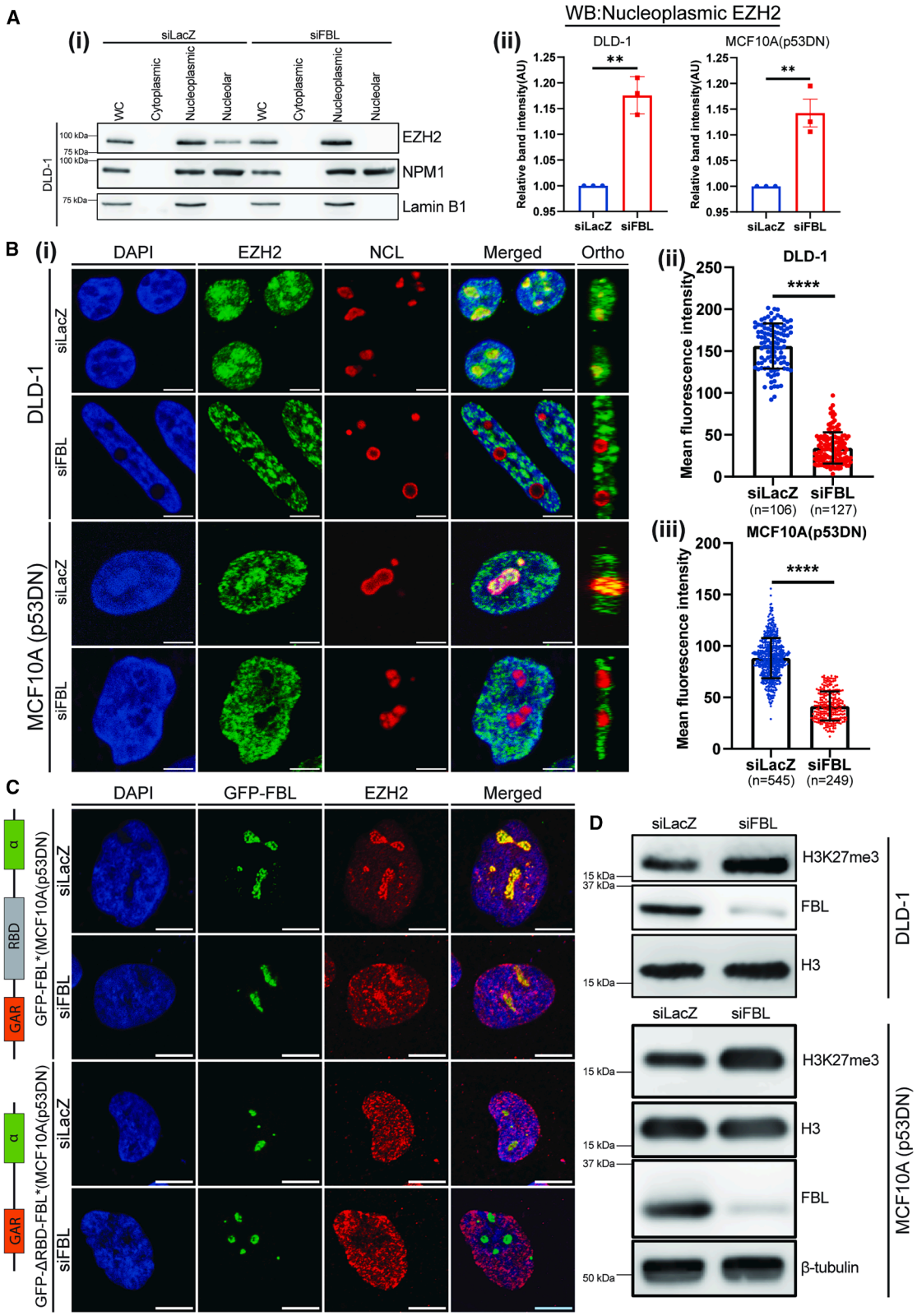

(legend on next page)

internalization, and suppresses cell migration. In contrast, EZH2 overexpression directly downregulates SCRIB expression by increased deposition of H3K27me3 on the SCRIB promoter.

EZH2 translocates from the nucleolus to the nucleoplasm upon FBL depletion

We found that FBL depletion caused a significant increase in the enrichment of EZH2 (∼0.11% ± 0.01%; Figure 3A) on the SCRIB promoter, while the total levels of EZH2 were unaltered. We next asked if FBL depletion impacts the subcellular localization of EZH2, using two independent approaches: (1) immunoblotting to determine total protein levels by subcellular fractionation and (2) immunofluorescence staining at the single-cell level. Interestingly, FBL depletion hardly showed any localization of EZH2 in the nucleolus in both cell lines. This was accompanied by a concomitant and significant increase (∼16% ± 1%) in the nucleoplasmic fraction of EZH2 (Figures 4A(i–ii) and S12E). Furthermore, IFAs showed a significant reduction of EZH2 in the nucleolus (demarcated by nucleolin [NCL]) upon FBL depletion (Figures 4B(i–iii) and S11A(i–ii) and S11B(i–ii); Videos S3 and S4).

FBL has an RNA-binding domain (RBD) that interacts with the CXC domain of EZH2.[42] We therefore generated an FBL mutant with a deletion of the RBD domain to investigate if the abrogation of FBL-EZH2 interaction impacts the relocalization of EZH2 into the nucleoplasm. We expressed an RBD-deleted, siRNA-resistant mutant of FBL tagged with GFP (GFP-ΔRBD FBL) in a background of endogenous FBL depletion, which showed a striking displacement of EZH2 from the nucleolus (∼50% ± 10%; Figures 4C and S13A and S13B; Videos S5, S6, S7, and S8). The disruption of FBL-EZH2 interaction was further validated using co-IP (Figure S12C). Consistent with this finding, the levels of H3K27me3 showed a concomitant increase upon FBL depletion, as monitored by IFA (∼6-fold) and immunoblotting assay (∼60% ± 10%; Figures 4D and S12A, S12B(i–ii), and S12D(i–ii)).

Interestingly, the total levels of EZH2 were unaltered upon FBL depletion. On closer inspection of cells labeled by IFA, nucleolar EZH2 showed a decrease by ∼30% ± 7%, while the amount of nucleoplasmic EZH2 increased by ∼27% ± 4%, further supporting the translocation of EZH2 from the nucleolus to the nucleoplasm (Figure S11C(i–iii)). Taken together, these results reveal that FBL plays a crucial role in sequestering a subpopulation of EZH2 within the nucleolus.

FBL-mediated nucleolar retention of EZH2 sustains Scribble expression

It is well established that EZH2 interacts with the PRC2 components SUZ12 and EED1.[43–45] Upon FBL depletion, the EZH2 that is released from the nucleolus (henceforth, "nucleolar EZH2") interacts with the nucleoplasmic PRC2 complex. Consistent with the enrichment of H3K27me3 and EZH2 on the SCRIB promoter, we investigated the contribution of nucleolar EZH2 to the downregulation of SCRIB expression. To this end, we utilized BioID2 ChIP-qPCR to tag and monitor nucleolar EZH2 upon FBL knockdown.[46] Cells stably expressing BioID2-FBL (WT) were supplemented with 50 μM biotin. The cells were harvested upon FBL knockdown (for ∼24 h), followed by ChIP. The sonicated chromatin was used for pull-down using streptavidin Dynabeads, followed by ChIP-qPCR analysis. We validated the pull-down of EZH2 using immunoblotting (Figure S14C). Interestingly, the ChIP-qPCR results showed increased occupancy of biotinylated EZH2 on the SCRIB promoter upon FBL depletion (Figures 5A and S15E).

Since we observed that the abrogation of FBL-EZH2 interaction increased nucleoplasmic EZH2, and BioID2 ChIP-qPCR revealed enrichment of the translocated EZH2 on the SCRIB promoter, we determined the impact of abrogating FBL-EZH2 interaction on cell-cell adhesion. We performed IFAs, which revealed a striking internalization of E-cadherin in GFP-ΔRBD FBL(siRes) or vector control (GFP) overexpressing cells, in a background of endogenous FBL depletion (Figures 5B and S14B(i–ii)). Immunoblotting showed a downregulation of Scribble expression due to the loss of FBL-EZH2 interaction (Figures 5C and S14A(i–ii)). Remarkably, the abrogation of FBL-EZH2 interaction also showed an increase in cell migration rates, as quantified from scratch wound assays (Figures 5D and 5E). Taken together, loss of FBL-EZH2 interaction translocates EZH2 from the nucleolus to the nucleoplasm, downregulating Scribble expression, accompanied by the concomitant internalization of E-cadherin and the consequent elongation and loss of

Figure 4. EZH2 translocates from the nucleolus to the nucleoplasm following fibrillarin depletion

(A) (i) Representative immunoblots of cell fractions derived from siLacZ- and siFBL-transfected DLD-1 cells (∼48 h), showing whole-cell lysate (WC), cytoplasmic, nuclear, and nucleolar fractions. IB: lamin B1 and nucleophosmin1 (NPM1) serve as nuclear and nucleolar loading controls, respectively. (ii) Quantification of IB (DLD-1 and MCF10A) shows a significant increase in nucleoplasmic EZH2. Data were pooled from $N = 3$ biological replicates. p values were derived from an unpaired t test.

(B) (i) Representative images of immunofluorescence showing a depletion of nucleolar EZH2, with NCL (red) demarcating the nucleolus from the nucleoplasm, in DLD-1 and MCF10A(p53DN) cells transfected with siLacZ and siFBL for ∼48 and ∼36 h, respectively. The nucleus is visualized via DAPI staining. EZH2: green and NCL: red. Data were pooled from $N = 3$ independent biological replicates. Scale bar, ∼20 μm. (ii) Scatterplot (bar overlaid) showing reduction in levels of nucleolar EZH2 upon transfecting DLD-1 cells with siFBL- compared to siLacZ-transfected (control) cells (for ∼48 h). The data were pooled from $n = 233$ nucleoli across $N = 3$ independent biological replicates. p values were pooled using an unpaired t test. (iii) Scatterplot (bar overlaid) showing reduction in levels of nucleolar EZH2 upon transfecting MCF10A(p53DN) cells with siFBL- (for ∼36 h) compared to siLacZ-transfected (control) cells. The data were pooled from $n = 794$ nucleoli across $N = 3$ independent biological replicates. p values were pooled using an unpaired t test.

(C) Representative immunofluorescence images for EZH2 (red) and nucleus (DAPI; blue) from GFP-FBL(siRes)- and ΔRBD-GFP-FBL(siRes)-overexpressing DLD-1 cells transfected with siLacZ and siFBL (for ∼48 h; $n \geq 120$ nucleoli). Data were pooled from $N = 3$ independent biological replicates. Scale bar, ∼20 μm. Quantification of colocalization of EZH2 and GFP is in Figure S11B(ii).

(D) Representative western blots showing a significant increase in H3K27me3 levels in siLacZ- (control) and siFBL-transfected DLD-1 and MCF10A(p53DN) cells for ∼48 and ∼36 h, respectively. Loading control: H3 and β-tubulin in siLacZ- and siFBL-transfected MCF10A(p53DN) cells. Data were pooled from $N = 3$ independent biological replicates. Scale bar, ∼20 μm. Quantification is in Figure S12D(i–ii).

Error bars indicate SD. $^{*}p < 0.1$, $^{**}p < 0.01$, $^{***}p < 0.001$, and $^{****}p < 0.0001$.

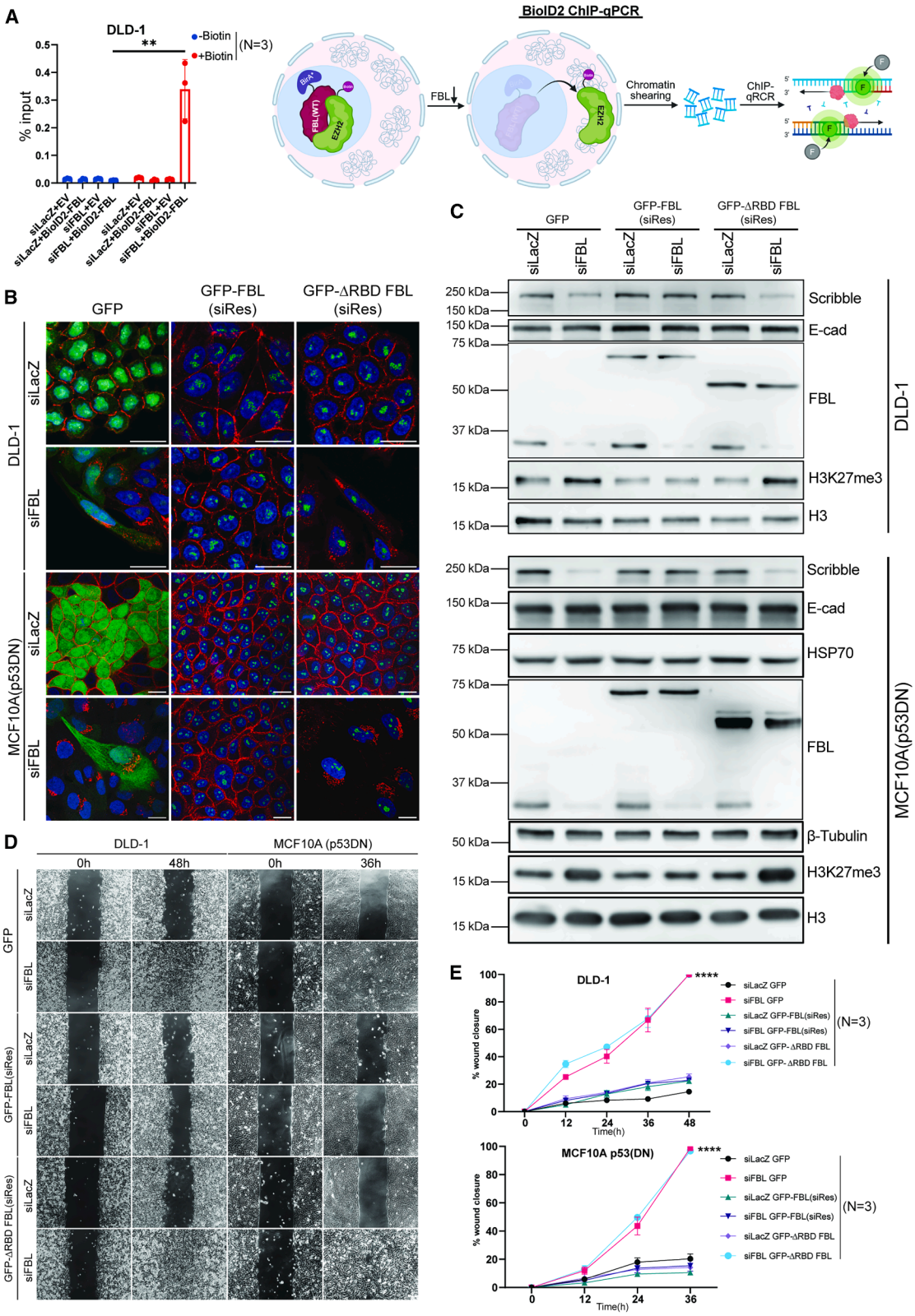

(legend on next page)

the cobblestone morphology that define epithelial cells (Figure S15C).

We next performed ChIP-qPCR to examine the occupancy of EZH2 on the SCRIB promoter. Loss of FBL-EZH2 interaction in an endogenous FBL-depleted background showed an increased occupancy of EZH2 on the SCRIB promoter, which downregulates Scribble expression (Figure 5C and S15D). Downregulation of Scribble manifests as mislocalization of E-cadherin and enhanced cell migration. Additionally, we performed a graded overexpression of EZH2 under a doxycycline (Dox)-inducible promoter, which caused an increase in EZH2 levels and downregulation of Scribble (Figures S15A and S15B).

Taken together, the interaction between FBL and EZH2 regulates Scribble expression and cell migration. Disrupting this interaction induces the translocation of nucleolar EZH2 into the nucleoplasm, thereby increasing H3K27me3 deposition on the SCRIB promoter and its consequent downregulation. Collectively, this results in the mislocalization of E-Cadherin, enhancing cell migration, which suggests that the FBL-EZH2 interaction plays a crucial role in the maintenance of the epithelial state of cells.

FBL depletion induces EMT by downregulating Scribble levels

FBL depletion showed a significant reduction in Scribble levels. Decreased Scribble levels induce EMT in the epithelial breast cell line MCF10A.[47] This transition is facilitated by the inactivation of the Hippo signaling pathway and the subsequent stabilization of TAZ, since TAZ promotes the expression of Snail and FOXC2, which are associated with EMT.[48] Furthermore, Scribble interacts with PHLPP1 to inhibit the phosphorylation or activation of Akt.[49] Activated Akt phosphorylates EZH2 at Ser21, altering the binding affinity of EZH2 for histone H3, resulting in the loss of methylating activity of EZH2 on histone H3.[50]

Since Scribble depletion induces EMT in breast epithelial cells (MCF10A), we examined whether FBL depletion induces EMT in MCF10A(p53DN) cells. Surprisingly, while FBL depletion hardly showed any alteration in the levels of EMT markers at the end of ~36 h, prolonging FBL depletion for ~72 h caused a significant increase in the levels of mesenchymal markers Snail1, Twist1, and Zeb1 (master transcription factors that promote EMT).[51,52] This was accompanied by decreased levels of cell adhesion proteins E-cadherin and occludin (Figures 6A and S19D). Furthermore, a reduction in H3K27me3 levels correlated with Akt activation (Figures 6A and S16A(i)). The levels of E-cadherin (decreased) and vimentin (increased) were further corroborated by IFA and immunoblotting, respectively (Figures 6B and S16E(i–ii)). Scribble levels were relatively lower in FBL-depleted cells (~36-h post-transfection), which, interestingly, recovered upon prolonged FBL depletion (~72 h). ChIP-qPCR showed a significant reduction in the occupancy of EZH2 and H3K27me3 on the SCRIB promoter after ~72 h of FBL depletion (Figure S16D), correlating with global H3K27me3 reduction and recovery of Scribble expression (Figure 6A). IFA revealed that Scribble was predominantly localized in the cytoplasm rather than the cell membrane at ~72 h (Figures 6C and S16B).

Since we previously identified that the interaction between FBL-EZH2 sustains the levels of Scribble, we abrogated FBL-EZH2 interaction by overexpressing GFP-ΔRBD FBL(siRes) in a background of endogenous FBL depletion (~72 h) in MCF10A(p53DN). Remarkably, immunoblotting showed upregulated levels of mesenchymal markers vimentin, Snail, Twist, Zeb1, and TAZ, with a concomitant decrease in the levels of epithelial markers E-cadherin and occludin upon GFP-ΔRBD-FBL(siRes) overexpression in an FBL-depleted background (Figures 6D and S16C(i–ii)). IFAs further showed elevated levels of vimentin and reduced levels of E-cadherin and occludin (Figures 6F and S17A(i–ii)).

Since pAkt was activated upon FBL depletion and Scribble is an antagonist of Akt activation,[49] we examined the role of pAkt in EMT in the context of FBL depletion in MCF10A(p53DN) cells. We inhibited Akt by treating cells with the Akt inhibitor GSK690693[53] at 2 nM for ~72 h. This further curtailed EMT progression, as it decreased Snail, Twist, Zeb1, and vimentin levels and rescued epithelial markers E-cadherin and occludin (Figures 6E and S17C).

Taken together, these studies establish that FBL depletion induces EMT in breast epithelial cells (MCF10A (p53DN)) by collectively (1) disrupting the presence of Scribble at the cell membrane, (2) activating Akt, and (3) reducing EZH2 activity. These events synergistically upregulate Snail, Twist, and Zeb1, while decreasing epithelial markers. However, overexpression of GFP-ΔRBD-FBL(siRes) does not rescue EMT in an endogenous FBL-depleted background, underscoring a requirement for an interaction between FBL-EZH2 for the maintenance of the epithelial state of cells. Furthermore, Akt inhibition rescues

Figure 5. FBL-mediated nucleolar retention of EZH2 is crucial for maintaining Scribble expression

(A) Bar plot representing BioID2-ChIP-qPCR enrichment of EZH2 (biotinylated and non-biotinylated) on the SCRIB promoter in DLD-1 and MCF10A(p53DN) cells in siLacZ- and siFBL-transfected cells ($N = 3$) for ~24h. p values derived from an unpaired t test. The schematic represents the steps involved in BioID2-ChIP-qPCR.

(B) Representative images of immunofluorescence for E-cadherin (red) upon overexpression of GFP, GFP-FBL(siRes), and ΔRBD-GFP-FBL(siRes) in DLD-1 and MCF10A(p53DN) cells transfected with siLacZ and siFBL for ~48 and ~36 h respectively. GFP or GFP-tagged proteins are shown in green. Nucleus (blue) stained with DAPI. Data were pooled from $N = 3$ independent biological replicates. Scale bar, ~20 μm. Quantification shown in Figure S14B(i) and (ii).

(C) Representative immunoblots showing Scribble, E-cadherin, FBL, and H3K27me3. Loading controls: HSP70, β-tubulin, H3, and GAPDH from GFP-, GFP-FBL(siRes)-, and ΔRBD-GFP-FBL(siRes)-overexpressing DLD-1 and MCF10A(p53DN) cells transfected with siLacZ and siFBL for ~48 and ~36 h respectively. Data were pooled from $N = 3$ independent biological replicates. Quantification in Figure S12A(i–ii).

(D) Representative phase-contrast images of scratch wound assay performed on DLD-1 and MCF10A(p53DN) cells expressing GFP, GFP-FBL(siRes), and ΔRBD-GFP-FBL(siRes) transfected with siLacZ- and siFBL-transfected cells. Data were pooled from $N = 3$ independent biological replicates.

(E) Quantitative analysis of scratch wound assay from Figure 5D. Two-way ANOVA with Sidak's test was performed to calculate the p value.

Error bars indicate SD. $^{*}p < 0.05$, $^{**}p < 0.01$, and $^{****}p < 0.0001$.

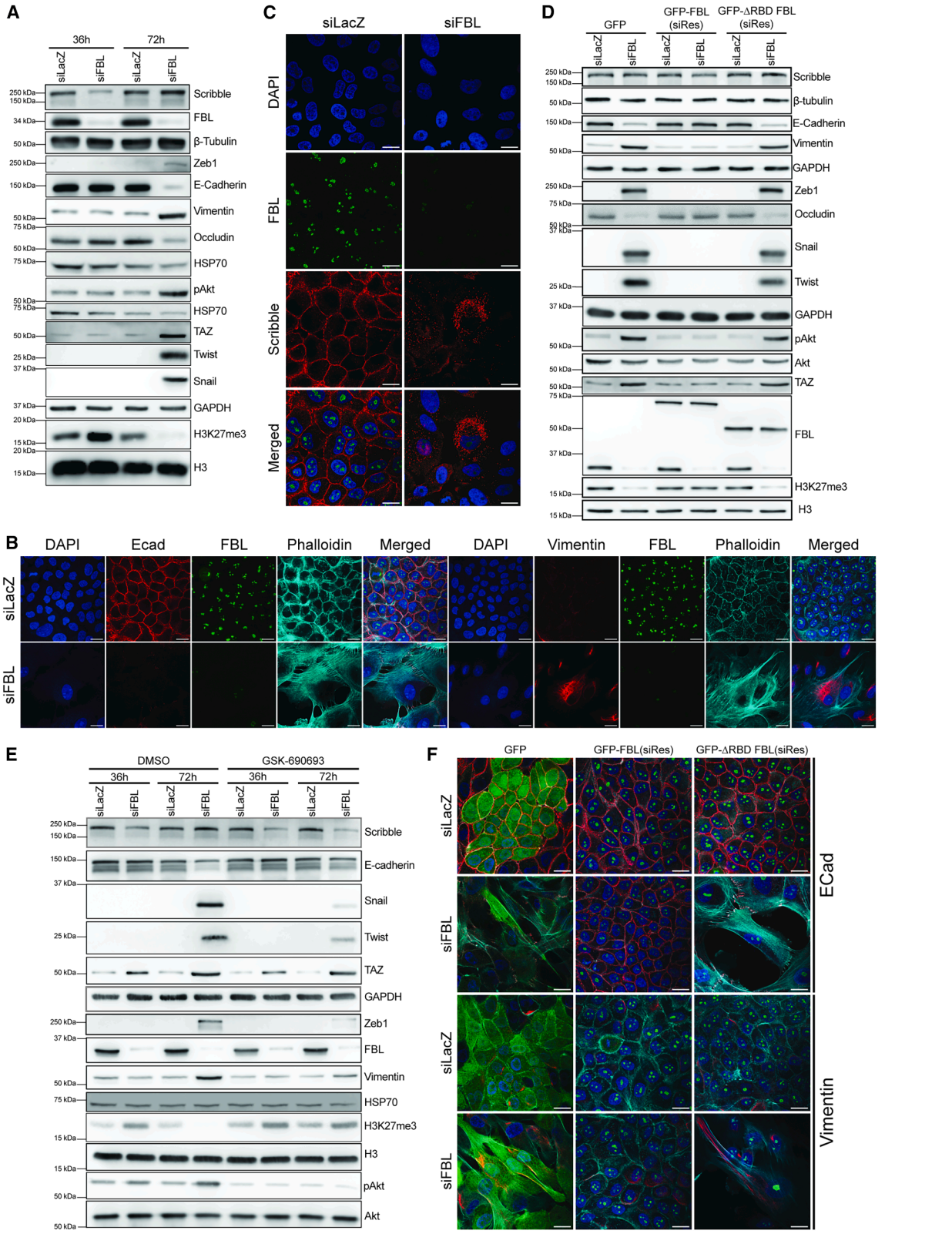

(legend on next page)

EMT, highlighting the role of Akt activation in EMT induction upon FBL depletion.

FBL depletion increases tumorigenicity and lung metastasis

We next investigated the contribution of FBL depletion to tumorigenesis. To this end, we subcutaneously injected FBL-depleted DLD-1 cells (stably expressing shFBL under a Tet-ON inducible promoter) into NOD-SCID mice. FBL depletion was sustained by administering Dox supplemented in drinking water, replaced every ~72 h. Tumor growth was monitored until harvest on day 35 post-injection, which showed a significant increase in tumor growth in FBL-depleted mice (Dox-treated [+Dox] mice, ~40%, compared to control mice [−Dox]; Figure 7B). Consistently, volumes and weights of tumors showed a significant increase upon FBL depletion (+Dox mice; Figure 7C(i–ii)).

To further investigate the crosstalk between FBL and EZH2 in primary cells, the tumors were enzymatically digested using a triple enzyme mix to isolate tumor cells. Notably, FBL depletion upon Dox induction in mice showed a significant decrease (~4-fold) in the localization of EZH2 in the nucleolus, as monitored by its colocalization with NCL, a key marker of the granular component (GC) of the nucleolus (Figures 7D and S20C). Additionally, analysis of tumor lysates revealed a significant decrease in the levels of Scribble and increased H3K27me3 (Figures 7E and S20B), reinforcing that FBL loss decreases Scribble levels, as determined in cultured cells. These findings present a crucial role for FBL depletion in enhancing tumorigenesis.

Since we established that FBL knockdown increases cell migration, we also asked if FBL depletion increases cell invasion and metastasis. We therefore performed tail vein injections of FBL-depleted DLD-1 cells (stably expressing shFBL under a Tet-ON inducible promoter) in immunocompromised NOD-SCID mice. FBL depletion was sustained by administering Dox, supplemented in drinking water, replaced every ~72 h. The mice were sacrificed ~60 days post-injection. We performed a careful visual inspection of the organs, closely examining the lungs, the primary site for metastasis of trapped circulating tumor cells and a known colonization site for DLD-1 upon tail vein injection, making them a preferable organ for assessing metastatic burden.[54] We harvested and processed the lungs for hematoxylin-eosin staining. FBL depletion (+Dox) showed enhanced lung metastasis in mice. Further quantification of metastatic nodules in the lung sections revealed increased metastatic burden upon FBL depletion in +Dox mice (Figures 7F(i–ii) and S20E). This implies that FBL depletion induces the cells to be more invasive and metastatic in nature.

In summary, FBL depletion increases cell invasiveness, as corroborated by xenograft models, which showed increased tumorigenic burden and metastasis, highlighting a novel role for FBL in the regulation of tumorigenesis.

DISCUSSION

FBL is a nucleolar protein required for post-transcriptional modifications and stability of rRNA. Here, we show that FBL plays a critical role in the maintenance of the integrity of the epithelial cells by regulating cell-cell adhesion. FBL depletion disrupts E-cadherin localization, leading to its internalization via clathrin-mediated endocytosis, compromising the stability of tight junctions. The destabilization of cell-cell adhesion is accompanied by the downregulation of Scribble, a key protein that determines apico-basal cell polarity,[55,56] repressed by increased occupancy of the inactive histone mark (H3K27me3), deposited by EZH2 upon FBL loss. Furthermore, FBL depletion translocates EZH2 from the nucleolus to the nucleoplasm, promoting transcriptional silencing of SCRIB, which enhances cell migration. Prolonged downregulation of Scribble stabilizes TAZ and decreases the deposition of H3K27me3 and SNAI1, ZEB1, and TWIST1 expression, synergistically, contributing to EMT in breast epithelial cells MCF10A(p53DN), as evidenced by the upregulation of mesenchymal markers. Taken together, our findings establish FBL as a crucial regulator of epithelial

Figure 6. FBL depletion induces EMT by modulating Scribble expression levels

(A) Representative immunoblots showing Scribble, occludin, E-cadherin, vimentin, Snail, Zeb1, Twist, pAkt, TAZ, FBL, and H3K27me3. Loading controls: 1st HSP70 is the loading control for Zeb1, E-cadherin, vimentin, and occludin, 2nd HSP70 is the loading control for pAkt, β-tubulin, H3, and GAPDH from MCF10A(p53DN) cells transfected with siLacZ and siFBL for 36 and 72h. Data were pooled from $N = 3$ independent biological replicates. Quantification shown in Figure S16A(i–ii).

(B) Representative immunofluorescence images showing FBL (green), E-cadherin (red), F-actin (phalloidin; cyan), and nucleus (DAPI; blue) upon FBL depletion (~72 h) lead to decreased E-cadherin and increased levels of vimentin. Data were pooled from $n = 416$ cells and $N = 3$ independent biological replicates. Quantification shown in Figure S16E(i–ii).

(C) Representative immunofluorescence images showing the internalization of SCRIB transfected with siLacZ and siFBL for 72 h ($n = 211$ cells) show the nucleus via DAPI staining, Scribble (red), and FBL (green). Data were from $N = 3$ independent biological replicates. Scale bar, 20 μm. Quantification is shown in Figure S16B.

(D) Representative immunoblots showing induction of EMT by ~72 h upon abrogating the FBL-EZH2 interaction in GFP-, GFP-FBL(siRes)-, and ΔRBD-GFP-FBL(siRes)-overexpressing MCF10A(p53DN) cells transfected with siLacZ and siFBL. IB: Scribble, occludin, E-cadherin, vimentin, Snail, Zeb1, Twist, pAkt, TAZ, FBL, and H3K27me3 using HSP70, β-tubulin, H3, AKt, and GAPDH as loading controls. Data were from $N = 3$ independent biological replicates. Scale bar, 20 μm. Quantification shown in Figure S16C(i–ii).

(E) Representative immunoblots show rescue of EMT upon the inhibition of Akt. IB: Scribble, E-cadherin, vimentin, Snail, Zeb1, Twist, pAkt, TAZ, FBL, and H3K27me3. Loading controls: HSP70, β-tubulin, H3, AKt, and GAPDH as loading controls from MCF10A(p53DN) cells transfected with siLacZ and siFBL for ~36 and ~72h, respectively, upon treatment with GSK690693 (2 nM) with DMSO (control). Data were pooled from $N = 3$ independent biological replicates. Quantification shown in Figure S17C.

(F) Representative images of immunofluorescence for E-cadherin (red) and vimentin (red), F-actin (phalloidin; cyan), and nucleus (DAPI; blue) for MCF10A(p53DN) cells from GFP-, GFP-FBL(siRes)-, and ΔRBD-GFP-FBL(siRes)-overexpressing MCF10A(p53DN) cells transfected with siLacZ and siFBL for 72h ($N = 3$). Data were pooled from $N = 3$ independent biological replicates. Quantification shown in Figure S17A(i–ii).

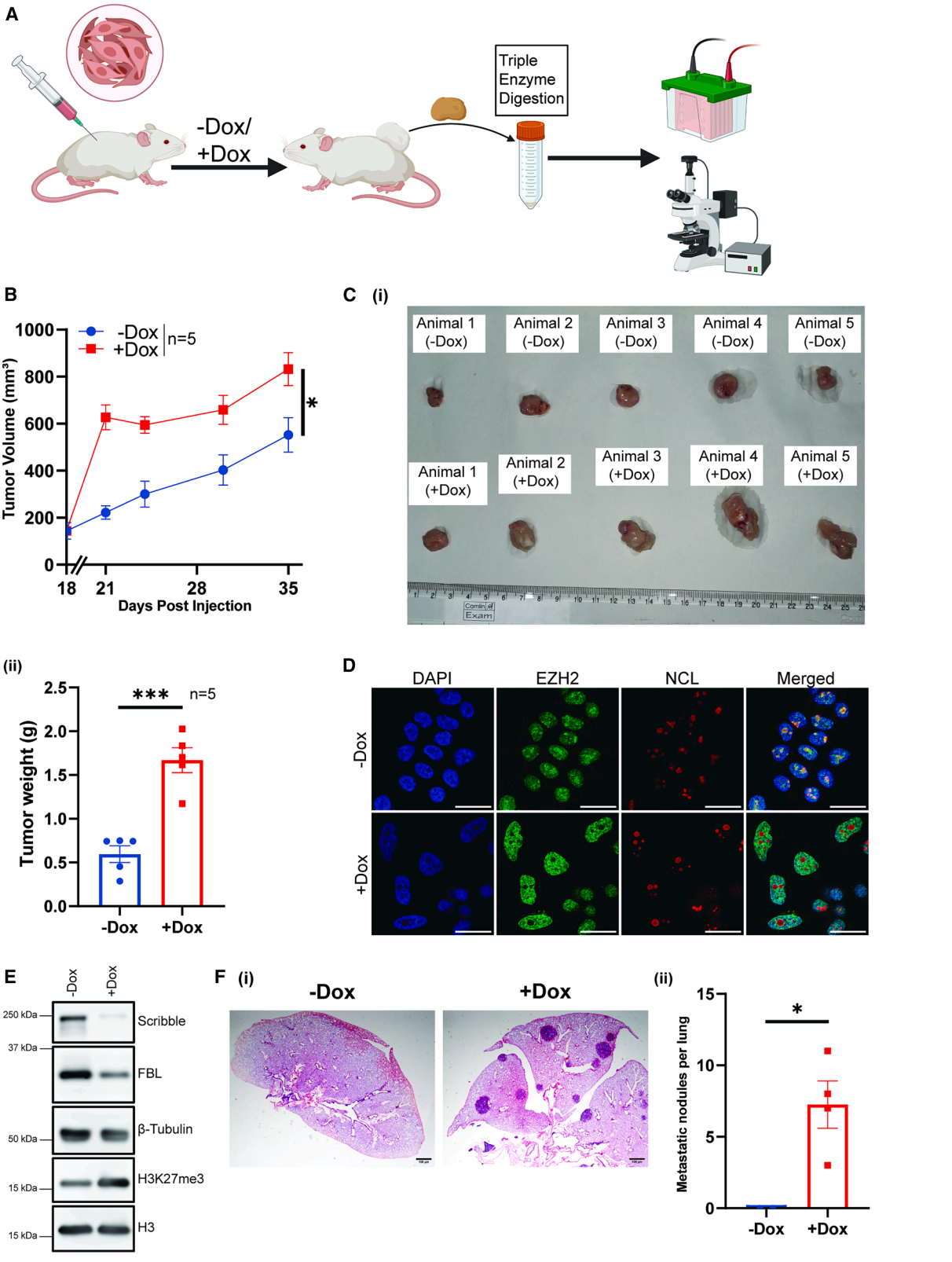

(legend on next page)

homeostasis, as FBL loss drives cell migration and EMT, regulated by Scribble and EZH2 dynamics.

FBL depletion disrupts cell-cell adhesion and enhances migration

Our study, for the first time, demonstrates that the depletion of FBL profoundly alters cell-cell adhesion in epithelial cells, enhancing cell migration in two independent epithelial cell types: (1) colorectal cancer (DLD-1) and (2) breast epithelial cells (MCF10A(p53DN)). We independently validated the internalization of E-cadherin upon FBL depletion using a proteinase K protection assay (Figure S2E). The generalizability of FBL depletion-mediated E-cadherin internalization was further validated in lung cancer A549 cells (Figure S4C(i-ii)).

While a direct loss of lamins typically manifests as an increase in cell migration in most cancer cells,[57,58] FBL depletion did not show any significant alterations in lamin levels, as determined by RNA-seq analysis.[59] This suggests that FBL depletion promotes cell migration while potentially bypassing nuclear lamins. We surmise that FBL loss reorganizes indirect interactions of LINC complex proteins with cell-cell adhesion molecules, likely creating differential tension on the nuclei of migrating cells.[60]

FBL is required for rRNA biogenesis and modification, and its depletion is likely to impact rates of rRNA and protein synthesis.[22,23] Interestingly, the SUnSET assay did not show a significant difference in protein synthesis rates (Figure S2F).[61] We surmise that (1) the residual levels of FBL post depletion are sufficient for processing nascent 45S rRNA, since FBL depletion does not show a significant effect on 28S and 18S rRNA (Figure S3D), and (2) decreased Scribble on the cell membrane activates the Akt/mTOR/S6K signaling pathway, upregulating global translation,[62] compensating for potential disruptions in protein homeostasis.

FBL depletion downregulates Scribble expression, leading to cell migration

FBL depletion not only affects E-cadherin localization but also results in its accumulation in the Golgi, as it colocalizes with the Golgi marker GM130 (Figure 2A). E-cadherin has a ubiquitination site at the cytoplasmic domain, which is protected by p120 protein, thereby sustaining the localization and integrity of E-cadherin on the cell membrane. Scribble, a key apical-basal polarity protein, further stabilizes the p120 and E-cadherin interaction at the cell membrane.[36] Decrease in Scribble levels upon FBL depletion led to increased cell elongation, along with concomitant fragmentation of Golgi (Figure 2A), potentially an indirect effect of actin remodeling during cell elongation[63] although a direct role of FBL in modulating Golgi fragmentation and function remains unclear.

It is well established that a multifactorial process maintains the stability of E-cadherin at the cell membrane, such as Discs large homolog 5 (DLG5),[64] CTNND1 (delta-catenin),[65] Epsin3 (EPN3),[66] VANGL planar cell polarity protein 2 (VANGL2),[67] Discoidin domain receptor family member 1 (DDR1),[68] and Scribble (SCRIB).[36] Transcriptome analyses of FBL depletion in DLD-1 cells did not show a significant decrease in the transcript levels of DLG5 and DDR1, otherwise implicated in the internalization of E-cadherin (Figure 2F). Interestingly, RNA sequencing revealed a significant downregulation of Scribble, which regulates E-cadherin trafficking (Figure 2F). Collectively, our study unravels a fundamental mechanistic link between FBL and Scribble in maintaining and regulating the integrity of epithelial cells.

FBL loss enhances H3K27me3 enrichment and silences SCRIB expression

It is well established that EZH2 occupancy and its histone methyltransferase activity modulate its interactions with PRC2 components EED and SUZ12. Notably, SUZ12 interacts with either EZH1 or EZH2, resulting in a transition of the SET domain (Su(var)3-9, enhancer-of-zeste, and trithorax) from an autoinhibitory to an active configuration, which enhances its methyltransferase activity.[45,69] The SCRIB promoter is potentially bivalent due to the co-occupancy of H3K27me3 and H3K4me3 in differentiated hESCs (5 days post-differentiation; Figure S5D). Such a bivalent state maintains robust expression and dynamic turnover of SCRIB, despite the pre-occupancy of H3K27me3. These findings implicate EZH2 in the regulation of Scribble upon FBL depletion.

EZH2 translocates to the nucleoplasm and represses Scribble upon FBL depletion

We show that the depletion of FBL relocalizes EZH2 from the nucleolus to the nucleoplasm, which correlates with an

Figure 7. FBL depletion promotes tumorigenesis

(A) Schematic representation of xenograft assays performed in NOD/SCID mice showing tumor induction, harvest, and further processing for immunoblotting and immunofluorescence assays.

(B) Quantification of tumor volumes across 35 days in +/− doxycycline (Dox)-administered mice ($n = 5$). Error bars indicate SD; $^{*}p < 0.5$.

(C) (i) Representative images of tumors harvested from mice 35 days post-injection ($n = 5$). (ii) Weight of tumors after harvesting from mice ($n = 5$). Error bars indicate SD. $^{***}p < 0.001$.

(D) Representative images of immunofluorescence for EZH2 and NCL from MCF10A(p53DN) and DLD-1 cells transfected with siLacZ and siFBL ($n \geq 90$) show the nucleus via DAPI staining, EZH2 via green fluorescence, and NCL via red fluorescence. Scale bar, 20 μm, ($N = 3$). Quantification of colocalization analysis of EZH2 and nucleolin (NCL) in Figure 20C.

(E) Representative immunoblots of Scribble, E-cadherin, FBL, and H3K27me3 using β-tubulin and H3 as loading controls from cells harvested from tumors. Quantification in Figure S20B.

(F) (i) Representative hematoxylin and eosin (H&E)-stained lung sections from NOD-SCID mice 60 days after tail vein injection of DLD-1 cells expressing shRNA targeting FBL (shFBL) under the Dox-inducible promoter. Lungs from Dox-administered (+Dox) mice exhibited numerous, well-defined metastatic nodules distributed across the lung parenchyma, whereas shFBL-expressing mice displayed markedly fewer and smaller metastatic lesions. Scale bars, 100 μm. (ii) Quantification of metastatic burden in lungs from NOD-SCID mice following tail vein injection of DLD-1 cells expressing Dox-inducible shFBL. Data are shown as mean ± SEM, with each dot representing each lung sample.

$^{*}p < 0.05$, unpaired *t* test.

increased deposition of H3K27me3 on the SCRIB promoter, repressing Scribble expression.

We examined the generalizability of FBL depletion in two additional colorectal cancer cell lines, HCT116 and SW480. These cell lines showed a decrease in the levels of nucleolar EZH2 (Figures S13C and S13D(i–ii)). EZH2 showed a significant decrease in the nucleoli upon FBL depletion, consistent with observations in DLD-1 and MCF10A(p53DN) (Figure 4B). This further demonstrates that FBL depletion causes relocalization of EZH2 from the nucleoli to the nucleoplasm.

Elevated expression of EZH2 has been implicated in promoting metastasis across various cancer types. In breast cancers, increased EZH2 levels are significantly associated with invasive carcinomas and metastasis.[70] Similarly, in prostate cancer, EZH2 overexpression correlates with advanced stages and metastatic progression. Increased EZH2 expression positively correlates with aggressive forms of bladder cancer, endometrial cancer, and melanoma, where it is linked to enhanced metastatic potential.[71,72] In ovarian cancers, EZH2 enhances metastasis through TGF-β signaling.[73] EZH2 regulates tumor suppressors by transcriptionally silencing adenosylmethionine decarboxylase 1 (AMD-1).[72] Collectively, these findings underscore the critical role of EZH2 in facilitating cancer metastasis across multiple cancer subtypes. Our study unravels Scribble as a key target of EZH2 overexpression.

FBL depletion induces EMT and enhances tumor growth

FBL depletion induces EMT by downregulating Scribble, stabilizing TAZ, and enhancing Akt activation, which reduces EZH2 activity. In MCF10A(p53DN) cells, FBL loss increased mesenchymal markers and reduced epithelial markers. Scribble levels declined by ∼36 h and partially recovered by ∼72 h but remained cytoplasmic. Using membrane anchoring-deficient Scribble mutants (C4S, C10S, and P305L), we found that cytoplasmic retention alone elevated pAkt (S473), corroborating its sufficiency for Akt activation (Figures S19A, S19B, and S19C).[62] We propose that Snail, which appears by ∼72 h, drives cytoplasmic retention of Scribble, consistent with elevated levels of Snail-high triple-negative breast cancer cells (MDAMB231).[74] Thus, prolonged FBL depletion promotes EMT by sustaining mislocalization of Scribble and activating Akt signaling.

FBL depletion-mediated downregulation of Scribble, the consequent disruption of PTEN proximal to the cell membrane, and decreased levels of PTEN in tumor cells (Figure S20F),[75,76] further function as key targets of FBL-dependent tumorigenesis.[77,78]

Gain-of-function mutations in EZH2, particularly in B cell lymphomas, enhance its methyltransferase activity, leading to aberrant gene repression and oncogenesis. The well-characterized Y641 mutation in the SET domain increases H3K27 trimethylation, promoting malignant transformation.[79] Similarly, the A687V mutation, also in the SET domain, alters substrate specificity and enhances methylation activity, further contributing to lymphoma development.[80] Additionally, the W113C mutation in the SET activation loop stabilizes the active conformation of EZH2, amplifying its catalytic function and driving oncogenesis.[81] Collectively, these studies show that a hyperactive mutation of EZH2 mediates excessive deposition of H3K27me3, playing a critical role in cell proliferation and tumor progression, consistent with our finding that the enhanced deposition of H3K27me3 upon FBL depletion enhances tumorigenesis.

Future directions

Consistent with elevated levels of FBL and its association with increased chemoresistance and proliferation in cancer cells, therapeutic interventions that modulate FBL expression are key. Among the various approaches for regulating protein levels, proteolysis-targeting chimeras (PROTACs) have emerged as promising therapeutic agents. However, our findings indicate that targeting FBL for degradation via PROTACs may not be a viable therapeutic strategy, as reduced FBL levels can compromise epithelial integrity. A potential therapeutic strategy is to develop small molecule-based stabilizers of the FBL-EZH2 interaction, likely to promote greater retention of EZH2 within the nucleolus rather than the nucleoplasm (Figure 4B). Such stabilizers include small molecules or peptide chimeras with high binding affinity to the FBL-EZH2 interface. Recently, the development of LOCKTACs—compounds that slow dissociation to stabilize natural protein interactions without generating new ones—has opened new avenues in drug design.[82] LOCKTACs function by binding directly within or adjacent to a protein-protein interface or by acting as heterobifunctional molecules that stabilize complexes without directly engaging the interface. Unlike allosteric drugs, which act at distal sites to induce conformational changes, LOCKTACs operate by reinforcing native interactions. To enable intracellular delivery, such stabilizers could be conjugated to cell-penetrating peptides (CPPs), short, positively charged sequences that facilitate membrane translocation via endocytosis or direct penetration.[83] Cyclic peptides generated via click chemistry provide an additional delivery route, offering improved stability and, in some cases, passive cell entry.[84] Delivering these interaction-stabilizing molecules, particularly during early stages of cancer, could preserve epithelial organization and suppress EMT-like phenotypic transitions without perturbing the canonical role of FBL in ribosome biogenesis, thereby preventing metastatic spread. In parallel, enzymatic inhibition of FBL activity also presents a therapeutic opportunity, as disabling its enzymatic function does not significantly affect cell proliferation.[9] Optimized use of FBL enzymatic inhibitors in cancers with elevated FBL levels could reduce rRNA methylation and subsequently limit cap-independent translation of key oncogenes, including IGF1R, MYC, and VEGFA.[8,85] Importantly, previous findings are consistent with ours, which reveal that FBL knockdown does not alter 28S or 18S rRNA levels by more than ∼10% (Figure S3D).[86] Moreover, cells can tolerate substantial reductions in FBL levels (>60%) without compromising ribosome production or viability.[6,9,87] Furthermore, this is consistent with our data, which indicate that when the p53-p21 axis is disabled, FBL depletion does not significantly affect cell viability (Figure S3B). Furthermore, SUnSET assays did not reveal any change in the global protein synthesis rates upon FBL depletion.

Limitations of the study

The molecular mechanisms by which FBL regulates nucleolar retention of EZH2 and the temporal control of its redistribution to the nucleoplasm are incompletely understood and require

detailed investigation across cancers. Mechanistically, it is crucial to map the epigenomic consequences of EZH2 relocalization to determine its direct and indirect targets and, consequently, the pathways altered upon FBL loss. Complementary to chromatin mapping, focused studies of membrane trafficking are essential to determine the underlying mechanisms by which E-cadherin internalizes but fails to recycle back to the cell membrane, impacting epithelial integrity. Furthermore, the study of tumorigenesis and metastasis needs to be expanded to additional paradigms of cancer progression employing iRFP-labeled[88] cells for *in vivo* imaging for a more comprehensive understanding of the role of FBL in metastasis. Since FBL is involved in rRNA synthesis, the finding that 45S pre-rRNA decreases while mature 18S and 28S levels remain stable implies compensatory homeostasis, which can potentially modulate cell polarity proteins. Consistent with the role of FBL in rRNA methylation, RiboMethSeq[89] would be a useful approach to profile rRNA methylation, and ribosome profiling could elucidate downstream consequences on translation to uncover the effect of modulating nucleolar proteins such as FBL in cancers. Collectively, these studies aim to address the underlying mechanisms by which FBL constrains epithelial plasticity and metastatic progression.

RESOURCE AVAILABILITY

Lead contact

Further information and requests for resources and reagents should be directed to and will be fulfilled by the lead contact, Prof. Kundan Sengupta (kunsen@iiserpune.ac.in).

Materials availability

All unique/stable reagents generated in this study are available from the lead contact without restriction.

Data and code availability

- RNA-seq data have been deposited at the GEO database with accession ID: GSE289801.
- This paper does not report any original code.

ACKNOWLEDGMENTS

The authors gratefully acknowledge the Microscopy and FACS facilities and especially Krishnaveni, National Facility for Gene Function in Health and Disease at IISER Pune, for her constant support and technical assistance with the animal experiments. We acknowledge Ayantika Sengupta for her pioneering work on FBL depletion and its role in enhancing cell migration, which laid the foundation for this study and was an integral part of her doctoral thesis. We thank the RNA-sequencing facility of the National Center for Biological Sciences (NCBS), Bangalore, for providing sequencing services. We acknowledge Richa Rikhy, Biology, IISER Pune, and the Biology department for reagents and useful discussions. We thank Jomon Joseph (NCCS, Pune) and Nagaraj Balasubramaniam (IISER, Pune) for reagents. Most illustrations were created using BioRender.com. We gratefully acknowledge funding support from ANRF, Department of Science and Technology (DST), Science and Engineering Research Board (SERB; grant no. CRG/2020/002563), Ministry of Education (grant no. MoE-STARS/STARS-2/2023-0603), Department of Biotechnology (DBT) MedDevice (grant no. BT/PR49745/MED/32/925/2023), Department of Biotechnology (BT/PR52973/MED/30/2535/2024), Intermediate Fellowship of the Wellcome Trust-DBT India Alliance (grant no. 500164/Z/09/Z), and intramural funding from IISER-Pune.

AUTHOR CONTRIBUTIONS

Conceptualization, S.S. and K.S.; experimental design, S.S. and K.S.; performance of experiments, S.S., A.K.B., and S.M.; data analysis, S.S. and A.K.B.; writing – original draft preparation, S.S.; writing – review and editing, S.S., K.S., A.K.B., and D.N.; visualization, S.S.; supervision, K.S.; project administration, K.S.; funding acquisition, K.S. All authors have read and agreed to the published version of the manuscript.

DECLARATION OF INTERESTS

The authors declare no competing interests.

DECLARATION OF GENERATIVE AI AND AI-ASSISTED TECHNOLOGIES IN THE WRITING PROCESS

During the preparation of this work, the author(s) used some portions of the language editing and initial drafting by OpenAI's ChatGPT. All content was subsequently reviewed and verified by the authors. After using this tool/service, the author(s) reviewed and edited the content as needed and take(s) full responsibility for the content of the published article.

STAR★METHODS

Detailed methods are provided in the online version of this paper and include the following:

- KEY RESOURCES TABLE
- EXPERIMENTAL MODELS AND STUDY PARTICIPANT DETAILS
  - Mice
  - Cell lines
- METHOD DETAILS
  - Cell culture and treatment
  - Generation of constructs
  - siRNA-mediated knockdown
  - Generation and transduction of viral particles
  - RNA sequencing
  - ChIP PCR
  - Chromatin fragmentation
  - Immunoprecipitation
  - Reverse crosslinking and DNA purification
  - PCR amplification and analysis
  - BioID2 ChIP PCR
  - Immunofluorescence assay
  - Western blotting
  - Cell fractionation
  - Proteinase K protection assay
  - Transferrin uptake assay
  - Scratch wound
  - Invasion assay
  - Image analysis
  - Segmentation analysis
  - Subcutaneous xenograft assay in NOD-SCID mice
  - Tail vein injection assay
  - Hematoxylin and eosin (H&E) staining of paraffin-embedded lung and tumor tissues
- QUANTIFICATION AND STATISTICAL ANALYSIS

SUPPLEMENTAL INFORMATION

Supplemental information can be found online at https://doi.org/10.1016/j.celrep.2025.116608.

Received: May 23, 2025
Revised: October 6, 2025
Accepted: November 4, 2025
Published: November 25, 2025

REFERENCES

1. Incarnato, D., Anselmi, F., Morandi, E., Neri, F., Maldotti, M., Rapelli, S., Parlato, C., Basile, G., and Oliviero, S. (2017). High-Throughput Single-Base Resolution Mapping of RNA 2′-O-Methylated Residues. Nucleic Acids Res. *45*, 1433–1441. https://doi.org/10.1093/nar/gkw810.
2. Tollervey, D., Lehtonen, H., Carmo-Fonseca, M., and Hurt, E.C. (1991). The Small Nucleolar RNP Protein NOP1 (Fibrillarin) Is Required for Pre-rRNA Processing in Yeast. EMBO J. *10*, 573–583. https://doi.org/10.1002/j.1460-2075.1991.tb07984.x.
3. Watkins, N.J., and Bohnsack, M.T. (2012). The Box C/D and H/ACA snoRNPs: Key Players in the Modification, Processing and the Dynamic Folding of Ribosomal RNA. Wiley Interdiscip. Rev. RNA *3*, 397–414. https://doi.org/10.1002/wrna.117.
4. Kiss-László, Z., Henry, Y., Bachellerie, J.P., Caizergues-Ferrer, M., and Kiss, T. (1996). Site-Specific Ribose Methylation of Preribosomal RNA: A Novel Function for Small Nucleolar RNAs. Cell *85*, 1077–1088. https://doi.org/10.1016/s0092-8674(00)81308-2.
5. Sharma, S., Marchand, V., Motorin, Y., and Lafontaine, D.L.J. (2017). Identification of Sites of 2'-O-Methylation Vulnerability in Human Ribosomal RNAs by Systematic Mapping. Sci. Rep. *7*, 11490. https://doi.org/10.1038/s41598-017-09734-9.
6. Iyer-Bierhoff, A., Krogh, N., Tessarz, P., Ruppert, T., Nielsen, H., and Grummt, I. (2018). SIRT7-Dependent Deacetylation of Fibrillarin Controls Histone H2A Methylation and rRNA Synthesis during the Cell Cycle. Cell Rep. *25*, 2946–2954.e5. https://doi.org/10.1016/j.celrep.2018.11.051.
7. Elliott, B.A., Ho, H.-T., Ranganathan, S.V., Vangaveti, S., Ilkayeva, O., Abou Assi, H., Choi, A.K., Agris, P.F., and Holley, C.L. (2019). Modification of Messenger RNA by 2'-O-Methylation Regulates Gene Expression in Vivo. Nat. Commun. *10*, 3401. https://doi.org/10.1038/s41467-019-11375-7.
8. Marcel, V., Ghayad, S.E., Belin, S., Therizols, G., Morel, A.-P., Solano-Gonzàlez, E., Vendrell, J.A., Hacot, S., Mertani, H.C., Albaret, M.A., et al. (2013). P53 Acts as a Safeguard of Translational Control by Regulating Fibrillarin and rRNA Methylation in Cancer. Cancer Cell *24*, 318–330. https://doi.org/10.1016/j.ccr.2013.08.013.
9. Sun, X., Gao, C., Xu, X., Li, M., Zhao, X., Wang, Y., Wang, Y., Zhang, S., Yan, Z., Liu, X., and Wu, C. (2023). FBL Promotes Cancer Cell Resistance to DNA Damage and BRCA1 Transcription via YBX1. EMBO Rep. *24*, e56230. https://doi.org/10.15252/embr.202256230.
10. Zhi, Y., Guo, Y., Li, S., He, X., Wei, H., Laster, K., Wu, Q., Zhao, D., Xie, J., Ruan, S., et al. (2025). FBL Promotes Hepatocellular Carcinoma Tumorigenesis and Progression by Recruiting YY1 to Enhance CAD Gene Expression. Cell Death Dis. *16*, 348. https://doi.org/10.1038/s41419-025-07684-z.
11. Nguyen Van Long, F., Lardy-Cleaud, A., Carène, D., Rossoni, C., Catez, F., Rollet, P., Pion, N., Monchiet, D., Dolbeau, A., Martin, M., et al. (2022). Low Level of Fibrillarin, a Ribosome Biogenesis Factor, Is a New Independent Marker of Poor Outcome in Breast Cancer. BMC Cancer *22*, 526. https://doi.org/10.1186/s12885-022-09552-x.
12. Takeichi, M. (1991). Cadherin Cell Adhesion Receptors as a Morphogenetic Regulator. Science *251*, 1451–1455. https://doi.org/10.1126/science.2006419.
13. Zaidel-Bar, R. (2013). Cadherin Adhesome at a Glance. J. Cell Sci. *126*, 373–378. https://doi.org/10.1242/jcs.111559.
14. van Roy, F., and Berx, G. (2008). The Cell-Cell Adhesion Molecule E-Cadherin. Cell. Mol. Life Sci. *65*, 3756–3788. https://doi.org/10.1007/s00018-008-8281-1.
15. Lamouille, S., Xu, J., and Derynck, R. (2014). Molecular Mechanisms of Epithelial-Mesenchymal Transition. Nat. Rev. Mol. Cell Biol. *15*, 178–196. https://doi.org/10.1038/nrm3758.
16. Bilder, D., Li, M., and Perrimon, N. (2000). Cooperative Regulation of Cell Polarity and Growth by Drosophila Tumor Suppressors. Science *289*, 113–116. https://doi.org/10.1126/science.289.5476.113.
17. Humbert, P., Russell, S., and Richardson, H. (2003). Scribble and Lgl in Cell Polarity, Cell Proliferation and Cancer. Bioessays *25*, 542–553. https://doi.org/10.1002/bies.10286.
18. Zihni, C., Mills, C., Matter, K., and Balda, M.S. (2016). Tight Junctions: From Simple Barriers to Multifunctional Molecular Gates. Nat. Rev. Mol. Cell Biol. *17*, 564–580. https://doi.org/10.1038/nrm.2016.80.
19. Burute, M., Prioux, M., Blin, G., Truchet, S., Letort, G., Tseng, Q., Bessy, T., Lowell, S., Young, J., Filhol, O., and Théry, M. (2017). Polarity Reversal by Centrosome Repositioning Primes Cell Scattering during Epithelial-to-Mesenchymal Transition. Dev. Cell *40*, 168–184. https://doi.org/10.1016/j.devcel.2016.12.004.
20. Yao, R.-W., Xu, G., Wang, Y., Shan, L., Luan, P.-F., Wang, Y., Wu, M., Yang, L.-Z., Xing, Y.-H., Yang, L., and Chen, L.-L. (2019). Nascent Pre-rRNA Sorting via Phase Separation Drives the Assembly of Dense Fibrillar Components in the Human Nucleolus. Mol. Cell *76*, 767–783.e11. https://doi.org/10.1016/j.molcel.2019.08.014.
21. Bursac, S., Brdovcak, M.C., Donati, G., and Volarevic, S. (2014). Activation of the Tumor Suppressor P53 upon Impairment of Ribosome Biogenesis. Biochim. Biophys. Acta *1842*, 817–830. https://doi.org/10.1016/j.bbadis.2013.08.014.
22. Castillo Duque de Estrada, N.M., Thoms, M., Flemming, D., Hammaren, H.M., Buschauer, R., Ameismeier, M., Baßler, J., Beck, M., Beckmann, R., and Hurt, E. (2023). Structure of Nascent 5S RNPs at the Crossroad between Ribosome Assembly and MDM2-P53 Pathways. Nat. Struct. Mol. Biol. *30*, 1119–1131. https://doi.org/10.1038/s41594-023-01006-7.
23. Scala, F., Brighenti, E., Govoni, M., Imbrogno, E., Fornari, F., Treré, D., Montanaro, L., and Derenzini, M. (2016). Direct Relationship between the Level of P53 Stabilization Induced by rRNA Synthesis-Inhibiting Drugs and the Cell Ribosome Biogenesis Rate. Oncogene *35*, 977–989. https://doi.org/10.1038/onc.2015.147.
24. Yang, K., Yang, J., and Yi, J. (2018). Nucleolar Stress: Hallmarks, Sensing Mechanism and Diseases. Cell Stress *2*, 125–140. https://doi.org/10.15698/cst2018.06.139.
25. Donati, G., Brighenti, E., Vici, M., Mazzini, G., Treré, D., Montanaro, L., and Derenzini, M. (2011). Selective Inhibition of rRNA Transcription Downregulates E2F-1: A New P53-Independent Mechanism Linking Cell Growth to Cell Proliferation. J. Cell Sci. *124*, 3017–3028. https://doi.org/10.1242/jcs.086074.
26. Hahn, W.C., Dessain, S.K., Brooks, M.W., King, J.E., Elenbaas, B., Sabatini, D.M., DeCaprio, J.A., and Weinberg, R.A. (2002). Enumeration of the Simian Virus 40 Early Region Elements Necessary for Human Cell Transformation. Mol. Cell Biol. *22*, 2111–2123. https://doi.org/10.1128/MCB.22.7.2111-2123.2002.
27. Shaulian, E., Zauberman, A., Ginsberg, D., and Oren, M. (1992). Identification of a Minimal Transforming Domain of P53: Negative Dominance through Abrogation of Sequence-Specific DNA Binding. Mol. Cell Biol. *12*, 5581–5592. https://doi.org/10.1128/mcb.12.12.5581-5592.1992.
28. Lock, J.G., and Stow, J.L. (2005). Rab11 in Recycling Endosomes Regulates the Sorting and Basolateral Transport of E-Cadherin. Mol. Biol. Cell *16*, 1744–1755. https://doi.org/10.1091/mbc.E04-10-0867.
29. Mu, F.T., Callaghan, J.M., Steele-Mortimer, O., Stenmark, H., Parton, R.G., Campbell, P.L., McCluskey, J., Yeo, J.P., Tock, E.P., and Toh, B.H. (1995). EEA1, an Early Endosome-Associated Protein. EEA1 Is a Conserved Alpha-Helical Peripheral Membrane Protein Flanked by Cysteine "Fingers" and Contains a Calmodulin-Binding IQ Motif. J. Biol. Chem. *270*, 13503–13511. https://doi.org/10.1074/jbc.270.22.13503.
30. Khurana, H., Baratam, K., Bhattacharyya, S., Srivastava, A., and Pucadyil, T.J. (2023). Mechanistic Analysis of a Novel Membrane-Interacting Variable Loop in the Pleckstrin-Homology Domain Critical for Dynamin Function. Proc. Natl. Acad. Sci. USA *120*, e2215250120. https://doi.org/10.1073/pnas.2215250120.

31. Macia, E., Ehrlich, M., Massol, R., Boucrot, E., Brunner, C., and Kirchhausen, T. (2006). a Cell-Permeable Inhibitor of Dynamin. Dev. Cell *10*, 839–850. https://doi.org/10.1016/j.devcel.2006.04.002.

32. Izumi, G., Sakisaka, T., Baba, T., Tanaka, S., Morimoto, K., and Takai, Y. (2004). Endocytosis of E-Cadherin Regulated by Rac and Cdc42 Small G Proteins through IQGAP1 and Actin Filaments. J. Cell Biol. *166*, 237–248. https://doi.org/10.1083/jcb.200401078.

33. Kon, S., Tanabe, K., Watanabe, T., Sabe, H., and Satake, M. (2008). Clathrin Dependent Endocytosis of E-Cadherin Is Regulated by the Arf6GAP Isoform SMAP1. Exp. Cell Res. *314*, 1415–1428. https://doi.org/10.1016/j.yexcr.2007.11.006.

34. Le, T.L., Yap, A.S., and Stow, J.L. (1999). Recycling of E-Cadherin. J. Cell Biol. *146*, 219–232. https://doi.org/10.1083/jcb.146.1.219.

35. Tria, S., Jimison, L.H., Hama, A., Bongo, M., and Owens, R.M. (2013). Sensing of EGTA Mediated Barrier Tissue Disruption with an Organic Transistor. Biosensors (Basel) *3*, 44–57. https://doi.org/10.3390/bios3010044.

36. Lohia, M., Qin, Y., and Macara, I.G. (2012). The Scribble Polarity Protein Stabilizes E-Cadherin/P120-Catenin Binding and Blocks Retrieval of E-Cadherin to the Golgi. PLoS One *7*, e51130. https://doi.org/10.1371/journal.pone.0051130.

37. Subramanian, A., Tamayo, P., Mootha, V.K., Mukherjee, S., Ebert, B.L., Gillette, M.A., Paulovich, A., Pomeroy, S.L., Golub, T.R., Lander, E.S., and Mesirov, J.P. (2005). Gene Set Enrichment Analysis: A Knowledge-Based Approach for Interpreting Genome-Wide Expression Profiles. Proc. Natl. Acad. Sci. USA *102*, 15545–15550. https://doi.org/10.1073/pnas.0506580102.

38. Qin, Y., Capaldo, C., Gumbiner, B.M., and Macara, I.G. (2005). The Mammalian Scribble Polarity Protein Regulates Epithelial Cell Adhesion and Migration through E-Cadherin. J. Cell Biol. *171*, 1061–1071. https://doi.org/10.1083/jcb.200506094.

39. Oki, S., Ohta, T., Shioi, G., Hatanaka, H., Ogasawara, O., Okuda, Y., Kawaji, H., Nakaki, R., Sese, J., and Meno, C. (2018). ChIP-Atlas: A Data-Mining Suite Powered by Full Integration of Public ChIP-Seq Data. EMBO Rep. *19*, e46255. https://doi.org/10.15252/embr.201846255.

40. Sharma, V., Malgulwar, P.B., Purkait, S., Patil, V., Pathak, P., Agrawal, R., Kulshreshtha, R., Mallick, S., Julka, P.K., Suri, A., et al. (2017). Genome-Wide ChIP-Seq Analysis of EZH2-Mediated H3K27me3 Target Gene Profile Highlights Differences between Low- and High-Grade Astrocytic Tumors. Carcinogenesis *38*, 152–161. https://doi.org/10.1093/carcin/bgw126.

41. McCabe, M.T., Ott, H.M., Ganji, G., Korenchuk, S., Thompson, C., Van Aller, G.S., Liu, Y., Graves, A.P., Della Pietra, A., Diaz, E., et al. (2012). EZH2 Inhibition as a Therapeutic Strategy for Lymphoma with EZH2-Activating Mutations. Nature *492*, 108–112. https://doi.org/10.1038/nature11606.

42. Yi, Y., Li, Y., Meng, Q., Li, Q., Li, F., Lu, B., Shen, J., Fazli, L., Zhao, D., Li, C., et al. (2021). A PRC2-Independent Function for EZH2 in Regulating rRNA 2'-O Methylation and IRES-Dependent Translation. Nat. Cell Biol. *23*, 341–354. https://doi.org/10.1038/s41556-021-00653-6.

43. Cao, R., Wang, L., Wang, H., Xia, L., Erdjument-Bromage, H., Tempst, P., Jones, R.S., and Zhang, Y. (2002). Role of Histone H3 Lysine 27 Methylation in Polycomb-Group Silencing. Science *298*, 1039–1043. https://doi.org/10.1126/science.1076997.

44. Kuzmichev, A., Nishioka, K., Erdjument-Bromage, H., Tempst, P., and Reinberg, D. (2002). Histone Methyltransferase Activity Associated with a Human Multiprotein Complex Containing the Enhancer of Zeste Protein. Genes Dev. *16*, 2893–2905. https://doi.org/10.1101/gad.1035902.

45. Pasini, D., Bracken, A.P., Jensen, M.R., Lazzerini Denchi, E., and Helin, K. (2004). Suz12 Is Essential for Mouse Development and for EZH2 Histone Methyltransferase Activity. EMBO J. *23*, 4061–4071. https://doi.org/10.1038/sj.emboj.7600402.

46. Kim, D.I., Jensen, S.C., Noble, K.A., Kc, B., Roux, K.H., Motamedchaboki, K., and Roux, K.J. (2016). An Improved Smaller Biotin Ligase for BioID Proximity Labeling. Mol. Biol. Cell *27*, 1188–1196. https://doi.org/10.1091/mbc.E15-12-0844.

47. Cordenonsi, M., Zanconato, F., Azzolin, L., Forcato, M., Rosato, A., Frasson, C., Inui, M., Montagner, M., Parenti, A.R., Poletti, A., et al. (2011). The Hippo Transducer TAZ Confers Cancer Stem Cell-Related Traits on Breast Cancer Cells. Cell *147*, 759–772. https://doi.org/10.1016/j.cell.2011.09.048.

48. Lei, Q.-Y., Zhang, H., Zhao, B., Zha, Z.-Y., Bai, F., Pei, X.-H., Zhao, S., Xiong, Y., and Guan, K.-L. (2008). TAZ Promotes Cell Proliferation and Epithelial-Mesenchymal Transition and Is Inhibited by the Hippo Pathway. Mol. Cell Biol. *28*, 2426–2436. https://doi.org/10.1128/MCB.01874-07.

49. Li, X., Yang, H., Liu, J., Schmidt, M.D., and Gao, T. (2011). Scribble-Mediated Membrane Targeting of PHLPP1 Is Required for Its Negative Regulation of Akt. EMBO Rep. *12*, 818–824. https://doi.org/10.1038/embor.2011.106.

50. Cha, T.-L., Zhou, B.P., Xia, W., Wu, Y., Yang, C.-C., Chen, C.-T., Ping, B., Otte, A.P., and Hung, M.-C. (2005). Akt-Mediated Phosphorylation of EZH2 Suppresses Methylation of Lysine 27 in Histone H3. Science *310*, 306–310. https://doi.org/10.1126/science.1118947.

51. Batlle, E., Sancho, E., Francí, C., Domínguez, D., Monfar, M., Baulida, J., and García De Herreros, A. (2000). The Transcription Factor Snail Is a Repressor of E-Cadherin Gene Expression in Epithelial Tumour Cells. Nat. Cell Biol. *2*, 84–89. https://doi.org/10.1038/35000034.

52. Sánchez-Tilló, E., Lázaro, A., Torrent, R., Cuatrecasas, M., Vaquero, E.C., Castells, A., Engel, P., and Postigo, A. (2010). ZEB1 Represses E-Cadherin and Induces an EMT by Recruiting the SWI/SNF Chromatin-Remodeling Protein BRG1. Oncogene *29*, 3490–3500. https://doi.org/10.1038/onc.2010.102.

53. Rhodes, N., Heerding, D.A., Duckett, D.R., Eberwein, D.J., Knick, V.B., Lansing, T.J., McConnell, R.T., Gilmer, T.M., Zhang, S.-Y., Robell, K., et al. (2008). Characterization of an Akt Kinase Inhibitor with Potent Pharmacodynamic and Antitumor Activity. Cancer Res. *68*, 2366–2374. https://doi.org/10.1158/0008-5472.CAN-07-5783.

54. Kato, H., Semba, S., Miskad, U.A., Seo, Y., Kasuga, M., and Yokozaki, H. (2004). High Expression of PRL-3 Promotes Cancer Cell Motility and Liver Metastasis in Human Colorectal Cancer: A Predictive Molecular Marker of Metachronous Liver and Lung Metastases. Clin. Cancer Res. *10*, 7318–7328. https://doi.org/10.1158/1078-0432.CCR-04-0485.

55. Kallay, L.M., McNickle, A., Brennwald, P.J., Hubbard, A.L., and Braiterman, L.T. (2006). Scribble Associates with Two Polarity Proteins, Lgl2 and Vangl2, via Distinct Molecular Domains. J. Cell. Biochem. *99*, 647–664. https://doi.org/10.1002/jcb.20992.

56. Stephens, A.D., Liu, P.Z., Banigan, E.J., Almassalha, L.M., Backman, V., Adam, S.A., Goldman, R.D., and Marko, J.F. (2018). Chromatin Histone Modifications and Rigidity Affect Nuclear Morphology Independent of Lamins. Mol. Biol. Cell *29*, 220–233. https://doi.org/10.1091/mbc.E17-06-0410.

57. Jia, Y., Vong, J.S.-L., Asafova, A., Garvalov, B.K., Caputo, L., Cordero, J., Singh, A., Boettger, T., Günther, S., Fink, L., et al. (2019). Lamin B1 Loss Promotes Lung Cancer Development and Metastasis by Epigenetic Derepression of RET. J. Exp. Med. *216*, 1377–1395. https://doi.org/10.1084/jem.20181394.

58. Zuo, L., Zhao, H., Yang, R., Wang, L., Ma, H., Xu, X., Zhou, P., and Kong, L. (2018). Lamin A/C Might Be Involved in the EMT Signalling Pathway. Gene *663*, 51–64. https://doi.org/10.1016/j.gene.2018.04.040.

59. Amin, M.A., Matsunaga, S., Ma, N., Takata, H., Yokoyama, M., Uchiyama, S., and Fukui, K. (2007). a Nucleolar Protein, Is Required for Normal Nuclear Morphology and Cellular Growth in HeLa Cells. Biochem. Biophys. Res. Commun. *360*, 320–326. https://doi.org/10.1016/j.bbrc.2007.06.092.

60. Uzer, G., Rubin, C.T., and Rubin, J. (2016). Cell Mechanosensitivity Is Enabled by the LINC Nuclear Complex. Curr. Mol. Biol. Rep. *2*, 36–47. https://doi.org/10.1007/s40610-016-0032-8.

61. Schmidt, E.K., Clavarino, G., Ceppi, M., and Pierre, P. (2009). SUnSET, a Nonradioactive Method to Monitor Protein Synthesis. Nat. Methods *6*, 275–277. https://doi.org/10.1038/nmeth.1314.

62. Feigin, M.E., Akshinthala, S.D., Araki, K., Rosenberg, A.Z., Muthuswamy, L.B., Martin, B., Lehmann, B.D., Berman, H.K., Pietenpol, J.A., Cardiff, R.D., and Muthuswamy, S.K. (2014). Mislocalization of the Cell Polarity Protein Scribble Promotes Mammary Tumorigenesis and Is Associated with Basal Breast Cancer. Cancer Res. *74*, 3180–3194. https://doi.org/10.1158/0008-5472.CAN-13-3415.

63. Khuntia, P., Rawal, S., Marwaha, R., and Das, T. (2022). Actin-Driven Golgi Apparatus Dispersal during Collective Migration of Epithelial Cells. Proc. Natl. Acad. Sci. USA *119*, e2204808119. https://doi.org/10.1073/pnas.2204808119.

64. Liu, J., Li, J., Li, P., Wang, Y., Liang, Z., Jiang, Y., Li, J., Feng, C., Wang, R., Chen, H., et al. (2017). Loss of DLG5 Promotes Breast Cancer Malignancy by Inhibiting the Hippo Signaling Pathway. Sci. Rep. *7*, 42125. https://doi.org/10.1038/srep42125.

65. Nanes, B.A., Chiasson-MacKenzie, C., Lowery, A.M., Ishiyama, N., Faundez, V., Ikura, M., Vincent, P.A., and Kowalczyk, A.P. (2012). P120-Catenin Binding Masks an Endocytic Signal Conserved in Classical Cadherins. J. Cell Biol. *199*, 365–380. https://doi.org/10.1083/jcb.201205029.

66. Schiano Lomoriello, I., Giangreco, G., Iavarone, C., Tordonato, C., Caldieri, G., Serio, G., Confalonieri, S., Freddi, S., Bianchi, F., Pirroni, S., et al. (2020). A Self-Sustaining Endocytic-Based Loop Promotes Breast Cancer Plasticity Leading to Aggressiveness and pro-Metastatic Behavior. Nat. Commun. *11*, 3020. https://doi.org/10.1038/s41467-020-16836-y.

67. Nagaoka, T., Inutsuka, A., Begum, K., Bin hafiz, K.M., and Kishi, M. (2014). Vangl2 Regulates E-Cadherin in Epithelial Cells. Sci. Rep. *4*, 6940. https://doi.org/10.1038/srep06940.

68. Chen, H.-R., Yeh, Y.-C., Liu, C.-Y., Wu, Y.-T., Lo, F.-Y., Tang, M.-J., and Wang, Y.-K. (2016). DDR1 Promotes E-Cadherin Stability via Inhibition of Integrin-\beta1-Src Activation-Mediated E-Cadherin Endocytosis. Sci. Rep. *6*, 36336. https://doi.org/10.1038/srep36336.

69. Antonysamy, S., Condon, B., Druzina, Z., Bonanno, J.B., Gheyi, T., Zhang, F., MacEwan, I., Zhang, A., Ashok, S., Rodgers, L., et al. (2013). Structural Context of Disease-Associated Mutations and Putative Mechanism of Autoinhibition Revealed by X-Ray Crystallographic Analysis of the EZH2-SET Domain. PLoS One *8*, e84147. https://doi.org/10.1371/journal.pone.0084147.

70. Alford, S.H., Toy, K., Merajver, S.D., and Kleer, C.G. (2012). Increased Risk for Distant Metastasis in Patients with Familial Early-Stage Breast Cancer and High EZH2 Expression. Breast Cancer Res. Treat. *132*, 429–437. https://doi.org/10.1007/s10549-011-1591-2.

71. Bachmann, I.M., Halvorsen, O.J., Collett, K., Stefansson, I.M., Straume, O., Haukaas, S.A., Salvesen, H.B., Otte, A.P., and Akslen, L.A. (2006). EZH2 Expression Is Associated with High Proliferation Rate and Aggressive Tumor Subgroups in Cutaneous Melanoma and Cancers of the Endometrium, Prostate, and Breast. J. Clin. Oncol. *24*, 268–273. https://doi.org/10.1200/JCO.2005.01.5180.

72. Zingg, D., Debbache, J., Schaefer, S.M., Tuncer, E., Frommel, S.C., Cheng, P., Arenas-Ramirez, N., Haeusel, J., Zhang, Y., Bonalli, M., et al. (2015). The Epigenetic Modifier EZH2 Controls Melanoma Growth and Metastasis through Silencing of Distinct Tumour Suppressors. Nat. Commun. *6*, 6051. https://doi.org/10.1038/ncomms7051.

73. Rao, Z.-Y., Cai, M.-Y., Yang, G.-F., He, L.-R., Mai, S.-J., Hua, W.-F., Liao, Y.-J., Deng, H.-X., Chen, Y.-C., Guan, X.-Y., et al. (2010). EZH2 Supports Ovarian Carcinoma Cell Invasion and/or Metastasis via Regulation of TGF-B1 and Is a Predictor of Outcome in Ovarian Carcinoma Patients. Carcinogenesis *31*, 1576–1583. https://doi.org/10.1093/carcin/bgq150.

74. Olmeda, D., Moreno-Bueno, G., Flores, J.M., Fabra, A., Portillo, F., and Cano, A. (2007). SNAI1 Is Required for Tumor Growth and Lymph Node Metastasis of Human Breast Carcinoma MDA-MB-231 Cells. Cancer Res. *67*, 11721–11731. https://doi.org/10.1158/0008-5472.CAN-07-2318.

75. Jarome, T.J., Perez, G.A., Hauser, R.M., Hatch, K.M., and Lubin, F.D. (2018). EZH2 Methyltransferase Activity Controls Pten Expression and mTOR Signaling during Fear Memory Reconsolidation. J. Neurosci. *38*, 7635–7648. https://doi.org/10.1523/JNEUROSCI.0538-18.2018.

76. Gan, L., Xu, M., Hua, R., Tan, C., Zhang, J., Gong, Y., Wu, Z., Weng, W., Sheng, W., and Guo, W. (2018). The Polycomb Group Protein EZH2 Induces Epithelial–Mesenchymal Transition and Pluripotent Phenotype of Gastric Cancer Cells by Binding to PTEN Promoter. J. Hematol. Oncol. *11*, 9. https://doi.org/10.1186/s13045-017-0547-3.

77. Sun, H., Lesche, R., Li, D.M., Liliental, J., Zhang, H., Gao, J., Gavrilova, N., Mueller, B., Liu, X., and Wu, H. (1999). PTEN Modulates Cell Cycle Progression and Cell Survival by Regulating Phosphatidylinositol 3,4,5,-Trisphosphate and Akt/Protein Kinase B Signaling Pathway. Proc. Natl. Acad. Sci. USA *96*, 6199–6204. https://doi.org/10.1073/pnas.96.11.6199.

78. Nguyen, L.X.T., and Mitchell, B.S. (2013). Akt Activation Enhances Ribosomal RNA Synthesis through Casein Kinase II and TIF-IA. Proc. Natl. Acad. Sci. USA *110*, 20681–20686. https://doi.org/10.1073/pnas.1313097110.

79. Béguelin, W., Teater, M.R., Meydan, C., Phillip, J.M., and Melnick, A. (2019). EZH2 Gain-of-Function Mutations Generate a Lymphoma-Permissive Immune Niche. Blood *134*, 2768. https://doi.org/10.1182/blood-2019-132263.

80. Majer, C.R., Jin, L., Scott, M.P., Knutson, S.K., Kuntz, K.W., Keilhack, H., Smith, J.J., Moyer, M.P., Richon, V.M., Copeland, R.A., and Wigle, T.J. (2012). A687V EZH2 Is a Gain-of-Function Mutation Found in Lymphoma Patients. FEBS Lett. *586*, 3448–3451. https://doi.org/10.1016/j.febslet.2012.07.066.

81. Chu, L., Tan, D., Zhu, M., Qu, Y., Ma, X., Song, B.-L., and Qi, W. (2023). EZH2 W113C Is a Gain-of-Function Mutation in B-Cell Lymphoma Enabling Both PRC2 Methyltransferase Activation and Tazemetostat Resistance. J. Biol. Chem. *299*, 103073. https://doi.org/10.1016/j.jbc.2023.103073.

82. Deshaies, R.J., and Potts, P.R. (2025). Load and Lock: An Emerging Class of Therapeutics That Influence Macromolecular Dissociation. Science *389*, eadx3595. https://doi.org/10.1126/science.adx3595.

83. Madani, F., Lindberg, S., Langel, U., Futaki, S., and Gräslund, A. (2011). Mechanisms of Cellular Uptake of Cell-Penetrating Peptides. J. Biophys. *2011*, 414729. https://doi.org/10.1155/2011/414729.

84. Rezai, T., Yu, B., Millhauser, G.L., Jacobson, M.P., and Lokey, R.S. (2006). Testing the Conformational Hypothesis of Passive Membrane Permeability Using Synthetic Cyclic Peptide Diastereomers. J. Am. Chem. Soc. *128*, 2510–2511. https://doi.org/10.1021/ja0563455.

85. Erales, J., Marchand, V., Panthu, B., Gillot, S., Belin, S., Ghayad, S.E., Garcia, M., Laforêts, F., Marcel, V., Baudin-Baillieu, A., et al. (2017). Evidence for rRNA 2'-O-Methylation Plasticity: Control of Intrinsic Translational Capabilities of Human Ribosomes. Proc. Natl. Acad. Sci. USA *114*, 12934–12939. https://doi.org/10.1073/pnas.1707674114.

86. Ren, X., Hu, B., Song, M., Ding, Z., Dang, Y., Liu, Z., Zhang, W., Ji, Q., Ren, R., Ding, J., et al. (2019). Maintenance of Nucleolar Homeostasis by CBX4 Alleviates Senescence and Osteoarthritis. Cell Rep. *26*, 3643–3656.e7. https://doi.org/10.1016/j.celrep.2019.02.088.

87. Tessarz, P., Santos-Rosa, H., Robson, S.C., Sylvestersen, K.B., Nelson, C.J., Nielsen, M.L., and Kouzarides, T. (2014). Glutamine Methylation in Histone H2A Is an RNA-Polymerase-I-Dedicated Modification. Nature *505*, 564–568. https://doi.org/10.1038/nature12819.

88. Honda, M., Yogosawa, S., Kamada, M., Kamata, Y., Kimura, T., Koike, Y., Harada, T., Takahashi, H., Egawa, S., and Yoshida, K. (2017). A Novel Near-Infrared Fluorescent Protein, iRFP720, Facilitates Transcriptional Profiling of Prostate Cancer Bone Metastasis in Mice. Anticancer Res. *37*, 3009–3013.

89. Marchand, V., Blanloeil-Oillo, F., Helm, M., and Motorin, Y. (2016). Illumina-Based RiboMethSeq Approach for Mapping of 2'-O-Me Residues in RNA. Nucleic Acids Res. *44*, e135. https://doi.org/10.1093/nar/gkw547.

90. Jacobus, A.P., and Gross, J. (2015). Optimal Cloning of PCR Fragments by Homologous Recombination in Escherichia Coli. PLoS One *10*, e0119221. https://doi.org/10.1371/journal.pone.0119221.

91. Gerard, G.F., Collins, S., and Smith, M.D. (2002). Excess dNTPs Minimize RNA Hydrolysis during Reverse Transcription. Biotechniques *33*, 984–990. https://doi.org/10.2144/02335bm03.

92. Tang, D., Chen, M., Huang, X., Zhang, G., Zeng, L., Zhang, G., Wu, S., and Wang, Y. (2023). A Free Online Platform for Data Visualization and Graphing. PLoS One *18*, e0294236. https://doi.org/10.1371/journal.pone.0294236.

93. Ge, S.X., Jung, D., and Yao, R. (2020). A Graphical Gene-Set Enrichment Tool for Animals and Plants. Bioinformatics *36*, 2628–2629. https://doi.org/10.1093/bioinformatics/btz931.

94. Suzuki, K., Bose, P., Leong-Quong, R.Y., Fujita, D.J., and Riabowol, K. (2010). A Two Minute Cell Fractionation Method. BMC Res. Notes *3*, 294. https://doi.org/10.1186/1756-0500-3-294.

95. Liang, Y.M., Wang, X., Ramalingam, R., So, K.Y., Lam, Y.W., and Li, Z.F. (2012). Novel Nucleolar Isolation Method Reveals Rapid Response of Human Nucleolar Proteomes to Serum Stimulation. J. Proteomics *77*, 521–530. https://doi.org/10.1016/j.jprot.2012.09.031.

96. Sen Gupta, A., and Sengupta, K. (2017). Lamin B2 Modulates Nucleolar Morphology, Dynamics, and Function. Mol. Cell Biol. *37*, e00274-17. https://doi.org/10.1128/MCB.00274-17.

97. Ozawa, M., Hoschützky, H., Herrenknecht, K., and Kemler, R. (1990). A Possible New Adhesive Site in the Cell-Adhesion Molecule Uvomorulin. Mech. Dev. *33*, 49–56. https://doi.org/10.1016/0925-4773(90)90134-8.

STAR★METHODS

KEY RESOURCES TABLE

REAGENT or RESOURCE	SOURCE	IDENTIFIER
Antibodies		
Mouse monoclonal anti-FBL(IB, IFA)	Abcam	Cat#ab4566; RRID:AB_304523
Rabbit polyclonal anti-FBL (IB, IFA)	Abcam	Cat#ab5821; RRID:AB_2105785
Rabbit monoclonal anti-E-cadherin(IB)	Cell Signaling Technology	E-Cadherin (24E10) Rabbit mAb Cat#3195; RRID:AB_2291471
Mouse monoclonal anti-E-cadherin(IB, IFA)	Abcam	Cat#ab1614(HECD-1); RRID:AB_300946
Mouse monoclonal anti-E-cadherin(IB, IFA)	Abcam	Cat#ab11512 (DECMA-1); RRID:AB_298118
Rabbit polyclonal Anti-ZO-1(IFA)	Abcam	Cat#ab59724, RRID:AB_946249
Mouse monoclonal anti-GM130 (IFA)	BD Biosciences	Cat#35/GM130; RRID:AB_398141
Mouse monoclonal anti-Scribble(IB)	SantaCruz	Cat#sc-55543; RRID:AB_2238926
Rabbit monoclonal anti-Scribble(IB, IFA)	Cell Signaling Technology	Scribble Antibody #4475
Mouse monoclonal anti-HSP70(IB)	Abcam	Cat#ab47455; RRID:AB_881520
Mouse monoclonal anti-GAPDH(IB)	SantaCruz	Cat#sc-32233; RRID:AB_627679
Rabbit polyclonal anti-GAPDH(IB)	Merck	Cat#G9545; RRID:AB_796208
Rat monoclonal anti-Beta-tubulin(IB)	Abcam	Cat#[YOL1/34](ab6161); RRID:AB_305329
Mouse monoclonal anti-Beta-tubulin(IB)	DHSB	Cat#E7; RRID:AB_528499
Rabbit polyclonal anti-H3K27me3(IB, IFA)	Merck	Cat#07-449, RRID:AB_310624
Rabbit polyclonal anti-H3(IB)	Abcam	Cat#ab1719; RRID:AB_302613
Rabbit monoclonal anti-EZH2(IB, IFA)	Cell Signaling Technology	Ezh2 (D2C9) XP® Rabbit mAb Cat#5246; RRID:AB_10694683
Rabbit polyclonal anti-EZH2(IB)	Merck	Cat#07-1562
Rabbit polyclonal anti-Zeb1(IB)	Abcam	Cat#ab203829; RRID:AB_2921369
Rabbit polyclonal anti-Vimentin(IB)	Abcam	Cat#ab92547 [EPR3776]; RRID:AB_10562134
Rabbit polyclonal anti-Occludin(IB, IFA)	Abcam	Cat#ab216327 [EPR20992]; RRID:AB_2737295
Rabbit monoclonal anti-pAkt(Ser473)(IB)	Cell Signaling Technology	Cat#9271; RRID:AB_329825
Rabbit monoclonal anti-Akt(IB)	Cell Signaling Technology	Cat#9272; RRID: AB_329827
Rabbit polyclonal anti-TAZ(IB)	Abcam	Cat#ab84927; RRID: AB_1925489
Mouse monoclonal anti-Twist(IB)	Abcam	Cat#ab50887; RRID: AB_883294
Rabbit polyclonal anti-Snail(IB)	Abcam	Cat#ab85931
Rabbit monoclonal anti-Rab11(IFA)	Cell Signaling Technology	Cat#Rab11 (D4F5) XP® Rabbit mAb #5589; RRID: AB_10693925
Mouse monoclonal anti-EEA-1(IFA)	BD Biosciences	Clone 14/EEA1 (RUO); RRID: AB_397830
Mouse monoclonal anti-PTEN(IB)	BD Biosciences	Clone A2B1 (RUO); RRID: AB_1645437
Goat anti-Mouse IgG (H + L) Cross-Adsorbed Secondary Antibody, Alexa Fluor™ 488	Invitrogen	Cat#A-11029; RRID:AB_2534088
Goat anti-Mouse IgG (H + L) Cross-Adsorbed Secondary Antibody, Alexa Fluor™ 568	Invitrogen	Cat#A-11004; RRID:AB_2534072
Goat anti-Rabbit IgG (H + L) Cross-Adsorbed Secondary Antibody, Alexa Fluor™ 488	Invitrogen	Cat#A-11008; RRID: AB_143165

(*Continued on next page*)

Continued

REAGENT or RESOURCE	SOURCE	IDENTIFIER
Goat anti-Rabbit IgG (H + L) Cross-Adsorbed Secondary Antibody, Alexa Fluor™ 568	Invitrogen	Cat#A-11011; RRID: AB_143157
Peroxidase AffiniPure® Goat Anti-Mouse IgG (H + L)	Jackson ImmunoResearch	Cat#115-035-003; RRID: AB_10015289
Peroxidase AffiniPure® Goat Anti-Rabbit IgG (H + L)	Jackson ImmunoResearch	Cat#111-035-003; RRID: AB_2313567
Goat anti-rat IgG H&L (HRP)	Abcam	Cat#ab97057; RRID: AB_10680316
Bacterial and virus strains		
E.coli DH5α	Lab generated	N/A
Biological samples		
N/A	N/A	N/A
Chemicals, peptides, and recombinant proteins		
Protease inhibitor cocktail complete EDTA-free	Roche	Cat#4693132001
DynaBeads	Invitrogen	Cat#10002D
Streptavidin DynaBeads	Invitrogen	Cat#65801D
GSK-126	MedChemExpress	Cat#HY-13470
GSK-690693	MedChemExpress	Cat#HY-10249
Sodium Deoxycholate	SigmaAldrich	Cat#S1827
Nonidet P-40	SigmaAldrich	Cat#74385-1L
Tris free base	SigmaAldrich	Cat#T1503
Glycine	Thermo Fisher Scientific	Cat#Q24755
NaCl	SigmaAldrich	Cat#S7653
HEPES	SigmaAldrich	Cat#H3375
EDTA	SigmaAldrich	Cat#E9884
DTT	SigmaAldrich	Cat#D0632
Tween 20	SigmaAldrich	Cat#P9416
SDS	SigmaAldrich	Cat#L3771
BSA	SigmaAldrich	Cat#A7906
MgCl2	SigmaAldrich	Cat#M1028
DMEM-F12	Invitrogen	Cat#11330-032
EGF	Peprotech	Cat#AF-100-15
Bovine Insulin	Sigma	Cat#I-1882
Cholera toxin	Sigma	Cat#C-8052
Hydrocortisone	Sigma	Cat#H-0888
Horse Serum	Invitrogen	Cat#16050-122
Pen/Strep	Invitrogen	Cat#15070-063
RPMI-1640	Invitrogen	Cat#31800-022
Fetal Bovine Serum (Brazil oragin)	Invitrogen	Cat#10270106
Texas Red® Conjugated Human Transferrin	Invitrogen	Cat#T2875; Lot# 1848488
Critical commercial assays		
PrimeScript™ 1st strand cDNA Synthesis Kit	Takara	6110B
Deposited data		
RNA-sequencing	This paper	GEO: GSE289801
Experimental models: Cell lines		
DLD-1	ATCC	CCL-221
MCF10A	ATCC	CRL-10317

(*Continued on next page*)

Continued

REAGENT or RESOURCE	SOURCE	IDENTIFIER
MCF10A(p53DN)	This paper	N/A
A549(p53DN)	This paper	N/A
HCT116	ATCC	CCL-247
SW480	ATCC	CCL-228
HEK293T	ATCC	CRL-3216
Experimental models: Organisms/strains		
NOD-SCID male/female mice syngeneic	Animal House facility, IISER, Pune, India	N/A
Recombinant DNA		
pLKOMCS-GFP	This paper	N/A
pLKOMCS-GFP-FBL(siRes)	This paper	N/A
pLKOMCS-GFP-ΔRBD FBL(siRes)	This paper	N/A
pBabe-SCRIB-Puro	This paper	N/A
pBABE-hygro p53 DD	Addgene	Addgene #9058
Tet-pLKO-shFBL-puro	This paper	N/A
Tet-pLKO-shSCRIB-puro	This paper	N/A
MSCVhygro-F-Ezh2	Addgene	Addgene #24926
pCW57.1 F-EZH2; FBL-BioID2-HA pBabe-puro	This paper	N/A
MSCV Puro SCRIB P305L	This paper	N/A
MSCV Puro SCRIB C4S	This paper	N/A
MSCV Puro SCRIB C10S	This paper	N/A
Software and algorithms		
Graphpad prism V.8.0	N/A	https://www.graphstats.net/graphpad-prism
ImageJ	Schneider et al.	https://imagej.nih.gov/ij/
Galaxy	The Galaxy Community	https://doi.org/10.1093/nar/gkae410
T-scratch	Gebäck et al. (2018)	https://doi.org/10.2144/000113083
Imaris	N/A	RRID:SCR_007370

EXPERIMENTAL MODELS AND STUDY PARTICIPANT DETAILS

Mice

In vivo experiments were carried out using NOD-SCID syngeneic male/female mice at the Animal House Facility of IISER Pune, India, with the approval of Institutional Animal Ethics Committee (IAEC) (IISER_Pune/IAEC/2022_01/01) and all experiments conform to IAEC guidelines. Mice aged six to eight weeks were selected, and their body weights were recorded prior to injections. Each mouse received a subcutaneous injection of ∼7 million DLD-1 cells into a single flank for tumorigenesis studies. On day 35 post-injection, the tumors were excised and processed for subsequent analyses. For tumor infiltration studies each mouse was injected with ∼1 million DLD-1 cells via tail vein injection. On day 60 post-injection, lungs were excised and processed for subsequent analyses.

Cell lines

DLD-1 colorectal adenocarcinoma cells were maintained in RPMI-1640 supplemented with 10% FBS, L-glutamine, and antibiotics. MCF10A mammary epithelial cells were cultured in DMEM/F-12 with horse serum, EGF, hydrocortisone, cholera toxin, insulin, and antibiotics. HCT116, SW480, and A549 cells were grown in DMEM (Gibco, Brazil) with 10% FBS and antibiotics. All cultures were maintained at 37°C in a humidified incubator with 5% CO_2.

METHOD DETAILS

Cell culture and treatment

DLD-1 human colorectal adenocarcinoma cells were cultured in RPMI-1640 medium (Gibco) supplemented with 10% fetal bovine serum (FBS) (Invitrogen, 6140-079 Carlsbad, USA), 2 mM L-glutamine (Gibco), and 1% penicillin-streptomycin (100 U/mL penicillin and 100 μg/mL streptomycin), and maintained at 37°C in a humidified incubator with 5% CO_2. MCF10A human mammary epithelial cells were cultured in DMEM/F-12 (1:1) medium (Gibco, Thermo Fisher Scientific) supplemented with 5% horse serum

(Sigma-Aldrich), 20 ng/mL epidermal growth factor (EGF) (PeproTech), 0.5 μg/mL hydrocortisone (Sigma-Aldrich), 100 ng/mL cholera toxin (Sigma-Aldrich), 10 μg/mL insulin (Sigma-Aldrich), and 1% penicillin-streptomycin, and maintained under the same conditions. HCT116, SW480, and A549 cells were cultured in DMEM (Gibco, Brazil) supplemented with 10% FBS (Gibco, Brazil) and 1% penicillin-streptomycin, and maintained at 37°C in a humidified incubator with 5% CO_2.

Generation of constructs

FBL CDS was available in the pEGFP-C1-Fibrillarin construct (gift from Sui Huang, Northwestern University). We created an siRNA-resistant GFP-FBL by mutating the seed sequence by PCR amplifying the pEGFP-C1-Fibrillarin construct with partially overlapping mutagenic primers, as described previously.[90] The PCR reaction was subjected to *DpnI* (20 units) digestion for digesting parental plasmid, at 37°C for 3h and was transformed into *E.coli* DH5α. Subsequently the colonies were screened using Sanger sequencing.

The mutated GFP-FBL (siRes) was PCR amplified with BamHI and SalI flanking sites. The PCR reaction was incubated with *DpnI* (20 units) at 37°C for 3h. The amplicon was gel purified using commercially available kits (Qiagen) and 1μg of the purified amplicon was double-digested with *BamHI*(10U) and *SalI*(10U) overnight, at 37°C. The reaction was terminated by heat inactivation at 65°C for 20 min. Subsequently, for ligation reaction, 5μL of the double-digested amplicon was incubated with 30ng of double-digested pLKO-MCS vector (Addgene #185594) and 350U of T4 DNA Ligase, overnight at 16°C. Ultimately, 4μL of the ligation mixture was transformed into *E.coli* DH5α and the colonies were screened using colony PCR and Sanger sequencing. Similarly, FBL(WT) was cloned into MCS-BioID2-HA pBabe-puro (Addgene #120308, gift from Kyle Roux, University of South Dakota) by PCR amplifying FBL from pEGFP-C1-Fibrillarin plasmid and was cloned using BamHI and EcoRI ends. For cloning, Flag-EZH2 into pCW57.1 N-term GFP tTA (Addgene #107551), Flag-EZH2 was amplified from MSCVhygro-F-Ezh2 plasmid (Addgene #24926) with primers flanking NheI and EcoRI sites and was used for digestion and ligation as mentioned previously. Colonies were screened using colony PCR and Sanger sequencing.

SCRIB CDS was obtained from RNA purified from DLD-1. 2μg of the extracted RNA was converted to cDNA using Invitrogen SuperScript II Reverse Transcriptase. The reaction was set up by incubating the following components in a nuclease-free microcentrifuge tube: 1 μL of Oligo(dT)12–18 (500 μg/mL), along with 2μg of total RNA. Then, 2 μL of dNTP Mix (10 mM each) and sterile, distilled water were added to a final volume of 12 μL. Since SCRIB CDS is 4.8kb long, using usual cDNA synthesis protocols would yield fragmented CDS instead of a complete stretch of SCRIB CDS, therefore/We added 4mM (Final concentration) of dNTP mix, as mentioned previously.[91] The mixture was heated to 65°C for 5 min and immediately chilled on ice. After a brief centrifugation, 4 μL of 5X First-Strand Buffer, 2 μL of 0.1 M DTT, and 1 μL of RNaseOUT (40 units/μL) were added. The contents of the tube were gently mixed. The mixture was incubated at 42°C for 2 min. Following this, 1 μL (200 units) of SuperScript II RT was added and mixed gently by pipetting, and the volume was adjusted to 20 μL with Nuclease Free Water. The reaction was incubated at 42°C for the first 40 min, temperature was gradually increased to 55°C for the last 10 min, followed by inactivation through heating at 70°C for 15 min. SCRIB CDS was PCR amplified with BamHI and EcoRI site flanking primers. The amplicon was purified from the gel using commercially available Qiagen kits. Next, 3 μg of the purified amplicon was subjected to double digestion with *BamHI* (20U) and *EcoRI* (20U) overnight at 37°C. Enzyme denaturation at 65°C for 20 min was used to terminate the reaction. For the ligation step, 5 μL of the double-digested amplicon was incubated overnight at 16°C with 30 ng of double-digested pBABE (Plasmid #21836) and 350 U of T4 DNA Ligase. Finally, 4 μL of the ligation mixture was transformed into *E.coli* DH5α, and the resulting colonies were screened using colony PCR and Sanger sequencing.

shSCRIB and shFBL sequences were synthesized as oligos were cloned into Tet-pLKO-puro vector (Addgene #21915). The shRNA oligos were designed and synthesized according to the siRNA sequence. Equimolar amounts of the sense and antisense oligonucleotides were then mixed for phosphorylating the 5′ ends of the oligos, using T4 PNK (10U) in a 10 μL reaction. The reaction was incubated at 37°C for 45 min, and subsequently exposed to 95°C for 5 min, and was gradually cooled to 25°C using step-down PCR. The above reaction conditions simultaneously achieved 5′ end phosphorylation and annealing of the oligonucleotides with overhangs compatible with the restriction sites in the vector. The Tet-pLKO-puro vector was prepared by digesting it with the appropriate restriction enzymes, *AgeI* and *EcoRI*, to linearize it and generate ends compatible with the annealed shRNA insert. The annealed shRNA inserts (5 μL from the PNK reaction) were then ligated into the digested pLKO-Tet-On vector (30ng) using T4 DNA ligase (350U), with the ligation reaction incubated at 16°C overnight. The ligation mixture was subsequently introduced into *E.coli* DH5α. Individual colonies were screened using *XhoI* digestion of extracted plasmid and Sanger sequencing.

FBL(WT) was cloned into MCS-BioID2-HA pBabe-puro (Addgene #120308, gift from Kyle Roux), FBL CDS was amplified from pEGFP-C1-Fibrillarin plasmid and was cloned using BamHI and EcoRI ends. Flag-EZH2 was cloned into pCW57.1 N-term GFP tTA (Addgene #107551) after amplifying the amplicon with NheI and EcoRI ends from the MSCVhygro-F-Ezh2 plasmid (Addgene #24926).

siRNA-mediated knockdown

siRNA-mediated gene knockdown was carried out using siRNA oligonucleotides (AGGAGAACATGAAGCCGCAdTdT) obtained from Sigma and Dharmacon, USA. DLD-1 and MCF10A(p53DN) cells ($\sim 0.2 \times 10^6$) were seeded in six-well plates 24 h before transfection (till 50–60% confluency is attained). Transfection was performed using RNAiMax transfection reagent (Invitrogen, 13778) in Opti-MEM reduced serum medium (Gibco, 31985), with a final siRNA concentration of 75nM. After 6 h, the transfection medium was replaced with complete RPMI. MCF10A(p53DN) Cells were collected at 36 h and 72 h post-transfection for RNA extraction

or immunofluorescence, or western blot analysis. DLD-1 was incubated for 48- or 72-h post-transfection. siLacZ (CGUACGCGGAAUACUUCGAdTdT) was used as a negative control in RNA interference (RNAi) experiments.

Generation and transduction of viral particles

Lentiviral transduction was performed by generating lentiviral particles through the co-transfection of HEK293T cells with Lentiviral transfer plasmid constructs, along with second-generation lentiviral packaging plasmids psPAX2 (Addgene #12260) and pMD2.G (Addgene plasmid #12259), in 4:3:1 ratio, with total 20μg DNA being transfected, in a 65% confluent 100 mm dish. Seventy-two hours post-transfection, the viral supernatant was harvested, mixed with Polybrene (12 μg/mL) and used to transduce DLD-1 and MCF10A(p53DN) cells, followed by selection with Puromycin (4 μg/mL, Invitrogen, A1113802) or FACS sorting for fluorophore-tagged cells. To verify the expression of the transduced gene, RT-PCR or immunoblotting was performed. FBL and SCRIB depletion was induced with 1200 ng/mL and 1000 ng/mL Dox, respectively, for 48 h, a condition consistently applied across experiments unless specified otherwise.

Retroviral transduction was carried out by generating retroviral particles through the co-transfection of HEK293T cells with retroviral transfer plasmid constructs, in combination with second-generation lentiviral packaging plasmids pBS-CMV-gagpol (Addgene #35614) and pCAG-VSVG (Addgene #35616), in 4:3:1 ratio, with total 20μg DNA being transfected, in a 65% confluent 100mm dish. Seventy-two hours post-transfection, the viral supernatant was collected, mixed with Polybrene (10 μg/mL) and subsequently used to transduce DLD-1 and MCF10A(p53DN) cells, followed by selection with Puromycin (4 μg/mL, Invitrogen, A1113802) or Hygromycin (50 μg/mL, Invitrogen, 10687010). To confirm the expression of the transduced gene, RT-PCR or immunoblotting was performed.

RNA sequencing

DLD-1 cells (∼0.6 million) were transfected and incubated for ∼72h. Isolation of total RNA from cells was performed by using a commercially available kit (Qiagen). Library preparation was carried out using the NEBNext Ultra II Directional RNA Library Preparation Kit, following the manufacturer's instructions. Paired-end reads of 51 bp were generated on the Illumina platform. RNA-Seq data submission GEO accession number: GSE289801.

Data Analyses: Quality control and preprocessing of raw sequencing reads involved filtering based on quality scores and adapter trimming using FastQC and Trimmomatic, respectively. The processed reads were aligned to the *Homo sapiens* GRCh38 reference genome using the splice-aware aligner HISAT2 on the Galaxy platform. Transcript assembly was performed using StringTie, which also quantified read counts and normalized gene expression levels using the Fragments Per Kilobase of transcript per Million mapped reads (FPKM) metric. Differential expression analysis was conducted with DESeq2, where raw read counts served as input. Genes with a p-value below 0.05 were considered significantly differentially expressed between the control and FBL knockdown conditions in DLD-1 cells. Upregulated genes were defined as those with a $\log_2FC > 1$, while downregulated genes had a $\log_2FC < -10$.

To identify differentially regulated pathways, gene ontology and pathway enrichment analyses were performed using Gene Set Enrichment Analysis (GSEA) on the GSEA desktop application, and key enriched gene sets were visualized through enrichment plots. The Gene Ratio corresponds to the Normalized Enrichment Score (NES) obtained from GSEA. Enrichment results are presented as the NES in GSEA. A false discovery rate (FDR) threshold of 0.05 was applied to ensure the inclusion of significantly enriched gene sets. Further details on RNA sequencing analysis are provided in key resources table. The GO (Gene Ontology) analysis of enriched Cellular components, Molecular functions, and Pathway network were performed on SR Plot[92] and ShinyGO,[93] respectively, with FDR = 0.05.

ChIP PCR

Chromatin crosslinking and cell lysis

Cells were cultured to approximately 80% confluency and crosslinked with 1% formaldehyde for 10 min at room temperature to preserve protein-DNA interactions. The reaction was quenched by adding glycine to a final concentration of 0.125 M, followed by a 5-min incubation at room temperature. Cells were subsequently washed twice with ice-cold phosphate-buffered saline (PBS, pH 7.4), harvested by scraping, and collected by centrifugation at 1,000 × g for 5 min at 4°C. The supernatant was discarded, and the cell pellet was resuspended in lysis buffer supplemented with protease inhibitors and incubated on ice for 10 min to facilitate nuclear extraction.

Chromatin fragmentation

Chromatin was sheared by sonication to generate DNA fragments ranging from 200 to 1000 bp. Chromatin shearing was performed using a Covaris focused ultrasonicator. DLD-1 cell lysates were prepared in 130 μL of lysis buffer and transferred to Covaris microTUBEs. Sonication was carried out at 6°C–7°C to prevent overheating. For Covaris M220, samples were processed at 75 W peak incident power, 60% duty factor, and 200 cycles per burst for 30 min, 30 s on 30 s off. Following sonication, samples were centrifuged at 16,000g for 10 min at 4°C, and the supernatant was collected for downstream ChIP assays. Chromatin fragmentation was assessed by agarose gel electrophoresis to confirm a fragment size range of 100–500 bp, and conditions were adjusted as necessary to achieve optimal shearing efficiency.

For MCF10A(p53DN), chromatin was sheared using a Covaris M220 focused ultrasonicator. 130 μL of cell lysate was put in Covaris microTUBEs. Sonication was performed at 75 W peak incident power, 60% duty factor, and 200 cycles per burst for 25 min, 30 s on 30 s off. The sample temperature was maintained at 6°C–7°C using a chiller. Following sonication, samples were centrifuged at

16,000g for 10 min at 4°C, and the supernatant was collected for further processing. DNA fragment size (100–500 bp) was assessed by agarose gel electrophoresis. The extent of shearing was assessed by agarose gel electrophoresis.

Immunoprecipitation

Sheared chromatin was pre-cleared by incubation with protein A/G Dynabeads for 1 h at 4°C with continuous rotation to reduce nonspecific binding. The pre-cleared chromatin was then incubated overnight at 4°C with an antibody specific to the target protein - 2μg for Histones and 5μg for EZH2, while an IgG control at similar quantities to that of specific antibodies was included to assess nonspecific interactions. The following day, protein A/G Dynabeads were added to captured immune complexes, followed by an additional 1–2 h of incubation at 4°C with rotation. Immunoprecipitates were sequentially washed with low-salt wash buffer (0.1% SDS, 1% Triton X-100, 2 mM EDTA (pH 8.0), 20 mM Tris-HCl (pH 8.0), 150 mM NaCl), high-salt wash buffer (0.1% SDS, 1% Triton X-100, 2 mM EDTA (pH 8.0), 20 mM Tris-HCl (pH 8.0), 500 mM NaCl), LiCl wash buffer (0.25 M LiCl, 1% NP-40, 1% sodium deoxycholate, 1 mM EDTA (pH 8.0), 10 mM Tris-HCl (pH 8.0)), and TE buffer (pH 8.0) to eliminate nonspecific binding.

Reverse crosslinking and DNA purification

Chromatin complexes were eluted using an elution buffer containing 1% sodium dodecyl sulfate (SDS) and proteinase K (200 μg/mL), followed by incubation at 65°C for 4–6 h to reverse crosslinking. DNA was purified using phenol-chloroform extraction or a commercially available DNA purification kit (Qiagen), followed by ethanol precipitation. The resulting DNA was resuspended in nuclease-free water and stored at −20°C for subsequent analysis.

PCR amplification and analysis

Purified ChIP-derived DNA (5ng) was subjected to PCR to amplify target genomic regions using specific primer pairs. PCR reactions were performed in a total volume of 10 μL containing template DNA, 2XTB Green Taq DNA polymerase mix (Takara), and gene-specific primers (0.3μM). Thermal cycling parameters were optimized for each target sequence. PCR products were resolved by agarose gel electrophoresis, stained with a nucleic acid dye, and visualized using a gel imaging system. Input DNA, representing a fraction of total chromatin before immunoprecipitation, and IgG controls were included to confirm the enrichment specificity.

BioID2 ChIP PCR

Cells (~4 million) constitutively expressing FBL(WT)-BirA* and EV were seeded on 100mm dishes and incubated with 50μM Biotin (for at least 16h) before being treated with siLacZ (Control) and siFBL with a final concentration of 75 nM. Cells were harvested 36h after siRNA transfection and were subjected to crosslinking with 1% formaldehyde for 10 min at room temperature to preserve protein-DNA interactions. The crosslinking reaction was terminated by the addition of glycine to a final concentration of 0.125M, followed by incubation at room temperature for 5 min. Cells were subsequently washed twice with ice-cold phosphate-buffered saline (PBS, pH 7.4), detached from the culture surface by scraping, and collected by centrifugation at 1,000 × g for 5 min at 4°C. The resulting cell pellet was resuspended in lysis buffer (50 mM HEPES-KOH pH 7.5, 140 mM NaCl, 1 mM EDTA (pH 8), 1% Triton X-100, 0.1% Sodium Deoxycholate, 0.1% SDS) supplemented with protease inhibitors and incubated on ice for 10 min to facilitate nuclear extraction. To achieve chromatin fragmentation, sonication was performed under optimized conditions to generate DNA fragments within the range of 200–600 bp while maintaining protein-DNA interactions. The efficiency of chromatin shearing was assessed by agarose gel electrophoresis. Fragmented chromatin was incubated with Streptavidin Dynabeads(100μL) at 4°C overnight with continuous rotation to minimize nonspecific binding.

The Dynabeads were isolated using a magnetic stand and subjected to sequential washes. Initially, they were washed twice with a 2% (wt/vol) SDS solution. This was followed by a wash with a buffer containing 0.1% deoxycholate, 1% Triton X-100, 500 mM NaCl, 1 mM EDTA, and 50 mM 4-(2-hydroxyethyl)-1-piperazineethanesulfonic acid (HEPES) at pH 7.5. Subsequently, precipitates were subjected to sequential washes using low-salt wash buffer (0.1% SDS, 1% Triton X-100, 2 mM EDTA (pH 8.0), 20 mM Tris-HCl (pH 8.0), 150 mM NaCl), high-salt wash buffer (0.1% SDS, 1% Triton X-100, 2 mM EDTA (pH 8.0), 20 mM Tris-HCl (pH 8.0), 500 mM NaCl), LiCl wash buffer (0.25 M LiCl, 1% NP-40, 1% sodium deoxycholate, 1 mM EDTA (pH 8.0), 10 mM Tris-HCl (pH 8.0)), and TE buffer (pH 8.0) to eliminate nonspecific binding. Precipitated chromatin was eluted using a buffer containing sodium dodecyl sulfate (SDS) and proteinase K, followed by incubation at 65°C for 4–6 h to reverse protein-DNA crosslinking. DNA was then extracted using a commercial purification kit (Qiagen). The purified DNA was resuspended in nuclease-free water and stored at −20°C for subsequent analysis.

To assess target DNA enrichment, PCR amplification was performed using ChIP-derived DNA (5ng) as a template. Each PCR reaction was conducted in a final volume of 10 μL containing template DNA, 2X TB Green Taq DNA polymerase mix (Takara), and gene-specific primers (0.3μM). PCR conditions were optimized based on the target sequence requirements. Amplified products were resolved by agarose gel electrophoresis, stained with a nucleic acid dye, and visualized using an imaging system. To confirm specificity, input DNA, representing total chromatin prior to immunoprecipitation, was included as an experimental control.

Immunofluorescence assay

0.2 million cells were cultured on 22 mm × 22 mm coverslips. Cells were subjected to two washes with 1× phosphate-buffered saline (PBS) (pH 7.4) for 5 min each and then fixed using 4% paraformaldehyde (PFA) in 1× PBS (pH 7.4) or for nuclear antigens cells were

pre-permeabilized with CSK buffer (100 mM NaCl, 300 mM Sucrose, 3 mM $MgCl_2$, 10 mM PIPES(pH 7.4), 0.5% Triton X-100) for 4mins on ice prior to PFA fixation. Cells were permeabilized with 0.5% Triton X-100 in PBS for 10 min and blocked with 1% Bovine Serum Albumin (BSA) for 30 min to reduce non-specific binding. The cells were incubated with primary antibodies for 2 h, followed by incubation with secondary antibodies for 60 min. Cells were counterstained with DAPI (0.05 μg/mL solution of 4′,6-diamidino-2-phenylindole (DAPI)) for 2 min at RT, followed by washes with 1X PBS. The cells were mounted using SlowFade Gold Antifade and stored at 4°C. For imaging, Zeiss LSM 710 and Zeiss LSM 780 confocal microscopes (Carl Zeiss, Thornwood, NJ, USA) were utilized, both equipped with a 63× Plan-Apochromat 1.4 NA oil immersion objective. Images were acquired using a zoom factor of 1.0–2.0, with a voxel size of 0.07 μm × 0.07 μm × 0.34μm and a frame resolution of 1912 × 1912 pixels, recorded at a pixel depth of 8-bit per channel. Line averaging was set to 4.0, and imaging was conducted in three/four-channel sequential mode.

Western blotting

Cell lysates were extracted utilizing Radio Immuno-Precipitation Assay (RIPA) Buffer and protein concentration was estimated with the Bicinchoninic Acid (BCA) Kit (Pierce, 23225). Subsequently, the samples were denatured by heating in 5× Laemmli Buffer before their separation on either a 12.5% or 15% acrylamide-bisacrylamide gel. Following electrophoresis, proteins were transferred onto a pre-activated polyvinylidene difluoride (PVDF) membrane at a constant voltage of 80 V for 180 min. The membrane was then subjected to blocking with 5% non-fat dried milk powder dissolved in 1× Tris-Buffered Saline with Tween 20 (0.1% v/v) (1× TBST). Primary and secondary antibodies were diluted in 0.5% milk in 1× TBST for 120 min and 60 min, respectively. The visualization of protein bands was accomplished using a chemiluminescent substrate (BioRad, Clarity Western ECL Substrate, Cat. no.1705061), with images captured at 10-s incremental exposures using the LAS4000 chemiluminescence system (GE). For molecular weight estimation, Precision Plus Protein Dual Color Standards (250–10kDa, Biorad, Cat. No. 161–0374) were utilized as molecular weight markers. Antibodies have been mentioned in the Supplementary Table.

Cell fractionation

Cytoplasmic and nuclear fraction isolation

Cytoplasmic and nuclear fractions had been prepared from 10 million cells. The cells were first rinsed with ice-cold phosphate-buffered saline (PBS) adjusted to pH 7.4. They were then detached on ice using a plastic cell scraper and collected into 1.5 mL microcentrifuge tubes containing 1 mL of ice-cold PBS. Brief centrifugation was performed for 10 s at 7500 rpm, after which the supernatant was discarded. The resulting cell pellets were resuspended in 900 μL of ice-cold 0.1% NP-40 in PBS and subjected to five rounds of mixing using a P1000 micropipette. From this lysate, 300 μL had been set aside as the "whole cell lysate". This fraction was mixed with 100μL of 5× Laemmli sample buffer and maintained on ice until sonication. The remaining 600μL was centrifuged for an additional 10 s, allowing for the collection of 300μL of the supernatant as the "cytosolic fraction," which was then combined with 100μL of 5× Laemmli sample buffer and boiled for 1 min. The remaining supernatant was discarded, and the pellet was resuspended in 1 mL of ice-cold 0.1% NP-40 in PBS. Following another centrifugation for 10 s, the supernatant was removed, and the final pellet, approximately 20 μL in volume, was resuspended in 180μL of 1× Laemmli sample buffer, designating this as the "nuclear fraction". Both the nuclear fractions and whole cell lysates containing DNA subsequently underwent sonication using microprobes set to level 2 for two cycles of 5 s each, followed by boiling for an additional minute. Finally, 10μL of whole cell lysate, 10μL of the cytoplasmic fraction, and 5μL of the nuclear fraction were loaded onto an SDS-PAGE gel for electrophoresis and were then transferred onto nitrocellulose membranes for further analysis.[94]

Nucleolar fraction isolation- Nucleolar isolation was performed as mentioned previously [4]. DLD-1 and MCF10A(p53DN) cells (~10^7) were thoroughly rinsed and harvested using an ice-cold solution composed of 0.5 mL of 0.5 M sucrose, 3 mM magnesium chloride ($MgCl_2$), and a 1× protease inhibitor cocktail (PIC). The collected cells were subjected to sonication on ice with a Sonics Vibracell, utilizing a protocol of five cycles, each consisting of 10 s of sonication followed by 10 s of rest, set at 50% amplitude. Following sonication, the resulting cell lysate was carefully layered onto 0.7 mL of Solution II, which contained 1.0 M sucrose and 3 mM $MgCl_2$ and was subsequently centrifuged at 1,800 × g for 5 min at 4°C. The supernatant was meticulously removed, and the resulting nucleolar pellet was then resuspended in RIPA buffer for immunoblotting.[95,96]

Proteinase K protection assay

Proteinase K protection assays were performed to assess the internalization of E-cadherin. DLD-1 cells were transfected with siLacZ (control) or siFBL for ~48 h. Cells were washed twice with ice-cold 1XHBS and incubated on ice with Proteinase K (100 μg/mL, final concentration) in 1XHBS containing 1 mM $CaCl_2$ for 30 min. Triton X-100 (0.5% final concentration) was added to the mentioned wells to permeabilize cells for Proteinase K. Lysates were cleared by centrifugation (14,000 × g, 10 min, 4°C), and equal amounts of protein were subjected to SDS–PAGE followed by immunoblotting for E-cadherin.

To enhance specificity toward the extracellular domain of E-cadherin, we optimized the protocol by using Rat anti-E-cadherin (DECMA-1) monoclonal antibody (during immunoblotting), which binds specifically to the extracellular domain of E-cadherin.[97]

Transferrin uptake assay

~0.2 million DLD-1 cells were seeded on a coverslip and transfected with siLacZ and siFBL for ~48h. Subsequently, cells were incubated with 50 μg/mL Texas Red-conjugated transferrin (Invitrogen) for 10, 20, and 30 min. For the negative control, siLacZ and siFBL

transfected cells were incubated at 4°C for 30 min. Following incubation with Texas Red-conjugated transferrin, unbound transferrin was removed by thorough acid wash (3X, 2 min each). Cells were fixed with 4% formaldehyde and further processed for confocal imaging after counterstaining with DAPI.

Scratch wound

Cells were cultured in Roswell Park Memorial Institute (RPMI) 1640 and Dulbecco's Modified Eagle Medium-F12 (DMEM-F12) following transfection with small interfering RNA (siRNA) or subsequent drug treatment. Twelve hours post-transfection, cells were reseeded in 24-well tissue culture plates at a density optimal for establishing a confluent monolayer. After another 12-h incubation, a sterile 200 μL pipette tip was utilized to meticulously create a linear scratch in the center of each well, ensuring the tip was held perpendicular to the substrate. Detached cells were then removed by gently washing the wells twice with phosphate-buffered saline (PBS), after which fresh medium was added. The assay was conducted using 0.5% serum-supplemented RPMI for DLD-1 cells and DMEM-F12 without epidermal growth factor (EGF), and Assay media for MCF10A(p53DN) cells. Following this, the cells were incubated for 48 h, or a modified duration as warranted by the specific cell type being examined. Imaging was carried out under consistent microscopic parameters, with the extent of wound closure or gap distance quantified for further analysis. The formula for measuring wound healing percentage used was-

Wound Closure % = (Initial Wound Area- Current Wound Area) $\times$100.

Where:

Initial Wound Area = the area of the wound at the beginning of observation (μm^2). Current Wound Area = the area of the wound at a later time (after treatment).

Wound Closure% represents the percentage of wound healing.

Invasion assay

To assess cell migration, $5X10^4$ cells per well were seeded in the upper chambers of Transwell inserts without a Matrigel coating, using serum-free media. The lower chamber contained 0.6 mL of RPMI or DMEM-F12 with 10% FBS or 5% Horse serum, acting as a chemoattractant. The plate was then incubated at 37°C for 36h hours (after transfection) to allow cell movement. After the incubation period, cells that had traversed to the lower membrane surface were fixed using 4% formaldehyde, and the nuclei were stained using DAPI.

Image analysis

Colocalization analysis

Colocalization analysis was performed using the Coloc module in Imaris (Bitplane, Oxford Instruments). Image datasets were imported into Imaris, and individual fluorescence channels were assigned to their respective markers. For analyses restricted to specific subcellular regions, a three-dimensional region of interest (ROI) was defined using the Surpass ROI tool. Colocalization between the two channels of interest was quantified using the Coloc wizard. Intensity thresholds for each channel were determined either automatically using the Costes method or set manually to exclude background signal. Voxels exceeding both thresholds were defined as colocalized, and a colocalization channel mask was generated for visualization. Quantitative colocalization metrics, including Pearson's correlation coefficient (PCC), Manders' overlap coefficients (M1 and M2), colocalized volume, and total number of colocalized voxels, were computed by the software. The resulting colocalization masks were rendered in 3D for qualitative assessment, and numerical data were exported for statistical analysis.

Segmentation analysis

Segmentation of fluorescence images was performed using the Surfaces module in Imaris. Image datasets were imported into Imaris, and each fluorescence channel was assigned to its corresponding marker. Segmentation was conducted on the channel of interest using either automatic thresholding based on the absolute intensity values or manual adjustment to exclude background signal. A surface creation wizard was used to generate 3D reconstructions, with background subtraction applied to improve object separation. Where necessary, smoothing filters were applied to reduce noise, and the "Split Touching Objects" function was used to separate adjacent structures. The minimum object size was defined to exclude spurious detections. For each segmented object, quantitative parameters including volume, surface area, mean fluorescence intensity, and total voxel count were computed. Segmented surfaces were rendered in 3D for qualitative visualization, and all statistical outputs were exported for further analysis.

Subcutaneous xenograft assay in NOD-SCID mice

To assess the tumorigenic impact of Fibrillarin (FBL) depletion, subcutaneous xenografts were established in NOD-SCID mice (NOD.CB17-Prkdc$^{scid/NcrCrl}$). All procedures were performed in accordance with institutional ethical guidelines and approved by the Institutional Animal Ethics Committee (IAEC).

DLD-1 cells stably expressing shFBL under a Tet-ON promoter were harvested at ~70–80% confluency, washed with sterile 1X PBS, and resuspended in a 1:1 mixture of 1X PBS at 1×10^7 cells/mL. A total of $\sim 7 \times 10^6$ cells (100 μL) were injected subcutaneously into the right flank of each mouse using a 26-gauge syringe. FBL knockdown was induced by administering doxycycline (2 mg/mL in drinking water supplemented with 5% sucrose), with water bottles changed every 72 h. Control mice received sucrose water without

doxycycline. Mice were monitored biweekly for tumor growth and general health. The formula for calculating the tumor size is given below-

$$V = (L \times W^2) / 2$$

V = Tumor volume (in cubic millimeters, mm^3).
L = Tumor length (the longest dimension of the tumor measured with calipers).
W = Tumor width (the shortest dimension perpendicular to the length).

Tail vein injection assay

To evaluate the metastatic potential of FBL-depleted cells, experimental lung colonization assays were performed by tail vein injection in NOD-SCID mice. Briefly, DLD-1 cells stably expressing Tet-ON–inducible shFBL were harvested at ~70–80% confluency, washed with sterile PBS, and resuspended at a density of 1×10^7 cells/mL in ice-cold PBS. A total of 1×10^6 cells (100 μL) were injected into the lateral tail vein of each mouse using a 29-gauge insulin syringe under brief isoflurane anesthesia. FBL knockdown was induced by doxycycline administration (2 mg/mL in 5% sucrose water, replaced every 72 h), while control animals received sucrose water alone. Mice were monitored for health and body weight throughout the study. After 6–8 weeks, lungs were harvested, fixed in 10% neutral-buffered formalin, paraffin-embedded, and subjected to H&E staining for histological assessment of metastatic burden.

Hematoxylin and eosin (H&E) staining of paraffin-embedded lung and tumor tissues

Formalin-fixed, paraffin-embedded (FFPE) lung and subcutaneous tumor tissues from NOD-SCID mice were subjected to standard H&E staining to assess tissue morphology and metastatic infiltration. Briefly, tissues were fixed in 10% neutral-buffered formalin (24–48 h, room temperature), dehydrated through graded ethanol, cleared in xylene, and embedded in paraffin. Sections (4–5 μm) were cut using a rotary microtome, floated on a 42°C water bath, mounted on charged slides, and baked at 60°C for 1 h.

For staining, slides were deparaffinized in xylene, rehydrated through graded ethanol, and rinsed in water. Nuclei were stained with Harris or Mayer's hematoxylin (4–5 min), differentiated in 0.3% acid alcohol, blued in 0.1% ammonia water, and rinsed. Cytoplasmic and extracellular components were counterstained with eosin Y (0.5–1%, 1–2 min). Sections were dehydrated through ascending ethanol, cleared in xylene, and mounted with a permanent medium (DPX). Stained slides were imaged under a brightfield microscope.

QUANTIFICATION AND STATISTICAL ANALYSIS

Statistical significance was assessed using an unpaired Student's *t* test, performed in GraphPad Prism version 8.0. Data are presented as mean ± SE with error bars, and a *p* value ≤ 0.05 was considered statistically significant. Details of the statistical tests, sample sizes, number of replicates, and definition of error bars are provided in the figure legends.

Nucleic Acids Research, 2026, gkaf1464
https://doi.org/10.1093/nar/gkaf1464
Gene regulation, Chromatin and Epigenetics

Phosphorylation-dependent modulation of the Lamin A/C-EZH2 complex regulates epithelial-mesenchymal plasticity

Balaji AK, Santam Saha, Kundan Sengupta *

B-216, Chromosome Biology Lab, Biology, Indian Institute of Science Education and Research (IISER), Pune, Dr Homi Bhabha Road, Pashan, Pune 411008, Maharashtra, India

*To whom correspondence should be addressed. Email: kunsen@iiserpune.ac.in

Abstract

Epithelial-to-mesenchymal transition (EMT) is essential for normal development and cancer progression. However, how nuclear Lamins regulate EMT is unclear. Here, we show that Lamin A/C modulates the epithelial–mesenchymal (E-M) plasticity of cells through its interaction with the chromatin organizer, EZH2. The overexpression of Lamin A reinforces an epithelial identity, while its depletion promotes a mesenchymal phenotype. This positions Lamin A/C as a crucial modulator of Epithelial-Mesenchymal plasticity. Furthermore, CDK1-mediated phosphorylation of Lamin A/C (Ser22) and EZH2 (Thr345) disrupts Lamin A/C–EZH2 interaction, destabilizing EZH2, with a concomitant decrease in the occupancy of the heterochromatin mark (H3K27me3) on the *SNAI1*, *TWIST1*, and *ZEB1* promoters, thereby facilitating a transition towards mesenchymal transcriptional programs. Conversely, phosphodeficient Lamin A/C (S22A) and EZH2 (T345A) mutants restore epithelial identity, highlighting a regulatory role of the Lamin A/C–EZH2 axis in maintaining epithelial homeostasis. *In vivo*, xenograft assays in NOD-SCID mice reveal that while phosphorylated Lamin A/C or EZH2 promote tumor growth and metastasis, phospho-deficient mutants markedly suppress it. Lamin A/C–EZH2 interaction regulates the expression of E–M-associated transcription factors, highlighting the role of this interaction in modulating transcriptional plasticity, thereby serving as a potential therapeutic target for regulating metastasis in breast cancers.

Graphical abstract

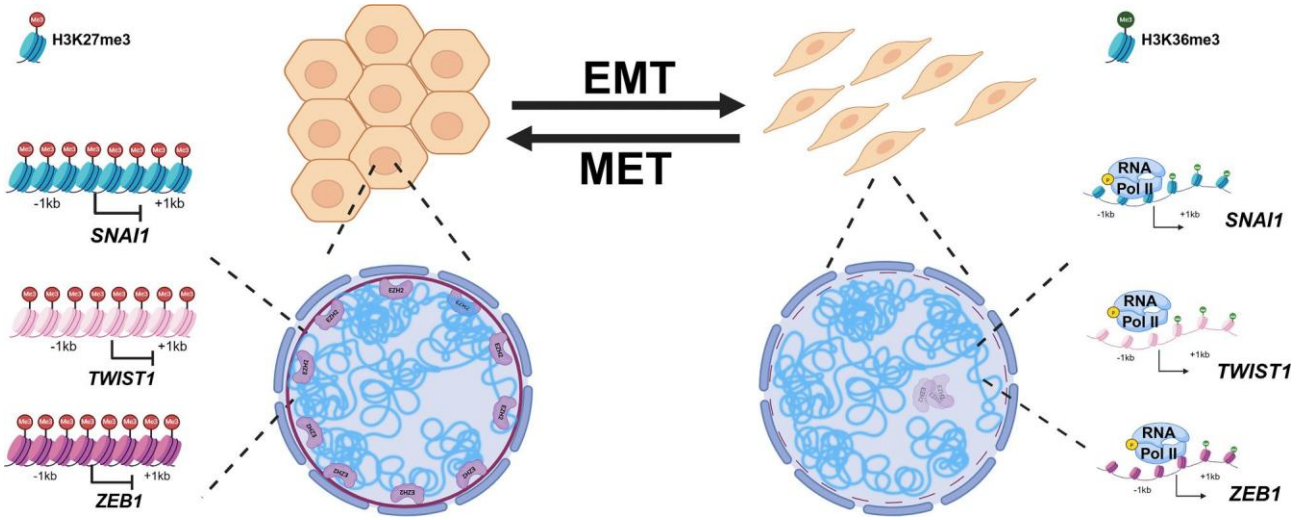

Introduction

Epithelial-to-Mesenchymal Transition (EMT) and Mesenchymal-to-Epithelial Transition (MET) are fundamental biological processes that play critical roles in embryonic development, wound healing, and tissue homeostasis [1]. EMT is essential for gastrulation, somite formation and neural crest cell migration, while the converse of EMT i.e. MET is essential for organogenesis, such as kidney development and the formation of epithelial somites surrounding the core of mesenchymal cells [2, 3]. During EMT, epithelial cells show

Received: June 3, 2025. **Revised:** November 26, 2025. **Accepted:** November 30, 2025

loss of polarity and cell–cell adhesion, which confer migratory and invasive characteristics that are typical of mesenchymal cells [4]. Conversely, MET induces enhanced cell–cell adhesion, decreases motility, restoring epithelial characteristics, enabling tissue differentiation and organogenesis [5]. While these processes are essential for normal physiology, they are subverted during cancer progression, fibrosis, and organ dysfunction [6]. EMT facilitates cells to invade the surrounding tissues and MET is crucial for the colonization of metastatic cells and integration into the secondary tissue. Rather than representing a binary switch, epithelial-to-mesenchymal plasticity (EMP) encompasses hybrid epithelial–mesenchymal (E-M) states that confer metastatic competence and survival advantages. Lineage-tracing and single-cell studies reveal that these hybrid states often underlie tumor dissemination, metastatic colonization, resistance to chemotherapy and recurrence, making it imperative to understand how tumor cells dynamically modulate EMP during cancer progression [7–10]. The transition between these phenotypic states (E and M) involves an intricate coordination among transcription factors, signalling pathways, and epigenetic mechanisms. However, the underlying mechanisms on how each of these processes crosstalk with one another are not fully understood [11].

During EMT, epithelial factors such as E-cadherin are downregulated, while mesenchymal markers—Vimentin, N-cadherin, and fibronectin—are upregulated, driven by transcription factors TWIST1, SNAI1, and ZEB1 [12]. Conversely, during MET, the activity of these transcription factors is attenuated, re-expressing epithelial factors, and suppressing mesenchymal properties [13]. However, the crosstalk between nuclear architecture and chromatin organization in regulating EM plasticity is unclear.

Lamin A/C, a core component of the nuclear lamina, provides structural support to the nucleus and maintains genome organization. It regulates chromatin architecture and gene expression, and its depletion increases nuclear deformability, alters chromatin accessibility, and enhances cellular plasticity [14–18]. Despite these broad nuclear functions, its direct role in EMT or MET remains unclear.

Lamin A/C regulates transcriptional programs through interactions with chromatin modifiers and transcriptional repressors. Notably, the Polycomb Repressive Complex 2 (PRC2), a histone methyltransferase, silences target genes via deposition of the repressive mark H3K27me3 [19, 20]. This connection suggests that Lamin A/C could modulate EM plasticity by coordinating with PRC2 components, such as EZH2 (the catalytic subunit of PRC2), thereby linking integrity of nuclear lamina to epigenetic regulation and transcriptional control. EZH2 is a well-established epigenetic regulator implicated in EMT [21]. However, the mechanisms by which Lamin A/C modulates EZH2 activity and if this interaction impacts E–M plasticity are largely unknown. Considering the central importance of epigenetic regulation in cancer initiation and progression, understanding the interplay between nuclear and chromatin organizers, namely Lamin A/C and EZH2 respectively, will uncover novel therapeutic targets to modulate EMT and MET dynamics in aggressive malignancies.

Here, we systematically investigate the role of Lamin A/C and EZH2 in EMT and MET using well-characterized paradigms of mammary breast epithelial cells and breast cancers. We demonstrate that depletion of Lamin A/C or EZH2 facilitates EMT, whereas its overexpression promotes MET, underscoring its role in maintaining epithelial identity. Furthermore, we identify that CDK1-mediated phosphorylation regulates the interaction between Lamin A/C-EZH2 altering their chromatin occupancy during EMT and MET. Integrative analyses involving transcriptomic, proteomic, and functional data, collectively provide crucial mechanistic insights into how nuclear Lamins contribute to EM plasticity. By elucidating the interplay between Lamin A/C and EZH2, this study elucidates the functional relevance of the interactome of nuclear Lamins in cancer progression. Our findings highlight the regulatory role of the phosphorylation of Lamin A/C in modulating EMT and implicate the Lamin A/C-EZH2 axis as a key target for novel therapeutic interventions in metastatic breast cancers.

Materials and methods

Cell culture

Immortalized human breast epithelial cell line MCF10A (CRL-10317) and cancer cell lines MCF7 (HTB-22), and MDAMB231 (HTB-26) were obtained from ATCC. MCF10A cells were maintained in Dulbecco's modified Eagle's medium (DMEM)/F12 (1:1) supplemented with 5% horse serum, EGF (20 ng/ml), hydrocortisone (0.5 mg/ml), cholera toxin (0.1 mg/ml), insulin (10 mg/ml), and 1% penicillin–streptomycin. MCF7 and MDAMB231 cells were cultured in DMEM and Roswell Park Memorial Institute (RPMI), respectively, supplemented with 10% fetal bovine serum (FBS), 1% L-glutamine, and 1% penicillin–streptomycin. All cells were grown at 37°C with 5% CO_2. The cell types were validated based on morphology (Supplementary Fig. S1A), chromosome numbers (Supplementary Fig. S1B), and profile of key E and M markers (Supplementary Fig. S1C–G). Furthermore, 4^{r},6-diamidino-2-phenylindole (DAPI) staining did not show any visible extranuclear staining, negating mycoplasma contamination.

EMT induction in MCF7 upon TWIST1 overexpression

MCF7 cells (~0.35 million) were seeded in six-well plates and allowed to adhere for ~10–12 h, to attain a confluency of ~50%. Cells were independently transfected with 2 μg of pEGFPN1 (Empty vector) or TWIST1 in Opti-MEM using polyethyleneimine (PEI; Sigma #408727-100ML) at a ratio of 1:3 plasmid: branched PEI. After ~6 h post-transfection, Opti-MEM was replaced with DMEM containing 10% FBS. Transfected cells were selected with G418 (890 μg/ml, Roche #4727878001) for 24 h. Cells were harvested for reverse transcriptase-polymerase chain reaction (RT-PCR), immunofluorescence assay, or immunoblotting at ~48 h post-transfection to assess for expression of E and M marks, respectively [22, 23].

TGF-β mediated EMT induction

MCF10A cells (~0.15 million) were seeded at a confluency of (~30%–40%) in each well of a six-well plate and allowed to adhere overnight (~16 h). MCF10A cells were treated with recombinant human TGF-β1 (10 ng/ml, PeproTech, #100-21) to induce EMT in complete growth medium. Media containing fresh TGF-β1 was replenished every ~48 h for a total duration of 7 days. Control cells were maintained in complete media without TGF-β [24, 25].

GRHL2 mediated MET induction

MET was induced by overexpression of GRHL2 using the lentiviral vector pLVX-TetOn-Puro-GRHL2 (gift from Dr Ruby Yun-Ju Huang, National Taiwan University). Lentiviral particles were generated by transfecting HEK293T cells ($\sim 1 \times 10^6$) with 8 μg plasmid DNA using branched PEI (1:3 DNA:PEI ratio). Viral supernatants collected at 48 and 72 h, were filtered using a 0.45 μm filter and used to transduce MDAMB231 cells ($\sim 1 \times 10^6$) in the presence of 8 μg/ml polybrene (Sigma #H9268). Cells were selected with puromycin (2 μg/ml, 2 days) and GRHL2 overexpression was validated by immunoblotting (Fig. 1I) [26, 27].

small interfering RNA (siRNA) transfection

MCF7, MCF10A, and MDA-MB-231 cells (~0.35 million) were seeded in six-well plates or 35 mm dishes ~24 h prior to transfection. Cells were cultured in Opti-MEM and transfected with 50 nM siRNA using 4 μl of RNAiMAX (Invitrogen #13778150). After ~6 h, Opti-MEM was replaced with DMEM with 10% FBS for a total duration of ~48 h. Cells were harvested for immunofluorescence assay, RT-PCR, or immunoblotting post-transfection.

Retroviral transduction

HEK293T cells (~1 million) were transfected with ~8 μg of the retroviral plasmid of interest (Supplementary Table 4), 4 μg of packaging plasmid Gag-Pol (Plasmid #14887), and VSV-G (2 μg, Plasmid #14888) using PEI (~42 μl), in the ratio of DNA:PEI = 1:3 (w/v). Viral supernatant (~8 ml) was collected ~48 h post-transfection from HEK293T cells and added to ~0.35 million cells (~1.5 ml; seeded at ~0.35 million cells per well in a six-well plate). Polybrene (10 μg/ml ~10 μl Sigma #H9268) was added to facilitate viral attachment and entry. This procedure was repeated at ~72 h post-transfection. Cells were selected using puromycin (2 μg/ml, Gibco #A1113802; for pBabe-Puro constructs) for ~48 h or hygromycin (50 μg/ml, Gibco #10687010; for MSCV-F-Hygro constructs) for ~24 h [28].

Lentiviral transduction

HEK293T cells were co-transfected with the transfer vector (8 μg), packaging plasmid psPAX2 (4 μg; Addgene #12260), and envelope plasmid pMD2.G (2 μg; Addgene #12259) using PEI (DNA:PEI = 1:3, w/v). Viral supernatants were collected at 48 and 72 h post-transfection and used to transduce target cells ($\sim 3.5 \times 10^5$ cells/well in a six-well plate) in the presence of 10 μg/ml polybrene. Transduced cells were selected with 2 μg/ml puromycin for 2 days [29].

Immunofluorescence

Cells ($\sim 3.5 \times 10^5$) were seeded on 22 × 22 mm coverslips and fixed with 4% paraformaldehyde in 1× phosphate buffered saline (PBS; pH 7.4) for 15 min at room temperature (RT), followed by permeabilization with 0.5% Triton X-100 for 10 min. After blocking with 1% bovine serum albumin (BSA) in 1× PBS for 30 min, cells were incubated with primary antibodies for 90 min at RT. Cells were incubated with Alexa Fluor-conjugated secondary antibodies (488 or 568; Invitrogen, 1:1000) for 1 h, followed by DAPI counterstaining (0.05 μg/ml, 2 min). Coverslips were mounted in SlowFade Gold Antifade Reagent (Invitrogen, S36937) and stored at 4°C until imaging. Dilutions and Catalogue numbers of antibodies used are listed in Supplementary Table 4.

Imaging and acquisition parameters

Confocal microscopy was performed using a Zeiss LSM 710 microscope (Carl Zeiss, Thornwood, NJ, USA) equipped with a 63 × Plan-Apochromat 1.4 NA oil immersion objective and an AxioCam MRm Rev.3 charge-coupled device camera (Zeiss). Images were acquired at a zoom of 1.0 as Z-stacks at a resolution of 512 × 512 pixels per frame with an 8-bit pixel depth per channel. Voxel size was set to 0.105 μm × 0.105 μm × 0.34 μm, with line averaging of 4.0 in sequential three-channel mode. Fluorescence signals were detected appropriately with filters for DAPI, Alexa Fluor-488, and Alexa Fluor-568. Image processing and analysis were performed using ImageJ software.

Immunoblotting

Cells were lysed in Radioimmunoprecipitation Assay (RIPA) buffer [50 mM Tris–HCl, pH 7.4–8.0, 150 mM NaCl, 1% NP-40, 0.1% sodium dodecyl sulphate (SDS), 0.5% sodium deoxycholate, 1 mM ethylenediaminetetraacetic acid (EDTA)] supplemented with protease and phosphatase inhibitors (Roche) for 10 min at 4°C. Protein concentration was determined using the Bicinchoninic Acid (BCA) assay. Equal amounts of protein were resolved on 12.5% sodium dodecyl sulphate–polyacrylamide gel electrophoresis (SDS–PAGE) and transferred to Polyvinylidene Fluoride (PVDF) membranes (0.45 μm; Millipore #IPVH00010) at 100 V for 2 h at 4°C. Membranes were blocked in 5% milk or 5% BSA in TBST (20 mM Tris–HCl, pH 7.5, 150 mM NaCl, 0.1% Tween-20) for 1 h and incubated overnight at 4°C with primary antibodies (1:1000 unless stated otherwise) against E-Cadherin, Vimentin, ZEB1, EZH2, pEZH2(T345), Lamin A/C, pLamin A/C(S22), pSmad3, Smad3, SUV39H1, Lamin B1, Lamin B2, Cyclin B1, Snail1, GRHL2, pCDK1, Twist1, GAPDH (1:7000) H3K27me3, H3K9me3, and H3 (1:3000). After washing, membranes were incubated with horseradish peroxidase-conjugated secondary antibodies (anti-rabbit #111-035-003; anti-mouse #515-035-003; Jackson Labs; 1:10 000) for 1 h at RT. Bands were visualized using ECL substrate (Bio-Rad #1705061) and imaged on LAS4000 (GE). Densitometric quantification was performed using ImageJ. Dilutions and Catalogue numbers of primary antibodies used are listed in Supplementary Table 4.

RT-PCR

RNA isolation

Cells ($\sim 3 \times 10^5$) were seeded in six-well plates and lysed in 1 ml TRIzol reagent (Invitrogen #15596018). Chloroform (100 μl per 500 μl TRIzol) was added, and samples were vortexed, incubated for 10 min at RT, and centrifuged at 12 000 × *g* for 15 min at 4°C. The aqueous phase was mixed with an equal volume of isopropanol, incubated for 15 min, and centrifuged at 12 000 × *g* for 15 min at 4°C. RNA pellets were washed with 70% ethanol, air-dried, and resuspended in nuclease-free water. RNA concentration and purity were measured using a NanoDrop spectrophotometer.

Complementary DNA synthesis and quantitative real-time PCR

Complementary DNA was synthesized from 1 μg total RNA using the PrimeScript RT Reagent Kit (Takara #6110B) with oligo(dT) and random hexamer primers. Quantitative PCR was performed using TB Green Premix Ex Taq II (Takara #RR820W) on a Bio-Rad CFX96 system under the following conditions: 95°C for 30 s, followed by 40 cycles of 95°C for 5 s and 60°C for 30 s. Melt-curve analysis (60–95°C, 0.3°C/s) confirmed amplicon specificity. Relative gene expression was calculated using the $2^{-\Delta\Delta Ct}$ method with GAPDH as the internal control and untreated samples as the reference.

Co-immunoprecipitation

Cells (~1 × 10^7) were lysed in co-immunoprecipitation (Co-IP) buffer (50 mM Tris–HCl, pH 8.0, 300 mM NaCl, 0.5% NP-40) supplemented with protease inhibitors (Roche #5892970001) and incubated on ice for 15 min. Lysates were cleared by centrifugation at 14 000 rpm for 15 min at 4°C, and protein concentration was determined by BCA assay. For each reaction, 2 μg of antibody or normal rabbit IgG (control) was pre-bound to Protein A–Sepharose beads (Roche #P3391) for 4 h at 4°C. Equal amounts of lysate (~500 μg total protein) were added and incubated overnight at 4°C with rotation. Beads were washed 5–6 times with a cold Co-IP buffer and eluted in 2 × Laemmli buffer at 95°C for 10 min. Eluates were resolved by SDS–PAGE and analyzed by immunoblotting. Antibodies used: anti-Lamin A/C (Abcam #ab108595), anti-EZH2 (CST #5246), and normal rabbit IgG (Invitrogen #10500C).

Chromatin immunoprecipitation

Cells (~1 × 10^7) were crosslinked with 1% formaldehyde in 1× PBS (pH 7.5) for 10 min at RT, and the reaction was quenched with 125 mM glycine for 5 min. Cells were washed twice with cold PBS and lysed in a buffer containing 1% SDS, 10 mM EDTA, and 50 mM Tris–HCl (pH 8.1) supplemented with protease inhibitors. Chromatin was sonicated (Covaris S220; 60% duty cycle, 30 s on/off for 30 min) to ~200–500 bp fragments, verified by agarose gel electrophoresis.

For each IP, 25 μg of chromatin was diluted in ChIP dilution buffer (0.01% SDS, 1% Triton X-100, 1.2 mM EDTA, 16.7 mM Tris–HCl, pH 8.1, 167 mM NaCl) and incubated overnight at 4°C with antibody-bound Protein A/G agarose beads. The following antibodies were used: Lamin A/C (Abcam #ab108595), EZH2 (CST #5246), H3K27me3 (Millipore #07-449), H3K36me3 (Abcam #ab9050), RNA Pol II (Ser2p; Covance #MMS-129R), and control IgG (Invitrogen #10500C). Beads were sequentially washed with low-salt, high-salt, LiCl, and TE buffers and eluted in 1% SDS, 0.1 M $NaHCO_3$. Eluates were treated with proteinase K (2 μl, 20 mg/ml, 55°C, 30 min), and crosslinks were reversed at 65°C for 4–6 h. DNA was purified using PCR purification columns (Promega #A9281) and analyzed by qPCR [30, 31].

Co-IP and mass spectrometry analysis

Endogenous Lamin A/C–interacting proteins were identified by Co-IP followed by Liquid Chromatography-Tandem Mass Spectrometry (LC–MS/MS) analysis [32, 33]. Briefly, MCF7−TWIST1(EV), MCF7+TWIST1, MDAMB231−Dox (−GRHL2), and MDAMB231+Dox (+GRHL2) cells (~1 × 10^7) were lysed in Co-IP buffer (50 mM Tris–HCl, pH 7.5; 150 mM NaCl; 1% NP-40) containing protease inhibitors. Clarified lysates (1 mg) were incubated overnight at 4°C with Protein A magnetic beads (SureBeads, Bio-Rad #161-4013) pre-bound to anti-Lamin A/C antibody (2 μg, Abcam #ab108595) or control IgG (Invitrogen #10500C). Immunocomplexes were washed, eluted in 2 × Laemmli buffer at 95°C, and resolved by SDS–PAGE.

Coomassie-stained gel bands (~2 cm) were excised, reduced (10 mM Dithiothreitol (DTT)), alkylated (55 mM iodoacetamide), and digested with sequencing-grade trypsin (Promega #V5111). Peptides were extracted, desalted on C18 columns, and analyzed on a Sciex TripleTOF 6600 mass spectrometer coupled to an Eksigent nano-LC 425 system. Data were processed using ProteinPilot (v2.0.1, Sciex) and searched against the human UniProt database.

The Lamin A/C interactome under EMT and MET conditions is provided in Supplementary Tables 2 and 3, respectively. The mass spectrometry (MS) data are available in the PRIDE repository (Dataset ID: PXD060831).

RNA sequencing

MCF10A cells (~0.35 million) were plated in six-well plates or 35 mm dishes around 24 h before transfection. The cells were maintained in Opti-MEM and transfected with 50 nM siRNA using 4 μl of RNAiMAX (Invitrogen #13778150). Transfection (was for ~6 h), after which the Opti-MEM medium was replaced with complete media, and the cells were incubated for ~48 h. Following transfection, MCF10A cells were collected in 1 ml TRIzol, and RNA sequencing (RNA-Seq) was outsourced to Medgenome, Bangalore. Quality control checks for the two independent biological replicates were confirmed through RNA Integrity Number (RIN) number analysis (RIN = 10, for all samples). RNA-Seq data are provided in Supplementary Table 1. The datasets have been deposited in Gene Expression Omnibus under accession number GSE289750.

Cell cycle analysis

Cells (~0.3 million) were harvested by trypsinization, washed with 1× PBS (pH = 7.5), and fixed in 70% ice-cold ethanol at 4°C, overnight. The fixed cell pellets were resuspended in 1× PBS and treated with RNase A (10 μg; Sigma, R6513-10MG) at 37°C for 45 min. Subsequently, propidium iodide (PI; 10 μg; Sigma, P4170-10MG) was added to the samples for DNA staining. The cell suspensions were passed through a 70 μm cell strainer (Corning, CLS431751) and processed for further analysis. Cell cycle profiling was performed using a fluorescence-activated cell scanner (BD FACSCalibur™, BD Biosciences) with approximately 10,000 events recorded per sample. Data were analyzed using FlowJO (V10.10) software.

Transwell migration (Boyden-chamber assay)

Cells (~3.5 × 10^5) were seeded in six-well plates and subjected to overexpression of Lamin A or EZH2, or their phosphodeficient (S22A-Lamin A, T345A-EZH2) or phosphomimetic (S22D-Lamin A, T345D-EZH2) variants. Approximately 5 × 10^4 cells were seeded in the upper chamber of 8 μm pore Transwell inserts (Corning #CLS3422) in serum-free media. Complete media (DMEM for MCF7 or RPMI for MDAMB231, 10% FBS) was added to the lower chamber and cells were allowed to migrate for ~36 h. Nonmigrated

cells were removed, and migrated cells were fixed with 4% paraformaldehyde for 10 min, washed, and stained with DAPI for 2 min. Nuclei were imaged at 10× on an EVOS microscope. Images were processed using the Threshold and Watershed functions, and nuclei were quantified with the "Analyze Particles" function (size 50 – ∞ pixels^2, circularity 0.5–1.0). Average nuclei per field were calculated and analyzed using imageJ.

Wound healing (scratch wound assay)

MCF10A cells (~3.5 × 10^5) were subjected to overexpression of Lamin A or EZH2, or their phosphodeficient (S22A-Lamin A, T345A-EZH2) or phosphomimetic (S22D-Lamin A, T345D-EZH2) variants. Cells were treated with 500 ng/ml doxycycline for ~48 h to induce endogenous Lamin A/C or EZH2 depletion, and EMT was induced with 10 ng/ml TGF-β. After ~48 h, ~5 × 10^4 cells were seeded per well in ibidi two-well inserts (ibidi #81176) in a 24-well plate overnight. Inserts were removed to create a wound gap, and migration into the wound area was monitored for 36 h (in assay media) using the Operetta High-Content Imaging System. Snapshots of wound closure was quantified with the integrated software in the Operetta Imaging System.

Animal studies

All animal procedures were conducted following approval from the Institutional Animal Ethics Committee (IISER-Pune/IAEC/2024–01/08) at the Indian Institute of Science Education and Research, Pune, in compliance with the Committee for the Purpose of Control and Supervision of Experiments on Animals (CPCSEA), Government of India. Mice were housed in the National Facility for Gene Function in Health and Disease (NFGFHD), IISER Pune, under standard laboratory conditions with unrestricted access to food and water.

In vivo tumor formation assay in NOD-SCID Mice

Female NOD-SCID mice (4–6 weeks old; Jackson Laboratory) were used for *in vivo* tumor formation studies. MDAMB231 cells expressing full-length (Lamin A or EZH2) or phosphodeficient (S22A-Lamin A, T345A-EZH2) or phosphomimetic (S22D-Lamin A, T345D-EZH2) variants were pre-treated with doxycycline for 48 h to deplete endogenous Lamin A/C or EZH2. Approximately 1 × 10^6 cells in 100 µl PBS were injected into the fourth mammary fat pad of each mouse. Knockdown was maintained via drinking water containing 1% sucrose and 500 ng/ml doxycycline, replenished every 72 h. Tumor growth was monitored, and volumes were calculated as (width^2 × length)/2. Mice were euthanized after 5 weeks, and tumors were harvested for analysis.

Tumor dissociation and primary cell culture

Excised tumors were minced using a scalpel and enzymatically digested in Hank's Balanced Salt Solution (HBSS) (Gibco, #14025050) containing collagenase IV (1 mg/ml, Sigma #C5138-1G), hyaluronidase V (0.1 mg/ml, Sigma #H6254-500MG), and DNase IV (20 mg/ml, Sigma #D5025-15KU) at RT. The suspension was filtered through a 70 µm mesh, centrifuged (1200 rpm, 5 min), and washed twice with HBSS. Cells were either lysed for Co-IP or plated in RPMI (Gibco, #11875093) for primary culture.

Proximity ligation assay

PLA was performed using the Duolink in Situ Detection Kit (Sigma #DUO92008) following the manufacturer's protocol. Cells were treated with cytoskeletal (CSK) buffer (10 mM PIPES, pH 6.8, 100 mM NaCl, 300 mM sucrose, 3 mM $MgCl_2$, 1 mM Ethylene Glycol Tetraacetic Acid (EGTA)), fixed in 4% Paraformaldehyde (PFA) (pH 7.4, 12 min), permeabilized with 0.5% Triton X-100 (10 min), and blocked with Duolink Blocking Solution (30 min, RT). Primary antibodies—Mouse anti-Lamin A/C (Jol2, Abcam #ab40567, 1:50), Rabbit anti-EZH2 (D2C9, CST #5246, 1:1000), and Rabbit anti-Phospho-cdc2 (Thr161, CST #9114, 1:500)—were applied overnight at 4°C.

PLA probes (anti-Mouse PLUS and anti-Rabbit MINUS, 1:5) were added and incubated at 37°C for 1 h, followed by ligation (Duolink ligase, 1 U/µl, 1:40) and amplification (Duolink polymerase, 10 U/µl, 1:80). Nuclei were counterstained with DAPI using Duolink Mounting Medium (#DUO82040).

Imaging and acquisition parameters

PLA images were acquired on a Zeiss anisotropy microscope (Carl Zeiss, Thornwood, NJ, USA) with a 63×/1.4 NA oil objective and AxioCam MRm Rev.3 camera using ZEN software. Z-stacks (512 × 512 pixels, 8-bit) were captured with a voxel size of 0.105 × 0.105 × 0.34 µm and line averaging of 4 in sequential two-channel mode. Fluorescence was detected for DAPI and Alexa Fluor-568. Images were processed and analyzed using ImageJ.

Statistical analysis

All statistical analyses were performed using GraphPad Prism version 8.4 (GraphPad Software, San Diego, CA, USA). Data are presented as mean ± standard deviation (SD) unless otherwise specified. Comparisons between the two groups were conducted using an unpaired two-tailed Student's *t*-test. For multiple-group comparisons, one-way or two-way analysis of variance (ANOVA) followed by Tukey's or Sidak's *post hoc* test was used, as appropriate. Statistical significance was defined as $P < 0.05$. Sample sizes and replicates for each experiment are detailed in the figure legends.

Results

Induction and reversal of EMT

EMT is a dynamic and reversible cellular process that plays a pivotal role in cancer progression [34]. EMT is involved in ~90% of cancers of epithelial origin, which increases cell migration while MET facilitates colonization and metastasis [35].

To elucidate the mechanisms that regulate EMT and MET, we selected three well-established cell types derived from the human breast, namely MCF7, MCF10A, and MDAMB231 [36]. The authenticity of these cell lines was validated by evaluating modal chromosome numbers (Supplementary Fig. S1A and B). We also performed phalloidin staining, followed by confocal imaging (Supplementary Fig. S1C), which showed an increased aspect ratio (AR) of mesenchymal [MDAMB231 cells (AR: 7.19±1.80)], as compared to epithelial cells [MCF7 (AR: 1.06±0.62) and MCF10A (AR: 1.09±0.59); Supplementary Fig. S1D]. Furthermore, immunoblotting and immunofluorescence assays at the single-cell level underscore

the epithelial nature of MCF7 cells, characterized by high E-cadherin expression and low Vimentin levels. In sharp contrast, MDA-MB-231 cells are mesenchymal, with relatively higher Vimentin and lower E-cadherin levels (Supplementary Fig. S1C and E–G).

We induced EMT in MCF7 cells by overexpressing hTWIST1-GFP for ~48 h. Immunoblotting analysis revealed a ~75% reduction in E-cadherin and a ~90% increase in Vimentin levels. Additionally, key mesenchymal transcription factors—Snail1, Twist1, and Zeb1—were significantly upregulated at the protein level (Fig. 1A). We corroborated these findings with immunofluorescence staining, which showed a decrease in E-cadherin and an increase in Vimentin expression in MCF7 cells overexpressing hTWIST1-GFP (Fig. 1B and D, methodological illustration in Fig. 1C), consistent with the immunoblot data. We treated MCF10A cells with TGF-β (10 ng/ml) for 7 days, which resulted in a striking reduction in E-cadherin expression (>70%) and a concomitant increase in Vimentin (~60%; Fig. 1E), consistent with EMT induction [24]. Immunofluorescence staining of these cells also showed a significant upregulation of Vimentin and downregulation of E-cadherin (Fig. 1F and H, methodological illustration in Fig. 1G). Furthermore, transcription factors that mark mesenchymal cells (Snail1, Twist1, and Zeb1) were significantly upregulated at the protein level (Fig. 1E).

We next overexpressed the transcription factor GRHL2 in the mesenchymal MDAMB231 cells for ~48 h [26, 27]. GRHL2 is a transcription factor that suppresses EMT by directly activating E-cadherin and repressing mesenchymal programs, thereby promoting MET, which makes it a useful model to study the reversibility of EMT [37, 38]. Overexpression of GRHL2 showed a striking increase in E-cadherin (>95%), decrease in Vimentin and mesenchymal transcription factors levels, leading to a transition in epithelial phenotype (Fig. 1I–L). Taken together, these representative cell lines derived from the E–M spectrum, serve as suitable models for studying EMT and its reversibility MET, offering a framework to investigate their regulatory mechanisms in the context of mammary epithelial and breast cancer respectively.

Impact of EMT induction on nuclear topology and Lamin A/C expression

EMT is accompanied by significant changes in cellular morphology and cytoskeletal organization. Altered cytoskeletal organization directly impacts nuclear morphology [39]. We examined the extent of changes in nuclear morphology upon EMT by overexpressing TWIST1 in MCF7 cells. This showed a significant decrease in the circularity and sphericity [from 0.86 ± 0.08 to 0.34 ± 0.06 in MCF7-TWIST1 cells ($P < 0.0001$)] of the nucleus, with no significant changes in either surface area or volume (Supplementary Fig. S2A–D). In contrast, GRHL2-mediated MET induction, restored nuclear shapes consistent with epithelial-like cells, with increased sphericity (from 0.35 ± 0.06 to 0.90 ± 0.06 in MDAMB231 +GRHL2 cells; Supplementary Fig. S2E and F). Taken together, these data reveal significant changes in nuclear morphology upon EMT or MET induction.

We next assessed the protein levels of Lamin A/C and B-type lamins, as lamins define nuclear structure and function [39, 40]. While EMT induction in the epithelial cells (MCF7 and MCF10A) showed a marked reduction in Lamin A/C levels (Fig. 2A–F), the levels of B-type Lamins were relatively unaltered (Supplementary Fig. S2G, H). Conversely, Lamin A/C levels were upregulated upon GRHL2-driven MET in MDAMB231 cells (Fig. 2G–I), without any significant changes in the expression levels of B-type lamins (Supplementary Fig. S2I and J).

We quantified the levels of A- and B-type lamins across a panel of 11 breast cancer cell lines spanning the EM spectrum [36]. Interestingly, Lamin A/C showed a progressive decline with increasing mesenchymal characteristics, whereas B-type lamin levels did not display such a trend (Fig. 2J), suggesting a selective downregulation of Lamin A/C during EMT.

Importantly, transcript levels of *LMNA* remained unchanged upon both EMT and MET (Fig. 2K), indicating that Lamin A/C is post-transcriptionally regulated [41]. To further determine if EMT impacts the stability of Lamin A/C, we performed a time-course cycloheximide (CHX) chase assay in MCF7 cells. TWIST1 overexpression, followed by CHX treatment (10 μg/ml) showed a temporal reduction in Lamin A/C protein levels, whereas Lamin A/C remained unaltered in control cells (Empty vector) over the same duration (Supplementary Fig. S3A and B). Furthermore, co-treatment with 1 μM MG132 and CHX restored the stability of Lamin A/C protein after ~8 h upon TWIST1 overexpression (Supplementary Fig. S3C and D), suggesting that EMT induces Lamin A/C degradation via a proteasome-dependent pathway.

Collectively, these results demonstrate that EM plasticity is associated with changes in Lamin A/C expression and nuclear morphology, with Lamin A/C being regulated by post-translational degradation during EMT.

Lamin A/C determines EM identity

To investigate the role of Lamin A/C in EM plasticity, we performed RNA-Seq analysis upon Lamin A/C depletion in MCF10A cells. Differential gene expression analysis (DESeq2) revealed a robust upregulation of mesenchymal-associated genes including *VIM, SNAI1, TWIST1,* and *ZEB1,* which were among the top 50 upregulated genes, accompanied by downregulation of epithelial markers such as *CLDN1, OCLN,* and *CDH1* (Fig. 3A and B) [42]. Consistent with these observations, Gene Ontology (GO) analysis showed a significant enrichment ($P < .05$) of genes associated with EMT regulation, cell migration, secondary neoplasms, cell–cell adhesion, and regulation of mitotic nuclear division (Fig. 3C) [43]. Kyoto Encyclopedia of Genes and Genomes (KEGG) pathway analysis revealed modulation of signalling pathways implicated in ECM–receptor interaction, TGF-β signalling pathway and regulation of actin cytoskeleton, while GO Cellular Component analysis highlighted ECM organization and cell migration (Supplementary Fig. S4A and B) [44]. Furthermore, Gene Set Enrichment Analysis (GSEA) enriched for cell adhesion and migration-related gene sets, both hallmarks of EMT (Fig. 3D; Principal Component Analysis (PCA) analyses of RNA seq data between independent replicates Supplementary Fig. S4C).

To validate these results in an independent epithelial context, Lamin A/C was depleted in MCF7 cells. Lamin A/C depletion showed an increase in the AR of MCF7 cells [si Lamin A/C: mean ± SD = 5.49 ± 2.09, si LacZ (control) mean ± SD = 1.02 ± 0.58] [Supplementary Fig. S5A, A(i), and A(ii)]. In contrast, overexpression of Lamin A in MDAMB231 cells, revealed the acquisition of cobblestone-like epithelial morphol-

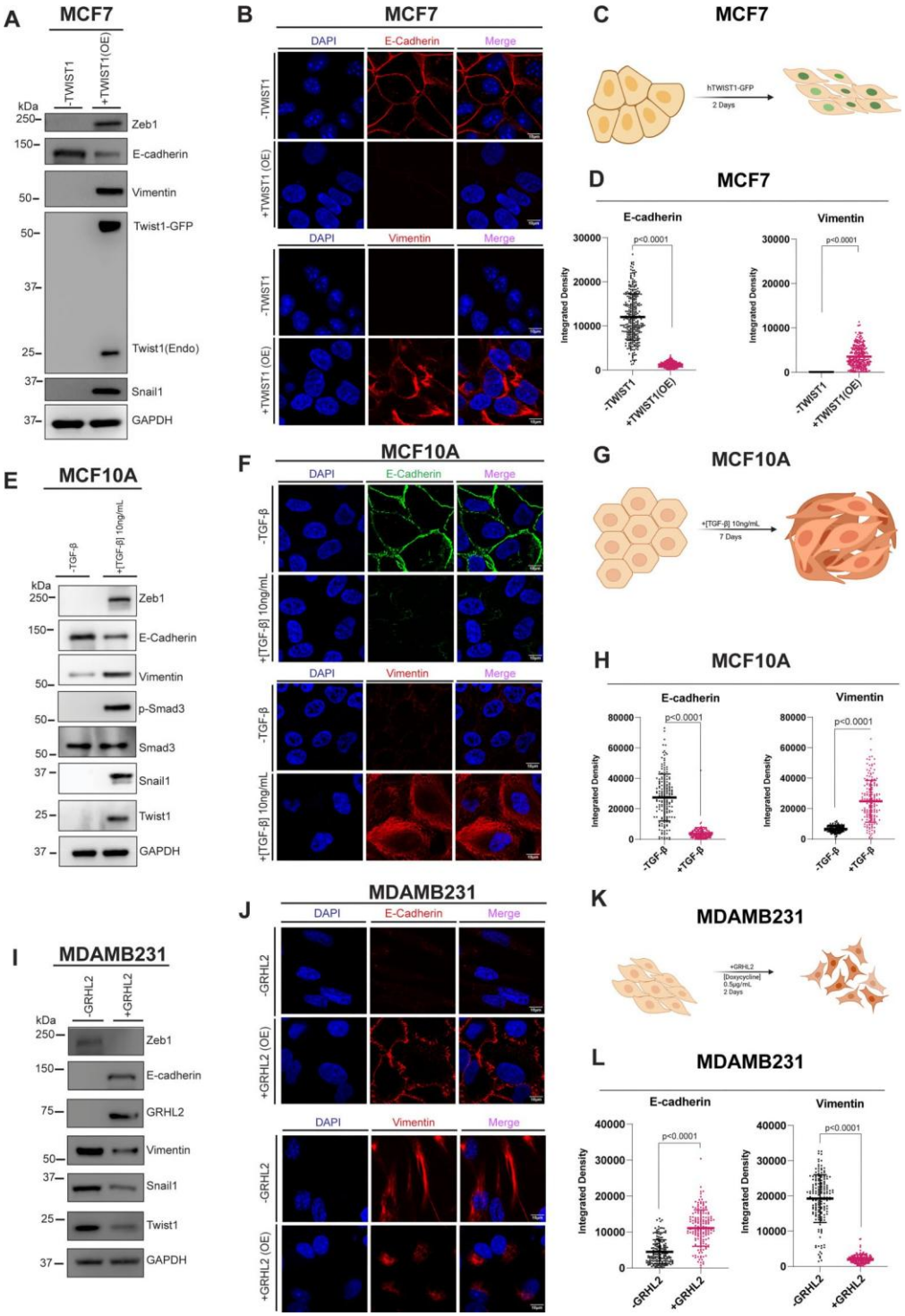

Figure 1. Induction and characterization of EMT and MET in breast cancer cell lines. **(A)** Immunoblot analysis of EMT induction in MCF7 cells transiently overexpressing TWIST1-GFP for 48 h. Cells were transfected with 2 μg of pEGFPN1 or hTWIST1-GFP **(B)** Immunofluorescence analysis of EMT in MCF7 cells overexpressing TWIST1-GFP or control pEGFPN1. E-cadherin and Vimentin (red), nucleus (DAPI, blue). Scale bar ~10 μm **(C)** Schematic representation of EMT induction in MCF7 cells **(D)** Scatter plot of immunofluorescence assay, showing relative changes in the integrated density of E-cadherin and Vimentin in MCF7 cells. Quantification for panel (B) (n = 200). Data represent mean ± standard deviation (SD) from N = 3 independent biological replicates. **(E)** Immunoblot analysis of EMT induction in MCF10A cells treated with 10 ng/ml TGF-β for 7 days **(F)** Immunofluorescence analysis of EMT in MCF10A cells treated with TGF-β. E-cadherin (green); Vimentin (red); nucleus (blue, DAPI). Scale bar ~10 μm **(G)** Schematic representation of EMT induction in MCF10A cells **(H)** Scatter plot of immunofluorescence assay, showing relative changes in the integrated density of E-cadherin and Vimentin in MCF10A cells [data shown in panel (F)] following EMT induction (n = 200). Data represent mean ± SD from N = 3 independent biological replicates **(I)** Immunoblot analysis of MET induction in MDAMB231 cells following doxycycline-induced GRHL2 overexpression for 48 h **(J)** Immunofluorescence analysis of MET in MDAMB231 cells overexpressing GRHL2. E-cadherin and Vimentin (red), nucleus (blue, DAPI). Scale bar ~10 μm **(K)** Schematic representation of MET induction in MDAMB231 cells **(L)** Scatter plot of immunofluorescence assay, showing relative changes in the integrated density of E-cadherin and Vimentin in MDAMB231 cells following MET induction [data shown in panel (J)] (n = 200). Data represent mean ± SD from three independent biological replicates. Unpaired Student's t-test was used to compute the P-value.

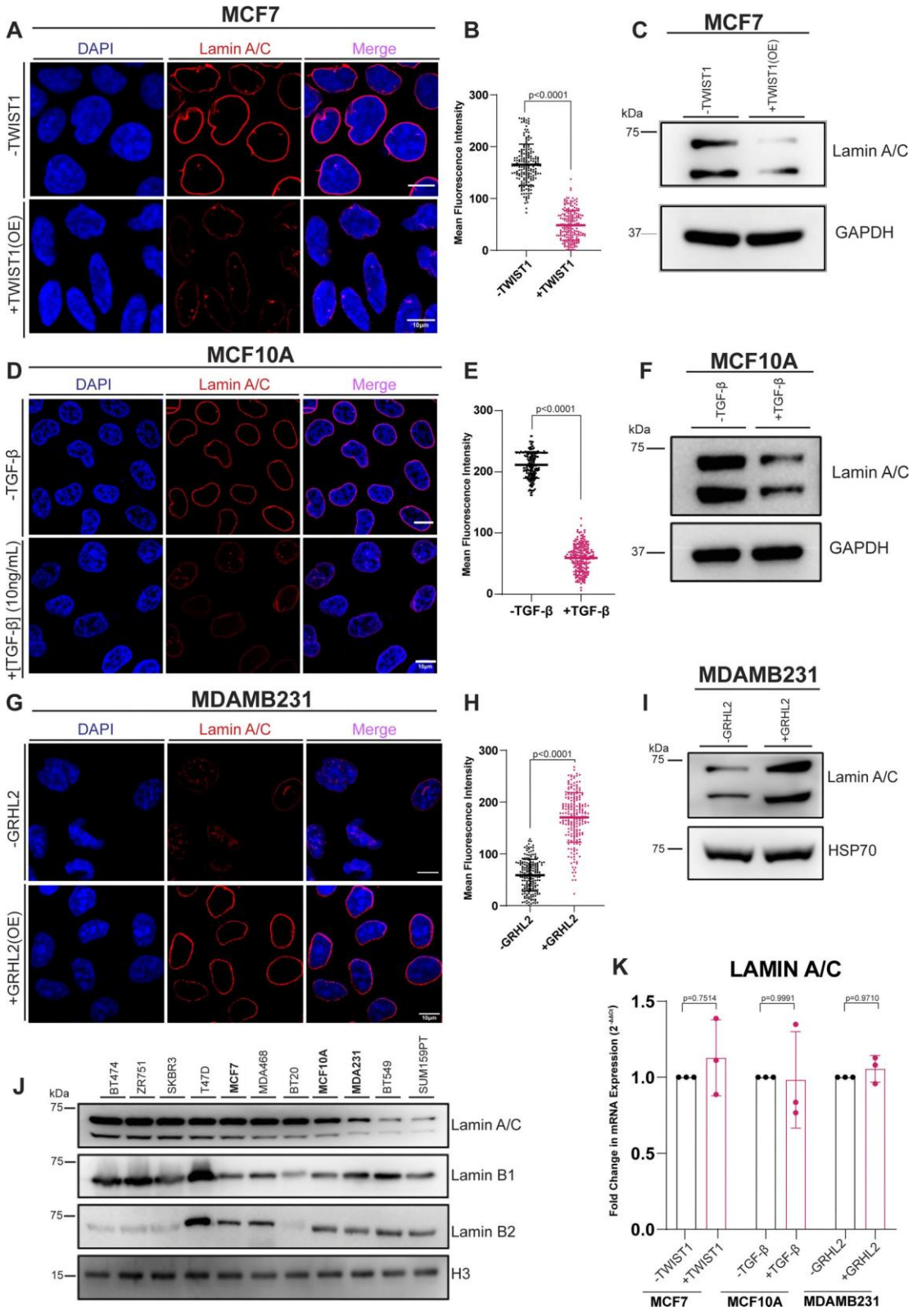

Figure 2. Impact of EMT induction on Lamin A/C expression. **(A, D, G)** Immunofluorescence analysis of Lamin A/C (red) in MCF7 **(A)**, MCF10A **(D)**, and MDAMB231 **(G)** cells upon EMT **(A, D)** or MET **(G)** nucleus (DAPI, blue). Scale bar ~10 μm. **(B, E, H)** Mean fluorescence intensity of Lamin A/C quantified by line scan analysis across the nucleus in MCF7 **(B)**, MCF10A **(E)**, and MDAMB231 **(H)** cells. Data represent mean ± SD from $N = 3$ independent biological replicates ($n = 250$). Unpaired Student's *t*-test was used to calculate *P*-values. **(C, F, I)** Immunoblot analysis of total Lamin A/C protein levels in MCF7 **(C)**, MCF10A **(F)**, and MDAMB231 **(I)** cells upon EMT **(C, F)** or MET **(I)** induction. GAPDH **(C, F)** and HSP70 **(I)** are loading controls. **(J)** Immunoblot analysis of Lamin A/C, Lamin B1, and Lamin B2 levels across 11 cell lines of breast origin with increasing mesenchymal characteristics. Loading control: Histone H3 **(K)** RT-qPCR analysis of LMNA transcript levels in MCF7 and MCF10A upon EMT and MET in MDAMB231 cells. Data represent mean ± SD ($N = 3$, $n = 9$). Unpaired Student's *t*-test was used to compute the *P*-values. Means are compared between **(B)** −Twist1 (control) and +Twist1; **(E)** −TGFβ (control) and **(H)** +TGFβ; −GRHL2 (control) and +GRHL2, statistical significance, *P*-value <0.05.

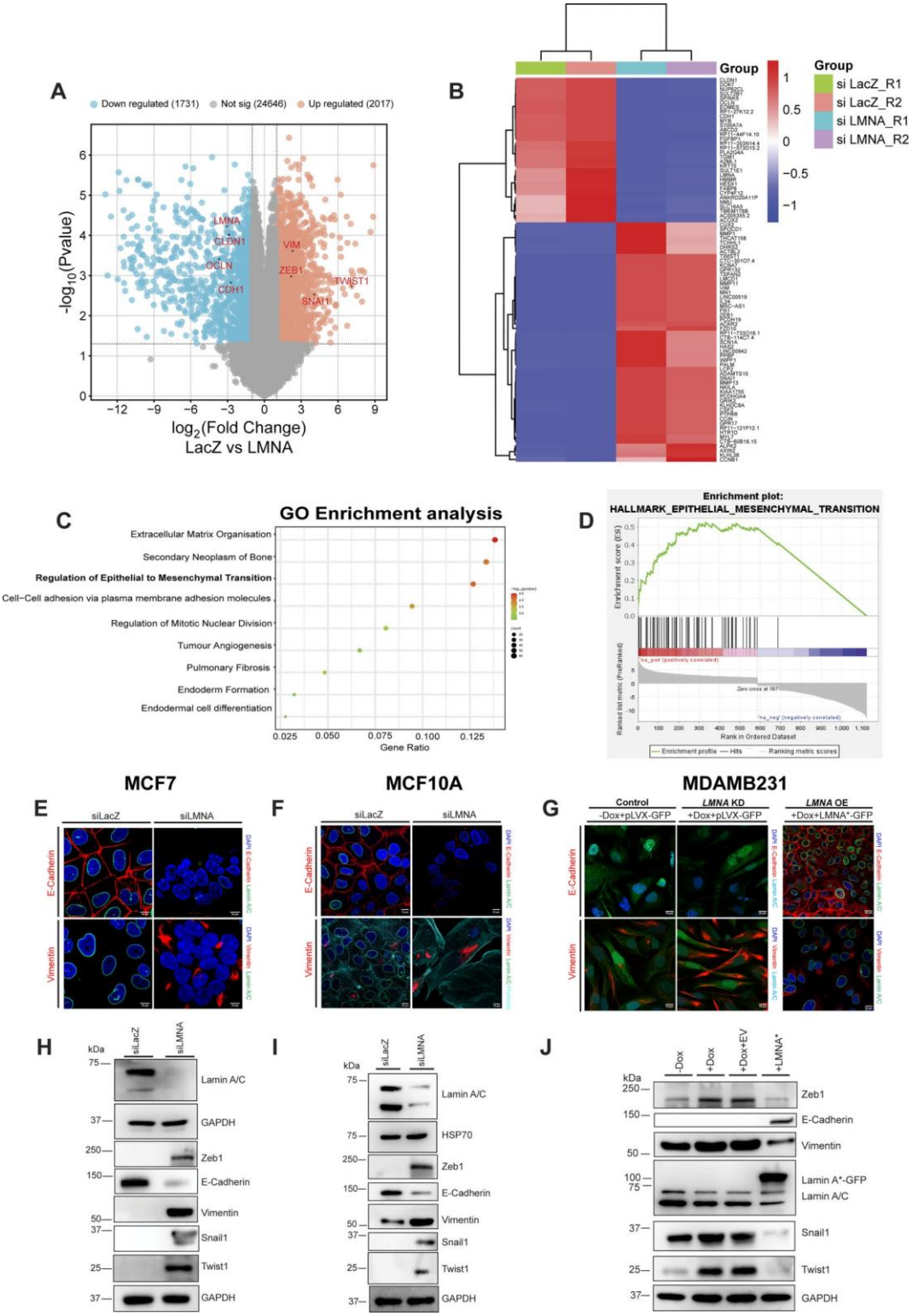

Figure 3. Effect of Lamin A/C perturbation on EMT and MET. **(A)** Volcano plot showing differentially expressed genes in MCF10A cells upon Lamin A/C knockdown. Downregulated, upregulated, and nonsignificant genes. **(B)** Heatmap of the top 50 [P <0.05; $\log_2$ Fold Change (FC) > 2] differentially expressed genes in MCF10A cells upon Lamin A/C knockdown. Downregulated and upregulated genes, respectively (N = 2 biological replicates). **(C)** GO enrichment analysis of differentially expressed genes ($P \leq 0.05$), showing the most enriched biological processes. **(D)** GSEA plot showing enrichment for EMT upon Lamin A/C knockdown (normalized enrichment score = 3.337). **(E, F)** Immunofluorescence analysis of MCF7 **(E)** and MCF10A **(F)** cells upon Lamin A/C knockdown. Lamin A/C, E-cadherin or Vimentin, and phalloidin. Nucleus (DAPI). Scale bars, ~10 μm **(G)** Immunofluorescence analysis of MDAMB231 cells overexpressing Lamin A*-GFP upon endogenous Lamin A/C depletion. E-cadherin (top panel) or Vimentin (bottom panel), and Lamin A/C (−Dox and +Dox panels only). Nucleus (DAPI). Scale bar ~10 μm. (**H-J**) Immunoblot analysis of EMT markers in MCF7 **(H)**, MCF10A **(I)** cells upon Lamin A/C knockdown, and MDAMB231 **(J)** cells upon Lamin A overexpression. RNA-Seq was performed in N = 2 independent biological replicates. Lamin A* denotes a full-length Lamin A construct resistant to doxycycline-induced depletion of endogenous Lamin A/C. Statistical significance, P-value <0.05.

ogy. This was corroborated by quantifications of AR, which showed a shift towards an epithelial-like architecture of cells [Supplementary Fig. S5B, B(i), and B(ii)].

Immunofluorescence analyses in both MCF10A and MCF7 cells showed a ~70% reduction in E-cadherin and a ~65% increase in Vimentin upon Lamin A/C loss (Fig. 3E and F; quantification: Supplementary Fig. S5C and D). Transcriptional upregulation of mesenchymal factors (*VIM, SNAI1, TWIST1*, and *ZEB1*) and decreased *CDH1*, was consistent with the mesenchymal morphology in MCF7 cells upon Lamin A/C depletion (Supplementary Fig. S5F). Immunoblotting showed a decrease in E-cadherin and increase in the levels of Vimentin, Snail1, Twist1, and Zeb1 in Lamin A/C–depleted cells (Fig. 3H and I).

In contrast, Lamin A overexpression in MDAMB231 cells (upon endogenous Lamin A/C depletion) showed a significant upregulation in the transcript levels of E-cadherin (~95% increase), and downregulation of mesenchymal regulators (*VIM, SNAI1, TWIST1*, and *ZEB1*; Supplementary Fig. S5G). Immunoblotting and immunofluorescence analyses reiterate these effects, showing enhanced E-cadherin expression and suppression of mesenchymal markers (Fig. 3G and J; quantification: Supplementary Fig. S5E).

We also determined the EM status in MCF7 and MDAMB231 cells upon depleting B-type Lamins (Lamin B1 and Lamin B2). Depletion of B-type Lamins did not significantly alter the expression of EM markers underscoring a specific role of Lamin A/C in regulating EM plasticity (Supplementary Fig. S5H and I).

Impact of EMT or MET induction on the lamin interactome

Nuclear Lamins play a critical role in the maintenance of nuclear integrity, chromatin organization and gene regulation [45]. Lamina-associated domains (LADs) are genomic regions enriched for nuclear Lamins and are marked by histone marks H3K9me3 and H3K27me3 associated predominantly with heterochromatin [46, 47]. We next performed immunoblotting upon EMT induction, which showed a decrease (~50%) in the total levels of H3K9me3 and H3K27me3, suggesting a marked decrease in inactive histone marks [Supplementary Fig. S6A(i) and B(i)]. In contrast, MET induction increased levels of these heterochromatic marks by ~60% [Supplementary Fig. S6C(i)]. Notably, Lamin A/C knockdown in the epithelial cells (MCF7 and MCF10A) also showed a significant reduction (~50%) in H3K27me3 and H3K9me3, reinforcing the functional association between Lamin A/C and chromatin compaction [Supplementary Fig. S6A(ii) and B(ii)]. Furthermore, Lamin A overexpression, showed an increase in H3K27me3 and H3K9me3 in MDAMB231 cells [Supplementary Figure S6C(ii)], consistent with the role of Lamin A/C in the maintenance of heterochromatin [48].

Given the dynamic changes in heterochromatin markers during EMT and MET, we next examined whether the interactors of Lamin A/C are differentially enriched across E and M states [19, 49, 50]. We performed Co-IP followed by MS to identify the sub-interactome of Lamin A/C in the epithelial and mesenchymal states. While, MS analyses identified 44 unique protein-protein interactors, including EZH2, in Lamin A/C pull-downs from epithelial MCF7 cells, 90 unique interactors including CCNB1 and pCDK1, among others were detected upon EMT induction in MCF7-TWIST1 cells. A total of 49 interactions (LMNB1, LMNB2, EHMT2, SUV39H1, PRRX1) were common to both the control and Twist1 overexpressing MCF7 cells (Fig. 4 A; PCA analysis Supplementary Fig. S6D). In contrast, MET induction in MDA-MB-231 cells markedly reconfigures the Lamin A/C interactome. In control cells, 103 unique interactors were identified involving (CCNB1 and pCDK1). In contrast, GRHL2 mediated MET-induction revealed 71 distinct interactors, including (EZH2). Notably, 72 proteins, including (LMNB1, LMNB2, CBX5, EHMT2, SUV39H1) were consistently associated with Lamin A/C in both control and GRHL2-overexpressing MDAMB231 cells (Fig. 4B; PCA analysis Supplementary Fig. S6E).

GO pathway enrichment analysis of the Lamin A/C interactome in epithelial MCF7 cells revealed that its interacting partners are primarily involved in the regulation of gene expression, messenger RNA (mRNA) metabolic processes, ribonucleoprotein complex assembly, and regulation of mRNA stability. In contrast, Twist1-mediated EMT shows a shift in the Lamin A/C interactome, enriching for pathways related to cell cycle regulation, nuclear envelope disassembly and DNA damage repair (Supplementary Fig. S7A and B). Remarkably, GRHL2-mediated MET re-established interactions between Lamin A/C and proteins involved in gene expression regulation, such as EZH2 (Supplementary Fig. S7C and D). These findings suggest that the Lamin A/C interactome is dynamically reprogrammed during EMT and MET, reflecting the functional requirements of epithelial versus mesenchymal cell states [51].

A key finding from the mass spectroscopy studies unravelled dynamic Lamin A/C interactome as it showed a reversible association with histone methyltransferase EZH2, which was enriched in MCF7 and upon MET induction in MDAMB231 cells. Interestingly, Lamin A/C-EZH2 interaction was undetectable in (i) MDAMB231 cells (ii) upon Twist1 induction in MCF7 cells. In contrast, Lamin A/C interacts with phosphorylated CDK1 (pCDK1) predominantly in the mesenchymal cells (MCF7-TWIST1 and control: MDAMB231). However, this interaction was undetectable upon MET induction (Fig. 4C and D). Taken together, these findings suggest a switch in the interactions of Lamin A/C, consistent with the cellular state, with Lamin A/C involved in chromatin-modifying functions via EZH2 in epithelial cells, while in mesenchymal states, Lamin A/C facilitates cell cycle regulation through its interaction with pCDK1.

To validate these findings, we performed Co-IP of Lamin A/C followed by immunoblotting for EZH2 upon EMT and MET induction. Co-IP results showed a loss of the Lamin A/C–EZH2 interaction upon EMT induction and its restoration during MET (Fig. 4E–G). Furthermore, immunoprecipitation with either of the B-type Lamins (Lamin B1 or B2), did not show an interaction with EZH2, indicating that this association with EZH2 is specific to Lamin A/C. However, both the B-type Lamins interact with the methyltransferases G9a and SUV39H1, consistent with previous studies [52]. Of note, these interactions with the B-type Lamins were unaltered upon EMT induction in MCF10A cells (Supplementary Fig. S7E and F).

To further determine if Lamin A/C interacts with PRC2 components other than EZH2, we performed Co-IP of Lamin A/C, followed by immunoblotting for PRC2 components—EED and Suz12—in MCF10A cells. This showed a specific association with EZH2, but not with other PRC2 components

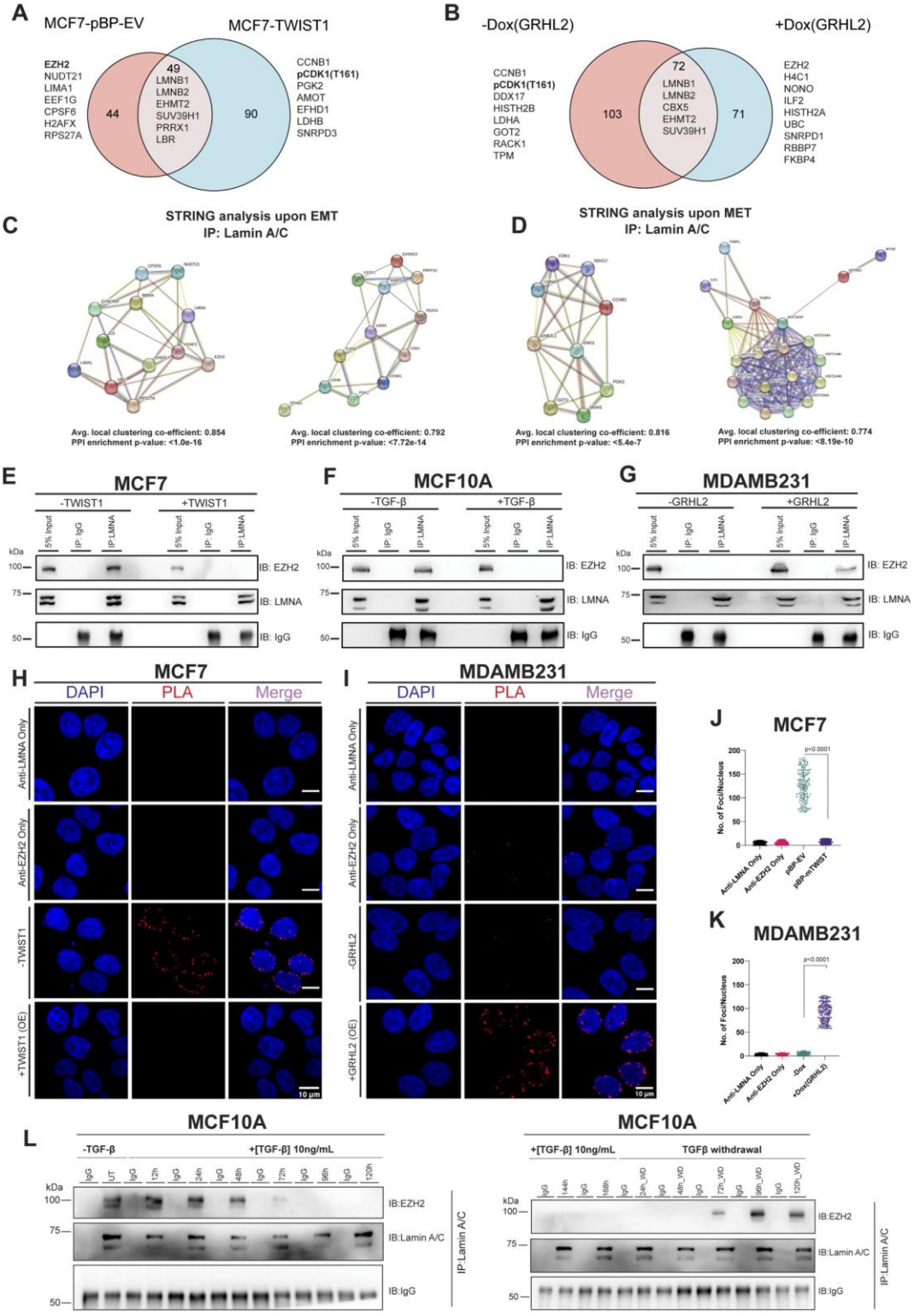

Figure 4. Dynamic Remodeling of the Lamin A/C Interactome During EMT and MET. **(A, B)** Venn diagrams showing unique and common interactors of Lamin A/C identified by (Immunoprecipitation - Mass Spectroscopy) IP-MS in MCF7 versus MCF7-TWIST1 **(A)** and MDAMB231 versus MDAMB231-GRHL2 **(B)**. **(C, D)** Representative STRING network analysis of Lamin A/C interactors in MCF7 versus MCF7-TWIST1 **(C)** and MDAMB231 versus MDAMB231-GRHL2 **(D)**. (**E-G**) Co-IP of Lamin A/C in MCF7 **(E)**, MCF10A **(F)**, and MDAMB231 **(G)** cells upon EMT **(E, F)** or MET **(G)** induction, followed by immunoblotting for EZH2 and Lamin A/C. IgG: isotype control, an approximately equal amount of antibody is used for immunoprecipitation. **(H, I)** Proximity ligation assay (PLA) detects Lamin A/C–EZH2 interaction in MCF7 **(H)** and MDAMB231 **(I)** cells upon EMT **(H)** or MET **(I)** induction. PLA signal (red), nucleus (blue, DAPI). Scale bar: ~10 µm. **(J, K)** Quantification of PLA signal in MCF7 **(J)** and MDAMB231 **(K)** cells. Data represent mean ± SD from $N = 3$, independent biological replicates, and P-values calculated by one-way ANOVA and means are compared between pBp-EV and pBP-Twist **(J)** and −Dox (GRHL2) and +Dox (GRHL2) **(K)**. **(L)** Time-course analysis of Lamin A/C–EZH2 interaction by immunoprecipitation of Lamin A/C in MCF10A cells during EMT progression [~12 to ~168 h (~7 days) post-TGF-β treatment] and MET recovery [5 days post-TGF-β withdrawal (WD)], assessed by Co-IP and immunoblotting. IgG: isotype control, statistical significance, P-value <0.05.

such as SUZ12 or EED (Supplementary Fig. S7G). To assess the integrity of the PRC2 complex upon EMT, EZH2 was immunoprecipitated from TGF-β-treated MCF10A cells, where it retained its association with SUZ12 and EED, indicating that the Lamin A/C–EZH2 interaction is independent of the PRC2 complex (Supplementary Fig. S7H).

To further substantiate the interaction between Lamin A/C and EZH2, we performed PLA upon EMT and MET induction. We detected a striking decrease (∼10-fold) in the number of PLA foci upon EMT induction, suggesting a loss of Lamin A/C–EZH2 interaction (Fig. 4H and J). In contrast, GRHL2-mediated MET induction re-established the interaction between Lamin A/C and EZH2, as demonstrated by a significantly higher number (∼10-fold) of PLA foci (Fig. 4I and K).

To investigate the temporal dynamics of the Lamin A/C–EZH2 interaction, we performed a time-course assay following EMT induction via TGF-β treatment and subsequent MET induction by withdrawal of TGF-β. Immunoprecipitation of Lamin A/C at different time points [∼12–168 h (∼7 days)] revealed a progressive loss of interaction with EZH2, with complete dissociation at ∼72 h post-EMT induction. Conversely, withdrawal of TGF-β [∼12–120 h (∼5 days)] restored Lamin A/C–EZH2 interaction after ∼72 h (Fig. 4L). These findings further corroborate a dynamic and reversible association between Lamin A/C and EZH2. In summary, these studies reveal that EMT induction disrupts the Lamin A/C–EZH2 interaction, with a concomitant decrease in heterochromatin marks, while MET promotes this interaction and re-establishes heterochromatin marks.

CDK1-mediated phosphorylation regulates Lamin A/C–EZH2 interaction and EMT progression

To address the molecular basis of Lamin A/C–EZH2 interaction, we performed HADDOCK, which predicted an interface between the head domain of Lamin A/C (Arg25, Arg28) and EZH2 (Asp136, Asp140; Supplementary Fig. S8A) [53]. We co-overexpressed GFP-tagged Lamin A and FLAG-tagged EZH2 deletion constructs into HEK293T cells. Co-IP revealed that Lamin A binds to EZH2 at the Ala301–Ala500 region, whereas reverse Co-IP (using Lamin A deletion constructs) shows that EZH2 interacts with the head domain of Lamin A (Fig. 5A and B).

Putative CDK1 phosphorylation sites were identified to be the region of interaction (through deletion experiments) between Lamin A/C and EZH2 (Supplementary Fig. S8B), suggesting CDK1 regulation. IP-MS also showed CDK1 enrichment with Lamin A/C in Twist1-overexpressing MCF7 and untreated MDAMB231 cells. PLA demonstrated that EMT induction in MCF10A cells enhanced the interaction of Lamin A/C with phosphorylated CDK1 (pCDK1-T161; Fig. 5C and F), which was further corroborated by Co-IP. In contrast, induction of MET in MDAMB231 cells abolished this interaction (Supplementary Fig. S8C–E).

Since CDK1 phosphorylates Lamin A/C and EZH2 independently, immunoblotting revealed increased ratios of pLMNA(S22)/LMNA and pEZH2(T345)/EZH2 along with elevated pCDK1-T161 levels during EMT, whereas MET induction markedly decreased these phosphorylation events (Supplementary Fig. S8F–I) [54, 55]. To address the effect of altered CDK1 activity during EMT/MET on cell cycle, we performed FACS profiling, which showed an increase in cell numbers in G2/M upon EMT (in MCF7 and MCF10A) and decreased cell numbers in G2/M upon MET (in MDAMB231; Supplementary Fig. S8J and K). We surmised that increased CDK1 activity could destabilize Lamin A/C–EZH2 binding during EMT. To validate this finding, we performed PLA, which showed a loss of Lamin A/C–EZH2 interaction upon EMT induction, which was restored upon CDK1 inhibition with RO-3306 (∼10-fold increase in PLA signal; Fig. 5D and G).

MCF10A cells treated with TGF-β showed an increase in mesenchymal markers (ZEB1, SNAI1, TWIST1, Vimentin) and reduction in E-cadherin. To determine if CDK1 inhibition alters the dynamics of EMT markers, EMT-induced cells were treated with the CDK1 inhibitor (RO-3306). This showed the attenuation of mesenchymal markers, while E-cadherin expression was sustained (Supplementary Fig. S9A and C–E). A similar effect was observed in Twist1-overexpressing MCF7 cells, where CDK1 inhibition suppressed EMT induction (Fig. 5H and K, and Supplementary Fig. S9I).

Since CDK1 phosphorylates EZH2 at Thr345, leading to its proteasomal degradation, we asked if phosphorylation contributes to the dissociation of EZH2 from Lamin A/C. Upon EMT induction, Lamin A/C levels were markedly reduced, resulting in the loss of colocalization with EZH2. However, this interaction was restored when cells were treated with the proteasomal inhibitor MG132 (Fig. 5I). Interestingly, MG132 treatment also attenuated EMT-associated phenotypic changes (Fig. 5J and L, and Supplementary Fig. S9B, F–H, and J).

To further assess the consequence of increased CDK1 activity in regulating cell cycle and EM status of cells, we synchronized MCF10A cells by double-thymidine block followed by release and treated cells with TGF-β. While Cyclin D1 levels remained unaltered, Cyclin B1 was upregulated at both mRNA (∼25-fold) and protein (∼15-fold) levels in mesenchymal cells (Supplementary Fig. S10A and B). Flow cytometry showed a ∼3-fold increase in the G2/M sub-population (Supplementary Fig. S10C and D). BrdU incorporation assays showed no changes in the intensity of BrdU, negating a G1 arrest (Supplementary Fig. S10E).

To determine the state of cells at G2/M, we examined the levels of H3S10p - a marker of late mitosis [56]. Immunofluorescence showed a marked reduction of H3S10p-positive cells in TGF-β-treated cells (∼0.67 ± 0.08%; control: ∼19 ± 7.8%; Supplementary Fig. S10F). Consistently, immunoblotting of synchronized, and FACS-sorted G2/M cells revealed reduced H3S10p in EMT-induced cells (Supplementary Fig. S10G). These results collectively indicate that the cells undergoing EMT are arrested at the late S-to-early G2 transition.

We next asked whether CDK1 activity per se, rather than cell cycle arrest, is essential for EMT. In Twist1-overexpressing MCF7 cells, nocodazole-induced prometaphase arrest did not impair EMT, whereas CDK1 inhibition with RO-3306 markedly suppressed EMT (Supplementary Fig. S11A). Similarly, TGF-β did not induce EMT in thymidine-arrested MCF10A cells, but ectopic overexpression of a phosphomimetic CDK1 mutant (T161D) restored EMT progression (Supplementary Fig. S11B).

To directly test whether CDK1 activity regulates Lamin A/C–EZH2 stability, we performed Co-IP assays in thymidine-arrested MCF10A cells expressing CDK1 phosphomutants. The Lamin A/C–EZH2 interaction was disrupted

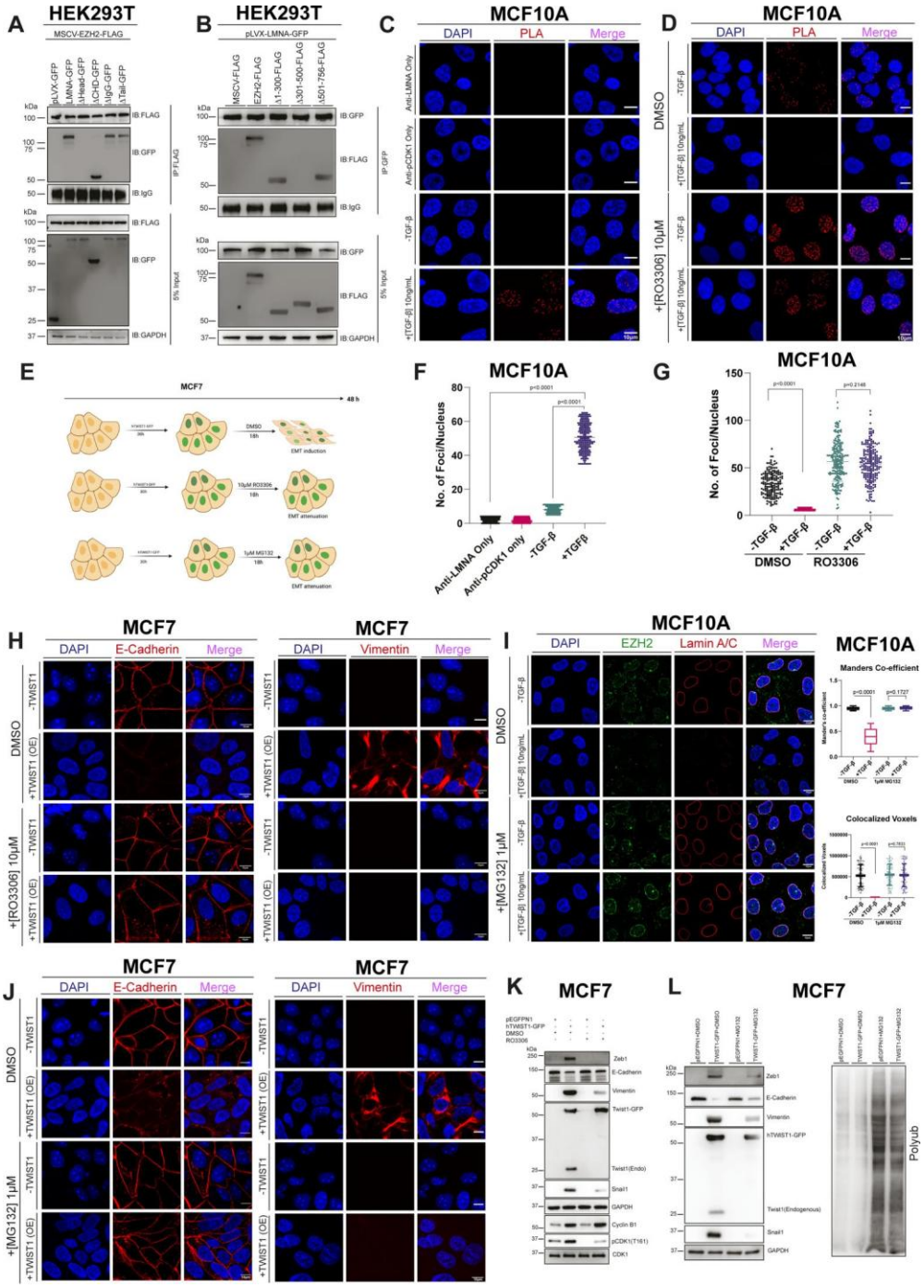

Figure 5. CDK1-mediated phosphorylation regulates Lamin A/C–EZH2 interaction and EMT progression. **(A)** Co-IP of FLAG in HEK293T cells co-transfected with full-length EZH2-FLAG and Lamin A-GFP deletion mutants (*Δ*Head 1–29, *Δ*Rod 31–387, *Δ*IgG 428–549, *Δ*Tail 550–664 of Lamin A). **(B)** Co-IP of GFP in HEK293T cells co-transfected with full-length Lamin A-GFP and EZH2-FLAG deletion mutants (*Δ*1–300, *Δ*301–500, *Δ*501–746 of EZH2). **(C)** PLA detects Lamin A/C–pCDK1(T161) interaction in MCF10A cells treated with 10 ng/ml TGF-β for ∼7 days. Nucleus (DAPI), PLA signal in red. Scale bar ∼10 μm **(D)** PLA detects Lamin A/C– EZH2 interaction in MCF10A cells treated with DMSO or 10 μM RO3306 for ∼18 h in the ± TGF-β for ∼7 days, nucleus (DAPI). PLA signal in red. Scale bar ∼10 μm. **(E)** Schematic representation of RO3306 and MG132 treatment in MCF7 cells **(F)** Quantification of PLA foci/nucleus of the data in **(C)**. *P*-values were calculated using ANOVA. Means are compared between +TGFβ and –TGFβ (control) conditions with the single antibody control. **(G)** Quantification of PLA foci/nucleus of the data in **(D)**. Statistical significance was determined using unpaired Student's *t*-tests. Means are compared between +TGFβ and –TGFβ (control) conditions within each group (DMSO and RO-3306). **(H)** Immunofluorescence of MCF7 cells transiently transfected with pEGFP-N1 or Twist1-GFP and treated with 10 μM RO3306 for 18 h. nucleus (DAPI). Scale bar ∼10 μm **(I)** Immunofluorescence and quantification of colocalized voxels and Mander's coefficient for Lamin A/C and EZH2 in MCF10A cells ± TGF-β and 1 μM MG132. Nucleus (DAPI). Scale bar ∼10 μm. Statistical significance was determined using unpaired Student's *t*-tests. Means are compared between +TGFβ and –TGFβ (control) conditions within each treatment group (DMSO and RO-3306). **(J)** Immunofluorescence of MCF7 cells treated with MG132 and transient overexpression of hTWIST1-GFP and stained for E-cadherin and Vimentin ; nucleus (DAPI). Scale bar ∼10 μm. **(K)** Immunoblotting for EMT markers in MCF7 treated with RO3306 and Twist1-GFP in MCF7 **(L)** Immunoblotting for EMT markers in MCF7 cells treated with MG132 and Twist1-GFP in MCF7. For all experiments, data are represented as mean ± SD from $N = 3$ three independent biological replicates, statistical significance, *P*-value <0.05.

upon expression of the phosphomimetic mutant (T161D; Supplementary Fig. S11C).

In summary, these findings suggest that EMT progression is driven by elevated CDK1 activity leading to late S-to-early G2 arrest. CDK1 phosphorylates Lamin A/C and EZH2, disrupts the Lamin A/C–EZH2 complex and promotes EZH2 degradation, thereby facilitating EMT [57–59].

Regulatory role of phosphorylation in the interaction of Lamin A/C-EZH2

Phosphorylation of nuclear lamins regulate nuclear organization and chromatin dynamics [60, 61]. Since Lamin A/C and EZH2 are involved in chromatin organization and transcriptional regulation, we surmised that perturbing their phosphorylation sites could modulate EMT/MET. Furthermore, CDK1-mediated phosphorylation impacts lamin organization, prompting an in-depth analysis of how CDK1 phosphorylation affects Lamin A/C–EZH2 binding. Specifically, Serine 22 (S22) in Lamin A/C and Threonine 345 (T345) in EZH2—both established CDK1 phosphorylation sites with roles in protein–protein interactions and nuclear dynamics—were selected for site-directed mutagenesis to mimic either a phosphorylated (phosphomimetic: Lamin A–S22D, EZH2–T345D) or nonphosphorylated (phospho-deficient: Lamin A–S22A, EZH2–T345A) state [62].

Lamin A/C knockdown lines (doxycycline-inducible) of MCF7 cells were generated, followed by ectopic overexpression of (i) GFP–Lamin A (shRNA resistant), (ii) S22A, and (iii) S22D constructs. To ensure homogeneity, GFP-positive cells were FACS-sorted. Additionally, TWIST1-GFP was transiently overexpressed (∼48 h) and selected with G418 to enrich TWIST1-expressing cells [(Fig. 6A), schematic for generation of EZH2 mutants (Fig. 6B)]. Immunoprecipitation of Lamin A/C followed by immunoblotting for EZH2 showed that full-length Lamin A and S22A retained their interaction with EZH2, independent of TWIST1-induced EMT, whereas the S22D variant did not bind to EZH2, irrespective of EMT status. These results indicate that phosphorylation at S22 disrupts Lamin A/C–EZH2 interaction (Fig. 6C).

We adopted a similar strategy in MDAMB231 cells stably expressing GRHL2 to induce MET. Consistent with findings in MCF7, full-length Lamin A and S22A interacted with EZH2, while the S22D variant did not (Fig. 6D). Thus, phosphorylation at Ser22 consistently inhibits Lamin A/C–EZH2 interaction during both EMT and MET.

To further delineate the role of EZH2 phosphorylation, T345A and T345D mutants were tested in MCF7 (±TWIST1) and MDAMB231 (±GRHL2) cells. In both contexts, full-length EZH2 and T345A retained their interaction with Lamin A/C, whereas the T345D variant failed to bind Lamin A/C (Fig. 6E and F).

Taken together, these data demonstrate that phosphorylation at either S22 in Lamin A/C or T345 in EZH2 prevents complex formation. We further validated the interaction between the mutants of Lamin A/C and EZH2 through immunofluorescence studies and found that the full length (control) and phosphodeficient mutants interact with each other (Lamin A/C and EZH2), while phosphomimetic mutants lost the interaction irrespective of the presence of TGF-β (Fig. 6G–J).

To determine if there is a requirement for dual phosphorylation of Lamin A and EZH2, we co-transfected HEK293T cells with combinations of Lamin A–GFP and EZH2–FLAG (wild-type, phospho-deficient, or phospho-mimetic). Co-IP revealed robust binding only when both proteins are in their unphosphorylated or phospho-deficient forms. Notably, phosphorylation of either Lamin A or EZH2 alone was sufficient to weaken or abolish this interaction. Lamin A/C–EZH2 complex is sensitive to phosphorylation of either partner. Therefore, the disruption of this interaction does not require both interacting partners to be phosphorylated (Supplementary Fig. S12A). Importantly, the localization of the Lamin A and EZH2 mutants was validated by immunofluorescence assays, which predominantly showed a nuclear localization (Supplementary Fig. S12B and C).

Since phosphorylation impacts cell cycle dynamics, we next examined how phosphomutants of Lamin A/C and EZH2 affect cell cycle progression. MCF10A cells expressing Lamin A or EZH2 mutants were synchronized by double-thymidine block and released (for ∼18 h), followed by FACS profiling. Notably, phosphomimetic mutants (∼25%–30%) showed an increased number of cells in G2/M compared with full-length and phospho-deficient forms (∼6%–9%; Supplementary Fig. S13A and B). To further examine the effect of phosphomutants of Lamin A and EZH2 on cell cycle, we performed PI-FACS, BrdU incorporation, and H3S10p staining. BrdU incorporation was comparable across full-length, phospho-deficient, and phospho-mimetic constructs (∼85% BrdU positive cells), which excluded G1 arrest (Supplementary Fig. S13C and D). However, H3S10p staining revealed that full-length and phospho-deficient mutants progressed normally through mitosis (∼10% H3S10p-positive cells), whereas phospho-mimetic mutants (S22D, T345D) stalled at G2/M as indicated by PI-FACS, but displayed markedly reduced H3S10p positivity (<2%), suggesting an arrest in late S-to early G2 phase of the cell cycle (Supplementary Fig. S13E and F).

Lamin A and EZH2 phosphorylation determines the dynamics of EMT

We next sought to determine the effect of Lamin A-EZH2 phosphorylation on EM plasticity. To address this question, we generated cell lines expressing either phosphodeficient or phosphomimetic mutants of Lamin A (S22A or S22D) and EZH2 (T345A or T345D) in the background of endogenous protein depletion.

Remarkably, the overexpression of the phosphomimetic Lamin A mutant (S22D) disrupts the Lamin A–EZH2 interaction, showing a pronounced mesenchymal phenotype, characterized by the upregulation of Vimentin, TWIST1, SNAI1, and ZEB1, and downregulation of E-cadherin, notwithstanding the absence of EMT inducers. In contrast, cells expressing either full-length Lamin A or the phosphodeficient mutant (S22A) retain their interaction with EZH2 and their epithelial features, even under EMT-inducing conditions such as TGF-β or TWIST1 overexpression (Fig. 7A, E, and F; quantification in Supplementary Fig. S14A–E).

Similarly, overexpression of full length or the phosphodeficient Lamin A (S22A) mutant (both capable of binding EZH2), was sufficient to induce a robust epithelial state, marked by high E-cadherin levels and reduced mesenchymal markers, even without GRHL2-mediated MET induction. In contrast, knockdown of Lamin A/C or overexpression of Lamin A (S22D)—which does not interact with EZH2—

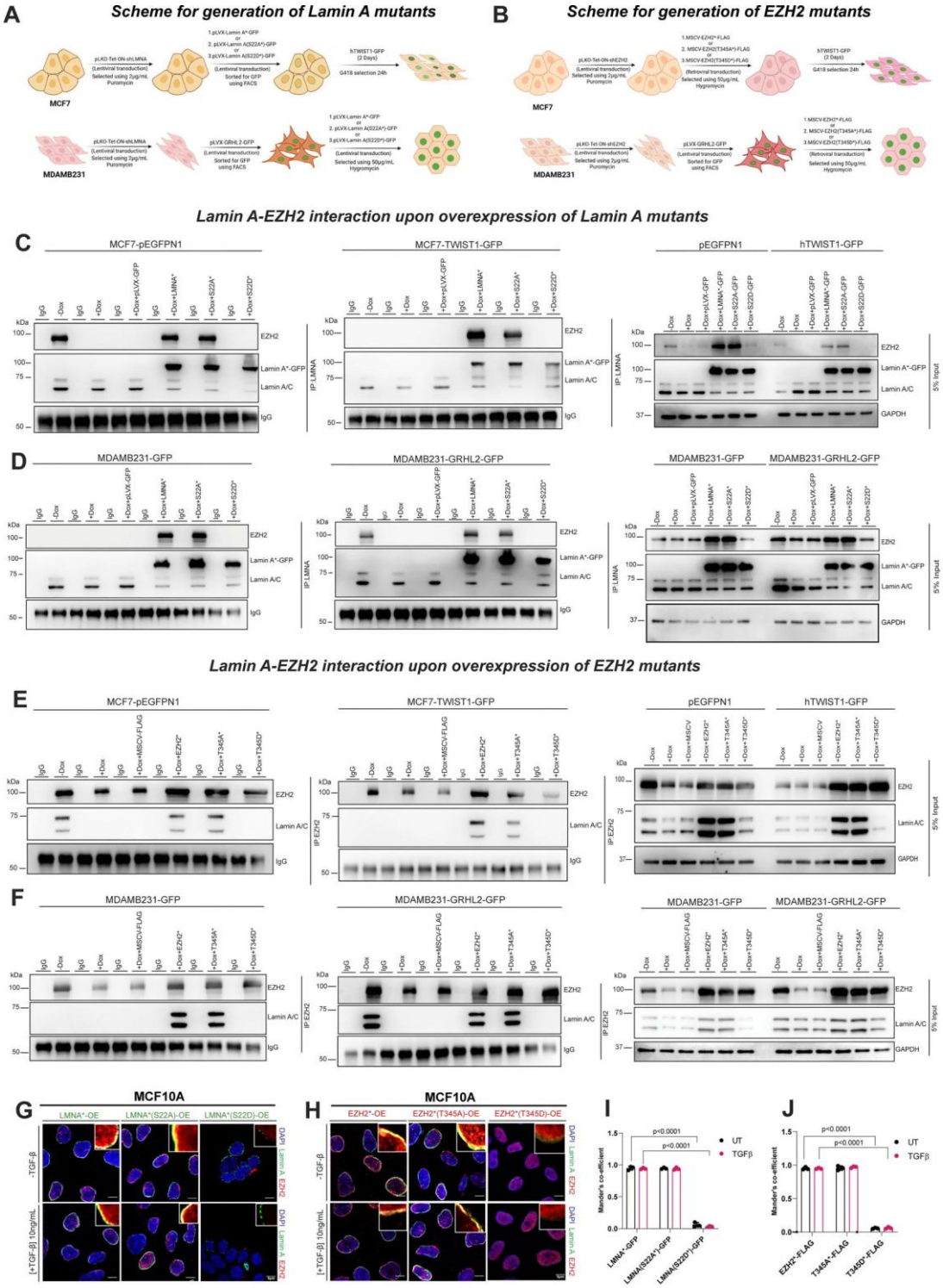

Figure 6. Phosphorylation-dependent regulation of Lamin A/C–EZH2 binding in EMT and MET. **(A, B)** Schematic representation of the workflow for generating stable cell lines with inducible knockdown of Lamin A **(A)** or EZH2 **(B)**, followed by rescue with full-length, phosphodeficient, or phosphomimetic mutants. **(C, D)** Co-IP of Lamin A in MCF7 and MDAMB231 cells after doxycycline-induced Lamin A/C depletion and rescue with full-length, phosphodeficient (S22A), or phosphomimetic (S22D) Lamin A. TWIST1-GFP was transiently overexpressed in MCF7 cells, and GRHL2-GFP was stably overexpressed in MDAMB231 cells. **(E, F)** Coimmunoprecipitation of EZH2 in MCF7 and MDAMB231 cells after doxycycline-induced EZH2 depletion and rescue with full-length, phosphodeficient (T345A), or phosphomimetic (T345D) EZH2. TWIST1-GFP was transiently overexpressed in MCF7 cells, and GRHL2-GFP was stably overexpressed in MDAMB231 cells. **(G)** Immunofluorescence images of MCF10A cells showing the extent of colocalization between Lamin A [full-length, phosphodeficient (S22A), or phosphomimetic (S22D)] and EZH2 ± TGF-β. Nucleus (DAPI). Scale bar ~10 μm. **(H)** Immunofluorescence images of MCF10A cells showing the extent of colocalization between EZH2 [full-length, phosphodeficient (T345A), or phosphomimetic (T345D)] nucleus (DAPI). Scale bar ~10 μm. **(I, J)** Quantification of Lamin A and EZH2 colocalization in MCF10A cells using Mander's coefficient. Unpaired Student's *t*-test was used to compute the *P*-value. Means are compared between **(I)** LMNA-GFP (UT; control) versus LMNA-S22D (UT) and LMNA-GFP (TGFβ; control) versus LMNA-S22D (TGFβ). **(J)** EZH2-FLAG (UT; control) versus EZH2-T345D (UT) and EZH2-FLAG (TGFβ; control) versus EZH2-T345D (TGFβ). Statistical significance, *P*-value <0.05.

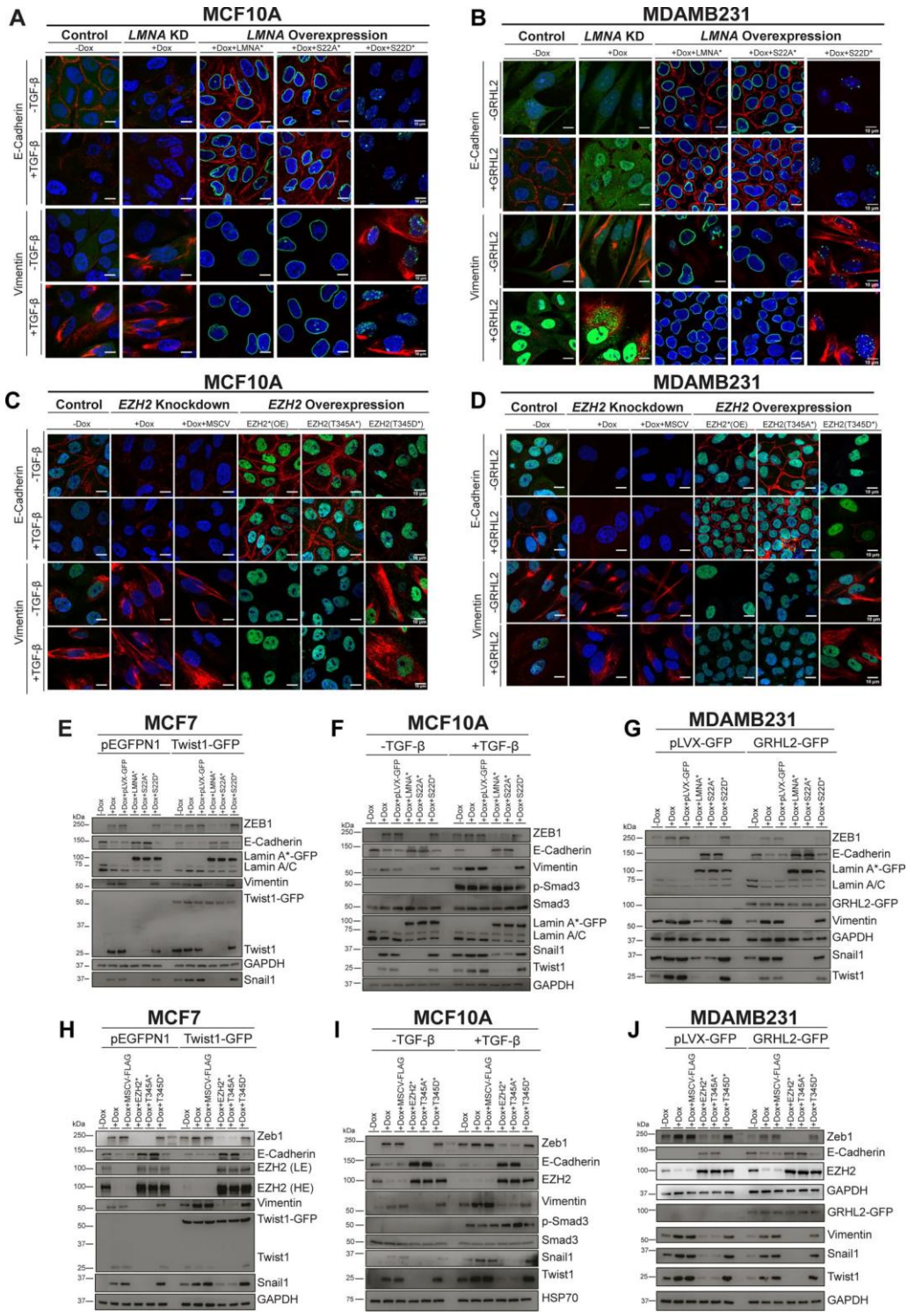

Figure 7. Phosphorylation-dependent regulation of EZH2 and Lamin A/C during EMT and MET. Representative mid-optical sections of immunofluorescence images showing the effect of Lamin A and EZH2 mutants on EMT (in MCF10A) and MET (in MDAMB231). MCF10A **(A, C)** and MDAMB231 **(B, D)**. Cells were transduced with full-length, phospho-deficient, or phospho-mimetic constructs of Lamin A **(A, B)** or EZH2 **(C, D)** following doxycycline-induced knockdown (0.5 μg/ml, 48 h) of endogenous Lamin A/C or EZH2. EMT was induced in MCF10A cells by TGF-β treatment (10 ng/ml, ~7 days), while MET was induced in MDAMB231 cells by stable, constitutive overexpression of GRHL2. EZH2 was immunostained in green; E-cadherin and Vimentin were immunostained in red. Lamin A constructs were GFP-tagged. Nucleus (blue, DAPI). Scale bar ~10 μm. **(E, F)** Immunoblot analysis of EMT marker expression in MCF7 and MCF10A cells upon Lamin A/C knockdown and rescue with full-length, phospho-deficient (S22A), or phospho-mimetic (S22D) Lamin A-GFP. EMT was induced by TWIST1 overexpression (~48 h) in MCF7 cells or by 10ng/ml TGF-β (~7 days) in MCF10A cells. **(G)** EM marker expression in cells with Lamin A/C knockdown was rescued with full-length, phospho-deficient (S22A) or phospho-mimetic (S22D) Lamin A/C. MET was induced by GRHL2 overexpression. **(H, I)** Immunoblot analysis of EMT marker expression in MCF7 and MCF10A cells upon EZH2 knockdown and rescue with full-length, phospho-deficient (T345A), or phospho-mimetic (T345D) EZH2-FLAG. EMT was induced by TGF-β (~7 days) in MCF10A cells or by TWIST1 overexpression (~48 h) in MCF7 cells. **(J)** EM marker expression in cells with EZH2 knockdown rescued with full-length, phospho-deficient (T345A), or phospho-mimetic (T345D) EZH2. MET was induced by GRHL2 overexpression.

resulted in the persistence of mesenchymal characteristics (Fig. 7B and G). Notably, MDAMB231 cells exhibited partial MET upon co-overexpression of GRHL2 and Lamin A (S22D), or GRHL2 overexpression combined with Lamin A/C depletion (Supplementary Fig. S14F–J). This reinforces the significance of the Lamin A–EZH2 interaction in facilitating MET and repressing mesenchymal genes.

To delineate the role of EZH2 phosphorylation in this regulatory axis, we introduced phosphodeficient (T345A) and phosphomimetic (T345D) EZH2 mutants in the background of EZH2 depletion in epithelial (MCF7, MCF10A) and mesenchymal (MDAMB231) cells. In MCF7 and MCF10A cells, overexpression of the phosphomimetic EZH2 mutant (T345D)—deficient in Lamin A/C binding—shows an EMT-like phenotype, including loss of E-cadherin and induction of mesenchymal markers, independent of external EMT induction. Conversely, overexpression of full length EZH2 or the phosphodeficient EZH2 mutant (T345A), which retains its interaction with Lamin A/C, maintained epithelial properties and resists EMT induction, even in the presence of TWIST1 or TGF-β (Fig. 7C, H, and I; quantification: Supplementary Fig. S14K–N).

Overexpression of full length or phosphodeficient EZH2 (T345A) promoted MET in MDAMB231 cells, consistent with elevated E-cadherin and suppression of mesenchymal markers, independent of GRHL2 overexpression. However, overexpression of the phosphomimetic EZH2 (T345D) or EZH2 knockdown (both of which abrogate Lamin A/C interaction), exacerbated mesenchymal properties. Overexpression of EZH2 (full length) or EZH2 (T345A) in the background of GRHL2 overexpression, facilitates transition of MDAMB231 cells to an epithelial-like phenotype [EZH2(OE) and EZH2(T345A)—E-cadherin (integrated density): 2108 ± 516 and 3560 ± 532, respectively], whereas EZH2 (T345D) or EZH2 depletion only partially reversed cells to an epithelial phenotype [EZH2(T345D)—E-cadherin (integrated density): 320 ± 58] as it maintains mesenchymal marker expression and a hybrid phenotype [Fig. 7D and J; quantification: Supplementary Fig. S14O–R).

Collectively, these data demonstrate that phosphorylation at Lamin A (S22) or EZH2 (T345) disrupts Lamin A/C–EZH2 interaction, activating mesenchymal transcription factors, thereby promoting EMT. In contrast, phosphodeficient mutants that preserve this interaction sustain epithelial identity and enable MET.

Lamin A/C promotes chromatin compaction suppressing EMT

To investigate the functional consequences of Lamin A/C–EZH2 interaction, we examined the effects of CDK1-mediated phosphorylation of Lamin A/C or EZH2 on the expression of mesenchymal transcription factors *SNAI1*, *TWIST1*, and *ZEB1*. RNA-Seq following Lamin A/C depletion in MCF10A cells showed a significant upregulation of these transcription factors, indicating a role of Lamin A/C in their transcriptional repression. This indicates that Lamin A/C and repressive chromatin factors work in coordination, which may arise from spatial–epigenetic coupling, whereby Lamin A/C anchors PRC2-enriched chromatin at the nuclear periphery, promoting robust H3K27me3 deposition and enforcing transcriptional repression at key EMT-regulatory loci.

Analysis of publicly available ChIP-seq data sets from ChIP-Atlas revealed an enrichment of Lamin A, EZH2, and H3K27me3 at the −1 kb regions of the SNAI1, TWIST1, and ZEB1 promoters in epithelial MCF7 cells, and a loss of this occupancy in mesenchymal MDAMB231 cells (Lamin A/C: Supplementary Fig. S15A–C; EZH2: Supplementary Fig. S16A–C, H3K27me3: Supplementary Fig. S17A) [63]. We overexpressed phosphodeficient or phosphomimetic mutants of Lamin A or EZH2 in MCF7 cells and performed ChIP-qPCR at the −1 kb regions of SNAI1, TWIST1, and ZEB1 (Fig. 8A and B). Twist mediated EMT induction showed a marked reduction of Lamin A/C, EZH2, and H3K27me3 occupancy on SNAI1, TWIST1, and ZEB1 promoters, but were otherwise enriched on these promoters in untreated MCF7 cells (control). Lamin A/C depletion markedly reduced EZH2 and H3K27me3 occupancy, while control regions (MYT1, positive control; *GAPDH*, negative control) showed no differences in their occupancy (Fig. 8C and D, and Supplementary Fig. S17B).

ChIP-qPCR for transcriptional elongation markers revealed reduced occupancy of H3K36me3 and RNA polymerase II Ser2P at the +1 kb regions of *SNAI1*, *TWIST1*, and *ZEB1* in control MCF7 cells, consistent with a reduced expression of mesenchymal genes in epithelial cells. However, Lamin A/C depletion and TWIST1 overexpression significantly increased the enrichment of H3K36me3 and RNA Pol II Ser2P on the promoters of mesenchymal transcription factors (Fig. 8E and Supplementary Fig. S17C and D).

We next analyzed the effect of Lamin A phosphorylation. Overexpression of full-length Lamin A or the phosphodeficient mutant S22A preserved Lamin A/C, EZH2, and H3K27me3 occupancy at the −1 kb regions of SNAI1, TWIST1, and ZEB1, even under EMT-inducing conditions. In contrast, the phosphomimetic mutant S22D showed reduced enrichment of Lamin A (Fig. 8C), EZH2 (Fig. 8D), and H3K27me3 (Supplementary Fig. S17B) at these loci, accompanied by increased H3K36me3 (Fig. 8E) and RNA Pol II Ser2P (Supplementary Fig. S17D) at the +1 kb regions of SNAI1, TWIST1, and ZEB1. A similar regulatory mechanism was observed for EZH2 phosphorylation. Overexpression of full-length EZH2 or the phosphodeficient mutant T345A enhanced Lamin A/C, EZH2, and H3K27me3 occupancy at the −1 kb regions of SNAI1, TWIST1, and ZEB1. Conversely, the phosphomimetic mutant T345D reduced this enrichment, with a corresponding increase in H3K36me3 and RNA Pol II Ser2P occupancy at the +1 kb regions (Fig. 8F–H, and Supplementary Fig. S18A and B). This was corroborated by analysis of primer efficiency profiles (Supplementary Fig. S18C–F).

Taken together, these findings demonstrate that Lamin A/C facilitates EZH2 mediated deposition of H3K27me3 on mesenchymal gene promoters. Furthermore, CDK1-mediated phosphorylation of either protein disrupts this repression, thereby facilitating EMT.

Impact of Lamin A/C-EZH2 phosphorylation on cancer progression

To investigate the functional role of Lamin A/C–EZH2 interaction in EM plasticity, we performed cell migration, and tumor induction assays. We performed Boyden-chamber assay (transwell to quantify migration) for MCF7 and MDAMB231 cells. In MCF7 cells, transient overexpression of hTwist1 followed by depletion of Lamin A/C or EZH2 increased migration by ~30%. Similarly, overexpression of the phosphomimetic mutants Lamin A (S22D) or EZH2 (T345D) en-

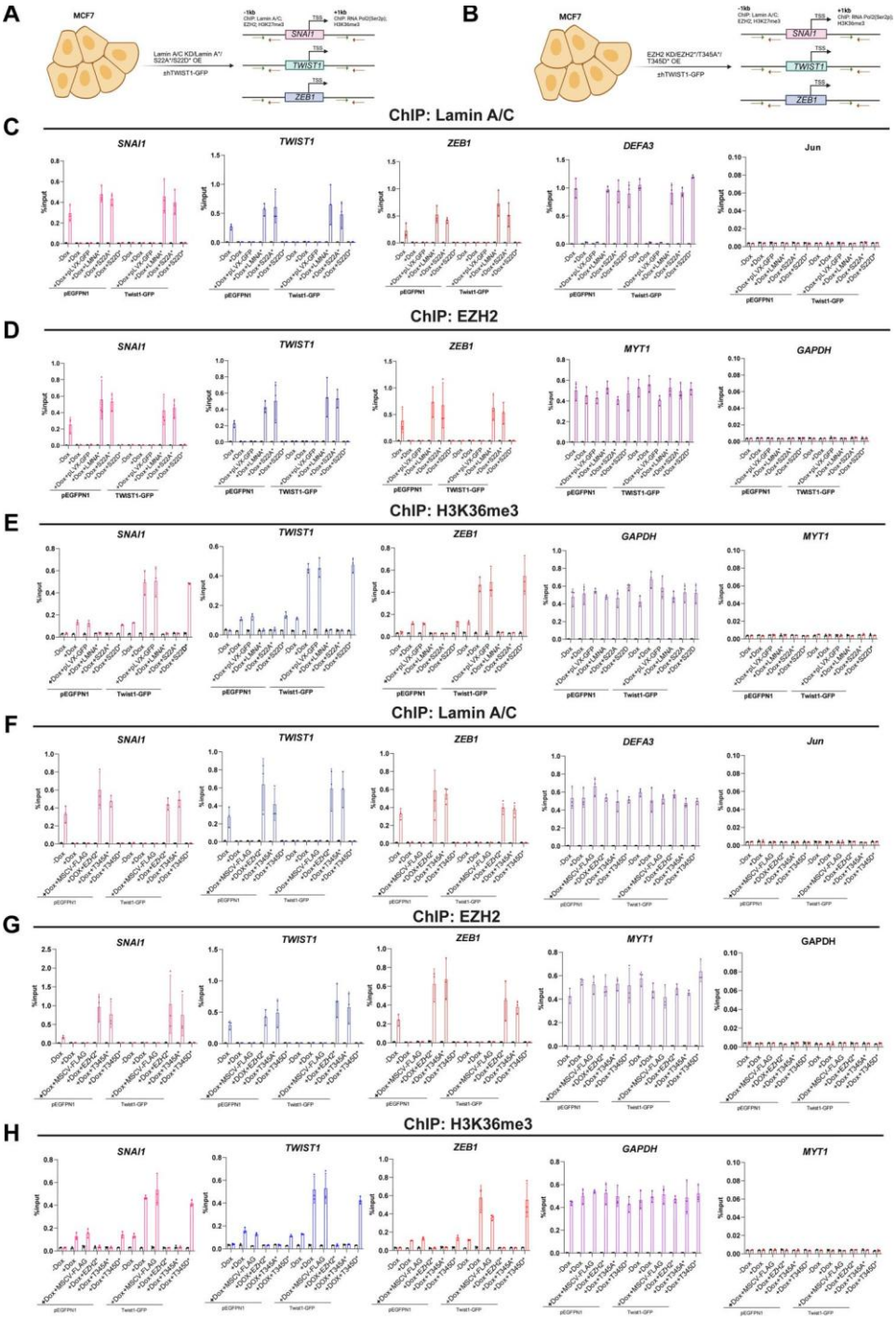

Figure 8. Lamin A/C promotes chromatin compaction suppressing EMT. **(A)** Schematic representation of chromatin immunoprecipitation (ChIP) experiments performed in MCF7 cells overexpressing TWIST1-GFP, following knockdown (KD) of Lamin A/C or overexpression (OE) of full-length Lamin A or phospho-mutant Lamin A (S22A: phospho-deficient; S22D: phospho-mimetic). ChIP was performed using antibodies against Lamin A/C, EZH2, H3K27me3 [−1 kb of transcription start sites (TSS)], and RNA Polymerase II (Ser2P) and H3K36me3 (+1 kb of TSS) at the promoters of key mesenchymal transcription factors SNAI1, TWIST1, and ZEB1. **(B)** Schematic representation of ChIP analysis in MCF7 cells with EZH2 knockdown or overexpression of full-length or phospho-mutant EZH2 (T345A: phospho-deficient; T345D: phospho-mimetic) in the context of TWIST1-GFP induction. Promoter occupancy of Lamin A/C, EZH2, and associated histone modifications (H3K27me3 and H3K36me3), as well as RNA Pol II (Ser2P), was examined at the TSS of SNAI1, TWIST1, and ZEB1. Green and red arrows indicate primers for the qPCR experiment. (**C**-**E**) ChIP PCR analysis in MCF7 cells stably transduced with full-length Lamin A, phosphodeficient (S22A), or phosphomimetic (S22D) variants, followed by transient transfection with pEGFP-N1 (control) or TWIST1-GFP for 48 h. ChIP occupancy of **(C)** Lamin A, **(D)** EZH2 at the −1 kb regions, and **(E)** H3K36me3 at the +1 kb regions of SNAI1, TWIST1, and ZEB1 were assessed. DEFA3 **(C)**, MYT1 **(D)**, and GAPDH **(E)** served as positive controls, while Jun **(C)**, GAPDH +1 kb **(D)**, and MYT1 **(E)** were negative controls for Lamin A/C, EZH2, and H3K36me3 respectively. (**F**-**H**) ChIP PCR analysis in MCF7 cells stably transduced with full-length EZH2, phosphodeficient (T345A), or phosphomimetic (T345D) variants, followed by transient transfection with pEGFP-N1 or TWIST1-GFP for 48 h. ChIP occupancy of **(F)** Lamin A, **(G)** EZH2 at the −1 kb regions, and **(H)** H3K36me3 at the +1 kb regions of SNAI1, TWIST1, and ZEB1 was assessed. DEFA3 **(F)**, MYT1 **(G)**, and GAPDH **(H)** served as positive controls, while Jun **(F)**, GAPDH +1 kb **(G)**, and MYT1 **(H)** were negative controls for Lamin A/C, EZH2, and H3K36me3 respectively. Data represent mean ± SD from three independent experiments.

hanced migration, whereas overexpression of the full-length proteins or their phosphodeficient mutants (Lamin A S22A, EZH2 T345A) reduced migration by ~20% (Supplementary Fig. S19A and B). In MDAMB231 cells, GRHL2 overexpression reduced migration, while depletion of Lamin A or EZH2 increased migration. When GRHL2 was overexpressed in cells lacking Lamin A or EZH2, migration was further elevated compared to GRHL2 overexpression alone. Consistently, the phosphomimetic Lamin A (S22D) and EZH2 (T345D) variants enhanced migration than their full-length or phosphodeficient counterparts (Supplementary Fig. S19C and D). We performed wound healing assays to determine the migratory ability of MCF10A cells. Depletion of Lamin A/C or EZH2 increased cell migration, comparable to that induced by TGF-β. While, overexpression of full-length Lamin A or EZH2, as well as their phosphodeficient mutants (S22A, T345A), suppressed migration in both untreated and TGF-β-treated cells. In contrast, the phosphomimetic mutants (S22D, T345D) enhanced migration, even in the absence of TGF-β (Supplementary Fig. S20A and B).

To investigate the *in vivo* implications of Lamin A (S22A and S22D) and EZH2 (T345A and T345D) mutants to form tumors, we orthotopically injected MDA-MB-231 cells (~1 × 10^6), overexpressing (i) full length (Lamin A or EZH2 – control), (ii) phospho-deficient (Lamin A S22A; EZH2 T345A) (iii) phospho-mimetic (Lamin A S22D; EZH2 T345D) forms into the mammary fat pad of female NOD-SCID mice (~6 weeks old). Tumour volume was monitored, and the experiment was terminated after ~5 weeks (Validation of Lamin A and EZH2 knockdown and overexpression are shown in Supplementary Fig. S21A and B). Both phosphomimetic Lamin A (S22D) and EZH2 (T345D) exhibited a marked increase in tumor growth, as reflected by both tumor volume and final tumor weight (Fig. 9A–F), as compared to their full-length and phospho-deficient counterparts (full length control in Supplementary Fig. S21C–H).

Previous studies have consistently shown that the lungs are a frequent site of metastasis in breast cancers. We therefore performed H&E staining of lung sections and quantified metastatic nodules to determine whether Lamin A and EZH2 phosphomutants (with respect to the full-length control) affect metastatic dissemination [64, 65]. Mice injected with phospho-mimetic mutants (S22D-Lamin A and T345D-EZH2) showed a significantly higher metastatic burden, whereas full length (LMNA-WT and EZH2-WT) and phospho-deficient mutants (S22A-Lamin A and T345A-EZH2) did not form detectable lung metastases. These findings demonstrate that CDK1-dependent phosphorylation of Lamin A/C and EZH2 promotes both primary tumor growth and *in vivo* metastatic dissemination of breast cancer cells (Fig. 9G and H; full length control in Supplementary Fig. S21I–L).

To further address the significance of the Lamin A/C-EZH2 interaction, we performed triple enzyme digestion followed by immunoprecipitation on primary tumor-derived cells. Phosphodeficient Lamin A (S22A) maintained its interaction with EZH2, whereas the phosphomimetic Lamin A (S22D) preferentially interacted with phosphorylated CDK1 (pCDK1-T161; Fig. 9I). Similarly, immunoprecipitation of EZH2 revealed that the phosphodeficient EZH2 (T345A) interacted with Lamin A/C, while phosphomimetic EZH2 (T345D) interacted with pCDK1 (Fig. 9J).

We performed immunofluorescence assays in cells (cultured for ~72 h) derived from the tumors (the EM state could not be examined *in situ*, as the subsequent assays necessitated culturing and expansion of cells). These assays also reveal morphological characteristics since the cells expressing phosphodeficient Lamin A or EZH2 mutants showed an epithelial-like morphology, whereas those expressing phosphomimetic mutants retained a mesenchymal phenotype (Fig. 9K–N).

In summary, these findings underscore a crucial role for Lamin A and EZH2 phosphorylation in modulating EM plasticity. Phosphomimetic modifications favour mesenchymal properties, whereas phosphodeficient or full-length variants reinforce epithelial characteristics.

Discussion

Summary of key results

In this study, we uncover a phosphorylation-sensitive interaction between the inner nuclear envelope protein Lamin A/C and the histone methyltransferase EZH2, revealing its pivotal role in regulating EM plasticity. Using a combination of models of EMT and its reversal (MET), we show that Lamin A/C interacts with EZH2 in epithelial cells, which renders a repressive chromatin environment on *SNAI1, TWIST1*, and *ZEB1* loci that encode for mesenchymal transcription factors (EMT-TF). To ensure comparable expression of empty vector and TWIST1 (in MCF7) or GRHL2 overexpression (in MDAMB231 cells; EGFP panel is included in Supplementary Fig. S25A–D). This interaction is disrupted upon EMT induction through CDK1-mediated phosphorylation of both Lamin A/C and EZH2, facilitating EMT-TF activation (Fig. 10). Phosphomimetic and phosphodeficient variants of Lamin A (S22D/S22A) and EZH2 (T345D/T345A) reveal their regulatory role of phosphorylation in controlling EMT. *In vivo*, phosphomimetic forms promote tumor growth and metastasis, whereas phosphodeficient forms maintain epithelial characteristics, decreasing tumor growth potential. These findings implicate Lamin A–EZH2 interaction as a critical epigenetic checkpoint modulated by phosphorylation in cancer progression.

Lamins and EMT: contributions of A- and B-type lamins

Nuclear lamins regulate nuclear architecture with genome organization and transcriptional control, and their altered expression or modification profoundly impacts cancer cell behavior by modulating nuclear mechanics and chromatin accessibility [66].

Lamin A/C restricts EMT by reinforcing nuclear stiffness and limiting chromatin openness. Its reduction decreases nuclear rigidity, increases chromatin accessibility, and promotes invasion by enhancing mesenchymal gene expression [67, 68].

Lamin B1, in contrast, acts as a context-dependent EMT regulator. Its loss in lung cancer cells suppresses E-cadherin, elevates fibronectin and N-cadherin, and activates rearranged during transfection proto-oncogene and MAPK/PI3K–AKT signaling, suggesting an EMT-restraining role [69]. Lamin B1 enrichment at TAD boundaries supports EMT programs, and its depletion disrupts them in NMuMG cells [70]. However, in our study, Lamin B1 levels remained stable, and depletion of Lamin B1 or B2 had no effect on EMT, indicating cell-type-specific variability. While Lamin B2 contributes to nuclear in-

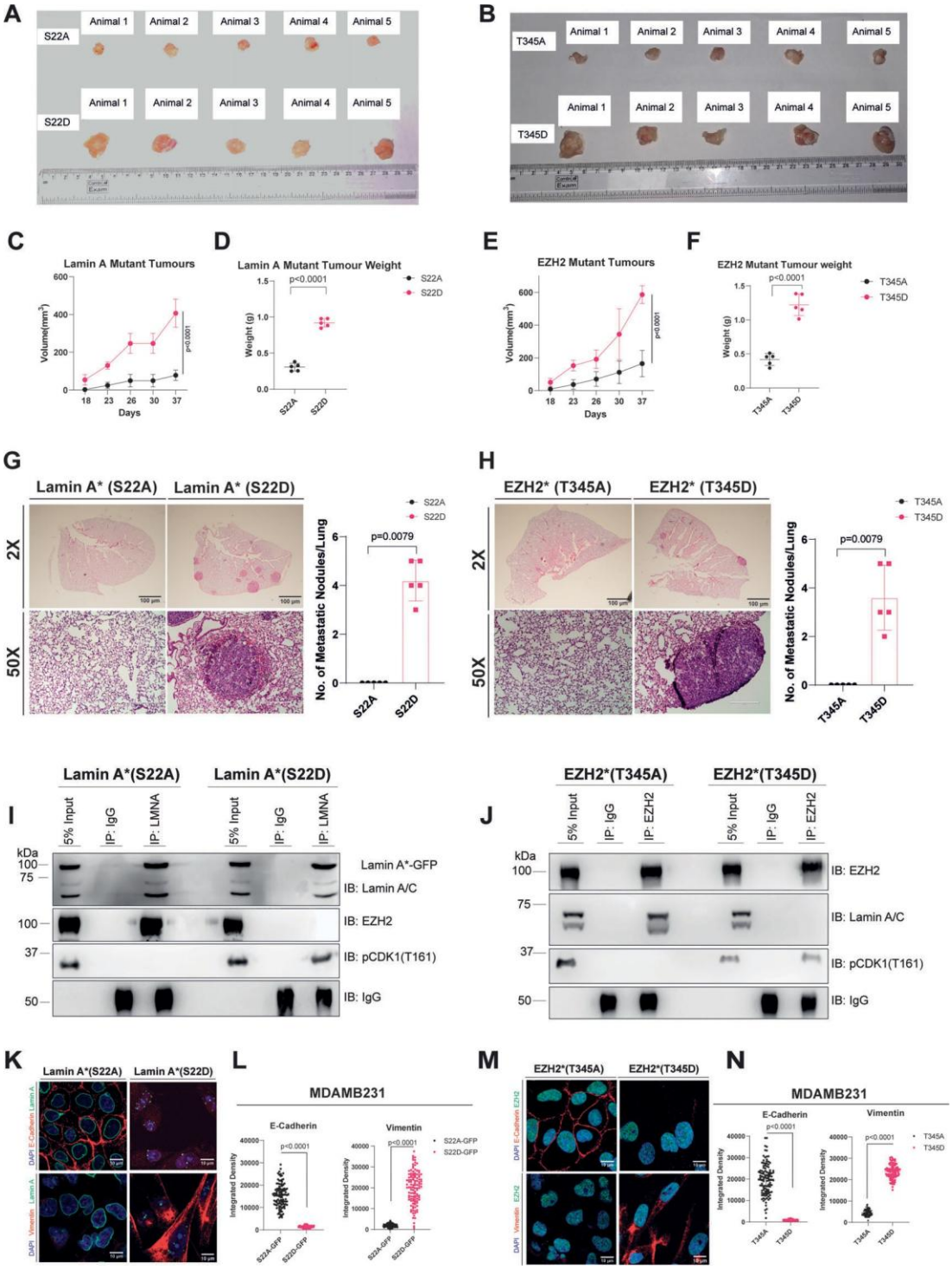

Figure 9. Impact of Lamin A/C–EZH2 phosphorylation on tumor progression. **(A, B)** Representative images of excised tumors from NOD-SCID female mice injected with MDAMB231 cells expressing either phospho-mutant Lamin A **(A)** or EZH2 **(B)**. $N = 5$ mice per group. **(C, D)** Quantification of tumor volume **(C)** and tumor weight **(D)** from Lamin A phospho-mutant xenografts. **(E, F)** Quantification of tumor volume **(E)** and tumor weight **(F)** from EZH2 phosphomutant xenografts. **(G)** Representative Hematoxylin and Eosin (H&E) images (2×, 50×) of lung metastases from MDA-MB-231 cells expressing phosphodeficient (S22A) or phosphomimetic (S22D) Lamin A. **(H)** Representative H&E images (2×, 50×) of lung metastases from MDA-MB-231 cells expressing phosphodeficient (T345A) or phosphomimetic (T345D) EZH2. Quantification of the number of nodules per lung is given alongside the H&E images. **(I)** Immunoprecipitation of Lamin A/C from tumor lysates followed by immunoblotting for EZH2 and phospho-CDK1 **(J)** Immunoprecipitation of EZH2 from tumor lysates followed by immunoblotting for Lamin A/C and phospho-CDK1 **(K)** Immunofluorescence of tumor-derived MDAMB231 cells stained for E-cadherin, Vimentin (red), and Lamin A (GFP). Nucleus (blue, DAPI). Scale bar ~10 μm. **(L)** Quantification of the integrated density of E-Cadherin and Vimentin upon overexpression of phosphomutants of Lamin A. Data represent mean ± SD. Statistical significance was determined using an unpaired two-tailed Student's *t*-test, *P*-value <0.05 **(M)** Immunofluorescence of tumor-derived MDAMB231 cells stained for E-cadherin, Vimentin and EZH2. Nucleus (DAPI). Scale bar ~10 μm. **(N)** Quantification of the integrated density of E-Cadherin and Vimentin upon overexpression of phosphomutants of EZH2. Data represent mean ± SD. Statistical significance was determined using an unpaired two-tailed Student's *t*-test. Means are compared between phosphodeficient (control) and phosphomimetic mutants.

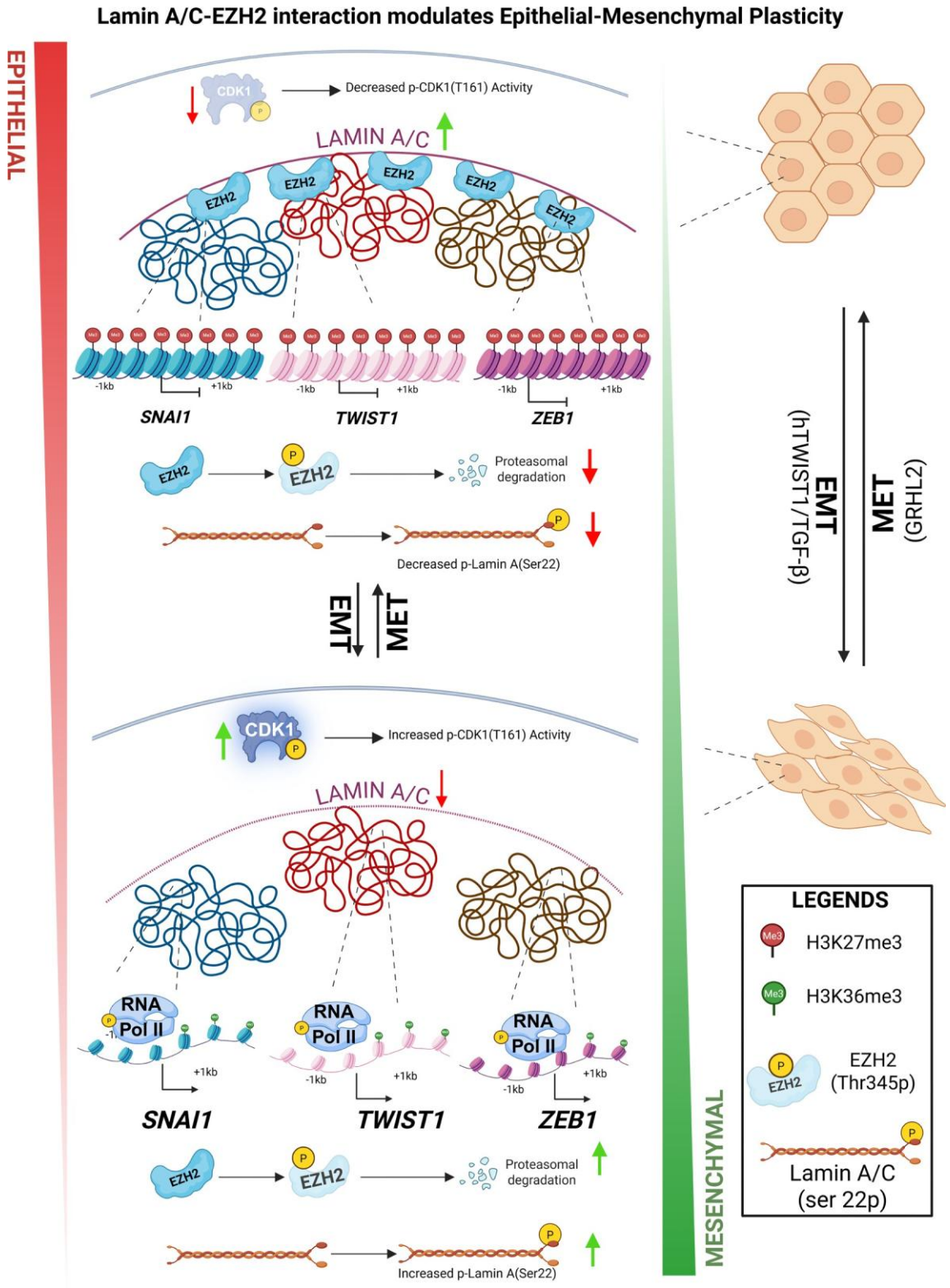

Figure 10. Lamin A/C-EZH2 interaction modulates EM plasticity. This schematic illustrates the dynamic regulation of EMT and MET by Lamin A/C–EZH2 signaling. In epithelial cells (top), high Lamin A/C levels promote the sequestration of EZH2 at the nuclear lamina, diminishing the transcriptional activation and expression of key EMT transcription factors (SNAI1, TWIST1, ZEB1) by enforcing H3K27me3-mediated repression at their promoters. Reduced CDK1 activity leads to reduced phosphorylation on both Lamin A/C (Ser22) and EZH2 (Thr345), limiting EZH2 degradation and further stabilizing chromatin repression. During EMT, increased CDK1 activity and phosphorylation of Lamin A/C (Ser22) and EZH2 (Thr345), results in proteasomal degradation of EZH2 which releases the repressive chromatin state, recruits active RNA polymerase II to EMT gene promoters, and upregulates EMT transcription factors, promoting mesenchymal properties. Created in BioRender. Sengupta, K.
(Schematic illustration of EMT and MET regulation by Lamin A/C-EZH2).

tegrity and metastasis in other cancers, it did not impact EMT in breast cancer [45, 71].

Overall, Lamin A/C consistently functions as a repressive scaffold maintaining epithelial identity, whereas B-type lamins show context-dependent roles. Loss or modification of Lamin A/C represents a critical step enabling EMT and invasiveness of cancer cells.

Coordination of Lamin A/C-PRC2 Interactions regulate EM Plasticity

Previous studies have reported divergent patterns of EZH2 expression during EMT, suggesting that its regulation may be context dependent [72]. While some reports did not observe a reduction of EZH2 in mesenchymal-like cells, our data reveal a modest but consistent decrease in EZH2 upon EMT induction and restoration during MET. This aligns with recent studies indicating that attenuation of PRC2/EZH2 function accompanies mesenchymal transition. Specifically, loss or dysfunction of PRC2 promotes a quasi-mesenchymal trajectory and enhance metastatic traits, implicating PRC2 as an organizer of the epithelial state [73]. In lung carcinoma cells, inhibition or knockout of EZH2 induces mesenchymal gene expression and a shift toward the mesenchymal phenotype [74], while in breast cancer models, EZH2 sustains epithelial identity by repressing mesenchymal programs [75]. Reduction in EZH2 levels, was undetected in other studies [76], underscoring that the relationship between EZH2 expression and EMT may vary across cellular contexts and experimental systems.

Since EZH2 levels are modulated during EMT, we next explored whether changes in the sub-interactome of Lamin A/C could explain these dynamics, focusing on Lamin A/C as a potential scaffold coordinating PRC2 activity and chromatin organization.

Lamin A/C-mediated chromatin reorganization during EMT and MET

Beyond its structural role, Lamin A/C serves as a dynamic scaffold that coordinates chromatin modifiers and transcriptional regulators to control EM plasticity. In epithelial MCF7 cells, Lamin A/C interacts with EZH2—the catalytic subunit of PRC2 responsible for H3K27 trimethylation—as well as other chromatin organizers such as NUDT21, LIMA1, and EHMT2 [67, 68]. During EMT, this interaction is lost, coinciding with Lamin A/C association with phosphorylated CDK1 and CCNB1, indicating a potential shift in the functional role of Lamin from chromatin organization to proliferative signaling [67].

A-type lamins associate with both euchromatin and heterochromatin, and loss of LAP2α redistributes Lamin A/C toward heterochromatin with altered histone modifications [77]. Similarly, reduced Lamin A/C decreases H3K27me3 levels and reorganizes, activating mesenchymal genes. Thus, Lamin A/C preserves a repressive chromatin environment, and its loss promotes chromatin relaxation and mesenchymal gene activation.

The Lamin A/C–EZH2 interaction is re-established upon MET, restoring PRC2 scaffolding and epithelial identity. [78]. Unlike A-type lamins, B-type lamins interact with G9a and SUV39H1, unaffected during EMT, emphasizing their distinct functional roles [45, 71].

Overall, Lamin A/C functions as a phosphorylation-dependent hub linking chromatin organization and cell cycle signaling. Its dynamic interaction with PRC2 and post-translationally modified EZH2 integrates nuclear architecture and epigenetic regulation to control EM plasticity, with MET-driven restoration of the Lamin A/C–EZH2 complex reinstating epithelial chromatin states.

pCDK1, Lamin A/C, and EMT-MET dynamics

During EMT, Lamin A/C associates with pCDK1 (T161), coinciding with loss of Lamin A/C–EZH2 interaction. BrdU incorporation in MCF10A cells undergoing EMT did not show G1 arrest, while decreased H3S10 phosphorylation indicated EMT-associated cell cycle arrest occurs between late S and early G2 phase.

Mechanistically, pCDK1 phosphorylates Lamin A/C and EZH2, disrupting their interaction, relieving PRC2-mediated H3K27me3 repression at mesenchymal loci, and activating EMT transcriptional programs. Upon MET, Lamin A/C–EZH2 interactions are restored, reinstating epithelial chromatin and transcriptional repression [67, 76].

These results are consistent with the finding that CDK1 phosphorylation modulates EMT, and frequently correlates with cell cycle stalling at late S/early G2 transition, coupling proliferative signalling with transcriptional reprogramming [57–59]. In line with recent studies highlighting the role of EMT-inducing transcription factors in late S/early G2-phase regulation, replication stress, and DNA damage responses [79–83], certain partial or metastatic EMT states are associated with transient G1 arrest or reduced proliferation, underscoring the temporal and contextual plasticity of EMT–cell cycle coupling [84, 85].

Collectively, our data suggest that cells undergoing EMT show cell cycle arrest at late S or early G2 phase, enabling pCDK1-dependent remodeling of Lamin A/C scaffolds, dissociation and degradation of EZH2, leading to activation of mesenchymal programs. Restoration of the Lamin A/C–EZH2 complex during MET underscores the reversible coupling between cell-cycle state, nuclear organization, and EM plasticity.

Decoding EMT plasticity through Lamin A and EZH2 phosphorylation

EMT and MET occur along a continuum, with hybrid epithelial/mesenchymal (E/M) states serving as key intermediates in tumor progression and metastasis. This hybrid population, marked by CD104 and CD44 co-expression [86].

During TWIST1-induced EMT, cells acquire a mesenchymal-like ($CD104^{+}CD44^{+}$) phenotype (Supplementary Fig. S22A and B), whereas overexpression of Lamin A or EZH2, with or without TWIST1, restores epithelial identity ($CD104^{+}CD44^{-}$), bypassing the hybrid state. In contrast, phospho-mimetic mutants (Lamin A S22D, EZH2 T345D) enrich hybrid populations in MCF7 cells, indicating that phosphorylation disrupts chromatin binding and repression of EMT-TFs such as SNAI1, TWIST1, and ZEB1. Under GRHL2-driven MET in MDA-MB-231 cells, these mutants maintain hybrid populations despite epithelial cues (GRHL2 overexpression).

Rescue experiments reveal that a complete commitment to an epithelial state requires unphosphorylated Lamin A and EZH2. Phospho-deficient mutants (S22A, T345A) restore epithelial identity ($CD104^{+}CD44^{-}$), while phospho-mimetic forms sustain hybrid states (Supplementary Figs S22C and D,

and S23A–D), consistent with Lamin A phosphorylation promoting nuclear softening and chromatin decondensation [87]. Overall, the hybrid E/M state is a regulated phenotype governed by post-translational modifications of Lamin A and EZH2. Phosphorylation-dependent disruption of their interaction enhances EM plasticity and sustains hybrid populations linked to metastasis.

Implications for diagnosis and treatment

The Lamin A–EZH2 interaction and their phosphorylation states offer potential diagnostic and therapeutic avenues. Phosphorylated Lamin A (S22) and EZH2 (T345) may serve as markers of mesenchymal transition and metastatic potential, detectable by mass spectrometry or immunohistochemistry to refine EMT-based prognosis.

CPTAC proteomics showed increased pLMNA(Ser22) and decreased total LMNA with tumor progression (Supplementary Fig. S24A), paralleled by elevated pEZH2(T345) and reduced total EZH2 (Supplementary Fig. S24B). TCGA data further revealed progressive CCNB1 upregulation and increased pCDK1(T161) across tumor stages, linking CDK1–CCNB1 activity to malignancy (Supplementary Fig. S24C and D) [88, 89].

Therapeutically, inhibiting CDK1 or stabilizing the Lamin A–EZH2 complex could restore heterochromatin and suppress EMT-TFs, promoting a less aggressive phenotype. However, broad PRC2 inhibition may disrupt Lamin A–EZH2 tumor-suppressive functions, emphasizing patient-tailored approaches. The reversibility of this interaction highlights tumor plasticity and its potential as a target to drive cells toward a more differentiated, less malignant state.

Limitations and future perspectives

This study identifies a phosphorylation-dependent Lamin A–EZH2 mechanism regulating EMT, but several aspects remain unresolved. The universality of this pathway beyond breast and liver carcinoma (HepG2; Supplementary Fig. S24E) needs validation, as tissue-specific factors may influence its function.

Although *in vivo* data support a phosphorylation-dependent Lamin A–EZH2 interaction in primary tumors, its role during metastasis and under therapeutic stress remains unclear. Determining whether EMT involves cell-cycle arrest specifically in late S or early G2 phases will further refine our understanding of this mechanism. Future studies employing high-resolution cell-cycle mapping approaches, such as short BrdU/EdU pulse labeling, combined DNA-content analysis with replication and mitotic markers, or single-cell cell-cycle indexing will be essential to definitively distinguish late S from early G2 states and clarify their contribution to EMT regulation.

Additionally, the phosphatases responsible for Lamin A and EZH2 dephosphorylation are yet to be identified. These enzymes are likely to mediate complex disassembly and chromatin reorganization, influencing EMT reversibility. Elucidating these regulatory layers will be key to fully defining the Lamin A–EZH2–CDK1 axis and its therapeutic relevance in tumor progression and chemoresistance.

Acknowledgements

We thank Ruby Yun-Ju Huang (National Taiwan University, Taiwan) for generously providing the GRHL2 constructs that were critical to this study. RNA sequencing was carried out by MedGenome (Bengaluru), and we acknowledge their contribution. We are grateful to the core facilities at IISER Pune, including the Mass Spectrometry Facility, Microscopy Facility, NFGFHD, and the FACS Facility, for their technical assistance. We also acknowledge the Revvity–IISER Pune Center of Excellence for providing access to the Operetta system. We thank Khushi Salvi and Madhura Kulkarni for providing protein lysates from breast cancer cell lines. We sincerely thank Richa Rikhy (IISER-Pune) for kindly providing PLA kits and reagents, as well as for valuable discussions throughout the course of this work. We are thankful to Anish Pandey for his help with HADDOCK simulations. Illustrations were created using BioRender, and we acknowledge their contribution to the visual presentation of our work. We thank Sanjeev Galande for providing access to the Covaris S220 for chromatin shearing. We thank Ellora Sen, NBRC, New Delhi, for her generous support with antibodies. We thank Sorab Dalal, ACTREC, Mumbai, for generously providing CDK1 construct. We thank Ajay S. Labade and CBL, IISER-Pune for insightful discussions during the preparation of this manuscript.

Author contributions: Balaji AK (Conceptualization [lead], Data curation [lead], Formal analysis [lead], Investigation [lead], Methodology [lead], Visualization [lead], Writing – original draft [equal], Writing – review & editing [equal], Santam Saha (Conceptualization [supporting], Data curation [supporting], Formal analysis [supporting], Methodology [supporting], Resources [supporting], Writing – original draft [supporting], Writing – review & editing [supporting], Kundan Sengupta (Conceptualization [lead], Formal analysis [supporting], Funding acquisition [lead], Investigation [lead], Methodology [supporting], Project administration [lead], Resources [supporting], Supervision [lead], Validation [supporting], Writing – original draft [supporting], Writing – review & editing [equal])

Supplementary data

Supplementary data is available at NAR online.

Conflict of interest

None declared.

Funding

We gratefully acknowledge funding support from ANRF, Department of Science and Technology, Science and Engineering Research Board (grant #CRG/2020/002563), Ministry of Education-STARS (grant #MoE-STARS/STARS-2/2023-0603), Department of Biotechnology (DBT) MedDevice (grant #BT/PR49745/MED/32/925/2023), Department of Biotechnology (BT/PR52973/MED/30/2535/2024), Intermediate Fellowship of the Wellcome Trust–DBT India Alliance (grant #500164/Z/09/Z) and Intramural funding from IISER-Pune.

Data availability

The RNA sequencing data generated in this study have been deposited in the Gene Expression Omnibus under accession number GSE289750.

The mass spectrometry proteomics data are available via the PRIDE repository with the dataset identifier PXD060831.

References

1. Thiery JP, Acloque H, Huang RYJ *et al.* Epithelial–mesenchymal transitions in development and disease. *Cell* 2009;139:871–90. https://doi.org/10.1016/j.cell.2009.11.007
2. Acloque H, Adams MS, Fishwick K *et al.* Epithelial–mesenchymal transitions: the importance of changing cell state in development and disease. *J Clin Invest* 2009;119:1438–49. https://doi.org/10.1172/JCI38019
3. Little MH, McMahon AP. Mammalian kidney development: principles, progress, and projections. *Cold Spring Harb Perspect Biol* 2012;4:a008300.
4. Kalluri R, Weinberg RA. The basics of epithelial–mesenchymal transition. *J Clin Invest* 2009;119:1420–8. https://doi.org/10.1172/JCI39104
5. Pitsidianaki I, Morgan J, Adams J *et al.* Mesenchymal-to-epithelial transitions require tissue-specific interactions with distinct laminins. *J Cell Biol* 2021;220:e202010154.
6. Brabletz T, Kalluri R, Nieto MA *et al.* EMT in cancer. *Nat Rev Cancer* 2018;18:128–34. https://doi.org/10.1038/nrc.2017.118
7. Jolly MK, Boareto M, Huang B *et al.* Implications of the hybrid epithelial/mesenchymal phenotype in metastasis. *Front Oncol* 2015;5:155. https://doi.org/10.3389/fonc.2015.00155
8. Jolly MK, Somarelli JA, Sheth M *et al.* Hybrid epithelial/mesenchymal phenotypes promote metastasis and therapy resistance across carcinomas. *Pharmacol Ther* 2019;194:161–84. https://doi.org/10.1016/j.pharmthera.2018.09.007
9. Pastushenko I, Mauri F, Song Y *et al.* Fat1 deletion promotes hybrid EMT state, tumour stemness and metastasis. *Nature* 2021;589:448–55. https://doi.org/10.1038/s41586-020-03046-1
10. Pastushenko I, Brisebarre A, Sifrim A *et al.* Identification of the tumour transition states occurring during EMT. *Nature* 2018;556:463–8. https://doi.org/10.1038/s41586-018-0040-3
11. Liu Q-L, Luo M, Huang C *et al.* Epigenetic regulation of epithelial to mesenchymal transition in the cancer metastatic cascade: implications for cancer therapy. *Front Oncol* 2021;11:657546. https://doi.org/10.3389/fonc.2021.657546
12. Lamouille S, Xu J, Derynck R. Molecular mechanisms of epithelial–mesenchymal transition. *Nat Rev Mol Cell Biol* 2014;15:178–96. https://doi.org/10.1038/nrm3758
13. Nieto MA, Huang RYJ, Jackson RA *et al.* EMT: 2016. *Cell* 2016;166:21–45. https://doi.org/10.1016/j.cell.2016.06.028
14. Solovei I, Wang AS, Thanisch K *et al.* LBR and lamin A/C sequentially tether peripheral heterochromatin and inversely regulate differentiation. *Cell* 2013;152:584–98. https://doi.org/10.1016/j.cell.2013.01.009
15. Kim J-K, Louhghalam A, Lee G *et al.* Nuclear lamin A/C harnesses the perinuclear apical actin cables to protect nuclear morphology. *Nat Commun* 2017;8:2123. https://doi.org/10.1038/s41467-017-02217-5
16. Capo-Chichi CD, Yeasky TM, Smith ER *et al.* Nuclear envelope structural defect underlies the main cause of aneuploidy in ovarian carcinogenesis. *BMC Cell Biol* 2016;17:37. https://doi.org/10.1186/s12860-016-0114-8
17. Wong KM, Song J, Wong YH. CTCF and EGR1 suppress breast cancer cell migration through transcriptional control of Nm23-H1. *Sci Rep* 2021;11:491. https://doi.org/10.1038/s41598-020-79869-9
18. Wang R-R, Qiu X, Pan R *et al.* Dietary intervention preserves β cell function in mice through CTCF-mediated transcriptional reprogramming. *J Exp Med* 2022;219:e20211779.
19. Cesarini E, Mozzetta C, Marullo F *et al.* Lamin A/C sustains PcG protein architecture, maintaining transcriptional repression at target genes. *J Cell Biol* 2015;211:533–51. https://doi.org/10.1083/jcb.201504035
20. Siegenfeld AP, Roseman SA, Roh H *et al.* Polycomb-lamina antagonism partitions heterochromatin at the nuclear periphery. *Nat Commun* 2022;13:4199. https://doi.org/10.1038/s41467-022-31857-5
21. Cardenas H, Zhao J, Vieth E *et al.* EZH2 inhibition promotes epithelial-to-mesenchymal transition in ovarian cancer cells. *Oncotarget* 2016;7:84453–67. https://doi.org/10.18632/oncotarget.11497
22. Xu Y, Qin L, Sun T *et al.* Twist1 promotes breast cancer invasion and metastasis by silencing Foxa1 expression. *Oncogene* 2017;36:1157–66. https://doi.org/10.1038/onc.2016.286
23. Zhang Y-Q, Wei X-L, Liang Y-K *et al.* Over-expressed twist associates with markers of epithelial mesenchymal transition and predicts poor prognosis in breast cancers via ERK and Akt activation. *PLoS One* 2015;10:e0135851. https://doi.org/10.1371/journal.pone.0135851
24. Paul I, Bolzan D, Youssef A *et al.* Parallelized multidimensional analytic framework applied to mammary epithelial cells uncovers regulatory principles in EMT. *Nat Commun* 2023;14:688. https://doi.org/10.1038/s41467-023-36122-x
25. Zhang J, Tian X-J, Zhang H *et al.* TGF-β-induced epithelial-to-mesenchymal transition proceeds through stepwise activation of multiple feedback loops. *Sci Signal* 2014;7:ra91. https://doi.org/10.1126/scisignal.2005304
26. Werner S, Frey S, Riethdorf S *et al.* Dual roles of the transcription factor grainyhead-like 2 (GRHL2) in breast cancer. *J Biol Chem* 2013;288:22993–3008. https://doi.org/10.1074/jbc.M113.456293
27. Chung VY, Tan TZ, Ye J *et al.* The role of GRHL2 and epigenetic remodeling in epithelial–mesenchymal plasticity in ovarian cancer cells. *Commun Biol* 2019;2:272. https://doi.org/10.1038/s42003-019-0506-3
28. Eremenko E, Taylor ZV, Khand B *et al.* An optimized protocol for the retroviral transduction of mouse CD4 T cells. *STAR Protocols* 2021;2:100719. https://doi.org/10.1016/j.xpro.2021.100719
29. Tan JYM, Tan JC, Wang C *et al.* Protocol for the simultaneous activation and lentiviral transduction of primary human T cells with artificial T cell receptors. *STAR Protocols* 2025;6:103685. https://doi.org/10.1016/j.xpro.2025.103685
30. Landt SG, Marinov GK, Kundaje A *et al.* ChIP-seq guidelines and practices of the ENCODE and modENCODE consortia. *Genome Res* 2012;22:1813–31. https://doi.org/10.1101/gr.136184.111
31. Bustin SA, Benes V, Garson JA *et al.* The MIQE guidelines: minimum information for publication of quantitative real-time PCR experiments. *Clin Chem* 2009;55:611–22. https://doi.org/10.1373/clinchem.2008.112797
32. Kumar K, Mhetre A, Ratnaparkhi GS *et al.* A Superfamily-wide activity atlas of serine hydrolases in *Drosophila melanogaster*. *Biochemistry* 2021;60:1312–24. https://doi.org/10.1021/acs.biochem.1c00171
33. Lagundžin D, Krieger KL, Law HCH *et al.* An optimized co-immunoprecipitation protocol for the analysis of endogenous protein-protein interactions in cell lines using mass spectrometry. *STAR Protocols* 2022;3:101234. https://doi.org/10.1016/j.xpro.2022.101234
34. Gaponova AV, Rodin S, Mazina AA *et al.* Epithelial-mesenchymal transition: role in cancer progression and the perspectives of antitumor treatment. *Acta Naturae* 2020;12:4–23. https://doi.org/10.32607/actanaturae.11010
35. Dongre A, Weinberg RA. New insights into the mechanisms of epithelial–mesenchymal transition and implications for cancer. *Nat Rev Mol Cell Biol* 2019;20:69–84. https://doi.org/10.1038/s41580-018-0080-4
36. Le AVP, Szaumkessel M, Tan TZ *et al.* DNA methylation profiling of breast cancer cell lines along the epithelial mesenchymal spectrum-implications for the choice of circulating tumour DNA methylation markers. *Int J Mol Sci* 2018;19:2553.
37. Cieply B, Riley P, Pifer PM *et al.* Suppression of the epithelial–mesenchymal transition by Grainyhead-like-2. *Cancer*

Res 2012;72:2440–53. https://doi.org/10.1158/0008-5472.CAN-11-4038
38. Wang Z, Coban B, Wu H *et al.* GRHL2-controlled gene expression networks in luminal breast cancer. *Cell Commun Signal* 2023;21:15. https://doi.org/10.1186/s12964-022-01029-5
39. Alisafaei F, Jokhun DS, Shivashankar GV *et al.* Regulation of nuclear architecture, mechanics, and nucleocytoplasmic shuttling of epigenetic factors by cell geometric constraints. *Proc Natl Acad Sci USA* 2019;116:13200–9. https://doi.org/10.1073/pnas.1902035116
40. de Leeuw R, Gruenbaum Y, Medalia O. Nuclear Lamins: thin filaments with major functions. *Trends Cell Biol* 2018;28:34–45. https://doi.org/10.1016/j.tcb.2017.08.004
41. Comaills V, Kabeche L, Morris R *et al.* Genomic instability is induced by persistent proliferation of cells undergoing epithelial-to-mesenchymal transition. *Cell Rep* 2016;17:2632–47. https://doi.org/10.1016/j.celrep.2016.11.022
42. Love MI, Huber W, Anders S. Moderated estimation of fold change and dispersion for RNA-seq data with DESeq2. *Genome Biol* 2014;15:550. https://doi.org/10.1186/s13059-014-0550-8
43. Ye J, Zhang Y, Cui H *et al.* WEGO 2.0: a web tool for analyzing and plotting GO annotations, 2018 update. *Nucleic Acids Res* 2018;46:W71–5. https://doi.org/10.1093/nar/gky400
44. Baldarelli RM, Smith CM, Finger JH *et al.* The mouse Gene Expression Database (GXD): 2021 update. *Nucleic Acids Res* 2021;49:D924–31. https://doi.org/10.1093/nar/gkaa914
45. Zheng X, Hu J, Yue S *et al.* Lamins organize the global three-dimensional genome from the nuclear periphery. *Mol Cell* 2018;71:802–15. https://doi.org/10.1016/j.molcel.2018.05.017e7.
46. Guelen L, Pagie L, Brasset E *et al.* Domain organization of human chromosomes revealed by mapping of nuclear lamina interactions. *Nature* 2008;453:948–51. https://doi.org/10.1038/nature06947
47. van Steensel B, Belmont AS. Lamina-associated domains: links with chromosome architecture, heterochromatin, and gene repression. *Cell* 2017;169:780–91. https://doi.org/10.1016/j.cell.2017.04.022
48. Wang Y, Elsherbiny A, Kessler L *et al.* Lamin A/C-dependent chromatin architecture safeguards naïve pluripotency to prevent aberrant cardiovascular cell fate and function. *Nat Commun* 2022;13:6663. https://doi.org/10.1038/s41467-022-34366-7
49. Liu B, Wang Z, Zhang L *et al.* Depleting the methyltransferase Suv39h1 improves DNA repair and extends lifespan in a progeria mouse model. *Nat Commun* 2013;4:1868. https://doi.org/10.1038/ncomms2885
50. Karoutas A, Szymanski W, Rausch T *et al.* The NSL complex maintains nuclear architecture stability via lamin A/C acetylation. *Nat Cell Biol* 2019;21:1248–60. https://doi.org/10.1038/s41556-019-0397-z
51. Ontology Consortium G, Aleksander SA, Balhoff J *et al.* The Gene Ontology knowledgebase in 2023. *Genetics* 2023;224:iyad031. https://doi.org/10.1093/genetics/iyad031
52. Kaneshiro JM, Capitanio JS, Hetzer MW. Lamin B1 overexpression alters chromatin organization and gene expression. *Nucleus* 2023;14:2202548. https://doi.org/10.1080/19491034.2023.2202548
53. de Vries SJ, van Dijk M, Bonvin AMJJ. The HADDOCK web server for data-driven biomolecular docking. *Nat Protoc* 2010;5:883–97. https://doi.org/10.1038/nprot.2010.32
54. Wu SC, Zhang Y. Cyclin-dependent kinase 1 (CDK1)-mediated phosphorylation of enhancer of zeste 2 (Ezh2) regulates its stability. *J Biol Chem* 2011;286:28511–9. https://doi.org/10.1074/jbc.M111.240515
55. Jeong S, Ahn J, Jo I *et al.* Cyclin-dependent kinase 1 depolymerizes nuclear lamin filaments by disrupting the head-to-tail interaction of the lamin central rod domain. *J Biol Chem* 2022;298:102256. https://doi.org/10.1016/j.jbc.2022.102256
56. Hendzel MJ, Wei Y, Mancini MA *et al.* Mitosis-specific phosphorylation of histone H3 initiates primarily within pericentromeric heterochromatin during G2 and spreads in an ordered fashion coincident with mitotic chromosome condensation. *Chromosoma* 1997;106:348–60. https://doi.org/10.1007/s004120050256
57. Yang L, Besschetnova TY, Brooks CR *et al.* Epithelial cell cycle arrest in G2/M mediates kidney fibrosis after injury. *Nat Med* 2010;16:535–43. https://doi.org/10.1038/nm.2144
58. Lovisa S, LeBleu VS, Tampe B *et al.* Epithelial-to-mesenchymal transition induces cell cycle arrest and parenchymal damage in renal fibrosis. *Nat Med* 2015;21:998–1009. https://doi.org/10.1038/nm.3902
59. Hu S, Lu Y, Yu G *et al.* Epithelial–mesenchymal transition couples with cell cycle arrest at various stages. bioRxiv, https://doi.org/10.1101/2025.02.24.639880, 28 February 2025, preprint: not peer reviewed.
60. Kochin V, Shimi T, Torvaldson E *et al.* Interphase phosphorylation of lamin A. *J Cell Sci* 2014;127:2683–96.
61. Ikegami K, Secchia S, Almakki O *et al.* Phosphorylated Lamin A/C in the nuclear interior binds active enhancers associated with abnormal transcription in progeria. *Dev Cell* 2020;52:699–713. https://doi.org/10.1016/j.devcel.2020.02.011
62. Liu S, Xiong F, Dou Z *et al.* Phosphorylation of Lamin A/C regulates the structural integrity of the nuclear envelope. *J Biol Chem* 2025;301:108033. https://doi.org/10.1016/j.jbc.2024.108033
63. Zou Z, Ohta T, Miura F *et al.* ChIP-Atlas 2021 update: a data-mining suite for exploring epigenomic landscapes by fully integrating ChIP-seq, ATAC-seq and Bisulfite-seq data. *Nucleic Acids Res* 2022;50:W175–82. https://doi.org/10.1093/nar/gkac199
64. Medeiros B, Allan AL. Molecular mechanisms of breast cancer metastasis to the lung: clinical and experimental perspectives. *Int J Mol Sci* 2019;20:2272.
65. Zhang J, Xie Q, Huo X *et al.* Impact of intestinal dysbiosis on breast cancer metastasis and progression. *Front Oncol* 2022;12:1037831. https://doi.org/10.3389/fonc.2022.1037831
66. Capo-chichi CD, Cai KQ, Simpkins F *et al.* Nuclear envelope structural defects cause chromosomal numerical instability and aneuploidy in ovarian cancer. *BMC Med* 2011;9:28. https://doi.org/10.1186/1741-7015-9-28
67. Danielsson BE, George Abraham B, Mäntylä E *et al.* Nuclear lamina strain states revealed by intermolecular force biosensor. *Nat Commun* 2023;14:3867. https://doi.org/10.1038/s41467-023-39563-6
68. Fan J-R, Chang S-N, Chu C-T *et al.* AKT2-mediated nuclear deformation leads to genome instability during epithelial–mesenchymal transition. *iScience* 2023;26:106992. https://doi.org/10.1016/j.isci.2023.106992
69. Jia Y, Vong JSL, Asafova A *et al.* Lamin B1 loss promotes lung cancer development and metastasis by epigenetic derepression of RET. *J Exp Med* 2019;216:1377–95. https://doi.org/10.1084/jem.20181394
70. Pascual-Reguant L, Blanco E, Galan S *et al.* Lamin B1 mapping reveals the existence of dynamic and functional euchromatin lamin B1 domains. *Nat Commun* 2018;9:3420. https://doi.org/10.1038/s41467-018-05912-z
71. Wazir U, Ahmed MH, Bridger JM *et al.* The clinicopathological significance of lamin A/C, lamin B1 and lamin B receptor mRNA expression in human breast cancer. *Cell Mol Biol Lett* 2013;18:595–611. https://doi.org/10.2478/s11658-013-0109-9
72. Tiwari N, Tiwari VK, Waldmeier L *et al.* Sox4 is a master regulator of epithelial–mesenchymal transition by controlling Ezh2 expression and epigenetic reprogramming. *Cancer Cell* 2013;23:768–83. https://doi.org/10.1016/j.ccr.2013.04.020
73. Zhang Y, Donaher JL, Das S *et al.* Genome-wide CRISPR screen identifies PRC2 and KMT2D-COMPASS as regulators of distinct EMT trajectories that contribute differentially to metastasis. *Nat Cell Biol* 2022;24:554–64. https://doi.org/10.1038/s41556-022-00877-0

74. Gallardo A, Molina A, Asenjo HG *et al.* EZH2 endorses cell plasticity to non-small cell lung cancer cells facilitating mesenchymal to epithelial transition and tumour colonization. *Oncogene* 2022;41:3611–24. https://doi.org/10.1038/s41388-022-02375-x
75. Gallardo A, López-Onieva L, Belmonte-Reche E *et al.* EZH2 represses mesenchymal genes and upholds the epithelial state of breast carcinoma cells. *Cell Death Dis* 2024;15:609. https://doi.org/10.1038/s41419-024-07011-y
76. Li Z, Wang D, Lu J *et al.* Methylation of EZH2 by PRMT1 regulates its stability and promotes breast cancer metastasis. *Cell Death Differ* 2020;27:3226–42. https://doi.org/10.1038/s41418-020-00615-9
77. Gesson K, Rescheneder P, Skoruppa MP *et al.* A-type lamins bind both hetero- and euchromatin, the latter being regulated by lamina-associated polypeptide 2 alpha. *Genome Res* 2016;26:462–73. https://doi.org/10.1101/gr.196220.115
78. Blanc RS, Richard S. Arginine methylation: the coming of age. *Mol Cell* 2017;65:8–24. https://doi.org/10.1016/j.molcel.2016.11.003
79. Johnson N, Cai D, Kennedy RD *et al.* Cdk1 participates in BRCA1-dependent S phase checkpoint control in response to DNA damage. *Mol Cell* 2009;35:327–39. https://doi.org/10.1016/j.molcel.2009.06.036
80. Schuhwerk H, Kleemann J, Gupta P *et al.* The EMT transcription factor ZEB1 governs a fitness-promoting but vulnerable DNA replication stress response. *Cell Rep* 2022;41:111819. https://doi.org/10.1016/j.celrep.2022.111819
81. Akhmetkaliyev A, Alibrahim N, Shafiee D *et al.* EMT/MET plasticity in cancer and Go-or-Grow decisions in quiescence: the two sides of the same coin? *Mol Cancer* 2023;22:90. https://doi.org/10.1186/s12943-023-01793-z
82. Schuhwerk H, Brabletz T. Mutual regulation of TGFβ-induced oncogenic EMT, cell cycle progression and the DDR. *Semin Cancer Biol* 2023;97:86–103. https://doi.org/10.1016/j.semcancer.2023.11.009
83. Perelli L, Zhang L, Mangiameli S *et al.* Evolutionary fingerprints of epithelial-to-mesenchymal transition. *Nature* 2025;640:1083–92. https://doi.org/10.1038/s41586-025-08671-2
84. Vega S, Morales AV, Ocaña OH *et al.* Snail blocks the cell cycle and confers resistance to cell death. *Genes Dev* 2004;18:1131–43. https://doi.org/10.1101/gad.294104
85. Pastushenko I, Blanpain C. EMT transition states during tumor progression and metastasis. *Trends Cell Biol* 2019;29:212–26. https://doi.org/10.1016/j.tcb.2018.12.001
86. Kröger C, Afeyan A, Mraz J *et al.* Acquisition of a hybrid E/M state is essential for tumorigenicity of basal breast cancer cells. *Proc Natl Acad Sci USA* 2019;116:7353–62.
87. Buxboim A, Swift J, Irianto J *et al.* Matrix elasticity regulates lamin-A,C phosphorylation and turnover with feedback to actomyosin. *Curr Biol* 2014;24:1909–17. https://doi.org/10.1016/j.cub.2014.07.001
88. Chandrashekar DS, Bashel B, Balasubramanya SAH *et al.* UALCAN: a portal for facilitating tumor subgroup gene expression and survival analyses. *Neoplasia* 2017;19:649–58. https://doi.org/10.1016/j.neo.2017.05.002
89. Chandrashekar DS, Karthikeyan SK, Korla PK *et al.* UALCAN: an update to the integrated cancer data analysis platform. *Neoplasia* 2022;25:18–27. https://doi.org/10.1016/j.neo.2022.01.001

Received: June 3, 2025. **Revised:** November 26, 2025. **Accepted:** November 30, 2025

frontiers | Frontiers in Cell and Developmental Biology

TYPE Review
PUBLISHED 16 December 2022
DOI 10.3389/fcell.2022.1068347

OPEN ACCESS

EDITED BY
Eric C. Schirmer,
University of Edinburgh,
United Kingdom

REVIEWED BY
Susana Gonzalo-Hervas,
Saint Louis University, United States
Fred Dick,
Western University, Canada
Jop Kind,
Hubrecht Institute (KNAW), Netherlands

*CORRESPONDENCE
Kundan Sengupta,
kunsen@iiserpune.ac.in

†These authors have contributed equally to this work

SPECIALTY SECTION
This article was submitted to Nuclear Organization and Dynamics, a section of the journal Frontiers in Cell and Developmental Biology

RECEIVED 12 October 2022
ACCEPTED 05 December 2022
PUBLISHED 16 December 2022

CITATION
Balaji AK, Saha S, Deshpande S, Poola D and Sengupta K (2022), Nuclear envelope, chromatin organizers, histones, and DNA: The many achilles heels exploited across cancers. *Front. Cell Dev. Biol.* 10:1068347. doi: 10.3389/fcell.2022.1068347

Nuclear envelope, chromatin organizers, histones, and DNA: The many achilles heels exploited across cancers

A. K. Balaji†, Santam Saha†, Shruti Deshpande†, Darshini Poola and Kundan Sengupta*

Chromosome Biology Lab (CBL), Indian Institute of Science Education and Research, Pune, Maharashtra, India

In eukaryotic cells, the genome is organized in the form of chromatin composed of DNA and histones that organize and regulate gene expression. The dysregulation of chromatin remodeling, including the aberrant incorporation of histone variants and their consequent post-translational modifications, is prevalent across cancers. Additionally, nuclear envelope proteins are often deregulated in cancers, which impacts the 3D organization of the genome. Altered nuclear morphology, genome organization, and gene expression are defining features of cancers. With advances in single-cell sequencing, imaging technologies, and high-end data mining approaches, we are now at the forefront of designing appropriate small molecules to selectively inhibit the growth and proliferation of cancer cells in a genome- and epigenome-specific manner. Here, we review recent advances and the emerging significance of aberrations in nuclear envelope proteins, histone variants, and oncohistones in deregulating chromatin organization and gene expression in oncogenesis.

KEYWORDS

lamins, heterochromatin, genome organization, nuclear envelope, oncohistones, histone variants

1 Introduction

Each chromosome occupies a unique sub-volume in the interphase nucleus, referred to as a chromosome territory (Cremer and Cremer, 2001). A chromosome territory encompasses intra- and inter-chromatin interactions, further fine-tuned by histone modifications. Analyses of chromatin interactions have revealed the organization of chromatin into two distinct compartments—A and B. Compartment A is composed of gene-rich, open chromatin localized toward the nuclear interior. In contrast, compartment B is gene-poor, has a compact conformation, and is localized toward the nuclear periphery. Closer inspection using variants of chromosome conformation capture assays, such as 3C, 4C, and Hi-C, reveals that the 3D genome architecture of a nucleus is intricately organized into Topologically Associating Domains (TADs), where

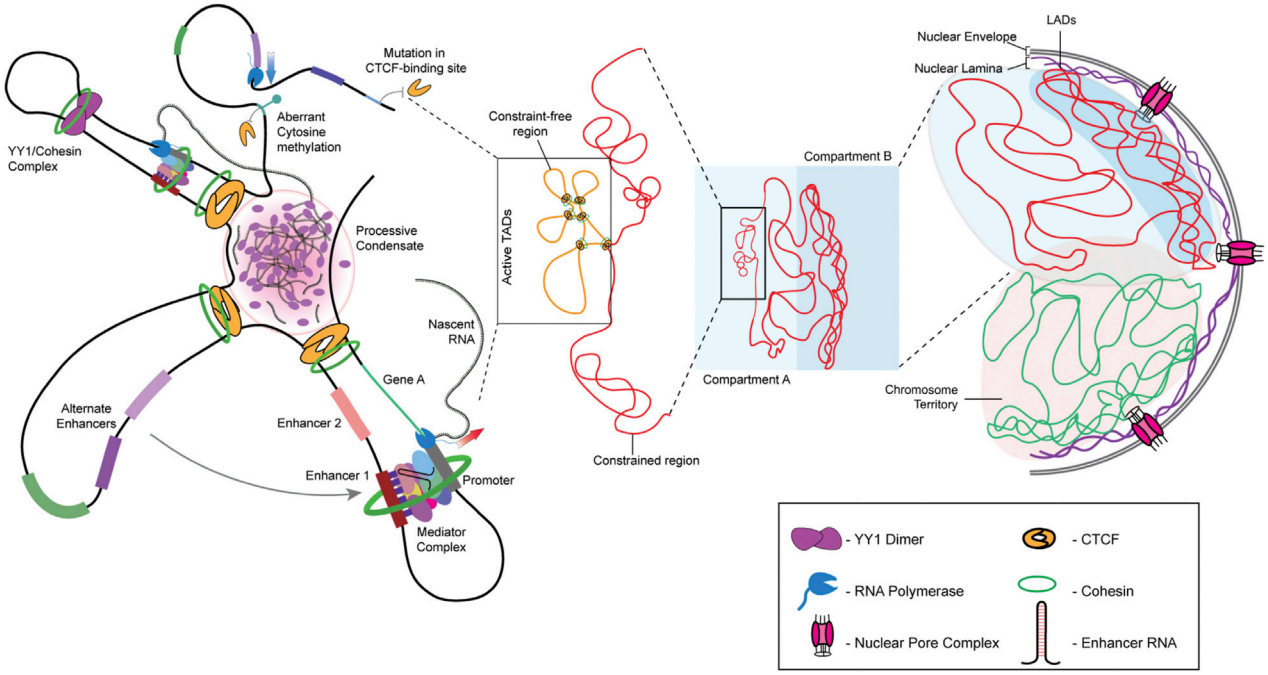

FIGURE 1
Hierarchy of genome organization. The involvement of lamins facilitates LAD organization at the nuclear periphery. Lamins organize the transcriptionally inactive B compartment of the TADs proximal to the nuclear envelope, while the transcriptionally active A compartment is maintained relatively toward the nuclear interior. The promoter-enhancer contacts are maintained by genome organizers such as cohesin, condensin, and CTCF. The presence of multiple such contacts within a TAD allows the formation of splicing condensates.

stretches of chromatin physically interact in a regulated manner to modulate gene expression within the TAD (Figure 1) (Szabo et al., 2019). The loop extrusion model of chromatin organization forms the basis of TAD-mediated genome organization, where chromatin loops are extruded by chromatin organizers and cohesin complexes and are delimited by CCCTC-binding factor (CTCF), another chromatin organizer (Fudenberg et al., 2016; Nuebler et al., 2018). TADs organize looping-in of sequences ~1 Mb (in mammals) apart within close proximity, enabling enhancer-promoter contacts for the spatiotemporal regulation of gene expression (Chetverina et al., 2017). Interestingly, chromatin stretches with the same type of histone modifications show a propensity to interact and compartmentalize in the 3D space of the nucleus, thus revealing CTCF-cohesin-independent chromatin folding mechanisms. For instance, H3K27me3 histone modifications function as a signal for long-range chromatin interactions during hematopoietic stem cell differentiation (Zhang X et al., 2020). Notably, in addition to CTCF, genome organizers such as cohesin and condensin are required for the recruitment of transcription cofactors. Cohesin and CTCF function as boundary elements that collectively maintain genome architecture, which is prudently rigid and guardedly dynamic (Phillips-Cremins et al., 2013). Furthermore, chromatin remodelers alter local chromatin dynamics in response to cell signaling events. The maintenance of TADs is critical since disruption of TAD organization is associated with developmental diseases and cancers (Lupiáñez et al., 2015; Akdemir et al., 2020). In cancers, the aberrant activation of cell signaling pathways relays erratic signals to the nucleus, which alters chromatin organization and transcriptional outputs of the cell. It remains to be examined how chromatin and its organizers respond to aberrant oncogenic signaling in cancer cells.

The double-membraned nucleus functions as the primary protector of the genome. In metazoans, the nucleus not only harbors the genome but also works in tandem with the differentially-compacted chromatin to regulate its tissue-specific spatial and functional organization. The nuclear envelope comprises the nuclear lamina that maintains nuclear integrity and regulates gene expression and is interspersed with Nuclear Pore Complexes (NPCs), whose primary function is to regulate nuclear transport (Lin et al., 2018). Though the chromatin in contact with the nuclear lamina is frequently repressed, NPCs additionally contribute to the regulation of gene expression. Furthermore, owing to the role of NPCs in chromatin organization and function, Nucleoporins (Nups), the class of proteins that comprise the NPC, are also involved in

regulating stemness and cell fate determination (D'Angelo et al., 2012). Interestingly, nucleoporins crosstalk with the chromatin organizer CTCF, which functions as a boundary element between TADs, while facilitating intra-TAD interaction. For instance, the nucleoporins Nup153 and Nup93, along with CTCF, regulate the transcriptional activity of the HOX gene cluster during early development and differentiation (Kadota et al., 2020; Labade et al., 2021).

In metazoans, type V intermediate filament proteins, the lamins, maintain the structural and functional integrity of the nucleus (Aebi et al., 1986; Gruenbaum and Foisner, 2015). The nuclear lamina is predominantly composed of two lamin sub-types—the A-type lamins that include lamins A and C (a spliced variant of lamin A), and the B-type lamins that comprise separately-encoded lamins B1 and B2 (in vertebrates). Each lamin sub-type harbors post-translational modifications (PTMs), exponentially increasing the functional diversity of lamins. Nuclear lamins regulate replication-dependent cell cycle progression, DNA damage repair, genome stability, and 3D organization of the genome (Moir et al., 2000; Bronshtein et al., 2015; Earle et al., 2020). Nuclear lamina interacts with stretches of chromatin that are in proximity to the nuclear periphery, referred to as Lamina-Associated Domains (LADs). LADs are typically repressed, barring exceptions where a subset of euchromatin interacts with lamin B1 and are categorized as euchromatic LADs (eLADs) (Guelen et al., 2008; Pascual-Reguant et al., 2018).

Chromatin in eukaryotes is organized as DNA wrapped around histone octamers, forming nucleosomes. Further, the linker histone H1 is incorporated with the nucleosomes constituting the fundamental units of the chromatin fiber—the chromatosomes (Zhang and Li, 2017). Histones are among the most widely modified proteins, and each modification has the unique ability to regulate gene expression (Turner, 1993; Millán-Zambrano et al., 2022). Actively transcribing genomic regions localized away from the nuclear periphery are often associated with active histone marks such as H3K4me3, H3K9ac, and H3K27ac, deposited by histone remodelers such as KMT2, CBP, and p300, respectively (Ogryzko et al., 1996; Rao and Dou, 2015). On the other hand, histone modifications such as H3K9me2/3, H3K27me3, and H4K20me1 are associated with transcriptional repression. The combination of active and inactive marks fine-tunes transcriptional output (Kimura, 2013; Talbert and Henikoff, 2021). Of note, repressive histone marks such as H3K9me2/3 and H3K27me3, deposited by INM-interacting histone-remodeling complexes such as SUV39H1/2 and the Polycomb Repressor Complex 2 (PRC2) complex, are often enriched on LADs (Shumaker et al., 2006; Cesarini et al., 2015; Harr et al., 2015). These histone-remodeling complexes interact with lamins and maintain the associated chromatin in a state of repression (Marullo et al., 2016; Salvarani et al., 2019; Bianchi et al., 2020; Siegenfeld et al., 2022).

Cancer cells exhibit a remarkable interplay between aberrant genome organization and deregulated transcription. The cancer genome harbors mutations in both coding and non-coding regions, selectively providing tumorigenic cells with a proliferative advantage to outcompete normal cells (Moreno and Basler, 2004; Pon and Marra, 2015; Bailey et al., 2021). For instance, incorporating non-canonical histone variants alters nucleosome stability, often resulting in altered replication and transcription (Bönisch et al., 2012; Henikoff and Smith, 2015; Buschbeck and Hake, 2017). In solid tumors, mutant chromatin remodelers differentially recruit histone modifiers that confer chemoresistance (Drosos et al., 2022). These cancer-associated mutant histones are referred to as oncohistones, which are now emerging as a class of prominent biomarkers of cancers (Bočkaj et al., 2021). In this review, we address the molecular and mechanistic underpinnings of nuclear envelope factors, their crosstalk with chromatin, and their pivotal role in cancer initiation and progression.

2 Nuclear envelope and lamins

The nuclear envelope is a crucial barrier between the cytoplasm and the nucleus and functions as a protector of the genome. The nuclear envelope consists of an outer and inner nuclear membrane (ONM and INM, respectively) and NPCs. The INM is lined on the inner side by a protein meshwork referred to as the nuclear lamina, which is composed of type V intermediate filament proteins—the A- and B-type lamins. The A-type lamins, lamin A/C, are produced as two somatic isoforms of prelamin A by alternative mRNA splicing at exon 10 of the LMNA gene (Machiels et al., 1996). Lamin A bears a CaaX motif at its C-terminal end, which is farnesylated, in contrast to lamin C, which does not contain the CaaX motif or undergo farnesylation (Vorburger et al., 1989). Notably, mature lamin A is formed by the loss of farnesylation inside the nucleus. On the other hand, the predominant B-type lamins—lamins B1 and B2 are permanently-farnesylated products of two separate genes—LMNB1 and LMNB2. Lamins interact with chromatin, either directly or through transmembrane proteins of the INM—lamin B receptor (LBR), MAN1, and Emerin (Ye and Worman, 1996; Holaska and Wilson, 2007; Demmerle et al., 2012). Apart from biochemical cues, the nucleus directly perceives mechanical signals through the LINC complex, involving Nesprin and SUN proteins (Figure 2). Nesprins, which extend from the ONM to the perinuclear space, directly interact with cytoskeletal proteins such as vimentin, actin, and microtubules (Ketema et al., 2013; Gimpel et al., 2017; Li et al., 2021). Mechanical cues are subsequently propagated *via* the interaction with the SUN and KASH domain proteins (Starr and Fischer, 2005; Tzur et al., 2006). These lines of evidence suggest that the coordinated functioning of nuclear lamins, nucleoporins, and LINC complex factors is central to the functional organization of the nucleus and the genome.

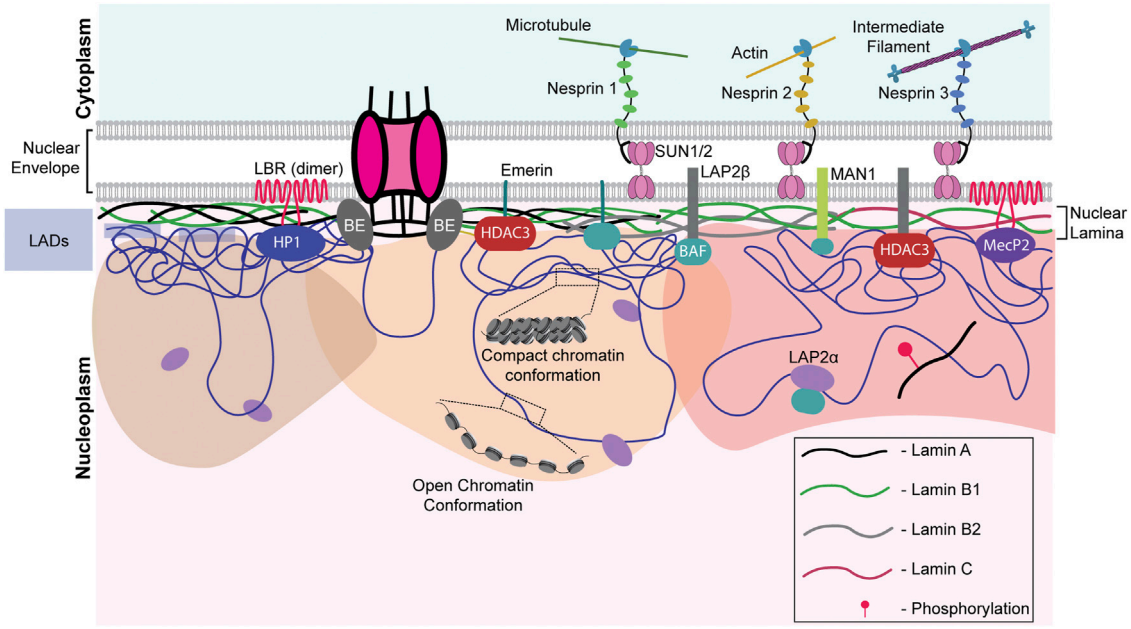

FIGURE 2
Nuclear envelope architecture and its role in genome organization. A schematic model showing the INM proteome involved in maintaining genome organization. Nesprins communicate external mechanical cues to the nucleus *via* the SUN1/2 complex. The regions of the genome contacting the nuclear lamina, the LADs, are maintained in a heterochromatic state. Phosphorylated lamin A binds to active enhancers in the nuclear interior. LAP2α interacts with intra-nuclear lamin A/C and could be regulating its functioning. Chromatin remodelers such as HDACs and sirtuins are often associated with the INM proteins such as emerin, MAN1, LAP2β, lamins, and LBR. NPCs are also associated with chromatin. LAP2α - lamina Associated Peptide 2α, LBR - lamin B receptor, BE - Barrier Element, HP1—Heterochromatin Protein 1, HDAC—histone deacetylase, SUN1/2—Sad1/unc-84 protein-like 1/2 and MeCP2—methyl CpG-binding protein 2.

Aberrations in nuclear morphology, such as invaginations, blebs, and micronuclei, serve as histological markers for grading tumor progression and often correlate with carcinogenesis. For instance, Haematoxylin-Eosin (HE) staining of papillary thyroid carcinoma cells and colon adenocarcinoma revealed enlarged nuclei with irregular morphology compared to normal cells with smaller and spherical nuclei (Fischer, 2020). Furthermore, nearly 90% of solid tumors are characterized by aneuploidy, which predominantly involves deletions and amplifications at the whole chromosomal and sub-chromosomal levels (Holland and Cleveland, 2012). CIN leads to transcriptional imbalances in a cell- and tissue-specific manner (Bakhoum et al., 2018; Benhra et al., 2018). Here, we focus on the mechanisms by which defects in the nuclear envelope manifest themselves, resulting in genomic instability and thereby contributing to cancer progression.

2.1 Role of aberrant nuclear envelope factors in cancers

The stability and integrity of LINC complex proteins and nuclear lamins are crucial for maintaining chromatin organization and genome stability, aberrations of which are associated with various cancers (Sur et al., 2014). For instance, immunohistochemistry showed decreased expression of LMNA and LMNB1 in 7/8 primary gastric cancers and 6/8 gastric cancers, respectively (Moss et al., 1999). In addition, nuclear envelope proteins regulate chromosomal stability as they participate in cell cycle progression, chromosome segregation, and nuclear envelope assembly post-mitosis (Dechat et al., 2007; Kuga et al., 2014; Dubińska-Magiera et al., 2019).

Remarkably, nuclear morphology plays a vital role in modulating cell fate in the continuum of cancer progression (Capo-Chichi et al., 2016; Smith et al., 2018; Fischer, 2020). In particular, the loss of emerin and lamin A show aberrations in nuclear morphology, accompanied by an increased aggressiveness of cancer cells (Reis-Sobreiro et al., 2018; Bell et al., 2022). Consistent with this finding, ovarian cancers show decreased emerin and lamin A/C levels, accompanied by a progressive destabilization of the nuclear envelope (Capo-chichi et al., 2011). Lamin A/C-emerin co-depletion alters chromatin mobility, suggestive of their role in the maintenance of genome organization and function (Ranade et al., 2019). Intriguingly, depletion of lamin A/C mislocalized emerin, resulting in altered nuclear morphology and increased invasiveness of DU145 prostate cancer cells (Kong et al., 2012; Reis-Sobreiro et al., 2018).

The nuclear lamina is composed of three lamin sub-types and interacts with the LINC complex genes, and this confers a molecular redundancy on lamin function, which counters abrupt alterations in the lamina—predominantly in response to external cues. For instance, keratinocytes and fibroblasts of the skin derived from lamin A/C-knockout mice showed prolonged expression of LBR as compared to wild-type cells (Solovei et al., 2013). Similar buffering mechanisms were uncovered in EMD- and LMNA-null mice during development. While LAP2α was upregulated in myogenic cells derived from $LMNA^{-/-}$ mice, cells derived from EMD-null mice showed a compensatory increase in lamin A expression (Melcon et al., 2006). However, the mechanistic basis of the transcriptional feedback circuits between lamin A/C and the nuclear envelope factors remains to be examined in greater detail.

The nuclear lamina functions as a docking site for anchoring LADs enriched in heterochromatin. For example, LBR tethers heterochromatin to the nuclear envelope in actively proliferating cancer cells during the early stages of mammalian development, while lamin A/C is a chromatin anchor in differentiated cells (Solovei et al., 2013; Lukášová et al., 2017). It is interesting to note that the loss of both LBR and lamin A/C results in the inversion of chromatin with heterochromatin toward the nuclear interior (Solovei et al., 2013), reiterating the significance of the nuclear lamina in chromatin organization and function. Furthermore, lamin B1 loss significantly increases nuclear bleb formation, while the depletion of lamin A/C shows morphological aberrations such as nuclear atypia, in addition to aneuploidy and CIN (Lammerding et al., 2006; Capo-chichi et al., 2011). Furthermore, destabilization of the nuclear envelope shows enhanced nuclear blebbing and micronuclei formation, which contribute to chromosomal losses and aneuploidy (Capo-Chichi et al., 2016). In addition to A and B-type lamins, peripheral heterochromatin provides additional stiffness, and its deregulation foreseeably weakens the nuclear envelope, contributing to the formation of nuclear blebs (Stephens et al., 2018). In summary, a stable nuclear envelope composition is required for genome organization facilitated by the maintenance of nuclear integrity by reinforcing nuclear stiffness.

Interestingly, the loss of lamin B1 shows CIN and DNA damage by destabilizing key Homologous Recombination (HR) pathway proteins such as Rad51 in U2OS cells (Liu et al., 2015). Correspondingly, A-type lamins regulate HR through transcriptional co-regulation of RAD51 and BRCA1 while modulating Non-Homologous End Joining (NHEJ) through 53BP1 in breast cancer cells (Redwood et al., 2011). Lamin A also regulates DNA damage repair (DDR) *via* its direct interaction with Hsp90—a molecular chaperone involved in protein folding and stability in ovarian cancer cells (Wang et al., 2021). Furthermore, whether the differential stoichiometry of the A and B-type lamins modulates NHEJ or HR pathways to repair damaged DNA in a cell-type- and cancer-specific manner remains an open question.

2.2 Role of nucleoporins in genome organization and cancers

Nuclear pore complexes (NPCs) are ~120 nm-wide structures in the nuclear envelope, which mediate selective transport in and out of the nucleus. In vertebrates, NPCs comprise nucleoporins (Nups), a group of ~30 proteins, to form a ~125MDa protein complex (Cronshaw et al., 2002; Cohen et al., 2012). In addition to nuclear transport, the NPCs regulate chromatin interaction and function (Zhou and Panté, 2010; Kadota et al., 2020). Further, Nups are classified into 1) on-pore Nups that are associated with the NPC and 2) off-pore Nups that exist both in the NPC and nucleoplasm. Nups that interact with and regulate essential genes in the genome include Nup93 (on-pore) and Nup153 (off-pore), which interact with super-enhancers, and function as major chromatin regulators (Baumann, 2016; Ibarra et al., 2016). Nup153 and Nup98, present near the nuclear basket of the NPC, communicate with a wide range of poised genes through interactions with CTCF (Pascual-Garcia et al., 2017). Certain on-pore Nups, such as Nup93, interact with and repress HOXA genes which are essential for early development (Labade et al., 2016). In the context of cancer progression, Nup93 facilitates metastasis by enhancing β-catenin import and upregulating EMT target genes, thus inducing epithelial-to-mesenchymal transition (EMT) in breast and hepatocellular cancers (Lin et al., 2022; Nataraj et al., 2022). The on-pore Nup210 interacts with SUN2 to regulate the expression of prometastatic mechanosensitive genes by impeding the spread of heterochromatin (Amin et al., 2021). Intriguingly, a non-canonical extranuclear function of the Nup107-160 complex is to stabilize bipolar spindle arrangement and prevent aneuploidy during each cell division, thus maintaining genome integrity (Orjalo et al., 2006).

Nups contribute to cancer progression by forming fusion proteins. For instance, the off-pore Nup98 is involved in multiple fusion proteins with transcriptional coactivators, histone methyltransferases, helicases, and in some instances, even orphan proteins (Wang et al., 2007; Yassin et al., 2010; Gough et al., 2011). During hematopoietic stem cell differentiation, HoxA7, HoxA9, and HoxA10 levels are upregulated, which progressively decrease as the hematopoietic cells differentiate further into various lineages. The Nup98 fusion protein alters gene expression resulting in Acute Myeloid Leukemia (AML). Intriguingly, in Nup98-NSD1 fusion protein-mediated AML, the fusion protein is recruited to the HoxA7, HoxA9, and HoxA10 gene loci. The FG-repeat (originating from Nup98) of the fusion protein interacts with HAT CBP/p300, leading to overexpression of the aforementioned Hox genes, contributing to AML. Nup98-PHD fusion proteins also promote AML progression *via* a similar mechanism (Wang et al., 2007, 2009). Thus, the aberrant localization and expression of Nups impact genome organization, contributing to oncogenesis. Taken together, the cellular machinery effectively copes with aberrant

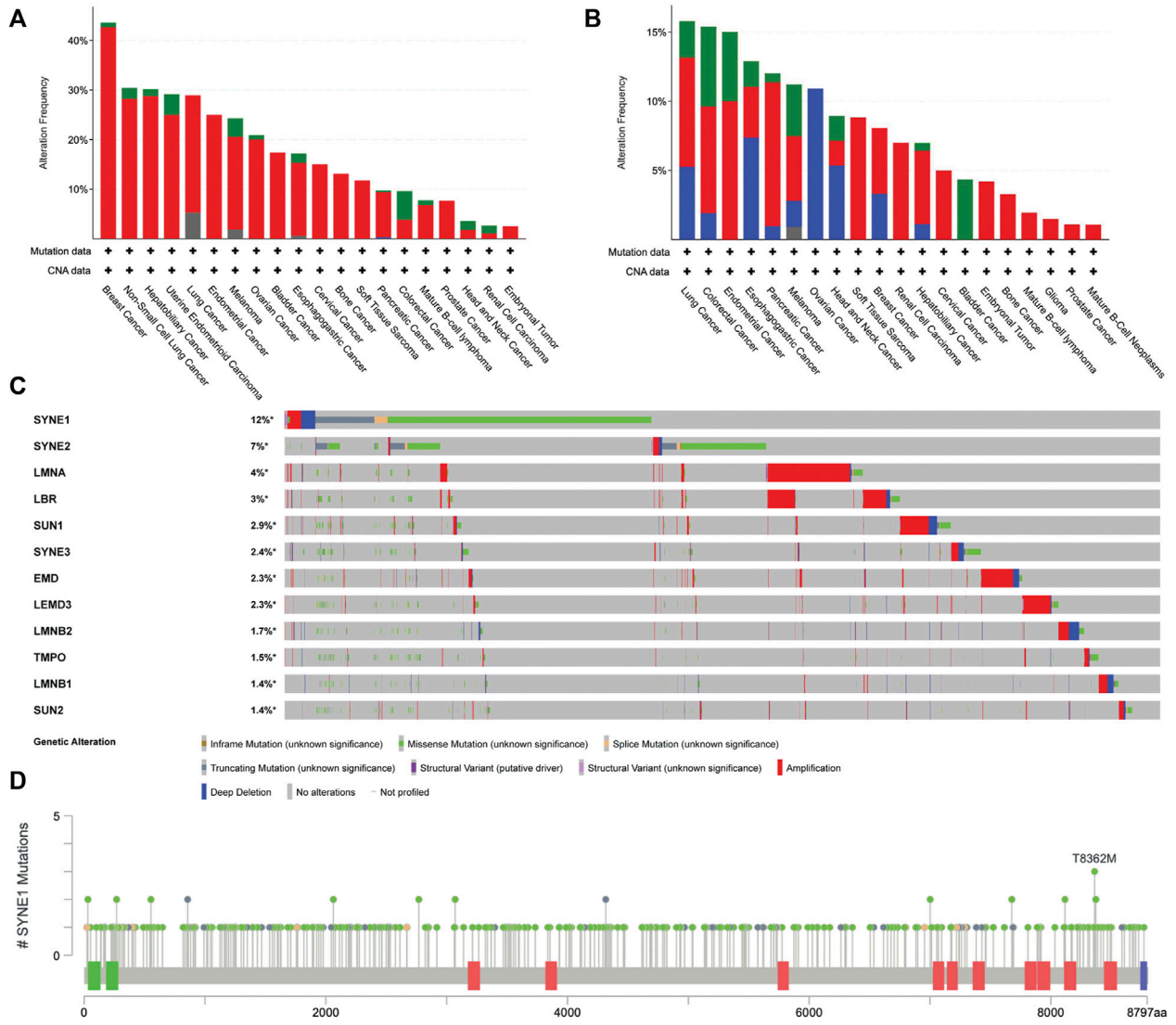

FIGURE 3
Analysis of genetic alterations in nuclear envelope genes in cancer patients using cBioPortal data (ICGC/TCGA Pan-Cancer Analysis of Whole Genomes Consortium 2020) CNAs in **(A)** LMNA **(B)** LMNB (B1 and B2) **(C)** Oncoprint of 10 nuclear envelope genes across 10967 cancer patient samples arranged in descending order based on the frequency of missense mutations **(D)** Localization and frequency of SYNE1 mutations in cancer patients using lollipop plot of cBioPortal (Cerami et al., 2012; Gao et al., 2013).

gene expression—a major target for future therapeutic approaches.

2.3 Lamins modulate copy number alterations in cancers

Assessing alterations in chromosome numbers is a key method for cancer diagnostics. Tumorigenesis often involves the progressive acquisition of genetic alterations in specific genes. Copy Number Alterations (CNAs) have been identified and characterized across a wide range of cancer types using high-density single nucleotide polymorphism (SNP) arrays (Chen et al., 2013). Determining therapeutic strategies in the case of deep deletions becomes especially difficult owing to the absence of the gene in the cancer cell genome, with its functional redundancy prepending an added layer of complexity. Teasing apart whether CNAs serve as drivers of cancers or silent passengers of its effects remains an area of active investigation. Here, we review the most recent advances in our understanding of the interplay between CNAs and cancer progression through data curated from cBioportal Figure 3 (Cerami et al., 2012; Gao et al., 2013).

2.3.1 Amplifications

It is well established that CIN and aneuploidy involving whole chromosomal and focal amplifications and deletions in the genome are defining features of cancer initiation and progression (Watanabe et al., 2001; Zhou et al., 2002; Kops et al., 2004). Interestingly, genes that encode for lamins are strikingly amplified as compared to the other nuclear envelope genes, implying that the very mechanisms that protect genomic integrity aberrate in cancers. TCGA analyses of nuclear envelope genes across patient samples revealed CNAs of the LMNA-coding sequence in ~13% of cancers. Breast cancer patient samples show the maximum extent of CNAs in LMNA in ~40% of the 211 patient samples (Figure 3A). However, the extent to which gene amplifications in LMNA correlate with changes in its transcript level remains unclear. An intriguing possibility is that transcriptional deregulation of lamin A/C potentially impacts expression levels of B-type lamins or LINC genes as a consequence of copy number amplifications of lamins and the stability of their interacting partners in a cell-type-specific manner.

2.3.2 Deletions

Interestingly, the LMNB1 gene shows a significant number of deletions across cancers. It is unique that LMNB1 and LMNB2 genes showed only deep deletions in ovarian cancers (Figures 3B,C). In ovarian cancer cells (HO-8910PM), decreased expression levels of lamin A/C correlate with increased cell migration and poor prognosis (Wang et al., 2019). Moreover, the lamin A:B stoichiometric ratio shows a dominance of A-type lamins in stiffer cartilaginous tissues, while B-type lamins are more prominent in softer tissues such as the brain (Swift et al., 2013). Nevertheless, if lamin A:B stoichiometry does modulate the malignant potential of cancer cells, the extent of complementation and the mechanisms that regulate the altered sub-interactome of the A- and B-type lamins remain to be uncovered.

2.3.3 Mutations in nuclear envelope genes—Nesprin (SYNE1)

We examined the status of mutations in genes that encode the nuclear envelope proteins across cancers using cBioPortal. This analysis revealed recurrent mutations in the Nesprin-1 gene—SYNE1 (Figure 3D). Markedly, the SYNE1 gene accumulates the highest number of missense mutations (271), followed by truncating (41) and splice mutations (12). A mutation in exon 33 of the SYNE1 gene modifies a conserved residue in spectrin repeat 11, showing aberrant mitotic phenotypes such as altered distance between the centrosome and the nucleus, potentially contributing to CIN in human hepatoma-derived Huh7 cells (Sur-Erdem et al., 2020). Furthermore, mutation analysis of SYNE1 revealed frequent missense mutations of T8362M across three different cancers—medulloblastoma, pancreatic adenocarcinoma, and ovarian epithelial tumor. However, the physiological significance of these mutations remains to be elucidated. Do mutations in SYNE1 destabilize or hyperactivate mechanochemical signals into the nucleus and chromatin as a consequence of its altered interaction with LINC complex factors and actin? This could further contribute to increased communication with the microenvironment and the consequent proliferation of cancer cells.

3 Chromatin organizers in carcinogenesis

The genome is a highly dynamic collection of genes, their regulators, and massive stretches of DNA whose function is yet to be discovered. Maintenance of genome organization involves the concerted function of numerous proteins required for the regulation of chromatin organization and gene expression. The aberrant function of chromatin organizers is associated with cancers (Table 1). Here, we examine the contribution of major chromatin organizers, namely CTCF, cohesins, and condensins, to cancer progression.

3.1 CTCF

CCCTC-binding factor (CTCF) is a conserved zinc-finger protein that functions as a chromatin organizer and transcription factor. In association with cohesin, CTCF regulates the organization of gene loci and alternative splicing primed by its sequence-specific binding to CTCF sites. In addition, CTCF functions as an insulator to restrict the expansion of repressive marks (Dixon et al., 2012; Holwerda and de Laat, 2013). The human genome has ~55,000–65,000 CTCF binding sites, amongst which around ~5,000 are highly conserved across species (Yusufzai et al., 2004; Chen et al., 2012; Holwerda and de Laat, 2013), though CTCF occupancy remains tissue- and cancer-specific (Hanssen et al., 2017; Debaugny and Skok, 2020). As per the loop extrusion model for TAD formation, the cohesin complex moves along the chromatin, establishing a loop until it encounters an oriented CTCF dimer. Consequently, further advancement of the cohesin complex is aborted, thus demarcating TAD boundaries enriched in CTCF binding sites (Sanborn et al., 2015; Fudenberg et al., 2016). CTCF also prevents non-specific promoter-enhancer interaction by delimiting the loop size, thus augmenting enhancer-blocking mechanisms (Amankwaa et al., 2022). The Yin Yang 1 (YY1) protein interacts with cohesin and is enriched near enhancer-promoter contact sites, thus assisting CTCF in augmenting enhancer-promoter interaction (Figure 1) (Weintraub et al., 2017).

Aberrant expression or occupancy of CTCF is associated with breast, lung, endometrial, gastrointestinal, prostate, and skin

TABLE 1 Role of chromatin organizers in cancers.

Chromatin organizer	Gene	Cancer	Effect of dysregulation of gene	Reference
Cohesin	STAG2	Glioblastoma	Mutation in STAG2 leads to aneuploidy while its rescue enhances the chromosomal stability	Solomon et al. (2011)
	RAD21	Breast	Overexpression of RAD21 in MDA-MB-231 cells leads to poor prognosis and chemoresistance, while its knockdown reduces chemoresistance	Xu et al. (2011)
Condensin	NCAPH	Colorectal	In HCT116, NCAPH depletion decreases cell migration, arrests the cells in G2/M, and enhances apoptosis	Yin et al. (2017)
	NCAPG	Liver	NCAPG has a pro-proliferative effect in adenocarcinoma patients	Zhang et al. (2022)
	NCAPH	Prostate	Upregulation of NCAPH in prostate cancers promotes cell proliferation and helps in bypassing replication checkpoints, which might hinder cancer progression	Kim et al. (2019)
CTCF		Breast	CTCF and EGR1 reduce cell migration in TNBC cell line MDA-MB-231 by inducing the expression of Nm23-H1	Wong et al. (2021)

Mutations in genes that encode for chromatin organizers are implicated in carcinogenesis and impact chromosome organization, stability and transcriptional regulation.

cancers (Eldholm et al., 2014; Kemp et al., 2014; Poulos et al., 2016; Guo et al., 2018; Höflmayer et al., 2020). Of note, multiple mutations map to the DNA-binding zinc finger domain of CTCF across cancers (Bailey et al., 2021). CTCF binding to its target sites is sensitive to their methylation states. For instance, hypermethylation of CTCF binding sites shows a loss of insulation in isocitrate dehydrogenase (IDH) mutant gliomas (Flavahan et al., 2016). This further leads to the ectopic interaction of the IDH enhancer with PDGFRA (platelet-derived growth factor receptor alpha), leading to its constitutive expression and the development of gliomas (Figure 1). However, not all cancer-specific mutations in CTCF affect its binding. For instance, stop codon mutations in its N- and C-terminals, as well as in the zinc finger domain, may exhibit a dominant-negative effect by hindering interactions with functionally important cofactors, thus impeding CTCF function (Debaugny and Skok, 2020).

Analyzing patient data sets from TCGA reveals frequent loss of the CTCF gene in breast and prostate cancer patients, correlating with hypermethylation of CpG islands and hypomethylation of other parts of the genome. CTCF depletion in a prostate cancer cell line, HPECE6/E7, shows hypermethylation of CTCF binding sites, further downregulating respective gene expression (Damaschke et al., 2020). This indicates that CTCF binding to its target sites prevents CpG hypermethylation and safeguards chromatin architecture, not just by organizing the chromatin but also by maintaining it. This study further reveals that drug-induced hypomethylation using 5-aza-2 deoxycytidine (5dAza) rescued chromatin organization, reaffirming the importance of CTCF and its binding sites in cancers. However, 5dAza interacts with a wide range of targets and fails to act precisely on distinct TADs, thus raising the question of specificity in cancer therapies.

CTCF functions as a double-edged sword, acting both as an oncogene as well as a tumor suppressor in a cancer subtype-specific manner. Ovarian cancers exemplify the oncogenic potential of CTCF, where metastatic lesions display elevated CTCF expression. Further, the depletion of CTCF in ovarian cancer cell lines (SKOV3 and A2780) decreased cell migration by consistently downregulating three metastasis-associated genes, including CTBP1, SRC, and SERPINE (Zhao et al., 2017). In contrast, CTCF positively regulates the expression of the metastatic suppressor, Nm23-H1, in breast cancers. Studies in the highly invasive MDA-MB-231 and the less invasive MCF-7 cells show that CTCF-dependent Nm23-H1 levels inversely correlate with cancer aggressiveness (Wong et al., 2021). The mechanism by which CTCF functions in a cancer-specific manner remains poorly understood.

Overall, changes in genome organization due to altered levels or aberrant recruitment of chromatin organizers contribute to cancer progression However, experiments performed in cell culture models need to be complemented with insights from animal models and patient-derived tumor samples. Since adherent cell culture studies are usually performed on a monolayer of cells, these approaches do not mimic the tumor microenvironment, discounting factors such as nutrient accessibility, barrier tissue formation, and variation in drug response, among others. What effects chemotherapeutic agents have on TAD organization and gene expression *in vivo* remains an area of active study. Moreover, it is intriguing that environmental factors, such as diet and social interaction, also impinge on CTCF function and, therefore, chromatin organization and function (Davis et al., 2022; Wang R et al., 2022)—an interesting finding, given that extraneous environmental factors considerably contribute to an increase in the incidence of cancers.

3.2 Cohesin

Cohesins are multi-protein complexes essential for mitosis and meiosis, conserved from yeast to humans. The canonical

function of cohesins is to clasp sister chromatids together during the metaphase-to-anaphase transition. Apart from the aforementioned function, cohesin plays a vital role in maintaining inter-TAD and intra-TAD boundaries by looping chromatin in the interphase nucleus, allowing for regulated inter- and intra-TAD interactions (Matthews and Waxman, 2018; Barrington et al., 2019). This promotes enhancer-promoter contacts in a cell type-specific manner.

Through genome-wide sequencing, it is now apparent that cohesin accumulates a number of mutations in the coding region that alter the way it binds the chromatin and promotes aberrant genomic contacts leading to anomalous expression of various genes. Depletion of RAD21, a component of the cohesin complex, promotes enhanced expression of mesenchymal genes such as ITGA5 and TGF-B1 by altering the intrachromosomal chromatin contacts and creating active transcriptional units (Yun et al., 2016). Recent exome sequencing revealed that the STAG2 protein of cohesin is frequently mutated in cancers (Lawrence et al., 2014). It is interesting to note that STAG2 is involved in promoting regulated chromosomal contacts, the depletion of which enhances the loop extrusion and promotes aberrant genomic contacts (Adane et al., 2021; Richart et al., 2021). It remains unclear how the mutated STAG2 functions in cancer, elucidation of which might uncover a new therapeutic candidate. Moreover, the loss of cohesin function in cancers leads to increased replication stress and genomic instability (Leylek et al., 2020; Minchell et al., 2020). We surmise that cohesin mutations enhance genomic instability, facilitate clonal expansion, or enhance tumorigenic potential, eventually leading to cohesin loss of function in the clonal population. However, various lines of evidence suggest that mutations in the cohesin genes contribute to cancer initiation and progression by disrupting chromosome organization and transcriptional regulation (Table 1) (Leeke et al., 2014; Kojic et al., 2018; Antony et al., 2021).

3.3 Condensin

Like cohesins, condensins are multi-protein complexes required for chromosome assembly, condensation, and segregation during mitosis and meiosis. While cohesin clasps the sister chromatids together, condensin facilitates mitotic chromosome compaction by uniting the two distant portions of a single chromatid. Condensin isoforms have conserved structural maintenance of chromosome (SMC) proteins, SMC2 and SMC4, but differ in their non-SMC components. Interestingly, decreased condensin expression triggers CIN, consequently driving colorectal cancer progression (Baergen et al., 2019). In addition, mutations in the C-terminal residues R551 and S556 of CAPH2, a condensin II subunit, lead to genomic instability in the human retinal pigment epithelial (RPE1) cell line (Weyburne and Bosco, 2021). Another line of evidence shows the involvement of the condensin complex in maintaining chromosomal stability *via* its recruitment to the pericentromeric regions. The binding of cell cycle regulators pRB and E2F1 to the pericentromeric regions cause replication stress. Studies reveal that these factors recruit condensin II to form a complex in the pericentromeric chromatin, thus regulating replication fidelity and cell ploidy (Coschi et al., 2014). This agrees with an increase in the γH2A.X marker at the pericentromeric region, accompanied by enhanced repeat instability, on depletion of condensin (Samoshkin et al., 2012). However, the precise function of condensin II and the mechanistic basis of its safeguarding function against replicative stress remains to be deciphered.

Apart from chromatin compaction, condensins also play moonlighting roles that include facilitating enhancer RNA transcription and enhancer-promoter looping in condensin-bound ERα (Estrogen Receptor α)-sensitive enhancers in breast cancers by recruiting p300 and RIP140 (Li et al., 2015). Immunoprecipitation of condensins followed by mass spectroscopy or Rapid immunoprecipitation mass spectrometry of endogenous proteins (RIME) during dynamic processes such as cell transformation may reveal other non-canonical functions (Mohammed et al., 2016). Considering the limited number of therapeutic approaches available to combat triple-negative breast cancers (TNBC), it is encouraging that the knockdown of condensin I complex protein NCAPD2 curtailed cell proliferation and invasion. These lines of evidence implicate NCAPD2 expression as a prognostic marker of TNBC patients suggesting a potential therapeutic candidate (Zhang Y et al., 2020). An in-depth biochemical and molecular characterization assumes significance as condensins emerge as potential therapeutic targets for human cancers (Wang et al., 2018).

4 Impact of non-canonical histones and oncohistones on chromatin organization in cancers

Non-canonical histone variants occasionally replace canonical histones in the genome, often serving two main purposes. First, histone variants are dynamically incorporated throughout the interphase with the regular nucleosomal turnover of canonical histones to sustain nucleosomal stability. Secondly, additional regulatory domains, interactors, and PTMs in non-canonical histones offer supplementary mechanisms for the control of epigenetic regulation. Since cancers are characterized by large-scale remodeling of their epigenetic landscape, canonical histones in cancers are occasionally interchanged with histone variants (Vardabasso et al., 2015). Structurally, histones are composed of amino- and carboxy-terminal tails and a globular histone fold domain (HFD). Specific mutations in histone genes tend to confer oncogenic

properties to cells, and these mutant histones are referred to as oncohistones (Mohammad and Helin, 2017). Mutations occur both in the tail and globular domains, with different consequences. While tail domain mutants cause a global loss of both active and inactive histone marks, the globular domain destabilizes the nucleosome. Here, we review the functional diversity and regulatory mechanisms involved in genome organization by some non-canonical and oncohistones while discussing the scope for further research in the field.

4.1 H3 variants

The histone variant H3.3 functions as a space-filling histone when canonical H3 is evicted from the nucleosome, thus maintaining nucleosomal stability (Ray-Gallet et al., 2011). The incorporation of histone H3.3 facilitates the enrichment of active marks on chromatin associated with dynamic histone turnovers, such as transcriptionally active promoters and enhancers of active genes (Lin et al., 2013; Ha et al., 2014). Contrastingly, histone H3.3 is also incorporated in repeat-rich and repressed telomeres, where H3.3 is incorporated into the nucleosomes and further methylated to H3.3K9me3. The H3.3K9me3 mark is vital for maintaining the integrity of constitutively heterochromatinized telomeres (Udugama et al., 2015). Specific chaperone complexes facilitate the incorporation of the histone H3.3 into different regions in the genome. In the euchromatin, H3.3 is incorporated by the HIRA complex (Shi et al., 2017; Yu et al., 2021; Yang et al., 2022), while DAXX/ATRX complexes incorporate H3.3 in the telomeric and pericentric heterochromatin (Goldberg et al., 2010; Lewis et al., 2010; Heaphy et al., 2011). Of note, DAXX/ATRX is mutated in classes of gliomas, sarcomas, and pancreatic neuroendocrine tumors and is involved in differential H3.3 deposition, thereby deregulating gene expression profiles (Heaphy et al., 2011; Yuen and Knoepfler, 2013; Ren et al., 2018). Deposition of the H3.3 variant in the telomeric regions might potentially contribute to the maintenance of cancer stem cells within tumors by activating embryonic stem cell dynamics and promoting alternative lengthening of telomeres (ALT) (Wong et al., 2009; Gulve et al., 2022). Moreover, the H3.3 recruiter ATRX is also localized to the nuclear periphery with the lamins, suggesting a possible interaction between H3.3, the telomere complex, and lamins, which collectively regulate telomere organization (Pennarun et al., 2021; Teng et al., 2021).

Histone composition in the nucleosome, especially the incorporation of oncohistones, affects the expression of a wide range of genes. For instance, H3/H3.3K27M tail domain mutations accelerate neural stem cell self-renewal by dysregulating neural development genes in diffuse intrinsic pontine gliomas (DIPGs) (Mohammad and Helin, 2017; Larson et al., 2019; Nacev et al., 2019). H3G34V/R and H3.3G34W/L histone tail domain mutations are found in pediatric high-grade gliomas and giant cell tumors of the bone, respectively. Several *in vitro* and *in vivo* studies reveal that both the oncohistones, H3.3K27M and H3.3G34W/L/V/R, reduce H3K27me3 levels, resulting in the aberrant expression of Polycomb-group (PcG)-mediated heterochromatinized genes, though the results are more promising in *in vitro* systems (Mohammad and Helin, 2017). H3.3K27M tumors have enhanced expression of genes associated with neural development, where H3K27me3 loss released bivalent promoters from their poised state (Larson et al., 2019). Likewise, the H3.3K36M mutation, found in 90% of chondroblastomas, shows a parallel trend of decreasing H3K36 di- and tri-methylation, PTMs involved in RNA polymerase elongation (Jha and Strahl, 2014; Fang et al., 2016; Sahu and Lu, 2022). A possible mechanism is reducing methylation levels by the selective sequestration of histone methyltransferases, NSD2, SETD2, and PRC2, creating a dominant negative effect (Figure 4D). Intriguingly, these oncohistones affect multiple histone marks. For instance, the H3.3K36M mutation, despite decreasing H3K36 methylation, increases the deposition of H3K27me3 marks. This leads to the mobilization of the polycomb repressor complex 1 (PRC1) away from its target sites, resulting in aberrations of PcG-regulated heterochromatin and an altered epigenetic profile (Bjerke et al., 2013; Chan et al., 2013; Lu et al., 2016). It remains an open question as to why the tail domain mutants of H3.3 are spatially confined in a hindbrain tissue-specific manner. Surprisingly, the H3.3K27M mutant promotes CIN and induces NHEJ-mediated DNA damage response through the DNA end-processing enzyme Polynucleotide Kinase 3′-Phosphatase (PNKP) (Rondinelli et al., 2022). The rationale underlying the deposition of H3.3 mutants on stalled forks despite the presence of other canonical histones remains unclear. Although oncohistones function as discrete entities, the mechanistic basis underlying their potential regulatory crosstalk would be a tantalizing finding to unravel.

4.2 H2A and H2B variants

All histones exist as multiple variants that modulate gene expression, barring histone H4, which has only one variant. Histone H2A and H2B cumulatively have 15 non-canonical histone variants, out of which 11 are H2A variants—H2A.X, H2A.Z.1, H2A.Z.2.1, H2A.Z.2.2, H2A.Bbd, H2A.J, H2A.B, TH2A, H2A.P, macroH2A.1.1, macroH2A.2, and macroH2A1.2, and four are H2B variants—H2BE, H2B.S.M, TH2B, and H2B.W (Oberdoerffer and Miller, 2022), which are often dysregulated in cancers (Figure 4A). γH2A.X, a histone H2A subclass phosphorylated at S139, functions as a molecular beacon that detects DNA damage in the genome (Mah et al., 2010). Of note, the lack of H2A.X causes lethality in mice exposed to γ-irradiation, establishing its importance in

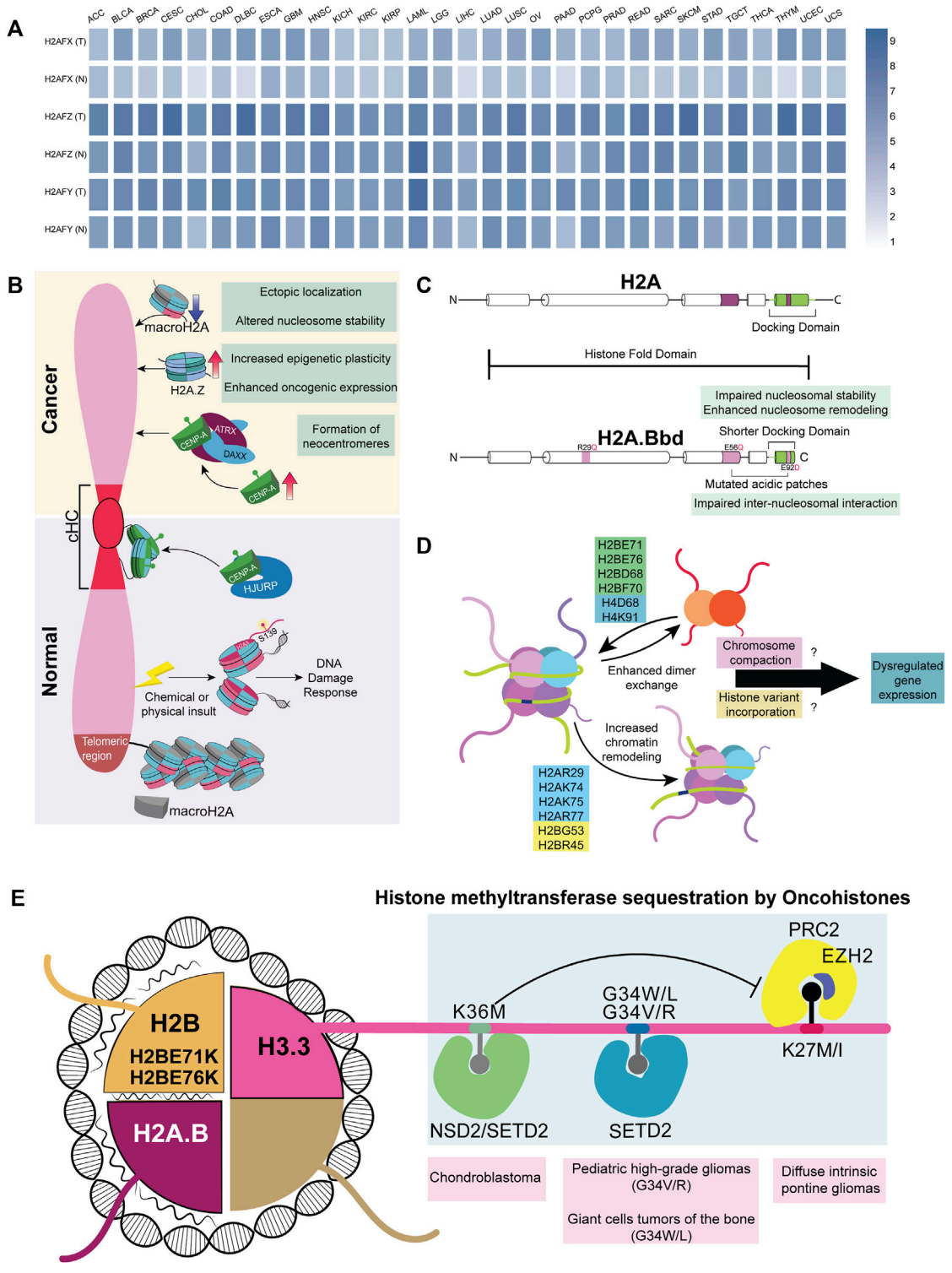

FIGURE 4
Histone variants and mutants in cancer **(A)** A heatmap representing various non-canonical histones across 31 different cancers; data curated from GEPIA2. Genes H2AFX, H2AFZ, and H2AFY code for H2A.X, H2A.Z.1, and macroH2A, respectively **(B)** Difference in the recruitment of non-canonical histones in normal versus cancer cells. cHC—Constitutive heterochromatin **(C)** Comparison between canonical H2A and non-canonical histone H2A.B **(D)** Mutations in the globular domain of core histones (H2B, H2A, and H4) to enhance dimer exchange and chromatin remodeling. This further dysregulates the expression of genes involved in differentiation **(E)** Oncohistones, mutations in the tail and globular domains are found in different cancers. Tail domain mutations sequester histone methyltransferases, while globular domain mutants destabilize the nucleosome, altering the expression of various genes.

maintaining genome stability (Celeste et al., 2002). Surprisingly, H2A.X is also involved in sustaining the self-renewal capacity of pluripotent stem cells (Turinetto et al., 2012). We speculate an H2A.X-dependent mechanism involved in the sustenance and regulation of cancer stem cells (Kim et al., 2012). As the guardian of the genome, the significance of H2A.X in facilitating metastasis was demonstrated when the knockdown of H2A.X induced EMT through the upregulation of transcription factors Twist1, ZEB, and SLUG (mesenchymal markers) in HCT116 colorectal cancer and MCF10A non-tumorigenic breast epithelial cell lines (Weyemi et al., 2016). This strongly suggests alternate functions of H2A.X in various aspects of gene regulation in addition to its role in the DNA damage response machinery.

Both H2A.Z and H3.3 maintain an open conformation of chromatin in nucleosome-depleted regions of the promoter for transcription factors to interact with gene promoters resulting in their transcriptional upregulation (Jin et al., 2009). Consistent with the requirement to transcribe genes, H2A.Z facilitates access to transcribing genomic regions by destabilizing the nucleosome, which is important in regulating stem-cell renewal and differentiation (Buschbeck and Hake, 2017). In cancers, canonical H2A is often replaced by its non-canonical variants H2A.Z.1.1 and H2A.Z.2. Remarkably, these isoforms are upregulated and positively correlate with resistance to chemotherapy in malignant stages of melanoma and pancreatic ductal adenocarcinoma (Vardabasso et al., 2015; Ávila-López et al., 2021). Furthermore, overexpression of H2A.Z correlates with poor prognosis in estrogen receptor-positive breast cancer (Hua et al., 2008). The non-canonical histone variant, macroH2A (mH2A), has a macro-domain and is involved in the inactivation of the X chromosome in mammals (Chadwick et al., 2001). In contrast to other histones, mH2A has a stabilizing effect on the nucleosome and can mediate both gene activation and repression. Notably, the depletion of mH2A dysregulates gene expression in at least nine cancers (Zink and Hake, 2016). However, the recruitment mechanism of mH2A is yet to be completely elucidated.

H2A.Bbd, a member of the short H2A family, is a testis and brain-specific histone variant overexpressed predominantly in Diffuse Large B-cell Lymphomas (DLBCLs) (Chew et al., 2021). Interestingly, H2A.B harbors multiple H2A mutations in its sequence. These include R29Q (DNA binding site mutant) and E92L (acidic-patch mutant) (Figure 4C). Furthermore, H2A.B's truncated C-terminal tail compromises its nucleosomal compaction and, if expressed ectopically, might cause dysregulated gene regulation (González-Romero et al., 2008; Bagert et al., 2021; Chew et al., 2021; Kohestani and Wereszczynski, 2021). From a vantage point, wild-type H2A.B has already evolved into an oncohistone with the ability to promote nucleosomal instability (Bagert et al., 2021). H2B, another histone H2 variant, has the highest number of nucleosome-destabilizing mutations in the globular domain at E71 and E76 (Nacev et al., 2019; Bagert et al., 2021).

Essentially, tail-domain mutants are well-characterized, but not limited to, H3.3. The same is true for globular domain mutations, which are better documented for histone H2 (Nacev et al., 2019). Mutation data shows that 80% of the most frequent mutations in histones occur in their globular domain (Nacev et al., 2019). Many of these mutations in the globular domain enhance chromatin remodeling and histone dimer exchange, which correlates with the altered expression of genes involved in differentiation across patients with different cancers (Bagert et al., 2021). However, the mechanism and contribution of these mutations to cancers remain largely uncharacterized. We surmise that mutations in the globular domain of histones induce nucleosomal instability, which affects chromatin compaction both during mitosis and interphase. Moreover, histones bearing mutations in their globular domains mutant histones can increase the chances of incorporating histone variants, potentially altering gene expression. The temporal preference for the incorporation of histones, both dependent on and independent of replication, adds an additional layer of complexity (Figure 4E). Interestingly, 47% of the missense mutations in histones H2A, H2B, H3, and H4 show a conversion of glutamic acid residues to lysine or glutamine (Nacev et al., 2019), suggestive of 1) altered DNA-histone interactions 2) aberrations in PTM patterns of histones owing to an increase in the number of lysine and glutamine residues. Such a contribution of novel histone PTMs to carcinogenesis remains to be elucidated.

4.3 CENP-A

Apart from the role of histones in regulating transcription, histones are essential for modulating DNA damage response, genome organization, and chromosome maintenance. CENP-A, a centromere-specific H3 variant, is necessary and sufficient to ensure the structural and functional organization of the centromere. Heterochromatinization at the centromere is achieved by recruiting RNAi-based DICER machinery and SUV methyltransferases (Peters et al., 2003; Folco et al., 2008). Moreover, heterochromatic regions are associated with the nuclear envelope components, contributing to an additional layer of regulation (Towbin et al., 2012; Solovei et al., 2013; Ebrahimi et al., 2018; Iglesias et al., 2020). For instance, LBR and B-type lamins are involved in the organization of the pericentric heterochromatin in the interphase nucleus (Shimi et al., 2008; Dechat et al., 2010; Lukášová et al., 2018). Centromeres and telomeres are enriched in constitutive heterochromatin marks that frequently localize to the LADs in the genome (Haaf and Schmid, 1991; Weierich et al., 2003; Raz et al., 2008; Bloom, 2014), with a subset of heterochromatic domains clustering

around nucleoli as perinucleolar heterochromatin (Alcobia et al., 2000; Gdula et al., 2013).

The two fundamental functions of CENP-A include 1) centromere formation and maintenance and 2) nucleation of checkpoint assembly proteins involved in chromosomal segregation. The organization of the centromere is dynamic during the various cell cycle stages, contributing to chromatin reorganization. During the early G1 phase, CENP-A molecules form a rosette-like structure nucleated by HJURP, facilitating a 3D ring-like organization during the G1 phase (Figure 4B). During mitosis, this structure is reoriented to form a rod-like pattern (Andronov et al., 2019). Elevated levels of CENP-A form neo-centromeres due to its mislocalization along the chromosomal arms, resulting in the misorientation of microtubule fibers on the kinetochore. This leads to the abnormal segregation of chromosomes, resulting in chromosomal translocations and breakage (Barnhart et al., 2011; Sun et al., 2016). It is now established that CENP-A is recruited to DNA double-strand breaks, and its depletion leads to an impaired DDR (Zeitlin et al., 2009; Lawrence et al., 2015; Stirpe and Heun, 2022). This highlights that CENP-A is recruited to sites other than the centromeric regions, although the exact role of CENP-A in DDR remains to be characterized. The ectopic overexpression of CENP-A increases the tolerance limit to DNA insults and enhances chemoresistance (Lacoste et al., 2014). The mechanism of CENP-A recruitment to DNA breakage sites and the consequent molecular signals required for its residence and dislodgement remains to be elucidated.

5 Chromatin organization during senescence

Cellular senescence is a state of dormancy where the cell ceases to divide. Senescence involves shortened telomeres, increased DNA damage, stalled replication, nuclear deformities, mitochondrial dysfunction, and aberrant genome organization (Di Micco et al., 2021). After a somatic cell crosses the Hayflick limit, it reaches replicative senescence because of the end replication problem, i.e., progressive shortening of telomeres with each division cycle due to the inherent inability of DNA polymerases to correctly replicate the cytosine-rich telomere lagging-strand (Hayflick and Moorhead, 1961; Harley et al., 1990). Interestingly, this limit is often bypassed by neoplastic cells, making them immortal (Autexier and Greider, 1996). As aging progresses, the DDR machinery is compromised, predominantly increasing the predisposition to breast, prostate, lung, and colon cancers (Rossi et al., 2007; de Magalhães, 2013). Normally, these functions are tightly regulated, and the activation of oncogenes leads to aberrant replication fork progression, resulting in Oncogene-Induced Senescence (OIS) (Serrano et al., 1997; Di Micco et al., 2006; Rocha et al., 2022). It is noteworthy that cancer cells often evade OIS by altering cellular levels of $p16^{INK4A}$, a cell cycle blocker (McLaughlin-Drubin et al., 2013).

Remarkably, extensive topological changes in chromatin compartmentalization accompany senescence, obfuscating the spatial separation between the A and B compartments. Microscopy and polymer modeling of chromatin reveals that the spatial organization of chromatin compartments is drastically altered in tumor cells. Following this finding, an additional intermediate Compartment I has been proposed that interacts with both A and B compartments in normal tissue and inclines toward the B compartment in cancerous tissue (Johnstone et al., 2020). Cells undergoing OIS show dramatic changes in chromatin architecture, with the formation of Senescence Associated Heterochromatin Foci (SAHF), characteristically enriched with facultative heterochromatic marks such as H3K9me1/2, H3K20me3, along with high-mobility group proteins and non-canonical histones such as mH2A (Narita et al., 2003; Zhang et al., 2007; Nelson et al., 2016). Chromatin polymer modeling suggests that SAHF can mobilize specific loci adjacent to heterochromatic domains in close proximity to each other in the 3D space of the nucleus, enhancing their activity in cell adhesion and cancer-related signaling (Sati et al., 2020). Alongside activating specific genes, the SAHF also affects cell proliferation by epigenetically repressing E2F target genes through the recruitment of pRB and heterochromatin factors (Narita et al., 2003). Moreover, SAHFs are not found in cells going through quiescence (Aird and Zhang, 2013). In agreement with this, the silencing of E2F-responsive elements and the formation of SAHF are characteristic of only irreversibly arrested cells, thus hinting towards an Rb-mediated mechanism for stabilizing the senescent phenotype.

The induction of senescence in cancer cells serves as a traditional therapeutic approach by targeting p53, mTOR, PI3K, and BCL-2 family proteins using senolytic agents (Lee et al., 2010; Muñoz-Espín et al., 2013; Laberge et al., 2015). However, challenges in targeting cancer cells are contributed to by tumor heterogeneity since aged patients have higher numbers of senescent cells, which can lead to fatal off-target effects by senolytic agents (Wang L et al., 2022).

6 Perspectives

6.1 Effect of lamin mutations on genome organization during cancer progression and senescence

The LADs are parts of chromatin domains that are largely in a state of repression. Surprisingly, the simultaneous loss of all lamin forms in mouse embryonic stem cells did not change the overall TAD structure but reorganized the inter- and intra-TAD interactions, further altering transcriptional

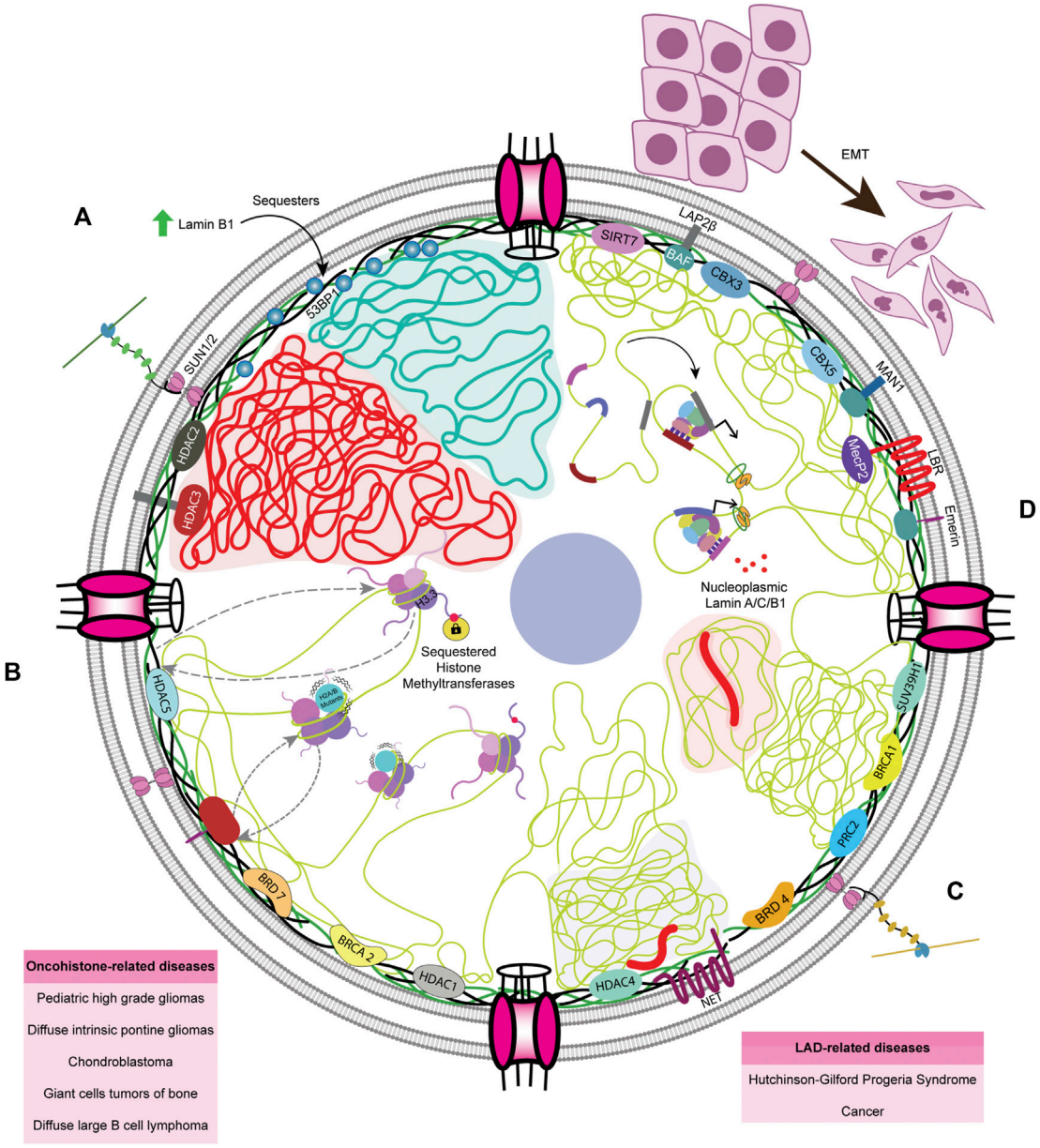

FIGURE 5
Lacunae in the field of genome organization and nuclear envelope **(A)** Lamin B1 is upregulated in most cancers, as per TCGA data, and overexpression of Lamin B1 expression sequesters 53BP1, a major orchestrator of NHEJ pathway. The precise mechanisms as to how cancer cells overcome 53BP1 sequestration is unknown **(B)** Incorporation of both tail and globular domain mutants leads to dysregulated gene expression through various mechanisms, though it remains unclear whether nuclear lamina has any role in either mitigating or worsening it. Globular domain mutations, when associated with the LADs, could be altering the spatial localization of gene loci. **(C)** The nuclear envelope maintains heterochromatin. LADs form a significant portion of the human genome and are regulated by the lamina and its associated complexes, the deregulation of which often leads to HGPS and cancer **(D)** Furthermore, in EMT and cancer progression, phosphorylated lamin A/C and B1 are associated with enhancer sequences, but the role of this association remains to be elucidated.

output (Zheng et al., 2018). It is interesting to note that although lamins are known to organize heterochromatin proximal to the nuclear border, they also modulate the organization of transcriptionally-active euchromatin within the nuclear interior (Pascual-Reguant et al., 2018; Ikegami et al., 2020).

Ovarian cancers harbor homozygous deletion in the LMNB1 gene, while the loss of lamin A/C leads to poor

prognosis and enhanced metastatic potential of cells (Capochichi et al., 2011). In the context of senescence, lamin A/C directly interacts with the telomeric protein TRF2, which facilitates the insertion of 3′ overhangs into telomeric DNA, resulting in T-loop formation that protects the telomere ends and slows cellular senescence in a cell-type specific manner. Mutations in LMNA, like those found in Hutchinson-Gilford progeria syndrome (HGPS), destabilize lamin A/C-TRF2 interaction, further leading to telomere loss and accelerated cellular aging (Wood et al., 2014).

Additionally, TCGA data retrieved from GEPIA2 shows that most of the cancers show upregulated levels of lamin B1. It is known that lamin B1 overexpression sequesters 53BP1, a crucial mediator of the NHEJ pathway (Etourneaud et al., 2021). It remains to be elucidated how a majority of the cancers overexpressing lamin B1 manage to steer the DDR to specific NHEJ pathways (Bouwman et al., 2010) (Figure 5A). Furthermore, lamins repress the activation of mobile transposable elements that trigger chromosomal instability (Andrenacci et al., 2020). During the later stages of cellular aging, the association of lamin with transposable elements declines, coupled with the loss of heterochromatin, leading to aberrant gene expression and type-I interferon response (De Cecco et al., 2019; Cenni et al., 2020). The mechanisms by which chromatin organizers function in cancer cells will facilitate the design of specific small molecule inhibitors.

6.2 Interactors of LMNA during cancer progression

Lamin A regulates gene expression by interacting with various chromatin modifiers, the deregulation of which promotes cancers. For instance, lamin A directly interacts with and prevents the proteasomal degradation of SUV39H1, the writer of the H3K9me3 inactive mark (Liu et al., 2013), the dysregulation of which results in HGPS (Figure 5C). Correspondingly, the PcG proteins that deposit the H3K27me3 inactive mark interact with lamins (Cesarini et al., 2015; Marullo et al., 2016). Notably, lamin loss leads to an anomalous distribution of PcG proteins, eventually resulting in dysregulated gene expression and accelerated cancer progression. HDAC2 also plays an active role in heterochromatinization by interacting with LMNA at the nuclear periphery (Mattioli et al., 2018; Santi et al., 2020; Murray-Nerger and Cristea, 2021). However, the molecular mechanisms involving lamin-mediated regulation of inactive H3K9me3 and H3K27me3 and active H3K4me3 marks are yet to be uncovered.

In cancers, chromatin organizers harbor mutations in various domains, resulting in their deregulated activity and altered binding to chromatin or lamins. For instance, sarcomas harbor high-frequency H3.3G34R and H3.3K36M mutations that directly prevent the binding of H3K36me2/3 writer NSD1/2, thus reducing PRC2-H3K36me2 interaction and increasing H3K27me3 levels (Lu et al., 2016). The interaction between SMARCB1 and NSD1 is essential for the deposition of H3K36me2 in the genome, which is a marker for better prognosis in sarcoma. Mutated SMARCB1 is unable to bind to NSD1 but binds to PRC2, leading to an increase in H3K27me3 with poor prognosis in cancer patients (Drosos et al., 2022). Such atypical deposition of inactive histone marks dilutes their occupancy in normally-repressed genes, reorienting the genomic regions localized to the nuclear periphery. As a result, genes typically localized to the nuclear periphery, such as the mesenchymal progenitor genes in the facultative LADs, become de-repressed (Lu et al., 2016). Hence, we surmise a potential crosstalk between the nuclear lamins, chromatin regulators, and oncohistones in the initiation and sustenance of cancer progression.

6.3 Crosstalk between the nuclear envelope and oncohistones

The nuclear lamina is primarily associated with inactive histone marks at the nuclear periphery. However, lamins also modulate active euchromatin (Zheng et al., 2018). How the peripheral and nucleoplasmic pools of lamins engage in chromatin dynamics and impinge on the transcriptional regulation mediated by oncohistones such as H3.3K27M/I, H3.3G34W/V/L/R, H3.3K36M, or sH2A is unclear (Figure 5B). In addition, components of the nuclear envelope, namely Nups and LINC complex factors, also participate in chromatin organization. Moreover, lamins are required for chromatin organization, although their potential role in the incorporation of oncohistones by chaperones remains unclear (Figure 5B). The extent of lamin A/C phosphorylation correlates with lamin A/C levels in the DU145 prostate cancer cell line, though this remains to be verified experimentally across cancers (Kong et al., 2012). Phosphorylated lamin A/C and unphosphorylated, probably nucleoplasmic lamin B1, associate with active enhancers and transcribing genes, respectively, which contradicts the conventional function of LADs in gene repression (Guelen et al., 2008; Ikegami et al., 2020). However, the exact role of phosphorylated Lamin A/C in modulating enhancer regions remains an enigma. In addition, the association of lamin B1 with eLADs and higher expression of fibronectin, vimentin, and twist highlight the role of lamin B1 in metastasis (Pascual-Reguant et al., 2018), although its exact purpose of lamin B1 in compartment A remains to be elucidated (Figure 5D). Interestingly, lamin B1 has been shown to localize to the TAD borders of eLADs, opening the possibility of its interaction with border elements such as CTCF and cohesin.

7 Conclusion

In summary, it is beyond any doubt that genetic mutations, aberrations in chromatin organization, incorporation of oncohistones, deregulated transcription, and defects in nuclear envelope organization and function collectively deregulate the cellular and molecular processes of cancers. Novel therapeutic targets will be identified by leveraging high-resolution single-cell approaches, such as sc-ChIP-seq, sc-ATAC-seq, and sc-Hi-C, with high-content imaging, including high-resolution FISH. Furthermore, molecular and biochemical assays remain the mainstay for the elucidation of molecular mechanisms. Collectively, these lines of evidence reveal that aberrant genome architecture serves as a precursor and promoter of cancer initiation and progression.

Author contributions

AKB, SS, SD, DP, and KS wrote the manuscript. SS, SD, and DP prepared the illustrations.

Funding

We gratefully acknowledge support from Science & Engineering Board (SERB), Grant#CRG/2020/002563 and intramural funding support from IISER-Pune.

Conflict of interest

The authors declare that the research was conducted in the absence of any commercial or financial relationships that could be construed as a potential conflict of interest.

Publisher's note

All claims expressed in this article are solely those of the authors and do not necessarily represent those of their affiliated organizations, or those of the publisher, the editors and the reviewers. Any product that may be evaluated in this article, or claim that may be made by its manufacturer, is not guaranteed or endorsed by the publisher.

References

Adane, B., Alexe, G., Seong, B. K. A., Lu, D., Hwang, E. E., Hnisz, D., et al. (2021). STAG2 loss rewires oncogenic and developmental programs to promote metastasis in Ewing sarcoma. *Cancer Cell* 39, 827–844. e10. doi:10.1016/j.ccell.2021.05.007

Aebi, U., Cohn, J., Buhle, L., and Gerace, L. (1986). The nuclear lamina is a meshwork of intermediate-type filaments. *Nature* 323, 560–564. doi:10.1038/323560a0

Aird, K. M., and Zhang, R. (2013). Detection of senescence-associated heterochromatin foci (SAHF). *Methods Mol. Biol.* 965, 185–196. doi:10.1007/978-1-62703-239-1_12

Akdemir, K. C., Le, V. T., Chandran, S., Li, Y., Verhaak, R. G., Beroukhim, R., et al. (2020). PCAWG Structural Variation Working Group, PCAWG ConsortiumDisruption of chromatin folding domains by somatic genomic rearrangements in human cancer. *Nat. Genet.* 52, 294–305. doi:10.1038/s41588-019-0564-y

Alcobia, I., Dilão, R., and Parreira, L. (2000). Spatial associations of centromeres in the nuclei of hematopoietic cells: Evidence for cell-type-specific organizational patterns. *Blood* 95, 1608–1615. doi:10.1182/blood.V95.5.1608.005k32_1608_1615

Amankwaa, B., Schoborg, T., and Labrador, M. (2022). <i>Drosophila</i> insulator proteins exhibit *in vivo* liquid-liquid phase separation properties. *Life Sci. Alliance* 5, e202201536. doi:10.26508/lsa.202201536

Amin, R., Shukla, A., Zhu, J. J., Kim, S., Wang, P., Tian, S. Z., et al. (2021). Nuclear pore protein NUP210 depletion suppresses metastasis through heterochromatin-mediated disruption of tumor cell mechanical response. *Nat. Commun.* 12, 7216. doi:10.1038/s41467-021-27451-w

Andrenacci, D., Cavaliere, V., and Lattanzi, G. (2020). The role of transposable elements activity in aging and their possible involvement in laminopathic diseases. *Ageing Res. Rev.* 57, 100995. doi:10.1016/j.arr.2019.100995

Andronov, L., Ouararhni, K., Stoll, I., Klaholz, B. P., and Hamiche, A. (2019). CENP-A nucleosome clusters form rosette-like structures around HJURP during G1. *Nat. Commun.* 10, 4436. doi:10.1038/s41467-019-12383-3

Antony, J., Chin, C. V., and Horsfield, J. A. (2021). Cohesin mutations in cancer: Emerging therapeutic targets. *Int. J. Mol. Sci.* 22, 6788. doi:10.3390/ijms22136788

Autexier, C., and Greider, C. W. (1996). Telomerase and cancer: Revisiting the telomere hypothesis. *Trends biochem. Sci.* 21, 387–391. doi:10.1016/S0968-0004(96)10042-6

Ávila-López, P. A., Guerrero, G., Nuñez-Martínez, H. N., Peralta-Alvarez, C. A., Hernández-Montes, G., Álvarez-Hilario, L. G., et al. (2021). H2A.Z overexpression suppresses senescence and chemosensitivity in pancreatic ductal adenocarcinoma. *Oncogene* 40, 2065–2080. doi:10.1038/s41388-021-01664-1

Baergen, A. K., Jeusset, L. M., Lichtensztejn, Z., and McManus, K. J. (2019). Diminished condensin gene expression drives chromosome instability that may contribute to colorectal cancer pathogenesis. *Cancers (Basel)* 11, 1066. doi:10.3390/cancers11081066

Bagert, J. D., Mitchener, M. M., Patriotis, A. L., Dul, B. E., Wojcik, F., Nacev, B. A., et al. (2021). Oncohistone mutations enhance chromatin remodeling and alter cell fates. *Nat. Chem. Biol.* 17, 403–411. doi:10.1038/s41589-021-00738-1

Bailey, C. G., Gupta, S., Metierre, C., Amarasekera, P. M. S., O'Young, P., Kyaw, W., et al. (2021). Structure-function relationships explain CTCF zinc finger mutation phenotypes in cancer. *Cell. Mol. Life Sci.* 78, 7519–7536. doi:10.1007/s00018-021-03946-z

Bakhoum, S. F., Ngo, B., Laughney, A. M., Cavallo, J.-A., Murphy, C. J., Ly, P., et al. (2018). Chromosomal instability drives metastasis through a cytosolic DNA response. *Nature* 553, 467–472. doi:10.1038/nature25432

Barnhart, M. C., Kuich, P. H. J. L., Stellfox, M. E., Ward, J. A., Bassett, E. A., Black, B. E., et al. (2011). HJURP is a CENP-A chromatin assembly factor sufficient to form a functional de novo kinetochore. *J. Cell Biol.* 194, 229–243. doi:10.1083/jcb.201012017

Barrington, C., Georgopoulou, D., Pezic, D., Varsally, W., Herrero, J., and Hadjur, S. (2019). Enhancer accessibility and CTCF occupancy underlie asymmetric TAD architecture and cell type specific genome topology. *Nat. Commun.* 10, 2908. doi:10.1038/s41467-019-10725-9

Baumann, K. (2016). Nuclear organization: NUP-Tial binding to super-enhancers. *Nat. Rev. Mol. Cell Biol.* 17, 738–739. doi:10.1038/nrm.2016.158

Bell, E. S., Shah, P., Zuela-Sopilniak, N., Kim, D., Varlet, A.-A., Morival, J. L. P., et al. (2022). Low lamin A levels enhance confined cell migration and metastatic capacity in breast cancer. *Oncogene* 41, 4211–4230. doi:10.1038/s41388-022-02420-9

Benhra, N., Barrio, L., Muzzopappa, M., and Milán, M. (2018). Chromosomal instability induces cellular invasion in epithelial tissues. *Dev. Cell* 47, 161–174. doi:10.1016/j.devcel.2018.08.021

Bianchi, A., Mozzetta, C., Pegoli, G., Lucini, F., Valsoni, S., Rosti, V., et al. (2020). Dysfunctional polycomb transcriptional repression contributes to lamin A/C-dependent muscular dystrophy. *J. Clin. Invest.* 130, 2408–2421. doi:10.1172/JCI128161

Bjerke, L., Mackay, A., Nandhabalan, M., Burford, A., Jury, A., Popov, S., et al. (2013). Histone H3.3. mutations drive pediatric glioblastoma through upregulation of MYCN. *Cancer Discov.* 3, 512–519. doi:10.1158/2159-8290.CD-12-0426

Bloom, K. S. (2014). Centromeric heterochromatin: The primordial segregation machine. *Annu. Rev. Genet.* 48, 457–484. doi:10.1146/annurev-genet-120213-092033

Bočkaj, I., Martini, T. E. I., de Camargo Magalhães, E. S., Bakker, P. L., Meeuwsen-de Boer, T. G. J., Armandari, I., et al. (2021). The H3.3K27M oncohistone affects replication stress outcome and provokes genomic instability in pediatric glioma. *PLoS Genet.* 17, e1009868. doi:10.1371/journal.pgen.1009868

Bönisch, C., Schneider, K., Pünzeler, S., Wiedemann, S. M., Bielmeier, C., Bocola, M., et al. (2012). H2A.Z.2.2 is an alternatively spliced histone H2A.Z variant that causes severe nucleosome destabilization. *Nucleic Acids Res.* 40, 5951–5964. doi:10.1093/nar/gks267

Bouwman, P., Aly, A., Escandell, J. M., Pieterse, M., Bartkova, J., van der Gulden, H., et al. (2010). 53BP1 loss rescues BRCA1 deficiency and is associated with triple-negative and BRCA-mutated breast cancers. *Nat. Struct. Mol. Biol.* 17, 688–695. doi:10.1038/nsmb.1831

Bronshtein, I., Kepten, E., Kanter, I., Berezin, S., Lindner, M., Redwood, A. B., et al. (2015). Loss of lamin A function increases chromatin dynamics in the nuclear interior. *Nat. Commun.* 6, 8044. doi:10.1038/ncomms9044

Buschbeck, M., and Hake, S. B. (2017). Variants of core histones and their roles in cell fate decisions, development and cancer. *Nat. Rev. Mol. Cell Biol.* 18, 299–314. doi:10.1038/nrm.2016.166

Capo-chichi, C. D., Cai, K. Q., Simpkins, F., Ganjei-Azar, P., Godwin, A. K., and Xu, X.-X. (2011). Nuclear envelope structural defects cause chromosomal numerical instability and aneuploidy in ovarian cancer. *BMC Med.* 9, 28. doi:10.1186/1741-7015-9-28

Capo-Chichi, C. D., Yeasky, T. M., Smith, E. R., and Xu, X.-X. (2016). Nuclear envelope structural defect underlies the main cause of aneuploidy in ovarian carcinogenesis. *BMC Cell Biol.* 17, 37. doi:10.1186/s12860-016-0114-8

Celeste, A., Petersen, S., Romanienko, P. J., Fernandez-Capetillo, O., Chen, H. T., Sedelnikova, O. A., et al. (2002). Genomic instability in mice lacking histone H2AX. *Science* 296, 922–927. doi:10.1126/science.1069398

Cenni, V., Capanni, C., Mattioli, E., Schena, E., Squarzoni, S., Bacalini, M. G., et al. (2020). Lamin A involvement in ageing processes. *Ageing Res. Rev.* 62, 101073. doi:10.1016/j.arr.2020.101073

Cerami, E., Gao, J., Dogrusoz, U., Gross, B. E., Sumer, S. O., Aksoy, B. A., et al. (2012). The cBio cancer genomics portal: An open platform for exploring multidimensional cancer genomics data. *Cancer Discov.* 2, 401–404. doi:10.1158/2159-8290.CD-12-0095

Cesarini, E., Mozzetta, C., Marullo, F., Gregoretti, F., Gargiulo, A., Columbaro, M., et al. (2015). Lamin A/C sustains PcG protein architecture, maintaining transcriptional repression at target genes. *J. Cell Biol.* 211, 533–551. doi:10.1083/jcb.201504035

Chadwick, B. P., Valley, C. M., and Willard, H. F. (2001). Histone variant macroH2A contains two distinct macrochromatin domains capable of directing macroH2A to the inactive X chromosome. *Nucleic Acids Res.* 29, 2699–2705. doi:10.1093/nar/29.13.2699

Chan, K.-M., Fang, D., Gan, H., Hashizume, R., Yu, C., Schroeder, M., et al. (2013). The histone H3.3K27M mutation in pediatric glioma reprograms H3K27 methylation and gene expression. *Genes Dev.* 27, 985–990. doi:10.1101/gad.217778.113

Chen, G. K., Chang, X., Curtis, C., and Wang, K. (2013). Precise inference of copy number alterations in tumor samples from SNP arrays. *Bioinformatics* 29, 2964–2970. doi:10.1093/bioinformatics/btt521

Chen, H., Tian, Y., Shu, W., Bo, X., and Wang, S. (2012). Comprehensive identification and annotation of cell type-specific and ubiquitous CTCF-binding sites in the human genome. *PLoS ONE* 7, e41374. doi:10.1371/journal.pone.0041374

Chetverina, D., Fujioka, M., Erokhin, M., Georgiev, P., Jaynes, J. B., and Schedl, P. (2017). Boundaries of loop domains (insulators): Determinants of chromosome form and function in multicellular eukaryotes. *BioEssays* 39 (3), 1600233. doi:10.1002/bies.201600233

Chew, G.-L., Bleakley, M., Bradley, R. K., Malik, H. S., Henikoff, S., Molaro, A., et al. (2021). Short H2A histone variants are expressed in cancer. *Nat. Commun.* 12, 490. doi:10.1038/s41467-020-20707-x

Cohen, S., Etingov, I., and Panté, N. (2012). Effect of viral infection on the nuclear envelope and nuclear pore complex. *Int. Rev. Cell Mol. Biol.* 299, 117–159. doi:10.1016/B978-0-12-394310-1.00003-5

Coschi, C. H., Ishak, C. A., Gallo, D., Marshall, A., Talluri, S., Wang, J., et al. (2014). Haploinsufficiency of an RB-E2F1-Condensin II complex leads to aberrant replication and aneuploidy. *Cancer Discov.* 4, 840–853. doi:10.1158/2159-8290.CD-14-0215

Cremer, T., and Cremer, C. (2001). Chromosome territories, nuclear architecture and gene regulation in mammalian cells. *Nat. Rev. Genet.* 2, 292–301. doi:10.1038/35066075

Cronshaw, J. M., Krutchinsky, A. N., Zhang, W., Chait, B. T., and Matunis, M. J. (2002). Proteomic analysis of the mammalian nuclear pore complex. *J. Cell Biol.* 158, 915–927. doi:10.1083/jcb.200206106

Damaschke, N. A., Gawdzik, J., Avilla, M., Yang, B., Svaren, J., Roopra, A., et al. (2020). CTCF loss mediates unique DNA hypermethylation landscapes in human cancers. *Clin. Epigenetics* 12, 80. doi:10.1186/s13148-020-00869-7

D'Angelo, M. A., Gomez-Cavazos, J. S., Mei, A., Lackner, D. H., and Hetzer, M. W. (2012). A change in nuclear pore complex composition regulates cell differentiation. *Dev. Cell* 22, 446–458. doi:10.1016/j.devcel.2011.11.021

Davis, L., Rayi, P. R., Getselter, D., Kaphzan, H., and Elliott, E. (2022). CTCF in parvalbumin-expressing neurons regulates motor, anxiety and social behavior and neuronal identity. *Mol. Brain* 15, 30. doi:10.1186/s13041-022-00916-9

De Cecco, M., Ito, T., Petrashen, A. P., Elias, A. E., Skvir, N. J., Criscione, S. W., et al. (2019). L1 drives IFN in senescent cells and promotes age-associated inflammation. *Nature* 566, 73–78. doi:10.1038/s41586-018-0784-9

de Magalhães, J. P. (2013). How ageing processes influence cancer. *Nat. Rev. Cancer* 13, 357–365. doi:10.1038/nrc3497

Debaugny, R. E., and Skok, J. A. (2020). CTCF and CTCFL in cancer. *Curr. Opin. Genet. Dev.* 61, 44–52. doi:10.1016/j.gde.2020.02.021

Dechat, T., Adam, S. A., Taimen, P., Shimi, T., and Goldman, R. D. (2010). Nuclear lamins. *Cold Spring Harb. Perspect. Biol.* 2, a000547. doi:10.1101/cshperspect.a000547

Dechat, T., Shimi, T., Adam, S. A., Rusinol, A. E., Andres, D. A., Spielmann, H. P., et al. (2007). Alterations in mitosis and cell cycle progression caused by a mutant lamin A known to accelerate human aging. *Proc. Natl. Acad. Sci. U. S. A.* 104, 4955–4960. doi:10.1073/pnas.0700854104

Demmerle, J., Koch, A. J., and Holaska, J. M. (2012). The nuclear envelope protein emerin binds directly to histone deacetylase 3 (HDAC3) and activates HDAC3 activity. *J. Biol. Chem.* 287, 22080–22088. doi:10.1074/jbc.M111.325308

Di Micco, R., Fumagalli, M., Cicalese, A., Piccinin, S., Gasparini, P., Luise, C., et al. (2006). Oncogene-induced senescence is a DNA damage response triggered by DNA hyper-replication. *Nature* 444, 638–642. doi:10.1038/nature05327

Di Micco, R., Krizhanovsky, V., Baker, D., and d'Adda di Fagagna, F. (2021). Cellular senescence in ageing: From mechanisms to therapeutic opportunities. *Nat. Rev. Mol. Cell Biol.* 22, 75–95. doi:10.1038/s41580-020-00314-w

Dixon, J. R., Selvaraj, S., Yue, F., Kim, A., Li, Y., Shen, Y., et al. (2012). Topological domains in mammalian genomes identified by analysis of chromatin interactions. *Nature* 485, 376–380. doi:10.1038/nature11082

Drosos, Y., Myers, J. A., Xu, B., Mathias, K. M., Beane, E. C., Radko-Juettner, S., et al. (2022). NSD1 mediates antagonism between SWI/SNF and polycomb complexes and is required for transcriptional activation upon EZH2 inhibition. *Mol. Cell* 82, 2472–2489. e8. doi:10.1016/j.molcel.2022.04.015

Dubińska-Magiera, M., Kozioł, K., Machowska, M., Piekarowicz, K., Filipczak, D., and Rzepecki, R. (2019). Emerin is required for proper nucleus reassembly after mitosis: Implications for new pathogenetic mechanisms for laminopathies detected in EDMD1 patients. *Cells* 8, 1. doi:10.3390/cells8030240

Earle, A. J., Kirby, T. J., Fedorchak, G. R., Isermann, P., Patel, J., Iruvanti, S., et al. (2020). Mutant lamins cause nuclear envelope rupture and DNA damage in skeletal muscle cells. *Nat. Mat.* 19, 464–473. doi:10.1038/s41563-019-0563-5

Ebrahimi, H., Masuda, H., Jain, D., and Cooper, J. P. (2018). Distinct "safe zones" at the nuclear envelope ensure robust replication of heterochromatic chromosome regions. *eLife* 7, e32911. doi:10.7554/eLife.32911

Eldholm, V., Haugen, A., and Zienolddiny, S. (2014). CTCF mediates the TERT enhancer-promoter interactions in lung cancer cells: Identification of a novel enhancer region involved in the regulation of TERT gene. *Int. J. Cancer* 134, 2305–2313. doi:10.1002/ijc.28570

Etourneaud, L., Moussa, A., Rass, E., Genet, D., Willaume, S., Chabance-Okumura, C., et al. (2021). Lamin B1 sequesters 53BP1 to control its recruitment to DNA damage. *Sci. Adv.* 7, eabb3799. doi:10.1126/sciadv.abb3799

Fang, D., Gan, H., Lee, J.-H., Han, J., Wang, Z., Riester, S. M., et al. (2016). The histone H3.3K36M mutation reprograms the epigenome of chondroblastomas. *Science* 352, 1344–1348. doi:10.1126/science.aae0065

Fischer, E. G. (2020). Nuclear morphology and the biology of cancer cells. *Acta Cytol.* 64, 511–519. doi:10.1159/000508780

Flavahan, W. A., Drier, Y., Liau, B. B., Gillespie, S. M., Venteicher, A. S., Stemmer-Rachamimov, A. O., et al. (2016). Insulator dysfunction and oncogene activation in IDH mutant gliomas. *Nature* 529, 110–114. doi:10.1038/nature16490

Folco, H. D., Pidoux, A. L., Urano, T., and Allshire, R. C. (2008). Heterochromatin and RNAi are required to establish CENP-A chromatin at centromeres. *Science* 319, 94–97. doi:10.1126/science.1150944

Fudenberg, G., Imakaev, M., Lu, C., Goloborodko, A., Abdennur, N., and Mirny, L. A. (2016). Formation of chromosomal domains by loop extrusion. *Cell Rep.* 15, 2038–2049. doi:10.1016/j.celrep.2016.04.085

Gao, J., Aksoy, B. A., Dogrusoz, U., Dresdner, G., Gross, B., Sumer, S. O., et al. (2013). Integrative analysis of complex cancer genomics and clinical profiles using the cBioPortal. *Sci. Signal.* 6, pl1. doi:10.1126/scisignal.2004088

Gdula, M. R., Poterlowicz, K., Mardaryev, A. N., Sharov, A. A., Peng, Y., Fessing, M. Y., et al. (2013). Remodeling of three-dimensional organization of the nucleus during terminal keratinocyte differentiation in the epidermis. *J. Invest. Dermatol.* 133, 2191–2201. doi:10.1038/jid.2013.66

Gimpel, P., Lee, Y. L., Sobota, R. M., Calvi, A., Koullourou, V., Patel, R., et al. (2017). Nesprin-1α-Dependent microtubule nucleation from the nuclear envelope via Akap450 is necessary for nuclear positioning in muscle cells. *Curr. Biol.* 27, 2999–3009. doi:10.1016/j.cub.2017.08.031

Goldberg, A. D., Banaszynski, L. A., Noh, K.-M., Lewis, P. W., Elsaesser, S. J., Stadler, S., et al. (2010). Distinct factors control histone variant H3.3 localization at specific genomic regions. *Cell* 140, 678–691. doi:10.1016/j.cell.2010.01.003

González-Romero, R., Méndez, J., Ausió, J., and Eirín-López, J. M. (2008). Quickly evolving histones, nucleosome stability and chromatin folding: All about histone H2A.Bbd. *Gene* 413, 1–7. doi:10.1016/j.gene.2008.02.003

Gough, S. M., Slape, C. I., and Aplan, P. D. (2011). NUP98 gene fusions and hematopoietic malignancies: Common themes and new biologic insights. *Blood* 118, 6247–6257. doi:10.1182/blood-2011-07-328880

Gruenbaum, Y., and Foisner, R. (2015). Lamins: Nuclear intermediate filament proteins with fundamental functions in nuclear mechanics and genome regulation. *Annu. Rev. Biochem.* 84, 131–164. doi:10.1146/annurev-biochem-060614-034115

Guelen, L., Pagie, L., Brasset, E., Meuleman, W., Faza, M. B., Talhout, W., et al. (2008). Domain organization of human chromosomes revealed by mapping of nuclear lamina interactions. *Nature* 453, 948–951. doi:10.1038/nature06947

Gulve, N., Su, C., Deng, Z., Soldan, S. S., Vladimirova, O., Wickramasinghe, J., et al. (2022). DAXX-ATRX regulation of p53 chromatin binding and DNA damage response. *Nat. Commun.* 13, 5033. doi:10.1038/s41467-022-32680-8

Guo, Y. A., Chang, M. M., Huang, W., Ooi, W. F., Xing, M., Tan, P., et al. (2018). Mutation hotspots at CTCF binding sites coupled to chromosomal instability in gastrointestinal cancers. *Nat. Commun.* 9, 1520. doi:10.1038/s41467-018-03828-2

Ha, M., Kraushaar, D. C., and Zhao, K. (2014). Genome-wide analysis of H3.3 dissociation reveals high nucleosome turnover at distal regulatory regions of embryonic stem cells. *Epigenetics Chromatin* 7, 38. doi:10.1186/1756-8935-7-38

Haaf, T., and Schmid, M. (1991). Chromosome topology in mammalian interphase nuclei. *Exp. Cell Res.* 192, 325–332. doi:10.1016/0014-4827(91)90048-y

Hanssen, L. L. P., Kassouf, M. T., Oudelaar, A. M., Biggs, D., Preece, C., Downes, D. J., et al. (2017). Tissue-specific CTCF-cohesin-mediated chromatin architecture delimits enhancer interactions and function *in vivo*. *Nat. Cell Biol.* 19, 952–961. doi:10.1038/ncb3573

Harley, C. B., Futcher, A. B., and Greider, C. W. (1990). Telomeres shorten during ageing of human fibroblasts. *Nature* 345, 458–460. doi:10.1038/345458a0

Harr, J. C., Luperchio, T. R., Wong, X., Cohen, E., Wheelan, S. J., and Reddy, K. L. (2015). Directed targeting of chromatin to the nuclear lamina is mediated by chromatin state and A-type lamins. *J. Cell Biol.* 208, 33–52. doi:10.1083/jcb.201405110

Hayflick, L., and Moorhead, P. S. (1961). The serial cultivation of human diploid cell strains. *Exp. Cell Res.* 25, 585–621. doi:10.1016/0014-4827(61)90192-6

Heaphy, C. M., de Wilde, R. F., Jiao, Y., Klein, A. P., Edil, B. H., Shi, C., et al. (2011). Altered telomeres in tumors with ATRX and DAXX mutations. *Science* 333, 425. doi:10.1126/science.1207313

Henikoff, S., and Smith, M. M. (2015). Histone variants and epigenetics. *Cold Spring Harb. Perspect. Biol.* 7, a019364. doi:10.1101/cshperspect.a019364

Höflmayer, D., Steinhoff, A., Hube-Magg, C., Kluth, M., Simon, R., Burandt, E., et al. (2020). Expression of CCCTC-binding factor (CTCF) is linked to poor prognosis in prostate cancer. *Mol. Oncol.* 14, 129–138. doi:10.1002/1878-0261.12597

Holaska, J. M., and Wilson, K. L. (2007). An emerin "proteome": Purification of distinct emerin-containing complexes from HeLa cells suggests molecular basis for diverse roles including gene regulation, mRNA splicing, signaling, mechanosensing, and nuclear architecture. *Biochemistry* 46, 8897–8908. doi:10.1021/bi602636m

Holland, A. J., and Cleveland, D. W. (2012). Losing balance: The origin and impact of aneuploidy in cancer. *EMBO Rep.* 13, 501–514. doi:10.1038/embor.2012.55

Holwerda, S. J. B., and de Laat, W. (2013). Ctcf: The protein, the binding partners, the binding sites and their chromatin loops. *Philos. Trans. R. Soc. Lond. B Biol. Sci.* 368, 20120369. doi:10.1098/rstb.2012.0369

Hua, S., Kallen, C. B., Dhar, R., Baquero, M. T., Mason, C. E., Russell, B. A., et al. (2008). Genomic analysis of estrogen cascade reveals histone variant H2A.Z associated with breast cancer progression. *Mol. Syst. Biol.* 4, 188. doi:10.1038/msb.2008.25

Ibarra, A., Benner, C., Tyagi, S., Cool, J., and Hetzer, M. W. (2016). Nucleoporin-mediated regulation of cell identity genes. *Genes Dev.* 30, 2253–2258. doi:10.1101/gad.287417.116

Iglesias, N., Paulo, J. A., Tatarakis, A., Wang, X., Edwards, A. L., Bhanu, N. V., et al. (2020). Native chromatin proteomics reveals a role for specific nucleoporins in heterochromatin organization and maintenance. *Mol. Cell* 77, 51–66. e8. doi:10.1016/j.molcel.2019.10.018

Ikegami, K., Secchia, S., Almakki, O., Lieb, J. D., and Moskowitz, I. P. (2020). Phosphorylated lamin A/C in the nuclear interior binds active enhancers associated with abnormal transcription in progeria. *Dev. Cell* 52, 699–713. doi:10.1016/j.devcel.2020.02.011

Jha, D. K., and Strahl, B. D. (2014). An RNA polymerase II-coupled function for histone H3K36 methylation in checkpoint activation and DSB repair. *Nat. Commun.* 5, 3965. doi:10.1038/ncomms4965

Jin, C., Zang, C., Wei, G., Cui, K., Peng, W., Zhao, K., et al. (2009). H3.3/H2A.Z double variant-containing nucleosomes mark "nucleosome-free regions" of active promoters and other regulatory regions. *Nat. Genet.* 41, 941–945. doi:10.1038/ng.409

Johnstone, S. E., Reyes, A., Qi, Y., Adriaens, C., Hegazi, E., Pelka, K., et al. (2020). Large-scale topological changes restrain malignant progression in colorectal cancer. *Cell* 182, 1474–1489. doi:10.1016/j.cell.2020.07.030

Kadota, S., Ou, J., Shi, Y., Lee, J. T., Sun, J., and Yildirim, E. (2020). Nucleoporin 153 links nuclear pore complex to chromatin architecture by mediating CTCF and cohesin binding. *Nat. Commun.* 11, 2606. doi:10.1038/s41467-020-16394-3

Kemp, C. J., Moore, J. M., Moser, R., Bernard, B., Teater, M., Smith, L. E., et al. (2014). CTCF haploinsufficiency destabilizes DNA methylation and predisposes to cancer. *Cell Rep.* 7, 1020–1029. doi:10.1016/j.celrep.2014.04.004

Ketema, M., Kreft, M., Secades, P., Janssen, H., and Sonnenberg, A. (2013). Nesprin-3 connects plectin and vimentin to the nuclear envelope of Sertoli cells but is not required for Sertoli cell function in spermatogenesis. *Mol. Biol. Cell* 24, 2454–2466. doi:10.1091/mbc.E13-02-0100

Kim, J. H., Youn, Y., Kim, K.-T., Jang, G., and Hwang, J.-H. (2019). Non-SMC condensin I complex subunit H mediates mature chromosome condensation and DNA damage in pancreatic cancer cells. *Sci. Rep.* 9, 17889. doi:10.1038/s41598-019-54478-3

Kim, S.-Y., Rhee, J. G., Song, X., Prochownik, E. V., Spitz, D. R., and Lee, Y. J. (2012). Breast cancer stem cell-like cells are more sensitive to ionizing radiation than non-stem cells: Role of ATM. *PLoS ONE* 7, e50423. doi:10.1371/journal.pone.0050423

Kimura, H. (2013). Histone modifications for human epigenome analysis. *J. Hum. Genet.* 58, 439–445. doi:10.1038/jhg.2013.66

Kohestani, H., and Wereszczynski, J. (2021). Effects of H2A.B incorporation on nucleosome structures and dynamics. *Biophys. J.* 120, 1498–1509. doi:10.1016/j.bpj.2021.01.036

Kojic, A., Cuadrado, A., De Koninck, M., Giménez-Llorente, D., Rodríguez-Corsino, M., Gómez-López, G., et al. (2018). Distinct roles of cohesin-SA1 and cohesin-SA2 in 3D chromosome organization. *Nat. Struct. Mol. Biol.* 25, 496–504. doi:10.1038/s41594-018-0070-4

Kong, L., Schäfer, G., Bu, H., Zhang, Y., Zhang, Y., and Klocker, H. (2012). Lamin A/C protein is overexpressed in tissue-invading prostate cancer and promotes prostate cancer cell growth, migration and invasion through the PI3K/AKT/PTEN pathway. *Carcinogenesis* 33, 751–759. doi:10.1093/carcin/bgs022

Kops, G. J. P. L., Foltz, D. R., and Cleveland, D. W. (2004). Lethality to human cancer cells through massive chromosome loss by inhibition of the mitotic checkpoint. *Proc. Natl. Acad. Sci. U. S. A.* 101, 8699–8704. doi:10.1073/pnas.0401142101

Kuga, T., Nie, H., Kazami, T., Satoh, M., Matsushita, K., Nomura, F., et al. (2014). Lamin B2 prevents chromosome instability by ensuring proper mitotic chromosome segregation. *Oncogenesis* 3, e94. doi:10.1038/oncsis.2014.6

Labade, A. S., Karmodiya, K., and Sengupta, K. (2016). HOXA repression is mediated by nucleoporin Nup93 assisted by its interactors Nup188 and Nup205. *Epigenetics Chromatin* 9, 54. doi:10.1186/s13072-016-0106-0

Labade, A. S., Salvi, A., Kar, S., Karmodiya, K., and Sengupta, K. (2021). Nup93 and CTCF modulate spatiotemporal dynamics and function of the HOXA gene locus during differentiation. *J. Cell Sci.* 134, jcs259307. doi:10.1242/jcs.259307

Laberge, R.-M., Sun, Y., Orjalo, A. V., Patil, C. K., Freund, A., Zhou, L., et al. (2015). MTOR regulates the pro-tumorigenic senescence-associated secretory

phenotype by promoting IL1A translation. *Nat. Cell Biol.* 17, 1049–1061. doi:10.1038/ncb3195

Lacoste, N., Woolfe, A., Tachiwana, H., Garea, A. V., Barth, T., Cantaloube, S., et al. (2014). Mislocalization of the centromeric histone variant CenH3/CENP-A in human cells depends on the chaperone DAXX. *Mol. Cell* 53, 631–644. doi:10.1016/j.molcel.2014.01.018

Lammerding, J., Fong, L. G., Ji, J. Y., Reue, K., Stewart, C. L., Young, S. G., et al. (2006). Lamins A and C but not lamin B1 regulate nuclear mechanics. *J. Biol. Chem.* 281, 25768–25780. doi:10.1074/jbc.M513511200

Larson, J. D., Kasper, L. H., Paugh, B. S., Jin, H., Wu, G., Kwon, C.-H., et al. (2019). Histone H3.3 K27M accelerates spontaneous brainstem glioma and drives restricted changes in bivalent gene expression. *Cancer Cell* 35, 140–155. doi:10.1016/j.ccell.2018.11.015

Lawrence, K. S., Chau, T., and Engebrecht, J. (2015). DNA damage response and spindle assembly checkpoint function throughout the cell cycle to ensure genomic integrity. *PLoS Genet.* 11, e1005150. doi:10.1371/journal.pgen.1005150

Lawrence, M. S., Stojanov, P., Mermel, C. H., Robinson, J. T., Garraway, L. A., Golub, T. R., et al. (2014). Discovery and saturation analysis of cancer genes across 21 tumour types. *Nature* 505, 495–501. doi:10.1038/nature12912

Lee, J. J., Lee, J. H., Ko, Y. G., Hong, S. I., and Lee, J. S. (2010). Prevention of premature senescence requires JNK regulation of Bcl-2 and reactive oxygen species. *Oncogene* 29, 561–575. doi:10.1038/onc.2009.355

Leeke, B., Marsman, J., O'Sullivan, J. M., and Horsfield, J. A. (2014). Cohesin mutations in myeloid malignancies: Underlying mechanisms. *Exp. Hematol. Oncol.* 3, 13. doi:10.1186/2162-3619-3-13

Lewis, P. W., Elsaesser, S. J., Noh, K.-M., Stadler, S. C., and Allis, C. D. (2010). Daxx is an H3.3-specific histone chaperone and cooperates with ATRX in replication-independent chromatin assembly at telomeres. *Proc. Natl. Acad. Sci. U. S. A.* 107, 14075–14080. doi:10.1073/pnas.1008850107

Leylek, T. R., Jeusset, L. M., Lichtensztejn, Z., and McManus, K. J. (2020). Reduced expression of genes regulating cohesion induces chromosome instability that may promote cancer and impact patient outcomes. *Sci. Rep.* 10, 592. doi:10.1038/s41598-020-57530-9

Li, W., Hu, Y., Oh, S., Ma, Q., Merkurjev, D., Song, X., et al. (2015). Condensin I and II complexes license full estrogen receptor α-dependent enhancer activation. *Mol. Cell* 59, 188–202. doi:10.1016/j.molcel.2015.06.002

Li, Y.-L., Cheng, X.-N., Lu, T., Shao, M., and Shi, D.-L. (2021). Syne2b/Nesprin-2 is required for actin organization and epithelial integrity during epiboly movement in zebrafish. *Front. Cell Dev. Biol.* 9, 671887. doi:10.3389/fcell.2021.671887

Lin, C.-J., Conti, M., and Ramalho-Santos, M. (2013). Histone variant H3.3 maintains a decondensed chromatin state essential for mouse preimplantation development. *Development* 140, 3624–3634. doi:10.1242/dev.095513

Lin, C.-S., Liang, Y., Su, S.-G., Zheng, Y.-L., Yang, X., Jiang, N., et al. (2022). Nucleoporin 93 mediates β-catenin nuclear import to promote hepatocellular carcinoma progression and metastasis. *Cancer Lett.* 526, 236–247. doi:10.1016/j.canlet.2021.11.001

Lin, D. H., Correia, A. R., Cai, S. W., Huber, F. M., Jette, C. A., and Hoelz, A. (2018). Structural and functional analysis of mRNA export regulation by the nuclear pore complex. *Nat. Commun.* 9, 2319. doi:10.1038/s41467-018-04459-3

Liu, B., Wang, Z., Zhang, L., Ghosh, S., Zheng, H., and Zhou, Z. (2013). Depleting the methyltransferase Suv39h1 improves DNA repair and extends lifespan in a progeria mouse model. *Nat. Commun.* 4, 1868. doi:10.1038/ncomms2885

Liu, N.-A., Sun, J., Kono, K., Horikoshi, Y., Ikura, T., Tong, X., et al. (2015). Regulation of homologous recombinational repair by lamin B1 in radiation-induced DNA damage. *FASEB J.* 29, 2514–2525. doi:10.1096/fj.14-265546

Lu, C., Jain, S. U., Hoelper, D., Bechet, D., Molden, R. C., Ran, L., et al. (2016). Histone H3K36 mutations promote sarcomagenesis through altered histone methylation landscape. *Science* 352, 844–849. doi:10.1126/science.aac7272

Lukášová, E., Kovařík, A., and Kozubek, S. (2018). Consequences of lamin B1 and lamin B receptor downregulation in senescence. *Cells* 7, 1. doi:10.3390/cells7020011

Lukášová, E., Kovarõík, A., Bacõíková, A., Falk, M., and Kozubek, S. (2017). Loss of lamin B receptor is necessary to induce cellular senescence. *Biochem. J.* 474, 281–300. doi:10.1042/BCJ20160459

Lupiáñez, D. G., Kraft, K., Heinrich, V., Krawitz, P., Brancati, F., Klopocki, E., et al. (2015). Disruptions of topological chromatin domains cause pathogenic rewiring of gene-enhancer interactions. *Cell* 161, 1012–1025. doi:10.1016/j.cell.2015.04.004

Machiels, B. M., Zorenc, A. H., Endert, J. M., Kuijpers, H. J., van Eys, G. J., Ramaekers, F. C., et al. (1996). An alternative splicing product of the lamin A/C gene lacks exon 10. *J. Biol. Chem.* 271, 9249–9253. doi:10.1074/jbc.271.16.9249

Mah, L. J., El-Osta, A., and Karagiannis, T. C. (2010). gammaH2AX: a sensitive molecular marker of DNA damage and repair. *Leukemia* 24, 679–686. doi:10.1038/leu.2010.6

Marullo, F., Cesarini, E., Antonelli, L., Gregoretti, F., Oliva, G., and Lanzuolo, C. (2016). Nucleoplasmic Lamin A/C and Polycomb group of proteins: An evolutionarily conserved interplay. *Nucleus* 7, 103–111. doi:10.1080/19491034.2016.1157675

Matthews, B. J., and Waxman, D. J. (2018). Computational prediction of CTCF/cohesin-based intra-TAD loops that insulate chromatin contacts and gene expression in mouse liver. *eLife* 7, e34077. doi:10.7554/eLife.34077

Mattioli, E., Andrenacci, D., Garofalo, C., Prencipe, S., Scotlandi, K., Remondini, D., et al. (2018). Altered modulation of lamin A/C-HDAC2 interaction and p21 expression during oxidative stress response in HGPS. *Aging Cell* 17, e12824. doi:10.1111/acel.12824

McLaughlin-Drubin, M. E., Park, D., and Munger, K. (2013). Tumor suppressor p16INK4A is necessary for survival of cervical carcinoma cell lines. *Proc. Natl. Acad. Sci. U. S. A.* 110, 16175–16180. doi:10.1073/pnas.1310432110

Melcon, G., Kozlov, S., Cutler, D. A., Sullivan, T., Hernandez, L., Zhao, P., et al. (2006). Loss of emerin at the nuclear envelope disrupts the Rb1/E2F and MyoD pathways during muscle regeneration. *Hum. Mol. Genet.* 15, 637–651. doi:10.1093/hmg/ddi479

Millán-Zambrano, G., Burton, A., Bannister, A. J., and Schneider, R. (2022). Histone post-translational modifications - cause and consequence of genome function. *Nat. Rev. Genet.* 23, 563–580. doi:10.1038/s41576-022-00468-7

Minchell, N. E., Keszthelyi, A., and Baxter, J. (2020). Cohesin causes replicative DNA damage by trapping DNA topological stress. *Mol. Cell* 78, 739–751. e8. doi:10.1016/j.molcel.2020.03.013

Mohammad, F., and Helin, K. (2017). Oncohistones: Drivers of pediatric cancers. *Genes Dev.* 31, 2313–2324. doi:10.1101/gad.309013.117

Mohammed, H., Taylor, C., Brown, G. D., Papachristou, E. K., Carroll, J. S., and D'Santos, C. S. (2016). Rapid immunoprecipitation mass spectrometry of endogenous proteins (RIME) for analysis of chromatin complexes. *Nat. Protoc.* 11, 316–326. doi:10.1038/nprot.2016.020

Moir, R. D., Spann, T. P., Herrmann, H., and Goldman, R. D. (2000). Disruption of nuclear lamin organization blocks the elongation phase of DNA replication. *J. Cell Biol.* 149, 1179–1192. doi:10.1083/jcb.149.6.1179

Moreno, E., and Basler, K. (2004). dMyc transforms cells into super-competitors. *Cell* 117, 117–129. doi:10.1016/s0092-8674(04)00262-4

Moss, S. F., Krivosheyev, V., de Souza, A., Chin, K., Gaetz, H. P., Chaudhary, N., et al. (1999). Decreased and aberrant nuclear lamin expression in gastrointestinal tract neoplasms. *Gut* 45, 723–729. doi:10.1136/gut.45.5.723

Muñoz-Espín, D., Cañamero, M., Maraver, A., Gómez-López, G., Contreras, J., Murillo-Cuesta, S., et al. (2013). Programmed cell senescence during mammalian embryonic development. *Cell* 155, 1104–1118. doi:10.1016/j.cell.2013.10.019

Murray-Nerger, L. A., and Cristea, I. M. (2021). Lamin post-translational modifications: Emerging toggles of nuclear organization and function. *Trends biochem. Sci.* 46, 832–847. doi:10.1016/j.tibs.2021.05.007

Nacev, B. A., Feng, L., Bagert, J. D., Lemiesz, A. E., Gao, J., Soshnev, A. A., et al. (2019). The expanding landscape of "oncohistone" mutations in human cancers. *Nature* 567, 473–478. doi:10.1038/s41586-019-1038-1

Narita, M., Nũnez, S., Heard, E., Narita, M., Lin, A. W., Hearn, S. A., et al. (2003). Rb-mediated heterochromatin formation and silencing of E2F target genes during cellular senescence. *Cell* 113, 703–716. doi:10.1016/s0092-8674(03)00401-x

Nataraj, N. B., Noronha, A., Lee, J. S., Ghosh, S., Mohan Raju, H. R., Sekar, A., et al. (2022). Nucleoporin-93 reveals a common feature of aggressive breast cancers: Robust nucleocytoplasmic transport of transcription factors. *Cell Rep.* 38, 110418. doi:10.1016/j.celrep.2022.110418

Nelson, D. M., Jaber-Hijazi, F., Cole, J. J., Robertson, N. A., Pawlikowski, J. S., Norris, K. T., et al. (2016). Mapping H4K20me3 onto the chromatin landscape of senescent cells indicates a function in control of cell senescence and tumor suppression through preservation of genetic and epigenetic stability. *Genome Biol.* 17, 158. doi:10.1186/s13059-016-1017-x

Nuebler, J., Fudenberg, G., Imakaev, M., Abdennur, N., and Mirny, L. A. (2018). Chromatin organization by an interplay of loop extrusion and compartmental segregation. *Proc. Natl. Acad. Sci. U. S. A.* 115, E6697–E6706. doi:10.1073/pnas.1717730115

Oberdoerffer, P., and Miller, K. M. (2022). Histone H2A variants: Diversifying chromatin to ensure genome integrity. *Semin. Cell Dev. Biol.* 135, 59–72. doi:10.1016/j.semcdb.2022.03.011

Ogryzko, V. V., Schiltz, R. L., Russanova, V., Howard, B. H., and Nakatani, Y. (1996). The transcriptional coactivators p300 and CBP are histone acetyltransferases. *Cell* 87, 953–959. doi:10.1016/s0092-8674(00)82001-2

Orjalo, A. V., Arnaoutov, A., Shen, Z., Boyarchuk, Y., Zeitlin, S. G., Fontoura, B., et al. (2006). The Nup107-160 nucleoporin complex is required for correct bipolar spindle assembly. *Mol. Biol. Cell* 17, 3806–3818. doi:10.1091/mbc.E05-11-1061

Pascual-Garcia, P., Debo, B., Aleman, J. R., Talamas, J. A., Lan, Y., Nguyen, N. H., et al. (2017). Metazoan nuclear pores provide a scaffold for poised genes and mediate induced enhancer-promoter contacts. *Mol. Cell* 66, 63–76. doi:10.1016/j.molcel.2017.02.020

Pascual-Reguant, L., Blanco, E., Galan, S., Le Dily, F., Cuartero, Y., Serra-Bardenys, G., et al. (2018). Lamin B1 mapping reveals the existence of dynamic and functional euchromatin lamin B1 domains. *Nat. Commun.* 9, 3420. doi:10.1038/s41467-018-05912-z

Pennarun, G., Picotto, J., Etourneaud, L., Redavid, A.-R., Certain, A., Gauthier, L. R., et al. (2021). Increase in lamin B1 promotes telomere instability by disrupting the shelterin complex in human cells. *Nucleic Acids Res.* 49, 9886–9905. doi:10.1093/nar/gkab761

Peters, A. H. F. M., Kubicek, S., Mechtler, K., O'Sullivan, R. J., Derijck, A. A. H. A., Perez-Burgos, L., et al. (2003). Partitioning and plasticity of repressive histone methylation states in mammalian chromatin. *Mol. Cell* 12, 1577–1589. doi:10.1016/s1097-2765(03)00477-5

Phillips-Cremins, J. E., Sauria, M. E. G., Sanyal, A., Gerasimova, T. I., Lajoie, B. R., Bell, J. S. K., et al. (2013). Architectural protein subclasses shape 3D organization of genomes during lineage commitment. *Cell* 153, 1281–1295. doi:10.1016/j.cell.2013.04.053

Pon, J. R., and Marra, M. A. (2015). Driver and passenger mutations in cancer. *Annu. Rev. Pathol.* 10, 25–50. doi:10.1146/annurev-pathol-012414-040312

Poulos, R. C., Thoms, J. A. I., Guan, Y. F., Unnikrishnan, A., Pimanda, J. E., and Wong, J. W. H. (2016). Functional mutations form at CTCF-cohesin binding sites in melanoma due to uneven nucleotide excision repair across the motif. *Cell Rep.* 17, 2865–2872. doi:10.1016/j.celrep.2016.11.055

Ranade, D., Pradhan, R., Jayakrishnan, M., Hegde, S., and Sengupta, K. (2019). Lamin A/C and Emerin depletion impacts chromatin organization and dynamics in the interphase nucleus. *BMC Mol. Cell Biol.* 20, 11. doi:10.1186/s12860-019-0192-5

Rao, R. C., and Dou, Y. (2015). Hijacked in cancer: The KMT2 (MLL) family of methyltransferases. *Nat. Rev. Cancer* 15, 334–346. doi:10.1038/nrc3929

Ray-Gallet, D., Woolfe, A., Vassias, I., Pellentz, C., Lacoste, N., Puri, A., et al. (2011). Dynamics of histone H3 deposition *in vivo* reveal a nucleosome gap-filling mechanism for H3.3 to maintain chromatin integrity. *Mol. Cell* 44, 928–941. doi:10.1016/j.molcel.2011.12.006

Raz, V., Vermolen, B. J., Garini, Y., Onderwater, J. J. M., Mommaas-Kienhuis, M. A., Koster, A. J., et al. (2008). The nuclear lamina promotes telomere aggregation and centromere peripheral localization during senescence of human mesenchymal stem cells. *J. Cell Sci.* 121, 4018–4028. doi:10.1242/jcs.034876

Redwood, A. B., Perkins, S. M., Vanderwaal, R. P., Feng, Z., Biehl, K. J., Gonzalez-Suarez, I., et al. (2011). A dual role for A-type lamins in DNA double-strand break repair. *Cell Cycle* 10, 2549–2560. doi:10.4161/cc.10.15.16531

Reis-Sobreiro, M., Chen, J.-F., Novitskaya, T., You, S., Morley, S., Steadman, K., et al. (2018). Emerin deregulation links nuclear shape instability to metastatic potential. *Cancer Res.* 78, 6086–6097. doi:10.1158/0008-5472.CAN-18-0608

Ren, X., Tu, C., Tang, Z., Ma, R., and Li, Z. (2018). Alternative lengthening of telomeres phenotype and loss of ATRX expression in sarcomas. *Oncol. Lett.* 15, 7489–7496. doi:10.3892/ol.2018.8318

Richart, L., Lapi, E., Pancaldi, V., Cuenca-Ardura, M., Pau, E. C.-S., Madrid-Mencía, M., et al. (2021). STAG2 loss-of-function affects short-range genomic contacts and modulates the basal-luminal transcriptional program of bladder cancer cells. *Nucleic Acids Res.* 49, 11005–11021. doi:10.1093/nar/gkab864

Rocha, A., Dalgarno, A., and Neretti, N. (2022). The functional impact of nuclear reorganization in cellular senescence. *Brief. Funct. Genomics* 21, 24–34. doi:10.1093/bfgp/elab012

Rondinelli, B., Giacomini, G., Piquet, S., Chevallier, O., Dabin, J., Bai, S.-K., et al. (2022). Aberrant DNA repair is a vulnerability in histone H3.3-mutant brain tumors. *BioRxiv* 1, 1. doi:10.1101/2022.09.29.510093

Rossi, D. J., Bryder, D., Seita, J., Nussenzweig, A., Hoeijmakers, J., and Weissman, I. L. (2007). Deficiencies in DNA damage repair limit the function of haematopoietic stem cells with age. *Nature* 447, 725–729. doi:10.1038/nature05862

Sahu, V., and Lu, C. (2022). Oncohistones: Hijacking the histone code. *Annu. Rev. Cancer Biol.* 6, 293–312. doi:10.1146/annurev-cancerbio-070120-102521

Salvarani, N., Crasto, S., Miragoli, M., Bertero, A., Paulis, M., Kunderfranco, P., et al. (2019). The K219T-Lamin mutation induces conduction defects through epigenetic inhibition of SCN5A in human cardiac laminopathy. *Nat. Commun.* 10, 2267. doi:10.1038/s41467-019-09929-w

Samoshkin, A., Dulev, S., Loukinov, D., Rosenfeld, J. A., and Strunnikov, A. V. (2012). Condensin dysfunction in human cells induces nonrandom chromosomal breaks in anaphase, with distinct patterns for both unique and repeated genomic regions. *Chromosoma* 121, 191–199. doi:10.1007/s00412-011-0353-6

Sanborn, A. L., Rao, S. S. P., Huang, S.-C., Durand, N. C., Huntley, M. H., Jewett, A. I., et al. (2015). Chromatin extrusion explains key features of loop and domain formation in wild-type and engineered genomes. *Proc. Natl. Acad. Sci. U. S. A.* 112, E6456–E6465. doi:10.1073/pnas.1518552112

Santi, S., Cenni, V., Capanni, C., Lattanzi, G., and Mattioli, E. (2020). PCAF involvement in lamin A/C-HDAC2 interplay during the early phase of muscle differentiation. *Cells* 9, 1. doi:10.3390/cells9071735

Sati, S., Bonev, B., Szabo, Q., Jost, D., Bensadoun, P., Serra, F., et al. (2020). 4D genome rewiring during oncogene-induced and replicative senescence. *Mol. Cell* 78, 522–538. doi:10.1016/j.molcel.2020.03.007

Serrano, M., Lin, A. W., McCurrach, M. E., Beach, D., and Lowe, S. W. (1997). Oncogenic ras provokes premature cell senescence associated with accumulation of p53 and p16INK4a. *Cell* 88, 593–602. doi:10.1016/s0092-8674(00)81902-9

Shi, L., Wen, H., and Shi, X. (2017). The histone variant H3.3 in transcriptional regulation and human disease. *J. Mol. Biol.* 429, 1934–1945. doi:10.1016/j.jmb.2016.11.019

Shimi, T., Pfleghaar, K., Kojima, S., Pack, C.-G., Solovei, I., Goldman, A. E., et al. (2008). The A- and B-type nuclear lamin networks: Microdomains involved in chromatin organization and transcription. *Genes Dev.* 22, 3409–3421. doi:10.1101/gad.1735208

Shumaker, D. K., Dechat, T., Kohlmaier, A., Adam, S. A., Bozovsky, M. R., Erdos, M. R., et al. (2006). Mutant nuclear lamin A leads to progressive alterations of epigenetic control in premature aging. *Proc. Natl. Acad. Sci. U. S. A.* 103, 8703–8708. doi:10.1073/pnas.0602569103

Siegenfeld, A. P., Roseman, S. A., Roh, H., Lue, N. Z., Wagen, C. C., Zhou, E., et al. (2022). Polycomb-lamina antagonism partitions heterochromatin at the nuclear periphery. *Nat. Commun.* 13, 4199. doi:10.1038/s41467-022-31857-5

Smith, E. R., Capo-Chichi, C. D., and Xu, X.-X. (2018). Defective nuclear lamina in aneuploidy and carcinogenesis. *Front. Oncol.* 8, 529. doi:10.3389/fonc.2018.00529

Solomon, D. A., Kim, T., Diaz-Martinez, L. A., Fair, J., Elkahloun, A. G., Harris, B. T., et al. (2011). Mutational inactivation of STAG2 causes aneuploidy in human cancer. *Science* 333, 1039–1043. doi:10.1126/science.1203619

Solovei, I., Wang, A. S., Thanisch, K., Schmidt, C. S., Krebs, S., Zwerger, M., et al. (2013). LBR and lamin A/C sequentially tether peripheral heterochromatin and inversely regulate differentiation. *Cell* 152, 584–598. doi:10.1016/j.cell.2013.01.009

Starr, D. A., and Fischer, J. A. (2005). KASH 'n karry: The KASH domain family of cargo-specific cytoskeletal adaptor proteins. *Bioessays* 27, 1136–1146. doi:10.1002/bies.20312

Stephens, A. D., Liu, P. Z., Banigan, E. J., Almassalha, L. M., Backman, V., Adam, S. A., et al. (2018). Chromatin histone modifications and rigidity affect nuclear morphology independent of lamins. *Mol. Biol. Cell* 29, 220–233. doi:10.1091/mbc.E17-06-0410

Stirpe, A., and Heun, P. (2022). The ins and outs of CENP-A: Chromatin dynamics of the centromere-specific histone. *Semin. Cell Dev. Biol.* 135, 24–34. doi:10.1016/j.semcdb.2022.04.003

Sun, X., Clermont, P.-L., Jiao, W., Helgason, C. D., Gout, P. W., Wang, Y., et al. (2016). Elevated expression of the centromere protein-A(CENP-A)-encoding gene as a prognostic and predictive biomarker in human cancers. *Int. J. Cancer* 139, 899–907. doi:10.1002/ijc.30133

Sur, I., Neumann, S., and Noegel, A. A. (2014). Nesprin-1 role in DNA damage response. *Nucleus* 5, 173–191. doi:10.4161/nucl.29023

Sur-Erdem, I., Hussain, M. S., Asif, M., Pınarbası, N., Aksu, A. C., and Noegel, A. A. (2020). Nesprin-1 impact on tumorigenic cell phenotypes. *Mol. Biol. Rep.* 47, 921–934. doi:10.1007/s11033-019-05184-w

Swift, J., Ivanovska, I. L., Buxboim, A., Harada, T., Dingal, P. C. D. P., Pinter, J., et al. (2013). Nuclear lamin-A scales with tissue stiffness and enhances matrix-directed differentiation. *Science* 341, 1240104. doi:10.1126/science.1240104

Szabo, Q., Bantignies, F., and Cavalli, G. (2019). Principles of genome folding into topologically associating domains. *Sci. Adv.* 5, eaaw1668. doi:10.1126/sciadv.aaw1668

Talbert, P. B., and Henikoff, S. (2021). Histone variants at a glance. *J. Cell Sci.* 134, jcs244749. doi:10.1242/jcs.244749

Teng, Y.-C., Sundaresan, A., O'Hara, R., Gant, V. U., Li, M., Martire, S., et al. (2021). ATRX promotes heterochromatin formation to protect cells from G-quadruplex DNA-mediated stress. *Nat. Commun.* 12, 3887. doi:10.1038/s41467-021-24206-5

Towbin, B. D., González-Aguilera, C., Sack, R., Gaidatzis, D., Kalck, V., Meister, P., et al. (2012). Step-wise methylation of histone H3K9 positions heterochromatin at the nuclear periphery. *Cell* 150, 934–947. doi:10.1016/j.cell.2012.06.051

Turinetto, V., Orlando, L., Sanchez-Ripoll, Y., Kumpfmueller, B., Storm, M. P., Porcedda, P., et al. (2012). High basal γH2AX levels sustain self-renewal of mouse embryonic and induced pluripotent stem cells. *Stem Cells* 30, 1414–1423. doi:10.1002/stem.1133

Turner, B. M. (1993). *Decoding the nucleosome minireview*: Cell Press. 75 (1), 5–8. doi:10.1016/S0092-8674(05)80078-9

Tzur, Y. B., Wilson, K. L., and Gruenbaum, Y. (2006). SUN-Domain proteins: "Velcro" that links the nucleoskeleton to the cytoskeleton. *Nat. Rev. Mol. Cell Biol.* 7, 782–788. doi:10.1038/nrm2003

Udugama, M., M Chang, F. T., Chan, F. L., Tang, M. C., Pickett, H. A., R McGhie, J. D., et al. (2015). Histone variant H3.3 provides the heterochromatic H3 lysine 9 tri-methylation mark at telomeres. *Nucleic Acids Res.* 43, 10227–10237. doi:10.1093/nar/gkv847

Vardabasso, C., Gaspar-Maia, A., Hasson, D., Pünzeler, S., Valle-Garcia, D., Straub, T., et al. (2015). Histone variant H2A.Z.2 mediates proliferation and drug sensitivity of malignant melanoma. *Mol. Cell* 59, 75–88. doi:10.1016/j.molcel.2015.05.009

Vorburger, K., Kitten, G. T., and Nigg, E. A. (1989). Modification of nuclear lamin proteins by a mevalonic acid derivative occurs in reticulocyte lysates and requires the cysteine residue of the C-terminal CXXM motif. *EMBO J.* 8, 4007–4013. doi:10.1002/j.1460-2075.1989.tb08583.x

Wang, G. G., Cai, L., Pasillas, M. P., and Kamps, M. P. (2007). NUP98-NSD1 links H3K36 methylation to Hox-A gene activation and leukaemogenesis. *Nat. Cell Biol.* 9, 804–812. doi:10.1038/ncb1608

Wang, G. G., Song, J., Wang, Z., Dormann, H. L., Casadio, F., Li, H., et al. (2009). Haematopoietic malignancies caused by dysregulation of a chromatin-binding PHD finger. *Nature* 459, 847–851. doi:10.1038/nature08036

Wang, L., Lankhorst, L., and Bernards, R. (2022). Exploiting senescence for the treatment of cancer. *Nat. Rev. Cancer* 22, 340–355. doi:10.1038/s41568-022-00450-9

Wang, R.-R., Qiu, X., Pan, R., Fu, H., Zhang, Z., Wang, Q., et al. (2022). Dietary intervention preserves β cell function in mice through CTCF-mediated transcriptional reprogramming. *J. Exp. Med.* 219, e20211779. doi:10.1084/jem.20211779

Wang, X., Hughes, A. C., Brandão, H. B., Walker, B., Lierz, C., Cochran, J. C., et al. (2018). *In vivo* evidence for ATPase-dependent DNA translocation by the Bacillus subtilis SMC condensin complex. *Mol. Cell* 71, 841–847. e5. doi:10.1016/j.molcel.2018.07.006

Wang, Y., Chen, Q., Wu, D., Chen, Q., Gong, G., He, L., et al. (2021). Lamin-A interacting protein Hsp90 is required for DNA damage repair and chemoresistance of ovarian cancer cells. *Cell Death Dis.* 12, 786. doi:10.1038/s41419-021-04074-z

Wang, Y., Jiang, J., He, L., Gong, G., and Wu, X. (2019). Effect of lamin-A expression on migration and nuclear stability of ovarian cancer cells. *Gynecol. Oncol.* 152, 166–176. doi:10.1016/j.ygyno.2018.10.030

Watanabe, T., Wu, T. T., Catalano, P. J., Ueki, T., Satriano, R., Haller, D. G., et al. (2001). Molecular predictors of survival after adjuvant chemotherapy for colon cancer. *N. Engl. J. Med.* 344, 1196–1206. doi:10.1056/NEJM200104193441603

Weierich, C., Brero, A., Stein, S., von Hase, J., Cremer, C., Cremer, T., et al. (2003). Three-dimensional arrangements of centromeres and telomeres in nuclei of human and murine lymphocytes. *Chromosome Res.* 11, 485–502. doi:10.1023/a:1025016828544

Weintraub, A. S., Li, C. H., Zamudio, A. V., Sigova, A. A., Hannett, N. M., Day, D. S., et al. (2017). YY1 is a structural regulator of enhancer-promoter loops. *Cell* 171, 1573–1588. doi:10.1016/j.cell.2017.11.008

Weyburne, E., and Bosco, G. (2021). Cancer-associated mutations in the condensin II subunit CAPH2 cause genomic instability through telomere dysfunction and anaphase chromosome bridges. *J. Cell. Physiol.* 236, 3579–3598. doi:10.1002/jcp.30113

Weyemi, U., Redon, C. E., Sethi, T. K., Burrell, A. S., Jailwala, P., Kasoji, M., et al. (2016). Twist1 and Slug mediate H2AX-regulated epithelial-mesenchymal transition in breast cells. *Cell Cycle* 15, 2398–2404. doi:10.1080/15384101.2016.1198864

Wong, K. M., Song, J., and Wong, Y. H. (2021). CTCF and EGR1 suppress breast cancer cell migration through transcriptional control of Nm23-H1. *Sci. Rep.* 11, 491. doi:10.1038/s41598-020-79869-9

Wong, L. H., Ren, H., Williams, E., McGhie, J., Ahn, S., Sim, M., et al. (2009). Histone H3.3 incorporation provides a unique and functionally essential telomeric chromatin in embryonic stem cells. *Genome Res.* 19, 404–414. doi:10.1101/gr.084947.108

Wood, A. M., Rendtlew Danielsen, J. M., Lucas, C. A., Rice, E. L., Scalzo, D., Shimi, T., et al. (2014). TRF2 and lamin A/C interact to facilitate the functional organization of chromosome ends. *Nat. Commun.* 5, 5467. doi:10.1038/ncomms6467

Xu, H., Yan, M., Patra, J., Natrajan, R., Yan, Y., Swagemakers, S., et al. (2011). Enhanced RAD21 cohesin expression confers poor prognosis and resistance to chemotherapy in high grade luminal, basal and HER2 breast cancers. *Breast Cancer Res.* 13, R9. doi:10.1186/bcr2814

Yang, Y., Zhang, L., Xiong, C., Chen, J., Wang, L., Wen, Z., et al. (2022). HIRA complex presets transcriptional potential through coordinating depositions of the histone variants H3.3 and H2A.Z on the poised genes in mESCs. *Nucleic Acids Res.* 50, 191–206. doi:10.1093/nar/gkab1221

Yassin, E. R., Abdul-Nabi, A. M., Takeda, A., and Yaseen, N. R. (2010). Effects of the NUP98-DDX10 oncogene on primary human CD34+ cells: Role of a conserved helicase motif. *Leukemia* 24, 1001–1011. doi:10.1038/leu.2010.42

Ye, Q., and Worman, H. J. (1996). Interaction between an integral protein of the nuclear envelope inner membrane and human chromodomain proteins homologous to Drosophila HP1. *J. Biol. Chem.* 271, 14653–14656. doi:10.1074/jbc.271.25.14653

Yin, L., Jiang, L.-P., Shen, Q.-S., Xiong, Q.-X., Zhuo, X., Zhang, L.-L., et al. (2017). NCAPH plays important roles in human colon cancer. *Cell Death Dis.* 8, e2680. doi:10.1038/cddis.2017.88

Yu, G., Zhang, Y., Gupta, V., Zhang, J., MacCarthy, T., Duan, Z., et al. (2021). The role of HIRA-dependent H3.3 deposition and its modifications in the somatic hypermutation of immunoglobulin variable regions. *Proc. Natl. Acad. Sci. U. S. A.* 118, e2114743118. doi:10.1073/pnas.2114743118

Yuen, B. T. K., and Knoepfler, P. S. (2013). Histone H3.3 mutations: A variant path to cancer. *Cancer Cell* 24, 567–574. doi:10.1016/j.ccr.2013.09.015

Yun, J., Song, S.-H., Kim, H.-P., Han, S.-W., Yi, E. C., and Kim, T.-Y. (2016). Dynamic cohesin-mediated chromatin architecture controls epithelial-mesenchymal plasticity in cancer. *EMBO Rep.* 17, 1343–1359. doi:10.15252/embr.201541852

Yusufzai, T. M., Tagami, H., Nakatani, Y., and Felsenfeld, G. (2004). CTCF tethers an insulator to subnuclear sites, suggesting shared insulator mechanisms across species. *Mol. Cell* 13, 291–298. doi:10.1016/s1097-2765(04)00029-2

Zeitlin, S. G., Baker, N. M., Chapados, B. R., Soutoglou, E., Wang, J. Y. J., Berns, M. W., et al. (2009). Double-strand DNA breaks recruit the centromeric histone CENP-A. *Proc. Natl. Acad. Sci. U. S. A.* 106, 15762–15767. doi:10.1073/pnas.0908233106

Zhang, H., and Li, T. (2017). Effects of spermidine and ATP on stabilities of chromatosomes and histone H1-depleted chromatosomes. *Bioorg. Med. Chem. Lett.* 27, 1149–1153. doi:10.1016/j.bmcl.2017.01.072

Zhang, R., Ai, J., Wang, J., Sun, C., Lu, H., He, A., et al. (2022). NCAPG promotes the proliferation of hepatocellular carcinoma through the CKII-dependent regulation of PTEN. *J. Transl. Med.* 20, 325. doi:10.1186/s12967-022-03519-z

Zhang, R., Chen, W., and Adams, P. D. (2007). Molecular dissection of formation of senescence-associated heterochromatin foci. *Mol. Cell. Biol.* 27, 2343–2358. doi:10.1128/MCB.02019-06

Zhang, X., Jeong, M., Huang, X., Wang, X. Q., Wang, X., Zhou, W., et al. (2020). Large DNA methylation nadirs anchor chromatin loops maintaining hematopoietic stem cell identity. *Mol. Cell* 78, 506–521. doi:10.1016/j.molcel.2020.04.018

Zhang, Y., Liu, F., Zhang, C., Ren, M., Kuang, M., Xiao, T., et al. (2020). Non-SMC condensin I complex subunit D2 is a prognostic factor in triple-negative breast cancer for the ability to promote cell cycle and enhance invasion. *Am. J. Pathol.* 190, 37–47. doi:10.1016/j.ajpath.2019.09.014

Zhao, L., Yang, Y., Yin, S., Yang, T., Luo, J., Xie, R., et al. (2017). CTCF promotes epithelial ovarian cancer metastasis by broadly controlling the expression of metastasis-associated genes. *Oncotarget* 8, 62217–62230. doi:10.18632/oncotarget.19216

Zheng, X., Hu, J., Yue, S., Kristiani, L., Kim, M., Sauria, M., et al. (2018). Lamins organize the global three-dimensional genome from the nuclear periphery. *Mol. Cell* 71, 802–815. doi:10.1016/j.molcel.2018.05.017

Zhou, L., and Panté, N. (2010). The nucleoporin Nup153 maintains nuclear envelope architecture and is required for cell migration in tumor cells. *FEBS Lett.* 584, 3013–3020. doi:10.1016/j.febslet.2010.05.038

Zhou, W., Goodman, S. N., Galizia, G., Lieto, E., Ferraraccio, F., Pignatelli, C., et al. (2002). Counting alleles to predict recurrence of early-stage colorectal cancers. *Lancet* 359, 219–225. doi:10.1016/S0140-6736(02)07448-2

Zink, L.-M., and Hake, S. B. (2016). Histone variants: Nuclear function and disease. *Curr. Opin. Genet. Dev.* 37, 82–89. doi:10.1016/j.gde.2015.12.002